THE ROLE OF METALS FROM MOLECULAR CLOUDS TO GALACTIC DISCS

Piyush Sharda

A thesis submitted for the degree of

Doctor of Philosophy

The Australian National University

Research School of Astronomy & Astrophysics

March 2022

To all the medical personnel for their services during COVID-19

Disclaimer

I hereby declare that the work undertaken in this thesis has been conducted by me alone, except where indicated in the text. I conducted this work between October 2018 and November 2021, during which period I was a PhD student at the Australian National University. This thesis, in whole or any part of it, has not been submitted to this or any other university for a degree.

This thesis has been compiled as a Thesis by Compilation in accordance with relevant ANU policies. Each of the seven main chapters in this thesis have been published in peer reviewed journals. I have made significant contribution to each of these journal articles and have written the text of the papers myself, except where indicated otherwise.

Piyush Sharda

27 March 2022

Acknowledgments

This PhD would not have been possible without the love, support and mentorship of several people, which enabled me to follow my passion and successfully conduct research in astronomy. I begin by acknowledging the custodians of the land on which this thesis was carried out - the Ngunnawal and Nambri people. I will always be grateful for their kind welcome and acceptance into the Australian society.

I would foremost like to thank my primary advisor, Mark Krumholz, for his everlasting support and guidance throughout the PhD. I am grateful to Mark for teaching me the art of doing research and for always indulging my ideas and polishing them to generate scientific results. I am grateful to my co-advisor Emily Wisnioski for her constant encouragement and motivation to look at the big picture, and to work in tandem with both observers and theorists. I am thankful to my co-advisor Elisabete da Cunha for her insight and thoughtfulness, and for inspiring me to pursue different research topics regardless of my experience. I also thank my co-advisor Christoph Federrath for his support, encouragement and constructive criticism that has enabled me to a better scientist.

I owe my sincere gratitude to my wonderful friends and colleagues who have supported me throughout my PhD. I would especially like to thank my best friend and fellow PhD student Stephanie Monty for her friendship and care throughout my PhD. I am also indebted to fellow graduate students Harrison Abbot, abdu Abohalima, Ayan Acharyya, Bella Gerrard, Lyla Jung, Umang Malik, Madeleine McKenzie, Rajsekhar Mohapatra, Aldo Mura, Arthur Puls, Adam Rains, Jamie Soon and Georgie Taylor who have been integral to my life in Canberra. I will always cherish our scientific and social discussions, and our common goal to make our community safer and more inclusive.

I have had immense guidance and mentorship from several postdoctoral researchers at the RSAA and elsewhere. I have greatly appreciated the time they have spent training me on various skills, as well as the emotional support they have provided me over the years. I am especially grateful to Katie Jameson for always being there for me, be it scientific or personal. I have always looked up to and been inspired by Noelia Rey, and she has been a crucial part of my success as a graduate student at RSAA. I also thank Lucia Armillotta, Carolyn Briggs, Sven Buder, Ioana Ciucâ, Jesse Cranney, Enrico Di Teodoro, Katie Grasha, Sarah Jeffreson, Meridith Joyce, Nickolas Pingel, Amita Seta, Maruša Žerjal and Henry Zovaro for their friendship, guidance and support throughout my PhD.

In addition to my supervisory panel, I have been very fortunate to engage with

This thesis contains seven chapters, each dedicated to the seven pets I have had the pleasure to share a house with during my stay in Canberra: Cedric, Clifford, Dill, Frankie, Inky, Knox and Maxi. They have all contributed to my research in their own ways, and have provided the much needed balance between work and life throughout my PhD.

This thesis would not have been possible without the sincere efforts of the emergency response personnel during the Australian Bushfires in 2019-2020, and then during the COVID-19 pandemic in 2020-2021. I thank them for their sacrifice and for keeping the community safe and protected so that we could continue to lead our lives as normally as possible.

I have gained much more than a PhD during my stay in Canberra, the most significant of them being my partner, Laura. I thank her for making Canberra home for me. Our pet cat Clemmy has vastly improved my quality of life, and she has been an equal partner in this journey. I look forward to the next chapter of my life with our little family.

Abstract

From the time the first generation of stars formed (redshift $z \sim 30$) to the present-day, elements that were not produced by the Big Bang (hereafter, *metals*) have witnessed the assembly of structure in the Universe in great detail. Although metals only form in stars and stellar remnants, they are ubiquitously present everywhere – from planetary cores to the intergalactic medium. However, we still do not understand how metals are effectively dispersed throughout the Universe, and what role do they play in shaping galaxies as we know today.

In this thesis, we use a multi-scale approach to study the role of metals in galaxy evolution, from pc-sized molecular clouds to kpc-sized galactic discs. On smaller scales, we focus on understanding the physical processes that shape up the initial mass function (IMF, with a particular emphasis on metal-free and metal-poor environments) that directly set the integrated yield of metals in the first and early galaxies. On larger scales, we focus on the physics of gas-phase metal distribution in diverse galaxies both in the local and the high-z Universe.

We develop a large suite of chemo-magnetohydrodynamic (chemo-MHD) simulations to study the formation of the first stars in metal-free environments. We find that initially weak magnetic fields exponentially grow in a short duration of time and suppress fragmentation in primordial molecular clouds, thereby preventing the formation of low mass first stars that would otherwise have lived to the present day. Magnetic fields grow via dynamo amplification during collapse, and later on in the accretion discs around the first stars. The overall impact of dynamically strong magnetic fields is that the mass distribution of the first stars shifts towards higher masses as compared to chemo-hydrodynamic simulations. An important consequence of our results is that the IMF of the first stars was likely top-heavy, as against the bottom-heavy IMF of the metal-rich Milky Way. We further create analytic models to explore the transition in the IMF as a function of the metallicity of the interstellar medium. We find that the IMF transitioned from top- to bottom-heavy in normal star-forming galaxies when the metallicity increased to $1/10000 - 1/100 \mathrm{Z}_\odot$. Our models also provide an explanation for the more bottom-heavy IMF observed in the centres of massive ellipticals.

Thanks to integral field unit (IFU) spectroscopy, spatially-resolved gas-phase metallicities have now been measured for several thousand galaxies. In particular, the last decade has seen a surge in the measurements of metallicity gradients in galaxies, wherein galaxy centres are typically more metal enriched as compared to the outskirts. We develop a new, first-principles model to understand the physics behind

these metallicity gradients. In contrast to existing models, our model incorporates all key modes of galactic metal transport (such as metal advection and diffusion), and allows for differential metal enrichment of galactic outflows. Further, the model is inherently linked to a galaxy evolution model, which ensures that metals are treated self-consistently with the gas in galactic discs and the number of free parameters in the model is restricted. We use our model to provide the first joint explanation for the mass-metallicity relation and the mass-metallicity gradient relation in local galaxies. We show that galaxies naturally transition from an advection-dominated to an accretion-dominated regime as they increase in mass. We also show that low mass galaxies preferentially loose more metals in galactic winds. Finally, we use the model to explore the complex relationship between metallicity gradients and galaxy kinematics, and use it to explain the trends observed in high-z galaxies.

Several features of our work will be directly tested using the upcoming James Webb Space Telescope (JWST) observations, like the variation of the IMF with metallicity through observations of ultra-faint dwarf galaxies, and the expected relationship between gas kinematics and metallicity through observations of a large number of star-forming galaxies at high-z. By studying the role of metals from pc to kpc scales, this research has set the scene to study the first galaxies and explore metal-poor environments of nearby dwarf galaxies. As we inch closer to the generation of Extremely Large Telescopes, studying the multi-scale structure formation in the early and the metal-poor Universe using metals will emerge as key focus areas in astronomy. Thus there is a vast scope in continuing to explore, understand and interpret the role of metals in the Universe.

Contents

List of Figures

List of Tables

Introduction

Much of the Universe as we see today has been shaped by metals. Not only do metals play a vital role in the assembly of structure in the Universe, they also act as some of the best tracers of the various physical processes that occur in nature. Thus, understanding the role of metals remains an area of key interest in astrophysics. However, measuring metal abundances requires probing special environments (e.g., stellar photospheres or emission and absorption lines in diffuse gas) at high precision, which makes it challenging to quantify how they are produced and get effectively dispersed across the Universe.

In this thesis, we use a multi-scale approach to reveal the role of metals in the interstellar medium (ISM) to galactic discs. Specifically, we first focus on formation of the first stars and their initial mass function (IMF) that subsequently set the scene for the production of the first metals. Then, we explore the physics behind the distribution of metals in the gas in galaxies to understand how small-scale metal production ultimately leads to metal enrichment on larger scales.

1.1 Star formation & metal enrichment in the early Universe

Stars are usually classified into three populations based on their metal content (Bond 1981; McDowell 1986). The generation of stars with the highest metallicity is known as Population I. Population II corresponds to stars that have relatively less metal content, and Population III is the hypothetical limit of stars that have no metals in them. Metal content also reflects formation time as a function of the age of the Universe. Population III stars are believed to have formed out of primordial species produced by the Big Bang, and hence have no metals in them. Population III is further classified into Population III.1 (the first generation of stars) and Population III.2 (primordial stars affected by radiation from other stars, McKee & Tan 2008; De Souza et al. 2011). While current day star formation is well studied thanks to

observations and simulations, the formation of the first generation of stars in the Universe still remains a mystery because of the lack of direct observations at spatially resolved scales beyond $z > 11.1$ (Oesch et al. 2016), and the lack of surviving first stars in the Local Group (Griffen et al. 2018; Hartwig et al. 2019).

The first stars are believed to form between $15 \leq z \leq 30$, at the center of dark matter minihalos that have high baryonic densities (see reviews by Abel et al. 2002; Bromm & Larson 2004; Glover 2005; Ciardi & Ferrara 2005). As Figure 1.1 shows, the first clouds of neutral hydrogen formed after the recombination of charged species by this epoch (Peebles 1968). These fragmented under the effects of self-gravity to give rise to the first stars. Since the first clouds only contain primordial elements (H, He, Li and their isotopes), cooling during the collapse is highly inefficient as compared to current day star formation where dust, molecular line and metal line emissions can significantly increase the cooling rate (Omukai et al. 2005). Figure 1.2 shows the evolution of temperature as a function of number density in collapsing clouds at different metallicities. As can be seen from Figure 1.2 , the cooling becomes less and less efficient as the metallicity drops, thus the Jeans mass (a measure of the stability of the cloud against collapse, see Jeans 1902) increases. A primary issue that hinders our understanding of first stars formation is primordial chemistry. It is significantly different than the present-day star formation because of the presence of dust in the latter which is a more efficient radiator than molecules. Once the density gets high enough for the dust-gas collisional energy exchange to be efficient (above $\sim 10^{4.5}\,\mathrm{cm}^{-3}$), the dust completely controls the temperature, and the gas chemistry ceases to matter because molecular line emission is tiny compared to dust emission. Thus, although primordial chemistry is simpler, the chemical state of the gas should be treated as accurately as possible in primordial star formation. Hence, any simulation or modeling in the context of first stars usually needs an explicit chemical network that should be solved to evolve the collapse of the cloud.

Early simulations of the first stars were conducted at low resolution without accounting for all important physical processes. They formed only a single massive ($M > 100\,M_\odot$) central protostar, leading to the belief that the first stars were very massive and evolved in isolation (Bromm et al. 2002; Abel et al. 2002; Yoshida et al. 2006; Glover & Jappsen 2007), thus eliminating any chances of a pristine first star being alive to this date. The reason the first simulations of first stars did not exhibit fragmentation is that they did not include sink particles. Thus, they were either limited to very low resolution, or had to stop as soon as the first collapsed object formed. It was only once the simulations started using sink particles that they could run for thousands of years past the initial collapse (Bate et al. 1995;
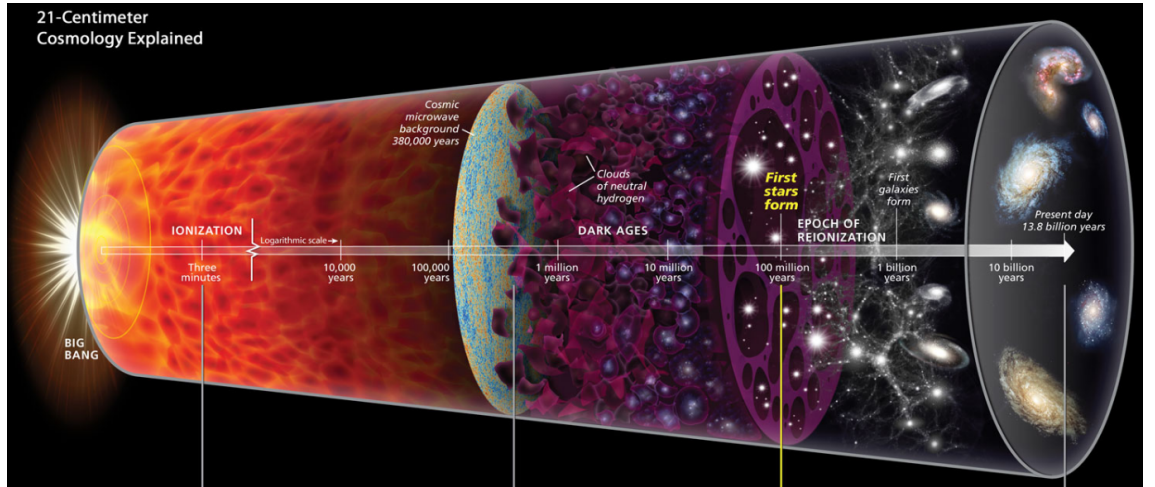
Figure 1.1: Figure taken from the Discovery magazine, depicting the epoch of the formation of the first stars in the cosmic context.
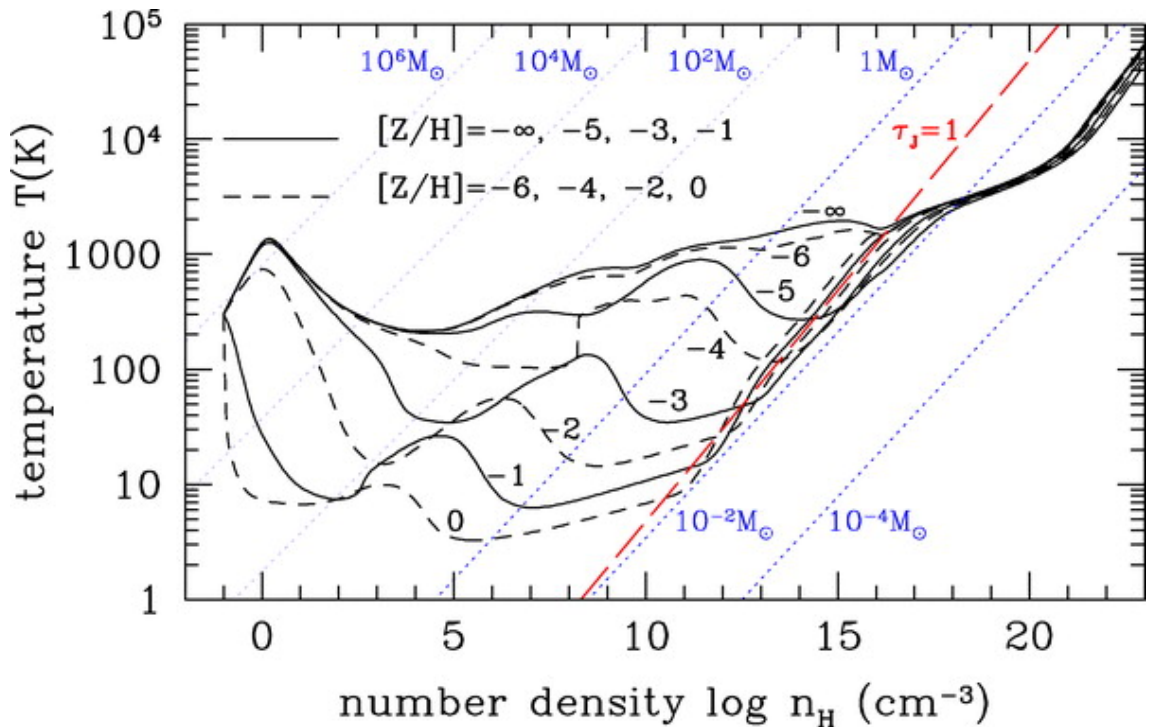
Figure 1.2: Figure adopted from Omukai et al. (2005), showing the 1-zone evolution of the temperature of star-forming clouds at different metallicities as a function of density after collapse sets in. Due to lack of efficient cooling pathways, first stars ($[Z/H] = -\infty$) are formed in primordial clouds that have higher Jeans mass compared to current day molecular clouds ($[Z/H] = 0$). The evolution is unaffected by chemistry once the high opacity continuum limit is reached ($\tau_{J=1}-$ red-dashed line), and all tracks merge.

Krumholz et al. 2004; Federrath et al. 2010a). Since then, fragmentation has been observed in almost all simulations of the first stars (Clark et al. 2011b). Moreover, it occurs very close to the central protostar, on scales as small as 1 au (Klessen 2018). This is because of the lack of an adiabatic core > 1 au even before protostar formation, as is observed in simulations of present day star formation (Larson 1969; Bate 1998; Bhandare et al. 2018). Thus, the circumstellar disk grows gradually and fragmentation occurs near the central protostar (Maki & Susa 2004).

The observation that fragmentation occurs in simulations has encouraged discussions on the IMF of the first stars, which has emerged as a central goal of research on this topic. Understanding the IMF of the first stars is crucial to determining the metal enrichment of the early Universe and photon budgets during the Epoch of Reionization (Sobral et al. 2015; Xu et al. 2016). It can also inform us about the nature of the first supernovae and black holes and help solve the mystery of supermassive blackholes observed in high-redshift galaxies (Fan 2006; Omukai et al. 2008; Silverman et al. 2008; Tanaka & Haiman 2009). The IMF is also important to understand the evolution of extremely metal-poor stars found in the Milky Way and nearby dwarf galaxies (Howes et al. 2015; Frebel & Norris 2015; Casey & Schlaufman 2015).

For a realistic simulation of first stars, one can take inspiration from cosmological simulations of the Universe that have successfully reproduced many of its large-scale properties (Springel 2005; Vogelsberger et al. 2013; Rocha et al. 2013; Schaye et al. 2015). Any realistic simulation of the first stars should be guided by initial conditions from such cosmological simulations together with the addition of key physical processes like primordial chemistry (Glover & Abel 2008; Grassi et al. 2014), turbulence (Clark et al. 2011b; Turk et al. 2012), magnetic fields (Machida et al. 2008b; Schober et al. 2012a), dark matter annihilation (Smith et al. 2012; Stacy et al. 2014), primordial streaming velocities (Tseliakhovich & Hirata 2010; Maio et al. 2011a) and radiation feedback (Hirano et al. 2014, 2015; Hosokawa et al. 2016). However, these simulations can only be followed up to a certain time after the collapse, before they become computationally expensive. Thus, they cannot yield a true distribution of the final population of first stars that forms within a reasonable computational time. In fact, no simulations yet exist that have taken all these different physical processes into account to yield the Population III IMF. Nonetheless, they can inform us about the earliest stages of primordial star formation that primarily set the mass distribution of the mature stellar population.

In addition to progress in simulations, high-resolution observational data is now becoming available through powerful and highly sensitive telescopes like the Ata-

cama Large Millimetre/submillimetre Array (ALMA), Keck, the Australian Square Kilometre Array Pathfinder (ASKAP), and the Australia Telescope Compact Array (ATCA, Wilson et al. 2011). For indirect observational constraints on the first stars, we expect data from JWST, and from the Giant Magellan Telescope (GMT), the European Extremely Large Telescope (ELT), Euclid, and the Wide-Field Infrared Survey Telescope (WFIRST, Martell et al. 2017). With these new surveys and observational facilities in place, the amount of data will dramatically increase in the next 15 years, requiring dedicated modelling of the physical processes that give rise to the observations.

Table 1.1 summarises all 3D hydrodynamic simulations of first star formation published before 2019 along with the physical processes that were included. The time listed in the Table 1.1 reflects that reached by the simulation after the formation of the first sink particle. AMR refers to adaptive mesh refinement, where the grid is adaptively refined (division of a parent cell into multiple child cells) or de-refined based on the density at a point (Berger & Colella 1989), a method that is critical to following the collapse accurately in locations where the densities are high or high Mach number shocks are present. Chemistry is ticked 'Y' if the simulation used an explicit primordial chemical network together with the hydrodynamic module. Similarly, turbulence and magnetic fields, if included in any form in the simulation, are marked as 'Y' in the respective row. There are many types of radiation feedback that should be considered for simulations of primordial star formation, for example, that from Lyman-Werner photons, cosmic rays, etc. If any one of these feedback processes are included in the simulation, the column entry is 'Y'.

The simulations that have been done over the last two decades cover a wide range of parameter space in terms of resolution (hence, density) and time period. A common feature in all these simulations is the formation of a central protostar. We notice that most of these simulations do not work with an adaptive grid that can be refined as the density increases and more resolution is required to resolve the small-scale structures. While the nested grid or particle based codes have certain advantages over an AMR based grid, they may not resolve the regions where high velocity shocks are present, for example, near the edge of accretion discs of protostars (Plewa 2001; O'Shea et al. 2005; Hubber et al. 2013a). Further, the chemical networks have been periodically updated every few years with more accurate rate constants and enthalpies, which can have significant effects on the evolution of the system. Thus, it becomes clear that there are many areas where we can contribute to the ongoing research on first stars.

Table 1.1: Summary of all 3D MHD simulations of the first stars published before 2019. Columns III and IV denote the maximum density reached and time after the first sink formed in the simulation. Column V denotes whether adaptive mesh refinement (AMR) was used for the simulations; it only applies to grid-based simulations. Column VI-IX denote whether chemistry, turbulence, magnetic fields and radiation feedback were explicitly included in the simulation setup, respectively. The last column denotes whether fragmentation of the cloud (or the accretion disc) leading to multiple first stars was observed.

S. No.	Work	Max Density (cm^{-3})	Time (yr)	AMR	Chemistry	Turb	Mag Fields	Rad Feedback	Disk Frag
1	Abel et al. (2002)	10^8	——	N	Y	N	N	N	N
2	Bromm et al. (2002)	10^{14}	——	Y	Y	N	N	N	N
3	Saigo et al. (2004)	10^{20}	200	N	N	N	N	N	Y
4	Yoshida et al. (2006)	10^{15}	——	N	Y	N	N	N	N
5	Gao et al. (2007)	10^{11}	——	N	Y	N	N	N	N
6	O'Shea & Norman (2007)	10^{15}	200000	Y	Y	N	N	N	N
7	Machida et al. (2008b)	10^{22}	3000	N	N	N	N	N	Y
8	Machida et al. (2008a)	10^{22}	0.4	N	N	N	Y	N	N
9	Turk et al. (2009)	10^{16}	200	Y	Y	N	N	N	Y
10	Stacy et al. (2010)	10^{12}	5000	N	Y	N	N	N	Y
11	Stacy et al. (2011)	10^{12}	5000	N	Y	N	N	N	Y
12	Hosokawa et al. (2011b)	10^{12}	13000	N	Y	N	N	Y	Y
13	Greif et al. (2011a)	10^{16}	1000	N	Y	N	N	Y	Y
14	Clark et al. (2011b)	10^{12}	3000	N	Y	Y	N	N	Y
15	Stacy et al. (2012)	10^{12}	5000	N	Y	N	N	Y	Y
16	Greif et al. (2012)	10^{19}	10	N	Y	N	N	N	Y
17	Turk et al. (2012)	10^{14}	——	Y	Y	Y	Y	N	Y

18	Susa (2013)	10^{13}	10^5	N	Y	N	N	Y	Y
19	Machida & Doi (2013)	10^{18}	1000	N	Y	N	Y	N	Y
20	Stacy & Bromm (2014)	10^{16}	5000	N	Y	N	N	Y	Y
21	Susa et al. (2014)	10^{12}	10^5	N	Y	N	N	Y	Y
22	Hirano et al. (2014)	10^{12}	5000	N	Y	N	N	Y	Y
23	Hummel et al. (2015)	10^{12}	5000	N	Y	N	N	Y	Y
24	Hummel et al. (2016)	10^{12}	5000	N	Y	N	N	Y	Y
25	Latif & Schleicher (2016a)	10^{16}	40	Y	Y	Y	N	N	Y
26	Stacy et al. (2016)	10^{16}	5000	N	Y	N	N	Y	Y
27	Hirano & Bromm (2017)	10^{15}	10^5	N	Y	N	N	N	Y
28	Hirano et al. (2018)	10^{12}	5000	N	Y	N	N	N	Y

1.1.1   Chemo-magnetohydrodynamical simulations

We aim to study the formation and evolution of systems bearing first stars through 3D chemo-magnetohydrodynamical (chemo-MHD) simulations using the grid-based AMR code FLASH (Fryxell et al. 2000; Dubey et al. 2008) where we can refine and derefine regions in the simulation based on the Jeans length which characterizes the collapse of a system (Jeans 1902). We carry out multiple realizations of these simulations at different resolutions. This not only helps build a statistical population of first stars and study their distributions, but also proves useful to check numerical convergence and report the effects of grid noise and limited resolution.

We utilize the KROME[1] package for primordial chemistry that has been developed for astrophysical applications (Grassi et al. 2014). KROME uses a subroutine of predesigned (re-writable) chemical networks for various astrophysical phenomena that can be embedded in numerical codes like FLASH. It uses the ODE solver `DLSODES`[2] to solve the reaction network and evolve the temperature and density of the system in accordance with the chemistry and the specified heating/cooling processes (Grassi et al. 2013; Bovino et al. 2013a). The reactions included for primordial chemistry have been taken from various works, either directly, or by fitting the reaction coefficients as obtained from observations (Aldrovandi & Pequignot 1973; Mitchell & Deveau 1983; Janev et al. 1987; Dalgarno & Lepp 1987; Cen 1992; Verner & Ferland 1996; Abel et al. 1997; Stancil et al. 1998; Galli & Palla 1998; Omukai 2001; Galli & Palla 2002; Savin et al. 2004; Yoshida et al. 2006; Capitelli et al. 2007; Glover & Abel 2008; Glover & Savin 2009; Stenrup et al. 2009; Kreckel et al. 2010; Glover et al. 2010; Coppola et al. 2011; Forrey 2013). We describe the details of the primordial chemistry network in Chapter 2.

Sink particles are frequently used in hydrodynamic simulations of star formation as a proxy for stellar sources. These Lagrangian particles can travel inside the grid, accrete gas from it and alter the local gravitational potential in the region. We use the `Sink` particle module in FLASH to track the evolution of overdense regions in the simulation which will eventually form protostellar cores (Federrath et al. 2010a, 2011a). FLASH uses a rigorous set of checks to ensure that bound and collapsing mass in regions crossing the density threshold at the highest level of refinement is converted into a sink while avoiding artificial fragmentation. Invented by Bate et al. (1995), sink particle techniques have been extensively employed in both AMR and smoothed particle hydrodynamics (SPH) MHD simulations of star formation (Krumholz et al. 2004; Jappsen et al. 2005; Wang et al. 2010; Padoan & Nordlund

---

[1]http://www.kromepackage.org/
[2]http://www.radford.edu/~thompson/vodef90web/

2011; Gong & Ostriker 2013; Hubber et al. 2013b; Bleuler & Teyssier 2014; Jones & Bate 2018).

Since we use sinks as a substitute for stellar sources in our simulations, the distribution of sink masses will thus be a crucial information to comment on the fragmentation of primordial discs under different physical processes. By following the algorithm used in Krumholz et al. (2012b) that calculates the number of bound sinks in a binary, triple or quadruple network, we also investigate the multiplicity fraction in these systems, which we expect to be high given that fragmentation occurs close to the primary star which will result in closely bound systems. Understanding the formation of Population III binaries has recently gained a lot of interest due to the possibility of them being gravitational wave sources in the primordial Universe (Inayoshi et al. 2016; Belczynski et al. 2017; Liu & Bromm 2020a; Liu et al. 2021).

1.1.2 Role of turbulence and magnetic fields

We find from Table 1.1 that most simulations of first stars done to date lack turbulence and/or magnetic fields. The quiescent early Universe has been conventionally assumed to be largely non-turbulent (Gibson 1996). However, once high-density baryonic regions are created in dark matter minihalos and begin to collapse, gas is driven to the center of these regions at high velocities. The Reynolds numbers of the resulting flows are very large, favouring the development of turbulence. Moreover, the streaming velocities between the dark matter and baryons can also contribute to turbulence (Fialkov et al. 2014). Further, even a small amount of seed turbulence can amplify the magnetic fields to large values through small-scale dynamo action (Brandenburg & Subramanian 2005; Federrath et al. 2011c; Brandenburg et al. 2012; Schober et al. 2012a; Federrath et al. 2014a). Hence, it is vital to understand how turbulence acts during the formation of the first stars and modulates the magnetic field strength during collapse. However, this is further complicated by the highly unconstrained primordial magnetic field strength, with values ranging around $10^{-34} - 10^{-9}$G on Mpc/h scales (Kahniashvili et al. 2013a, 2014; Saga et al. 2018; Cheera & Nigam 2018). Nonetheless, there are strong theoretical arguments for the existence of a weak, non-zero magnetic field in the early Universe. The relevant question for the Population III IMF then becomes: can magnetic fields grow to be sufficiently strongly during Population III star formation?

One possible way for the field to grow is through flux-freezing, where the field simply follows the gas as it collapses to high densities. Another way to grow the field (at exponential rates) is through the action of the turbulent or the mean field dynamo
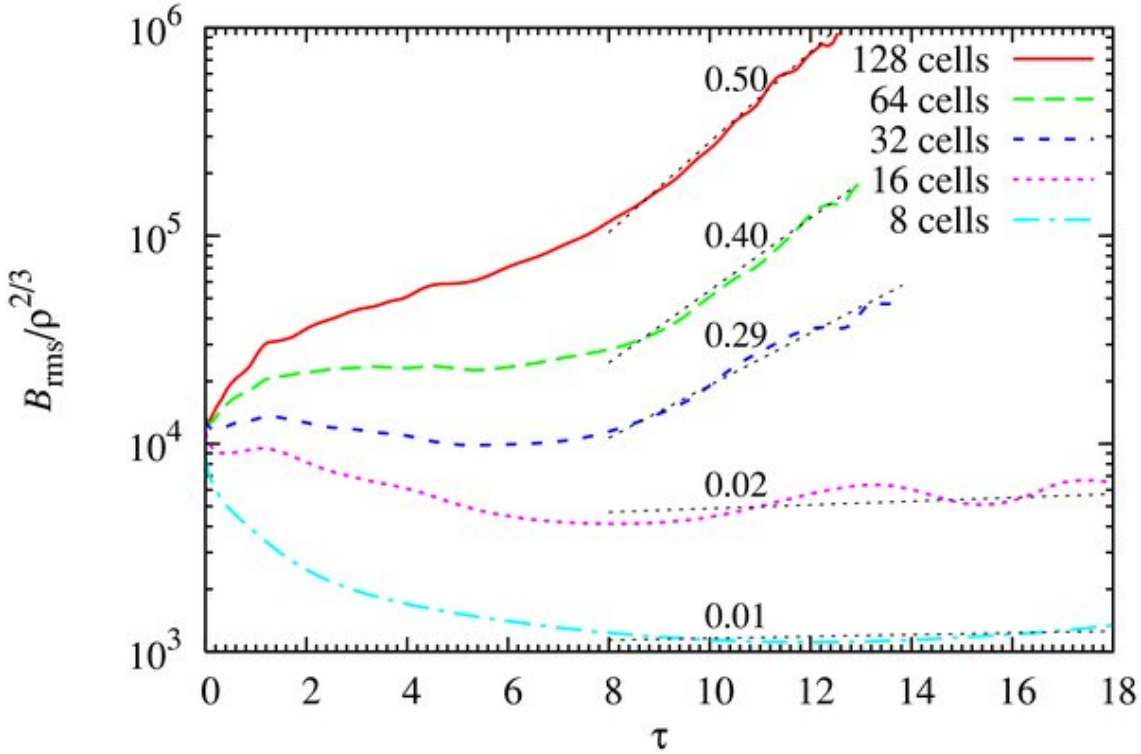
Figure 1.3: Figure adopted from Federrath et al. (2011c), showing the evolution of the rms component of magnetic field (or, the turbulent magnetic field) relative to the amplification by compression of the field ($\rho^{2/3}$) of star-forming clouds at different times during collapse. At least 32 cells per Jeans length are required to resolve the small-scale turbulence that can amplify the magnetic fields through the dynamo action (Brandenburg & Subramanian 2005). This is $8\times$ better resolution than is usually adopted for simulations of cloud collapse based on the Truelove criterion for resolving the Jeans length (Truelove et al. 1997).

that convert kinetic energy to magnetic energy (Brandenburg & Subramanian 2005). Numerous studies have shown that it is important to resolve the scales at which turbulence can amplify magnetic fields through the dynamo action. It is common to use the Truelove criterion for refinement in gravito-hydrodynamic simulations, which requires at least 4 cells per Jeans length to resolve the ongoing collapse of the system (Truelove et al. 1997). However, Federrath et al. (2011c) show that one needs at least 32 cells per Jeans length to resolve the scales at which turbulence can amplify magnetic fields (see Figure 1.3, Sur et al. 2010). In fact, using less than ∼30 grid cells per Jeans lengths leads to underestimates not only in the amplification, but also in the amount of kinetic energy that is resolved on the Jeans scale (Federrath et al. 2011c) and the structure of the gas (for example, the scale height of accretion discs; see Federrath et al. 2014a). Such a large difference in the refinement criteria is already a major improvement over other simulations that we implement.

It is well known that simulations cannot reproduce realistic Reynolds numbers found in turbulent environments in the primordial Universe, which are of the order of 10^6 (Schober et al. 2012a; see also, Haugen et al. 2004; Kitsionas et al. 2009). In the ideal case of infinite resolution, one would expect to see magnetic fields eventually saturate as turbulence converts kinetic energy into magnetic energy. Sur et al. (2014) show that even a weak turbulent seed can saturate the magnetic fields on timescales smaller than the free-fall timescale of collapse. We can achieve this by introducing a saturated magnetic field as expected from dynamo theory in our FLASH simulations. This allows us to perform a parameter study of the effects of different magnetic field strengths during the onset of collapse in primordial clouds.

It is well known that an ordered component of magnetic field can lead to the launching of jets and outflows from a system undergoing rotational motion (Pudritz & Norman 1986; Crutcher 1999; Wu et al. 2004; Banerjee & Pudritz 2006; Price & Bate 2007). Gerrard et al. (2019) recently carried out a study on outflows in the presence of different types of magnetic fields (ordered, mixed and turbulent) in the context of present day star formation. These authors show that different magnetic field geometries have a significant impact on the distribution of the underlying stellar population and thus may play a crucial role in determining the IMF. Given the highly turbulent flow in dark matter minihalos, the fields will be completely tangled up very quickly and there may not be an ordered component present. However, if the $\alpha\omega$ mean field dynamo works, it can generate and sustain an ordered component (Pariev & Colgate 2007; Pariev et al. 2007). This is so because the $\alpha\omega$ dynamo can transfer magnetic energy back and forth between different directions. The importance of protostellar outflows, if any, remains largely unexplored in Population III star formation.

1.1.3 Role of radiation feedback

It is vital to include a treatment of the different radiative processes that occur in star-forming clouds, because they can significantly influence the final masses and dynamical interactions of stars in a cluster. In the primordial case, it has been shown that radiation feedback can halt the growth of a protostar beyond $M_\star > 30 M_\odot$ (see Figure 1.4, adopted from Hosokawa et al. 2011b). However, in a recent study Jaura et al. (2022) reach the opposite conclusion; they attribute the results of previous studies to failure to resolve the scale height of the accretion disc, which leads them to overestimate the effectiveness of radiation feedback. In the case of primordial gas, cooling takes place due to line emissions instead of continuum emission as for present day star formation. It is harder to model radiative transfer in the former
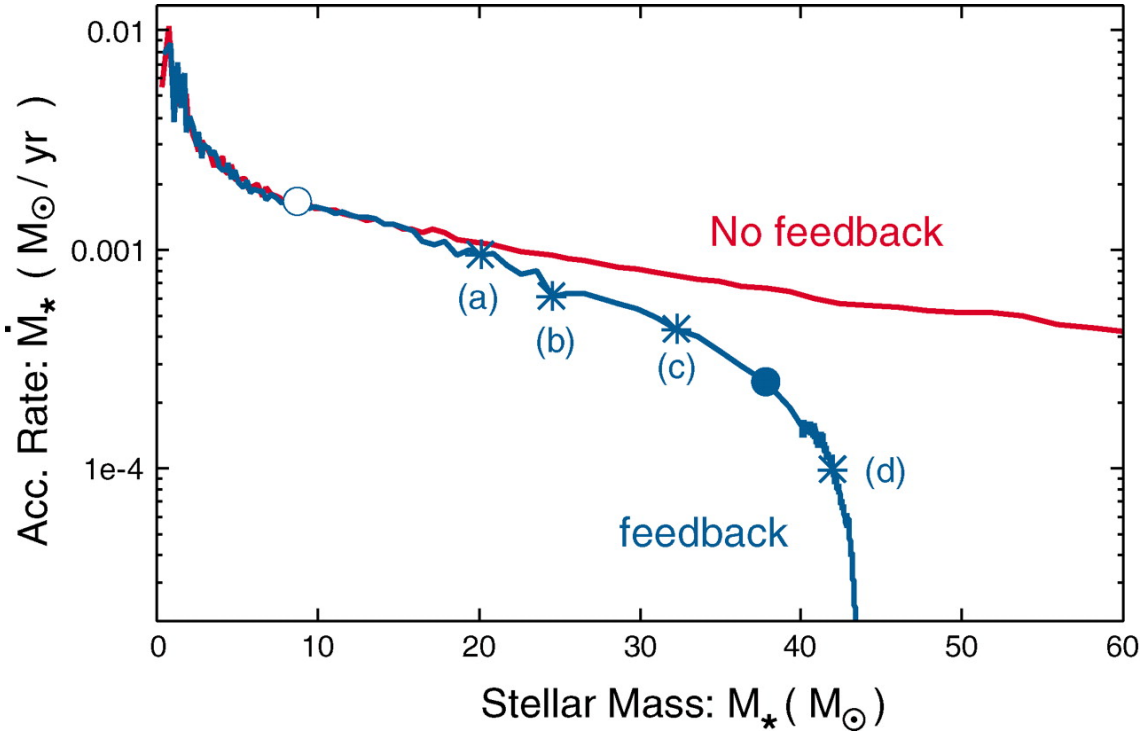
Figure 1.4: Figure adopted from Hosokawa et al. (2011b), showing the accretion rate of a first star with and without the presence of radiation feedback. Radiation feedback from the protostar can halt its growth by evaporating the accretion disk around it (EUV radiation).

case because the medium is not static and the lines overlap in high density regions, thus deviating significantly from Lorentzian profiles.

Lyman-Werner photons can potentially impact Population III star formation. These photons have energies $11.2 < h\nu < 13.6$ eV and are capable of photo-dissociating H_2 which is the primary coolant in primordial gas at high densities (Allison & Dalgarno 1969). They are produced from massive protostars and can escape their host minihalos. This effect can create a Lyman-Werner photon background, whose strength depends on the escape fraction, which can dissociate H_2 in minhalos that have not yet collapsed, thus affecting their star formation process (Schauer et al. 2017; Regan & Downes 2018). Figure 1.5 shows this calculation of the escape fraction approximated by Schauer et al. (2015), showing how it can rise to unity for massive first stars within a Myr.

The treatment of Lyman-Werner radiation is usually complemented by a prescription for calculating the stellar luminosity that is used to estimate the fraction of photons in the Lyman-Werner bands. In the absence of observations of surviving first stars, the stellar luminosity of the first protostars is approximated assuming that they follow the Hayashi and Henyey tracks (Stacy et al. 2016) as they evolve to reach the
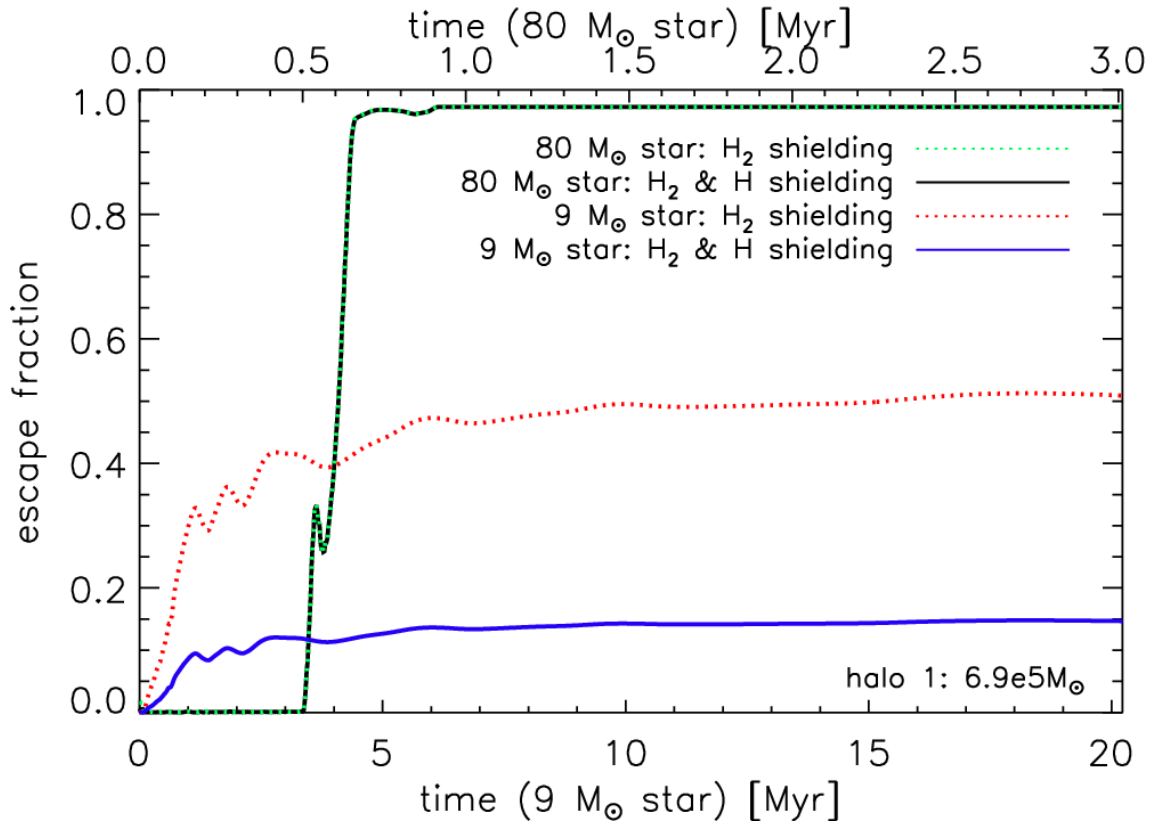
Figure 1.5: Figure adopted from Schauer et al. (2015), showing the escape fraction of Lyman-Werner photons for a massive and intermediate-mass star when shielding from H and H_2 is considered.

pre-main sequence phase

$$L_\star = L_{\mathrm{acc}} + L_{\mathrm{int}} \,, \tag{1.1}$$

by using a higher effective temperature than that suggested by these tracks (to find L_{int}) because the gas is metal-free (Stahler et al. 1986; Cassisi & Castellani 1993). The accretion luminosity can be estimated as $L_{\mathrm{acc}} = GM_*\dot{M}/R_\star$ (Hartmann 2008), where $\dot{M}$ is the accretion rate of the sink particle.

Another source of radiation feedback which is primarily important for the Pop III.2 star formation is cosmic rays driven by the Pop III.1 stars. It has been shown that the cosmic ray strength, even when varied for orders of magnitude, does not affect the evolution of a primordial cloud (Hummel et al. 2015, 2016). However, these studies were carried out at lower resolutions where the small-scale turbulent magnetic fields could not be resolved and amplified, which are the necessary drivers for cosmic ray diffusion (e.g., Gabici et al. 2007; López-Barquero et al. 2016).
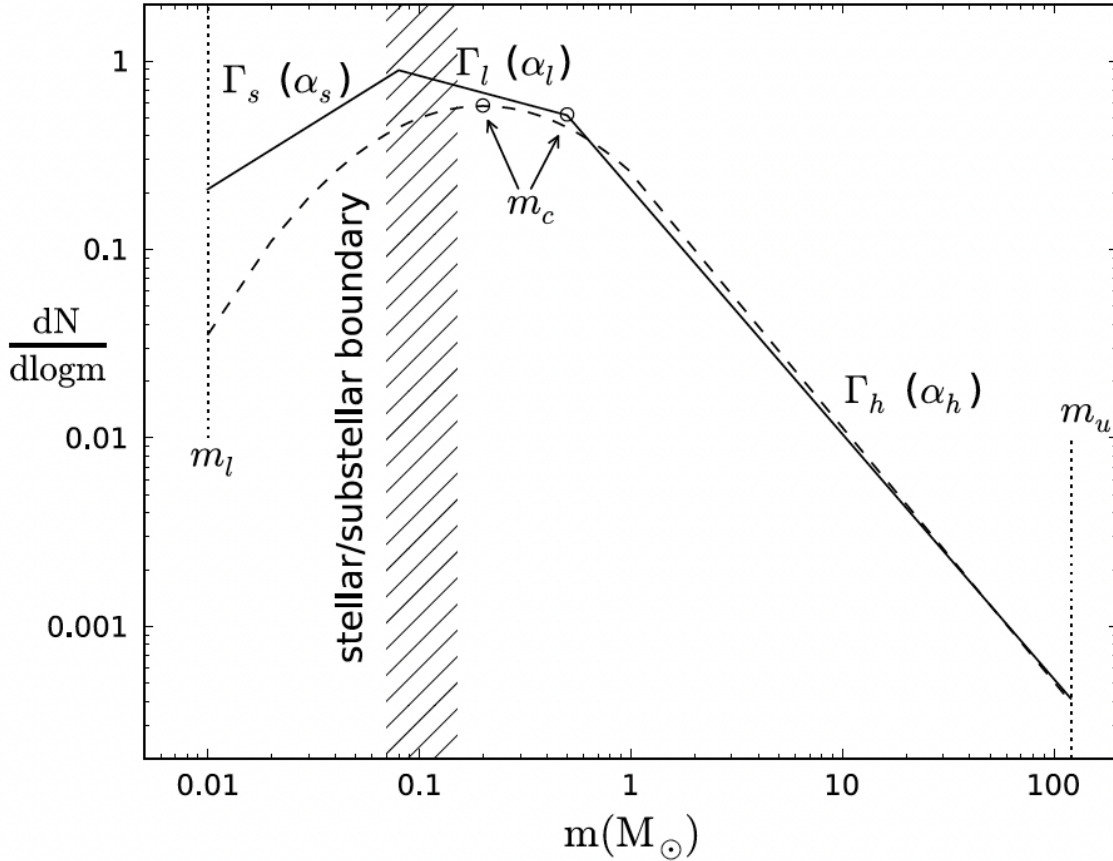
Figure 1.6: Figure adopted from Hopkins (2018), showing the IMF of the Milky Way. The IMF is typically parameterized by five key parameters: the low and the high truncation masses (m_l and m_u, respectively), the peak or the characteristic mass (m_c), and the slope at the low and the high mass ends (α_s, α_l and α_h).

1.1.4   IMF at zero and low metallicities

All the above physical processes play a big role in shaping up the IMF, which is one of the most fundamental properties for several key research areas in astrophysics. The IMF is simply defined as the mass distribution of stars at birth. It forms the basis for galaxy evolution, metal production, star formation feedback, star cluster formation, and significantly influences the lifecycle of molecular clouds and galactic discs. The IMF of the Milky Way has been extensively studied both in theory and observations. In fact, the literature on the IMF has grown so massive that several different and confusing terminologies have emerged as different groups have worked on it over the years (Hopkins 2018).

Figure 1.6 shows the IMF in the Milky Way. The IMF in the Milky Way is usually described by one of the three most popular functional forms: a power-law for all masses with an exponent -2.35 as found early on by Salpeter (1955), a broken power-law with breaks at $0.08\,\mathrm{M_\odot}$ and $0.5\,\mathrm{M_\odot}$ (Kroupa 2001), and a log-normal form

with a peak around $0.2\,\mathrm{M_\odot}$ (Chabrier 2003). The IMF is called top-heavy if the characteristic mass (peak mass in the log-normal case and the mass where the slope changes in the broken power-law case) is greater than $\mathrm{M_\odot}$, and bottom-heavy if it is less than $\mathrm{M_\odot}$. Several works have looked at how conditions during star formation and feedback on small scales, and galaxy evolution on large scales sets the slopes at the low and the high mass ends as well as the peak of the IMF. However, it becomes tricky to measure the substellar IMF in extragalactic regions due to insufficient resolution, and most extragalactic IMF studies have only focused on massive stars or the slope at the high mass end of the IMF.

Early works on the IMF found it to be quite similar despite the (limited) diversity of environments it was investigated in, leading to the belief that the IMF is universal. However, we now know that star formation is very sensitive to the environment. For example, the formation of the first stars in the absence of dust and metals takes place in a completely different thermodynamic regime as compared to metal-rich star formation (Omukai et al. 2005). As we describe above, even though no first stars have ever been observed, it is likely that the Population III IMF was top-heavy, unlike the bottom-heavy IMF in the Milky Way. These results already imply a transition in the IMF as a function of metallicity. In fact, there is now some observational evidence for IMF variations in super-Solar (like the centres of massive galaxies – van Dokkum & Conroy 2010) as well as very sub-Solar (like ultra-faint dwarf galaxies – Geha et al. 2013) environments, although some findings do not rule out a Milky Way-like IMF at more than $1-2\sigma$ level (El-Badry et al. 2017). Nevertheless, it is becoming clearer that the first step in understanding the evolution of zero and low metallicity systems (e.g., first and metal-poor stars, ultra-faint dwarf galaxies, and globular clusters) is to constrain their IMF. Theoretical progress in this area is highly desired given the upcoming JWST observations to explore the substellar part of the IMF in metal-poor dwarf galaxies (Geha 2014).

1.2   Metal distribution in galaxies

The distribution of metals in galaxies is inherently connected to small-scale physics that governs how metals are produced in stars and stellar remnants. The IMF decides the mass distribution of massive stars that directly sets the metal yield in galaxies. Thus, it is important to connect the small-scale metal enrichment to the large-scale metal distribution in galaxies. The overall metal content of galaxies can give us a great deal of information on how galaxies form and evolve over time. For example, it is now well known that galaxies follow a fundamental mass-metallicity
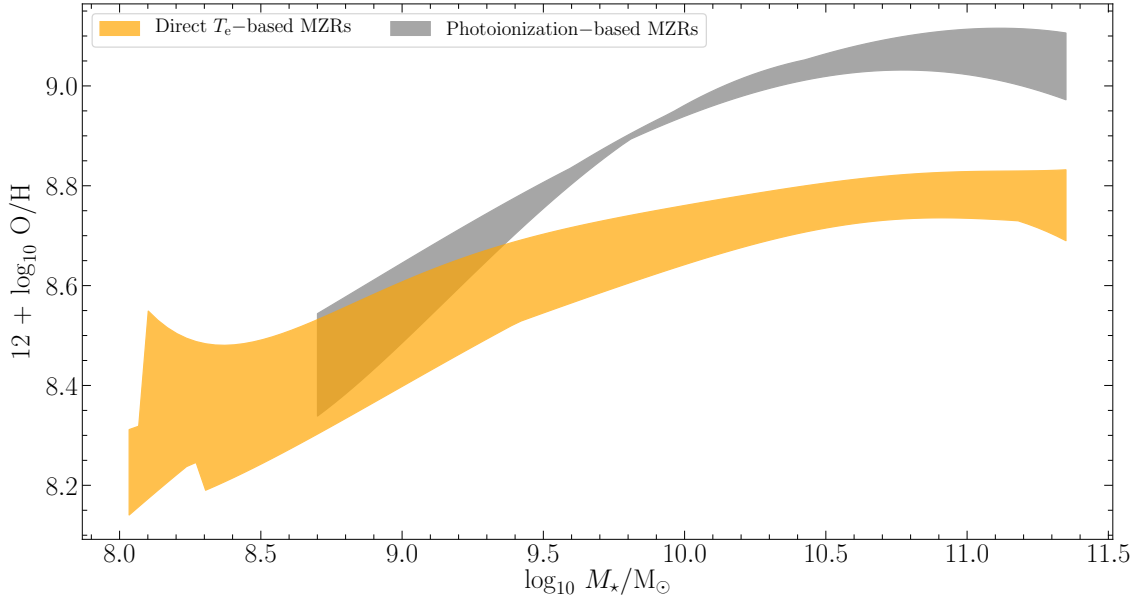
Figure 1.7: Figure depicting the mass-metallicity relation (MZR) in local galaxies, modified from Maiolino & Mannucci (2019) to show the two bands encompassing metallicity measurements from direct methods and photoionization modeling.

relation (MZR) whereby low mass galaxies have fewer metals per unit mass. Studying the shape and scatter in this relation in turn tells us about what drives galaxy evolution, and what regulates star formation and galactic metal content. The MZR has been the focus of several studies on galaxy evolution (see the reviews by Kewley et al. 2019b and Maiolino & Mannucci 2019). Recent works have also started exploring the MZR at high redshifts, finding how the mass content of galaxies in the early Universe correlate with their metal content (e.g., Jones et al. 2020; Sanders et al. 2021).

In addition to focusing on the overall metal content of galaxies, we can also study the distribution of metals in galaxies. Within the inside-out galaxy formation theory where the inner parts of the galaxy form first, it is expected that the inner parts of the galaxy will be more metal enriched as compared to the outskirts. This would lead to the development of a negative gradient in metallicity measured from inside out. Metallicity gradients are a useful tool to probe not only the overall evolution of galaxies, but also their assembly and inner structure. Such negative metallicity gradients have now been observed in thousands of galaxies thanks to integral field unit (IFU) spectroscopy. IFU spectroscopy uses different 'units' (often called as fibres or bundles) that can be positioned to cover different parts of a galaxy (see Figure 1.8) to provide spatially as well as spectrally-resolved data.

In this thesis, we develop a new model to understand the physics of metallicity gra-
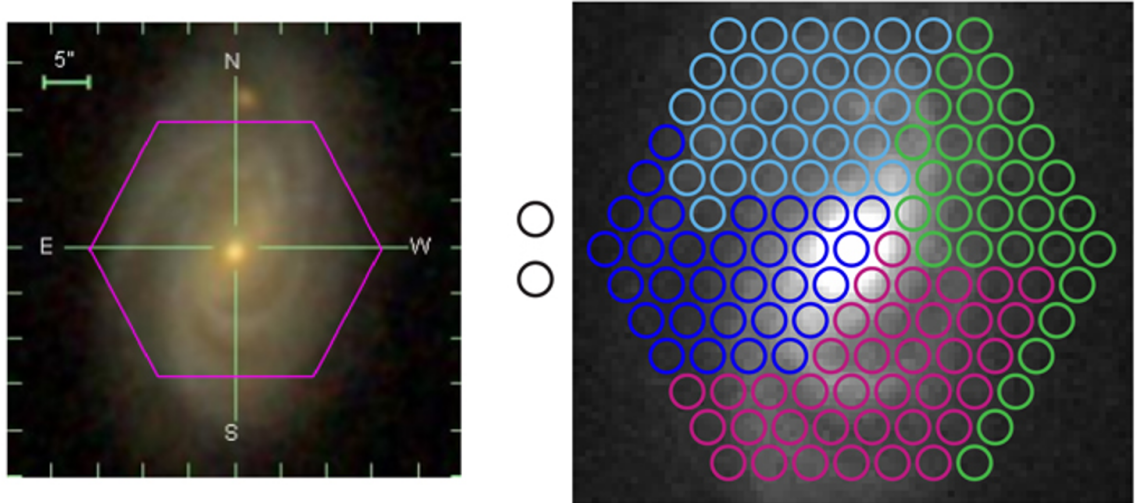
Figure 1.8: Figure adopted from Law et al. (2016), depicting how IFU spectroscopy can provide a spectrum for different parts of the galaxy over a 2D field of view instead of only providing an integrated spectrum from the entire galaxy.

dients, and provide a joint explanation for global as well as spatially-resolved metallicity trends observed in galaxies. For the purpose of this thesis, metals refers to the gas-phase oxygen abundance, unless explicitly stated otherwise. In the subsections below, we provide a brief overview on how gas-phase metallicities are measured, and present the current status of research on metal distribution in galaxies.

1.2.1 Lifecycle of metals in galaxies

To understand the distribution of metals and metallicity gradients in galaxies, it is essential to understand the lifecycle of metals. Figure 1.9 depicts the important components of galactic metal lifecycle - galaxies continuously accrete gas from the cosmic web and the intergalactic medium (IGM), which subsequently triggers star formation in the galactic disc. While a fraction of the metals produced get locked in low mass stars and stellar remnants, the majority of the metals are dumped back into the ISM, on timescales much shorter than the dynamical evolution time of galaxies (commonly termed as 'instantaneous recycling', following Tinsley 1980). Since the galactic disc is a dynamic and multiphase system, metals continuously get advected along with the bulk flow of the gas. Metals also diffuse due to turbulence in galactic discs, and are depleted onto dust grains in the ISM. Energetic feedback processes like supernovae and active galactic nuclei (AGN) can also eject metals out of the disc in the form of galactic winds. In fact, a fraction of the metals can be directly ejected out of the disc without ever mixing into the ISM. Depending on the kinetics of the wind, metals can fall back onto the disc in the form of a galactic fountain,
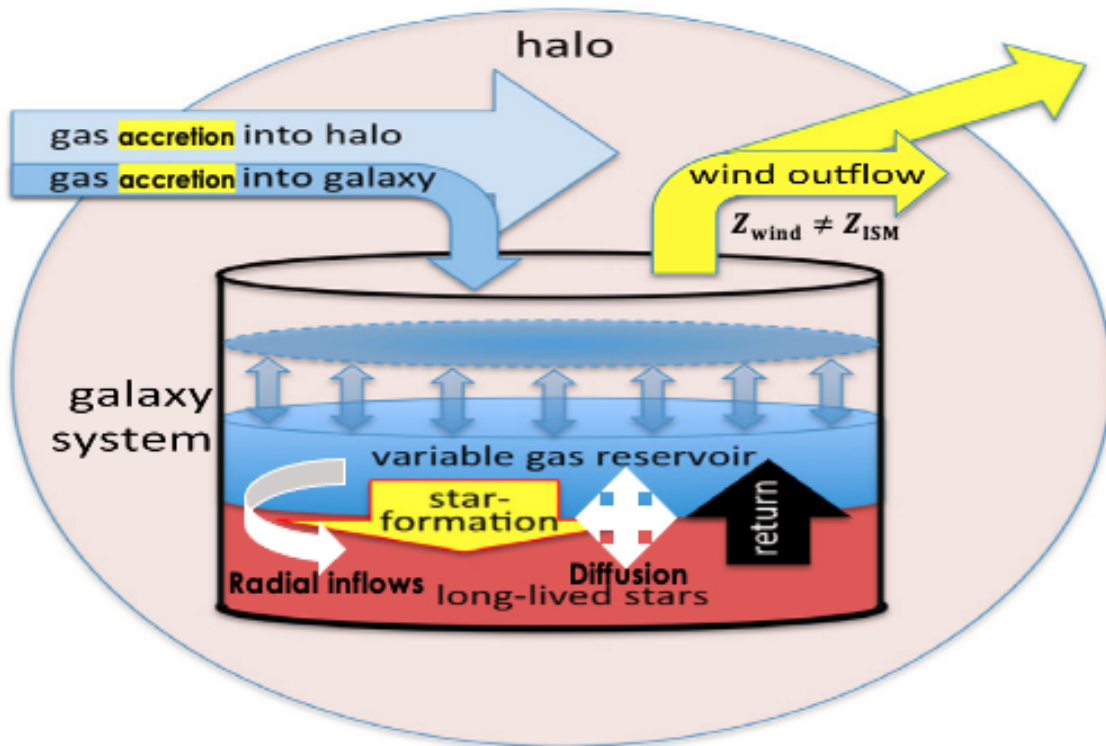
Figure 1.9: Figure depicting the bathtub model of chemical evolution (Lilly et al. 2013), modified to include all major modes of metal transport (radial inflows or advection, and diffusion) and to highlight differential enrichment of galactic winds.

enrich the circumgalactic medium (CGM), or leave the galactic halo entirely.

Some of these processes have not been taken into account in existing chemical evolution models, primarily because they only impact the distribution of metals in the disc, and not the overall metal content (for example, metal advection and diffusion). Additionally, many chemical evolution models invoke the assumption that the metallicity of galactic winds is identical to that of the galactic disc. We will show later in this thesis that this a strong assumption which is not necessarily true for all types of galaxies.

The lifecycle of metals is governed by a complex combination of different physical processes that shape galaxy evolution. Since these processes are often occurring simultaneously, and in different parts of the disc, the exact shape of the metallicity profile can be quite non-linear and asymmetric. Nonetheless, as a first order approximation that can be applied to a wide range of galaxies, it is common to fit the metallicity profile with a log-linear function (logarithmic in metallicity), the slope of which is called the metallicity gradient.

Note that the above description typically applies to isolated star-forming galaxies. However, we now know that most star-forming galaxies do not evolve in isolation for
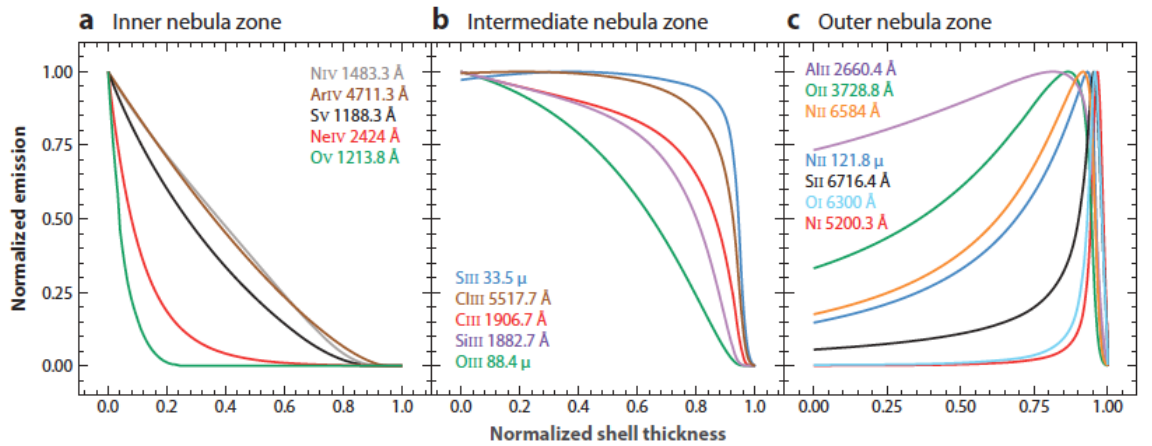
Figure 1.10: Figure reproduced from Kewley et al. (2019b), showing the ionization zones of different strong lines emitted in H II regions that are used to measure the ISM metallicity. Higher ionization states are usually observed in the innermost parts of the nebula.

a Hubble time. Galaxies often interact with other galaxies, and undergo flybys or mergers. Galaxies in a group and satellite galaxies often experience tidal interactions and ram pressure stripping. All such interactions can vastly alter the metal lifecycle in galaxies in a short amount of time. Recent observations have started to reveal the complexities of galaxy-galaxy interactions and how they impact galaxy metallicity, showing that such interactions often drive pristine gas inflows towards the galactic centres that dilute the metallicity. At the same time, interactions can often trigger star formation that ultimately leads to more metal enrichment.

1.2.2 Measuring gas-phase metallicity

The gas-phase metallicity is typically quoted as the oxygen abundance of the ISM on a logarithmic scale: $12 + \log_{10} \text{O/H}$. The gas-phase metallicity is usually obtained from gas ionized by H II regions (regions surrounding young massive stars that are impacted by high energy radiation from the star). The abundances of different chemical species in the gas can be measured from the flux of their emission lines that result due to collisional excitation of the ions. These emission lines cover a wide part of the electromagnetic spectrum – from X-rays to the infrared. Some of the most prominent emission lines that are observed at rest-frame optical wavelengths include those from oxygen, nitrogen and sulphur atoms. Higher ionization states are typically observed close to the radiating source, and very few lines are produced throughout the ionized nebula (see Figure 1.10).

There are various methods to measure and constrain the gas-phase metallicity of the ISM, which can broadly be grouped into two categories – direct methods and
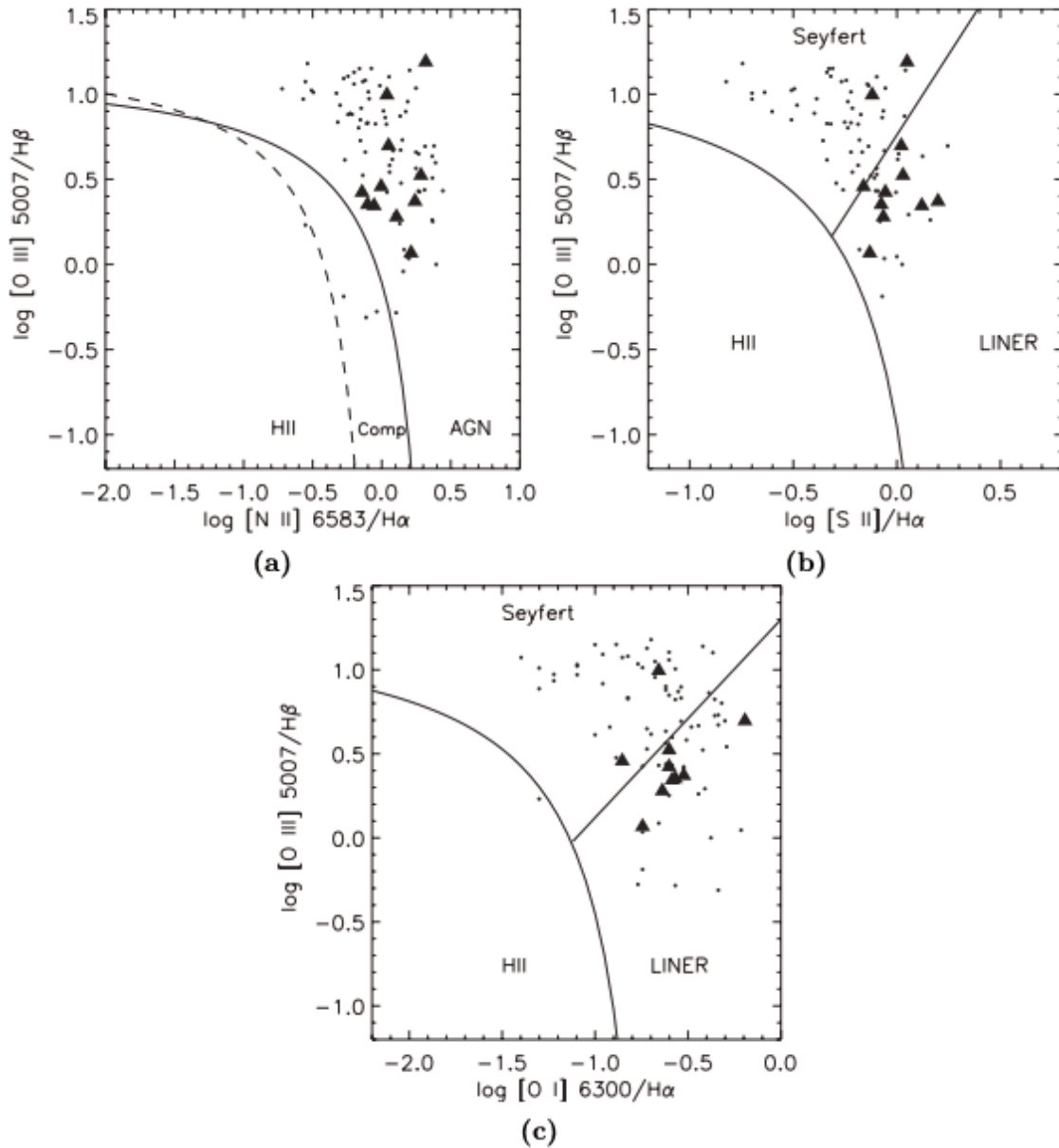
Figure 1.11: Figure reproduced from Zovaro (2020), showing the three different BPT diagrams from Ogle et al. (2010). These diagrams are very helpful in selecting only H II regionwhile measuring the gas-phase metallicity using strong line diagnostics, since these diagnostics are only calibrated against H II region, and any contamination from other sources like AGN or LINER/LIER can lead to an erroneous measurement of gas-phase metallicity. An updated version of this diagram also removes contamination from shocks (D'Agostino et al. 2019).

methods relying on photoionization modeling of the H II regions. Direct methods use a set of collisionally excited lines or recombination lines to determine the abundance of a specie given an emissivity and the thermodynamic structure of the emitting region (temperature and density). Photoionization modeling involves constraining the gas-phase metallicity based on the relative strength of different emission lines that can be compared against a grid of H II region models of different characteristics. Both the approaches have several advantages and limitations, which we describe in Section 1.2.3 and Section 1.2.4, respectively. A key difference between the two approaches is that while photoionization modeling predicts the 'overall' gas+dust-phase metallicity of the ISM, direct methods only produce the gas-phase metallicity. Thus, care needs to be taken while interpreting or comparing the metallicity from these two approaches with theoretical models.

The same emission lines can also be produced by other physical processes that have a source different than H II regions (for example, shocks and AGN). In extragalactic observations, it becomes essential to separate the emission line flux coming from H II regions in order to accurately estimate the gas-phase metallicity, since the underlying emission line modeling is often restricted only to radiation arising from young massive stars. As a way to separate H II regions from other possible sources of excitation, Baldwin et al. (1981) proposed a diagram that plots the [O III]$\lambda 5007$/Hβ ratio against [N II]$\lambda 6584$/Hα, [S II]$\lambda 6717,6730$/Hα or [O I]$\lambda 6300$/Hα ratios. Any combination of the above category of ratios is sensitive to the gas-phase metallicity, ionizing radiation, and abundance ratios of different species, and is thus a useful probe to separate emission from H II regions from shocks and AGN (see Figure 1.11). These diagrams are now well known as the BPT diagrams, named after the three authors of the original study.

Once a metallicity is derived for all the H II regions in a galaxy, the metallicity gradient is simply given by the slope of the linear fit to the observed trend between the logarithmic metallicity and the deprojected galactocentric distance. The metallicity gradient is typically quoted in the units of dex/kpc or dex/r_e, where r_e is the half-light radius of the galaxy. This is of course a first order approximation to the more complex metallicity profiles often seen in galaxies (Sánchez 2020a), but it has the power to inform us on the spatially-resolved structure and mass assembly in galaxies.

1.2.3 Metallicity diagnostics

There are various strong line metallicity diagnostics that are used to infer the ISM metallicity. We describe some of the common ones below, listing their benefits and

challenges:

1. *R23* It is one of the most popular metallicity diagnostics as it involves using two different ionisation states of oxygen: log ([O II]λ3727+ [O III]λ5007,4958)/Hβ. A wide range of calibrations have been proposed for this diagnostic (e.g., Pagel et al. 1979; Dopita & Evans 1986; Zaritsky et al. 1994; Kobulnicky & Kewley 2004). However, this diagnostic is sensitive to the ionization parameter (defined as the photon to baryon ratio in H II regions) and ISM pressure at high metallicities, and does not have a unique solution for the metallicity in some parts of the parameter space. Thus, most works relying on this diagnostic use it in conjunction with another diagnostic to constrain both the ionization parameter and the metallicity. Some authors have also separated *R23* into its constituents: *R2* (log[O II]λ3727/Hβ) and *R3* (log[O III]λ5007/Hβ), finding that *R2* suffers with similar issues (including dust reddening) as *R23*, but a tight relation exists between *R3* and metallicity driven by the ionization parameter (Curti et al. 2017).

2. *N2* It uses the [N II]λ6584 to Hα ratio as a measure of metallicity. Since both these lines are quite close to each other, this diagnostic has the advantage of being the least affected by dust reddening (Pettini & Pagel 2004). This is also the most common choice at high redshifts where other lines are often redshifted out of spectral coverage. However, this ratio has a weak dependence on the ionization parameter (Kewley et al. 2019b), and can give erroneous results if the nitrogen abundance in the target galaxy is quite different from the calibrated value (Maiolino & Mannucci 2019).

3. *O3N2* It uses a combination of [O III]λ5007, [N II]λ6584 and the first two hydrogen Balmer lines to calculate the metallicity. However, it involves similar caveats regarding the scatter in the nitrogen abundance and N/O ratio, is more accurate at high metallicities, and is sensitive to the ionization parameter (Kewley et al. 2019b).

4. *S2* It uses the [S II]λ6717,6730 and Hα lines to measure the metallicity, and has an advantage over nitrogen-based diagnostics since sulphur is an α element like oxygen. However, it is also sensitive to the ionization parameter. Using it together with [S III]λ9069,9532 lines removes the dependence on the ionization parameter (Vilchez & Esteban 1996; Oey & Shields 2000), however the [S III]λ9069,9532 lines are often out of spectral coverage that is available with optical facilities.

5. *N2O2* It uses the ratio of [N II]λ6584 and [O II]λ3727 lines to measure the metallicity. This ratio has the advantage that it is insensitive to the ionization

parameter and the ISM pressure over a wide range of parameters. This ratio has also been found to be least affected by AGN or diffuse ionized gas (DIG, Kewley et al. 2006b; Zhang et al. 2017). However, this ratio can also suffer from biases if the N/O ratio is significantly different from the calibrated value.

6. *N2S2* Proposed by Dopita et al. (2016), this diagnostic combines the *N2* and *S2* diagnostics to remove the dependence on both the ionization parameter and the ISM pressure. Furthermore, this diagnostic is often useful for high-redshift galaxies where only the red end of the spectrum can be observed. However, since it involves using the [N II]$\lambda6584$ line, the same caveats on the abundance of nitrogen and the assumed N/O-O/H relation apply (Curti et al. 2020a).

In addition to the optical diagnostic listed above, rest frame UV diagnostics are used to infer the metallicity from UV observations of H II regions (e.g., Feltre et al. 2016; Pérez-Montero & Amorín 2017; Byler et al. 2018). Some of the common UV emission lines used for this purpose include [N II]$\lambda2139,2143$, [O II]$\lambda2470$, [C III]$\lambda1908$, [C IV]$\lambda1549$, [O II]$\lambda1664$, and [He II]$\lambda1640$. However, these lines are also sensitive to the ionization parameter, and only trace the innermost part of H II regions. Some of these lines (e.g., [He II]$\lambda1640$) are also emitted by other sources like Wolf-Rayet stars, thus making it challenging to attribute them solely to H II regions. Another class of diagnostics uses strong lines in the infrared, however most lines in this part of the electromagnetic spectrum are also sensitive to the ionization parameter and the gas density (Afflerbach et al. 1997; Calabrò et al. 2018). The observational measurements that we use in this thesis come from strong line diagnostics in the optical, so we do not discuss UV and infrared diagnostics further.

1.2.4   Challenges in measuring and modeling metallicity

Measuring gas-phase metallicity using the techniques described above carry some uncertainties. As we note above, the accuracy of different metallicity diagnostics is very sensitive to the additional dependence they have on the physical structure of H II regions. Therefore, they carry significant systematic uncertainties, especially if only some of the strong lines are observed. This was highlighted by Poetrodjojo et al. (2021a) who used the SAMI survey to investigate the uncertainties in the mass-metallicity gradient relation due to different strong line diagnostics (see Figure 1.12). These authors show that the scatter in this relation can be as high as 0.11 dex/$r_{\rm e}$, and introduce new conversions between the different diagnostics (when only some lines are observed) to reduce the scatter.

Similarly, there is also a considerable discrepancy between metallicities estimated from photoionization modeling and direct methods, especially at high metallicities
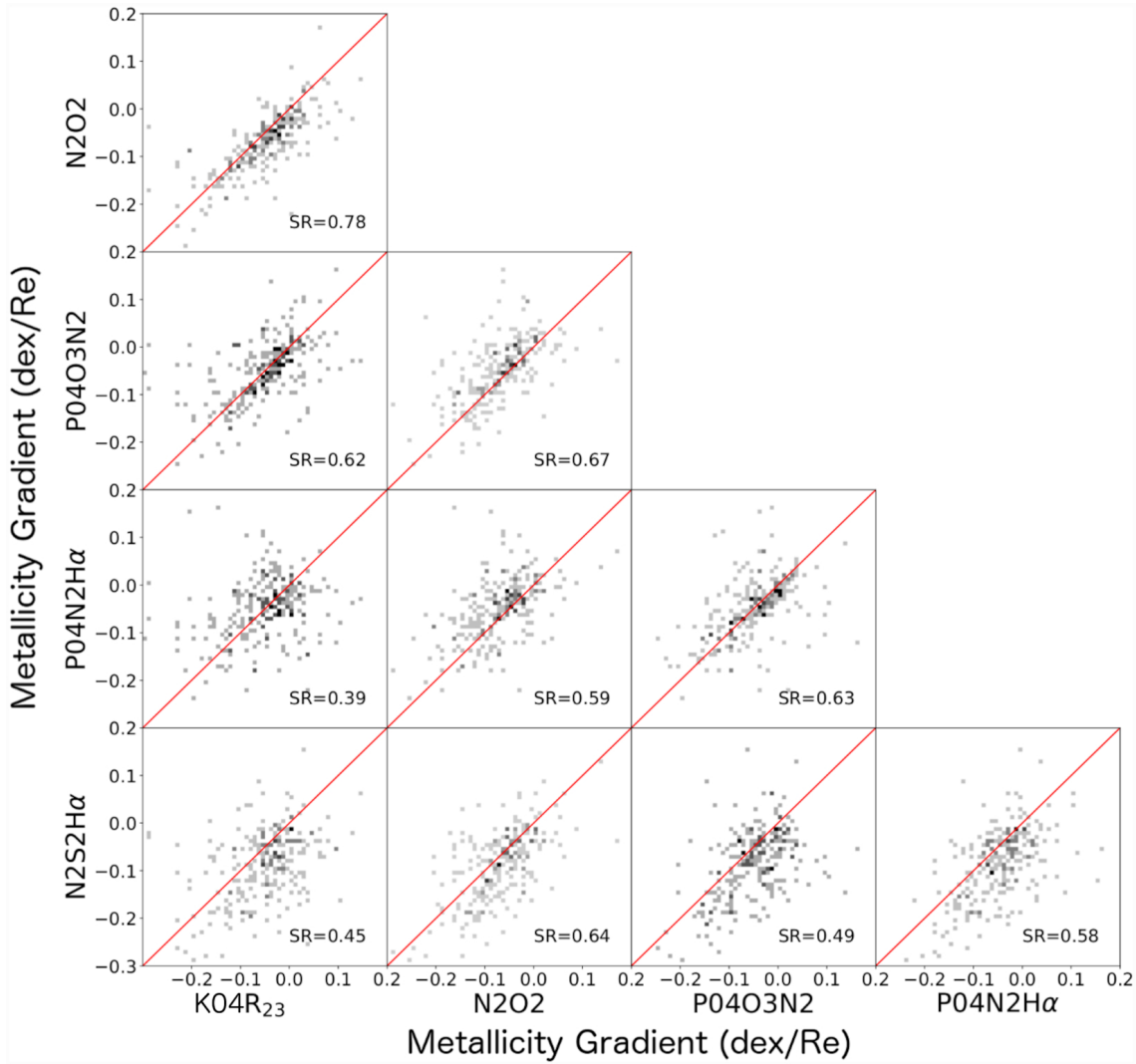
Figure 1.12: Figure adopted from Poetrodjojo et al. (2021a), showing how different gas-phase metallicity diagnostics compare against each other. The scatter around the 1:1 line in each panel reflects the systematic uncertainties in measuring metallicities using emission lines. 'SR' denotes the Spearman's coefficient between the diagnostics.

(see Figure 1.7). A part of this discrepancy is due to dust depletion. Some other factors that potentially contribute to this discrepancy include the assumed form of the energy and density distribution of electrons, geometrical configuration of H II regions and ionization correction factors. Lastly, it is worth noting that most of these diagnostics have been developed and calibrated for local H II regions, so the extent of their applicability at high redshifts is still debated (e.g., Kewley et al. 2013a; Shirazi et al. 2014; Kaasinen et al. 2017; Strom et al. 2018; Davies et al. 2020).

The spatial resolution in extragalactic studies is typically insufficient to separate H II regions from DIG, thus making it harder to properly estimate the metallicity. It is possible that the red end of the spectrum suffers more from DIG contamination (Vale Asari et al. 2019), which is a worry for measurements of metallicity gradients at high redshifts. Some studies have shown how the presence of DIG in the outer regions of a galaxy can make its metallicity gradient to appear shallower than the true value (e.g., Poetrodjojo et al. 2019). The reliability of the measured metallicity gradient is, to a lesser extent, also subject to noise in the data and the available S/N ratio (Acharyya et al. 2020).

On the theoretical side of galactic metal evolution, while there are several models that exist to explain global galaxy metallicities, there are only a handful that incorporate spatially-resolved (or, radially-resolved) information to explain the physics behind metallicity gradients. A key difference between the two categories of models is that explaining metallicity gradients also requires models and simulations to include metal transport processes that only change the distribution of metals but not its overall content. Additionally, a key challenge for metallicity gradient theory is to provide a joint explanation for both the global and spatially-resolved metallicities. Given these complexities, most chemical evolution models that can describe metallicity gradients are limited to Milky Way-like local spiral galaxies. Hence, they do not provide information on the cosmic evolution of metallicity gradients. As we show later in this thesis, the evolution of metallicity gradients is inherently connected to galactic winds and enrichment of the CGM. Thus, incorporating galactic winds and their enrichment is another important aspect of modeling metallicity gradients that several models have ignored.

Cosmological simulations have now started exploring metallicity gradients in galaxies, and provide a very rich dataset of simulated galaxies to probe the metal evolution of the disc as well as the CGM (e.g., Vogelsberger et al. 2014; Schaye et al. 2015; Dolag et al. 2017; Davé et al. 2019). However, these simulations do not have the resolution to explicitly include the small-scale physics that directly sets the overall

metal yield in galaxies, and they usually rely on sub-grid or empirical modeling of small-scale processes. Connecting cosmological simulations to small-scale physics is extremely important to understand the physics of metal evolution in galaxies, and it remains an active area of research in galaxy evolution (Naab & Ostriker 2017). This is where analytical and semi-analytical models have proved useful, as these computationally-feasible alternatives allow us to have a more explicit control on physical processes that are included, and enable us to explore a wide range of the parameter space. However, such models also suffer from limitations as they are more appropriate for looking at statistical trends and scatter in the data and generally do not contain the physical complexities that individual galaxies go through. All these characteristics introduce some uncertainties in providing predictions for or explaining the observed metallicity gradients.

1.3   Thesis outline

In this thesis, I aim to further our understanding of star formation and galaxy evolution by using metals (or their absence thereof) as tracers. On smaller scales corresponding to molecular clouds and the ISM, I aim to look at the IMF in zero- and low-metallicity environments. On larger scales corresponding to galactic discs, I aim to understand the physics of metal distribution in nearby as well as high-redshift galaxies. The thesis is organised as follows, and all the respective chapters have been published post peer reivew in Monthly Notices of the Royal Astronomical Society.

Chapter 2 presents a calculation detailing the most accurate treatment of the adiabatic index of dust- and metal-free molecular gas. Given that the adiabatic index can potentially impact gas thermodynamics, we check whether an accurate treatment of the adiabatic index results in any significant differences during the formation of the first stars. We use the AMR code FLASH to conduct chemo-hydrodynamical simulations for this purpose.

Chapter 3 investigates the role of magnetic fields in the formation of the first stars, and how magnetic fields can impact the IMF of the first stars. Understanding the role of different physical processes in shaping the Population III IMF is critical to understanding the production of the first metals, and metal enrichment in the early Universe, as the mass distribution of massive stars directly sets the overall metal yield. We use FLASH to perform the largest suite of chemo-MHD simulations of Population III star formation ever done to statistically study the impact of magnetic fields on the IMF.

Chapter 4 builds upon the results of Chapter 3 to provide an explanation for why magnetic fields play an important role in setting the IMF of the first stars. In this chapter, we conduct high resolution simulations to resolve the small-scale and large-scale dynamo processes that act in unison to exponentially amplify magnetic fields. This amplification that occurs in a very short time is responsible for the role magnetic fields play in the IMF of the first stars.

Chapter 5 presents analytical models that span a wide range of metallicity (from primordial-like to super-Solar like) in an effort to explore the transition in the IMF as a function of metallicity. We use these model to provide an answer for a pertinent question in astronomy: when did the IMF become bottom-heavy as the Universe increased in metal abundance over time?

Chapter 6 looks at the role of metals from a galactic perspective. It presents our first-principles modeling of the physics of spatially-resolved metal distributions in galaxies, and how metallicity gradients contain a wealth of information about processes that shape up galaxy evolution. We also present some applications of our model that look at the evolution of metallicity gradient in the Milky Way, as well as in all star-forming galaxies as a function of redshift.

Chapter 7 further uses the model presented in Chapter 6 to provide the joint first explanation for the well known mass-metallicity relation and the mass-metallicity gradient relation in local galaxies. The comparison between the data and the model also provides some interesting predictions that can be validated against future observations.

Chapter 8 uses the model presented in Chapter 6 to investigate the dependence of metallicity gradients on gas kinematics in high-redshift galaxies. In this observations + theory work, we first establish the trends between metallicity gradients and gas kinematics from restframe optical observations of high-redshift galaxies, and then use our model to provide an explanation for the observed trends.

Finally, we provide our conclusions in Chapter 9.

The role of the H_2 adiabatic index in the formation of the first stars

Context and Contribution

This chapter has been previously published as **'The role of the H_2 adiabatic index in the formation of the first stars', by Piyush Sharda, Mark R. Krumholz, and Christoph Federrath, 2019, MNRAS, 490, 513***. The work is presented here exactly as in the publication. I have ran the simulations described in this paper, and post-processed the simulation data for further analysis. I have written the majority of the paper, with inputs and suggestions from co-authors.*

Abstract

The adiabatic index of H_2 (γ_{H_2}) is non-constant at temperatures between $100 - 10^4 \, \mathrm{K}$ due to the large energy spacing between its rotational and vibrational modes. For the formation of the first stars at redshifts 20 and above, this variation can be significant because primordial molecular clouds are in this temperature range due to the absence of efficient cooling by dust and metals. We study the possible importance of variations in γ_{H_2} for the primordial initial mass function by carrying out 80 3D gravito-hydrodynamic simulations of collapsing clouds with different random turbulent velocity fields, half using fixed $\gamma_{H_2} = 7/5$ in the limit of classical diatomic gas (used in earlier works) and half using an accurate quantum mechanical treatment of γ_{H_2}. We use the adaptive mesh refinement code FLASH with the primordial chemistry network from KROME for this study. The simulation suite produces almost 400 stars, with masses from $0.02 - 50 \, \mathrm{M}_\odot$ (mean mass $\sim 10.5 \, \mathrm{M}_\odot$ and mean multiplicity fraction ~ 0.4). While the results of individual simulations do differ when we change our treatment of γ_{H_2}, we find no statistically significant differences in the overall mass or multiplicity distributions of the stars formed in the two sets of runs. We conclude that, at least prior to the onset of radiation feedback, approximating H_2 as a classical diatomic gas with $\gamma_{H_2} = 7/5$ does not induce significant errors

in simulations of the fragmentation of primordial gas. Nonetheless, we recommend using the accurate formulation of the H_2 adiabatic index in primordial star formation studies since it is not computationally more expensive and provides a better treatment of the thermodynamics.

2.1   Introduction

Stars are usually classified into three populations based on their metal content (Bond 1981; McDowell 1986). The generation of stars with the highest metallicity is known as Population I. Population II corresponds to stars that have relatively less metal content, and Population III is the hypothetical limit of stars that have no metals. Population III stars, also known as first stars, are believed to have formed in dust-free environments out of primordial species produced by the Big Bang (Saslaw & Zipoy 1967; Galli & Palla 1998). They are further classified into Population III.1 (the first generation of stars) and Population III.2 (primordial stars affected by radiation from other stars, see McKee & Tan 2008; De Souza et al. 2011). While contemporary star formation is well studied thanks to observations and simulations, the formation of the first generation of stars in the Universe still remains a mystery because of the lack of direct observations at spatially resolved scales beyond $z > 11.1$ (Oesch et al. 2016), and of zero-metallicity stars, if any, in the Local Group (Griffen et al. 2018; Hartwig et al. 2019).

The first stars are believed to have formed between redshifts $15 \leq z \leq 30$ (see reviews by Abel et al. 2002; Bromm & Larson 2004; Glover 2005; Ciardi & Ferrara 2005; Bromm 2013; Karlsson et al. 2013), at the center of dark matter minihalos that have high baryonic densities of the order of $\sim 10^4 \, \mathrm{cm}^{-3}$ (Abel et al. 2002; Bromm et al. 2002). By this epoch, the first clouds of neutral hydrogen had formed after recombination (Peebles 1968). Since the first clouds only contained primordial elements (H, He, Li and their isotopes), cooling during the collapse is inefficient as compared to contemporary star formation where dust and metal lines are present (Omukai et al. 2005; Bromm 2013).

Early simulations of the first stars did not have a long dynamical range in time and thus could not follow the large-scale evolution once the primordial clouds started to collapse. They showed no fragmentation, leading to the belief that the first stars were very massive and evolved in isolation (Bromm et al. 2002; Abel et al. 2002; Yoshida et al. 2006). Once numerical techniques were improved to include modules like sink particles and work with better and more efficient solvers, it became possible to simulate farther in time past the initial collapse. Since then, fragmentation has

been observed in almost all simulations of the first stars (for example, Clark et al. 2011b; Stacy et al. 2012; Hirano et al. 2014, 2015). However, it occurs very close to the central protostar, on scales as small as a few AU (Kratter & Matzner 2006; Susa et al. 2014; Klessen 2018). This is because of the lack of an adiabatic core larger than 1 AU even before protostar formation, as is observed in simulations of contemporary star formation (Larson 1969; Bate 1998). Thus, in the case of the first stars, the circumstellar disc grows gradually and fragmentation occurs near the central protostar. The observation that primordial gas clouds do fragment naturally raises the question of what initial mass function (IMF) this process yields. Determining the IMF of first stars has thus become a central goal of modern first star research (Tumlinson et al. 2004; Schneider et al. 2006b; Susa 2013; Susa et al. 2014; Ishigaki et al. 2018).

In this work, we investigate the sensitivity of this IMF, and closely related quantities such as the multiplicity statistics of first stars, to the thermodynamics of molecular hydrogen. This molecule controls the thermal and chemical evolution of collapsing primordial clouds, and becomes the dominant chemical state of hydrogen once the density is high enough. While there has been extensive work on the importance of H_2 as a coolant, no published 3D simulations of first star fragmentation to date have systematically investigated another potential role it might play in controlling fragmentation, via the dependence of the adiabatic index on the H_2 mass fraction and temperature.

The adiabatic index is potentially important to the IMF because it determines how easy or hard it is to compress the gas, and thus how much the gas resists fragmentation. A gas with higher γ is more resistant to fragmentation because, for the same level of pressure fluctuation, it will respond with a smaller density fluctuation than a gas with lower γ. In the context of contemporary star formation, Boley et al. (2007) show that simulations of gravitationally-unstable protoplanetary discs using a correct quantum treatment of γ_{H_2} produce qualitatively different amounts of fragmentation than those where γ_{H_2} is approximated as constant; Bitsch et al. (2013) show that there are also differences in the subsequent accretion and migration of the fragments. Vaytet et al. (2014) show that variations in γ_{H_2} lead to changes in the dynamics of the first Larson (1969) cores that result from collapse. Gravitationally-unstable discs seem particularly sensitive to the adiabatic index of the gas, and this is precisely the mode of fragmentation that determines the IMF of the first stars. Moreover, first star formation occurs in gas clouds at temperatures of hundreds of Kelvin (Omukai et al. 2005), which is precisely the temperature range at which the rovibrational modes of H_2 first become excited, and thus the departure from classical

behaviour is largest. However, no analogous studies have been performed to look for systematic effects of γ_{H_2} on formation of the first stars, where at least potentially the effects of variable γ_{H_2} are much larger. The few studies that do include non-constant γ_{H_2} (Silk 1983; Omukai & Nishi 1998; Abel et al. 2002; Yoshida et al. 2006; Ahn & Shapiro 2007; McKee & Tan 2008; Greif 2014; Stacy et al. 2016) have not systematically studied its effects, and have also included only variability due to vibrational degrees of freedom, not rotational ones. Our goal in this paper is to carry out a comprehensive study comparing a full quantum mechanical treatment of the H$_2$ molecule to the classical approximation adopted in most earlier 3D simulations.

This paper is organised as follows: Section 2.2 discusses how we compute the adiabatic index of H$_2$; Section 2.3 describes the simulation setup and the physics included; Section 2.4 presents our results and findings; finally, Section 2.5 summarises our analysis.

2.2 Adiabatic Index of H$_2$

The adiabatic index of a gas partly composed of H$_2$ depends on the temperature, mass fraction of H$_2$ and the ratio of ortho to para H$_2$ (which are the two nuclear spin orientations of the molecule, see Omukai & Nishi 1998; Glover & Abel 2008; Matthews et al. 2011). To calculate this dependence, we follow the approach of Krumholz (2014a), though equivalent calculations may be found in Boley et al. (2007) and Tomida et al. (2013). Consider a gas containing multiple chemical species, each with mass fraction x_s, such that $\sum_s x_s = 1$. The relation between the net adiabatic index of all species and density is

$$\gamma_{net} = \frac{d \ln P}{d \ln \rho} \tag{2.1}$$

where P is the pressure. ρ is the volume density, which is related to the number density (n_s) and mass fraction (x_s) as

$$n_s = \frac{x_s \rho}{A_s m} \tag{2.2}$$

where m is one a.m.u., and A_s is the mass number of the species. The net adiabatic index for the system can be written as the ratio of specific heats at constant pressure and volume

$$\gamma_{net} = \frac{c_p/k_B}{c_v/k_B} = \frac{c_v/k_B + 1}{c_v/k_B}, \tag{2.3}$$

where c_p and c_v are the specific heats per H nucleon at constant volume and pressure, respectively. We obtain these from the internal energy per unit volume,

$$e_{\mathrm{g}} = n_{\mathrm{H}} k_{\mathrm{B}} T \frac{\mathrm{d}\ln z}{\mathrm{d}\ln T}, \tag{2.4}$$

where z is the ensemble partition function given by the product of partition functions for the translational, rotational and vibrational degrees of freedom $z = Z_{\mathrm{trans}} Z_{\mathrm{rot}} Z_{\mathrm{vib}}$, T is the temperature and n_{H} is the number density of H nuclei (which is invariant under chemical reactions). The specific heat per H nucleon at constant volume is related to e_{g} by

$$\frac{c_v}{k_B} = \frac{1}{n_{\mathrm{H}}} \frac{\partial e_{\mathrm{g}}}{\partial T}. \tag{2.5}$$

Using partition functions and mass fractions for ortho and para H_2 ($Z_{\mathrm{rot}} = Z_{\mathrm{pH_2}} Z_{\mathrm{oH_2}}$, as defined below), this becomes:

$$\begin{aligned}
\frac{c_v}{k_{\mathrm{B}}} = \frac{3}{2} &+ x_{\mathrm{pH_2}} \frac{\partial}{\partial T}\left(\frac{T^2}{Z_{\mathrm{pH_2}}} \frac{\partial Z_{\mathrm{pH_2}}}{\partial T}\right) + x_{\mathrm{oH_2}} \frac{\partial}{\partial T}\left(\frac{T^2}{Z_{\mathrm{oH_2}}} \frac{\partial Z_{\mathrm{oH_2}}}{\partial T}\right) \\
&+ (x_{\mathrm{oH_2}} + x_{\mathrm{pH_2}})\frac{\theta_{\mathrm{vib}}^2 \exp(-\theta_{\mathrm{vib}}/T)}{T^2[1 - \exp(-\theta_{\mathrm{vib}}/T)]^2}
\end{aligned} \tag{2.6}$$

where $x_{\mathrm{H_2}} = x_{\mathrm{oH_2}} + x_{\mathrm{pH_2}}$, and we have assumed that all species other than H_2 have no internal degrees of freedom. While an exact calculation of the partition function should also include contributions from electronic and nuclear degrees of freedom, these modes are not excited in the range of temperatures relevant to this study; hence they can safely be ignored, and we can simply adopt $\gamma = 5/3$ for monoatomic species like He. Similarly, we ignore the effects of overlap between higher vibrational levels, vibrational continuum and electronically excited levels of H_2 that occur at temperatures much higher than those we study in this work. We also use a fixed ortho:para ratio for reasons we discuss further below. The last term in equation 2.6 corresponds to vibrational degrees of freedom of H_2, where $\theta_{\mathrm{vib}} = 5987$ K (Draine et al. 1983).

The rotational partition functions of para- and ortho-H_2 are given by

$$Z_{\mathrm{pH_2}} = \sum_{J\,\mathrm{even}} (2J+1)\exp\left[-\frac{J(J+1)\theta_{\mathrm{rot}}}{T}\right] \tag{2.7}$$

$$Z_{\mathrm{oH_2}} = e^{2\theta_{\mathrm{rot}}/T}\left(\sum_{J\,\mathrm{odd}} 3(2J+1)\exp\left[-\frac{J(J+1)\theta_{\mathrm{rot}}}{T}\right]\right) \tag{2.8}$$

where $\theta_{\mathrm{rot}} = 85.4$ K (Black & Bodenheimer 1975). The leading exponential term in the ortho H_2 partition functions ensures that rotation only contributes to internal

energy when the rotational states are excited (Boley et al. 2007).

Figure 2.1 shows the variation of the net adiabatic index of the system (γ_{net}) as a function of temperature (T) at different mass fractions of H_2 (x_{H_2}), assuming an ortho- to para-ratio of 3:1 (see below). When the gas is completely molecular (*i.e.,* $\gamma_{H_2} = \gamma_{\mathrm{net}}$), it can be described as monoatomic (3 translational degrees of freedom) at low temperatures ($T < 50\,\mathrm{K}$) with $\gamma_{H_2} = 5/3$, and diatomic at high temperatures (3 translational, 2 rotational and 2 vibrational degrees of freedom) where the continuum limit is reached ($T \gtrsim 10^4\,\mathrm{K}$) with $\gamma_{H_2} = 9/7$.[1] Primordial star formation sits squarely in between these two regimes, where first the rotational modes are excited during collapse and then the vibrational modes are excited in accretion shocks around first stars, leading to the complex behaviour of γ_{H_2} as a function of T shown in Figure 2.1.

It should be noted that our calculation of the adiabatic index depends on our choice of the ratio of ortho-H_2 to para-H_2, and any possible dependence of this ratio on temperature or density. However, Glover & Abel (2008) show that the ortho-to-para is not very sensitive to temperature at the redshifts important for Population III star formation, and the standard assumption of an ortho-to-para ratio of 3:1, *i.e,* $x_{oH_2} = 3x_{pH_2}$, as usually found in the present-day Universe (Sternberg & Neufeld 1999), produces results similar to a more detailed treatment. Due to interconversions facilitated by collisions with H^+ in the primordial gas, this ratio drops down to 0.25:1 at $z \approx 20$ in environments where the mass fraction of H_2 drops to 10^{-6} (Flower & Pineau des Forêts 2000; Flower & Harris 2007), but at such low H_2 abundances, the value of γ_{net} is essentially independent of γ_{H_2} in any event (Figure 2.1). Keeping these studies in mind, we fix the ortho-to-para ratio to be 3:1 for our simulations.

2.3 Numerical and Physical Ingredients

2.3.1 Numerical Hydrodynamics

We use the adpative mesh refinement (AMR, Berger & Colella 1989) code FLASH (Fryxell et al. 2000; Dubey et al. 2008). We utilize an approximate Riemann solver for our hydrodynamic simulations (Bouchut et al. 2007, 2010) which was developed for FLASH by Waagan (2009) and Waagan et al. (2011). We treat the self-gravity of the gas with a tree-based solver (Wünsch et al. 2018). We use the sink particle technique developed for FLASH (Federrath et al. 2010a, 2011a, 2014a) to follow the evolution of collapsing gas at high resolutions at late times. Sink particles are

---

[1] Since H_2 is collisionally dissociated at temperatures well below 10000 K, in reality it never reaches the high temperature continuum limit.
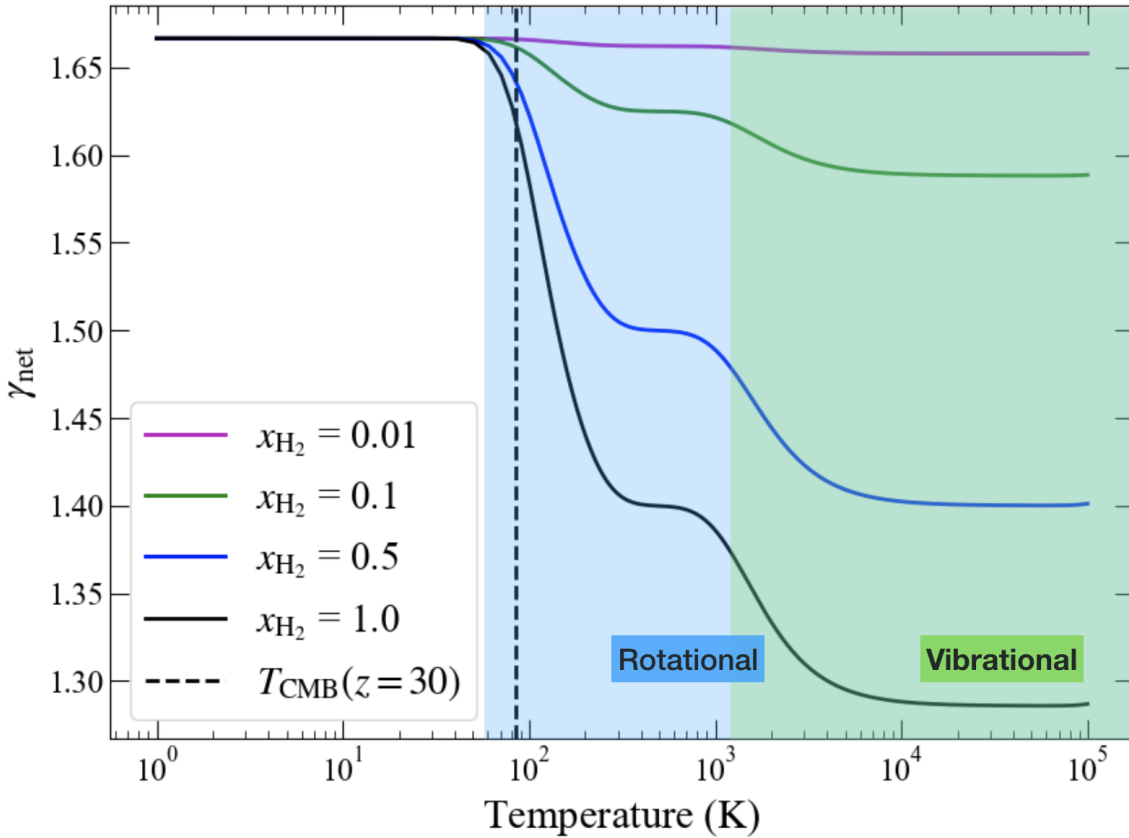
Figure 2.1: Net adiabatic index (γ_{net}) as a function of temperature for primordial gas with varying fractional abundances of H_2, assuming an ortho- to para-ratio of 3:1 and no other species have any internal degrees of freedom. The dashed-black line marks the cosmic microwave background (CMB) floor at $z = 30$. The temperature range indicated in blue is dominated by the rotational degrees of freedom of H_2 whereas that in green is dominated by its vibrational degrees of freedom. The deviation of γ_{net} from the standard values is greatest for a completely molecular gas, and negligible if $x_{H_2} \lesssim 0.01$.

frequently used in hydrodynamic simulations of star formation as a proxy for stellar sources (Bate et al. 1995; Krumholz et al. 2004; Jappsen et al. 2005; Wang et al. 2010; Padoan & Nordlund 2011; Gong & Ostriker 2013; Hubber et al. 2013b; Bleuler & Teyssier 2014; Jones & Bate 2018). These Lagrangian particles can travel inside the grid, accrete gas and contribute to the gravitational potential in the region. The sink particle method developed in Federrath et al. (2010a) uses a rigorous set of checks to ensure that only Jeans unstable gas that is converging and bound and has a gravitational potential minimum in cells at the sink density threshold at the highest level of refinement is converted into a sink, thus avoiding artificial fragmentation. The density threshold where sink particles are created at the standard resolution used in our simulations (see below) is $1.45 \times 10^{-11}\,\mathrm{g\,cm^{-3}}$. We use the distribution of sink masses to study fragmentation around the primary sink. As the numerical

scale we use in this work is much larger than the radii of actual protostars, we do not allow the merging of sink particles in our simulations (see, for example, Susa et al. 2014; Riaz et al. 2018).

In order to completely encompass the cloud that collapses to form stars, we define a cubical box of size $L = 2.4\,\mathrm{pc}$ to run our simulations. We set the boundary conditions to be outflow-type to enable mass-loss from the cloud, if any, during star formation[2]. The boundary condition for gravity is 'isolated' (*i.e.*, not periodic). We use a base grid of 8^3 cells plus 14 levels of refinement in this work, which results in a unit cell length at the highest level of refinement of $dx = 7.6\,\mathrm{AU}$ and a maximum resolvable density $n \sim 10^{15}\,\mathrm{cm}^{-3}$; the maximum effective resolution of the simulation is 65536^3. This choice is motivated by optimizing the trade-off between higher resolution and computational costs. We repeat three representative simulations with different random seeds of turbulence (see Section 2.3.3) at 12, 13, 14 and 15 levels of refinement to check numerical convergence; we present the results of our convergence study in Appendix A and show that it is reasonable to believe convergence has been achieved to first order at resolution 14.

Numerous studies have shown that it is important to resolve the scales at which turbulence can amplify magnetic fields through small-scale dynamo action (Sur et al. 2010; Federrath et al. 2010a; Schleicher et al. 2010; Schober et al. 2012a; Brandenburg et al. 2012; Schober et al. 2012b; Bovino et al. 2013b; Latif et al. 2013b). The required resolution in this case is at least 30 cells per Jeans length (Federrath et al. 2011c), which is 7.5 times more than the Truelove criterion to avoid artificial collapse in gravito-hydrodynamic simulations (Truelove et al. 1997). Although we do not include magnetic fields in this work, we satisfy the criterion suggested by Federrath et al. (2011c) by using 32 cells per Jeans length, to maintain self-consistency with other works (P. Sharda et al., in prep.). In fact, using less than 30 grid cells per Jeans length leads to underestimates not only of the amplification of magnetic fields, but also of the amount of kinetic energy that is resolved on the Jeans scale (Federrath et al. 2011c) and the structure of the gas (for example, the scale height of accretion discs; see Federrath et al. 2014a).

2.3.2 Primordial Chemistry

We utilize the KROME package for primordial chemistry, which has been developed to include chemistry in hydrodynamic simulations for astrophysical applications (Grassi et al. 2014). KROME uses a subroutine of pre-designed and re-writable chemical networks for various astrophysical phenomena which can be embedded

---

[2]Note that outflow in FLASH also means that inflow can occur.

in numerical codes like FLASH. It uses the differential solver DLSODES (Hindmarsh 1980; Radhakrishnan & Hindmarsh 1993) to solve the reaction network and evolves the temperature and density of the system in accordance with the chemistry and the specified heating and cooling processes (Grassi et al. 2013; Bovino et al. 2013a). The network of primordial chemical reactions we use in our simulations is `react_primordial_3` which is the most robust primodial chemistry network and includes the following species: H, H_2, H^+, H^-, He, He^+, He^{++}, H_2^+ and e^-.

We include a variety of chemical and radiative heating and cooling processes, all of which are computed by KROME. The cooling processes we include are: 1) cooling by H_2 through excitation of rovibrational modes in H_2 and subsequent emission of photons, 2) cooling through collisionally induced emission (CIE) which occurs due to the formation of 'supermolecules' with finite electric dipole from collisions between different molecules, 3) cooling due to endothermic chemical reactions, 4) atomic cooling due to collisional ionisation, collisional excitation and recombination of primordial species and bremsstrahlung emission from ionised species, and 5) cooling due to Compton scattering of cosmic microwave photons by free electrons. In addition, we impose a constraint on the minimum temperature such that it never decreases beyond the cosmic microwave background temperature at the assumed redshift ($T_{CMB}(z = 30) = 84.63\,\mathrm{K}$). The heating processes we include are 1) chemical heating generated from reaction enthalpies and 2) compressional heating (as computed by the hydrodynamics module).

At high densities, the cooling rates are suppressed by opacity effects. For cooling due to H_2, we approximately account for this by using the H_2 cooling function provided by Ripamonti & Abel (2004). This approximation diverges from the more detailed treatment of opacity by Hirano & Yoshida 2013 (see also, Greif 2014; Hartwig et al. 2015) when $x_{H_2} \lesssim 0.5$. However, in practice these cooling functions differ only where the gas is dense enough to be optically thick, and has also been heated by adiabatic compression to the point where H_2 undergoes significant collisional dissociation. Such conditions prevail only at densities $\gtrsim 10^{16}$ cm^{-3}, an order of magnitude higher than those we resolve. Thus, over the density range we cover, the Ripamonti & Abel (2004) and Hirano & Yoshida (2013) H_2 cooling functions are very similar. Apart from this, the Lyman-α cooling formulation that we include in our simulations (in KROME) diverges from its true value in optically-thick regimes where both the densities and temperatures are high; such regions constitute the accretion disks around sink particles, as we later show in Section Section 2.4. However, we do not expect this effect to significantly alter the temperature because the Lyman-α cooling rate is extraordinarily sensitive to temperature and only very weakly sensitive to

optical depth (see, for example, Section 2.1 of Ge & Wise 2017); thus even fairly large optical depths alter the temperature relatively little. We also omit cooling due to H^-. While this can be important in regions where H^- is abundant, due to its large cross section, the H^- abundance is very low at densities $\lesssim 10^{15}\,\text{cm}^{-3}$ (Omukai 2001; Van Borm et al. 2014), the highest we resolve in this work.

Our chosen chemical network does not include deuterium, which was also produced by the Big Bang (Epstein et al. 1976). We choose to omit it because deuterium has no significant impact on the adiabatic index because of the low fractional abundance of HD as compared to H or H_2. HD can be an important coolant in low density regions ($10^5 \le n \le 10^8\,\text{cm}^{-3}$) at temperatures of the order of $100\,\text{K}$ (Galli & Palla 2002; Nagakura & Omukai 2005; Yoshida et al. 2007) in cases where the primordial gas does not go through an ionized phase (Johnson & Bromm 2006; Glover & Abel 2008). However, as we show below, our simulations start at $n \sim 10^4\,\text{cm}^{-3}$ and fragmentation occurs at densities that are 10^{4-5} times the density range quoted above. Similarly, we do not include primordial Li (Fields 2011), since it has been shown that its contribution to both chemistry and cooling is unimportant (Lepp & Shull 1984; Lepp et al. 2002; Galli & Palla 2013; Liu & Bromm 2018).

2.3.3 Initial Conditions

We initiate our simulations by setting up a spherical cloud core with a homogeneous density. Taking inspiration from cosmological simulations that form dark matter minihalos where baryonic cores form in overdense regions, we begin from a core of mass $M_{\text{core}} = 1000\,\text{M}_\odot$ and radius $R_{\text{core}} = 1\,\text{pc}$ (Abel et al. 2000, 2002; Bromm et al. 2002). These parameters are similar to that for Bonnor-Ebert spheres on the verge of collapse, and are often used in such simulations as initial conditions (for example, Machida & Doi 2013; Susa et al. 2014; Hirano et al. 2014; Stacy & Bromm 2014; Hummel et al. 2016; Riaz et al. 2018). Our initial density ($n_{\text{core}} = 9050\,\text{cm}^{-3}$) is thus in good agreement with the overdensity observed in cosmological simulations. Based on 1D calculations of primordial cloud collapse using KROME that we run from low densities ($n = 1\,\text{cm}^{-3}$) and temperatures ($T = 100\,\text{K}$), we find that the temperature reaches 265 K by the time the density has reached $n \sim 10^4\,\text{cm}^{-3}$. Thus, we set $T_{\text{core}} = 265\,\text{K}$. This 1D model also sets the initial mass fractions of all species for our simulations. Specifically, we use $x_{\text{H}} = 0.7502$, $x_{\text{H}_2} = 0.0006$ and $x_{\text{He}} = 0.2492$, which also agree well with initial mass fractions for several other simulations at the same initial temperature and density; the He abundance is that predicted by the Big Bang nucleosynthesis (Steigman 2007; Galli & Palla 2013). To ensure the simulation box is in pressure equilibrium, we set the corresponding

Table 2.1: Initial conditions of the spherically homogeneous primordial cloud.

Parameter	Symbol	Value
Cloud Mass	M_{core}	$1000\,M_\odot$
Cloud Radius	R_{core}	$1\,pc$
Cloud Number Density	n_{core}	$9050\,cm^{-3}$
Cloud Temperature	T_{core}	$265\,K$
Rotational / Gravitational Energy	E_{rot}/E_{grav}	0.03
Mass Fraction of H	x_H	0.7502
Mass Fraction of H_2	x_{H_2}	0.0006
Mass Fraction of He	x_{He}	0.2492
CMB Temperature at $z = 30$	T_{CMB}	$84.63\,K$
Turbulence	v_{rms}	$1.84\,km\,s^{-1}$
Sound Speed	c_s	$1.84\,km\,s^{-1}$

background density and temperature to be 100 times lower and higher, respectively. We put the initial core into solid body rotation around the $\hat{z}$ axis, with the initial angular velocity set such that the rotational energy is 3 per cent of the gravitational energy. This choice is motivated by the angular momentum of minihalos observed in cosmological simulations (Bromm et al. 2002; Yoshida et al. 2006), and is roughly what is expected for a random turbulent field (Goodman et al. 1993; Burkert & Bodenheimer 2000; Lewis & Bate 2018).

Our initial velocity includes a random turbulent component on top of the organised rotational field. We only change the random seed value of turbulence between different runs. Our reasons for including turbulence are two-fold: 1) cosmological simulations show that turbulence is driven in dark matter minihalos by the motion of baryons towards the center of the minihalo, leading to the formation of overdense regions ($n \sim 10^4\,cm^{-3}$) where collapse takes place (Greif et al. 2008; Prieto et al. 2012; Cornuault et al. 2018); and 2) turbulence can also be generated by streaming velocities between the dark matter and baryons (Fialkov et al. 2014) or primordial magnetic fields (Brandenburg et al. 1996; Kahniashvili et al. 2016). Taking this into account and following Greif et al. (2008), we introduce rms velocity fluctuations (v_{rms}) equal to the sound speed (c_s) in the simulation box (*i.e.*, we set an initially sonic turbulence with Mach 1; see also, Clark et al. 2011a; Schober et al. 2012a; Riaz et al. 2018). The initial turbulent velocity field that we add has a power spectrum $P_v \sim k^{-1.8}$ from wavenumbers $k/(2\pi/L) = 2 - 20$ where L is the side length of the computational domain. We choose the above scaling to model sonic turbulence that we include, which lies between the Kolmogorov turbulence ($k^{-1.67}$, for incompressible subsonic fluids) and Burgers turbulence (k^{-2}, for compressible supsersonic fluids) and has been studied in detail in numerous works (for example,

Kritsuk et al. 2007; Federrath 2013a). We summarise all properties of our initial conditions in Table 2.1.

2.4 Results

We carry out two sets of simulations. One set uses a fixed value $\gamma_{H_2} = 7/5$, as is the common practice in first stars simulations; we refer to these runs as *Fixed* γ_{H_2}. The second set uses a value of γ_{H_2} computed via a full quantum mechanical treatment, as described in Section 2.2; we refer to these as the *Variable* γ_{H_2} simulations. We carry out 40 realisations of each type of simulation, using different turbulent velocity fields. Velocity fields are matched in pairs of fixed and variable γ_{H_2} simulations, so the same 40 turbulent fields are used in each simulation set. We note that simulations with variable γ_{H_2} are not computationally expensive, and take the same time and resources as those with fixed γ_{H_2}. Thus, irrespective of the results, we highly recommend variable γ_{H_2} formulation be used for future studies of primordial star formation since it is more accurate. We define a sink formation efficiency

$$\text{SFE} = \frac{\sum M_{\text{sink}}}{M_{\text{core}}} \tag{2.9}$$

and present all analysis at SFE = 5%. In other words, the analysis and figures we present is at the time when the sink particles have collectively accreted 5 per cent of the initial cloud mass. The reason for this is radiation feedback, which is not included in our simulations, can inhibit the growth of massive protostars $\gtrsim 25\,\text{M}_\odot$ (Hosokawa et al. 2011b; Schauer et al. 2015; Hosokawa et al. 2016). By limiting our analysis to the time when a relatively small mass has been accreted, we limit ourselves to considering the time before which our simulations will substantially deviate from reality.

2.4.1 Qualitative Outcome

Figure 2.2 shows the density-weighted projections of number density (through the $\hat{z}$ axis) in three representative runs from the fixed and variable γ_{H_2} cases where we find no (top panel), some (middle panel) and high fragmentation (bottom panel), respectively[3]. The white dots marked with black boundaries in each panel represent the locations of sink particles in the corresponding runs. All the projections are focused on the 0.01 pc region around the most massive sink particle. While the

---

[3]A movie showing the evolution of density and γ_{H_2} as collapse and fragmentation occur in a representative run is available as supplementary online material.

runs with no fragmentation after the first sink is formed show a dense accretion disk around it, we detect diverse filamentary and spiral structures around the sink particles in other runs where subsequent fragmentation has occurred. The densities we reach in the simulations are of the order of $10^{15}\,\mathrm{cm}^{-3}$ where we begin to run into optically thick media. However, we expect the optically thick cooling rate approximation used from Ripamonti & Abel (2004) in KROME to remain accurate, because the densest regions that we resolve are almost fully molecular, as we notice from Figure 2.3, which shows the mass fraction of H$_2$ in the same region as illustrated in Figure 2.2. However, where strong accretion shocks are present, H$_2$ has been dissociated into H. The presence of shocks can be seen through the velocity quivers overplotted on the pair of projection maps in the upper panel of Figure 2.3 and the temperature field shown in Figure 2.4. The temperature range has a strict lower-limit given by the CMB temperature at our assumed redshift ($z = 30$, see Table 2.1) as well as a loose upper-limit set by the onset of atomic cooling at temperatures greater than $10^4\,\mathrm{K}$. The typical Mach numbers we find in the runs are between $2 - 35$.

The qualitative outcome of our simulations, including the diversity in level of fragmentation are similar to the results of other simulations of first star formation that include turbulence (Turk et al. 2012; Schober et al. 2012a; Riaz et al. 2018). Stars forming in highly-fragmented systems often experience fragmentation-induced starvation that limits the gas per star available for accretion (Kratter & Matzner 2006; Peters et al. 2010; Girichidis et al. 2012). This effect is more prominent for Population III star formation than for contemporary star formation, due to the smaller distances from the the primary at which fragmentation occurs.

Figure 2.5 shows the joint distributions of number density as a function of temperature, mass fraction of H$_2$ ($x_{\mathrm{H_2}}$), adiabatic index of H$_2$ ($\gamma_{\mathrm{H_2}}$) and the net adiabatic index of all species (γ_{net}) for a representative simulation of the variable $\gamma_{\mathrm{H_2}}$ case. We show these characteristics just before the formation of the first sink particle and at the end point of our simulations where SFE = 5%. We sample these distributions over all the cells within $0.5\,\mathrm{pc}$ of the most massive sink in the simulation at SFE = 5%. The evolution of temperature with density in the collapsing cloud closely follows the one zone model of Omukai et al. (2005), as can be noticed from the mean value of the $n - T$ distribution plotted as the black curve on the top panels in Figure Figure 2.5. For comparison, we also plot the mean value of the corresponding fixed $\gamma_{\mathrm{H_2}}$ case in magenta. It is clear that the mean value between the two cases only slightly differs throughout the collapse of the cloud. The diverging behavior from the mean at higher densities is due to the formation of accretion discs

around sink particles that contain a huge diversity of cells with different positions in the $n - T$ space. There is a clear scatter in the distributions that is a result of variations in temperature and mass fraction of H_2, and the variance of the distribution of γ_{H_2} increases monotonically with time. The distributions have a number of features whose physical origin is easy to understand. At densities $n \lesssim 10^7 \text{ cm}^{-3}$, γ_{net} is very close to 5/3 because the H_2 fraction is tiny, as can be noticed from the second panel of Figure 2.5. Only above this density does an appreciable H_2 fraction build up due to 3-body reactions (Omukai et al. 2005; Glover & Abel 2008; Grassi et al. 2013); it also undergoes rapid dissociation due to high temperatures, thus leading to negligible x_{H_2}. At higher densities, the value of γ_{net} ranges from near 5/3 to near 7/5, tracking both H_2 fraction and temperature. The adiabatic index of the H_2 alone, γ_{H_2}, has a mean value of 1.39 with a standard deviation of 0.02, but there are excursions to both higher and lower values. Excursions to higher γ_{H_2} represent cells that have cooled to near the CMB floor of 85 K, cold enough for the rotational degrees of freedom to freeze out, while those to low γ_{H_2} are preferentially cells at temperatures of a few thousand K, where the vibrational degrees of freedom become excited and γ_{H_2} reaches an absolute minimum $= 9/7 \approx 1.28$.

2.4.2 Mass Distribution of Sinks

We next examine the distribution of sink particle masses in the two sets of simulations. The fixed and variable γ_{H_2} cases form 186 and 192 sink particles in total, respectively. Figure 2.6 shows the probability distribution function (PDF) and cumulative distribution function (CDF) of the sink masses at the instant when 5 per cent of the total initial cloud mass has been accreted (*i.e.*, SFE = 5%), summed over all 80 simulations. We remind the reader that these are not the final masses, since we have not run to 100% accretion, and do not include the feedback that would be required to do so. However, comparison of early fragmentation in the two simulation sets is nonetheless revealing of whether changes in the H_2 adiabatic index matter. We find that the mass distribution peaks around $1 \, M_\odot$ in both the fixed and variable γ_{H_2} cases, and rapidly declines for subsolar masses. Both the fixed and the variable γ_{H_2} cases have sink particles masses between $0.02 - 50 \, M_\odot$, with a mean of $10.5 \, M_\odot$. The two subsets further show quantitatively similar accretion rates of the different sink particles that form in the system. The apparent bi-modality in the distribution caused by the peak at $50 \, M_\odot$ is due to the fact that one-third of all the simulations only form a single massive star (no signs of fragmentation until SFE = 5%). In such runs, the single sink particle accretes $50 \, M_\odot$.

To search for differences between the mass distributions for fixed and variable γ_{H_2},
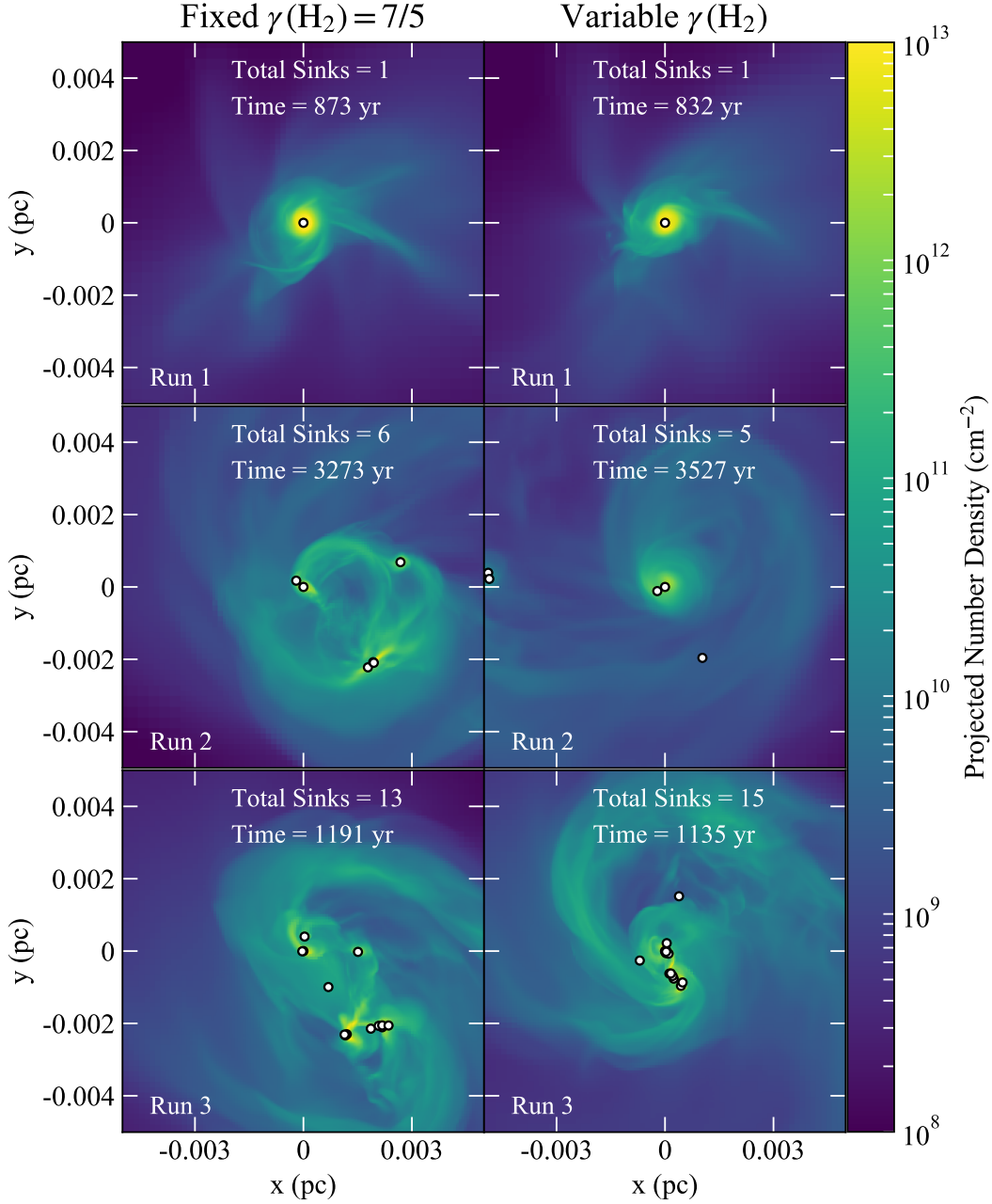
Figure 2.2:   Face-on density-weighted projection maps of the number density (through the $\hat{z}$ axis) for a pair of three representative runs showing no (*top panels*), some (*middle panels*) and high fragmentation (*bottom panels*) for fixed (left) and variable (right) γ_{H_2}, respectively. All the snapshots are taken when the sink(s) (shown in white circles with black boundaries) have collectively accreted 5 per cent of the initial cloud mass (SFE = 5%, see equation 2.9). The snapshots cover a spherical region of radius 0.01 pc, centered on the most massive sink in the simulation. The time printed in each panel is the time since the formation of the first sink particle in each run. Each of the paired fixed and variable γ_{H_2} cases shown begins from identical initial conditions, so the differences seen in the corresponding maps are solely due to variations in γ_{H_2}.
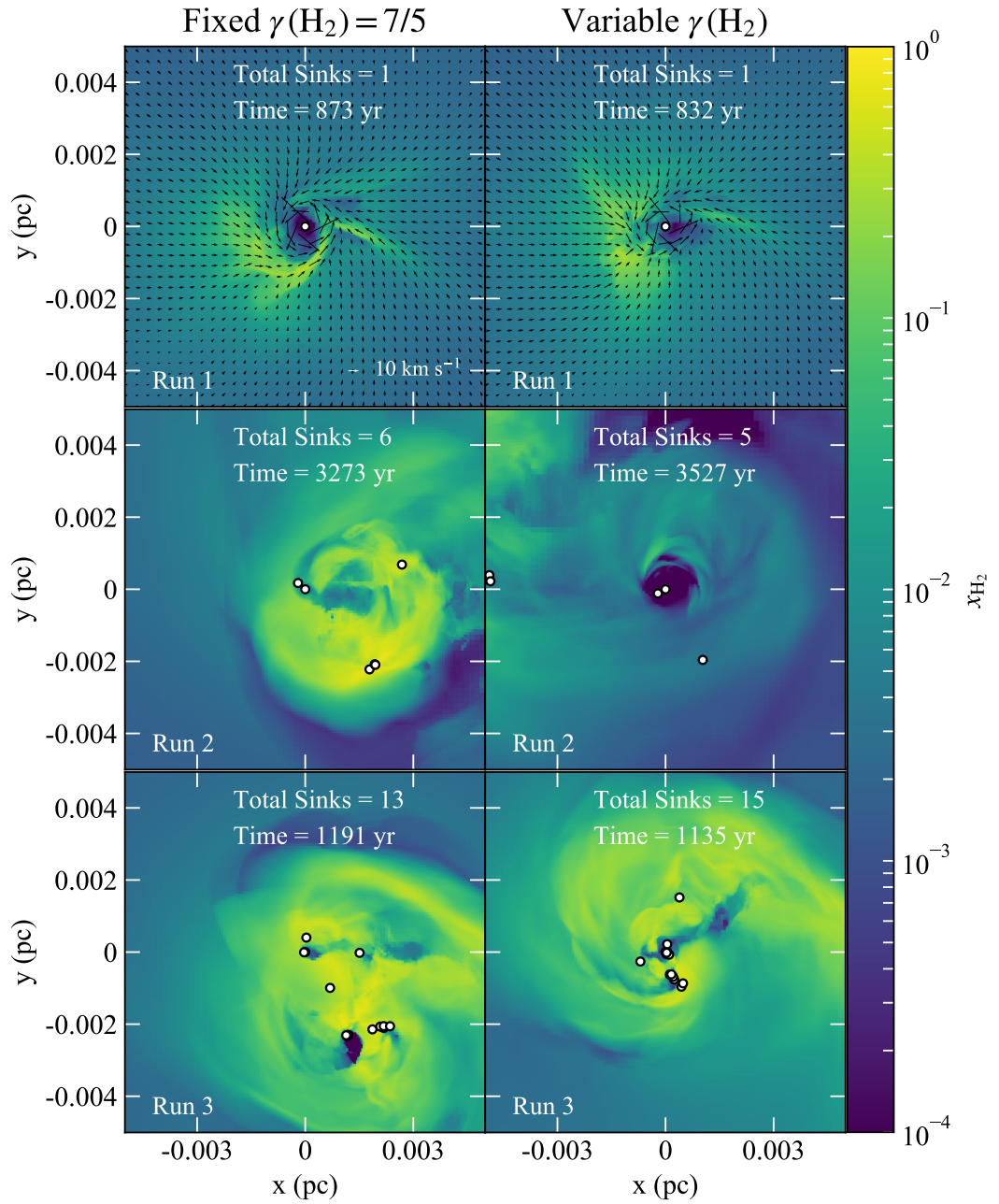
Figure 2.3: Same as Figure 2.2 but showing the density-weighted mean mass fraction of H_2 (x_{H_2}). Quivers plotted on the top panels represent the velocity vectors.
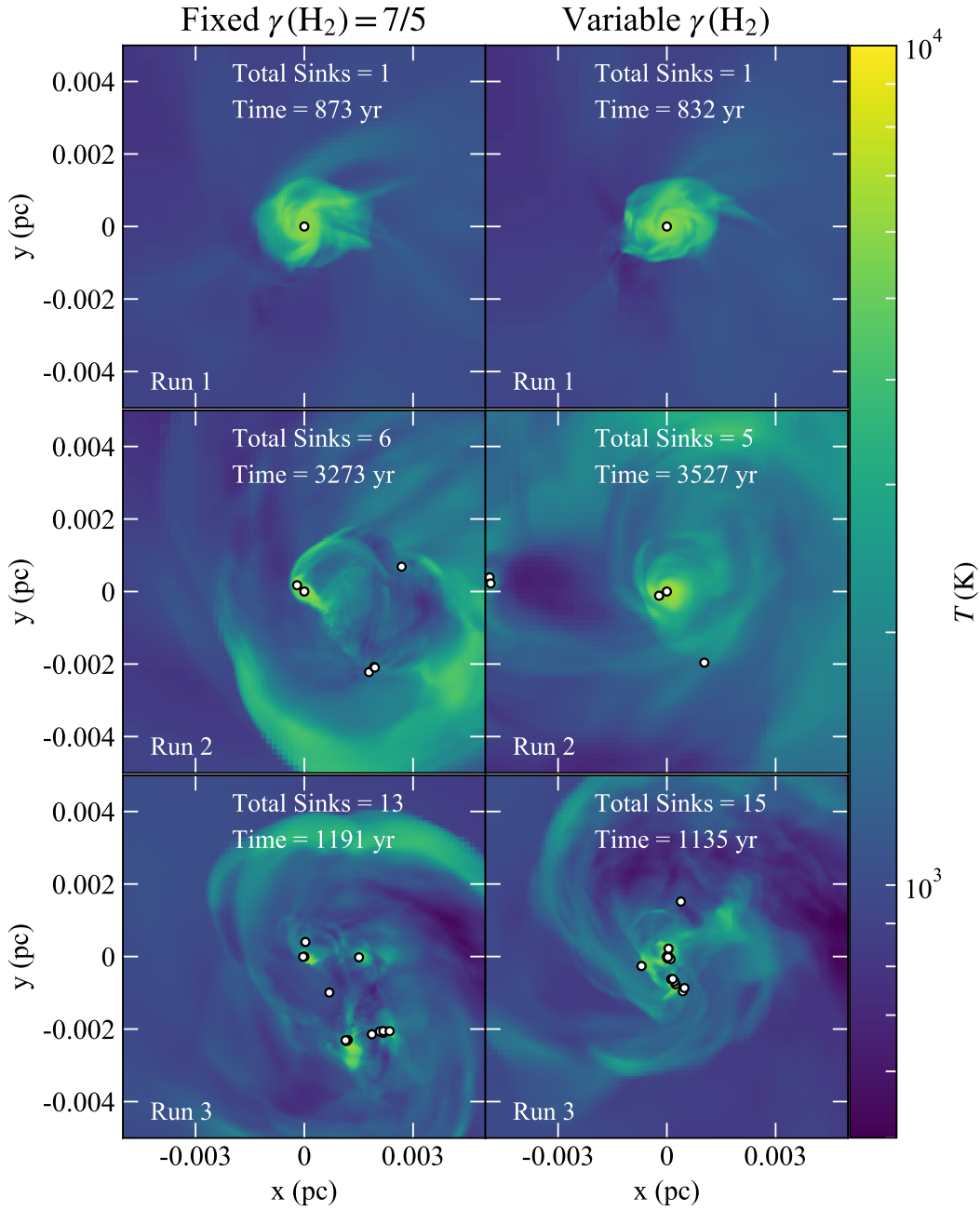
Figure 2.4: Same as Figure 2.2 but showing the density-weighted mean temperature.
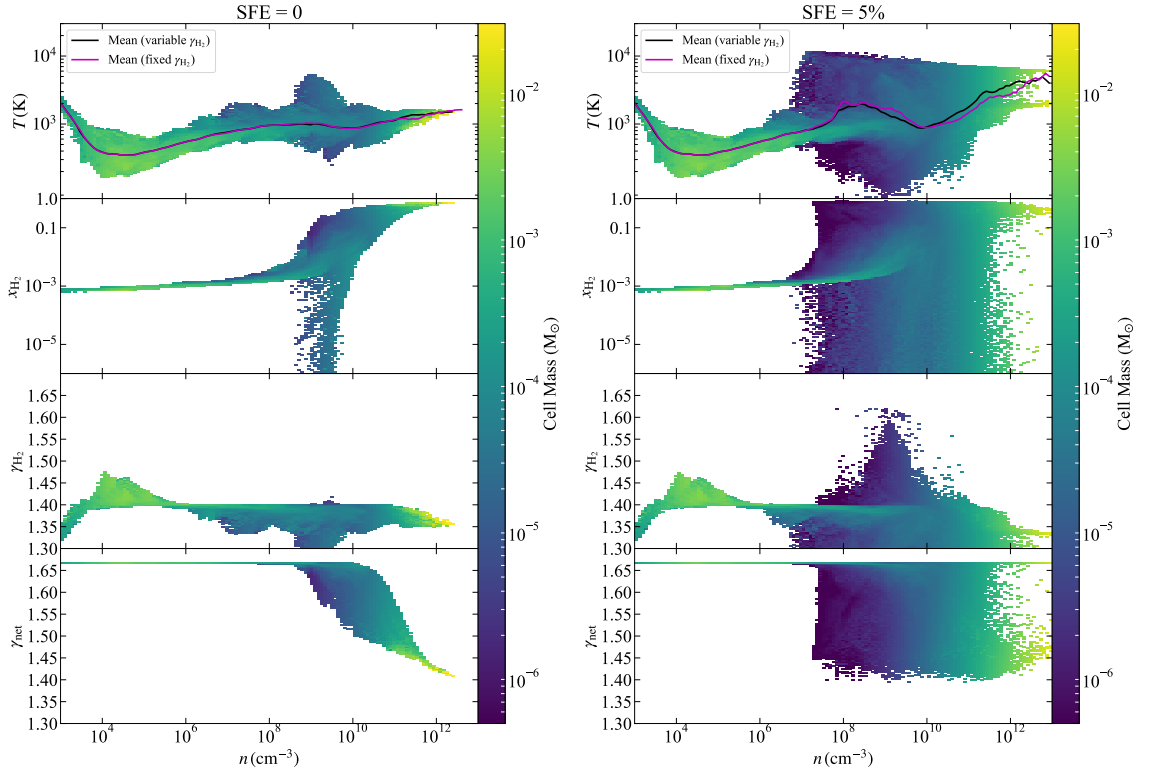
Figure 2.5: Joint distributions of number density (n) as a function of temperature (T, *first panel*), mass fraction of H_2 (x_{H_2}, *second panel*), adiabatic index of H_2 alone (γ_{H_2}, *third panel*) and of all gas (γ_{net}, *fourth panel*) in a spherical volume of radius $0.5\,\mathrm{pc}$ centered on the most massive sink particle. The two figures reflect the characteristics of the system just before the formation of the first sink and at SFE = 5%. They belong to one of the 40 runs randomly selected from the variable γ_{H_2} subset. Also plotted in the top panels is the mean trend of T as a function of n for the variable (black) and the corresponding fixed γ_{H_2} (magenta) run.

we apply the Kolmogorov-Smirnov test (KS-test), which yields a p value of 0.28, implying that we cannot rule out the null hypothesis that the mass distribution is unaffected by our differing treatments of γ_{H_2}. Hence, even though the physical properties of the two cases are different (as discussed in Section 2.4.1), the mass distribution of the sink particles is statistically the same. Of course we cannot rule out the possibility that a difference might become apparent if we performed a larger number of runs, or included feedback enabling the runs to continue further. However, at the level of data available (378 distinct sink particles, measured at SFE = 5%), changing our treatment of γ_{H_2} has no detectable effect.

2.4.3 Multiplicity Fraction

Given that our simulations frequently yield multiple stars (see Figure 2.2), we next examine the multiplicity properties of the stars. A simulation that produces a
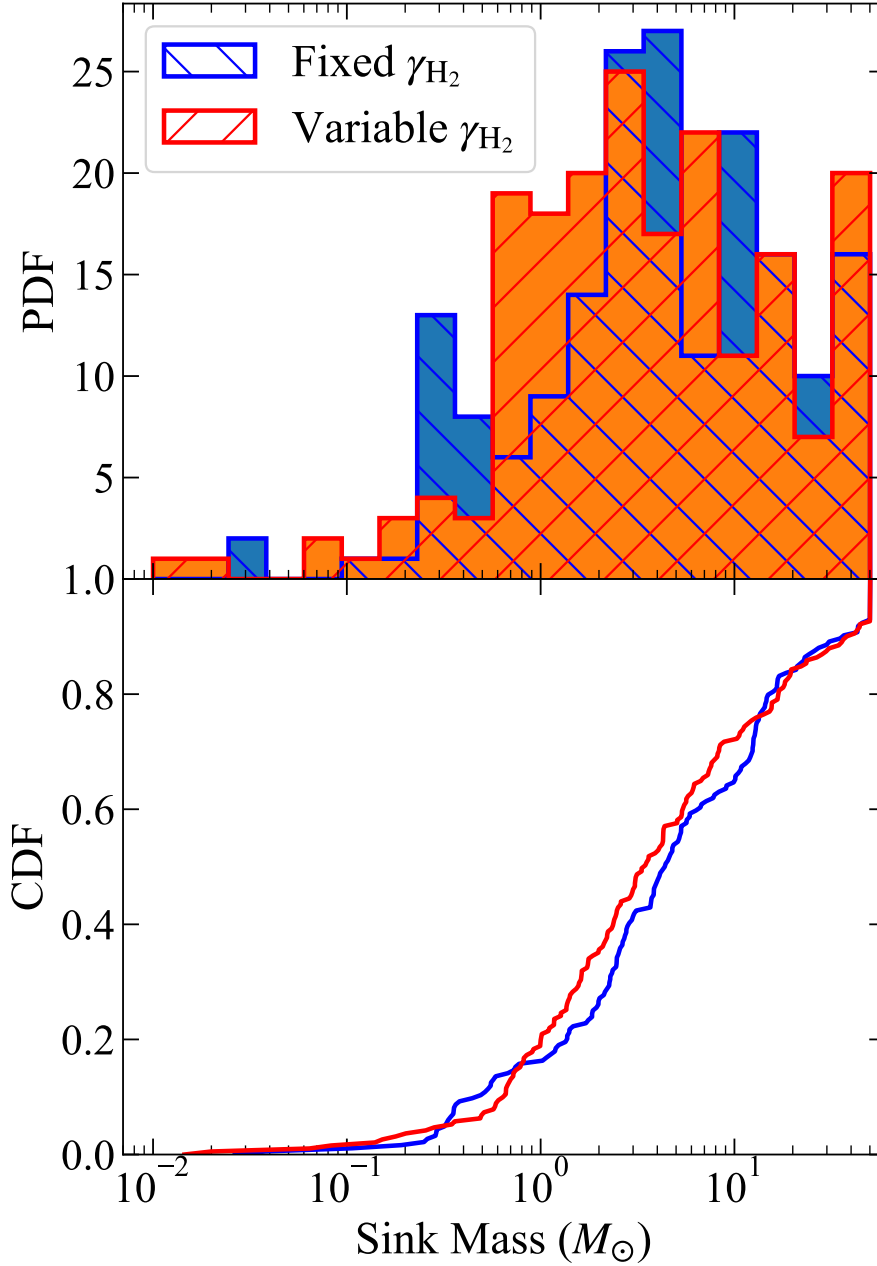
Figure 2.6: Probability distribution function (PDF; *top panel*) and cumulative distribution function (CDF; *bottom panel*) of sink particle masses formed in all 80 simulations. The fixed γ_{H_2} case (blue) forms a total of 186 sink particles up to the point where 5 per cent of the initial cloud mass has been deposited in sink particles in each run (SFE = 5%). The variable γ_{H_2} case (red) creates 192 sink particles. Comparing the two distributions with a KS test yields a p value of 0.28, implying that we cannot rule out the null hypothesis that the two sets of sink particle masses were drawn from the same parent distribution. The peak at $50\,M_\odot$ in the PDF and the corresponding jump in the CDF in both sets of runs is due to runs where no fragmentation occurs, and our condition of stopping at SFE = 5% therefore results in a single sink particle of mass $50\,M_\odot$.

realistic IMF of the first stars should also be able to explain or predict the fraction of Population III binaries or higher-order bound systems (Weidner et al. 2009; Stacy et al. 2010), which is a crucial input to estimates of the rate of black hole or neutron star mergers, and similar high-energy phenomena.

We define multiplicity in our simulations following the algorithm of Bate (2009a). In this algorithm, we recursively find the most bound pair of sinks (*i.e.,* sinks for which the sum of gravitational potential energy and kinetic energy around their common center of mass is most negative) and replace them with a single sink at their center of mass, with mass equal to the sum of masses of the constituent sinks. The velocity of the replaced sink is then the velocity of the center of mass of the constituent pair. Every iteration likewise finds the most bound pair in the system and replaces it with a single sink. This can lead to aggregation of sinks to higher orders, for example, when a sink that replaced two sinks in an earlier iteration now forms the most bound pair with a third sink. The exception to this rule is if aggregating the most bound pair would lead to a quintuple or higher system, which would almost certainly disintegrate dynamically were the simulation to be run long enough; if aggregating the most-bound pair would lead to such an outcome, we skip it and proceed to the next-most-bound pair that can be combined to produce an aggregate of < 5 individual stars. The algorithm terminates if during any iteration there are no more bound pairs that can be aggregated to yield a combined system with multiplicity < 5.

The final result of this algorithm is that all sinks in each simulation are placed in multiplicity groups: isolated sinks that are not bound to any other sinks (S), bound pairs (B), triples (T) or quadruples (Q). Then, the multiplicity fraction is given as (for example, Kouwenhoven et al. 2010; Bate 2012a; Krumholz et al. 2012b)

$$\mathrm{mf} = \frac{B + T + Q}{S + B + T + Q} . \tag{2.10}$$

This empirical definition has proven robust for use on observations because it does not change if the number of components in a bound system is updated (Hubber & Whitworth 2005), for example, if a system initially classified as a binary is later discovered to contain a third member.

Figure 2.7 shows the CDF of mass for singles, binaries, triples and quadruples in our simulations; note that the CDF we plot is the distribution of masses for *all* stars identified at a given multiplicity, not just for the primary in each system. The (fixed, variable) $\gamma_{\mathrm{H_2}}$ cases form $(48, 53)$ single stars, $(16, 24)$ binaries, $(30, 15)$ triples and $(92, 100)$ quadruples, respectively. The mean value of mf we find for the fixed
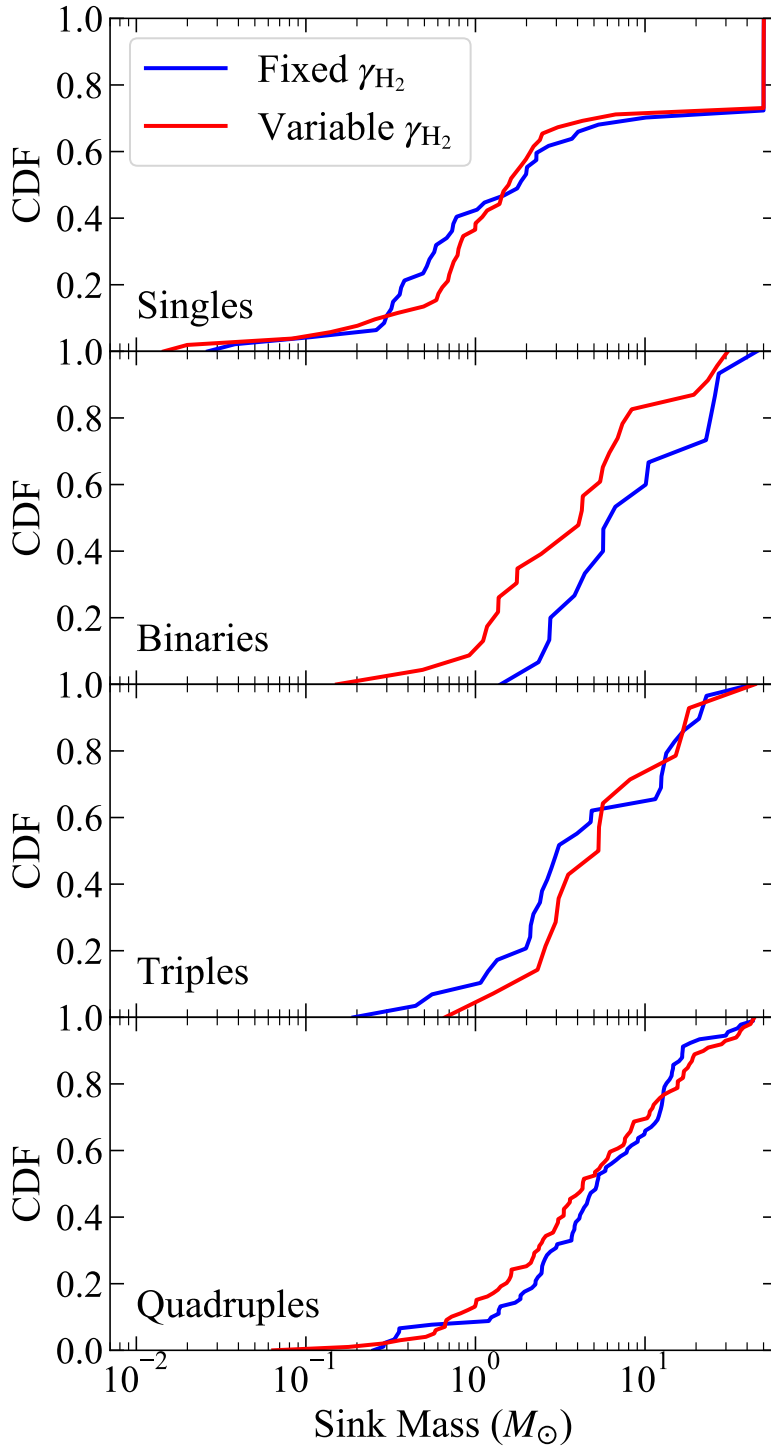
Figure 2.7: Cumulative mass distribution for stars classified as single, binary, triple, and quadruple (top to bottom) in the two cases of fixed and variable γ_{H_2}, at a time when 5 per cent of the initial cloud mass has been accreted by sink particles (SFE = 5%). Stars are classified by multiplicity as described in the main text. The sudden vertical jump at $50 \, M_\odot$ in the case of single stars represents the runs that show no fragmentation until SFE = 5%. Comparisons of the plotted mass distributions via KS tests yields p values consistent with the null hypothesis that both runs are drawn from the same parent distribution.
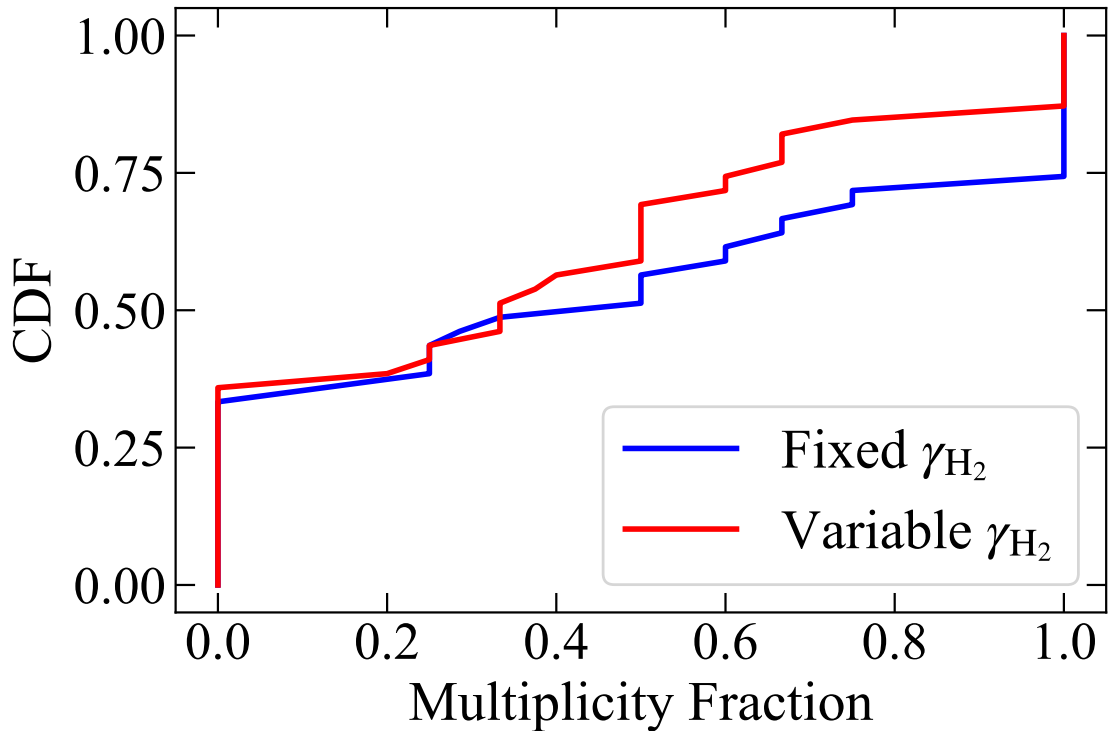
Figure 2.8: CDF of the multiplicity fraction (mf) sampled from 80 simulations for the fixed and variable γ_{H_2} cases, calculated using equation 2.10. The high fraction of mf at 0 multiplicity represents one-third of the total runs where no fragmentation is observed. Similarly, runs where all the stars are bound (*i.e.*, no singles) contribute to the jump seen at $mf = 1$. The KS-test p-value for the two distributions of mf corresponding to the fixed and variable γ_{H_2} cases is 0.72.

and variable γ_{H_2} cases is 0.45 and 0.37, respectively. Although the differences in the number of binaries and triples for the two cases is 33 and 100 per cent respectively, we cannot classify them as significant because of the low number of such systems that form in our simulations. We compare the fixed and variable γ_{H_2} CDFs in each multiplicity bin using a KS test, obtaining p values of 0.43, 0.17, 0.58 and 0.75, for singles, binaries, triples, and quadruples, respectively. As with the mass distribution for all stars, we detect no statistically-significant difference between the fixed and variable γ_{H_2} runs for the singles, binaries, triples and quadruples. We speculate that part of the reason that including variable γ_{H_2} has little effect is that a cancellation occurs: as shown in Figure 2.1, depending on the density and temperature regime, values of γ_{H_2} both lower and higher than the classical value of 1.4 can occur. The former favours fragmentation (since a gas with lower γ is more compressible), while the latter opposes it, but since there are deviations to both lower and higher γ_{H_2} the effects roughly cancel out.

We can also compare the multiplicity fractions directly. Figure 2.8 shows the CDF
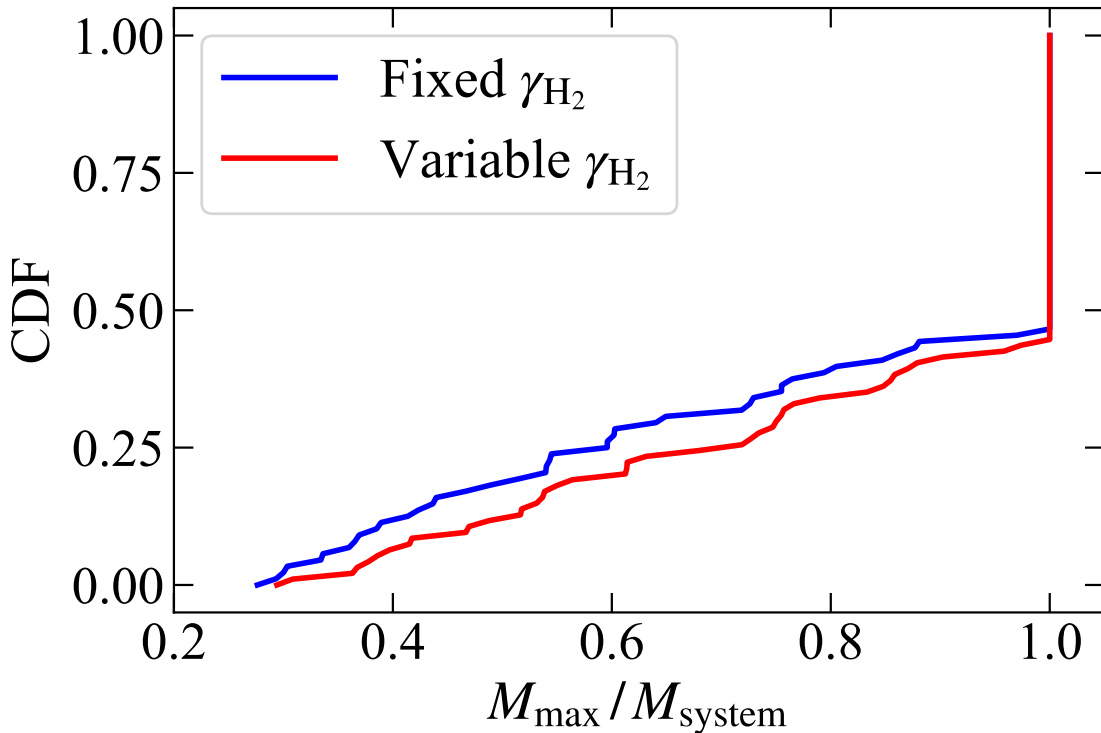
Figure 2.9: CDF of the ratio of the primary (most massive) star (M_{max}) to the sum of masses of stars in a bound system (M_{system}) that can be a binary, triple or quadruple. The substantial fraction of non-fragmented runs lead to this ratio being 1 with a high frequency.

of the multiplicity fraction for the two cases. A KS test comparison of the two distributions yields a p value of 0.72, indicating that the differences in multiplicity fraction are, like the differences in mass, not statistically significant. Figure 2.9 shows the fraction of the mass in multiple systems that is in the primary (most massive star). Values close to unity indicate systems consisting of a dominant primary with small companions, and usually correspond to runs where fragmentation occurs only shortly before we reach SFE = 5%, or to cases where fragments form earlier but are not able to accrete much mass. On the other hand, ratios farther from unity indicate more equal multiples, which generally result from near-simultaneous fragmentation at locations very close to each other, although there can be other possibilities. The p value returned by a KS comparison of the variable and fixed γ_{H_2} distributions is 0.81, again revealing no statistically-significant differences.

2.5   Conclusions

In this work, we study the effects of the adiabatic index of molecular hydrogen (γ_{H_2}) on the fragmentation and mass distribution of the first protostars. H$_2$ is the

primary component of the star-forming gas and the dominant cooling agent in zero metallicity primordial clouds where there is no dust. Thus, the thermodynamics are primarily controlled by H_2 and as such it is necessary to check whether the common approximation of treating H_2 as a classical diatomic gas with fixed adiabatic index $\gamma_{H_2} = 7/5$ is valid. The reason for concern is that, at the temperatures of a few hundred K found in primordial clouds and the accretion discs of the first stars, rotational and vibrational levels of H_2 are only starting to become excited, and thus H_2 behaves non-classically. Instead, its adiabatic index is a complex function of both temperature and the ratio of ortho- to para-H_2 .

We perform two sets of 3D simulations at high resolution (7.6 AU) using the AMR hydrodynamic code FLASH. In the first set we fix $\gamma_{H_2} = 7/5$, and in the second we compute γ_{H_2} as a function of temperature and ortho- to para- ratio using a full quantum mechanical treatment. We follow all simulations up to the time when 5 per cent of the initial cloud mass is accreted by sink particles, yielding a total of 378 sink particles from 80 simulations with different initial random turbulent velocity fields, with a mean sink particle mass of $10.5\,M_\odot$. We show that primordial systems can undergo high fragmentation at distances as close as 5 AU from the primary star, thus resulting in stars being bound to others soon after their formation; the mean multiplicity fraction is 0.4. However, around one-third of our simulations show no fragmentation even when the first star has accreted $50\,M_\odot$. Hence, unless feedback effectively halts accretion on to the isolated massive stars, it seems likely that a great diversity of Population III stars existed, from single massive stars evolving in isolation to clustered formation of significantly less massive stars.

Comparing runs using identical initial conditions run with fixed and variable γ_{H_2} reveals clear differences in physical properties such as density and temperature distributions, especially in regions where the net adiabatic index of all species (γ_{net}) is dominated by γ_{H_2} due to the high mass fraction of H_2 . We compare and analyze the mass distribution and multiplicity of the fixed and variable γ_{H_2} simulations; we find no statistically significant differences between the two. We also do not see any evidence of preferential formation of clustered systems in either of the two cases. Within the domains covered by this analysis, we therefore conclude that the standard approximation of molecular hydrogen as a classical diatomic gas during the formation of the first stars is valid, at least to first order during the first few thousand years after collapse of the formation of the first star. This may change with feedback, as feedback will alter the temperature distribution and hence the value of γ_{H_2}. Thus it is possible that a full quantum mechanical treatment of the H_2 molecule will prove more important at later stages of the primordial star formation process.

Nonetheless, we recommend following the accurate treatment of the H$_2$ adiabatic index in future studies of formation of the first stars because it is not computationally more expensive as compared to the classical treatment.

Acknowledgements

The importance of magnetic fields for the initial mass function of the first stars

Context and Contribution

Abstract

Magnetic fields play an important role for the formation of stars in both local and high-redshift galaxies. Recent studies of dynamo amplification in the first dark matter haloes suggest that significant magnetic fields were likely present during the formation of the first stars in the Universe at redshifts of 15 and above. In this work, we study how these magnetic fields potentially impact the initial mass function (IMF) of the first stars. We perform 200 high-resolution, three-dimensional (3D), magneto-hydrodynamic (MHD) simulations of the collapse of primordial clouds with different initial turbulent magnetic field strengths as predicted from turbulent dynamo theory in the early Universe, forming more than 1100 first stars in total. We detect a strong statistical signature of suppressed fragmentation in the presence of strong magnetic fields, leading to a dramatic reduction in the number of first stars with masses low enough that they might be expected to survive to the present day. Additionally, strong fields shift the transition point where stars go from being mostly single to mostly multiple to higher masses. However, irrespective of the field strength, in-

dividual simulations are highly chaotic, show different levels of fragmentation and clustering, and the outcome depends on the exact realisation of the turbulence in the primordial clouds. While these are still idealised simulations that do not start from cosmological initial conditions, our work shows that magnetic fields play a key role for the primordial IMF, potentially even more so than for the present-day IMF.

3.1 Introduction

Magnetic fields are ubiquitous in the Universe, and have a major impact on the behaviour of objects whose sizes range from planetary cores (Stevenson 2003; Balogh 2010) to the intracluster medium (Carilli & Taylor 2002; Durrer & Neronov 2013). The relevance of magnetic fields in contemporary star formation has been extensively studied in theory, simulations and observations (see reviews by Shu et al. 1987; McKee & Ostriker 2007; Crutcher 2012; Han 2017; Krumholz & Federrath 2019; Hennebelle & Inutsuka 2019). Nonetheless, several questions that concern magnetic fields still remain unanswered; for example, how are they generated? How are they amplified or dissipated? How are they sustained and how do they evolve across different scales? And importantly, how do they affect the stellar initial mass function (IMF)?

Magnetic fields have also been proposed to be of importance in the high-redshift Universe (Zweibel 2006; Kronberg et al. 2008; Bernet et al. 2008), especially during the formation of the first generation of stars around $z \sim 20 - 30$ (Bromm 2013; Klessen 2019). However, the magnetic field strength at such high redshifts is extremely difficult to measure and to constrain; moreover, any constraints that arise can only inform us of the field strength and/or topology on scales much larger than that of molecular clouds where actual star formation takes place. Several physical processes can lead to the production of a magnetic field in the early Universe (Grasso & Rubinstein 2001; Subramanian 2016), including cosmological phase transitions (10^{-40} s after the Big Bang) that drive electric currents (Kibble 1980; Vachaspati 1991; Sigl et al. 1997; Kahniashvili et al. 2013b), excitation of charged scalar fields during inflation (10^{-30} s) (Guth 1981; Guth & Pi 1982; Turner & Widrow 1988), and baryogenesis (10^{-10} s) that leads to asymmetry between baryons and antibaryons (Greenstein 1969; Matese & O'Connell 1970; Ng & Vachaspati 2010). We recommend the reader to the introduction of Mosquera Cuesta & Lambiase (2009) and the review by Widrow et al. (2012) for a discussion of additional candidates. Regardless of the fields' origin, their importance on large scales at $15 \leq z \leq 30$ continues to

be a mystery (Vazza et al. 2014). It is believed that an efficient Biermann Battery mechanism during these redshifts can amplify the initial seed field (Biermann 1950; Xu et al. 2008; Doi & Susa 2011); there are a number of other possible amplification mechanisms, including vorticity present in the primordial plasma during the radiation era (Harrison 1970; Baierlein 1978) or an inverse energy cascade where magnetic energy is transferred from small to large scales (Brandenburg et al. 1996; Field & Carroll 2000; Christensson et al. 2001).

Given the disagreement even over field amplification mechanisms, it is not surprising that there is a great deal of uncertainty about the field strength, which is exponentially sensitive to the source and physical parameters used (Brandenburg & Subramanian 2005). Published estimates of the primordial magnetic field on correlation lengths of 50 kpc or more range from 10^{-34} G $- 10^{-9}$ G (Tashiro & Sugiyama 2006; Kawasaki & Kusakabe 2012; Kahniashvili et al. 2013a; Hutschenreuter et al. 2018; Donnert et al. 2018). For example, Ichiki et al. (2006) use the cosmological power spectrum of magnetic fields to predict field strengths at the onset of primordial star formation of 10^{-18} G on 1 Mpc and 10^{-14} G on 10 kpc scales, respectively. Similarly, Banerjee & Jedamzik (2004) propose that primordial magnetic fields of strength $\sim 10^{-11}$ G exist in galaxy clusters with correlation lengths of a few kpc. Maki & Susa (2004, 2007), Susa et al. (2015), and Higuchi et al. (2018) show that primordial molecular clouds are closer than modern-day ones to the limit of ideal magnetohydrodynamics (MHD) due to higher ionization fraction in the early Universe (see, however, Nakauchi et al. 2019). No matter how the field is generated, it can be quickly amplified within a collapsing molecular cloud as a result of fluxfreezing. Fields can be even further amplified during the collapse by the small-scale dynamo, which converts the kinetic energy of collapse-driven motions to magnetic energy (Brandenburg & Subramanian 2005). Simulations show that this mechanism rapidly increases the magnetic energy density to a significant fraction (up to ~ 50 per cent) of the kinetic energy density (Federrath et al. 2011b; Sur et al. 2014; Schober et al. 2015; Federrath 2016). All the necessary conditions for the existence of a small-scale dynamo are fulfilled in the early Universe prior to primordial star formation (Sur et al. 2010, 2012; Schober et al. 2012a; Wagstaff et al. 2014), as cosmological simulations directly predict the existence of turbulence at the onset of primordial cloud collapse (Wise & Abel 2007; Wise et al. 2008; Greif et al. 2008).

While these studies strongly favour the presence of a dynamically-significant magnetic field during the formation of the first stars, there have been only limited explorations of how this affects the star formation process, and in particular the IMF of the first stars. Some of the first 3D nested-grid MHD simulations were performed

by Machida et al. (2006, 2008b,a), who find that strong, ordered magnetic fields lead to the formation of jets and outflows. Turk et al. (2012) and Latif et al. (2013b) simulate the effects of magnetic fields on Population III star formation starting from cosmological structure conditions. They show that the field can be quickly amplified by the action of the small-scale dynamo if the resolution is sufficient to resolve the turbulent motions of the gas. However, they are unable to study the primordial IMF because their numerical techniques do not allow them to run past the formation of the first collapsed object. Machida & Doi (2013) perform MHD simulations of primordial clouds with varying magnetic field strengths and find that fragmentation scales with the inverse of the field strength, with stronger fields resulting in the formation of a single, massive star. However, their resolution is insufficient to capture dynamo effects, and their numerical method precludes them from considering turbulent initial conditions. Thus, it becomes clear that the effects of magnetic fields on Population III star formation largely remain unexplored (Bromm 2013; Klessen 2019; Haemmerlé et al. 2020).

This work adds on to earlier investigations of magnetic fields during primordial star formation in two straightforward ways: (1.) we study the effects of turbulent, non-uniform magnetic field structures, which has not been investigated in previous simulations. Once the collapse sets in, the turbulence being driven by gravity in the center of the minihalo will quickly convert even an originally uniform field to a tangled one with a randomly oriented geometry (Schekochihin et al. 2004; Brandenburg & Subramanian 2005), and (2..) we carry out 200 simulations with different realisations of the initial turbulent velocity and magnetic field distribution, so that we can sample enough stars to conduct a meaningful analysis of the resulting mass distribution. As we show later (see also, Wollenberg et al. 2020), the amount of fragmentation highly varies within different realizations of the same field strength, thus, we cannot draw statistically meaningful conclusions unless we collect enough statistics to overcome the effects of stochasticity (Hopkins & Christiansen 2013; Young & Clarke 2016).

This paper is organised as follows: Section 3.2 discusses how we setup the simulation and the turbulent magnetic field strengths we use, Section 3.3 presents our results, with a discussion in Section 3.4. We summarise our findings and conclusions in Section 3.5.

3.2 Numerical simulation methods

3.2.1 Simulation Setup

We utilize the adaptive mesh refinement (AMR) code FLASH (Fryxell et al. 2000; Dubey et al. 2008, 2013) for our MHD simulations. We largely adopt the simulation setup of Sharda et al. (2019a), with important additions including magnetic fields and deuterium chemistry. We use a tree-based solver to solve the Poisson equation for self-gravity (Wünsch et al. 2018), the five-wave approximate Riemann solver HLL5R to solve the MHD equations (Bouchut et al. 2007, 2010) adopted for FLASH by Waagan (2009); Waagan et al. (2011), and sink particles as a proxy for stellar particles that form during collapse (Federrath et al. 2010a, 2011a, 2014a). The sink particle module has been shown to work well for MHD simulations in FLASH because the grid-based implementation can ensure the magnetic field geometry remains intact during sink particle creation (Seifried et al. 2011; Duffin & Pudritz 2011); further, the checks required for a sink to form contain appropriate contributions from magnetic pressure (for Jeans mass) and energy (for virial checks).

Table 3.1 lists the initial conditions we utilize in this work. We start with a primordial cloud core of mass $1000\,M_\odot$ and a radius of $1\,\mathrm{pc}$. The size of the computational box we use is $L = 2.4\,\mathrm{pc}$. These initial conditions are in very good agreement with the overdense regions observed in dark matter mini-haloes in cosmological simulations that form around $z \sim 30$ (Hirano et al. 2015). Similarly, taking inspiration from cosmological simulations and MHD simulations of contemporary star formation, we initialise an angular velocity in the core to initiate a solid-body rotation around the $\hat{z}$ axis, such that the rotational energy is 3 per cent of the gravitational energy at the initial stage. Our base grid consists of 8^3 cells on top of which we add up to 14 levels of refinement; the maximum effective resolution of the simulations thus reaches 65536^3 cells. The maximum physical resolution and number density the simulations reach is given by the minimum cell size of $dx = 7.6\,\mathrm{au}$, and maximum gas density of $n \sim 10^{13}\,\mathrm{cm}^{-3}$ (equivalent to a mass density $\rho \sim 10^{-11}\,\mathrm{g\,cm}^{-3}$), respectively.

3.2.2 Primordial chemistry

Since chemical evolution timescales in primordial clouds are comparable to collapse times (Omukai & Nishi 1998), it is necessary to solve the chemical network associated with them in order to self-consistently compute the temperature as a function of the density during the collapse. We use the chemistry package KROME (Grassi et al. 2014), which is designed to be incorporated in astrophysical simulations where

treating the chemistry and hydrodynamics together is a crucial requirement (Grassi et al. 2013). Specifically, we utilize the primordial chemistry network in KROME, which includes the following species: H, D, H_2, HD, H^+, D^+, H^-, D^-, He, He^+, HD^+, He^{++}, H_2^+ and e^-. We run a 1D primordial cloud collapse model in KROME to generate initial mass fractions, core temperature and density that we supply as inputs to our 3D simulations[1]. The mass fractions of the ionized species returned by KROME are scaled to ensure charge neutrality is maintained. We also follow an accurate calculation of the H_2 adiabatic index (γ_{H_2}) implemented by Sharda et al. (2019a), which takes into account that, in the temperature range crucial for the formation of the first stars, quantum effects for H_2 are non-negligible, and thus the gas is not well-approximated as a classical diatomic gas with $\gamma_{H_2} = 7/5$. For all other species, we assume their adiabatic indices to be $5/3$, apart from the remaining diatomic species (HD, HD^+ and H_2^+) for which we assume it to be $7/5$. The net adiabatic index of the gas is then given by the mass-weighted average of adiabatic indices of all species. Further, we implement a strict temperature floor given by the CMB temperature at our assumed redshift $z = 30$.

KROME also contains inbuilt functions to estimate the net heating and cooling contributed by the chemistry during the collapse. Specifically, we include cooling due to H_2, Lyman-α cooling, collisionally-induced emission (CIE) cooling, cooling due to Compton scattering of CMB photons, cooling due to HD, and cooling and heating due to chemical reactions that can be either exothermic and/or endothermic. At high densities, we use the opacity correction given by Ripamonti & Abel (2004) in the cooling function for H_2. We refer the reader to Sharda et al. (2019a, their Section 3.2) for a discussion of the caveats associated with the implementation of these processes, and point out that the density and temperature spaces covered by our simulations are not significantly affected by the approximations used in KROME, at least prior to the onset of radiation feedback which we do not consider in this work.

3.2.3 Turbulence

Once an overdense region starts forming in the center of the mini-halo, it creates a potential well that pulls the baryons inwards and causes an infall of the gas. The dynamics of such a collapsing system naturally lead to the production of turbulence

---

[1]In the primordial chemistry network in KROME, we have adjusted the break-point in temperature of the reaction rate coefficient for the reaction $H_2 + D \rightarrow HD + H$ (adopted from reaction IX17, Appendix A of Glover & Savin 2009) for maintaining numerical stability at high densities where the flux of this reaction is high. This adjustment ensures that the rate coefficient changes smoothly as a function of temperature, and is consistent with the experimental estimates originally provided by Mielke et al. (2003) for this reaction.

(Greif et al. 2008), which is a crucial ingredient for star formation. Turbulence can also be generated in the early Universe due to streaming velocities of the baryons with respect to the dark matter particles as per the λCDM model (Tseliakhovich & Hirata 2010; Greif et al. 2011c; Maio et al. 2011b), and by primordial magnetic fields through density perturbations (Kim et al. 1996). Further, turbulence can be sustained and driven by gravity that creates compressive as well as solenoidal flows of gas during infall (Federrath et al. 2011c), increasing the density and temperature. Taking this into account, we initialize our simulations with different random turbulent fields such that the root-mean-square (rms) Mach number ($\mathcal{M}_{\mathrm{rms}}$) is 1, *i.e.,* the initial velocity fluctuations equal the local sound speed. The initial velocity power spectrum goes as $P_{\mathrm{v}} \sim k^{-1.8}$ from wave numbers $k/(2\pi/L) = 2 - 20$ where L is the length of the cubic computational domain (e.g., Federrath 2013a; Gerrard et al. 2019; Kuruwita & Federrath 2019). We select the power-law scaling to be between the Kolmogorov ($k^{-5/3}$, Kolmogorov 1941) and Burgers (k^{-2}, Burgers 1948) turbulence. Since both these kinds of turbulence are primarily driven on large scales, the results do not sensitively depend on the initial spectrum (Federrath et al. 2011c). The turbulence is driven by mixed modes comprised of solenoidal as well as compressive motions (Federrath et al. 2010b; Federrath & Klessen 2012).

We note that the turbulence here is artificially driven by setting up an initially turbulent velocity field as described above, but that there is no subsequent mechanism to continue driving the turbulence. In reality, the kinetic energy on the largest model scales would be provided by even larger scale interactions in the cosmic web, thus continuously driving the turbulence on model scales. In practice, this makes little difference for our simulations, because the duration of our runs is relatively small compared to the turnover time of the largest turbulent structures, which is comparable to the free-fall time evaluated at the initial mean density. Thus, little turbulent decay occurs within the duration of our runs. However, we are currently in the process of constructing cosmological simulations that will be used as initial conditions for zoom-in simulations, in a forthcoming study. This will allow runs with significantly longer durations. A possible alternative to cosmological initial conditions would be to continuously drive the turbulence, but in a much larger computational domain containing multiple collapsing cores. However, this is not as realistic as cosmological initial conditions, and is computationally much more expensive, because if there are multiple collapsing cores present, then each must advance in time using the most stringent time step constraint that applies to any of them. This constraint would effectively mean that we could not follow the simulation much past the point where the first few cores collapsed.

Additionally, in line with the arguments made by several previous works about the necessity of sufficiently resolving Jeans length to capture the effects of the small-scale dynamo (Sur et al. 2010; Federrath et al. 2011c; Turk et al. 2012; Latif et al. 2013a), we set our AMR refinement condition to maintain at least 32 cells per Jeans length. Note that in AMR MHD simulations, it is also common to refine the grid based on derivatives of the velocity field (such as vorticity or divergence), as they can better capture the turbulent energy cascade responsible for shocks, especially in cases where the evolution of low-density regions is crucial (Kritsuk et al. 2006; Iapichino et al. 2008; Kritsuk et al. 2009; Vazza et al. 2009; Schmidt et al. 2009; Vazza et al. 2014; Iapichino et al. 2017). However, Kritsuk et al. (2007) and Schmidt et al. (2009) show that such refinement criteria can be more computationally expensive than Jeans refinement, because they are extremely sensitive to the conditions at the shock front that can change by a large margin, thus reducing the simulation timestep and making long-duration runs difficult to accomplish. Furthermore, using such criteria would lead us to refine large portions of the computational domain that contain mostly low-density material that will never be accreted or interact with the dense regions that are the focus of this study, highly increasing the computational cost for no gain in accuracy in the regions about which we care. We can capture the regions in which we are interested sufficiently well by resolving the Jeans length with 32 cells, including the turbulent energy content on the Jeans scale (Federrath et al. 2011c).

3.2.4   Magnetic Fields

We use four model cases with different magnetic field strengths to study the role of magnetic fields in setting fragmentation early on during the collapse of primordial clouds. The four cases, as we show in Table 3.1, are named $B_0 - B_3$, and have initial rms field strengths of $0\,\mathrm{G}$, $1\,\mathrm{fG}$, $9\,\mu\mathrm{G}$ and $28\,\mu\mathrm{G}$, respectively. B_0 is an ideal case with no magnetic field strength that acts as a control simulation. Our motivation for case B_1 is to test an unlikely condition where an initial seed field has not already been amplified due to the small-scale dynamo at the onset of collapse, and the field strength is close to the pre-dynamo values discussed in Section 3.1; such a case seems unlikely because if the small-scale dynamo is present, it will very quickly amplify any weak seed magnetic field (Federrath et al. 2011c; Federrath 2016; Subramanian 2016), even before the presence of a protostellar disc (Schleicher et al. 2010). In fact, saturation of the field due to the small-scale dynamo is also observed very early on ($n \sim 10^5\,\mathrm{cm}^{-3}$) even when non-ideal MHD effects like ambipolar and Ohmic diffusion are considered (Schober et al. 2012a).

The cases B_2 and B_3 demand a more qualitative as well quantitative reasoning. Even though simulations are now able to resolve the action of the small-scale dynamo by efficiently resolving the Jeans length, they have not yet reached convergence. In other words, the higher the number of cells per Jeans length are used, the more the amplification of the magnetic field during the formation of the first stars is observed (Sur et al. 2010; Federrath et al. 2011c; Turk et al. 2012; Latif et al. 2013a). This is because the simulations can only reach kinematic Reynolds numbers (the ratio of flow scale to viscous dissipation scale) of up to 10^{2-4} (Kritsuk et al. 2009; Jones et al. 2011), in best possible cases up to 10^5 (Federrath 2013a, 2020), whereas star-forming regions and the ISM in the Universe typically have Reynolds numbers of the order of 10^7 (Kritsuk et al. 2011; Krumholz 2014b). Since the current MHD simulations are not able to reach convergence, they cannot reliably show the limit in which the dynamo action saturates. Dynamo saturation occurs when the back reaction of the magnetic field on the gas due to the Lorentz force causes the peak of the magnetic energy spectrum to shift to the largest possible spatial scales. This is thought to occur when the diffusivity equals the growth rate of magnetic fields (Subramanian 1999; Schekochihin et al. 2002; Schober et al. 2015).

Nevertheless, theoretical developments as well as isothermal MHD simulations of turbulence in a box (Haugen et al. 2004; Federrath et al. 2011c, 2014a; Schober et al. 2015) predict that the saturation rate of magnetic energy produced by the turbulent dynamo can be anywhere between a fraction of a per cent to a few tens of per cent of the turbulent kinetic energy, depending on the turbulent Mach number, Reynolds number of the flow and magnetic Prandtl number (ratio of magnetic to hydrodynamic Reynolds number). Given that the magnetic Prandtl numbers in the early Universe were high (Childress & Gilbert 1995; Kulsrud 1999; Schober et al. 2012a), we expect the dynamo to have saturated at a few per cent of the turbulent kinetic energy at our chosen initial sonic Mach number (see Figure 3 of Federrath et al. 2011c, Figure 2 of Federrath et al. 2014a and Figure 4 of Federrath 2016). It has also been shown that the field will saturate very quickly if strong accretion shocks are present (Latif et al. 2014). Hence, we initialize cases B_2 and B_3 with magnetic field strengths such that the initial magnetic energy is 1 and 10 per cent, respectively, of the total turbulent kinetic energy in the system. This gives $B_2 = 9\,\mu\mathrm{G}$ and $B_3 = 28\,\mu\mathrm{G}$, respectively.

The associated initial magnetic power spectrum goes as $k^{3/2}$ over a wide range of wave numbers ($2 \leq k \leq 20$) in the simulation box, the so-called Kazantsev spectrum resulting from turbulent dynamo amplification (Kazantsev 1968; Kazantsev et al. 1985; Bhat & Subramanian 2014). There is no well-defined orientation of the field

Table 3.1: Initial conditions of the spherically homogeneous primordial cloud. The RMS magnetic field strength in cases B_2 and B_3 is also expressed as a fraction of the turbulent kinetic energy ($E_{\text{turb,kin}}$).

Parameter	Symbol	Value
Cloud Mass	M_{core}	$1000 \, M_\odot$
Cloud Radius	R_{core}	$1 \, \text{pc}$
Cloud Number Density	n_{core}	$9050 \, \text{cm}^{-3}$
Cloud Temperature	T_{core}	$265 \, \text{K}$
Rot. / Grav. Energy	$E_{\text{rot}}/E_{\text{grav}}$	0.03
Mass Fraction of H	x_{H}	0.7502
Mass Fraction of D	x_{D}	4.56×10^{-5}
Mass Fraction of H_2	x_{H_2}	0.0006
Mass Fraction of He	x_{He}	0.2492
Mass Fraction of HD	x_{HD}	3.82×10^{-8}
Mass Fraction of e^-	x_{e^-}	4.72×10^{-9}
CMB Temperature at $z = 30$	T_{CMB}	$84.63 \, \text{K}$
Turbulence	v_{rms}	$1.84 \, \text{km s}^{-1}$
Sound Speed	c_{s}	$1.84 \, \text{km s}^{-1}$
RMS Magnetic Field	B_0	0
	B_1	$1 \, \text{fG}$
	B_2	$9 \, \mu\text{G} \, (0.01 \, E_{\text{turb,kin}})$
	B_3	$28 \, \mu\text{G} \, (0.10 \, E_{\text{turb,kin}})$

with respect to the rotation axis since we work with non-ordered fields as expected from the action of the small-scale dynamo[2]. We note that certain MHD simulations have shown that a strong magnetic field can alter the underlying velocity power spectrum (Lemaster & Stone 2009; Collins et al. 2012; Beattie & Federrath 2020). Thus, the velocity power spectrum could take a sightly different form for magnetized versus non-magnetized simulations; however, we ignore any such effects here as they would not significantly change the exponent of -1.8 appropriate for trans-sonic turbulence, which is a reasonable intermediate value between the Kolmogorov and Burgers exponents of -5/3 and -2, respectively.

3.3   Results

We run a total of 200 simulations, 50 realizations each for the four different initial magnetic field strengths we use, as shown in Table 3.1. We only change the random seeds of the initial turbulence and magnetic field distributions between the different runs. The set of 50 random seeds is identical for each magnetic field strength, so,

---

[2]There is still a possibility of an ordered component of the magnetic field that can be generated later on in the core via the $\alpha\omega$ type large-scale dynamo (Subramanian 2016; Latif & Schleicher 2016b; Liao et al. 2019).

for example, run 1 for cases B_0 - B_3 has the same initial velocity field and the same magnetic field structure in all four cases; only the field strength differs. Given that star formation is well known to be a stochastic process (e.g., Gerola & Seiden 1978; Seiden et al. 1979; Kauffmann et al. 2006; Fumagalli et al. 2011a), such simulations are an ideal way to study the overall pattern and distribution of a sample since they collectively take into account the changes one would expect simply from stochasticity (Wollenberg et al. 2020).

Similar to Sharda et al. (2019a), we parameterize the time for which we run our simulations by the star formation efficiency, defined as the ratio of the total mass of sink particles M_{sink} to the initial cloud mass M_{cloud}, i.e., SFE $= M_{\mathrm{sink}}/M_{\mathrm{cloud}}$. We stop our simulations when SFE $= 5$ per cent, since we do not include radiation feedback, which starts to become significant for primordial stars $\gtrsim 50\ M_\odot$ (Hosokawa et al. 2011b; Sugimura et al. 2020). This threshold is usually achieved between $500 - 5000\,\mathrm{yr}$ after the first sink particle is formed. All the runs collectively form a total of 1157 sink particles.

3.3.1   Morphology of discs and star systems

As the primordial cloud collapses, infall towards the center compresses the gas, leading to the creation of high-density peaks that ultimately form sink particles. In all cases, an accretion disc forms around the primary sink particle that may or may not fragment further to produce more sinks. We also find that the onset of collapse is delayed in cases where the magnetic field is strong. This is simply because magnetic pressure exerted on the cloud supports it against gravitational collapse (Hosking & Whitworth 2004; Price & Bate 2007).

In Figure 3.1, we show the projection of number density along the z axis at SFE $=$ 5 per cent for three pseudo-random realisations of each magnetic field strength that are selected to show no, few and high secondary fragmentation after the first sink particle has formed, respectively. Animated versions of this and related figures are available in the supplementary online material. It is straightforward to notice the diversity of systems formed in different cases only by changing the random seeds of turbulence or magnetic field. In runs where only one sink particle is formed, the accretion disc around it remains hot, inhibiting any further fragmentation, as seen in Figure 3.2. In cases where high fragmentation is observed, the discs are generally cooler. This is because the angular momentum transport causes the disc to spread out in radius, which allows the growth of density perturbations that can form multiple high-density peaks, which collapse to give rise to more sink particles (Burkert & Bodenheimer 1993). In such cases, we find that sinks often tend to
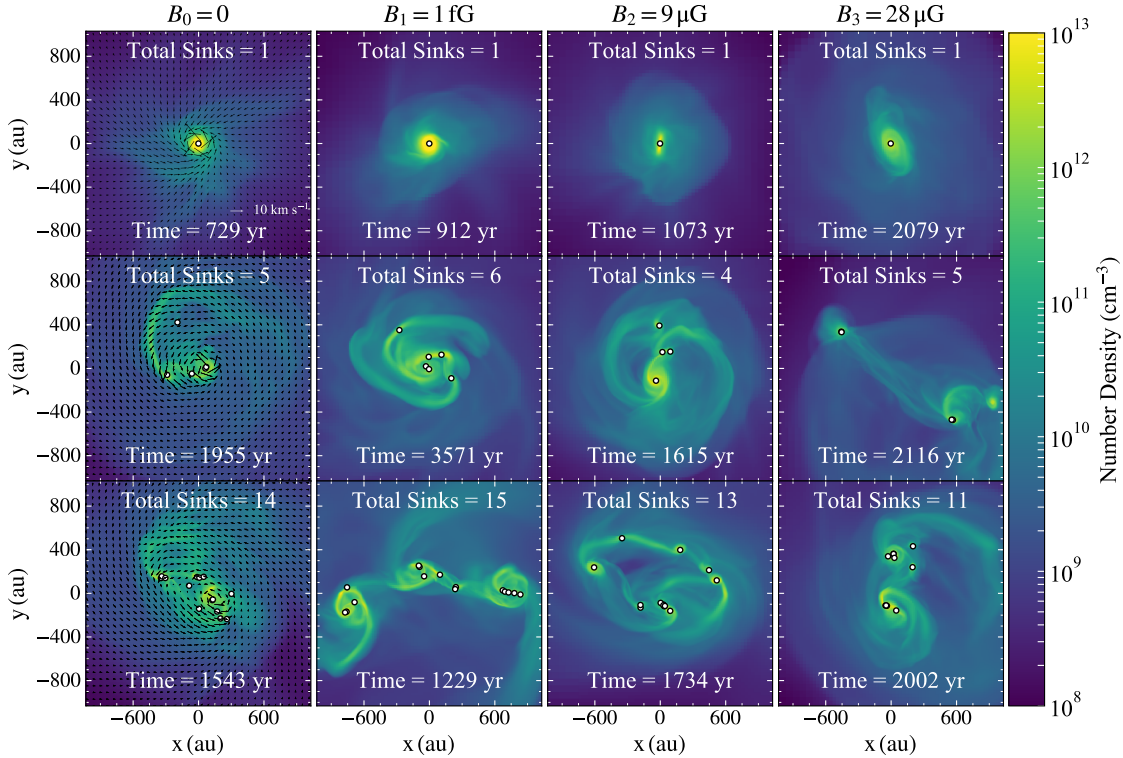
Figure 3.1: Density-weighted projection maps (through the $\hat{z}$ axis) of the number density (n) for three randomly selected realizations from each of the four cases with different initial magnetic field strengths in each column. The random seed for the simulations shown in the first row is the same for all four cases, while it differs for the other two rows. These realizations depict the central $0.01\,\mathrm{pc}$ region and result in no, medium and high fragmentation, respectively (from top to bottom in every column). The maps correspond to a time when all the sink particles (white circles with black boundaries) have collectively accreted 5 per cent of the initial cloud mass (SFE = 5 per cent). Time in the panels is given as time since the formation of the first sink particle. The contours on the first column depict the velocity vectors of the gas in the $x - y$ plane.

redistribute themselves to form clusters (at least for a short period of time), with an accretion disc associated with each cluster and large-scale high-density spiral patterns. They also result in the formation of numerous sub-solar and solar-type sinks, many of which remain bound to a massive ($M_\star > 20\,M_\odot$) primary (Stacy et al. 2016). Figure 3.1 and Figure 3.3 show the coupling between magnetic field and primordial gas that results due to flux-freezing.

In general, we observe reduced fragmentation as we increase the magnetic field strength. Random seeds which lead to the formation of only one sink particle in the B_0 case also form just one sink particle in all other cases. However, there are exceptions to this general trend, in the form of realisations where we observe more fragmentation in runs with strong fields. Fragmentation often also occurs in spiral
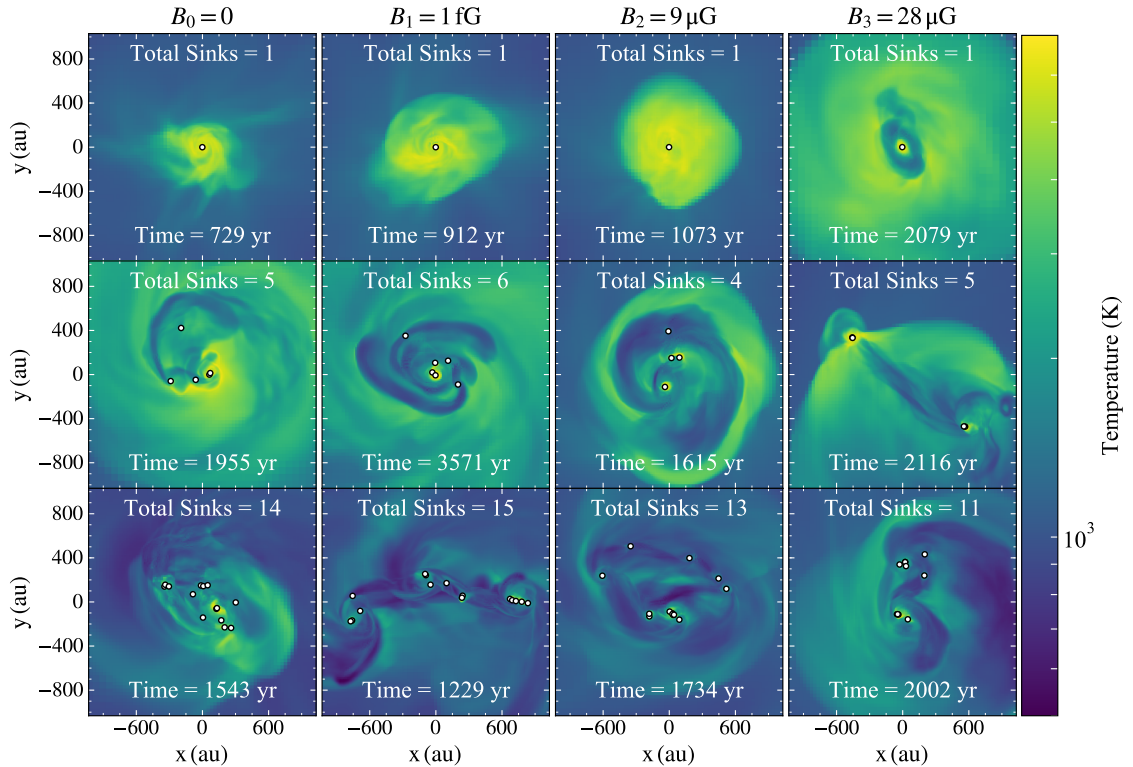
Figure 3.2: Same as Figure 3.1 but for the density-weighted temperature. Both hot and cold accretion flows as well as spiral density patterns are noticeable. Cooler regions are highly molecular with H_2 being the dominant species. Lyman-α cooling becomes effective at temperatures ¿ 10^4 K.

density waves that develop due to gravitational instabilities and decreased local Jeans mass and sound speed (Forgan & Rice 2011), as can be seen from Figure 3.2. Runs where high fragmentation is observed often result in all sink particles being co-planar, as we see from projections along all the three axes.

3.3.2   Evolution with time and gas density

In Figure 3.4, we plot the accretion rates of all sink particles averaged over bins of sink mass; the blue curve in each panel depicts the accretion rate of the first sink particle that is formed in the simulations. The accretion rates are generally in good agreement with similar studies (e.g., Clark et al. 2011a; Latif et al. 2013a; Hirano et al. 2014; Stacy & Bromm 2014; Riaz et al. 2018; Wollenberg et al. 2020). We also find that the accretion rates seldom drop below $10^{-4}\,M_\odot\,\mathrm{yr}^{-1}$ till SFE = 5 per cent where the effects of protostellar ultraviolet (UV) feedback becomes important (Latif & Schleicher 2015). The first row shows how magnetic fields affect accretion onto the sink particles by systematically lowering the peak as well as the overall accretion rate with time, similar to the findings of Price & Bate (2007) for present-day star
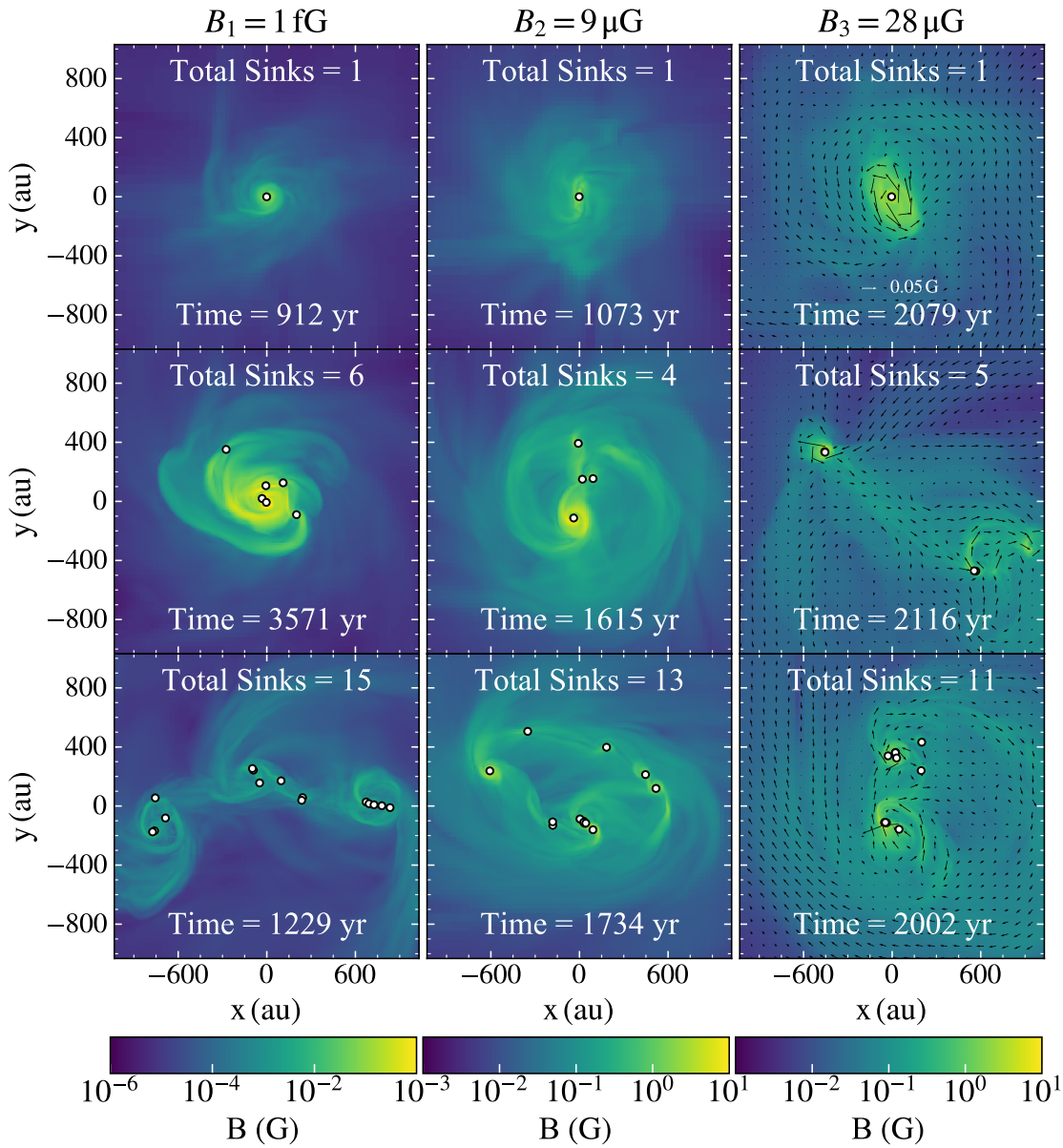
Figure 3.3: Same as Figure 3.1 but for the density-weighted magnetic field strength in the three non-zero magnetic field cases. Arrows in the third panel mark the xy components of magnetic field vectors. The length of all other vectors is a fraction (in log) of the vector with the highest magnitude; for example, a vector half the length of the legend represents a field strength that is 10 times smaller.
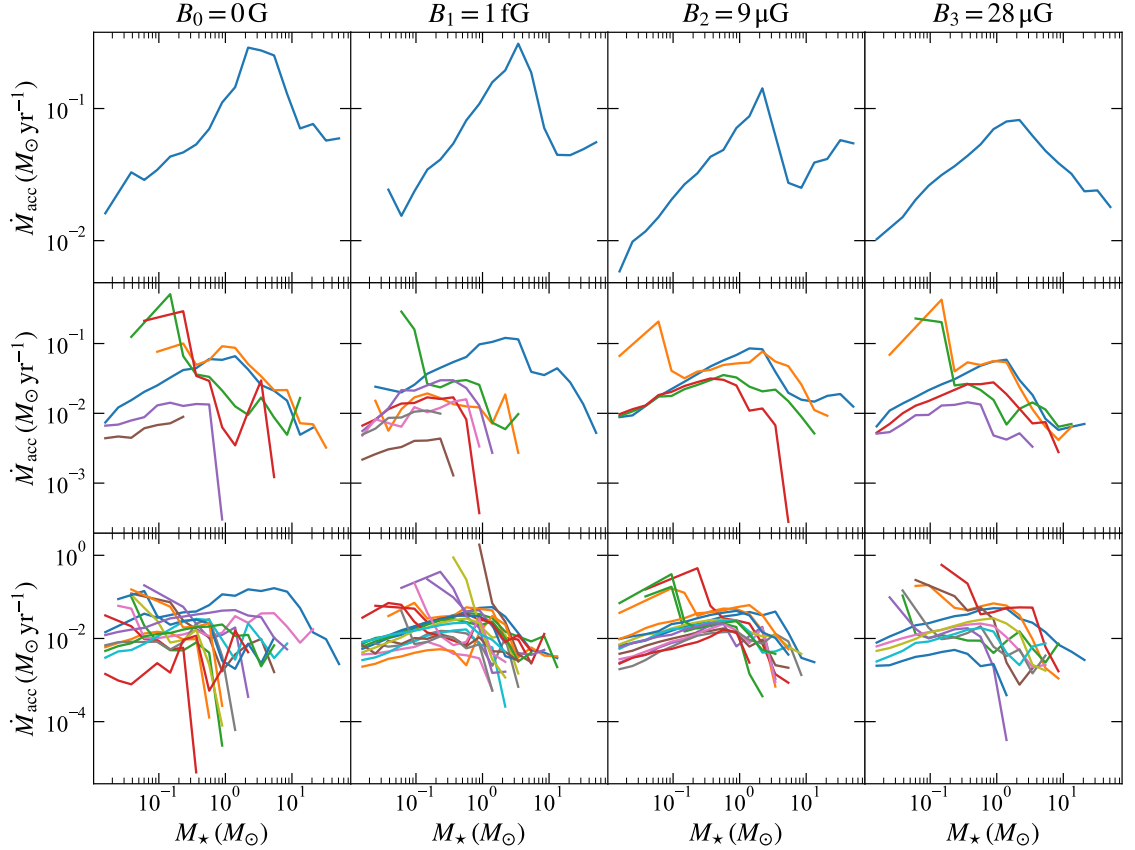
Figure 3.4: Evolution of accretion rate against sink mass for the same simulations shown in Figure 3.1, averaged over bins of sink mass. Each colored line represents an individual sink particle, with the blue depicting the first sink particle that forms in each case.

formation.

Figure 3.5 shows the evolution of temperature, mass fractions of H_2 and HD, and the magnetic field strength as a function of number density just after the formation of the first sink particle (*i.e.,* at SFE = 0) in randomly selected realizations from each case. The mean thermal evolution as shown in the first row is broadly in good agreement with the one-zone calculations of Omukai et al. (2005), and all other reported simulations of the first stars. The distributions of mass fractions of H_2 and HD show a tighter correlation with their mass-weighted mean as the field strength increases. The dip in the temperature at low densities ($n \sim 10^5 \, \text{cm}^{-3}$) is a result of the onset of cooling due to the formation of HD during collapse at these densities (Bromm et al. 2002; Nakamura & Umemura 2002; Omukai et al. 2005). Even though the initial field strength for cases B_2 and B_3 differs by a factor of 3, the maximum field strength at the end of the simulation is similar. This might be due to the back reaction of the strong field on the density. We provide a more thorough analysis of the growth of magnetic field with density and its implications for dynamo action in
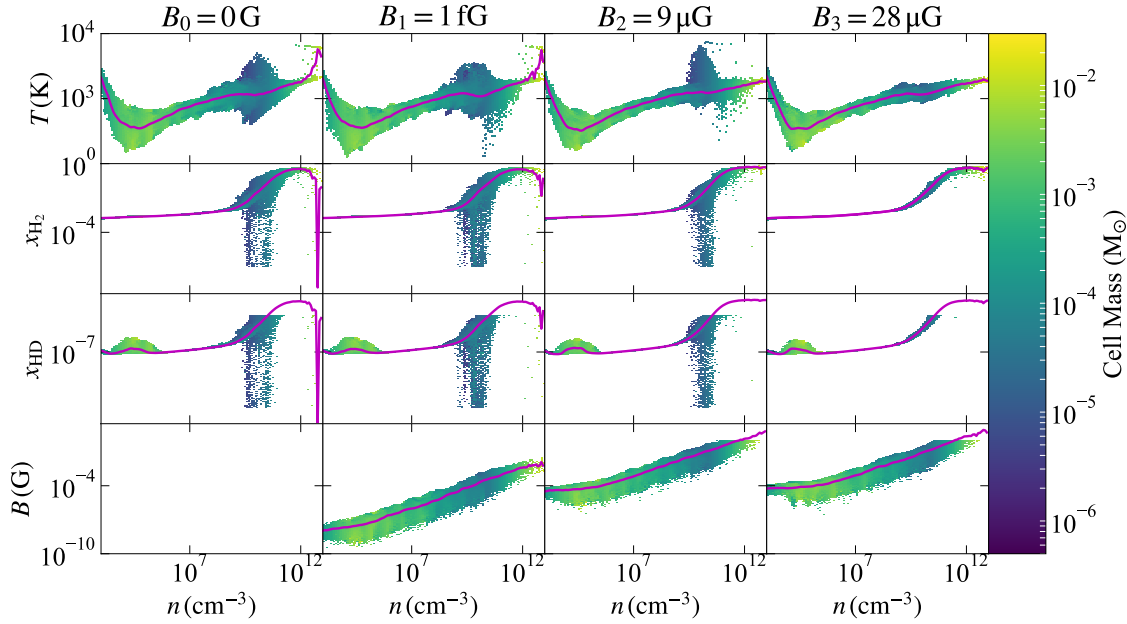
Figure 3.5: Joint distributions of number density (n) as a function of temperature (T, first row), mass fraction of H_2 (x_{H_2}, second row), HD (x_{HD}, third row), and the magnetic field strength (B, fourth row) of the gas in a randomly selected realization with the same random seed for all the four cases. These distributions represent a 0.5 pc sized region centered at the single sink particle that has just formed in the simulation. Magenta curves show the mean value of the quantity on the y-axis in bins of n.

a companion paper (P. Sharda et al., in preparation).

Another noteworthy feature of Figure 3.5 is that cells with the highest densities have lower mean temperatures in the strong-field cases (B_2 and B_3) than in the weak-field cases (B_0 and B_1); they also have correspondingly higher H_2 fractions, due to the lack of gas warm enough to induce collisional dissociation. This change occurs because, in the strong-field cases, shock compression that leads to temperature enhancements are limited by magnetic pressure. Our finding here is broadly consistent with that of Schleicher et al. (2009), who find that magnetic fields can change the thermal evolution of a collapsing primordial cloud. More importantly, it is also strong evidence that magnetic pressure plays a crucial role in reducing fragmentation: the more strongly-magnetised cases fragment less *despite* having lower temperatures and thus less thermal support at high densities.
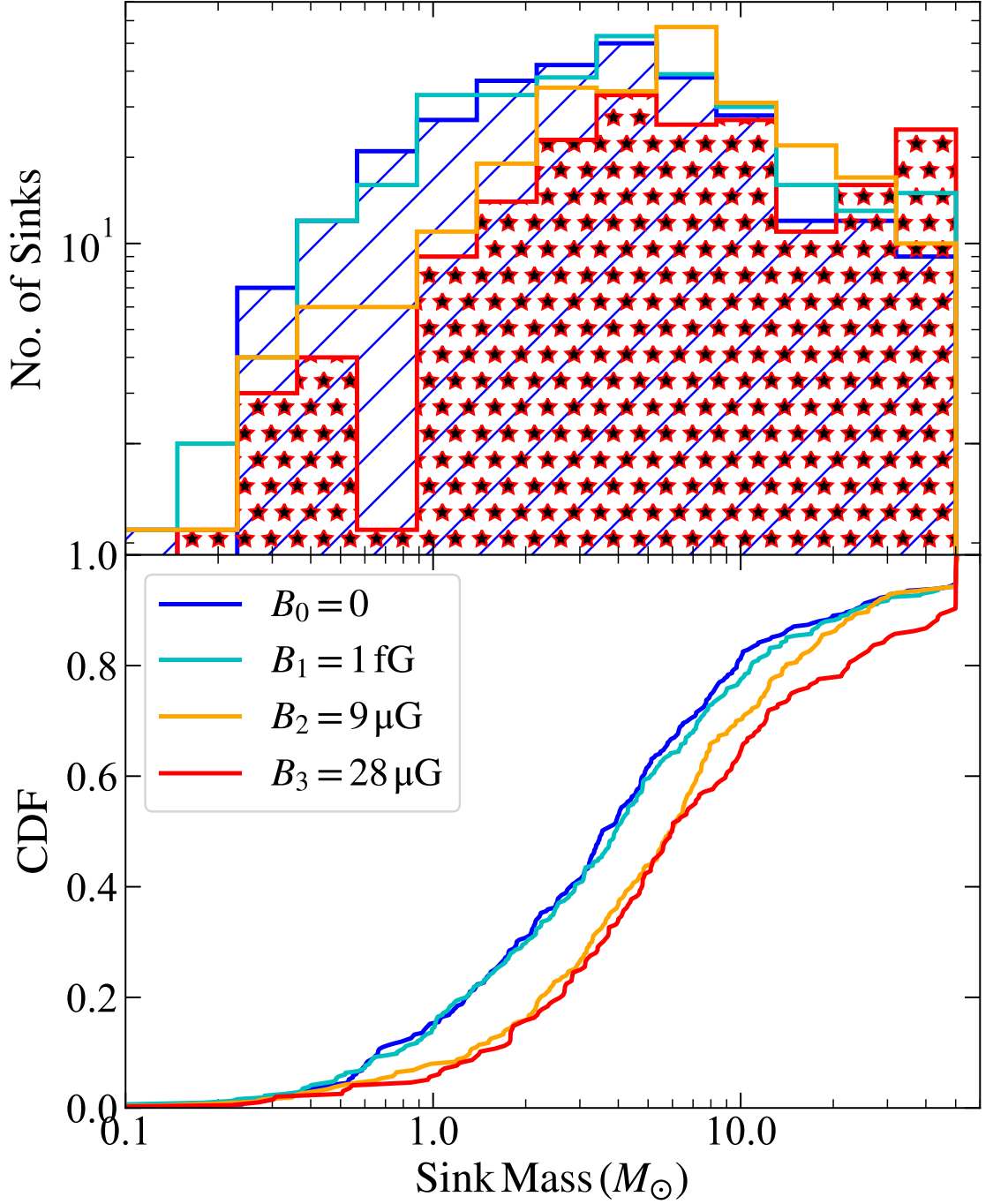
Figure 3.6: Number of sink particles and their cumulative distribution function (CDF; *bottom panel*) from all 200 simulations with different initial magnetic field strengths. The peak at $50\,M_\odot$ in the top panel and the corresponding jump in the CDF is due to runs where no fragmentation occurs, and our condition of stopping at SFE = 5 per cent therefore results in a single sink particle of mass $50\,M_\odot$.

Table 3.2: KS test p-values for different pairs of magnetic field strengths. If p-value ¡ 0.01, there is less than a 99 per cent chance that the two sink mass distributions corresponding to the two magnetic field strengths are different.

p-value	B0	B1	B2	B3
B0	1.0	0.87	4.5×10^{-5}	7.2×10^{-5}
B1	0.87	1.0	5.2×10^{-4}	4.5×10^{-4}
B2	4.5×10^{-5}	5.2×10^{-4}	1.0	0.25
B3	7.2×10^{-5}	4.5×10^{-4}	0.25	1.0
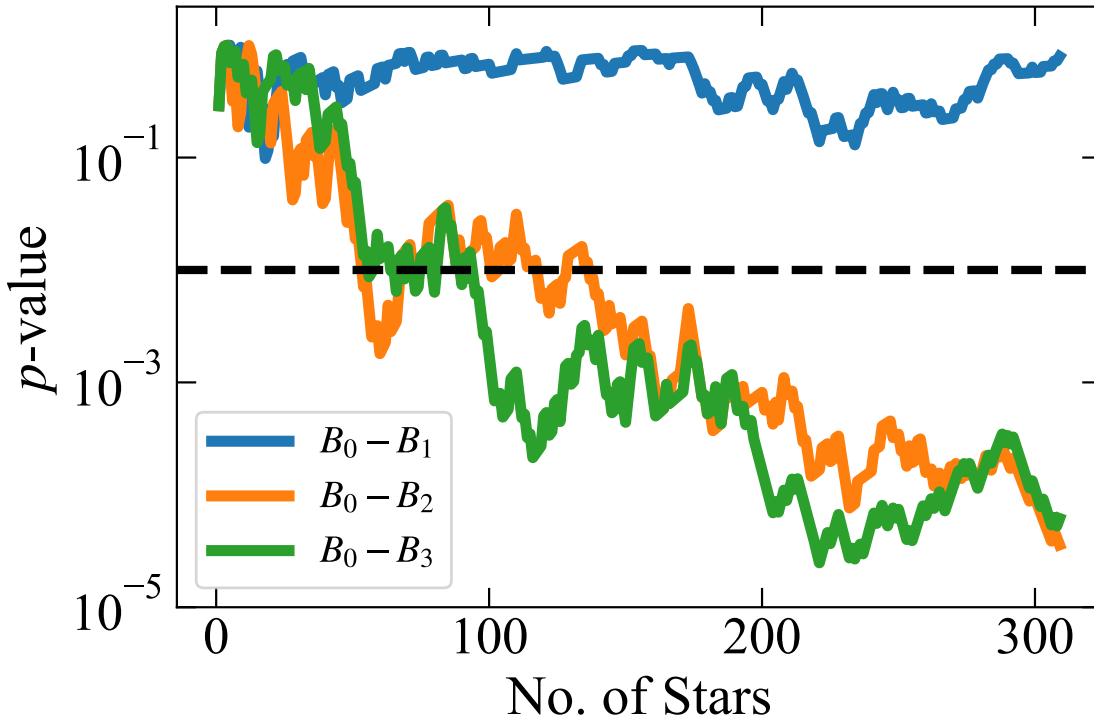
Figure 3.7: Change in the p-value returned by comparing simulation B_0 to the other three cases (B_1 - B_3, as indicated in the legend) as a function of the mean number of stars being compared (*i.e.*, a value of 100 means an average of 100 stars from each of the two runs). To construct this plot, we compute the p-value by comparing one realisation of B_0 to one realisation of B_1, then two realisations of each case, and so forth, and similar for B_2 - B_4. The dashed line denotes a p-value of 0.01, our adopted threshold for a significant detection.

3.3.3 Initial mass function and multiplicity of the first stars

Sink Mass Distribution

With 1157 sink particles formed across all simulations, we can perform a rigorous statistical analysis of the properties of the first stars that form under different initial magnetic field strengths. Figure Figure 3.6 shows the number of sinks and the cumulative distribution function (CDF) of the masses of sink particles formed in the four different magnetic field cases. The peak of the distribution of sink masses does not change appreciably between the four runs, however, a second peak at $50\,M_\odot$ becomes more and more prominent as the field strength increases. The latter simply represents the growing number of systems that remain single to SFE = 5 per cent, where we stop the simulations. Another prominent difference between the runs with zero/weak and strong magnetic fields is the smaller number of less massive sink particles (almost by a factor ~ 2 as seen in Figure 3.6), in runs where secondary fragmentation takes place; this is also clear from the separation in the CDFs for sink masses $> 0.5\,M_\odot$. Thus, three important conclusions that we can draw from these observations are: (1) as the field strength increases, so does the chance of a first star evolving in isolation without any companions, (2) even if turbulent primordial clouds with strong initial magnetic fields do fragment, they tend to form fewer stars on average, and (3) strong magnetic fields suppress the formation of low-mass stars by a factor ~ 2 compared to cases where the field is weak or non-existent.

To check whether the sink mass distributions resulting from simulations with different initial field strengths differ by a statistically-significant amount, we use the Kolmogorov-Smirnoff (KS) test, the output of which is a p-value with which we can rule out the null hypothesis that the sink masses in any given set of simulations were drawn from the same underlying distribution. Following Sharda et al. (2019a), we consider two distributions to be different if their corresponding KS test yields p-value < 0.01, meaning we can rule out the null hypothesis at > 99 per cent confidence. Table 3.2 lists the p-values of the KS tests that we conduct between all possible pairs of simulations. The extremely low p-value for any pairs of B_0 or B_1 on one hand and B_2 or B_3 on the other, is strong evidence that the underlying sink mass distributions that result from the collapse of turbulent primordial clouds with weak/zero and strong magnetic fields are significantly different, with stronger fields yielding fewer, more massive fragments. This is consistent with expectations for contemporary star formation, where additional magnetic pressure increases the total (magnetic + thermal) Jeans mass and suppresses fragmentation (Federrath &

Klessen 2012; Hopkins 2013; Krumholz & Federrath 2019).

Note that we derive this result based on 200 realisations in total. Figure 3.7 demonstrates why such a large number of realisations is necessary, by showing how the p-value between the B_0 and other cases changes as we add more and more stars (from more and more independent simulations) to the sample. We see that detecting the difference between the mass distribution in case B_0 and those produced in cases B_2 or B_3 requires $\gtrsim 100$ stars (on average for each case, so $\gtrsim 200$ in total) for reliable detection. Smaller samples would be insufficient. This result reinforces our expectation, laid out in Section 3.1, that multiple realisations are necessary to draw strong conclusions about the characteristics of chaotic systems like turbulent star-forming molecular clouds.

Multiplicity

We next examine the number of singles, binaries, triples and quadruples formed in our simulations. The first step in our investigation is to classify stars by multiplicity. This is not a trivial task, since we cannot assume that all the stars formed in a single simulation constitute a bound system – in some cases there are complex interactions between fragments in the disc that lead to one or more stars being ejected, such that they would likely end up single. To handle this issue, we classify every star formed in each simulation as single (S), or as belonging to a binary (B), triple (T) or quadruple (Q) system, following the algorithm given by Bate (2009a). Briefly, this algorithm recursively finds the most bound stellar pair and replaces the constituent stars with a single star at their center of mass with a velocity equal to their center of mass velocity. The algorithm moves on to the next pair if the subsequent bound pair would lead to the formation of a quintuple, since such high-order multiples would almost certainly disintegrate dynamically. If no more bound pairs can be formed, the algorithm moves on to the next most bound pair among the remaining stars. The algorithm terminates if there are no more bound pairs, or if the only bound pairs remaining would, if combined, yield an aggregate of > 4 stars. Once this state has been reached, the algorithm has classified every star in a given simulation into the type of system – S, B, T, or Q – to which it belongs.

Figure 3.8 plots the ratio of the number of singles, binaries, triples and quadruple systems to the total number of sink particles formed in each case. Following Krumholz et al. (2012b), we calculate the statistical uncertainty on these fractions by assuming that the number of stars we have in each case are random variates drawn from a binomial distribution for which the true probability that a randomly chosen star is single is f (and similarly for all other multiplicities). We assume a flat

prior on f from $[0,1]$. Then, if the sample produced by our simulations constitutes exactly M singles from a total of N stars, the 16th percentile (f_{16}) on the posterior probability distribution for f is then implicitly given by

$$\int_0^{f_{16}} \binom{N}{M} f^M (1-f)^{N-M} \, df = 0.16 \,, \tag{3.1}$$

and the 84th percentile (f_{84}) is

$$\int_{f_{84}}^1 \binom{N}{M} f^M (1-f)^{N-M} \, df = 0.16 \,. \tag{3.2}$$

The median value $f_{50} = N/M$, not surprisingly. We see that, independent of magnetic field strength, almost one-third of all sink particles formed are single. Most interestingly, we find that the magnetic field strength has no effect on the multiplicity distribution. All four cases produce fractions of singles, binaries, triples, and quadruples that are identical within the statistical uncertainties, despite our large sample size.

We can understand how to reconcile the apparent insensitivity of multiplicity to magnetic field strength with the clear dependence of the IMF on it by examining the mass functions broken down by stars that are classified into different multiplicity groups. To this end, we perform KS tests to check whether each pair of runs differs significantly for a particular multiplicity, for example, we ask whether the mass function for singles formed in case B_0 is statistically-distinguishable from the mass function for singles formed in cases B_1, B_2 or B_3. We provide the results of this analysis in Table 3.3 where we list the KS test p-values between the different pairs of multiples for different cases of initial magnetic field strength. This table provides us with important information on what drives the sink mass distributions with zero/weak fields to differ from those produced in simulations with strong fields. As we report in Section 3.3.3, the p-value between $B_0/B_1 - B_2/B_3$ cases is extremely low, indicating that the overall mass functions are statistically very different. From Table 3.3, we see that the p-value for the distribution of binaries between these cases is very low, thus, it is clear that the binary population is strongly affected by the presence of magnetic fields. On the other hand, the p-value for triples and quadruples is high (except for quadruples of B_1 and B_2). Similarly, the p-value between the single sink distributions of $B_0/B_1 - B_2/B_3$ is also low. Thus, Table 3.3 indicates that the difference in the overall mass function between weak-field and strong-field cases arises primarily in cases where little or no fragmentation takes place, and the result is a single or binary. In cases where many fragments form,

yielding a triple or higher, there is little difference.

A final metric by which we can compare our simulations is by examining their multiplicity fractions,

$$mf = \frac{B + T + Q + ...}{S + B + T + Q + ...}, \tag{3.3}$$

as a function of mass of the primary (Hubber & Whitworth 2005; Bate 2012a). Figure 3.9 is analogous to Figure 17 of Bate (2012a) and Figure 14 of Krumholz et al. (2012b) where we plot the multiplicity fraction against the mass of the primary in different bound systems, including single stars. The markers denote the central values of each logarithmic mass bin and the width of the rectangular boxes for cases B_0 and B_3 denote the width of the mass bin. The height of the boxes shows the 16th and 84th percentiles of the multiplicity fraction in that bin, which we calculate using equation 3.1 and equation 3.2. Figure 3.9 shows that the multiplicity fraction changes as a function of the primary mass with the change in field strength. In line with what is observed in contemporary star formation (Bate 2012a; Krumholz et al. 2012b), mf increases with increasing primary mass, implying that more massive stars have more companions on average. The sharp drop in the last mass bin should be treated with caution, because it is an artifact of our choice to halt simulations at 5 per cent SFE: this guarantees by construction that all 50 $M_\odot$ stars are single. That said, we argue below that these cases likely do represent stars that will be single regardless of how far the simulation is run. Omitting these cases of very massive single stars, we find that the transition from mostly singles to mostly multiples occurs at a higher mass in the presence of a strong magnetic field; for example, we see from Figure 3.9 that a 2 $M_\odot$ star is more likely to have companions in the absence of a magnetic field.

3.4   Discussion

3.4.1   Implications for the primordial versus contemporary IMF

It is interesting to compare our results for the effects of magnetic fields on primordial star formation with work on present-day star formation, with an eye to understanding the implications for the primordial IMF. Simulations of present-day systems paint a somewhat complex picture of the effect of magnetic fields on fragmentation. While magnetic fields appear to suppress fragmentation in simulations that do not include radiative feedback (e.g., Machida et al. 2005; Hennebelle & Teyssier 2008), the effects in simulations that do are more subtle. Simulations of monolithic massive
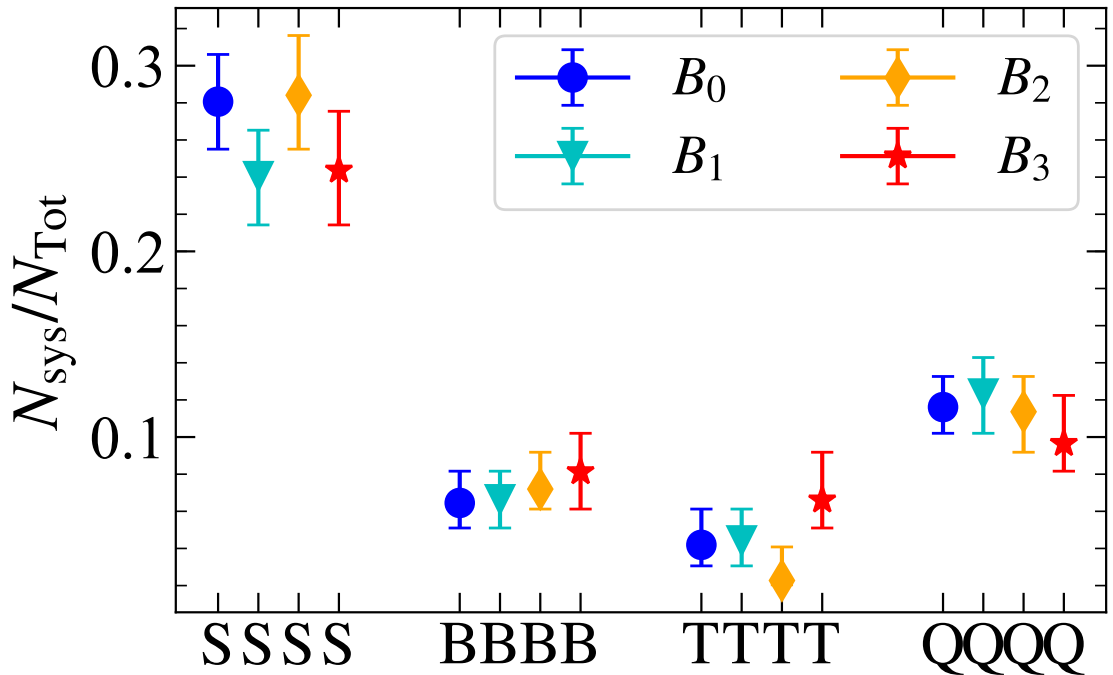
Figure 3.8: Number of singles (S), binaries (B), triples (T) and quadruples (Q) formed in all the four main simulation cases (with different magnetic field strengths) divided by the total number of stars formed at the SFE = 5 per cent threshold, summed over all realizations. The error bars shown indicate the 16th to 84th percentile uncertainty range.

cores tend to find that magnetic fields also suppress fragmentation in them (e.g., Commerçon et al. 2010; Myers et al. 2013), but simulations that follow the formation of entire star clusters on larger scales generally find that magnetic fields may be less important compared to radiation feedback at suppressing fragmentation (e.g., Myers et al. 2014a; Cunningham et al. 2018a; Wurster et al. 2019). This is because, by the time the cascade of collapse has produced a $\sim 1\ M_\odot$ core, thermal pressure fed by radiation feedback from the protostar at the center of the core dominates over magnetic pressure (Krumholz et al. 2016a). However, the magnetic field changes the gas distribution of the clouds already before the formation of cores starts, making the field a crucial ingredient for the initial conditions that leads to their fragmentation (Hennebelle & Teyssier 2008; Padoan & Nordlund 2011; Molina et al. 2012; Federrath 2015, 2018, 2020). In this respect our finding here is more similar to the simulations of present-day massive cores, or those without radiation feedback.

This makes sense in light of some of the important differences between present-day and population III star formation. First, the typical "core" that arises from cosmological simulations, and that we choose as an initial condition, is much more massive and less turbulent than a modern-day massive protostellar core, due to
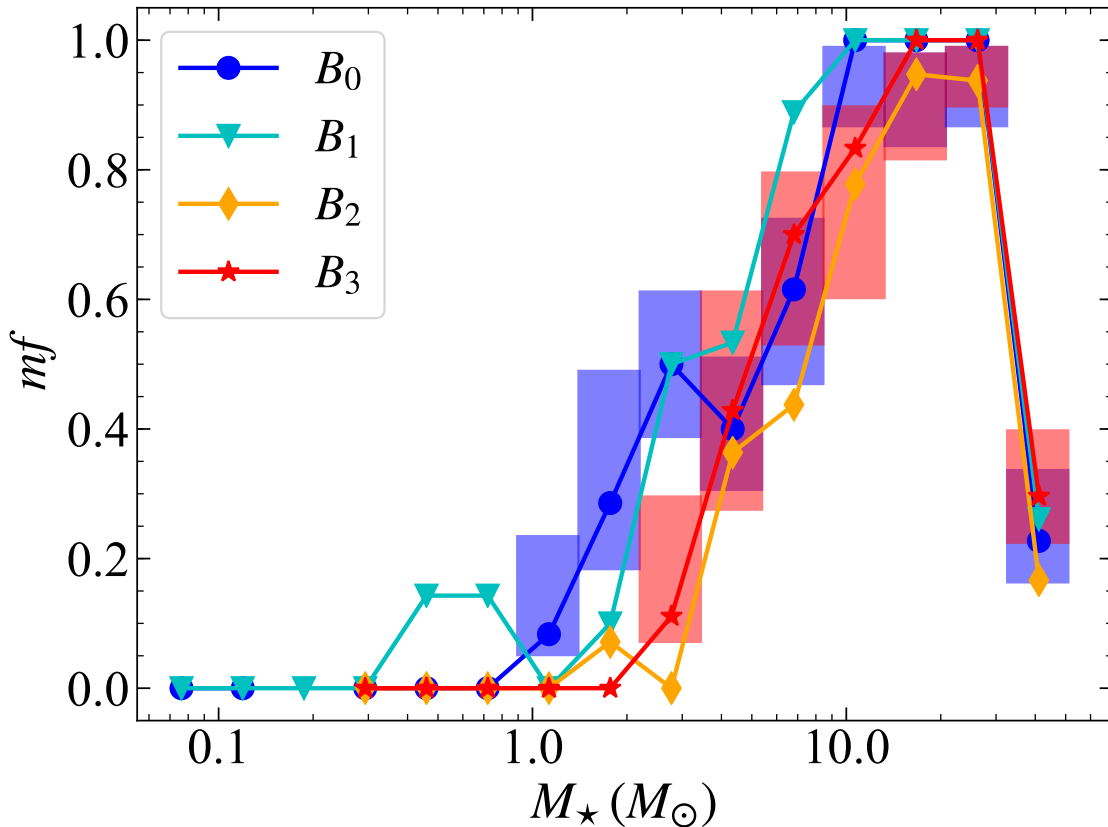
Figure 3.9: Multiplicity fraction for each bin of primary mass, analogous to Figure 17 of Bate (2012a) and Figure 14 of Krumholz et al. (2012b) for simulations of contemporary star formation. Markers denote the central value of each mass bin. The width of the rectangular boxes denotes the extent of the mass bin and the height denotes the 16th and 84th percentiles on the measured multiplicity fraction by assuming it to be a binomial distribution. For clarity, only the percentiles for cases B_0 and B_3 are shown.

its higher temperature and thus lower Mach number (~ 1 for a primordial core, versus $\sim 5 - 10$ for a colder modern-day core – Tan et al. 2014). Second, due to the efficient coupling between stellar radiation and gas provided by dust grains, radiation feedback plays a much more important role in present-day star formation, and at a much earlier stage, than it does for primordial star formation. Indeed, radiation feedback appears to be the most important ingredient to suppress fragmentation in present-day star formation (e.g., Bate 2009a; Offner et al. 2009a; Krumholz 2011a; Krumholz et al. 2016a; Guszejnov et al. 2016a; Federrath et al. 2017a), leaving only a lesser role for magnetic fields at the later stages when cores have already formed. By contrast, in the case of primordial star formation, the inability of the gas to cool renders the entire system hotter and thus harder to affect by radiation, and the lack of solid material to couple the gas to the dust leaves a more important role for magnetic fields in primordial star formation compared to contemporary star

Table 3.3: KS test p-values for comparisons between the mass functions produced by various cases for stars of the indicated multiplicity (see main text). Thus, for example, the top row of the table means that the p-value we obtain by comparing the mass distribution of singles formed in case B_0 to those of the singles formed in cases B_0, B_1, B_2, and B_3, respectively, are 1.0 (by construction), 0.84, 0.006, and 0.02. The next row gives the corresponding values for comparing binaries in case B_0 to the other cases, and so forth. Low p-values imply that the null hypothesis that the two underlying distributions are the same can be rejected with high confidence.

		B_0	B_1	B_2	B_3
	S	1.0	0.84	0.006	0.02
B_0	B	1.0	0.12	10^{-5}	10^{-6}
	T	1.0	0.32	0.09	0.22
	Q	1.0	0.84	0.02	0.23
	S	0.84	1.0	0.003	0.009
B_1	B	0.12	1.0	0.04	0.02
	T	0.32	1.0	0.03	0.23
	Q	0.84	1.0	0.007	0.10
	S	0.006	0.003	1.0	0.19
B_2	B	10^{-5}	0.04	1.0	0.29
	T	0.09	0.03	1.0	0.43
	Q	0.02	0.007	1.0	0.66
	S	0.02	0.009	0.19	1.0
B_3	B	10^{-6}	0.02	0.29	1.0
	T	0.22	0.23	0.43	1.0
	Q	0.23	0.10	0.66	1.0

formation.

In this light, the role of magnetic fields in shaping the primordial IMF appears to be particularly important. Even though our simulations form more than 1100 sink particles, the total number of sub-solar sinks formed in the simulations is only 15 and 6 per cent, for cases B_0 and B_3, respectively. We emphasise that this is an upper limit, since, at the time we halt the simulations, many of these low-mass sinks are still accreting, while few new fragments are emerging (see below). Thus, our simulations suggest not only that the primordial IMF was top-heavy, as has long been expected based on non-MHD arguments (Schneider et al. 2006b; Susa et al. 2014; Stacy et al. 2016), but that it formed a very small number of sub-solar stars that could have survived to the present day. The latter is almost entirely due to the influence of magnetic fields, which strongly suppress the disc fragmentation that otherwise seems to produce low-mass stars. In this sense magnetic fields in primordial stars appear to play the role that radiation feedback takes in present-day star formation, *i.e.,* it stabilises discs and thus prevents the generation of large numbers of fragments whose masses are well below the peak of the mass function

that is produced by primary fragmentation. These observations seem consistent with the fact that no surviving low-mass Population III stars have been discovered so far.

3.4.2   Caveats

While our results conclusively show that magnetic fields will have an impact on the primordial IMF, there are various caveats that we should keep in mind while interpreting its implications. We list them below and comment on how significant they can be:

1. *Resolution.* This can be broken into two parts: the effects of resolution on fragmentation (minimum cell length that can be resolved) as well as on the number of cells per Jeans length used.

    (a) Gravitational fragmentation. The sink mass distribution we analyze is resolution-dependent; at high resolution, there is a possibility that sinks with lower masses will be formed, or a different level of fragmentation will be observed. However, we showed in Sharda et al. (2019a) that convergence (in terms of the number of sink particles) is achieved at the level of refinement we use for the same initial conditions. While the overall shape of the distribution of sink masses formed in isothermal MHD turbulence simulations is scale-free (Krumholz & Federrath 2019), there is no reason to believe this would be the case for non-isothermal simulations like ours where chemistry and hydrodynamics both dictate the thermodynamics of the system. However, we cannot go to higher resolutions to perform a large number of runs, due to computational limitations.

    (b) Dynamo amplification. As we mention in Section 3.2.3, we use 32 cells per Jeans length as recommended by Federrath et al. (2011c) so that minimum dynamo action is resolved in the weak-field case (B_1), whereas we do not expect any dynamo to operate in the strong-field cases (B_2 and B_3) as they are already saturated (e.g., Federrath et al. 2011b; Federrath 2016). We discuss the details of the dynamo action on the core and disc in a companion paper (P. Sharda et al., in preparation); here, we simply note that, while Federrath et al. (2011c) show that 32 cells per Jeans length is the minimum resolution required to capture the dynamo at all, even at this resolution the growth rate of the dynamo is underestimated. Thus, it is possible that at higher resolution (more cells per Jeans length), case B_1 would behave more similarly to B_2 or B_3, since its field would grow

more rapidly. However, even if this were to occur, it would in no way contradict our conclusion that primordial magnetic fields will suppress fragmentation and affect the shape of the IMF.

2. *Initial Conditions.* While we initialise our simulations to be consistent with results from cosmological simulations and several similar simulations of primordial star formation, we cannot take into account more realistic cloud geometries, and distribution of temperature and velocity in the cloud, which can be directly derived from structure formation in the early Universe (see, for example, Turk et al. 2012). However, simulations that start from cosmological conditions are difficult to follow on scales on which the primordial clouds ultimately collapse to form the first stars. Additionally, it is highly computationally expensive to run the large number of realisations of such simulations that would be needed to perform rigorous statistical analyses to appropriately sample the IMF as we do in this work (c.f., Figure 3.7). Thus, there remains a trade-off between selecting more realistic initial conditions and the number of such simulations that are feasible.

3. *Radiation Feedback.* A crucial ingredient missing in our simulations is radiation feedback. Earlier works have conclusively showed that radiation feedback can halt accretion onto massive first stars, thereby limiting their final masses (McKee & Tan 2008; Hosokawa et al. 2011b; Stacy et al. 2012; Tanaka et al. 2017; Sugimura et al. 2020), especially if the accretion rates are low (Hirano et al. 2014; Latif & Schleicher 2015). This is precisely why we choose SFE = 5 per cent as our threshold beyond which we expect our results to deviate from reality. Analyses such as ours are crucial precursors to a suite of complete radiation MHD simulations of the first stars because they can disentangle the effects of magnetic fields alone.

4. *Jets and Outflows.* Jets are well known to emerge from the inner accretion disc of protostars (Frank et al. 2014; Offner et al. 2014). They can carry away mass from the protostellar-accretion disc system, thus reducing the final stellar mass and consequently impacting the IMF. Machida et al. (2006) study the formation and launching of strong jets in simulations of the first stars where an ordered magnetic field is assumed, showing that the stellar mass can be reduced in such cases. However, recent present-day star formation simulations by Gerrard et al. (2019) show the absence of a jet in cases where the magnetic field is completely tangled and does not have an ordered component, similar to what we expect for primordial star formation at least in the early stages. Thus, jets might not have a significant impact on the primordial IMF if the

field were highly tangled; however, even a very tangled field can generate an ordered component during protostellar accretion by the action of the $\alpha\omega$ dynamo (Beck et al. 1996; Malapaka & Müller 2013; Falceta-Gonçalves & Kowal 2015). How strong an ordered component could be generated is an open question. However, we do not have the resolution in our simulations to resolve the regions of jet launching where this might take place (Federrath et al. 2014a).

5. *Non-ideal MHD effects.* Note that we perform ideal MHD simulations to study the role of magnetic fields during the formation of the first stars. As in the present-day Universe (e.g., Bai & Stone 2011; Nolan et al. 2017; Wurster et al. 2018; Wurster & Li 2018), non-ideal MHD effects are potentially important in the primordial Universe as well. For example, Schleicher et al. (2009) and Nakauchi et al. (2019) show that ambipolar diffusion has an impact on the thermal evolution $(n-T)$ of primordial clouds. Additionally, we do not include Li as a chemical species since its importance for both chemistry and cooling have shown to be negligible (Galli & Palla 2013; Liu & Bromm 2018). However, Li has the highest ionization potential in all the primordial species and also becomes the main charge carrier at $n > 10^8\,\mathrm{cm}^{-3}$ (Glover & Savin 2009), both of which can impact the collapse. Nonetheless, (Schober et al. 2012a, see their Figure 8) show that the growth rate of the field due to dynamo amplification is orders of magnitude more than the dissipation caused by ambipolar diffusion and Ohmic effects, except around $n \sim 10^9\,\mathrm{cm}^{-3}$ (see also, Machida & Doi 2013).

6. *Subsequent fragmentation and multiplicity.* We cannot ignore the fact that we stop our simulations only a few thousand yr after the formation of the first sink particle. Any subsequent fragmentation that we cannot capture has the potential to change the sink mass distributions and multiplicity. The multiplicity can also change even without fragmentation as dynamical interactions take place. However, this is unlikely to alter our conclusions, because when we continue to run the simulations past the threshold, we find additional sinks appearing in only a small fraction of our runs; the number of such new sinks is less than 15 per cent of the sinks already formed in the extra time computationally feasible in which the SFE reaches 10 per cent. This is because almost all secondary fragmentation, if any, already occurs within our specified threshold, and is consistent in cases of single-star runs with the results of Latif et al. (2013a).

7. *Final stellar masses.* A common and well-known feature of all simulations

of Population III star formation is that they cannot be run for millions of yr in proper time once the stars have formed. Thus, the final masses of star particles in such simulations cannot be ascertained (see, however, McKee & Tan 2008; Hirano et al. 2014). Nonetheless, the lack of knowledge of the final stellar masses should not change the conclusions of this work; if magnetic fields already affect the distribution of Population III protostars soon after they have formed, their presence will certainly impact the distribution of their final masses.

3.5 Conclusions

In this work, we investigate how a dynamo-induced magnetic field in pre-collapse primordial clouds affects the primordial initial mass function. We do so by generating one of the largest suites of high-resolution ideal MHD simulations of the formation of the first stars. We follow 50 realizations of an isolated, initially-turbulent primordial core that only differ in the initial random turbulence and unordered magnetic field structure, for three different initial magnetic field strengths each, as motivated by various arguments for generation, sustenance and amplification of primordial magnetic fields. We also carry out control simulations where the magnetic field is absent. The 200 simulations in total form more than 1100 sink particles (used as a proxy for stars), thus providing us with a sample size sufficient to characterise the Population III IMF.

We show that the sink mass distributions of cases with weak/zero magnetic field strength are statistically different from those produced by simulations with strong magnetic fields. We find that strong fields suppress fragmentation in primordial clouds, reducing the number of low-mass stars almost by a factor of 2. As a result of this shift, our strongly-magnetised simulations produce almost no first stars at masses $\lesssim 1\ M_\odot$, small enough that they might be expected to survive to the present day. In contrast, in the non-magnetised cases such low-mass stars are smaller than average, but are not a very uncommon outcome. We emphasise, however, that the results of individual simulations are highly chaotic, so that sample sizes of several hundred stars are required to detect the IMF shift we observe with confidence. Studies using only a single realisation of each magnetic field strength, or even ~ 10 may not yield a statistically-robust signal. We also caution that, since our simulations include only an isolated core, we lack a turbulent cascade from larger scales, as would be present for fully cosmological initial conditions. We intend to explore the effects of these more realistic initial conditions in a forthcoming study.

We also find that the population of singles and binaries differ in the strong-field cases from the control simulation. The field tends to affect those simulations more where little fragmentation is present, leading to the formation of single or binary stars. In contrast, the magnetic field strength has no detectable impact on the overall clustering and multiplicity fraction of first stars. The effect we observe is simply that strong fields shift the entire mass distribution to larger values, and in the process, shift the transition where first stars go from being mostly single to mostly multiple to higher masses.

In summary, we find strong evidence that magnetic fields impact the primordial IMF to a greater extent than they do for the present-day IMF. Even with all the caveats as listed in Section 3.4.2, it is clear that magnetic fields will have a significant impact on the primordial IMF, primarily by suppressing the formation of lower-mass stars even before radiation feedback kicks in to halt accretion onto massive stars. There are convincing arguments in the literature that project a strong magnetic field during the collapse of primordial clouds, due to amplification by flux-freezing and the small-scale, turbulent dynamo. Thus, future works that discuss the primordial IMF should take into account the role magnetic fields play in setting the formation and evolution of Population III stars.

Acknowledgements

Magnetic field amplification in accretion discs around the first stars: implications for the primordial IMF

Context and Contribution

This chapter have been previously published as '**Magnetic field amplification in accretion discs around the first stars: implications for the primordial IMF**', *by* **Piyush Sharda, Christoph Federrath, Mark R. Krumholz, and Dominik R. G. Schleicher, 2021, MNRAS, 503, 2014**. *The work is presented here exactly as in the publication. I initiated and led the idea behind this work. I have ran the simulations described in this paper, and post-processed the simulation data for further analysis. I have written the majority of the paper, with inputs and suggestions from co-authors.*

Abstract

Magnetic fields play an important role in the dynamics of present-day molecular clouds. Recent work has shown that magnetic fields are equally important for primordial clouds, which form the first stars in the Universe. While the primordial magnetic field strength on cosmic scales is largely unconstrained, theoretical models strongly suggest that a weak seed field existed in the early Universe. We study how the amplification of such a weak field can influence the evolution of accretion discs around first stars, and thus affect the primordial initial mass function (IMF). We perform a suite of 3D ideal magneto-hydrodynamic (MHD) simulations with different initial field strengths and numerical resolutions. We find that, in simulations with sufficient spatial resolution to resolve the Jeans scale during the collapse, even initially weak magnetic fields grow exponentially to become dynamically important

due to both the so-called *small-scale turbulent dynamo* and the *large-scale mean-field dynamo*. Capturing the small-scale dynamo action depends primarily on how well we resolve the Jeans length, while capturing the large-scale dynamo depends on the Jeans resolution as well as the maximum absolute resolution. Provided enough resolution, we find that fragmentation does not depend strongly on the initial field strength, because even weak fields grow to become strong. However, fragmentation in runs with magnetic fields differs significantly from those without magnetic fields. We conclude that the development of dynamically strong magnetic fields during the formation of the first stars is likely inevitable, and that these fields had a significant impact on the primordial IMF.

4.1   Introduction

From the formation of molecular clouds to their collapse into protostar-accretion disc systems, turbulence and magnetic fields play several roles in setting the overall direction for a star formation episode. While extensive studies have been carried out to investigate the role of turbulent magnetic fields in present-day star formation (see reviews by Crutcher 2012; Han 2017; Wurster & Li 2018; Hennebelle & Inutsuka 2019; Krumholz & Federrath 2019; Crutcher & Kemball 2019; Zhao et al. 2020), only a handful of 3D simulations have looked at their role in the early Universe, especially during the formation of the first generation of stars (Machida et al. 2008a; Sur et al. 2010; Schleicher et al. 2010; Turk et al. 2012; Latif et al. 2013b; Machida & Doi 2013; Latif et al. 2014; Liao et al. 2019; Grete et al. 2019). This is primarily due to the lack of solid constraints on the magnetic field strength and topology in the early Universe (Widrow 2002; Giovannini 2004; Widrow et al. 2012; Ryu et al. 2012; Wagstaff et al. 2014; Subramanian 2016). However, there is a growing consensus on the presence of a cosmic-scale primordial field, no matter how weak (Brandenburg et al. 1996; Hammond et al. 2012; Subramanian 2016; Planck Collaboration et al. 2016b). This motivates studying magnetic fields that may be amplified from the primordial field during the collapse of molecular clouds, leading to Population III star formation.

Several studies have conclusively shown that the presence of a turbulent dynamo (Kazantsev 1968; Meneguzzi et al. 1981; Brandenburg & Subramanian 2005; Subramanian 2016) can exponentially amplify any weak seed field to near-saturation values (e.g., Federrath et al. 2011c; Schober et al. 2012a; Federrath et al. 2014a; Schober et al. 2015; Federrath 2016; Xu & Lazarian 2016; McKee et al. 2020). In the early Universe, the presence of such a turbulent dynamo driven by gravity is

expected when baryonic matter starts collapsing towards the centre of dark matter minihaloes (Greif et al. 2008; Wise et al. 2008; Turk et al. 2012; Grete et al. 2019). This infall leads to the creation of overdense regions that harbour the first molecular clouds where Population III star formation ultimately takes place (see reviews by Bromm 2013; Klessen 2019; Haemmerlé et al. 2020). Apart from the action of the small-scale turbulent dynamo, it is also expected that accretion discs around Population III stars may contain a large-scale mean field component (Liao et al. 2019). This can occur if discs undergo differential rotation and angular momentum transport through viscous stresses, thereby generating a large-scale dynamo from a seed field that can sustain a dynamically strong and coherent mean field component (Ruzmaikin et al. 1988b; Brandenburg et al. 1995; Hawley et al. 1996; Stone et al. 1996). In fact, given that the characteristic diffusion timescale in accretion discs is very short ($10^2 - 10^4$ s) as compared to viscous timescales (order of few yr), dynamically strong magnetic fields that last for the lifetime of the disc can only be generated by a dynamo operating in accretion discs (Ruediger et al. 1995).

The expectation that dynamically-significant magnetic fields might be present during the formation of Population III stars naturally raises the question of how such fields might affect the initial mass function (IMF) of the first stars. In a recent work, Sharda et al. (2020a, hereafter, SFK20), we presented the first suite of 3D magneto-hydrodynamical (MHD) simulations of Population III star formation aimed at answering this question. We showed that dynamically strong magnetic fields, if present during the formation of the first stars, suppress fragmentation in primordial clouds, thereby increasing the mean stellar mass and greatly decreasing the prevalence of low-mass Population III stars that could potentially survive to the present day. Several works that include radiative transfer (Price & Bate 2009; Bate 2009a, 2012a), protostellar heating feedback (Guszejnov et al. 2016b; Federrath et al. 2017b; Mathew & Federrath 2020a), or both (Offner et al. 2009b; Krumholz et al. 2010; Urban et al. 2010; Myers et al. 2014a; Hennebelle et al. 2020a) highlight that radiation feedback plays an important role in setting the present-day stellar IMF, potentially even more so than magnetic fields (Krumholz et al. 2016b; Cunningham et al. 2018a; Wurster et al. 2019; Krumholz & Federrath 2019; Lee & Hennebelle 2019; see, however, Rosen & Krumholz 2020, who find that, for present-day massive stars, magnetically-driven outflows are more important than radiation feedback). However, SFK20 argue that this might not be the case for Population III stars because the late onset of radiation feedback due to the absence of dust (Hosokawa et al. 2011b, 2012; Sugimura et al. 2020) allows a much longer period when magnetic effects and magnetic pressure can dominate and consequently impact the primordial IMF. However, the results of SFK20 do not fully resolve the question of whether

magnetic fields significantly influence the first star IMF, because they did not determine the magnetic field strength self-consistently; they only showed that, if fields near dynamo-saturation levels are present, they have a significant effect on the IMF of the first stars. Calculating the field strength self-consistently is a challenging numerical problem, because dynamo amplification is exquisitely sensitive to numerical dissipation, and thus, very high resolution is required to recover even qualitatively correct estimates for the rate of dynamo growth (Federrath et al. 2014a; Schober et al. 2015; Federrath 2016; McKee et al. 2020). The simulations of SFK20 only marginally resolve the dynamo action, and thus leave the question of the true magnetic field strength in primordial star-forming regions unsolved.

In this study, we answer this question by studying in detail how dynamo amplification can occur in first star discs. We find that, given sufficient resolution in the disc, even an initially weak field can be exponentially amplified due to the presence of both the small-scale and the large-scale dynamo; the former primarily amplifies the turbulent component of the field whereas the latter amplifies the mean component. We show that the resulting saturation level of the field is high enough that magnetic effects on the IMF are inevitably significant. The remainder of this paper is organised as follows. In Section 4.2, we describe our suite of simulations. In Section 4.3 we present our simulation results and discussions; in Section 4.4, we comment on how our results can potentially impact the primordial IMF, and we summarise the implications of our findings in Section 4.5.

4.2   Simulation suite

The simulations presented here are similar to those described in SFK20, where we motivate in detail the choice of initial conditions and numerical methods. Here, we only summarise the key aspects of the simulation setup and methods. For details, we refer the reader to SFK20.

4.2.1   MHD code and basic initial conditions

We perform 3D ideal MHD simulations of Population III star formation using the adaptive mesh refinement (AMR) code FLASH (Fryxell et al. 2000; Dubey et al. 2008), together with the primordial chemistry network from the astro-chemistry package KROME (Grassi et al. 2014). We use sink particles to represent stars (Federrath et al. 2010a); the density threshold for sink particle formation is $n_{\mathrm{sink}} \sim 10^{13}\,\mathrm{cm}^{-3}$. We start the simulations from a spherical core of mass $M_{\mathrm{cl}} = 10^3\,\mathrm{M}_\odot$, with uniform density ($n = 9.05 \times 10^3\,\mathrm{cm}^{-3}$), temperature ($265\,\mathrm{K}$) and composition

(with mass fractions $x_{\mathrm{H}} = 0.7502$, $x_{\mathrm{H_2}} = 0.0006$, $x_{\mathrm{He}} = 0.2492$) as appropriate for the formation of the first stars at the centre of dark matter minihaloes at a redshift of 30 (Sharda et al. 2019a, and references therein). The simulation box is of size 2.4 pc and the boundary conditions are outflow/inflow for the hydrodynamics and isolated for computing gravitational interactions. The initial conditions also include a driven, mixed mode of turbulence (Federrath et al. 2010b, 2011b) that initially follows a velocity power spectrum $P_{\mathrm{v}} \propto k^{-1.8}$, where k is the wave number that spans $2 \leq k \leq 20$. The initial Mach number is trans-sonic, such that the velocity fluctuations equal the local sound speed at the initial temperature. The maximum resolution of the simulations is $\Delta x = 7.6$ au, equivalent to a maximum effective resolution of $65,536^3$ grid cells. A limitation of our work is that we do not include radiation feedback in our simulations, which can halt accretion onto massive stars provided the accretion rates are low (Hosokawa et al. 2011b, 2012, 2016; Sugimura et al. 2020). We also discuss caveats associated with the exclusion of non-ideal MHD effects in Section 4.3.4.

4.2.2   Criteria for resolving dynamo action and initial conditions for the magnetic field

In our previous simulations (SFK20), the refinement criteria were set so as to guarantee that, on all levels at or above the finest, the Jeans length (Federrath et al. 2010a),

$$\lambda_{\mathrm{J}} = \sqrt{\frac{\pi c_{\mathrm{s}}^2}{G\rho}} \tag{4.1}$$

is resolved by at least 32 cells at all times (here, c_{s} is the sound speed). These simulations used three different initially turbulent magnetic field strengths of 1 fG, 9 μG and 30 μG. The latter two of these correspond to plausible scenarios whereby the turbulent dynamo saturates at a ratio of magnetic energy, E_{mag}, to turbulent kinetic energy, $E_{\mathrm{turb,kin}}$, of 0.01 and 0.1, respectively (Federrath et al. 2014a; Schober et al. 2015; Federrath 2016). The magnetic power spectrum goes as $P_{\mathrm{mag}} \propto k^{1.5}$ for $2 \leq k \leq 20$. We use the first and third sets, that is, runs with a field strength of 1 fG and 30 μG, in this analysis[1]. We call these runs weakJ32 and strongJ32, to represent that they start with a weak and strong field, respectively, and the Jeans length is refined with 32 cells at all times. SFK20 provide 50 realisations of each of these cases, which are identical in their mean properties, but differ in the random realisation of the turbulent velocity and magnetic fields. We use half of their suite

---

[1]The statistical outcomes of the runs with an initial field strength of 9 and 30 μG are very similar, so we use only the latter for simplicity.

Table 4.1: List of simulations used in this work. B is the initial root-mean-square magnetic field strength. J represents the number of cells per Jeans length used, Δx is the minimum cell size at the highest level of the AMR grid, and N_{r} is the number of realizations per run. All the realizations between the different runs are matched in pairs of initial random seeds for the turbulence and the magnetic field.

ID	B	J	Δx	N_{r}	Source
weakJ32	1 fG	32	7.6 au	25	SFK20
weakJ64	1 fG	64	7.6 au	25	This Work
strongJ32	30 μG	32	7.6 au	25	SFK20
strongJ64	30 μG	64	7.6 au	25	This Work

(25 realisations of each magnetic field strength) in this study.

As we discuss in Section 4.1, dynamo simulations are extremely sensitive to resolution. We therefore repeat these earlier simulations, but at a higher resolution of 64 cells per Jeans length instead of 32 as used by SFK20. We call these two sets of runs weakJ64 and strongJ64, respectively. Our motivation to go to higher Jeans resolution is to check the operation of the turbulent dynamo in the weak-field case; we expect the strong-field case not to show any small-scale dynamo action, since the initially turbulent field should be close to saturation. Note that a higher Jeans resolution does not mean that we resolve the grid to a smaller cell size; higher Jeans resolution simply implies that the grid creates more cells (of the same size) to better resolve the Jeans length. Thus, the minimum value of Δx remains the same in runs between 32 and 64 cells per Jeans length. However, we also discuss two cases below where we increase the maximum resolution, but these are not part of our main simulation suite, because we are unable to perform a large number of such simulations due to computational expense. Indeed, increasing only the Jeans resolution requires substantially more computational time (Federrath et al. 2011c). For example, runs with 64 cells per Jeans length are up to 8 times more expensive than the respective runs with 32 cells per Jeans length. This increased cost of the simulations precludes us from performing higher-resolution runs for the entire suite of 50 simulations presented in SFK20. However, Figure 7 of SFK20 indicates that 25 realisations constitute a large enough sample to allow us to recover the true statistics of the sink mass distribution with reasonable accuracy. In particular, even 25 realisations are sufficient to show a clear distinction between the distributions of sink particle masses produced in magnetised versus purely hydrodynamic simulations, which is the critical question for us. We summarise the full simulation set we use in this paper in Table 4.1.

4.3   Results and Discussions

Following SFK20, we stop the runs at a time when the sink particle has accreted $50\,M_\odot$, corresponding to a parameterized star formation efficiency, SFE $= \sum M_{\mathrm{sink}}/M_{\mathrm{cl}} = 0.05$, where $M_{\mathrm{cl}} = 10^3\,M_\odot$ is the initial cloud mass. We stop the simulations based on this criterion, because we do not include radiation feedback, which starts to play a dominant role for massive first stars (Hosokawa et al. 2011b, 2012, 2016; Sugimura et al. 2020). Note that for all the analysis except for the effects of Jeans resolution on fragmentation, we only use the subset of simulations that forms a single sink particle of mass $50\,M_\odot$ (~ 8 out of the 25 realizations in each case). This is because such simulations have a well-defined accretion disc, enabling a cleaner study of the effects of the magnetic-field amplification in the disc. The simulations where secondary fragmentation takes place form more complex disc-like structures characterised by strong spiral density waves and circum-binary or circum-ternary discs. In such cases, studying the amplification of the small- and/or large-scale dynamo is challenging as it would demand that all the accretion discs be well resolved, and the full simulation be followed to a significantly longer time. Thus, we only study magnetic field amplification in accretion discs around massive first stars.

4.3.1   Morphology and thermal evolution

We begin our discussion by examining the morphology and thermal structure of the discs formed in four representative realisations, one from each of the combinations of resolution and magnetic field strength listed in Table 4.1. Figure 4.1 shows the face-on and edge-on projections of density-weighted number density (n), temperature (T) and magnetic field strength (B) for these four example realisations. All the snapshots are centred at the single sink particle that forms in the simulations (noting again that for this part of the analysis we select simulations that only form one star), and show the time at which the simulation reaches SFE $= 5$ percent. T_{s} denotes the time elapsed since the formation of the sink particle. It is straightforward to notice that the morphology of the system varies significantly in the run weakJ32 as compared to the other three runs. In runs weakJ64, strongJ32 and strongJ64, the snapshots reveal the presence of a hot, spherical bubble that expands radially outwards with time (see movies M1 and M2 attached as online material with this paper for reference) such that there are higher temperatures inside the bubble that lead to more dissociation of H_2. A similar resolution-dependent effect has been noted by Turk et al. (2012) during the formation and collapse of dark matter minihaloes in their cosmological simulations with a seed magnetic field. However, this phenomenon
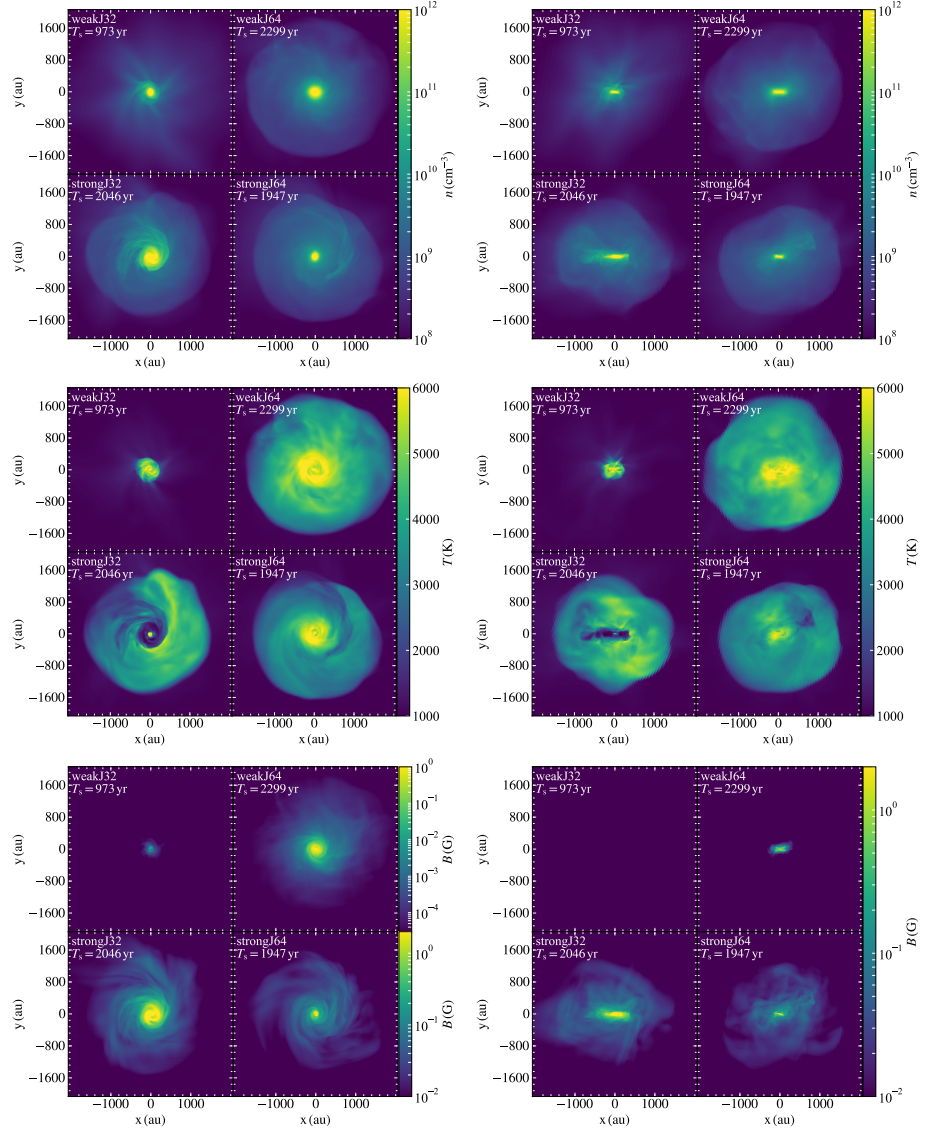
Figure 4.1: Density-weighted face-on (left) and edge-on (right) projections of the number density n (top panels), temperature T (middle panels), and magnetic field strength B (bottom panels) centred on position of the sink particle, for the four different categories of runs we study in this work (see Table 4.1). The snapshots correspond to the end of the simulation where SFE = 5 percent and the sink particle has accreted $50\,\mathrm{M_\odot}$. The simulations shown differ only in resolution and initial magnetic field strength.
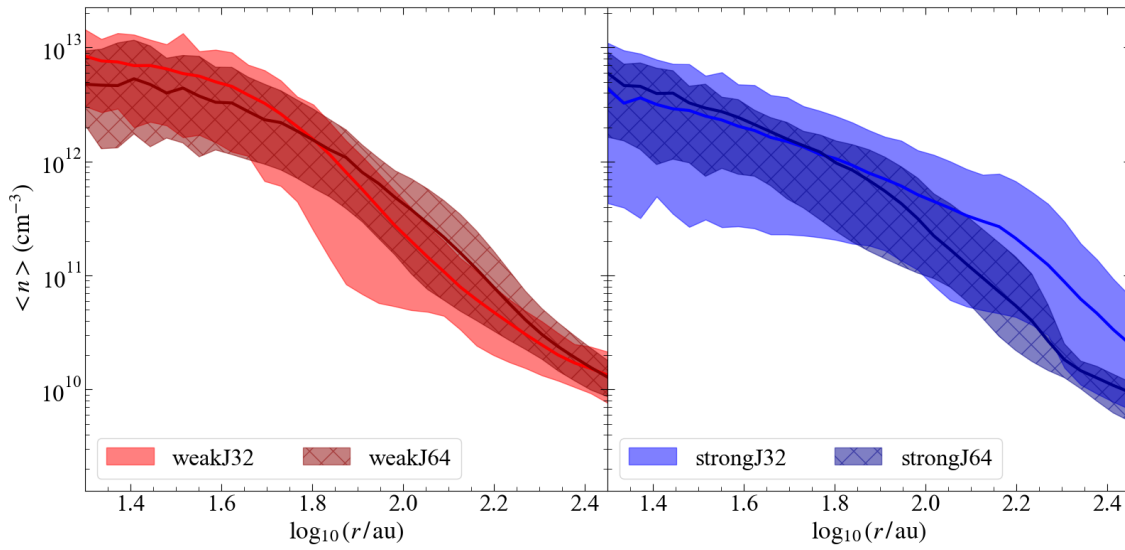
Figure 4.2: Azimuthally-averaged, mass-weighted radial profiles of the number density in the accretion discs around the central star for all the non-fragmenting set of realisations (*i.e.*, where only a single sink particle forms), shown at the end of the simulation when SFE = 5 percent (see Section 4.3). The four sets of simulations denoted in the legend represent weak and strong magnetic fields run with 32 and 64 cells per Jeans length (see Table 4.1). The solid curves represent the mean averaged over all the non-fragmenting realisations in each simulation category. The coloured bands mark the 5th to 95th percentile range. Note that the radial extent of these profiles only covers the accretion discs, and is smaller than the extent of the projections we show in Figure 4.1.
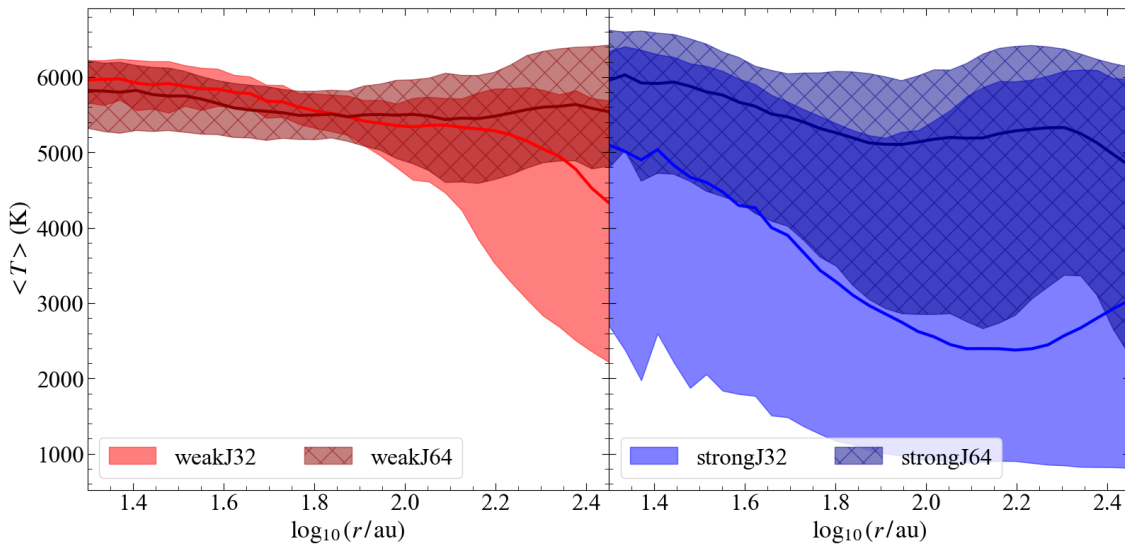
Figure 4.3: Same as Figure 4.2 but for the temperature in the discs.

does not occur primarily due to magnetic fields. We show in Appendix B that the qualitative difference in the outcome is a result of how well we resolve the length and timescales for chemical evolution and radiative cooling across shock fronts. However, the effect is not related to dynamo amplification, and has little impact on the overall results because the thermal pressure is dynamically-unimportant in all cases. For this reason, we do not discuss it further in the main text.

In addition to the hot spherical halo that extends across $\sim 2000\,\mathrm{au}$, the face-on and edge-on projections in Figure 4.1 also reveal the presence of an accretion disc a few $100\,\mathrm{au}$ in size (typically $\lesssim 500\,\mathrm{au}$ in diameter) in each run. The fact that discs form in our ideal MHD simulations even with strong magnetic fields implies the absence of the magnetic braking catastrophe, and could be a result of the misalignment between the rotation axis and the magnetic field, as has been found in Population I star formation (e.g., Seifried et al. 2013; Joos et al. 2013; Li et al. 2013c; Gray et al. 2018). Movies M1 and M2 in the supplementary material show the 3D orientation and geometry of the disc around the star in each of the four runs. The mass of accretion discs around the $50\,\mathrm{M_\odot}$ sink particle varies between $5-40\,\mathrm{M_\odot}$ within the different non-fragmenting runs, with a mean disc mass $\sim 16\,\mathrm{M_\odot}$ in all the four categories listed in Table 4.1. We also find that discs in the J64 runs are systematically more massive than the discs in the J32 runs irrespective of the magnetic field strength.

The difference that is of the greatest interest to us is in the magnetic fields (see bottom panel of Figure 4.1). Strikingly, we see that the magnetic field strength and morphology of the weakJ64 run is much closer to the results we find for strongJ32 or strongJ64 than to weakJ32. Despite having started from identical initial conditions, the field in weakJ64 is ~ 3 orders of magnitude stronger than in weakJ32. We explore this in detail in the following subsections.

Unless explicitly stated otherwise, we calculate all quantities of interest in the frame of reference of the disc once it is formed, averaging over a cylindrical region centred on the sink particle, with the symmetry axis of the cylinder aligned with the angular momentum vector of the mass within $500\,\mathrm{au}$ of the sink particle. We define the usual cylindrical basis vectors $(\hat{r}, \hat{\phi}, \hat{z})$ to denote position within this analysis region. We find that using an analysis region of diameter $500\,\mathrm{au}$ and half-height $50\,\mathrm{au}$ ensures that the resulting volume covers the entire disc in all our realisations. We have also verified that our results are relatively insensitive to the exact choice of radius and height for our analysis region (provided it is large enough to cover most of the mass of the disc), since we calculate mass-weighted quantities, which means that the low-density material does not contribute significantly to our quantitative analyses of the disc material.

4.3.2　Radial profiles

We next discuss the statistical properties of the discs formed in every non-fragmenting realisation. In Figure 4.2 and Figure 4.3 we show the azimuthally-averaged, mass-weighted radial profiles of the number density and the temperature in accretion discs at the end of the simulation where the SFE reaches 5 per cent. The solid curves show the mean value averaged over all the realisations we include, and the coloured bands denote the 5$^{\text{th}}$ to 95$^{\text{th}}$ percentile range. The profiles of number density in the accretion discs are quite similar in all the four runs, with somewhat larger scatter in the strong magnetic field runs. On the contrary, the radial profiles of temperature show significant differences, between strong and weak fields, as well as between runs with 32 and 64 cells per Jeans length. Simulations with strong magnetic fields show a much larger scatter in the disc temperatures as compared to simulations with the weak field.

In Figure 4.4, we plot the azimuthally-averaged, mass-weighted radial profiles of the different components of the velocity field in the accretion discs. We define the turbulent component of the velocity, $\mathbf{v}_{\text{turb}}$, as,

$$\mathbf{v}_{\text{turb}} = \left(v_{\text{r}} - \langle v_{\text{r}} \rangle\right) \hat{r} + \left(v_{\phi} - \langle v_{\phi} \rangle\right) \hat{\phi} + \left(v_{\text{z}_{+/-}} - \langle v_{\text{z}_{+/-}} \rangle\right) \hat{z} , \qquad (4.2)$$

where v_{r} and v_{ϕ} are the radial and toroidal cylindrical components of velocity, and v_{z_+} (v_{z_-}) denotes the component of velocity along the $\hat{z}$ axis of the disc in its upper (lower) half. Angle brackets indicate the azimuthal average of a given quantity; we denote the magnitude of the turbulent field as $v_{\text{turb}} \equiv |\mathbf{v}_{\text{turb}}|$. We subtract the mean components of v_{z_+} and v_{z_-} separately because $\langle v_{\text{z}} \rangle \approx 0$; this systematically removes the influence of any radial or vertical gradients and gives a reasonable estimate of the turbulent velocity (Flock et al. 2011). We see that in all cases our discs are dominated by azimuthal and turbulent motions, with much smaller radial inflow and vertical infall velocities. There is no obvious systematic difference in the results with either resolution or initial magnetic field strength.

Because differential rotation is important for large-scale dynamo action, it is important to characterise the degree of shear in our discs, which is given by $q = -\text{dln}\,(v_{\phi}/r)/\text{dln}\,r$. For a disc in rigid (non-differential) rotation, $q = 0$, whereas for a Keplerian disc, $q = 1.5$. Using the profiles of v_{ϕ} from Figure 4.4, we find $q \approx 1.4$. Thus, the discs are almost Keplerian, but there is some deviation from a perfect Keplerian disc, which is due to additional support from magnetic pressure. To demonstrate this, we define an effective Keplerian velocity $v_{\text{eff,Kep}}$ in the presence

of magnetic fields by subtracting the contribution of the Lorentz force,

$$\frac{v_{\text{eff,Kep}}^2}{r} = \frac{v_{\text{Kep}}^2}{r} - \frac{1}{4\pi\rho}\left[(\nabla \times B) \times B\right], \qquad (4.3)$$

where $v_{\text{Kep}} = \sqrt{GM_{\text{s}}/r}$, M_{s} is the mass of the sink particle, and ρ is the gas density; the final term represents the Lorentz acceleration. As an example, we plot the radial profile of $v_{\text{eff,Kep}}$ for one of the strongJ32 runs in Figure 4.5. We see that the v_ϕ is almost exactly $v_{\text{eff,Kep}}$ at all radii, and and the deviation from v_{Kep} is $\sim 10\%$. Thus we find that our discs are in near-Keplerian rotation, with a small deviation from a Keplerian profile due to magnetic support.

In Figure 4.6 we plot mass-weighted, azimuthally-averaged radial profiles of the different components of the magnetic fields. In analogy to $\mathbf{v}_{\text{turb}}$, we define the turbulent component of the field, $\mathbf{B}_{\text{turb}}$, as,

$$\mathbf{B}_{\text{turb}} = (B_{\text{r}} - \langle B_{\text{r}}\rangle)\,\hat{r} + (B_\phi - \langle B_\phi\rangle)\,\hat{\phi} + (B_{\text{z}} - \langle B_{\text{z}}\rangle)\,\hat{z}\,, \qquad (4.4)$$

where B_{r}, B_ϕ, and B_{z} are the cylindrical components of the total magnetic field, and we denote the magnitude of the turbulent field as $B_{\text{turb}} \equiv |\mathbf{B}_{\text{turb}}|$. In line with the morphological differences between weakJ32 and the other runs, we find that all the components of the field are substantially lower in weakJ32 compared to the other runs. We also see that while the initial magnetic field we imposed is completely random, in all cases except weakJ32, a substantial mean toroidal field develops in the disc, as is clear from the radial profile of $\langle B_\phi\rangle$ in Figure 4.6. This component is comparable in strength to the turbulent component.

By looking at the time evolution of the velocity and the magnetic field profiles (available as movie M3 in the supplementary material), we find that initially, when the sink forms, all the three components of the velocity and the magnetic field are of the same strength. As the disc around the sink starts to grow and expand outwards to conserve angular momentum, a strong toroidal component of velocity (v_ϕ) is generated, which winds up the magnetic field in the $\hat{\phi}$ direction, thus giving rise to a strong B_ϕ component. This happens through the development of the Ω effect that results from shear instabilities (Babcock 1961). We explore the Ω effect further in Section 4.3.3.

4.3.3   Magnetic field amplification

We have seen that in our weakJ64 simulations starting from an initially weak field, the simulations eventually develop both strong turbulent and mean fields. This
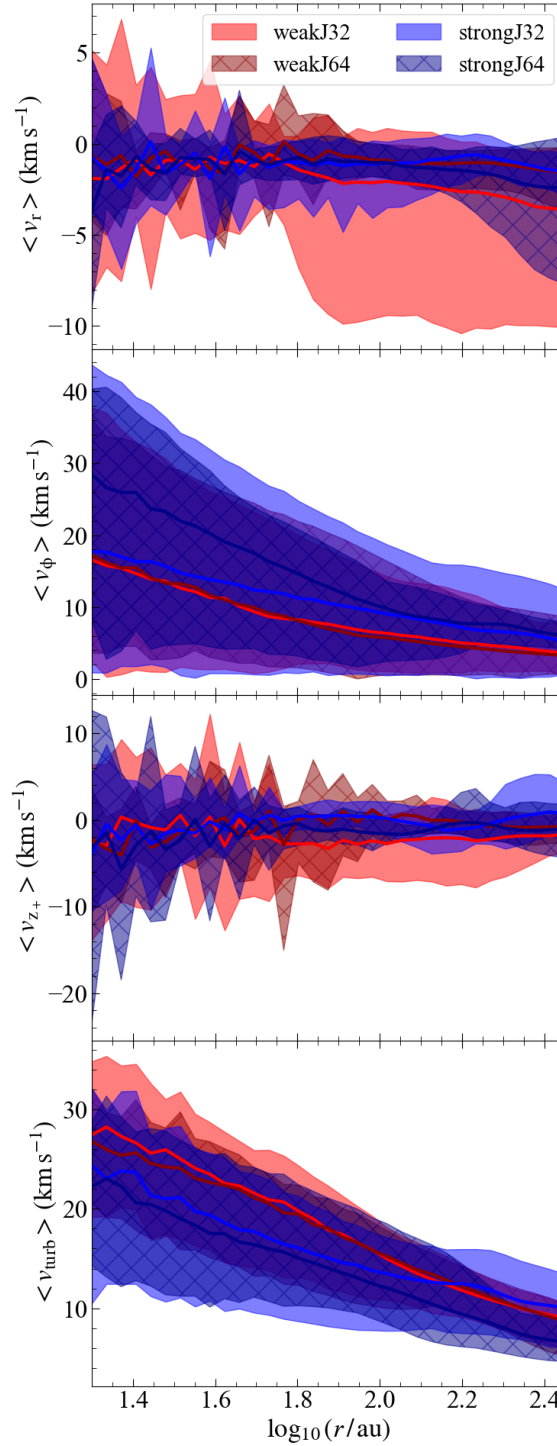
Figure 4.4: Azimuthally-averaged, mass-weighted radial profiles of different components of velocity in the accretion discs around the central star for all the non-fragmenting realisations in each set of simulations, shown at the end of the simulation when SFE = 5 percent. v_{z+} refers to the velocity component along the polar axis of the disc in its upper half (see Section 4.3.2 for details). $\langle v_{turb} \rangle$ in the last panel is the turbulent component of the velocity, defined in equation 4.2. Solid curves represent the mean value and coloured bands represent the 5th to 95th percentile range.
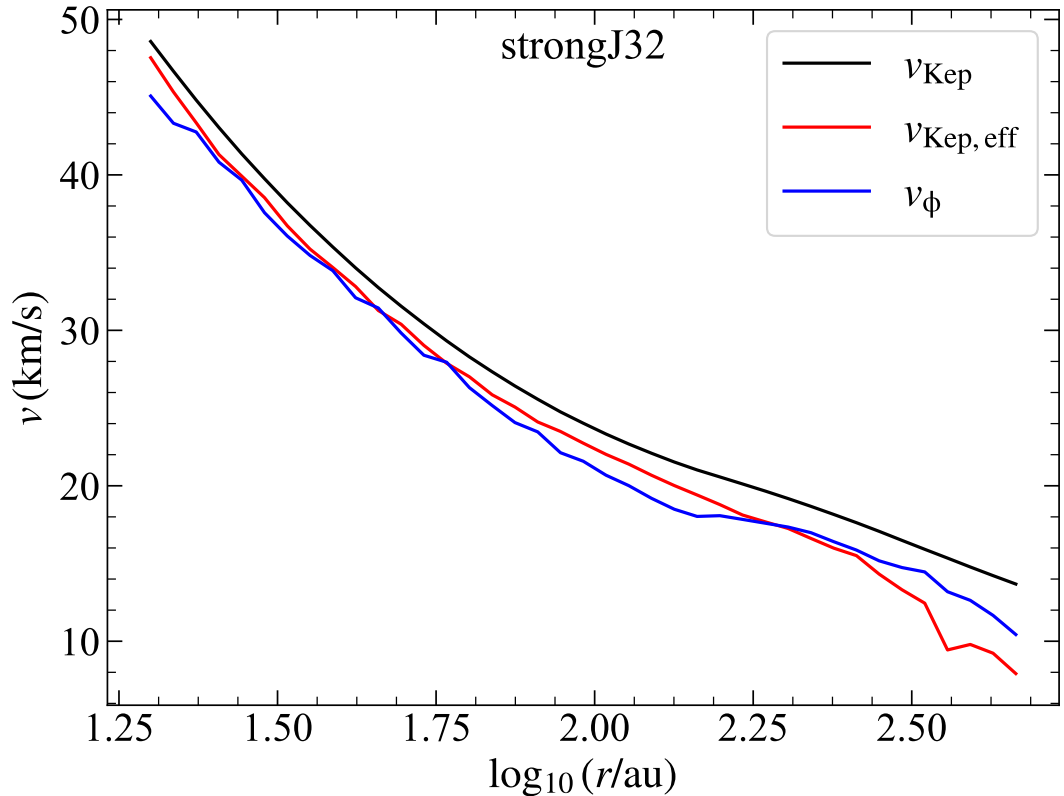
Figure 4.5: Comparison of the toroidal component of the velocity (v_ϕ, blue) with the Keplerian velocity (v_{Kep}, black) in the disc for a representative realisation of the simulation strongJ32. The effective Keplerian velocity ($v_{\mathrm{Kep,eff}}$, red) is obtained by subtracting the contribution due to the Lorentz force from the Keplerian velocity as defined in equation 4.3. The disc is slightly sub-Keplerian due to additional support from magnetic pressure.

suggests the operation of both the small-scale turbulent and the large-scale mean-field dynamo in the disc. Here, we attempt to separate the dynamos based on the scale of turbulent motions that amplify the small-scale dynamo and the scale at which inhomogeneties exist in a mean field generated through the large-scale dynamo (Rogachevskii et al. 2018). In principle, scale separation cannot be naively applied here, because we only have ~ 70 resolution elements across the disc, and we do not resolve the innermost part of the disc where we have less than 30 resolution elements across the disc scale height. Nevertheless, we have an effective magnetic Reynolds number in the discs of the order of $300-600$ (based on $(2r/\Delta x)^{4/3-3/2}$, where $\Delta x = 7.6\,\mathrm{au}$, and the exponents correspond to Kolmogorov and Burgers scaling, respectively; see Federrath et al. 2011c), which is sufficient to trigger the small-scale dynamo for magnetic Prandtl numbers close to unity (Haugen et al. 2004), but we cannot capture its full efficiency in our simulations. This is not unexpected, given that the viscous and Ohmic dissipation scales that control the
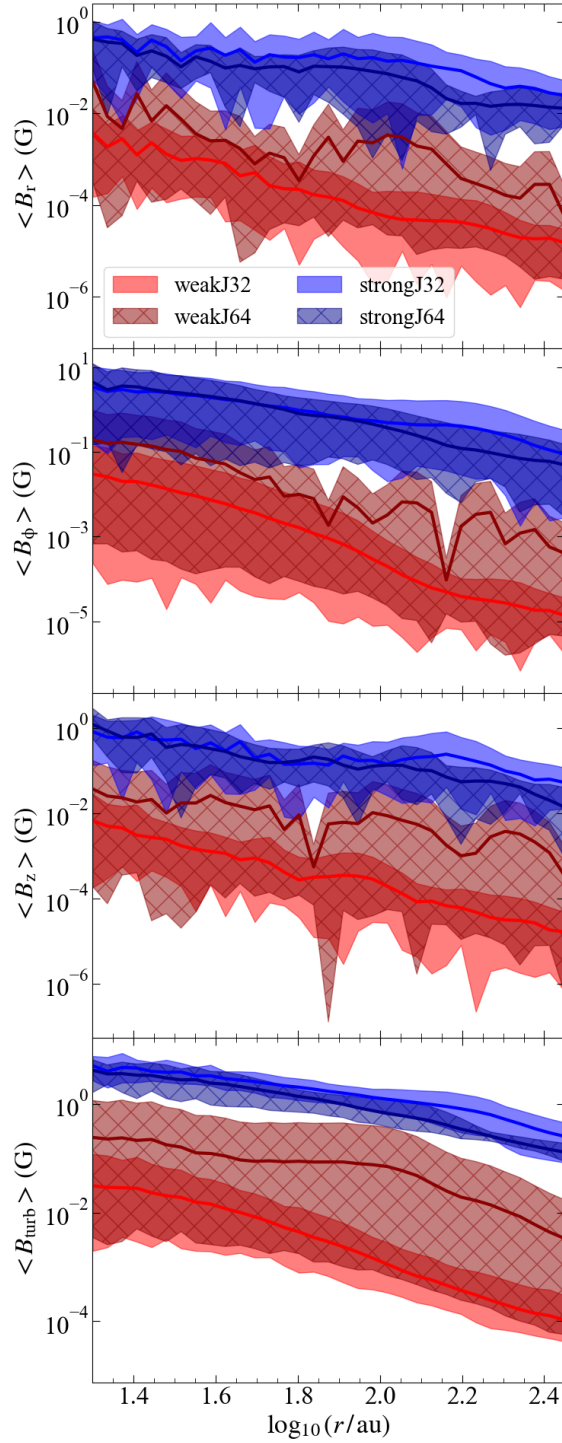
Figure 4.6: Same as Figure 4.4, but for the different components of the magnetic field. B_{turb} is defined as in equation 4.4. Note that $\langle B_\phi \rangle$ is the largest component, indicating a large-scale mean field in the toroidal direction. There is also a strong turbulent component, $\langle B_{\text{turb}} \rangle$, indicating the presence of the small-scale dynamo.

driving scale and the growth rate of the dynamo lie $2 - 3$ orders of magnitude below the current resolution that can be afforded by simulations like ours (Nakauchi et al. 2019, Figure 12). Similarly, since we resolve the scale height in the inner disc with less than 30 resolution elements, it means that we cannot fully capture the large-scale dynamo amplification. Resolving the dynamo action not only depends on the absolute resolution, but also on the Jeans resolution, such that increasing the Jeans resolution leads to more efficient dynamo amplification (Sur et al. 2010; Federrath et al. 2011c). Thus, scale separation is possibly also a function of the Jeans resolution. Keeping these caveats in mind, we caution that we may be in a transitionary regime in between the small-scale and the large-scale dynamo since we do not fully resolve the action of either dynamo. In fact, as Brandenburg & Subramanian (2005) note, the differentiation between a small-scale and a large-scale dynamo is artificial, and in reality, the two regimes are connected. It is believed that the small-scale dynamo acts first, possibly even before the disc is established, but the disc is needed for the large-scale dynamo to act.

In the next two subsections, we quantify the action of these dynamos in accretion discs around the sink particles in our simulations. We remind the reader that we only use those simulations that did not show any fragmentation (~ 8 out of the total 25 simulations in each category) and formed only a single sink particle of mass $50\,\mathrm{M_\odot}$ by SFE $= 5$ per cent, while studying the small-scale and the large-scale dynamo. Analysing multiple runs provides the benefit of overcoming statistical noise between different runs (e.g., Sharda et al. 2019a, 2020a; Wollenberg et al. 2020), but our choice of which simulations we include implies that we only study dynamo amplification in accretion discs around massive first stars.

Small-Scale dynamo

Traditionally, the presence of a small-scale dynamo is verified by an exponential increase in the ratio,

$$Q_{\mathrm{ss}} = \frac{(B_{\mathrm{turb}})_{\mathrm{rms}}}{\rho^{2/3}}\,, \tag{4.5}$$

over the lifetime of the simulation (e.g., Sur et al. 2010; Federrath et al. 2011c; Turk et al. 2012; Schober et al. 2012a; Latif et al. 2013b; Schober et al. 2015; Federrath 2016); here, $(B_{\mathrm{turb}})_{\mathrm{rms}}$ is the root-mean-square strength of the turbulent component of the magnetic field, averaged over some region of interest (see below). The motivation for the normalisation by $\rho^{2/3}$ in the definition of Q_{ss} is to remove the effects of flux-freezing: even in the absence of dynamo action, a collapse that increases the gas density will also increase the strength of the frozen-in field. The fastest growth occurs for the spherical collapse of a region with a dynamically-unimportant, tan-

gled field, in which case $B \propto \rho^{2/3}$ (Banerjee & Pudritz 2006; Crutcher et al. 2010); stronger fields that force anisotropic collapse produce scalings closer to $B \propto \rho^{1/2}$ (Ames 1973; Crutcher 1999; Desch & Mouschovias 2001; Li et al. 2004; Machida et al. 2006; Mocz et al. 2017; Hennebelle & Inutsuka 2019). Thus, Q_{ss} is either a conserved or decreasing quantity in the absence of dynamo action, and an increase in Q_{ss} indicates that the small-scale dynamo is operating.

We show the value of B_{turb} and Q_{ss} versus time for all of our non-fragmenting runs in the top and middle panels of Figure 4.7. For the purpose of this plot, we calculate all quantities in a spherical region of radius 0.01 pc centred on the point of maximum density before the sink particle forms, and then shift to a cylindrical geometry that represents the accretion disc around the sink, which we defined in Section 4.3.1. However, our results are quite insensitive to these choices, as long as the volume over which we compute Q_{ss} is large enough to capture the entire disc. In Figure 4.7, the solid lines are the mean values averaged over the ~ 8 non-fragmenting simulations in each category, and the colored bands denote the 5th and the 95th percentiles[2].

The initial amplification in Q_{ss} in the pre-sink phase ($T_s < 0$) is not accompanied by an increase in the ratio of the magnetic to the turbulent kinetic energy, $E_{mag}/E_{turb,kin}$, as shown in the bottom panel of Figure 4.7. Here, we define the turbulent kinetic energy as $E_{turb} = \sum (1/2) m v_{turb}^2$, where the sum is over all cells in the region of interest, m is the cell mass, and v_{turb} is the turbulent velocity as defined in equation 4.2. $E_{mag}/E_{turb,kin}$ remains constant because the ongoing collapse converts gravitational potential energy into turbulent motions and thence into magnetic fields (e.g., Xu & Lazarian 2020), resulting in an increase in both E_{mag} and $E_{turb,kin}$. This is a collapse-driven dynamo, as observed earlier by Sur et al. (2010) and Federrath et al. (2011b). There is a small plateau close to the sink formation time, $T_s = 0$, which results because the evolution is so fast that the snapshots we use (which are taken every 50 timesteps) do not resolve the time frames that we parameterize by the SFE.

Turning now to the phase of the simulation after sink formation, the plot shows that, on average, the weakJ64 runs show a substantial small-scale dynamo amplification. The value of Q_{ss} asymptotically approaches the value found in the strong-field runs. However, there is a large scatter, so the amount of dynamo amplification varies

---

[2]The percentiles requested can be outside the range that can be computed given the limited input sample size in our work. To take this into account, we use the `numpy` percentile function with the `linear` interpolation option such that if the request percentile is between two data points i and j, this operation returns $i + (j - i) \times f$, where f is the fractional part of the sample index between i and j; see the `numpy` user manual for further details (Oliphant 2006).
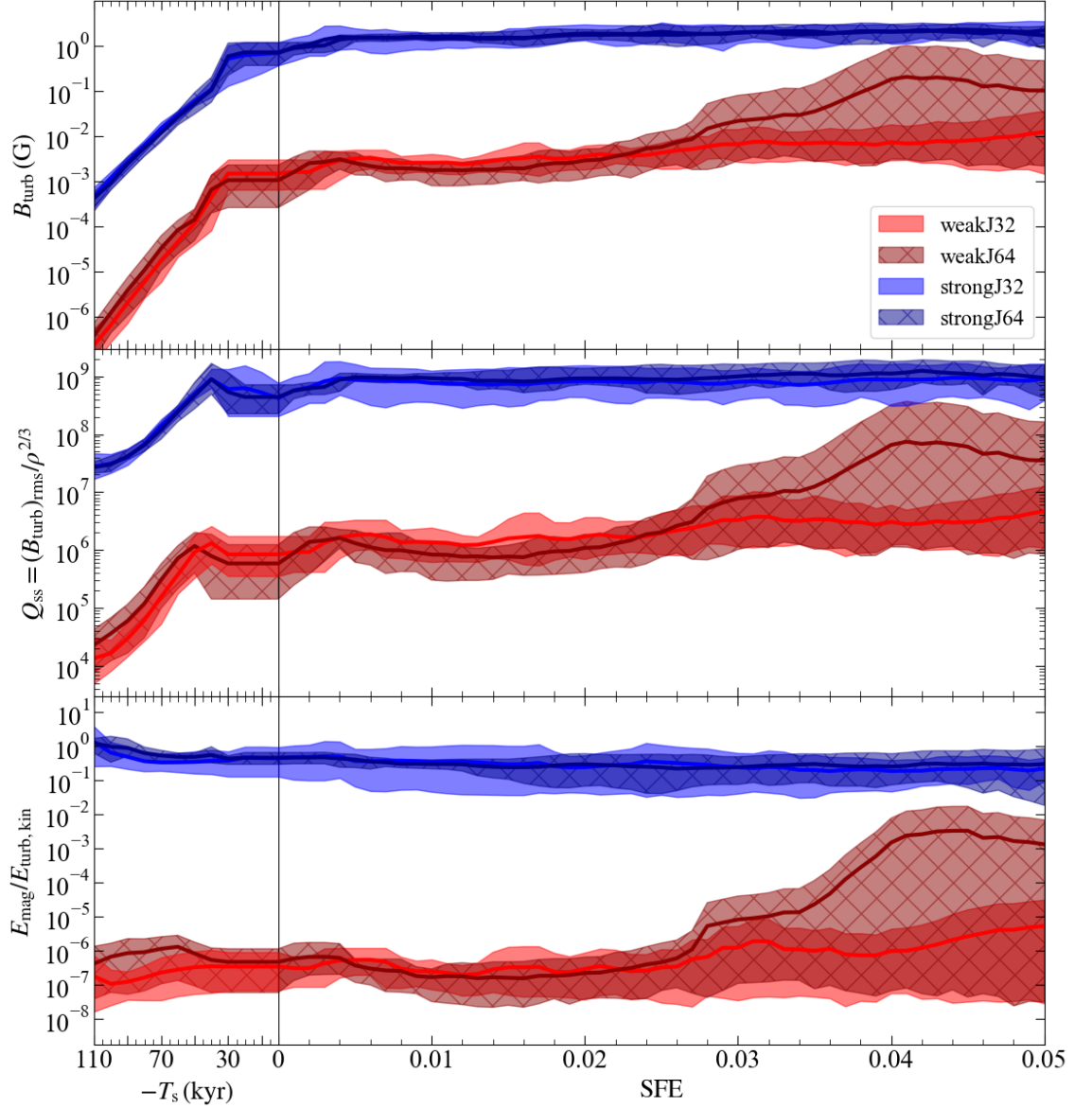
Figure 4.7: *Top panel:* Evolution of the mass-averaged turbulent magnetic field B_{turb} as a function of time in the core before the formation of the sink at time T_{s}, and as a function of star formation efficiency (SFE) in the disc around the sink after its formation (SFE $= 0.05$ implies that the sink particle has accreted $50\,\mathrm{M_\odot}$). We calculate B_{turb} using equation 4.4, averaging over a spherical volume of radius $0.01\,\mathrm{pc}$ before the collapse, and a cylindrical region of radius $500\,\mathrm{au}$ and half-height $50\,\mathrm{au}$, oriented to lie in the same plane as the accretion disc, afterwards. The solid lines represent the mean averaged over the non-fragmenting ($N_{\mathrm{r}} \sim 8$) realisations of each set of simulations with weak and strong magnetic fields at two different Jeans resolution as marked in the legend (see also, Table 4.1). The coloured bands represent the 5th to 95th percentile range. *Middle panel:* The evolution of the small-scale dynamo ratio, Q_{ss}, calculated using equation 4.5. *Bottom panel:* The bottom panel shows the ratio of magnetic to turbulent kinetic energy, which quantifies the growth and saturation of the small-scale dynamo.

significantly with the random seed for the initial turbulent velocity and magnetic field. On the other hand, runs with an initially strong magnetic field do not show any amplification in Q_{ss}, independent of resolution. This is in accordance with the expectations laid out in section 2 of SFK20, namely that the strong-field runs correspond to an initially saturated magnetic field that cannot be further amplified.

Consistent with our discussion of Q_{ss}, we see that the ratio $E_{\mathrm{mag}}/E_{\mathrm{turb,kin}}$ is nearly constant in the strong-field runs, further implying that the field is saturated. The saturation level is around $0.001 - 0.1$, in very good agreement with that expected from isothermal MHD turbulence simulations with similar Mach number and magnetic Prandtl number (Federrath et al. 2011b, 2014a; Federrath 2016), but here with realistic chemistry and cooling. Most interestingly, in the weakJ64 case, the ratio of energies increases from $\sim 10^{-7}$ for our initial state to $\sim 10^{-3} - 10^{-2}$ by the time the SFE has reached $4 - 5$ per cent. However, there is a great deal of scatter about this result, with some runs showing no increase in magnetic energy density at all, and others reaching a ratio of almost 0.1.

While it may seem from Figure 4.7 that the small-scale dynamo action is not resolved with 32 cells per Jeans length, this is not strictly the case. In fact, field amplification is only delayed, not suppressed entirely. To illustrate this point, we have continued one realisation of a weakJ32 run to an SFE of 12 percent; we show Q_{ss} and $E_{\mathrm{mag}}/E_{\mathrm{turb,kin}}$ for this run in Figure 4.8[3]. As the green curve in the top panel of Figure 4.8 shows, small-scale dynamo amplification does occur, but not until after SFE = 5 percent. Thus, the small-scale dynamo is active even at a J=32 Jeans resolution; however the time at which amplification begins seems to be both stochastic and resolution-dependent. This observation confirms that J $\sim$ 30 is a threshold for dynamo amplification (Sur et al. 2010; Federrath et al. 2011c) even in the presence of primordial chemistry and cooling.

We also use this realisation to test for the effects of increasing the maximum resolution, as opposed to changing the number of cells per Jeans length. To this end, we repeat the weak-field case with 32 and 64 cells per Jeans length but at a higher absolute resolution, such that $\Delta x = 3.8\,\mathrm{au}$ on the finest AMR level (instead of the $\Delta x = 7.6\,\mathrm{au}$ for all the other simulations). It is clear from Figure 4.8 that the runs with higher absolute resolution produce results that are very similar to the ones at our standard absolute resolution. While we are unable to repeat these higher-resolution tests in more cases due to the computational expense, the experiment

---

[3]We caution that the evolution at this point is largely unphysical, because we are not including stellar radiation feedback, which would be extremely important for a 120 $M_{\odot}$ star as it forms in this case; we should therefore think of this run as a numerical experiment to demonstrate a point about dynamo action, rather than a realistic simulation of the formation of a primordial star.

we have performed suggests that absolute resolution is less important for capturing small-scale dynamo effects than resolving the Jeans length by a sufficiently large number of cells. Further, we also find that the onset of the small-scale dynamo action depends on the degree of smoothness and circularity in the disc. We show this in the movie M4, by comparing the evolution of magnetic field strength in two realizations of the weakJ64 runs that show no and high amplification, respectively. This demands a detailed analysis of the interaction of disc dynamos with disc instabilities, which is beyond the scope of this work since the inner disc is not well resolved, as we discuss in Section 4.3.3.

Large-Scale dynamo

The kinetic helicity, $F = \int v \cdot W \, dV$ (where $W = \nabla \times v$ is the vorticity) is finite and non-zero in our simulations, thus suggesting the presence of helical turbulence (e.g., Kulsrud 1999; Brandenburg & Subramanian 2005; Brandenburg et al. 2019). It is well known that helical turbulence in the presence of a vertical density gradient (stratification) and differential rotation in discs can lead to the generation of a large-scale magnetic field through the $\alpha\Omega$ dynamo (Pudritz 1981b,a). While the small-scale dynamo generates field structures on smaller scales, it cannot lead to the production of a coherent field on large scales. The presence of the mean toroidal field as we observe in our simulation hints at the presence of a large-scale dynamo. This happens due to winding-up of the magnetic field in the toroidal direction by shearing motions (Ω effect, see Babcock 1961). However, the Ω effect alone cannot be classified as a dynamo. The amplified poloidal component that we observe in addition to the toroidal field implies that an additional field amplification is mechanism at work, likely the α effect (Steenbeck et al. 1966). The combination of the α and Ω effects is well known to give rise to the $\alpha\Omega$ large-scale dynamo (Brandenburg & Subramanian 2005). In our simulations, we speculate that the $\alpha\Omega$ dynamo acts to amplify the small-scale field produced by the small-scale dynamo (provided the resolution is high enough), and that this transforms the small-scale field into the large-scale one that we observe. While it is generally believed that the small-scale dynamo can quench the action of the mean-field dynamo (Kulsrud & Anderson 1992; Subramanian 1999; Schekochihin et al. 2004; Brandenburg & Subramanian 2005; Brandenburg et al. 2012), recent high-resolution simulations find that a large-scale mean field can co-exist with a small-scale field of comparable strength, if both shear and helical turbulence are present (Bhat et al. 2016; Singh et al. 2017; Bhat et al. 2019), due to the unified action of the two dynamos. Note that the studies we refer to above have quite different simulation setups that the one we use; for ex-
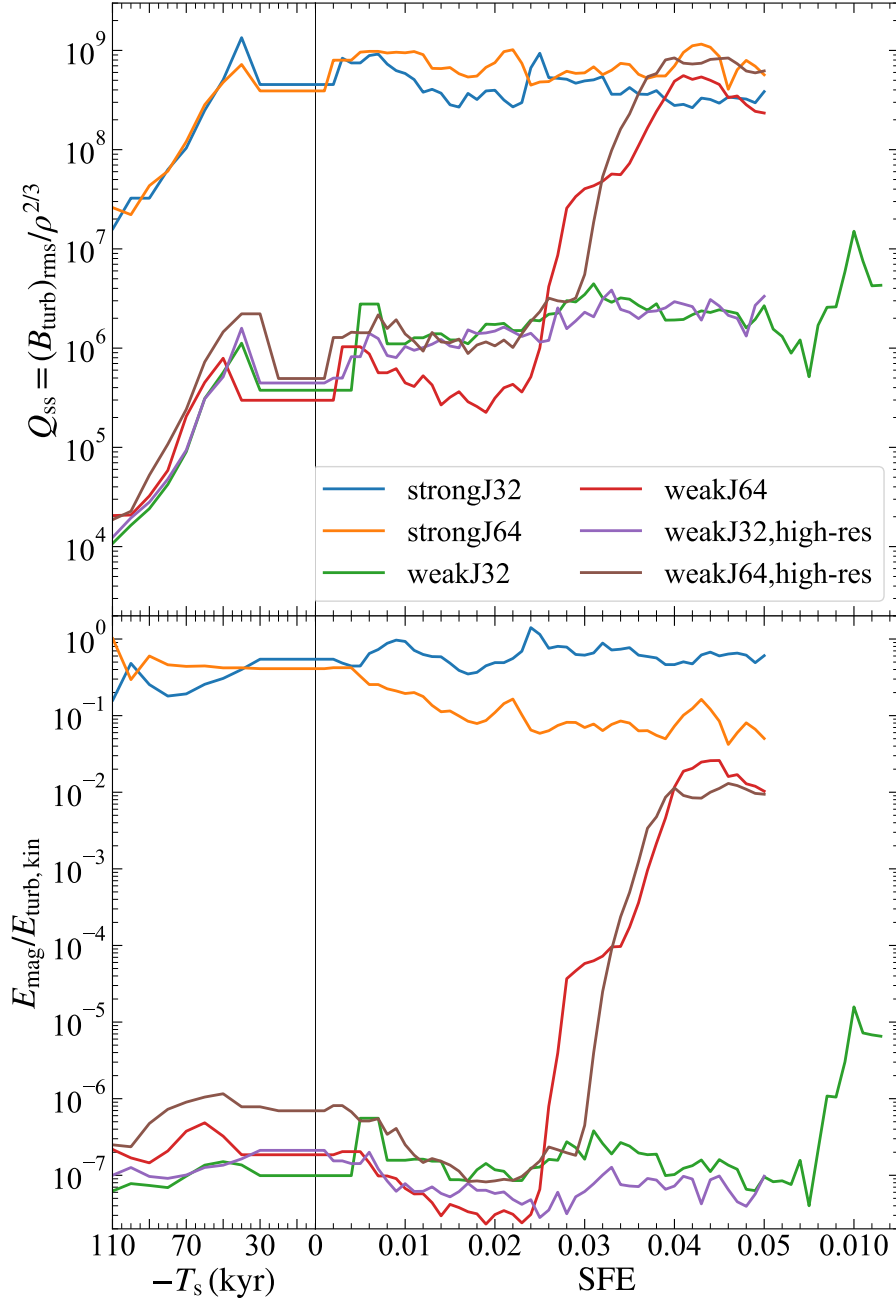
Figure 4.8: Same as Figure 4.7, but for one particular realization, including runs with the weak field at a higher absolute resolution. In this plot, the strongJ32, strongJ64, and weakJ64 cases are all run with the standard resolution. We run the weakJ32 case shown with the standard resolution as well, but allow the run to continue to SFE = 12 percent rather than 5 percent. Finally, for the two runs (weakJ32, high-res) and (weakJ64, low-res), we use the same initial conditions and refinement criteria as weakJ32 and weakJ64, but add an extra level of refinement, so the maximum resolution is $\Delta x = 3.8$ au rather than 7.6 au. The main conclusion from this is that higher Jeans resolution is more critical for resolving dynamo amplification than absolute maximum resolution.

ample, most of these studies assume incompressibility and isotropy, work with low Mach numbers, do not have density stratification, and do not include other relevant astrophysical processes like gravity, non-equilibrium chemistry, and non-isothermal thermodynamics; thus, they do not form or study the dynamo in a star-forming environment. Hence, results from these studies cannot be directly compared against our simulations, and the extent to which they apply to our work is limited. Nevertheless, these studies provide important basic insight and a reasonable starting point to discuss dynamo operation in astrophysical discs around the first stars.

The operation of the α effect depends on the competition between how efficiently the field is regenerated as compared to how quickly is it dissipated (by turbulence) in the poloidal direction. Similarly, the operation of the Ω effect depends on how efficiently the field is amplified as compared to how quickly is it dissipated in the toroidal direction. Thus, the two effects can be quantified under the assumption of axisymmetric accretion discs (Raedler 1986) by taking the ratio of field amplification rate to its dissipation rate (Pudritz 1981a; Ruzmaikin et al. 1988b; Stepinski & Levy 1990; Brandenburg & Subramanian 2005),

$$R_\alpha = \frac{\alpha h}{\eta_{\mathrm{T}}} \text{ and } R_\Omega = \frac{S h^2}{\eta_{\mathrm{T}}} \tag{4.6}$$

where h is the disc scale height at some radius r and S is the radial shear caused by differential rotation, $S = r\, \partial\Omega/\partial r$. Further, α is a pseudo-scalar[4] that represents the transport coefficient responsible for the α effect ($\alpha = 0$ if the turbulence is not helical), and η_{T} is the second transport coefficient, given as the sum of microscopic and turbulent magnetic diffusivity (Moffatt 1978; Krause & Raedler 1980; Ruzmaikin et al. 1988a; Brandenburg 2018). Theoretically, the operation of the large-scale dynamo requires that the large-scale dynamo number,

$$D_{\alpha\Omega} = R_\alpha R_\Omega\,, \tag{4.7}$$

be larger than unity, implying that the amplification of the field by the two effects is more rapid than dissipation[5].

---

[4]The pseudo-scalar, α, is actually a compressed version of the symmetric part of the α tensor, obtained under the assumption that the turbulent field is isotropic (invariant under rotation) and homogeneous (see equation 7.15 in Moffatt 1978). Certain simulations have calculated the different components of the α tensor (e.g., Schrinner et al. 2007; Warnecke et al. 2018; Viviani et al. 2019; Bendre et al. 2020), however, as we explain in the main text, this is not within the scope of this work.

[5]In practice, the critical dynamo number above which the dynamo operation is sustained is a function of the disc aspect ratio (Bera et al. 2019, see their Figure 2), however, it is generally expected to be of the order of $1-10$ in astrophysical systems with disc-like geometries (Ruzmaikin et al. 1988b,a).

In order to verify that a large-scale $\alpha\Omega$ dynamo is operating in our simulations, we must estimate α and η_{T}, so that we may compute R_α and R_Ω, and hence $D_{\alpha\Omega}$ (equation 4.7). For accretion discs, the microscopic diffusivity is much less than the turbulent magnetic diffusivity as the discs are highly conducting (e.g., Krause & Roberts 1976; Pudritz 1981b; Hartmann et al. 1998; see, however, Section 4.3.4, where we discuss the effects of non-ideal MHD, *i.e.,* the effects of microscopic diffusivities primarily giving rise to ambipolar diffusion). In a simulation such as ours, which does not include explicit resistivity and where the physical scale of magnetic diffusion is unresolved, the magnetic diffusivity is dictated solely by the finite resolution of the grid on which we discretise the MHD equations (Kowal et al. 2009; Santos-Lima et al. 2012; McKee et al. 2020). We can estimate the diffusivity by noting that, in the absence of explicit viscosity or resistivity, the dissipation scale is always of order the cell size Δx, and thus the fluid and magnetic Reynolds numbers Re and Rm must be close to unity for length scales $\ell \sim \Delta x$ (e.g., Haugen et al. 2004; Schekochihin et al. 2004; Balsara et al. 2004), giving a magnetic Prandtl number around 1 (Lesaffre & Balbus 2007; Federrath et al. 2011b; McKee et al. 2020). Thus, $\eta_{\mathrm{T}} \sim c_{\mathrm{s}}\Delta x \sim 10^{20}\,\mathrm{cm^2\,s^{-1}}$ (see, however, Section 4.3.4).

To calculate α, we make use of the fact that, in the presence of helical turbulence, the induction equation for the mean field has an additional term, χ, that depends on the turbulent velocity and magnetic field (Subramanian 2016, see their equation 151). Assuming spatially isotropic turbulence and a finite scale separation between small and large scales (Blackman & Field 2002), χ can be expressed under a first-order smoothing approximation (neglecting quadratic terms) in the kinematic regime as,

$$\chi = \langle \mathbf{v}_{\mathrm{turb}} \times \mathbf{B}_{\mathrm{turb}} \rangle = \alpha \langle \mathbf{B} \rangle - \eta_{\mathrm{T}}\, \nabla \times \langle \mathbf{B} \rangle\,. \tag{4.8}$$

Note that equation 4.8 can only be used if: (1) Rm is small (Cattaneo & Hughes 2009; see, however, Tobias & Cattaneo (2013) and Cattaneo & Tobias (2014) who show that the large-scale dynamo can persist even when Rm is high, provided there exists a strong shear), and (2) B_{turb} is small compared to $\langle B \rangle$. The latter assumption is violated in our simulations, since $B_{\mathrm{turb}} \sim \langle B \rangle$. However, direct numerical simulations report that equation 4.8 holds approximately even when $B_{\mathrm{turb}} \sim \langle B \rangle$ (Sur et al. 2008), especially in the case of accretion discs, because the turbulence correlation time is small compared to the turnover time (Pudritz 1981b; Brandenburg & Subramanian 2005; Rincon 2019). Since our goal is not to estimate an accurate value of α, but simply to check if the α effect operates in our simulations, we work under the first-order smoothing approximation introduced above. Plugging η_{T} into equation 4.8 gives $\langle\alpha\rangle \approx 3\,\mathrm{km\,s^{-1}}$. Note that we derive η_{T} (and by
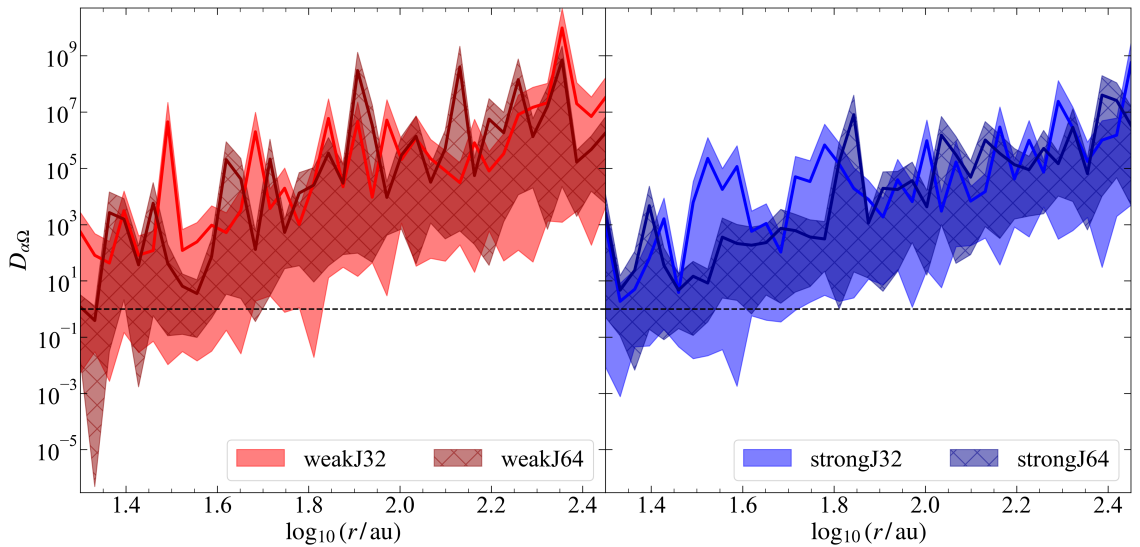
Figure 4.9: Azimuthally-averaged radial profile of the large-scale dynamo number, $D_{\alpha\Omega}$ (see equation 4.7), in the disc for different runs at SFE = 5 percent. The left and right panels and present results for weak and strong magnetic field cases with different Jeans resolution, respectively (cf. Table 4.1 for details). Similar to Figure 4.7, the solid lines represent the mean over all simulations that produced a single sink particle, and the colored bands represent the 5th and 95th percentiles. This mean-field dynamo likely operates due to the $\alpha\Omega$ effect in the disc, requiring a critical $D_{\alpha\Omega} > 1$, denoted by the dashed, black line. It does not act in the inner disc in some realisations due to coarser resolution there, but for $\log_{10}(r/\mathrm{au}) \gtrsim 1.5$, the weak-field models have $D_{\alpha\Omega} > 1$ and all models have $D_{\alpha\Omega} \gg 1$ further out in the disc ($r \gtrsim 100\,\mathrm{au}$), demonstrating the effectiveness of the $\alpha\Omega$ dynamo. However, note that we are likely overestimating the value of $D_{\alpha\Omega}$ in the case of strong fields since we do not include non-ideal MHD effects that can dissipate the field (see Section 4.3.4).

extension, α) based on the grid resolution. Nonetheless, the values we obtain are in very good agreement with that expected from the first-order smoothing approximation for $\langle v_{\mathrm{turb}} \rangle \sim 10\,\mathrm{km\,s^{-1}}$ as in our simulations (Sur et al. 2008, see their equation 16)[6].

Our results confirm the recent results of Liao et al. (2019), who also argue for the presence of a large-scale mean-field dynamo acting in Population III star formation. However, we note that Liao et al. used only 8 cells per Jeans length in their simulations, which is not sufficient to capture the small-scale dynamo (Federrath et al. 2011c). Thus, they likely miss the production of small-scale fields that can then be driven to large scales by the $\alpha\Omega$ effect. In addition, both Liao et al.'s simulations and ours likely underestimate the rate of $\alpha\Omega$ dynamo amplification because, as we show above, the dynamo number $D_{\alpha\Omega} \propto (h/\eta_{\mathrm{T}})^2$, which for a simulation dominated by grid dissipation ($\eta_{\mathrm{T}} \propto \Delta x$), implies a scaling $D_{\alpha\Omega} \propto (h/\Delta x)^2$. In practice, this

---

[6]If Rm ≤ 1, the first-order smoothing approximation estimates have to be scaled by Rm.

means that in order to capture the $\alpha\Omega$ effect well requires that the disc scale height be resolved by at least ~ 30 cells (Federrath et al. 2011c). We approach, but do not quite satisfy this requirement in the outer disc, and fall far short of it at smaller radii where the disc is thinner. We remind the reader that due to coarse resolution in the inner disc, we can thus only qualitatively comment on the scale separation between the small and the large-scale dynamo. We also point out that our analysis implies that the growth rate of the $\alpha\Omega$ dynamo depends on the absolute resolution, not just the number of cells per Jeans length.

Finally, we note that there can be additional large-scale dynamo amplification in the presence of helical turbulence and strong shear, for e.g., the shear current effect (Rogachevskii & Kleeorin 2003, 2004) or the incoherent α-shear dynamo (Hoyng 1988; Vishniac & Brandenburg 1997). We have not explored these effects in this work, so we cannot rule out the possibility that they might be operating as well.

4.3.4   Effects of non-ideal MHD

The results we have discussed so far are based on ideal MHD simulations, and it is important to highlight the effects of non-ideal processes on the operation of the dynamo. Nakauchi et al. (2019) use one-zone calculations to study the ionisation fraction and the effects of non-ideal MHD on primordial chemistry, and conclude that non-ideal processes do not suppress dynamo amplification when the field is weak, but they can have a significant impact in the case of strong fields. This is because at high densities ($\sim 10^{10} - 10^{13}\,\mathrm{cm^{-3}}$) in the presence of strong fields ($\sim 1\,\mathrm{G}$), magnetic diffusivities giving rise to ambipolar diffusion can be as high as $10^{21} - 10^{23}\,\mathrm{cm^2\,s^{-1}}$, which is $\sim 1-3$ orders of magnitude higher than the numerical diffusivity we estimated in Section 4.3.3. Similar order of magnitude estimates for the magnetic diffusivity are derived by McKee et al. (2020). Both these studies also find that Ohmic resistivity and the Hall effect are sub-dominant compared to ambipolar diffusion for the weakly-ionised primordial gas (see also, Schleicher et al. 2009). Thus, ambipolar diffusion can decrease the strength of the large-scale dynamo by several orders of magnitude (10^6 in the outer disc, and 10^2 in the inner disc; cf. equation 4.6), possibly even quenching it altogether when the field reaches $\sim 1\,\mathrm{G}$.

However, in our strong field simulations where the field strength reaches $\sim 1\,\mathrm{G}$, we did not see any amplification in any event, even with ideal MHD, simply because the field is already at or above saturation level when the disc forms. Thus, the relevant question is whether we would expect non-ideal effects to be significant for the field strengths typical of the weak-field cases. There, the field is $\sim 10^{-3}\,\mathrm{G}$

when the sink particle forms (cf., top panel of Figure 4.7), and the disc that forms thereafter has characteristic densities 10^{10}–10^{13} cm^{-3} (similar to what they are in the strong-field cases; cf., Figure 4.2). Since the effective resistivity provided by ambipolar diffusion scales as $\eta_{\mathrm{T}} \propto B$, for these physical conditions Nakauchi et al. (2019) find resistivities of order 10^{18}–10^{20} cm^2 s^{-1}, slightly smaller than our estimate of the numerical resistivity in the simulations. Thus, we conclude that non-ideal suppression of the dynamo is unimportant at least for the initial stages of amplification starting from a weak, sub-saturation field, consistent with the findings of Schober et al. (2012a).

A more subtle question is whether non-ideal effects might become important once significant amplification has taken place, and might thereby reduce the saturation field strength compared to what we find in our ideal MHD models. In the weakJ64 simulations where we see amplification, the runs saturate at peak field strengths of ~ 0.1 G, corresponding in Nakauchi et al.'s models to resisitivities of $\sim 10^{20}$–10^{22} cm^2 s^{-1} for the range of densities found in our discs. At the high end of the range, this is well in excess of our numerical resistivity, but seems unlikely to be sufficient to quench the dynamo: since $D_{\alpha\Omega} \propto \eta_{\mathrm{T}}^{-2}$, an increase from $\eta_{\mathrm{T}} \sim 10^{20}$ cm^2 s^{-1} (our numerical value) to $\eta_{\mathrm{T}} \sim 10^{22}$ cm^2 s^{-1} (from Nakauchi et al.'s models) at large disc radii, where the resistivity is largest, would correspond to a reduction in $D_{\alpha\Omega}$ by a factor of $\sim 10^4$ at those radii (cf. Figure 4.9). While this represents a weakening of the dynamo, even the reduced figure is well above the threshold for efficient large-scale dynamo amplification. We therefore tentatively conclude that non-ideal effects are unlikely to substantially reduce the saturated field strength compared to that found in our ideal simulations.

Non-ideal MHD effects can also have consequences for the formation and evolution of accretion discs around the first stars, though there has been limited exploration of this effect in the literature. Nevertheless, we can gain insight by considering work on present-day (Pop I) star formation where non-ideal MHD effects have been explored in detail (Wurster & Li 2018 and Zhao et al. 2020, and references therein). Recent SPH simulations find that non-ideal MHD effects can be quite significant for the evolution of accretion discs around low-mass Pop I stars (Wurster et al. 2017; Wurster & Lewis 2020; Wurster 2021); in particular, these simulations find that larger and more massive discs form in the non-ideal MHD runs as compared to the ideal MHD runs when the turbulence is sub- or trans-sonic. Certain simulations also find that outflows are weaker in non-ideal MHD runs as compared to ideal MHD runs (e.g., Masson et al. 2016; Wurster & Bate 2019; Marchand et al. 2020; Xu & Kunz 2021). The inclusion of non-ideal effects also solves the magnetic-

breaking catastrophe by suppressing the angular momentum transport that inhibits the formation of discs in ideal MHD (e.g., Tomida et al. 2015; Tsukamoto et al. 2015b; Zhao et al. 2016; Masson et al. 2016; Vaytet et al. 2018; Wurster et al. 2019). While ideal MHD does not hinder the formation of discs around first stars even in the case of strong fields (most likely due to the misalignment between the rotation axis and the tangled magnetic field in the presence of turbulence, as for Pop I stars; e.g., Seifried et al. 2013; Tsukamoto et al. 2015a, 2017; Wurster et al. 2019), it is an open question how the properties of the discs might change when non-ideal effects are taken into account. We speculate that Pop III discs are closer to the case of discs around massive stars in the present-day Universe, because both types of systems are characterised by the overwhelming dominance of gravity over thermal pressure. This in turn makes the ram pressure of the accretion flow a dominant force that governs the physical properties of the disc (e.g., Rosen et al. 2016; Rosen & Krumholz 2020).

In summary, it is clearly desirable to run a large suite of non-ideal MHD simulations to study the formation of the first stars, but the associated computational cost (due to the combination of required high resolution, large statistics, and small timesteps due to magnetic diffusion) restricts us from performing such simulations at this time. We hope to remedy this in the future, and explore how dynamo amplification is impacted by non-ideal MHD effects during the formation of the first stars through 3D simulations.

4.4   Implications for the IMF of the first stars

While the presence or absence of a dynamo in primordial accretion discs is interesting in itself, the main astrophysical question in which we are interested is how any resulting magnetic fields might affect the IMF of the first stars. This is something that does have at least potentially observable consequences. To investigate this question, we collect information on the sink mass distribution of all the four simulation categories: weakJ32, weakJ64, strongJ32, strongJ64, as well as the control case from SFK20, which did not include a magnetic field and the Jeans length was resolved by 32 cells; we refer to this as the HDJ32 case. As opposed to Section 4.3 where we only used a subset of our simulations to study field amplification, we use all the simulations in each category to study the sink mass distribution and the primordial IMF.

The total number of sink particles (used as a proxy for stars) formed in weakJ32, weakJ64, strongJ32 and strongJ64, over the 25 realisations, are 121, 175, 70 and
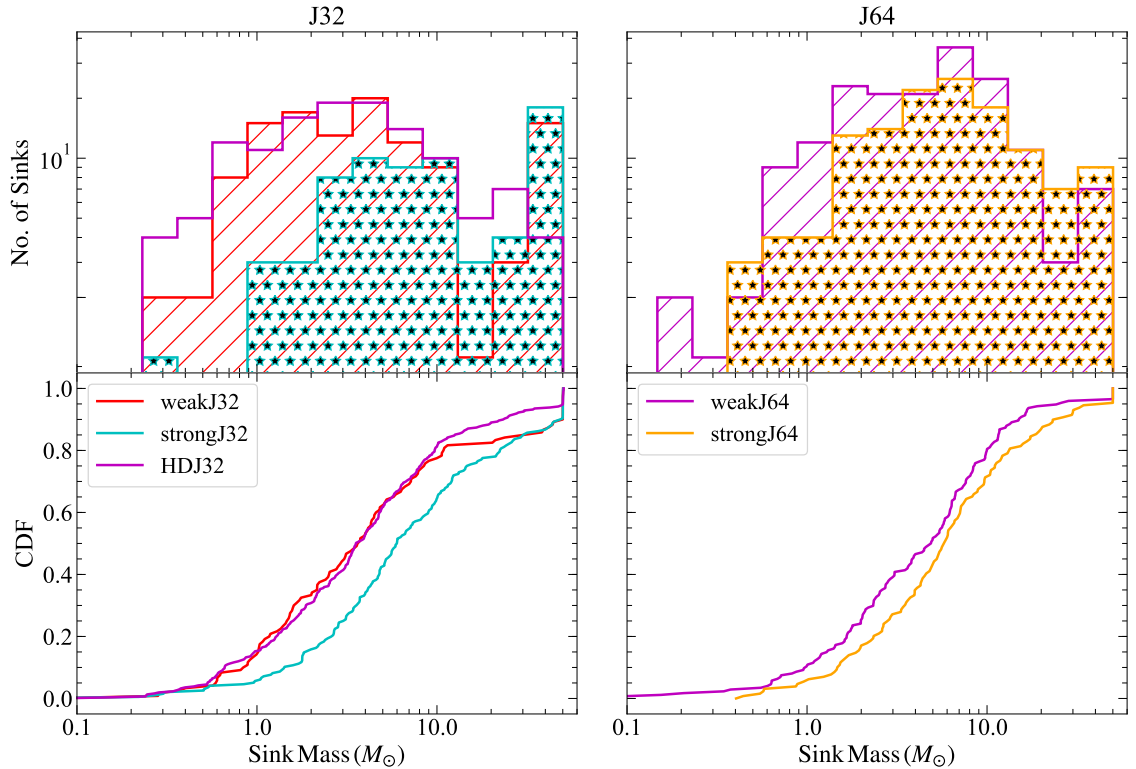
Figure 4.10: *Left panel*: The mass distribution (top) and the cumulative distribution (bottom) of sink particles that form till SFE = 5 percent in 25 realizations in the weak- and strong-field runs with 32 cells per Jeans length. We also show the distribution for HDJ32 (without magnetic fields), adopted from SFK20. *Right panel*: the same distributions resulting from runs with 64 cells per Jeans length.

130, respectively. This implies that higher Jeans resolution leads to more fragmentation in the MHD runs, by as high as a factor of 2. It is not easy to pin-point the cause of this finding, because the simulations are highly chaotic and non-linear. However, broadly speaking, we can attribute this effect to the fact that the accretion discs around the primary sink, and thus disc instabilities and sub-structure, are better resolved in J64 runs as compared to J32 runs. Given this result, we compare the sink mass distributions for the runs with 32 and 64 cells per Jeans length separately, so that we can disentangle the effects of magnetic fields and resolution. While this approach means that we are not necessarily capturing the true amount of fragmentation, since simulations are not fully converged, it does allow us to test with confidence how magnetic fields and dynamo amplification shift the IMF.

The left panel of Figure 4.10 shows the sink mass distribution for simulations with 32 cells per Jeans length. It is straightforward to see that the sink mass distribution of the strongJ32 runs is different from the other two, while the weakJ32 and HDJ32 runs are very similar, at least for $M \lesssim 10\,\mathrm{M_\odot}$. To confirm this visual impression quantitatively, we apply the Kolmogorov-Smirnoff (KS) test for each pair of the

runs shown in this panel. This test returns a p-value that describes the confidence level with which we can rule out the null hypothesis that the masses in each pair of runs were drawn from the same underlying distribution. Following Sharda et al. (2019a) and SFK20, we classify two distributions to be significantly different, if the p-value is < 0.01. The p-values for the pairs HDJ32−weakJ32, HDJ32−strongJ32 and weakJ32−strongJ32 come out to be 0.55, 5×10^{-5} and 8×10^{-4}, respectively. Thus, the sink mass distribution produced by the strong magnetic field runs has a different origin than that produced by the weak field and HD runs. This finding is consistent with that of SFK20. However, we note that the mass distributions for $M \gtrsim 10\,\mathrm{M}_\odot$ are much more similar between weakJ32 and strongJ32, both showing a significantly higher number of massive stars than HDJ32.

The right panel of Figure 4.10 shows the same distributions for the runs with 64 cells per Jeans length. Visually, the weakJ64 and strongJ64 distributions are much closer to one another than are the weakJ32 and strongJ32 cases. The p-value for the pair weakJ64−strongJ64 is 0.12, implying no statistically significant difference in fragmentation between the weak- and the strong-field runs at higher Jeans resolution. This is not entirely unexpected, given that weakJ64 runs show significant field amplification. Thus, we find that first star cores with an initial field that falls below equipartition by a factor of $\sim 10^7$ produce an IMF that is significantly different from those that start near equipartition when we do not resolve dynamo amplification, but that this difference greatly diminishes, to the point of statistical undetectability, when we do capture dynamo growth. As further evidence of this effect, we note that, while we do not have a set of non-magnetic simulations at 64 cells per Jeans length to enable a direct comparison, the weakJ64 run shows *less* fragmentation, and higher mean masses, than the HDJ32 case, despite having higher resolution, which tends to favour *more* fragmentation. Thus, the effect of the dynamo-amplified magnetic field in suppressing fragmentation outweighs the effect of increasing the resolution.

It is interesting to consider the implications of these findings in the context of previous work on the mass of first stars formed in simulations. For example, based on radiation hydrodynamics simulations of first stars, Susa et al. (2014, Figure 9) find that the mass spectrum peaks around $20\,\mathrm{M}_\odot$, and that most stars that form the earliest (prior to subsequent fragmentation) are more massive than $20\,\mathrm{M}_\odot$. While our conclusion of a top-heavy primordial IMF matches theirs, the exact location of the peak of the IMF is different. This is not entirely unexpected given the vast differences in physical (magnetic fields versus radiation feedback) and numerical schemes (initial conditions, AMR versus SPH, resolution, etc.) used in the two works. Hirano et al. (2014) produce a suite of 100 first stars from their 2D radiation hydrodynam-

ics simulations, finding stars as massive as $1000\,\mathrm{M}_\odot$. Hirano et al. (2015) perform cosmological simulations to study the primordial IMF, finding that it is top-heavy and the distribution is bimodal, peaking at $25\,\mathrm{M}_\odot$ and $250\,\mathrm{M}_\odot$, respectively. This bimodality is a result of the thermal evolution followed by accreting stars during the initial runaway collapse phase. It is difficult to directly compare the results of Hirano et al. (2014, 2015) with ours, given that we do not follow the protostellar accretion beyond $50\,\mathrm{M}_\odot$ in our 3D simulations without radiative feedback, whereas Hirano et al. (2015) perform 2D simulations without magnetic fields that do not capture the effects of fragmentation. The mass spectrum resulting from SPH-based 3D simulations of Stacy & Bromm (2013) and Stacy et al. (2016) is also top-heavy, but the distribution is relatively flat at early times and steepens later on, with several low-mass first stars forming in few thousand yr. Thus, while all simulations converge on the top-heavy nature of the primordial IMF, the intrinsic differences between them makes it difficult to compare them on a quantitative basis. This is further complicated by the fact that most simulations lack the necessary statistics to build up a statistically converged mass distribution.

It is also worth comparing the primordial IMFs resulting from simulations discussed above to the constraints provided by observations of metal-poor stars that are believed to have been impacted by the first supernovae. Ishigaki et al. (2018) find that the elemental abundance patterns measured in their compiled sample of extremely metal-poor stars ([Fe/H] ¡ -3) are best described by $< 40\,\mathrm{M}_\odot$ Pop III supernovae, with the majority of the patterns best fitted by a $25\,\mathrm{M}_\odot$ hypernova, confirming earlier results from Hansen et al. (2011) and Ishigaki et al. (2014). Similarly, Nordlander et al. (2019) find that the elemental abundance pattern in SMSS J160540.18-144323.1 − the most iron-poor star known to-date ([Fe/H] $= -6.2 \pm 0.2$), is best described by a $10\,\mathrm{M}_\odot$ Pop III supernova. Placco et al. (2016) find that the abundance pattern in several ultra metal-poor stars ([Fe/H] ¡ -4) is best described by Pop III supernovae with progenitor masses of $20 - 28\,\mathrm{M}_\odot$. On the other hand, the abundance pattern of another extremely metal-poor star is best fitted by a $40 - 60\,\mathrm{M}_\odot$ Pop III supernova (Bessell et al. 2015). de Bennassuti et al. (2017) find that observations of metal-poor stars are not in agreement with a flat mass distribution of the first stars with masses between $10 - 300\,\mathrm{M}_\odot$. Overall, these results indicate that at most a small fraction of first stars were more massive than $40\,\mathrm{M}_\odot$, which is not inconsistent with the predictions from at least some of the simulations we discuss above. However, both the observed and modeled abundance patterns are subject to uncertainties and free parameters that can significantly alter the resulting best-fits (e.g., Frebel et al. 2008; Joggerst et al. 2009; Heger & Woosley 2010; Nomoto et al. 2013; Amarsi et al. 2016; Nordlander et al. 2017; Magg et al. 2020). Additionally,

several works have remarked on the importance of considering multiple enrichment scenarios where yields from more than one Pop III supernova enriched the stars in their surroundings (Hartwig et al. 2018, 2019; Welsh et al. 2021), which further complicates the abundance pattern comparison. Nevertheless, these analyses remain one of the very few indirect ways through which we can put observational constraints on the primordial IMF.

In summary, we conclude that even if only a weak magnetic seed field was present in primordial clouds, it will be quickly driven to saturation by dynamo action and becomes dynamically important during Pop III star formation. This is important because it means that (1) strong magnetic fields were likely present during Pop III star formation, and (2) they had a significant impact on the primordial IMF.

4.5　Conclusions

In this work, we study how magnetic fields can be amplified through a dynamo mechanism both on small and large scales in the accretion discs around Population III stars. There is a growing consensus that seeds of primordial magnetic fields, no matter how weak, were present in the early Universe (Widrow et al. 2012; Subramanian 2016; Planck Collaboration et al. 2016b), and that they can be exponentially amplified during the collapse of minihaloes at $z \sim 20 - 30$ (Turk et al. 2012). Recent analysis has also shown that if dynamically strong magnetic fields were present during Population III star formation, they will significantly reduce fragmentation, thereby changing the IMF of the first stars (Sharda et al. 2020a). However, previous work has left unresolved the question of how strong can magnetic fields grow during first star formation, and thus of how strong magnetic effects on the IMF are likely to be. This uncertainty is largely a function of numerical limitations: resolving the amplification of magnetic fields by dynamo action requires far higher resolution than is traditionally used in simulations of gravitational collapse and fragmentation.

To address this question, we perform a series of simulations in which we systematically vary the resolution (32 and 64 cells per Jeans length) and the initial strength of the turbulent magnetic field ($1\,\mathrm{fG}$ and $30\,\mu\mathrm{G}$, see Table 4.1). We use a subset of our simulations that form a single (massive) star to study the action of the dynamo in the protostellar accretion discs. The simulations with initially strong magnetic fields are a control case; they do not show any small-scale dynamo operation at either Jeans resolution, implying that the field is already saturated, as expected given our choice of initial field strength. By contrast, in the simulations where the initial magnetic field is weak, we find that the small-scale dynamo acts in accretion discs

around the sink particles, amplifying the turbulent field strength such that, by the time a few percent of the initial cloud has accreted, the field in the disc reaches near saturation values similar to those in the runs where we start with the field already at saturation (see Figure 4.7). However, we also find that the timing and strength of field amplification is sensitive to resolution: simulations with 64 cells per Jeans length yield earlier and stronger field amplification than their lower-resolution counterparts.

We also find a strong, large-scale mean toroidal component of the field in all the simulations (see Figure 4.6) together with a non-zero poloidal component, which is likely due to the operation of a large-scale $\alpha\Omega$-type dynamo. In this type of large-scale dynamo, the Ω effect winds up the field in the toroidal direction due to differential rotation (shear), and the α effect regenerates and maintains the poloidal field. Figure 4.9 shows that the $\alpha\Omega$ dynamo acts efficiently in the outer disc, where we resolve the disc scale height with enough cells to capture its operation. Our findings are consistent with those of Federrath et al. (2011c), who suggest that fully capturing a dynamo process likely requires resolution of ~ 30 cells per Jeans length. Overall our results suggest a picture in which protostellar cores containing only seed fields with no organised structure and an energy density ~ 7 orders of magnitude below equipartition experience rapid growth of the field via both the small-scale dynamo, which increases the turbulent field strength to $\sim 1 - 10$ percent of equipartition, and the $\alpha\Omega$ dynamo, which moves a significant fraction of the energy stored in the disorganised, small-scale field into an organised, large-scale toroidal component. Although our simulations use ideal MHD, we also consider the likely effects of non-ideal processes in the context of recent work estimating the effective diffusivity due to Ohmic dissipation, the Hall effect, and ambipolar diffusion (Nakauchi et al. 2019; McKee et al. 2020). We tentatively find that these effects should not significantly impede dynamo amplification, because the diffusivity depends on the field strength. Thus non-ideal effects are very small when the dynamo becomes to operate, and even once the field strength saturates, the diffusivity is small enough that the dynamo number remains $\gg 1$. Confirmation of these conclusions, however, will have to await full 3D non-ideal MHD simulations.

The development of magnetic fields at $1 - 10$ percent of equipartition even in pro-tostellar cores that begin far below equipartition has profound implications for the IMF of the first stars. Sharda et al. (2020a) show that the presence of an initial near-equipartition field strongly reduces the fragmentation of first star discs, leading to an IMF that is significantly more top-heavy, and deficient in stars with mass $\lesssim 1 M_\odot$ that might survive to the present day. Our simulations here show that,

thanks to dynamo action, this effect operates even in cores where the initial field is many orders of magnitude smaller, and that simulations can capture this effect, if they reach sufficient resolution. Hence, we propose that a scenario where magnetic fields remain weak throughout a Population III star formation episode is likely unphysical: magnetic field effects are always non-negligible.

A more speculative implication from this would be that Population III star formation might be subject to significant magnetic field-induced feedback effects like magnetic bubbles or jets (Tan & Blackman 2004; Machida et al. 2006; Li et al. 2014; Frank et al. 2014; Dyda et al. 2018; see, however, Gerrard et al. 2019; Higuchi et al. 2019; McKee et al. 2020), and that it should be possible to detect these effects in simulations provided the innermost parts of the disc are sufficiently resolved. As the first massive stars explode, the first supernova explosions are likely to bring the magnetic fields into the interstellar medium, while also enriching it with metals (Greif et al. 2007; Sakuma & Susa 2009; Meiksin & Whalen 2013). The metal enrichment is expected to lead to the formation of lower-mass stars due to cooling via metals and dust grains (e.g., Schneider et al. 2003; Bromm & Loeb 2003; Omukai et al. 2005). For these Population II stars, the magnetic fields built up by dynamos around the first stars may become even more dynamically significant, and more important to limiting fragmentation (Latif et al. 2014), due to the diminished role of thermal pressure in gas subject to efficient cooling. The fields may also be further amplified in the haloes where this process takes place, via the same basic dynamo mechanisms we have explored here (Latif et al. 2013b; Grete et al. 2019). Self-consistent models of such environments should therefore always aim to incorporate the magnetic fields.

Acknowledgements

When did the IMF become bottom-heavy?

Context and Contribution

This chapter have been previously published as '**When did the IMF become bottom-heavy?**', *by* **Piyush Sharda and Mark R. Krumholz, 2022, MNRAS, 509, 1959**. *The work is presented here exactly as in the publication. I initiated and led the idea behind this work. I have created the models described in this work based on my co-author's original developments. I have contributed heavily to interpretation of the results and written the majority of the paper, with inputs and suggestions from the co-author.*

Abstract

The characteristic mass that sets the peak of the stellar initial mass function (IMF) is closely linked to the thermodynamic behaviour of interstellar gas, which controls how gas fragments as it collapses under gravity. As the Universe has grown in metal abundance over cosmic time, this thermodynamic behaviour has evolved from a primordial regime dominated by the competition between compressional heating and molecular hydrogen cooling to a modern regime where the dominant process in dense gas is protostellar radiation feedback, transmitted to the gas by dust-gas collisions. In this paper we map out the primordial-to-modern transition by constructing a model for the thermodynamics of collapsing, dusty gas clouds at a wide range of metallicities. We show the transition from the primordial regime to the modern regime begins at metallicity $Z \sim 10^{-4} Z_\odot$, passes through an intermediate stage where metal line cooling is dominant at $Z \sim 10^{-3} Z_\odot$, and then transitions to the modern dust- and feedback-dominated regime at $Z \sim 10^{-2} Z_\odot$. In low pressure environments like the Milky Way, this transition is accompanied by a dramatic change in the characteristic stellar mass, from $\sim 50 \, \mathrm{M_\odot}$ at $Z \sim 10^{-6} \, Z_\odot$ to $\sim 0.3 \, \mathrm{M_\odot}$ once radiation feedback begins to dominate, which marks the appearance of the

modern bottom-heavy Milky Way IMF. In the high pressure environments typical of massive elliptical galaxies, the characteristic mass for the modern, dust-dominated regime falls to $\sim 0.1\,\mathrm{M_\odot}$, thus providing an explanation for the more bottom-heavy IMF observed in these galaxies. We conclude that metallicity is a key driver of variations in the characteristic stellar mass, and by extension, the IMF. '

5.1 Introduction

The thermodynamics of modern (metal-rich) star formation is largely determined by the combined action of dust and stellar radiation feedback. At gas number densities $\lesssim 10^4 - 10^5$ cm^{-3}, dust and gas temperatures can differ, but once the density in a collapsing molecular cloud core exceeds this threshold, efficient gas-dust collisional coupling forces the gas and dust temperatures to track one another closely (e.g., Masunaga et al. 1998; Masunaga & Inutsuka 2000; Goldsmith 2001). This means that, prior to the formation of stellar sources capable of heating it, dust is the main coolant as molecular clouds collapse and compress on their way to star formation. In this regime the gas temperature is set by a competition between adiabatic compression of the gas due to collapse (possibly supplemented by cosmic ray heating) and cooling due to dust thermal emission (possibly supplemented by metal line cooling). The cooling processes initially keep the gas close to isothermal, allowing it to fragment to ever-smaller masses as the Jeans mass decreases with rising density (Guszejnov et al. 2016b, 2018), until the system reaches the so-called opacity limit for fragmentation (Low & Lynden-Bell 1976; Rees 1976). At this point a collapsing cloud becomes opaque and can no longer radiate away its gravitational potential energy on a free-fall timescale, preventing the gas from fragmenting any further (Omukai 2000). This transition occurs when the collapsed mass reaches $\sim 10^{-2}\,\mathrm{M_\odot}$.[1], and early simulations using an equation of state that stiffens at high density to mimic the effects of opacity found a mass spectrum that is essentially flat between $0.01 - 0.5\,\mathrm{M_\odot}$ (Bate et al. 2003; Bate 2005).

Once hydrostatic objects form the thermodynamic regime radically changes: the gravitational potential energy liberated as mass accretes onto $\sim 10^{-2}\,\mathrm{M_\odot}$ "seed" protostars is transformed into heat and then radiatively transferred outward. In the highly-opaque environment of a collapsing cloud, this radiation is in turn absorbed by and heats the surrounding dust, which then heats the gas to temperatures far higher than those that prevail prior to hydrostatic core formation. This suppresses the formation of small objects and shifts the peak in the stellar mass distribution

---

[1]Throughout this manuscript, we use '$\approx$' to imply 'approximately equal to' and '$\sim$' to imply 'of the order'.

to ~ 0.2 M$_\odot$ (Offner et al. 2009b; Bate 2009b, 2012b; Krumholz 2011b; Krumholz et al. 2011, 2012c; Myers et al. 2014a; Bate & Keto 2015; Guszejnov et al. 2016b; Federrath et al. 2017a; Cunningham et al. 2018b; Mathew & Federrath 2020b, 2021). This characteristic mass is effectively set by the "sphere of influence" that each hydrostatic object creates around itself by heating the gas therein to the point where it is unable to fragment (Krumholz et al. 2016a).

The thermodynamic behaviour of collapsing gas at much lower metallicities, characteristic of the formation of the first stars (Population III) and the generation that immediately followed them (Population II), is quite different. Stellar feedback in the form of heating (as opposed to ionisation or dissociation) is unimportant, since there is no dust to absorb the radiation and transmit it to the gas. In the absence of metals, molecular hydrogen is the dominant cooling agent that competes against compressional heating (Lepp & Shull 1984; Galli & Palla 1998). Nonetheless, because H_2 is a poor coolant, the characteristic gas temperature is much higher than during modern, dust-mediated star formation, even considering the elevated dust temperatures that prevail once hydrostatic objects form. Thus while some low-mass objects can form due to disc fragmentation even in the absence of metals (e.g., Clark et al. 2011c,a; Greif et al. 2011b; Stacy et al. 2012; Hirano et al. 2014; Latif & Schleicher 2015; Susa 2019; Sharda et al. 2020b, 2021a), the typical mass of a star formed under these thermodynamic conditions is far larger than in the present-day case (Bromm et al. 2009; Bromm 2013; Susa et al. 2014; Klessen 2019).

However, the transition between the two extremes of modern (metal-rich) and primordial (metal-poor) star formation, and in particular the role of dust coupling and stellar radiation feedback at low metallicity, has thus far received limited exploration. Krumholz (2011b) present analytic models for radiation feedback and predict a weak scaling of IMF peak mass with metallicity, while Myers et al. (2011) and Bate (2014, 2019) carry out radiation-hydrodynamic simulations of star formation over a metallicity range from $0.01 - 3\,Z_\odot$ and find negligible effects on gas fragmentation. However, these studies do not explore lower metallicities, despite available evidence for the existence of a low-metallicity ISM in the past through the discovery of stars with metallicities as low as 10^{-4} Z$_\odot$ (Caffau et al. 2011; Starkenburg et al. 2018), as well as several others with [Fe/H] < -5 (Christlieb et al. 2004; Keller et al. 2014; Frebel et al. 2015; Aguado et al. 2017, 2018; Nordlander et al. 2019; Ezzeddine et al. 2019). Coming from the opposite direction, Bromm et al. (2001) and Omukai et al. (2005, 2010) consider the thermodynamics of gas of increasing metallicity, and find that dust and metal line cooling permits fragmentation to reach masses $\lesssim 1$ M$_\odot$ only once the metallicity exceeds $\sim 10^{-3.5} Z_\odot$. Dust is a more efficient coolant

than metal lines, and permits fragmentation to lower masses at lower metallicity (e.g., Meece et al. 2014; Chiaki & Yoshida 2020; Shima & Hosokawa 2021), but exactly by how much depends on the poorly-known distribution of dust grain sizes in the early Universe (Schneider et al. 2006a, 2012; Omukai et al. 2010; Schneider & Omukai 2010; Chiaki et al. 2015). However, the early Universe star formation models are fundamentally misanalogous to the modern ones that consider decreasing metallicity, in that the early Universe models consider dust solely as a coolant that enables fragmentation, whereas the modern ones assign it a more nuanced role, as both a source of cooling and later, once stellar feedback begins, a source of heating – a changeover that seems crucial to explaining why the IMF in the present-day Universe peaks at $\sim 0.2\,\mathrm{M_\odot}$ rather than $\sim 10^{-2}\,\mathrm{M_\odot}$ (Kroupa 2001; Chabrier 2003, 2005).

Our goal in this paper is to explore the thermodynamics of star-forming gas, and the implications of those thermodynamics for fragmentation, across a wide range of metallicity, from near zero to super-Solar. In particular, we aim to study the transition in the peak of the IMF as a function of metallicity, and figure out when the IMF became bottom-heavy as the metal content of the Universe increased. Crucially, and in contrast with earlier work, we consider the evolving role of stellar radiation feedback, which is perhaps sub-dominant in the primordial Universe but evolves to a dominant effect in the present. We arrange the rest of the paper as follows: Section 5.2 describes the theoretical framework that we use to construct our models, Section 5.3 describes the resulting dust and gas temperatures and the characteristic stellar mass, and Section 5.4 presents a discussion of the robustness of the results. Section 5.5 looks at the evolution of the IMF in various stellar systems in the context of our models. We then use our models to explore implications for the cosmic star formation history in Section 5.6. Finally, we present a summary of our work in Section 5.7.

5.2   Theoretical Framework

The basic system we consider is a spherical cloud core shortly after its centre has collapsed and produced a first hydrostatic object of mass $\sim 10^{-2}\,\mathrm{M_\odot}$. We are interested in determining how much of the gas around this object is available to accrete onto it – thereby increasing the object's mass above the minimum imposed by the opacity limit for fragmentation and shifting the stellar mass distribution higher – and how much is likely to undergo independent collapse and form other objects. Since both analytic models and simulations show that fragmentation is

closely linked to the temperature structure of the gas, we address this question by first computing the expected gas temperature structure, which requires balancing heating against cooling, and then examining the implications of that temperature structure for fragmentation. For simplicity, we collect all the major parameters we use in this work and list them in Table 5.1.

Before proceeding further, however, we note an important caveat: the basic premise of our model is that the location of the IMF peak is set by thermal fragmentation, and, while this proposition has significant theoretical and numerical support (as discussed in Section 5.1), this is not the only possible explanation. For example, several early authors proposed that the IMF peak might be set by the feedback provided by protostellar outflows (Adams & Fatuzzo 1996; Shu et al. 2004), and more recently several have proposed that it is imposed by tidal forces that appear when a first Larson (1969) core forms (Lee & Hennebelle 2018; Hennebelle et al. 2019; Colman & Teyssier 2020; Hennebelle et al. 2020b). Our calculation will yield correct results only to the extent that the IMF peak is controlled by gas thermodynamics rather than outflows, tidal forces, or some other process that is insensitive to the temperature and pressure of the collapsing gas.

5.2.1   Physical model

Following numerical simulations of star formation at various metallicities (e.g., Krumholz et al. 2011; Federrath & Klessen 2013; Chiaki et al. 2016; Sharda et al. 2019a) as well as observations (Caselli & Myers 1995; van der Tak et al. 2000; Jørgensen et al. 2002; Mueller et al. 2002; Pirogov 2009; Schneider et al. 2015; Gieser et al. 2021), we assume that the volume density of the cloud has a radial profile $\rho(r) = \rho_0(r/R)^{-k_\rho}$ that can be fully described by three parameters; one of these is k_ρ, which both observations and simulations find is always in the range $k_\rho = 1 - 2$, and we therefore fix to 1.5. The other two can be the edge density ρ_0 and outer radius R, but we can equally well specify any two of the total mass (M), the mean surface density (Σ), or anything else related to these. For the purposes of exploring the parameter space, it is convenient to choose the two parameters to be the pressure at the cloud edge P and velocity dispersion at the cloud edge σ_v – the former because the pressure in a molecular cloud core will be at a minimum bounded below by the mean interstellar pressure in the galaxy wherein it resides, and the latter because observed velocity dispersions in molecular cloud cores span a

Table 5.1: List of the main parameters used in this work.

Parameter	Description	Reference
	Physical model	Section 5.2.1
P	Cloud pressure	equation 5.1
σ_{v}	Cloud velocity dispersion	
ρ_0	Density at the cloud edge	equation 5.1
Σ	Surface density at the cloud edge	equation 5.2
R	Cloud radius	equation 5.3
M	Cloud mass	equation 5.4
	Chemical model	Section 5.2.2
Z	Metallicity	. . .
$\mathcal{Z}$	$\log_{10} Z/Z_\odot$	. . .
δ	Dust to gas ratio	. . .
n_{H}	Number density per H nuclei	. . .
n	Free particle number density	. . .
μ	Mean mass per free particle	. . .
μ_{H}	Mean mass per H nucleon	. . .
	Dust temperature profile	Section 5.2.3
L	Luminosity	equation 5.11
T_{d0}	Dust temperature at cloud edge	equation 5.12
$T_{\mathrm{d}}(r)$	Dust temperature at radius r	equation 5.12
κ	Dust opacity	equation 5.14
	Gas temperature profile	Section 5.2.4
$T_{\mathrm{g}}(r)$	Gas temperature at radius r	. . .
Γ_{c}	Compressional heating	equation 5.17
Ψ_{gd}	Dust-gas energy exchange	equation 5.18
Λ_{M}	Metal line cooling	equation 5.26
$\Lambda_{\mathrm{H_2}}$	Molecular hydrogen cooling	equation 5.27
Λ_{HD}	Hydrogen deuteride cooling	. . .
$\Gamma_{\mathrm{H_2,3b}}$	3-body H_2 formation heating	equation 5.32
$\Gamma_{\mathrm{H_2,d}}$	Heating due to H_2 formation on dust	equation 5.33
Γ_{CR}	Cosmic ray heating	equation 5.34
$\mathcal{C}(\eta)$	Relative contribution of a process η to gas heating/cooling	equation 5.31
	Characteristic stellar mass	Section 5.2.5
$M_{\mathrm{enc}}(r)$	Enclosed mass as a function of r around a protostar	equation 5.29
$M_{\mathrm{BE}}(r)$	Bonnor-Ebert mass as a function of r around a protostar	equation 5.30
n_{crit}	Critical density where $M_{\mathrm{enc}} = M_{\mathrm{BE}}$	. . .
M_{ch}	Characteristic stellar mass	. . .

relatively narrow range. The edge density and radius are related to these by[2]

$$\rho_0 = \frac{P}{\sigma_{\mathrm{v}}^2} \tag{5.1}$$

$$\Sigma = \sqrt{\frac{20P}{3\pi\alpha_{\mathrm{vir}}G}} \tag{5.2}$$

$$R = \frac{(3-k_\rho)\Sigma}{4\rho_0} \tag{5.3}$$

$$M = \pi\Sigma R^2 \tag{5.4}$$

where $\alpha_{\mathrm{vir}} \approx 2$ is the virial ratio for a collapsing molecular cloud. Here, we have ignored the effects of magnetic pressure, which, if dominant (e.g., in high mass star formation regions), can lead to $\alpha_{\mathrm{vir}} \ll 1$ (Pillai et al. 2011; Kauffmann et al. 2013b). At least for modern star formation, Krumholz et al. (2016a) find that magnetic forces are unimportant on the small scales where fragmentation sets the IMF, even in simulations where the magnetic field is dynamically very strong on larger scales.

We vary the pressure between $10^4\,k_{\mathrm{B}}\,\mathrm{K\,cm^{-3}}$ (typical of Milky Way molecular clouds - Dame et al. 2001; Miville-Deschênes et al. 2017) and $10^8\,k_{\mathrm{B}}\,\mathrm{K\,cm^{-3}}$ (typical of molecular clouds in starburst environments - Turner et al. 2000; van Dokkum et al. 2008; Bolatto et al. 2008, or super star clusters - Bastian et al. 2006). Observed values of σ_{v} for molecular cloud cores are between $0.5 - 5\,\mathrm{km\,s^{-1}}$ (see also, Padoan et al. 1997; Myers et al. 2011; Chabrier et al. 2014). Note that not all combinations of P and σ_{v} are physically plausible, and some are plausible but not very probable. For example, a molecular cloud with a very high P in general cannot have a very high σ_{v} since high P corresponds to a high surface density, and the volume density is proportional to $1/\sigma_{\mathrm{v}}^2$; high P and high σ_{v} therefore corresponds to the implausible combination a very high surface density but a very low volume density.

5.2.2 Metallicity and chemical model

We parameterize the chemical composition of the gas in terms of the metallicity Z, which we vary between $10^{-6}\,Z_\odot$ (extremely metal-poor or primordial-like) and $2\,Z_\odot$ (super solar-like). This is of course a significant oversimplification. In reality, the chemical composition of a cloud changes according to the density, metallicity, and temperature, and may or may not be in steady state (e.g., Langer 2009; Krumholz & Gnedin 2011; Hu et al. 2021; Sternberg et al. 2021). This matters for the thermo-

---

[2]Note that the relationship between σ_{v}, M, and R in this system is the same as that in Myers et al. (2011, equation 14) within 20 per cent.

dynamics because, even for fixed abundances of elements such as C and O, the rate of cooling depends on whether these are mostly in the form of molecules such as CO, neutral atoms such as C I, or ions such as C II. Capturing this complexity in detail is possible only with the aid of a fully time-dependent chemodynamic simulation (e.g., Chiaki et al. 2016). However, we will see that the generic result we obtain below regarding the existence of different thermodynamic regimes and the locations of transitions between them is not qualitatively dependent on details of the chemical composition.

For the purposes of making a simple model, we will limit ourselves to considering the following chemical species, which are responsible for the great majority of cooling in neutral gas: H I, H_2[3], C I, C II, O I, and CO. We define x_S as the ratio of the number density of species S to the number density of H nuclei, where we distinguish between the abundance of the neutral state of a particular species and all atoms of that species by denoting the former with I, i.e., $x_{C I}$ is the number of neutral carbon atoms present per H nucleus, while x_C is the number of all carbon atoms per H nucleus in all chemical and ionisation states – ionised, free neutral, and bound into CO. We set total atomic abundances as a function of metallicity simply by scaling from local ISM gas-phase abundances, i.e., we set $x_C = x_{(C,MW)}(Z/Z_\odot)$, and similarly for O. Here $x_{(C,MW)}$ is the gas-phase abundance of C atoms in the local ISM; for the purposes of this paper, we adopt $x_{(C,MW)} = 1.4 \times 10^{-4}$ and $x_{(O,MW)} = 3.0 \times 10^{-4}$ following Draine (2011, table 23.1). The abundances of the various possible chemical states are then related by

$$1 = x_{H I} + 2x_{H_2} \tag{5.5}$$

$$x_C = x_{C I} + x_{C II} + x_{CO} \tag{5.6}$$

$$x_O = x_{O I} + x_{CO}, \tag{5.7}$$

which is equivalent to stating that all (gas-phase) O atoms are in the form of O I or CO, C atoms are in the form of C I, C II, or CO, and H atoms are H I or H_2.

In keeping with our simple approach, as a fiducial case we will adopt plausible scalings of x_{H_2}, $x_{C I}$, and x_{CO} with metallicity, guided by a combination of simulations and observations; the abundances of the remaining states can then be deduced from conservation. We therefore adopt

---

[3]In places where we make use of atomic data that distinguishes ortho-H_2 from para-H_2, we adopt a fixed ortho-H_2 to para-H_2 ratio of 3:1 - variations in this ratio as observed in clouds at different metallicities (e.g., Sternberg & Neufeld 1999; Flower & Pineau des Forêts 2000; Rodríguez-Fernández et al. 2000) make little difference to the results.

$$x_{\mathrm{H\,I}} = \begin{cases} 1 - 2x_{\mathrm{H_2,\,min}}, & \mathcal{Z} < -5 \\ (1 - 2x_{\mathrm{H_2,\,min}}) + \\ \quad 2(\mathcal{Z} + 5)\,(x_{\mathrm{H_2,\,min}} - x_{\mathrm{H_2,\,max}}), & -5 \leq \mathcal{Z} < -4 \\ 1 - 2x_{\mathrm{H_2,\,max}}, & \mathcal{Z} \geq -4\,, \end{cases} \tag{5.8}$$

where $\mathcal{Z} \equiv \log_{10}(Z/Z_{\odot})$, $x_{\mathrm{H_2,max}} = 0.5$ for a fully molecular composition, and we set $x_{\mathrm{H_2,min}} \approx 0.0007$ based on the results from Population III star formation simulations (Sharda et al. 2019a, 2020b). For CO, we adopt

$$\frac{x_{\mathrm{CO}}}{x_{\mathrm{C}}} = \begin{cases} 0, & \mathcal{Z} < -1 \\ 2\,(\mathcal{Z} + 1), & -1 \leq \mathcal{Z} < -0.5 \\ 1, & \mathcal{Z} \geq -0.5\,, \end{cases} \tag{5.9}$$

and for C I, we use

$$\frac{x_{\mathrm{C\,I}}}{x_{\mathrm{C}}} = \begin{cases} 0, & \mathcal{Z} < -4 \\ 4 + \mathcal{Z}, & -4 \leq \mathcal{Z} < -3 \\ 1, & -3 \leq \mathcal{Z} < -1 \\ -\,(1 + 2\mathcal{Z}), & -1 \leq \mathcal{Z} < -0.5 \\ 0, & \eta \geq -0.5 \end{cases} \tag{5.10}$$

We plot our adopted fiducial chemical abundances as a function of metallicity in Figure 5.1.

Qualitatively, these scalings describe a sequence of chemical states through which star-forming gas passes, starting with a purely atomic, moderately ionised composition (mostly H I, C II, O I) at the lowest metallicity, changing to one where the H converts to H_2 at higher metallicity (mostly H_2, C II, O I), then allowing the C to start transitioning to neutral as dust shielding increases (H_2, C I, O I), and finally reaching the CO-dominated composition observed to characterise modern star formation (H_2, CO). While our chemical setup is consistent with both theoretical (Omukai et al. 2005; Krumholz et al. 2009b; McKee & Krumholz 2010; Glover & Clark 2012b; Sternberg et al. 2014; Chiaki et al. 2015; Bialy & Sternberg 2015; Glover & Clark 2016; Chiaki & Yoshida 2020; Sternberg et al. 2021; Hu et al. 2021) and observational results (Langer 2009; Pineda et al. 2017; Schruba et al. 2017; Jameson et al. 2018; Madden et al. 2020), it is of course a simplification since the chemical composition also depends on cloud density and temperature as we describe above. We will show later in Section 5.4.3 that the choice of the chemical composition does not significantly impact our results on the transition of the IMF from primordial to modern-day.
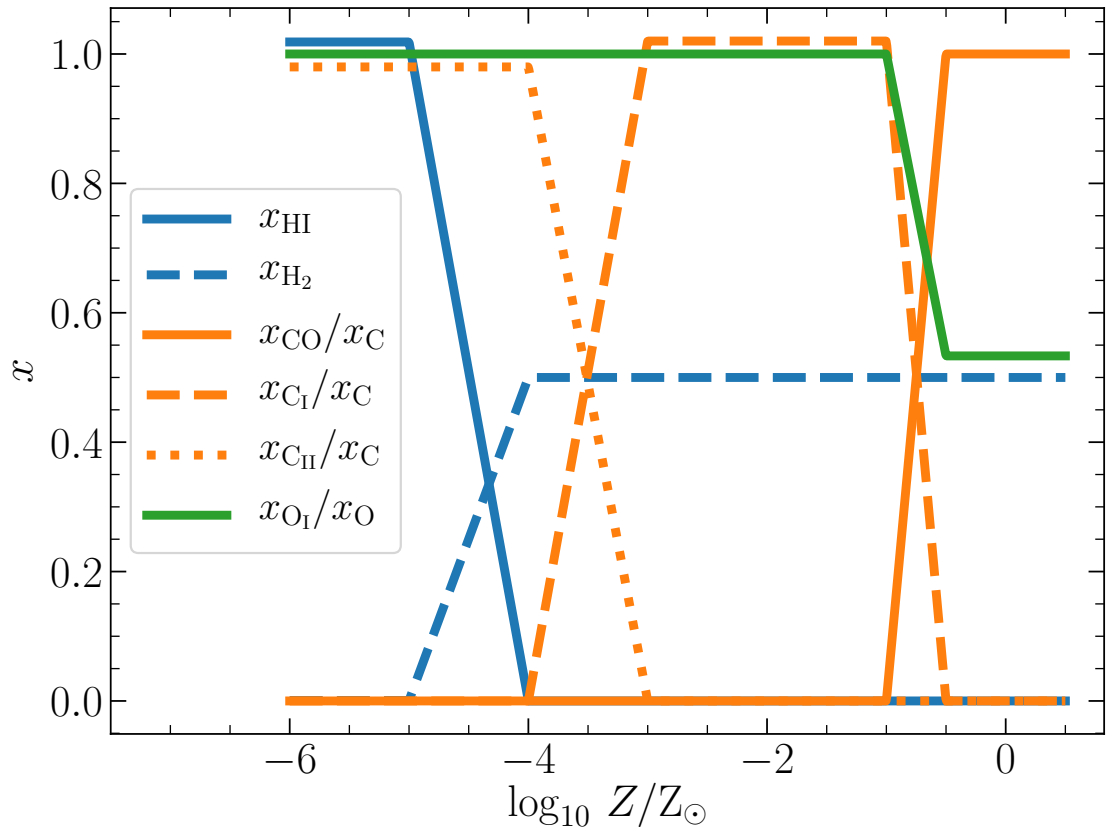
Figure 5.1: Number fraction of hydrogen, carbon and oxygen atoms in various forms – neutral (H I, C I, O I), ionized (C II), and molecular (H$_2$, CO), as a function of metallicity Z for the fiducial model (see equation 5.9 and equation 5.10). The curves for $x_{\mathrm{H\,I}}$ and $x_{\mathrm{O\,I}}/x_{\mathrm{O}}$ have been shifted by ± 2 per cent, respectively, for better visibility.

Since one of the main goals of this paper is to account for the effects of dust, as a fiducial model we also assume that the dust abundance scales linearly with total metallicity. Specifically, we adopt a dust to gas mass ratio $\delta_\odot = 1/162$ at $Z = \mathrm{Z}_\odot$ (Zubko et al. 2004), and at other metallicities adopt a mass ratio $\delta = \delta_\odot (Z/\mathrm{Z}_\odot)$. As with gas-phase chemical abundances, we also consider alternative scalings of δ with Z below in Section 5.4.4, and show that our qualitative results are not sensitive to the particular scaling that we adopt.

Finally, at various points in the following discussion, we will require conversions between mass density and number density, which depend on chemical composition. Assuming that H and He nuclei always dominate the mass, and the usual cosmic He abundance $x_{\mathrm{He}} = 0.1$, the mean mass per H nucleus, measured in units of m_{H}, is $\mu_{\mathrm{H}} = 1 + 4x_{\mathrm{He}} = 1.4$. The number density of H nuclei is related to the mass density by $n_{\mathrm{H}} = \rho/\mu_{\mathrm{H}} m_{\mathrm{H}}$. By contrast, the number of free particles per H nucleus is $1 - x_{\mathrm{H}_2} + x_{\mathrm{He}}$, so the mean mass per free particle is $\mu = \mu_{\mathrm{H}}/(1 - x_{\mathrm{H}_2} + x_{\mathrm{He}})$, and

the number density of free particles is $n = \rho/\mu m_{\mathrm{H}}$.

5.2.3   Dust temperature profile

Once a protostar appears in a star-forming molecular cloud, the temperature of the dust around the protostar is mainly governed by radiation feedback from the protostar. Thus, radiation feedback plays a key role in the thermodynamics of dust in such regions. During the early phases of star formation, this feedback is powered primarily by accretion, rather than by nuclear burning, and we calculate the accretion luminosity following Krumholz (2011b):

$$L = \epsilon_{\mathrm{L}}\epsilon_{\mathrm{M}}\mathcal{A}M\sqrt{\frac{3G\rho_0}{3 - k_\rho}} \,. \tag{5.11}$$

Here the factor under the square root is simply the inverse of the mean free-fall time (t_{ff}) in the cloud, so this expression amounts to a statement that the luminosity is proportional to an accretion rate of order M/t_{ff}. The other factors appearing in the proportionality are $\epsilon_{\mathrm{M}} \approx 0.5$, the fraction of the mass falling onto the protostar that is accreted rather than ejected from the inner disc in a wind (Matzner & McKee 2000; Alves et al. 2007; Enoch et al. 2008; Federrath & Klessen 2012; Federrath et al. 2014b), $\epsilon_{\mathrm{L}} \approx 0.75$, the fraction of accretion power that contributes to accretion luminosity rather than being used to drive the wind (McKee & Tan 2003), and $\mathcal{A} = GM_\star/R_\star$, the energy per unit mass released by accretion onto a protostar of mass $M_\star$ and radius $R_\star$. Krumholz (2011b, Figure 3a) point out that, due to deuterium burning during the star formation process, all protostars have similar, nearly-linear mass-radius relations, which yields an approximately constant value $\mathcal{A} = 2.5 \times 10^{14}\,\mathrm{erg\,g^{-1}}$ (see also, Stahler et al. 1980; Hosokawa et al. 2011a). We discuss how ϵ_{L}, ϵ_{M} and $\mathcal{A}$ impact the final results in Section 5.4.5.

To obtain the dust temperature from the luminosity and the physical structure of the cloud core, we use the analytic model developed by Chakrabarti & McKee (2005) to produce spectral energy distributions (SEDs) of non-overlapping[4] spherically-symmetric sources. This model has been shown to reproduce the SEDs in a wide variety of dusty environments, ranging from protostellar sources to high-redshift sub-mm galaxies (Chakrabarti & McKee 2008; Chakrabarti et al. 2013). Chakrabarti & McKee show that, for a dusty gas cloud with a powerlaw density profile such

---

[4]Non-overlapping means that the thermal influence zone of one source does not overlap with another, which is a valid approximation as long as the star formation efficiency per freefall time is less than 10 per cent (Krumholz et al. 2011), observed in almost all star-forming environments (Sharda et al. 2018, 2019b).

as we have assumed, the dust temperature profile also assumes an approximately powerlaw form, given by

$$T_{\rm d}(r) = T_{\rm d0} \left(\frac{r}{R}\right)^{-k_{\rm T}},\tag{5.12}$$

where, for a given wavelength-dependent dust opacity, the index $k_{\rm T}$ and the outer dust temperature $T_{\rm d0}$ are determined entirely by two parameters: the cloud luminosity-to-mass ratio L/M, and the surface density Σ. The index and outer dust temperature are in turn given by

$$k_{\rm T} \approx \frac{0.48 k_\rho^{0.005}}{\tilde{R}^{0.02 k_\rho^{1.09}}} + \frac{0.10 k_\rho^{5.5}}{\tilde{R}^{0.70 k_\rho^{1.09}}}\tag{5.13}$$

$$T_{\rm d0}^\gamma \approx \left(\frac{L/M}{6.4\sigma_{\rm SB}\tilde{R}^{0.1}}\right)^{k_\rho - 1 + \beta k_{\rm T}} \left[\frac{(3 - k_\rho)\delta\kappa_0}{4(k_\rho - 1)T_0^\beta}\right]^{4k_{\rm T} - 2}$$
$$\times \Sigma^{(4+\beta)k_{\rm T} + k_\rho - 3}\tag{5.14}$$

where $\gamma = 2\beta + 4(k_\rho - 1)$, $\sigma_{\rm SB}$ is the Stefan-Boltzmann constant, and the parameters β, δ, κ_0, and T_0 describe the dust opacity as a function of wavelength in the infrared, $\kappa = \delta\kappa_0(\lambda_0/\lambda)^\beta$, where $\lambda_0 = hc/k_B T_0$. We adopt $\beta = 2$ and $\kappa_0 = 0.27\,{\rm cm}^2\,{\rm g}^{-1}$ at $\lambda_0 = 100\,\mu{\rm m}$ from the dust opacity model of Weingartner & Draine (2001), which gives $T_0 = 144\,{\rm K}$.[5] Other dust opacity models such as those of Pollack et al. (1994) and Semenov et al. (2003) have been shown to make little difference in this calculation (Myers et al. 2011). Finally, the dimensionless constant $\tilde{R}$ is given by

$$\tilde{R} = \left[\frac{(L/M)(M/\pi R^2)^{(4+\beta)/\beta}}{6.4\sigma_{\rm SB}\tilde{R}^{0.1}} \left(\frac{\delta\kappa_0\,(3 - k_\rho)}{4\,(k_\rho - 1)\,T_0^\beta}\right)^{4/\beta}\right]^{-\beta/\gamma}.\tag{5.15}$$

Note that the dust opacity model we incorporate is only valid as long as most of the emission is longward of $30\,\mu{\rm m}$, implying that dust opacities cannot be written down as a powerlaw in frequency for $T_{\rm d} \gtrsim 480\,{\rm K}$. We show below that $T_{\rm d} < 480\,{\rm K}$ in the regime where dust matters for the characteristic stellar mass. Furthermore, we check that the application of the Chakrabarti & McKee model for our work remains valid across the entire parameter space by ensuring $\tilde{R} > 1$.

---

[5]Note that the dust opacity model we adopt does not take the effects of grain growth via coagulation into account. However, Chakrabarti & McKee (2005) show that for typical cloud densities, the coagulation timescale is two orders of magnitude more than the freefall time at which the cloud collapses. Additionally, dust coagulation changes β by at most 10 per cent (Ossenkopf & Henning 1994), which does not lead to any appreciable difference in $T_{\rm d}$. Thus, we do not expect dust coagulation to play a significant role in our work.

5.2.4   Gas temperature profile

The next step in our calculation is to determine the gas temperature T_{g} as a function of radius within the cloud. In thermal equilibrium, we can solve for T_{g} by balancing gas heating and cooling,

$$\Gamma_{\mathrm{c}} + \Psi_{\mathrm{gd}} + \Lambda_{\mathrm{M}} + \Lambda_{\mathrm{H_2}} + \Lambda_{\mathrm{HD}} = 0 \qquad (5.16)$$

where the Γ term represents heating processes (expressed as rate per unit mass, with units of energy per unit mass per unit time), Λ terms represent cooling processes, and Ψ is a term representing processes that can either heat or cool the gas depending on the circumstances. From left to right, the terms appearing in equation 5.16 represent heating due to adiabatic compression, heating/cooling due to dust-gas energy exchange, cooling due to metal lines, cooling due to molecular hydrogen, and cooling due to hydrogen deuteride, respectively. While this list of processes is by no means exhaustive, our list does cover the processes that dominate gas thermodynamics. In addition to these, we also consider the effects of H_2 formation heating and cosmic rays on gas thermodynamics later in Section 5.4. We next express all of the heating, exchange, and cooling terms in terms of the local gas density ρ and gas temperature T_{g}; since we have specified $\rho(r)$ (as well as the dust temperature $T_{\mathrm{d}}(r)$), doing so allow us to solve equation 5.16 to obtain the gas temperature profile $T_{\mathrm{g}}(r)$.

Heating processes

Compressional heating. Heating due to compression in a free-falling gas occurs at a rate (e.g., Masunaga et al. 1998; Masunaga & Inutsuka 2000)

$$\Gamma_{\mathrm{c}} \approx \frac{k_{\mathrm{B}} T_{\mathrm{g}}}{\mu} \sqrt{\frac{32 G \mu_{\mathrm{H}} n_{\mathrm{H}}}{3 \pi m_{\mathrm{H}}}} . \qquad (5.17)$$

This expression follows simply from the first law of thermodynamics, which requires that the work per unit mass done on the gas by compression be $P \, d(1/\rho)/dt$. equation 5.17 follows immediately from this by applying the ideal gas law to write P in terms of ρ and T_{g}, and taking the time derivative to be of order of the free-fall time $1/t_{\mathrm{ff}} = \sqrt{32 G \rho / 3\pi}$ (e.g., McKee & Ostriker 2007). We discuss some additional heating mechanisms that could potentially contribute to gas heating in some parts of the parameter space (for example, cosmic rays and H_2 formation heating) in Section 5.4, showing that they do not qualitatively alter our results on the trends in characteristic stellar mass as a function of metallicity.

Gas-dust energy exchange

The energy exchange per unit mass between the dust and the gas due to collisions is given by (Hollenbach & McKee 1979; Omukai 2000)

$$\Psi_{\mathrm{gd}} = 2\alpha_{\mathrm{gd}}\delta\mathcal{S}_{\mathrm{gd}}n_{\mathrm{H}}\sqrt{\frac{8k_{\mathrm{B}}T_{\mathrm{g}}}{\pi m_{\mathrm{H}}}}\,k_{\mathrm{B}}\left(T_{\mathrm{d}} - T_{\mathrm{g}}\right) \times \sum_{\mathrm{S}}\frac{x_{\mathrm{S}}}{\sqrt{\mu_{\mathrm{S}}}}\,, \tag{5.18}$$

where the sum is over the species H I, H_2, and He, μ_{S} is the species mass in units of m_{H} (1, 2, and 4 for H I, H_2, and He, respectively), α_{gd} is a factor between 0 and 1 that describes the inelasticity of dust-gas collisions (Burke & Hollenbach 1983), δ is the dust to gas ratio that we defined in Section 5.2.2, and $\mathcal{S}_{\mathrm{gd}}$ is the dust cross section per unit dust mass. Following results from experiments (Thomas 1967; Goodman 1974; Goodman & Wachman 1967), we set $\alpha_{\mathrm{gd}} \sim 0.5$. In the absence of low metallicity measurements, we fix $\mathcal{S}_{\mathrm{gd}} = 10^5\,\mathrm{cm^2\,g^{-1}}$ (based on observations of interstellar dust in the Milky Way - Schneider et al. 2012) at all Z, cautioning that this is very uncertain, since $\mathcal{S}_{\mathrm{gd}}$ depends primarily on the poorly-understood grain size distribution (Schneider et al. 2016). We discuss the effects of uncertainties in α_{gd} and $\mathcal{S}_{\mathrm{gd}}$ on the final results in Section 5.4.5.

It is clear from equation 5.18 that Ψ_{gd} acts as a heating source if $T_{\mathrm{d}} > T_{\mathrm{g}}$, and a cooling source when $T_{\mathrm{d}} < T_{\mathrm{g}}$. In the analysis that follows later, we will split Ψ_{gd} into its positive (heating) and negative (cooling) terms, and denote them by Γ_{gd} and Λ_{gd}, respectively. Our approach thus enables us to gauge the role of dust-gas energy exchange in the presence of stellar feedback by using T_{d} from the Chakrabarti & McKee (2005) model.

Cooling processes

The most important metal coolants in the ISM are carbon and oxygen, both of which can be present in different chemical forms (C II, C I, O I, CO). In atomic form, the most important coolants are the fine structure lines C II $158\,\mu\mathrm{m}$, O I 63 and $145\,\mu\mathrm{m}$, C I 230 and $610\,\mu\mathrm{m}$; when C and O are in molecular form, cooling is dominated by the low-J levels of CO. Based on the chemical composition we describe in equation 5.9 and equation 5.10, we can express Λ_{M} as the sum of cooling provided by C and O in their various chemical forms.

C II cooling. The ground spectroscopic term of C II is a ^2P doublet. In statistical equilibrium between the excited and the ground fine structure states, the cooling

rate per unit mass is given by[6]

$$\Lambda_{C\,II} = -\frac{x_{C\,II,1} A_{C\,II,10} k_B T_{C\,II}}{\mu_H m_H} \tag{5.19}$$

where $x_{C\,II,1}$ is the level population in the excited level of C II, $A_{C\,II,10}$ is the C II Einstein A coefficient for radiative de-excitation from the excited to the ground level, and $T_{C\,II}$ is the energy per k_B for the excited level of C II. We use the Leiden Atomic and Molecular Database (LAMDA, Schöier et al. 2005) to obtain $A_{C\,II,10} = 2.3 \times 10^{-6}\,s^{-1}$ and $T_{C\,II} \approx 91\,K$. The density in the upper level $x_{C\,II,1}$ can then be expressed as

$$x_{C\,II,1} = x_{C\,II} \times \left[1 + \frac{n_H \overline{k}_{C\,II,10} + A_{C\,II,10}}{n_H \overline{k}_{C\,II,01}}\right]^{-1}. \tag{5.20}$$

Here, $\overline{k}_{C\,II,10}$ is the number fraction-weighted rate of collisional de-excitation from the excited to the ground level due to collisions with H, ortho-H_2, para-H_2, and He at a given T_g,

$$\overline{k}_{C\,II,10} = x_{H\,I} k_{C\,II,10-H} + \frac{3}{4} x_{H_2} k_{C\,II,10-oH_2} + \frac{1}{4} x_{H_2} k_{C\,II,10-pH_2} + $$
$$x_{He} k_{C\,II,10-He}. \tag{5.21}$$

We adopt the collisional coefficient rates for collisions between C II and other species from the LAMDA database (Barinovs et al. 2005; Lique et al. 2013; Wiesenfeld & Goldsmith 2014).[7] $\overline{k}_{C\,II,01}$ is the number fraction-weighted rate of collisional excitation from the ground to the excited state, given by

$$\overline{k}_{C\,II,01} = \frac{g_{C\,II,1}}{g_{C\,II,0}} \overline{k}_{C\,II,10} e^{-T_{C\,II}/T_g} \tag{5.22}$$

where $g_{C\,II,1} = 4$ and $g_{C\,II,0} = 2$ are the statistical weights of the excited and the ground states of C II, respectively.

C I and O I cooling. Both C I and O I have similar atomic shell configurations since the former has 2 filled and the latter has 2 empty $2p$ shells. For both, cooling at low temperatures comes from fine structure transitions between the sub-states of

---

[6]Note that this calculation and the analogous ones that follow for C I and O I are only valid as long as the cooling lines are optically thin. We check that this is indeed the case by estimating the optical depth of each of the transitions of these species. The general result is that these species never become optically thick within the parameter space we cover in this work (at all Z); this is primarily because of the extremely low oscillator strengths of the fine structure transitions.

[7]The collisional rate coefficient for collisions between C II and He, $k_{C\,II,10-He}$, is not provided in the LAMDA database. So, we simply approximate $k_{C\,II,10-He} \approx \sqrt{2} k_{C\,II,10-oH_2}$, where the factor $\sqrt{2}$ accounts for the mass difference between He and ortho-H_2.

the lowest spectroscopic term, which is a ^3P triplet. In statistical equilibrium, the level populations in the three states can be implicitly expressed as

$$\left(n_{\mathrm{H}}\overline{\mathsf{K}} + \mathsf{A}\right)\mathbf{x}_{\mathrm{C\,I}} = \mathbf{0}, \tag{5.23}$$

where

$$\overline{\mathsf{K}} = \begin{pmatrix} \overline{k}_{\mathrm{C\,I},01} + \overline{k}_{\mathrm{C\,I},02} & -\overline{k}_{\mathrm{C\,I},10} & -\overline{k}_{\mathrm{C\,I},20} \\ -\overline{k}_{\mathrm{C\,I},01} & \overline{k}_{\mathrm{C\,I},10} + \overline{k}_{\mathrm{C\,I},12} & -\overline{k}_{\mathrm{C\,I},21} \\ -\overline{k}_{\mathrm{C\,I},02} & -\overline{k}_{\mathrm{C\,I},12} & \overline{k}_{\mathrm{C\,I},20} + \overline{k}_{\mathrm{C\,I},21} \end{pmatrix} \tag{5.24}$$

is the matrix of weighted collisional transition rates,

$$\mathsf{A} = \begin{pmatrix} 0 & -A_{\mathrm{C\,I},10} & -A_{\mathrm{C\,I},20} \\ 0 & A_{\mathrm{C\,I},10} & -A_{\mathrm{C\,I},21} \\ 0 & 0 & A_{\mathrm{C\,I},20} + A_{\mathrm{C\,I},21} \end{pmatrix} \tag{5.25}$$

is the matrix of radiative transition rates, $\mathbf{x}_{\mathrm{C\,I}} = (x_{\mathrm{C\,I},0}, x_{\mathrm{C\,I},1}, x_{\mathrm{C\,I},2})$ is a vector of the number fractions in the three fine structure sub-states (whose sum is constrained by $x_{\mathrm{C\,I},0} + x_{\mathrm{C\,I},1} + x_{\mathrm{C\,I},2} = x_{\mathrm{C\,I}}$), and $\mathbf{0}$ is the zero vector. The $\overline{k}_{\mathrm{C\,I},nm}$ and $A_{\mathrm{C\,I},nm}$ terms are the number fraction-weighted collisional rate coefficients and Einstein A coefficients for transition from state n to state m, respectively. The expression for O I is analogous. We again use temperature-dependent collision rates for collisions of C I or O I with H, He and ortho/para-H_2 taken from the LAMDA database (Launay & Roueff 1977; Schroder et al. 1991; Staemmler & Flower 1991; Lique et al. 2018). Once the level populations are known from the solution to equation 5.23, the cooling rate per unit mass can then be written as

$$\Lambda_{\mathrm{C\,I}} = -\frac{k_{\mathrm{B}}}{\mu_{\mathrm{H}}m_{\mathrm{H}}} \sum_{i=1}^{2} x_{\mathrm{C\,I},i} \sum_{j=0}^{i-1} A_{\mathrm{C\,I},i,j} T_{\mathrm{C\,I},i,j}. \tag{5.26}$$

The procedure for computing $\Lambda_{\mathrm{O\,I}}$ is analogous.

CO cooling. CO cooling is significantly more complex, because we cannot assume for it, as we do for the C and O fine structure lines, that the optical depth is small. We therefore handle CO using the software library `DESPOTIC` to estimate cooling rates and optical depths for molecular clouds of finite optical depth using the escape probability approximation (Krumholz 2014a). For this purpose, we create a 4D grid in n_{H}, T_{g}, CO column density N_{CO}, and σ_{v}, and interpolate across the grid to find the cooling rate due to CO (from all J states) for a given molecular cloud. We estimate the column density of CO for our model clouds as $N_{\mathrm{CO}} = x_{\mathrm{CO}}\Sigma/(\mu_{\mathrm{H}}m_{\mathrm{H}})$, with x_{CO} given by equation 5.9.

H$_2$ cooling. To implement H$_2$ cooling, we write the cooling rate per unit mass as

$$\Lambda_{\mathrm{H_2}} = -\Lambda_{\mathrm{H_2,thin}} \frac{x_{\mathrm{H_2}}}{n_{\mathrm{H_2}} \mu_{\mathrm{H}} m_{\mathrm{H}}} \times \min\left[1, \left(\frac{n}{8 \times 10^9 \,\mathrm{cm}^{-3}}\right)^{-0.45}\right], \tag{5.27}$$

where $\Lambda_{\mathrm{H_2,thin}}$ is the cooling rate in the optically thin regime assuming local thermodynamic equilibrium (LTE) that we obtain from Grassi et al. (2014, equation 9). The factor in the square parentheses in equation 5.27 accounts for a reduction in H$_2$ cooling due to optical depth effects at high densities, following Ripamonti & Abel (2004). Note that the optical depth correction we use is only approximate, and can deviate from a more accurate implementation especially at very high densities (Yoshida et al. 2006; Hartwig et al. 2015). This is not a problem; as we show below, the densities in which we are interested are $\lesssim 10^9\,\mathrm{cm}^{-3}$ for all P, σ_{v} and Z.

HD cooling. We follow Lipovka et al. (2005) to calculate cooling due to HD as a function of T_{g}, n_{H} and the number fraction of HD molecules that we approximate as $x_{\mathrm{HD}} = [\mathrm{D/H}] f_{\mathrm{HD}}$, where $[\mathrm{D/H}] \approx 10^{-5}$ (Tytler et al. 1996; O'Meara et al. 2001; Cooke et al. 2014). Here, f_{HD} represents the fraction of deuterium that exists in the form of HD. Typically, $f_{\mathrm{HD}} \sim 10^{-3}$ at $Z < 10^{-5}\,\mathrm{Z}_\odot$ but it can rise to 10 per cent at $Z \sim 10^{-4}\,\mathrm{Z}_\odot$ (see figure 4 of Omukai et al. 2005). While such elevated HD abundances do not significantly impact the characteristic mass at low metallicities where HD cooling can be important, we nonetheless fix $f_{\mathrm{HD}} = 0.1$, thus including the maximum possible contribution of HD cooling at all Z.

Consistency check. As a necessary check, we verify that the ratio of luminosity due to cooling radiation by all these processes to the luminosity due to blackbody cooling radiation never exceeds unity. This ratio is

$$\mathcal{L} = -\frac{4\pi r^3 \rho(r) \left(\Lambda_{\mathrm{M}} + \Lambda_{\mathrm{H_2}} + \Lambda_{\mathrm{HD}} - \min(\Psi_{\mathrm{gd}}, 0)\right)}{4\pi r^2 \sigma_{\mathrm{SB}} T_{\mathrm{g}}^4(r)} \tag{5.28}$$

where the minimum operator in the final term is to ensure that we include the contribution of dust only when it is a source of cooling, not a source of heating. Below we compute a critical radius that sets the characteristic mass, and we find that $\mathcal{L} < 0.004$ at this radius and everywhere outside it throughout our model grid for all models we discuss in this work.

5.2.5   Characteristic Stellar Mass

Now that we have found the gas temperature profile, we are in a position to estimate how fragmentation will proceed, and what characteristic stellar mass, M_{ch}, it will produce. We do so following the *ansatz* proposed by Krumholz (2011b), and which

direct tests against radiation-magnetohydrodynamic simulations (Krumholz et al. 2016a; Cunningham et al. 2018b) have shown is reasonably accurate: we consider a spherical region of radius r around the forming protostar, and within this region we compute both the mass enclosed

$$M_{\mathrm{enc}}(r) = \frac{8\pi\rho_0^2 R^3}{3\rho(r)}\,, \qquad (5.29)$$

and the minimum mass required for the gas to be unstable against gravitational collapse, which is given by the Bonnor-Ebert mass (Ebert 1955; Bonnor 1956, 1957)

$$M_{\mathrm{BE}}(r) = 1.18 \times \epsilon_{\mathrm{M}}\sqrt{\frac{\left(k_{\mathrm{B}}T_{\mathrm{g}}(r)/G\mu m_{\mathrm{H}}\right)^3}{\rho(r)}}\,, \qquad (5.30)$$

where the factor of ϵ_{M} is to account for the fraction of the mass that survives being blown out by protostellar jets. The enclosed mass scales as $M_{\mathrm{enc}} \propto \rho^{-1}$, while the Bonnor-Ebert mass scales as $T_{\mathrm{g}}^{3/2}\rho^{-1/2}$. So, for small radii, where ρ and T_{g} are both large, we have $M_{\mathrm{enc}} \ll M_{\mathrm{BE}}$. The physical meaning of this condition is that close to a protostar, the gas is prevented from fragmenting because its mass is unable to overcome thermal pressure support. It can accrete onto the already-existing protostar (or ejected as part of an outflow), but it cannot collapse to produce a new protostar. As one considers larger and larger regions, ρ and T_{g} both fall, such that there is a critical radius at which $M_{\mathrm{enc}} = M_{\mathrm{BE}}$, meaning that the enclosed mass is large enough to be unstable. Our *ansatz* is that this transition gives the approximate characteristic mass at which fragmentation can occur. Consequently, the characteristic mass M_{ch} can be read off at the location where $M_{\mathrm{enc}} = M_{\mathrm{BE}}$. Since we have specified $\rho(r)$ and $T_{\mathrm{g}}(r)$, we can solve for M_{ch} from any cloud of specified physical parameters – σ_{v} and P – and chemical composition – as parameterised by Z. Our goal in this work is to study how M_{ch} changes as we vary these parameters, particularly Z, and to understand which physical processes are responsible for driving these changes.

It is important to highlight how the formation of binary stars fits into our cloud configuration. It is well known that binaries form via two main modes – core fragmentation (e.g., Clarke & Pringle 1991; Goodwin et al. 2004; Fisher 2004; Offner et al. 2009b, 2010) and disc fragmentation (e.g., Adams et al. 1989; Bonnell & Bate 1994; Kratter & Matzner 2006; Krumholz et al. 2009a; Guszejnov et al. 2017a). However, it is not yet clear which mode of binary formation dominates near the characteristic stellar mass that sets the peak of the Galactic IMF (see, for example, Offner et al. 2010 versus Tokovinin & Moe 2020), with currently available observa-
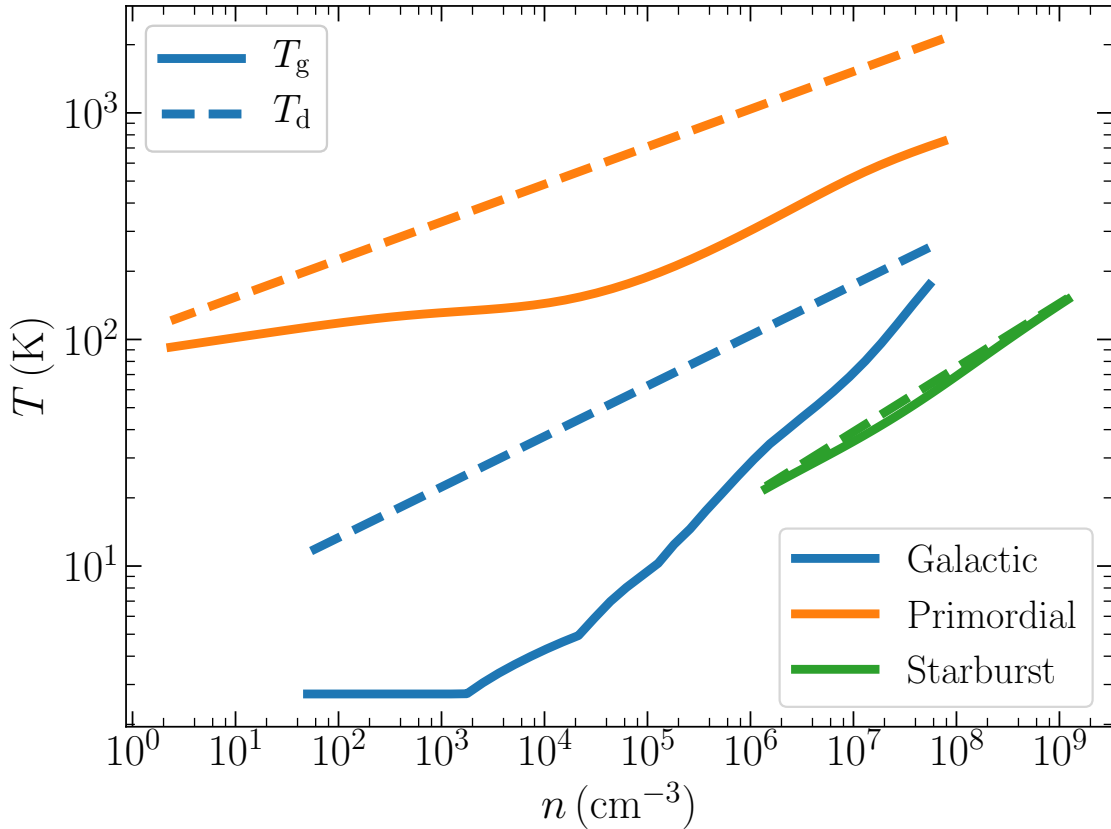
Figure 5.2: Gas and dust temperatures ($T_\mathrm{g}-$ solid, and $T_\mathrm{d}-$ dashed) as a function of free particle number density n in a molecular cloud in three different environments: Galactic (pressure $P/k_\mathrm{B} = 10^4\,\mathrm{K\,cm^{-3}}$, velocity dispersion $\sigma_\mathrm{v} = 5\,\mathrm{km\,s^{-1}}$, metallicity $Z = \mathrm{Z_\odot}$), primordial (same as Galactic but with $Z = 10^{-6}\,\mathrm{Z_\odot}$), and starburst ($P/k_\mathrm{B} = 10^8\,\mathrm{K\,cm^{-3}}$, $\sigma_\mathrm{v} = 0.5\,\mathrm{km\,s^{-1}}$, $Z = \mathrm{Z_\odot}$). Dust acts as a heating source for the gas if $T_\mathrm{d} > T_\mathrm{g}$, and vice-versa; it is unimportant for setting gas temperature in the primordial case due to the near-zero dust abundance.

tions providing support for both scenarios (Kraus et al. 2011; Tobin et al. 2016; Lee et al. 2017). The same conundrum also holds at extremely low or zero metallicity, where simulations find a ubiquitous presence of binary systems due to both modes of fragmentation (Machida et al. 2009; Machida & Nakamura 2015; Chon & Hosokawa 2019; Sharda et al. 2019a, 2020b; Sugimura et al. 2020; Chon et al. 2021; Liu et al. 2021), with a slight preference for disc fragmentation over core fragmentation (Chiaki & Yoshida 2020). Our model naturally incorporates the core fragmentation mode for binary formation but not the disc fragmentation mode. Thus, to the extent that core fragmentation dominates, we are able to predict the characteristic stellar mass of single star IMF. On the other hand, our predictions apply for the system IMF in the case disc fragmentation dominates binary star formation.
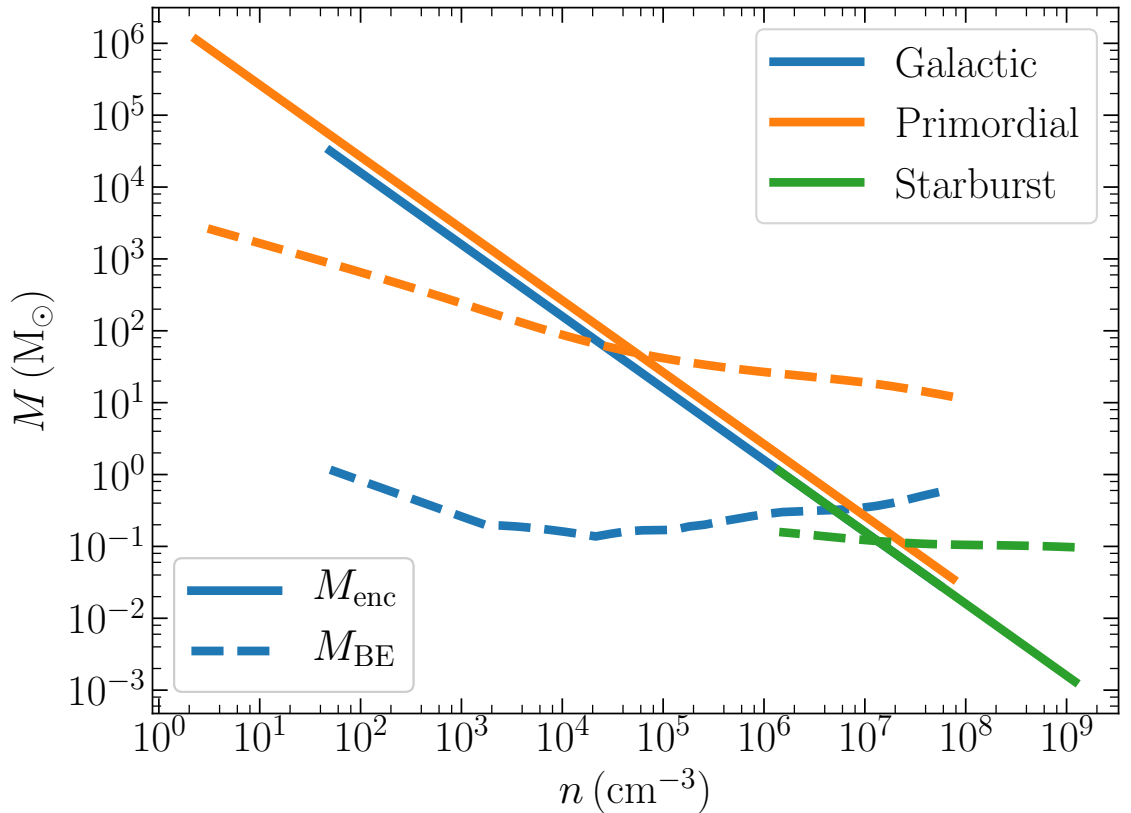
Figure 5.3: Mass enclosed around a protostar (M_{enc}, equation 5.29) and the Bonnor-Ebert mass (M_{BE}, equation 5.30) as a function of free particle number density n in a typical molecular cloud in different environments (Galactic, primordial, starburst) as in Figure 5.2. The characteristic stellar mass M_{ch} can be read off at the critical density n_{crit} where $M_{\mathrm{enc}} = M_{\mathrm{BE}}$.

5.3   Results

With the procedure complete, we can now look at the resulting models. We begin in Section 5.3.1 by walking through the procedure using some example models, to orient the reader and provide some intuition for the workings of the model. We then explore variations in the gas and dust temperatures across parameter space in Section 5.3.2, the physical processes driving these variations in Section 5.3.3, and finally the consequences for the characteristic stellar mass and the IMF in Section 5.3.4. We remind the reader that in this work we only focus on the characteristic stellar mass that sets the peak of the IMF. This is not sufficient by itself to fully describe the IMF since it consists of several other features (for example, the slopes at the low and the high-mass end, and the truncation mass) that we do not investigate in this work.

5.3.1 Profiles

We begin by presenting results for three example cases: a typical Galactic molecular cloud of pressure $P/k_{\mathrm{B}} = 10^4 \, \mathrm{K\,cm^{-3}}$, effective velocity dispersion $\sigma_{\mathrm{v}} = 5 \, \mathrm{km\,s^{-1}}$, and metallicity $Z = Z_{\odot}$, a near-primordial cloud with the same P and σ_{v} but $Z = 10^{-6} Z_{\odot}$, and a very compact cloud in a high-pressure starburst environment, with $P/k_{\mathrm{B}} = 10^8 \, \mathrm{K\,cm^{-3}}$, $\sigma_{\mathrm{v}} = 0.5 \, \mathrm{km \, s^{-1}}$, and $Z = Z_{\odot}$. In all cases we use our fiducial choice of chemical composition for the corresponding metallicity, though, as we will show below, the qualitative results are insensitive to this.

Figure 5.2 shows the profile of gas and the dust temperature as a function of density of free particles n that we obtain in each of the three cases following the theoretical framework we outline in Section 5.2. For the Galactic cloud, dust acts as a heating source throughout the cloud as it has been warmed by the central protostar; however, the gas and dust do not reach close to equality until the density rises to almost $10^6 \, \mathrm{cm^{-3}}$. By contrast, in the primordial case, the role of dust in gas thermodynamics becomes negligible, so even though $T_{\mathrm{d}} > 480 \, \mathrm{K}$ across some part of the cloud (likely invalidating the Chakrabarti & McKee 2005 model, since its assumption of a powerlaw dust opacity fails at such high temperatures), this makes no difference to the gas temperature, which is entirely set by $\mathrm{H_2/HD}$ cooling. Finally, in the starburst case, the density is so high that the dust and gas temperatures are very well coupled to each other throughout the cloud (shown by the overlapping solid and dashed green curves in Figure 5.2), and dust completely dominates gas thermodynamics. However, note that dust properties (e.g., surface area per unit mass) likely vary at least somewhat with physical conditions and metallicity, and we have ignored this effect thus far. We discuss this further in Section 5.4.5.

Figure 5.3 shows the radial profiles of M_{BE} and M_{enc} for the three example cases. As expected, we observe that in all cases the mass enclosed at high densities (corresponding to small radii) is much too small to collapse close to the protostar, i.e., $M_{\mathrm{enc}} \ll M_{\mathrm{BE}}$, but becomes unstable to collapse as one moves outward (away from the protostar). The density and mass at which this changeover occurs is different in the three examples. For the Galactic case, we find $M_{\mathrm{enc}} = M_{\mathrm{BE}}$ at $n \approx 6 \times 10^6$ $\mathrm{cm^{-3}}$. The resulting characteristic stellar mass in this case is $M_{\mathrm{ch}} = 0.31 \, \mathrm{M_{\odot}}$, within ≈ 10 per cent of the observed the peak of the Milky Way stellar IMF (Kroupa 2001; Chabrier 2003). Our model therefore naturally results in a characteristic stellar mass that is sub-solar at $Z = Z_{\odot}$, thereby resulting in a bottom-heavy Milky Way stellar IMF. This exercise also demonstrates that protostellar feedback is important to reproduce the peak of the IMF, at least at Solar metallicity and low pressure, consistent with findings from several numerical simulations (Offner et al. 2009b;

Krumholz et al. 2010; Urban et al. 2010; Myers et al. 2014b; Mathew & Federrath 2021).

For the primordial case, due to the high gas temperature, the enclosed mass only becomes sufficient to collapse by itself much farther out in the cloud (at low n), yielding $M_{\mathrm{ch}} = 60\,\mathrm{M_\odot}$. Thus, primordial-like star formation naturally gives rise to a super-solar characteristic mass, thereby hinting at the formation of a top-heavy IMF in primordial-like environments. Finally, for the starburst case, M_{BE} is nearly independent of n due to the combination of feedback and strong dust-gas coupling; feedback yields a dust temperature, and thus a gas temperature, that falls with radius in such a way as to keep $\sqrt{T^3/\rho} \propto M_{\mathrm{BE}}$ nearly constant. The resulting M_{ch} is $0.11\,\mathrm{M_\odot}$, close to the Galactic case but smaller by a factor of ≈ 3. We revisit this finding in the context of the IMF in the centres of massive elliptical galaxies in Section 5.5.1.

5.3.2   Gas and dust temperatures

Having built some intuition for the functioning of the models, we now begin to examine results across parameter space. We first seek to answer two related questions: how well-coupled are the dust and the gas? And where in parameter space is dust a source of cooling versus a source of heating, or where is it unimportant? Since our parameter space is three-dimensional $\{P, \sigma_{\mathrm{v}}, Z\}$, we address these questions by making slices through it. We first look at the 2D space in $\{P, \sigma_{\mathrm{v}}\}$ for the metallicities $Z = Z_\odot$ and $Z = 10^{-6} Z_\odot$. For each point in this parameter space, we find the location where the enclosed mass equals the Bonnor-Ebert mass (i.e., the location at which M_{ch} is determined) and measure the dust and gas temperatures there. Figure 5.4 and Figure 5.5 show the results. At $Z = Z_\odot$, we see that the gas and dust temperatures are well coupled to each other for all P and σ_{v}, consistent with our findings above that dust plays a crucial role in setting the gas temperature at high Z. Both the temperatures increase in tandem if either P or σ_{v} is increased. On the other hand, the gas temperatures are much less sensitive to P or σ_{v} for $Z = 10^{-6}\,Z_\odot$. The dust temperatures do change, and dust can both heat and cool the gas in this case, but its impact on the gas temperature is negligible.

We next explore variation with metallicity. Figure 5.6 plots the dust and gas temperatures as a function of Z at two choices of fixed P and σ_{v}, one corresponding to a low-density, Galactic-type case ($P/k_{\mathrm{B}} = 10^4$ K cm^{-3}, $\sigma_{\mathrm{v}} = 5$ km s^{-1}), and one to a dense, starburst-type environment ($P/k_{\mathrm{B}} = 10^8$ K cm^{-3}, $\sigma_{\mathrm{v}} = 0.5$ km s^{-1}). For the former, dust acts as a heating source for the gas since $T_{\mathrm{d}} > T_{\mathrm{g}}$ at all Z; however, this heating source becomes more and more feeble as we go to lower Z, such that the dust
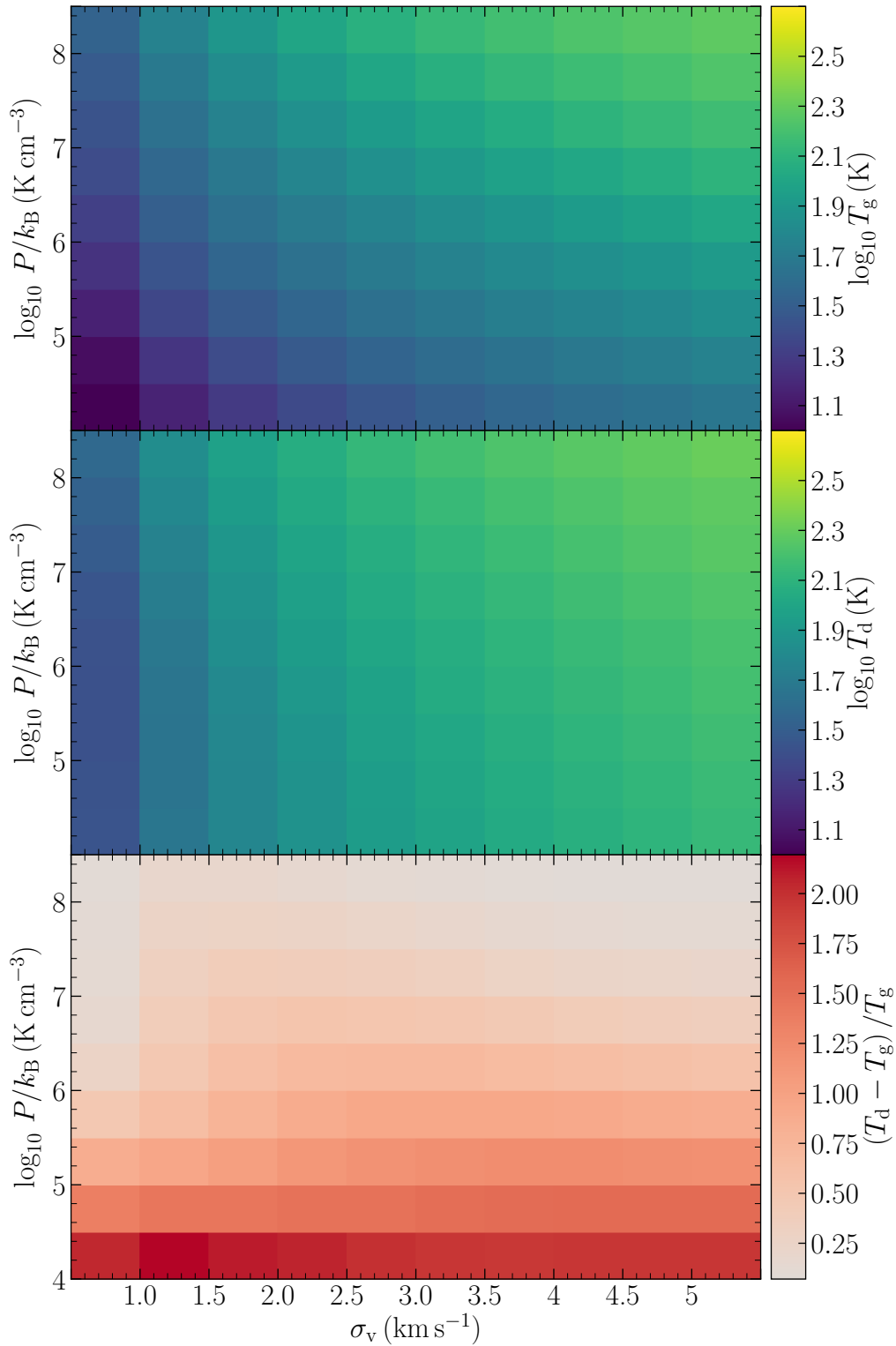
Figure 5.4: 2D plots of the gas and dust temperatures at the critical location that sets the characteristic mass as a function of cloud pressure P and velocity dispersion σ_{v} for $Z = Z_{\odot}$. Dust plays a crucial role in setting the gas temperature in this case, and is well-coupled to the gas.
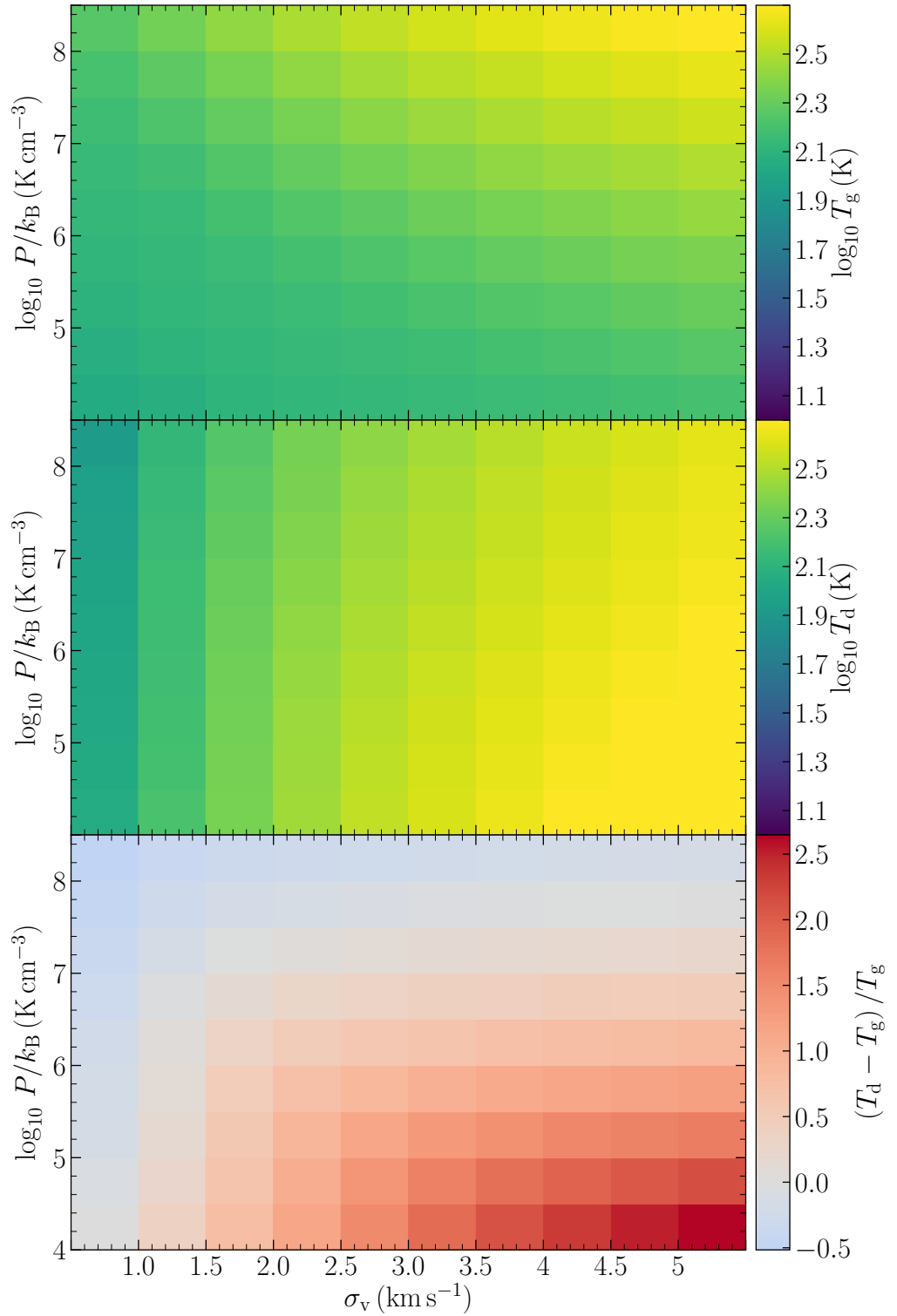
Figure 5.5: Same as Figure 5.4 but for an extremely metal-poor environment ($Z = 10^{-6}\,\mathrm{Z}_\odot$). Here, dust can act as both a heating and a cooling source for the gas, but is generally unimportant. Note the difference in colour scale in the bottom panel here as compared to Figure 5.4.
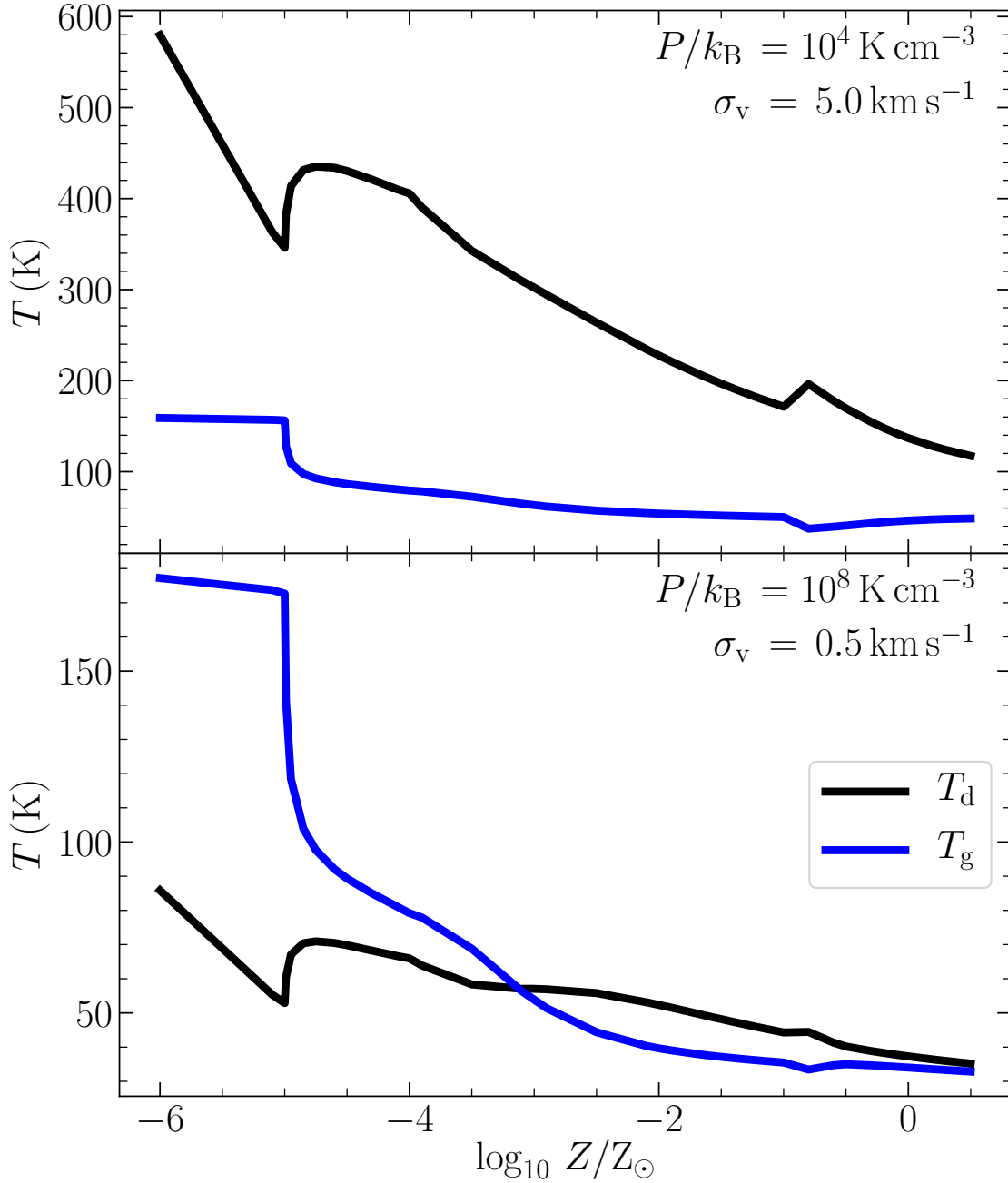
Figure 5.6: *Top panel:* Gas and dust temperatures ($T_{\rm g}$ and $T_{\rm d}$) at the location of the characteristic stellar mass $M_{\rm ch}$ as a function of metallicity Z for a Galactic-type environment with pressure $P/k_{\rm B} = 10^4\,{\rm K\,cm^{-3}}$ and velocity dispersion $\sigma_{\rm v} = 5\,{\rm km\,s^{-1}}$. *Bottom panel:* Same as the top panel but for a starburst environment with $P/k_{\rm B} = 10^8\,{\rm K\,cm^{-3}}$ and velocity dispersion $\sigma_{\rm v} = 0.5\,{\rm km\,s^{-1}}$.

and gas temperatures begin to diverge. For the latter case, we see a more non-linear behavior. Figure 5.6 shows that dust and gas temperatures are very well-coupled at high metallicities ($Z > 10^{-0.5}\,\mathrm{Z_\odot}$), but $T_\mathrm{g} < T_\mathrm{d}$ between $10^{-3.3} \leq Z/\mathrm{Z_\odot} \leq 10^{-0.5}$, implying that dust begins to act as a heating source for these metallicities. At $Z < 10^{-3.3}\,\mathrm{Z_\odot}$, dust begins to act as a cooling source for the gas. However the effects of dust cooling at such low metallicities are rather limited compared to metal and $\mathrm{H_2/HD}$ cooling, a topic we explore below in Section 5.3.3.

5.3.3   Gas thermal balance

We have already seen that, depending on the metallicity and environment, dust can be both a source of heating and of cooling, and the gas and dust temperatures can be closely locked or widely divergent. We now seek to place dust in the broader context of other heating and cooling mechanisms. To quantify the relative importance of all the various heating and cooling terms, we define

$$\mathcal{C}(\eta) = \frac{2\eta}{|\Gamma_\mathrm{c}| + |\Gamma_\mathrm{gd}| + |\Lambda_\mathrm{gd}| + |\Lambda_\mathrm{M}| + |\Lambda_{\mathrm{H_2}}| + |\Lambda_\mathrm{HD}|} \tag{5.31}$$

where $\mathcal{C}(\eta)$ represents the relative contribution of each term η that heats or cools the gas, evaluated at the location in the model cloud where $M_\mathrm{enc} = M_\mathrm{BE}$, i.e., at the point that determines how the gas fragments. Thus, for example, $\mathcal{C}(\mathrm{c})$ is the ratio of the compressive heating rate to the sum of the absolute values of all heating and cooling rates. By construction $-1 \leq \mathcal{C}(\eta) \leq 1$. Terms for which $\mathcal{C} < 0$ represent processes that cool the gas, and vice-versa; the sum of $\mathcal{C}(\eta)$ over all cooling terms is -1, and the sum over all heating terms is $+1$, giving $\mathcal{C}(\eta)$ an easy physical interpretation: it is the fraction of the total heating or cooling provided by some particular mechanism, such that mechanisms η for which $|\mathcal{C}(\eta)|$ is close to unity are dominant, while those for which is it close to zero do not play a significant role in gas thermodynamics. Note that, in computing $\mathcal{C}$, we group all cooling by metal line emission (i.e., via all lines of C I, C II, O I, and CO) into a single term Λ_M, and we separate the dust-gas energy exchange (Ψ_gd) into its corresponding heating (Γ_gd) and cooling (Λ_gd) parts; the latter is critical to ensuring that $\mathcal{C}$ properly captures situations such as the one we have already encountered in starburst conditions, where dust and gas are so tightly coupled that the gas temperature is set almost entirely by the balance between Γ_gd and Λ_gd, and other mechanisms are unimportant.

In Figure 5.7, we plot $\mathcal{C}(\eta)$ for all heating and cooling terms η as a function of metallicity at values of $P/k_\mathrm{B} = 10^4$ and $10^8\,\mathrm{K\,cm^{-3}}$, and $\sigma_\mathrm{v} = 0.5$ and $5\,\mathrm{km\,s^{-1}}$ – values that represent the outermost corners of our parameter space, though we
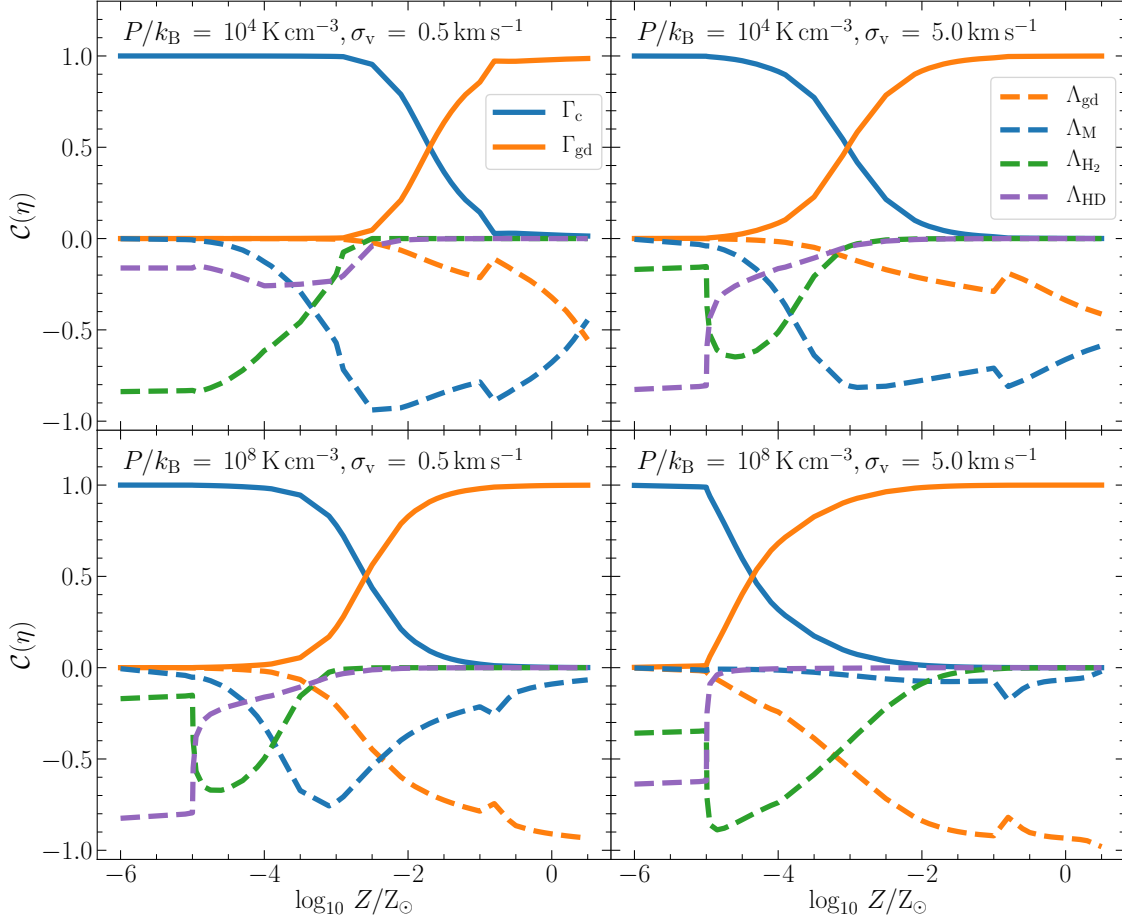
Figure 5.7: *Top panel:* Importance of different heating and cooling processes under thermal balance as a function of metallicity Z (normalised to Solar) for a given $P/k_{\rm B} = 10^4\,{\rm K\,cm^{-3}}$ and effective velocity dispersion $\sigma_{\rm v} = 0.5$ and $5\,{\rm km\,s^{-1}}$. $\mathcal{C}(\eta)$ is calculated for each term η as shown in the legend following equation 5.31. Solid curves show all the heating processes ($\Gamma_{\rm c}$ – adiabatic compression, $\Gamma_{\rm gd}$ – heating due to dust-gas coupling) that have $\mathcal{C}(\eta) > 0$ and dashed curves show all the cooling processes ($\Lambda_{\rm gd}$ – cooling due to dust-gas coupling, $\Lambda_{\rm M}$ – cooling due to metals, $\Lambda_{\rm H_2}$ – cooling due to H$_2$, $\Lambda_{\rm HD}$ – cooling due to HD) that have $\mathcal{C}(\eta) < 0$. The sum of the magnitudes of all heating and all cooling processes separately is unity. Values of $|\mathcal{C}(\eta)|$ close to unity indicate a dominant process, values close to zero indicate an unimportant process. *Bottom panel:* Same as the top panel but for $P/k_{\rm B} = 10^8\,{\rm K\,cm^{-3}}$.

remind the reader that the high P, high σ_v case is highly improbable. All these panels reveal a common trend: at very low metallicity, the most important heating process is adiabatic compression. The most important cooling processes are H_2 and (at the lowest densities) HD line emission; recall from Section 5.2.4 that the HD cooling rate we use is an upper limit. At Solar or higher metallicity, by contrast, heating is invariably dominated by dust, which provides a conduit to deposit energy from accretion into the thermal reservoir of the gas. Cooling is also dominated by dust when the density is high (i.e., at low σ_v or high P), with metal line cooling reaching a maximum ~ 50 per cent contribution at the lowest-density corner of our grid.

Thus far these findings confirm earlier results on the thermodynamics of present-day (modern) and primordial star formation. However, from Figure 5.7 we can also see evidence for a distinct, transitionary star formation regime at intermediate metallicity ($-3.5 \lesssim \log_{10} Z/Z_\odot \lesssim -1.5$), where cooling is dominated by metal line emission. The exact range in metallicity where this regime occurs is somewhat dependent on the physical conditions – it extends to higher metallicity at low pressure than at high pressure.

Nonetheless, the overall picture that emerges for gas thermal balance at the critical location that sets M_{ch} in the presence of protostellar feedback is that there are three regimes of star formation at all pressures: (1.) primordial-like at $Z \lesssim 10^{-4}\,Z_\odot$ where H_2 and/or HD cooling and adiabatic compression heating dominate, (2.) transitionary at $10^{-4} \lesssim Z/Z_\odot \lesssim 10^{-2}$ where metal cooling dominates and dust and compression heating are comparable, and (3.) modern day-like at $Z \gtrsim 10^{-2}\,Z_\odot$ where the gas temperature is mostly set by dust-gas coupling (with a contribution from metal line cooling in the lowest density regions), and the competition between dust cooling and heating. Since different heating and cooling mechanisms equilibrate at different gas temperatures, we expect the characteristic stellar mass to be different in the three different regimes we identify.

5.3.4 Characteristic stellar mass and the IMF

We now look at the resulting characteristic stellar mass, M_{ch}, as a function of Z in different star-forming environments. We estimate M_{ch} for each Z based on the procedure we outline in Section 5.2.5. As in the previous sections, we study the variations in M_{ch} as a function of Z at different P and σ_v.

Figure 5.8 shows M_{ch} as a function of Z for a range of P and σ_v values. We see that at all combinations of P and σ_v the characteristic stellar mass declines steadily from super-solar to sub-solar masses as the metallicity increases from near-zero to

$\approx 10^{-2}\,\mathrm{Z}_\odot$. Above this metallicity, the characteristic mass either flattens or rises slightly with Z, depending on the choice of P and σ_v. The absolute value of M_ch is also fairly sensitive to the choice of P and σ_v at low Z, but much less so at high Z. This is consistent with numerous simulations of Population III star formation that find a much broader mass spectrum than that in Population I star formation (Clark et al. 2011a; Susa et al. 2014; Chon et al. 2021). The exact location and depth of the inflection in M_ch at $10^{-2}\,\mathrm{Z}_\odot$ at low P that delineates the transition from the primordial to the modern regime depends on our assumed model for chemical composition as a function of Z (because CO provides more cooling than atomic lines at low temperature – Krumholz 2014a, figure 9), but the existence of this transition is independent of our chemical assumptions, as we show in Section 5.4.3. It is instead a result of the changeover from an H_2-dominated cooling regime to a metal line-dominated regime to a dust-dominated regime, which occurs regardless of the chemical state of C and O.

Another notable, though perhaps not surprising, result is that higher pressure environments favour lower mass stars. This implies that starburst environments at all Z should contain more low mass stars (consistent with earlier results of Chabrier et al. 2014 that did not include protostellar feedback), although the peak in very metal-poor environments ($Z \leq 10^{-4}\,\mathrm{Z}_\odot$) still remains top-heavy with $M_\mathrm{ch} \sim 15\,\mathrm{M}_\odot$. At solar metallicity the effects of pressure are much weaker, due to the dominance of dust in the thermodynamics, but we nonetheless find that starburst environments should typically have a slightly more bottom-heavy IMF than the average star-forming environment. We discuss this finding further in the context of massive elliptical galaxies in Section 5.5.1.

Thus, we can now answer the question: when does the IMF become bottom-heavy? We find that the transition from a top-heavy to a bottom-heavy IMF occurs between $10^{-4} \leq Z/\mathrm{Z}_\odot \leq 10^{-2}$ at low P (depending on the density), and around $Z \approx 10^{-4}\,\mathrm{Z}_\odot$ at high P irrespective of the density.

Figure 5.9 plots the characteristic mass as a function of the critical density, *i.e.*, density at the location where $M_\mathrm{enc} = M_\mathrm{BE}$ in the cloud, for three different metallicities. The apparent jitter in the curves arises from plotting all possible values of P and σ_v. We find that, at $Z = 10^{-6}\,\mathrm{Z}_\odot$, M_ch monotonically decreases as a function of n_crit, which can be best fit by a linear function with a slope ≈ -0.3. There is little evolution in the slope until the metallicity is high enough for dust to take control of gas thermodynamics, after which there is little variation in M_ch as a function of n_crit.
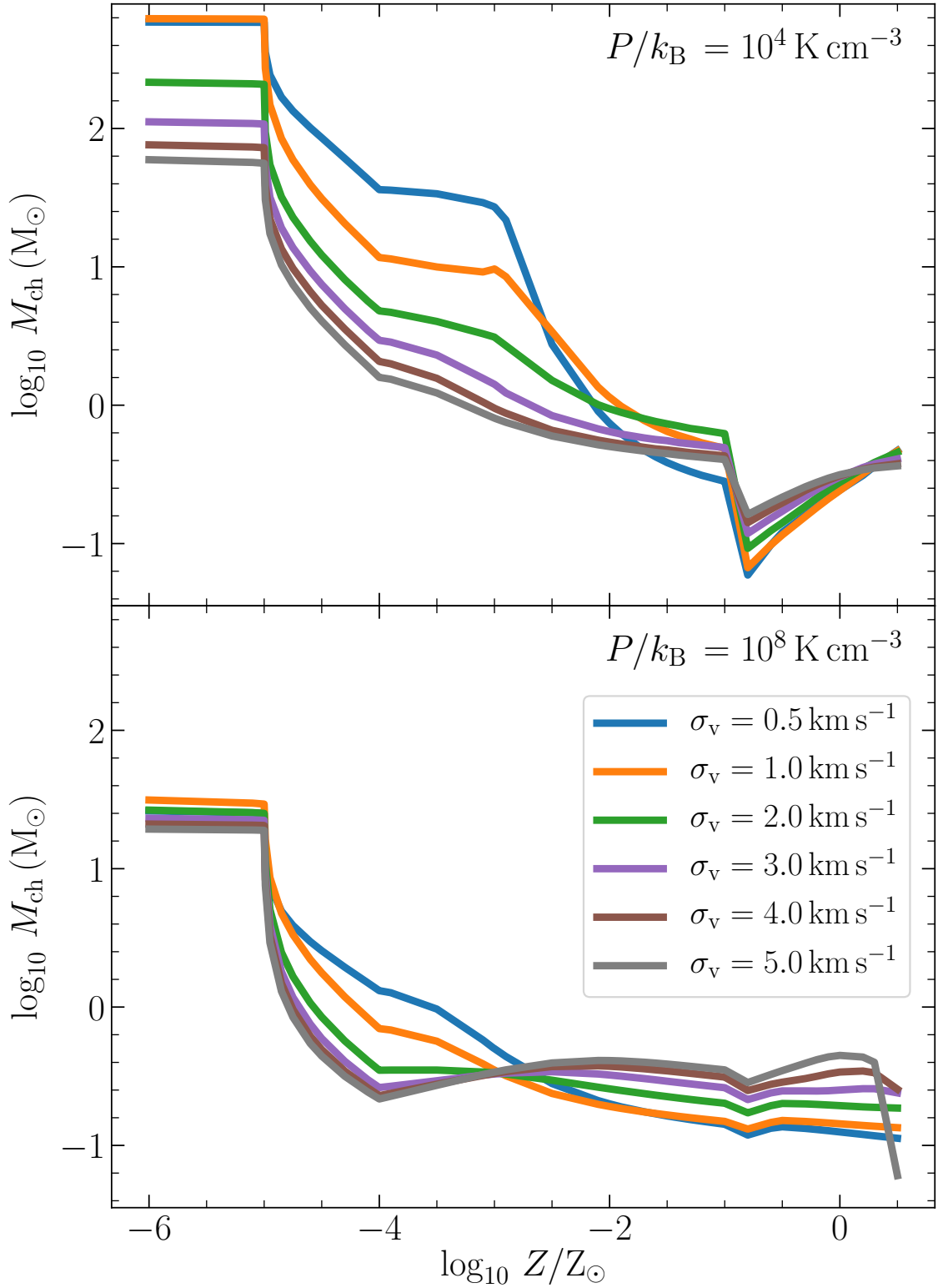
Figure 5.8: *Top panel:* Characteristic stellar mass, $M_{\rm ch}$, as a function of metallicity for a fixed cloud pressure $P/k_{\rm B} = 10^4\,{\rm K\,cm^{-3}}$ at different effective velocity dispersions $\sigma_{\rm v}$ as shown in the legend. *Bottom panel:* Same as the top panel but at a high pressure ($P/k_{\rm B} = 10^8\,{\rm K\,cm^{-3}}$), typical of starburst environments.
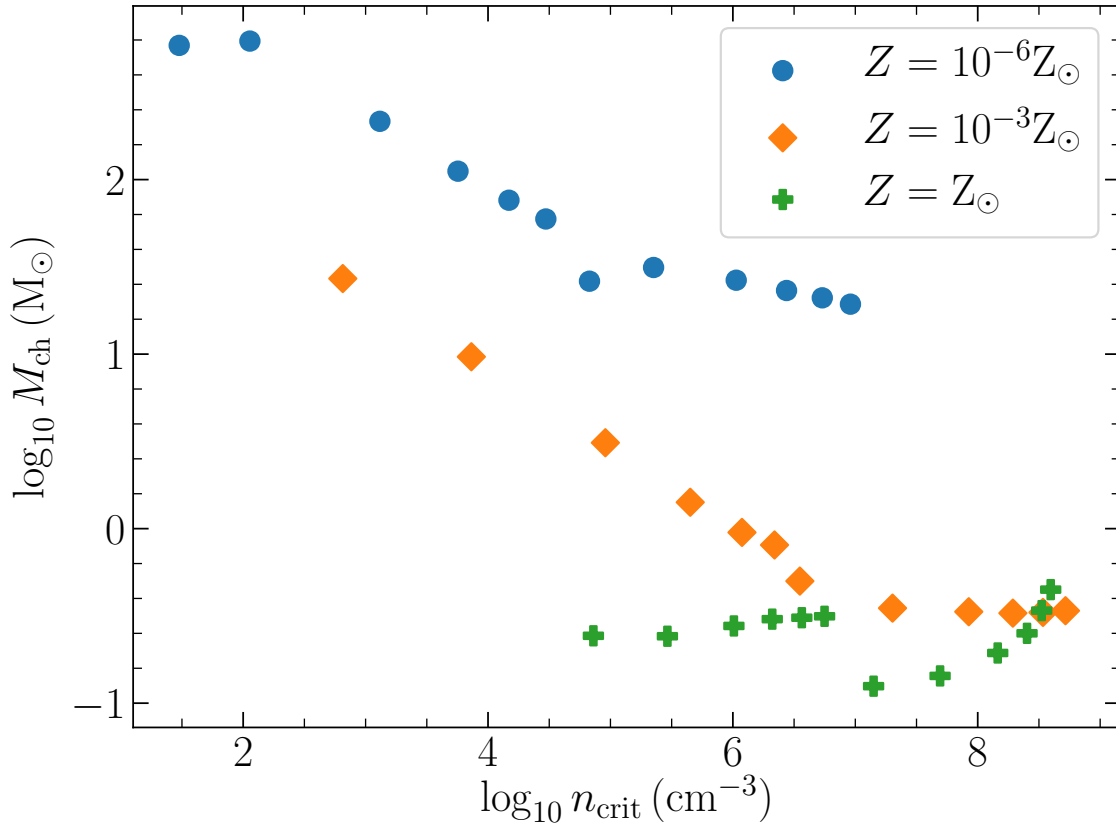
Figure 5.9: Characteristic stellar mass as a function of the critical density (where $M_{\mathrm{enc}} = M_{\mathrm{BE}}$) at three different metallicities.

5.4   Discussion

5.4.1   Effects of H$_2$ formation heating

In chemical equilibrium, H$_2$ formation or destruction cannot by itself be a source of heating or cooling, since the chemical energy liberated by formation is balanced by that lost to destruction; at best H$_2$ formation or destruction can act as a conduit by which other processes (e.g., cosmic rays or X-rays – Glassgold et al. 2012) can transfer energy to the gas. Thus, we need to only consider heating from H$_2$ formation when the formation process is non-equilibrium. For this case, we use equation 37 of Grassi et al. (2014) to write heating due to 3-body formation of H$_2$ as

$$\Gamma_{\mathrm{H_2,3b}} = E_{\mathrm{d}} f_{\mathrm{chem}} \frac{k_{\mathrm{H_2,3b}}}{\mu_{\mathrm{H}} m_{\mathrm{H}}} \left(x_{\mathrm{H\,I}} n_{\mathrm{H}} \right)^2 , \tag{5.32}$$

where $E_{\mathrm{d}} = 4.48\,\mathrm{eV}$ is the energy released due to formation of H$_2$, f_{chem} is the critical density factor that we obtain from equation 33 of Grassi et al. (2014), and $k_{\mathrm{H_2,3b}}$ is the rate coefficient for the reaction that we adopt from table C1 of Grassi et al.
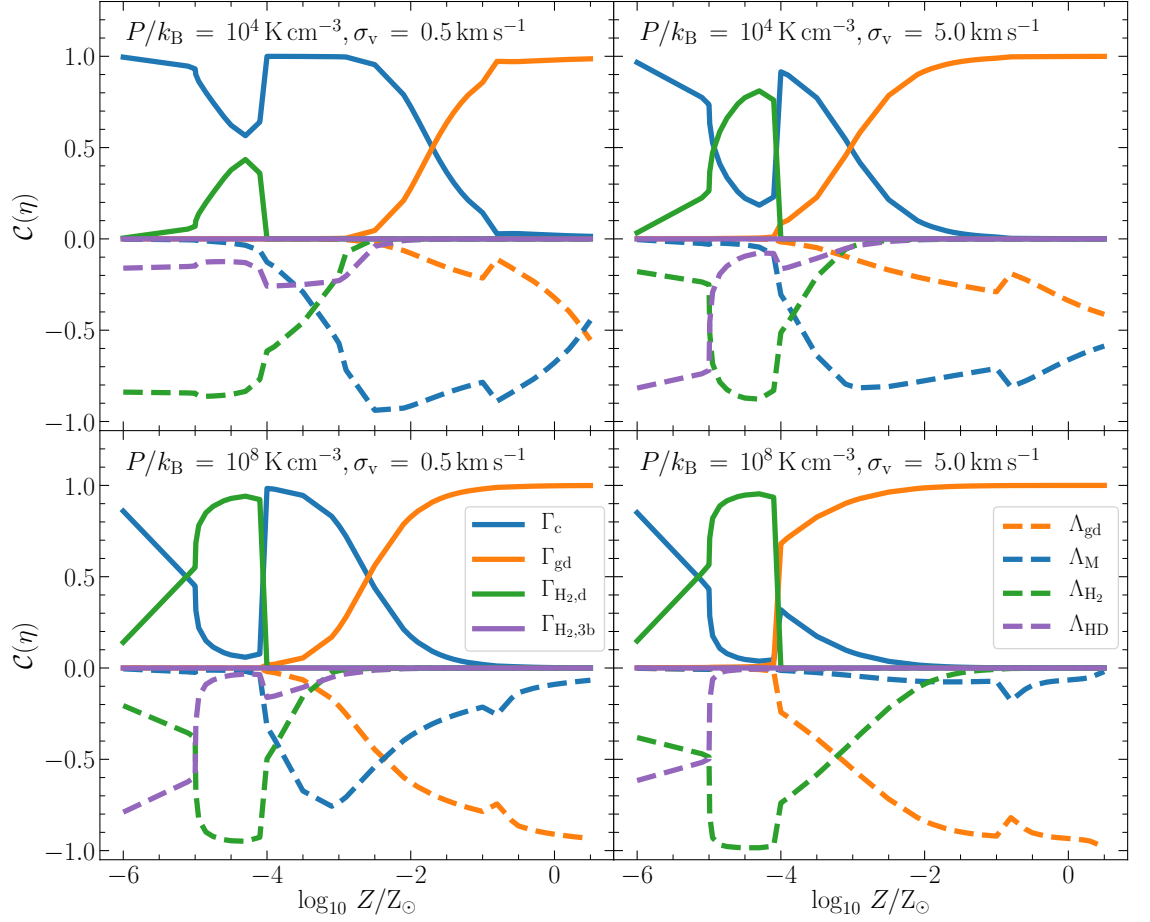
Figure 5.10: Same as Figure 5.7 but including H_2 formation heating due to dust (solid green) and 3-body reactions (solid purple).

(2014). Additionally, we follow Cazaux & Spaans (2009) to include heating due to H_2 formation on dust

$$\Gamma_{H_2,d} = R_{H_2,d} f_{H_2,d} E_d \frac{1}{\mu_H m_H n_H} \tag{5.33}$$

where $R_{H_2,d}$ is the formation coefficient (in $cm^{-3} s^{-1}$) that depends on the metallicity, sticking coefficient (following Hollenbach & McKee 1979), gas thermal velocity, and H_2 formation efficiency on different types of grains (Cazaux & Spaans 2009, equation 13). Here, we only work with C and Si grains. We adopt the formation efficiencies of these grains from Cazaux & Spaans (2009, equations 6 and 7). $f_{H_2,d} \approx 0.34$ denotes the fraction of energy released during H_2 formation on dust (E_d) that is available to heat the gas (Pantaleone et al. 2021).

Figure 5.10 shows the gas thermal balance at the critical location that sets M_{ch}, now in the presence of H_2 formation heating. We firstly see that heating due to 3-body H_2 formation is always negligible. On the other hand, heating due to H_2 formation on dust becomes important if the chemical composition is H I-dominated

(typically corresponding to low Z), and is zero otherwise. Cooling due to H_2 quickly compensates the additional heating provided by H_2 formation without a substantial change in the gas temperature since H_2 cooling is exponentially sensitive to the gas temperature (Galli & Palla 1998; Glover & Abel 2008). This yields minimal variation in the characteristic mass due to H_2 formation heating, as we illustrate in Figure 5.11.

We can understand the lack of importance of H_2 formation heating as follows. The characteristic timescale to convert a gas that is mostly $H\,\textsc{i}$ into one that is mostly H_2 is $t_{H_2} \sim 1/n_H R'_{H_2,d}$, where $R'_{H_2,d} = R_{H_2,d}/n_H^2$ is the rate coefficient in $\mathrm{cm}^3\,\mathrm{s}^{-1}$, and we have ignored heating due to 3-body H_2 formation. We can compare the timescale for H_2 formation to the timescale for collapse, which is $t_{\mathrm{ff}} \sim 1/\sqrt{Gn_H m_H}$, and to the corresponding rate of compressive heating, $\Gamma_c \sim k_B T_g \sqrt{Gn_H/m_H}$ (see equation 5.17). This ratio is $\Gamma_{H_2,d}/\Gamma_c \sim (E_d/k_B T_g) R'_{H_2,d} \sqrt{n_H/(Gm_H)}$, which is greater than unity, i.e., H_2 formation heating is significant compared to compressive heating, only if $n_H > (Gm_H/R'^2_{H_2,d})(k_B T_g/E_d)^2$, where we have omitted factors of order unity for simplicity. On the other hand, in order to be out of equilibrium we require $t_{H_2}/t_{\mathrm{ff}} > 1$, which is satisfied only if $n_H < Gm_H/R'^2_{H_2,d}$. Adopting the rough scaling $R'_{H_2,d} \approx 7 \times 10^{-15} Z/Z_\odot$ (Cazaux & Spaans 2009), and for $T_g \approx 100\,\mathrm{K}$ (expected if H_2 is important), this numerically evaluates to $4 \times 10^{-6}/(Z/Z_\odot)^2 < n_H/\mathrm{cm}^3 < 2 \times 10^{-3}/(Z/Z_\odot)^2$. We can immediately see that this condition is only satisfied at very low Z for typical values of $n = n_{\mathrm{crit}}$ we obtain, which is why H_2 formation heating does not play a significant role elsewhere.

5.4.2   Effects of cosmic rays

So far, we have ignored the effects of cosmic rays. While it is not yet known if cosmic rays threaded primordial/metal-poor star-forming clouds, we can use our models to study if they could have any any effects on the characteristic stellar mass or the IMF (e.g., Fontanot et al. 2018). Cosmic rays can impact our analysis in two major ways: by providing excess heating to the gas, and by providing free hydrogen atoms needed to form H_2.

Heating due to cosmic rays at different densities, pressures and metallicities is highly uncertain, so we adopt an empirical approach where we express cosmic ray heating normalized to that observed in the Milky Way

$$\Gamma_{\mathrm{CR}} = \frac{q_{\mathrm{CR}}}{\mu_H m_H}\zeta\,, \tag{5.34}$$
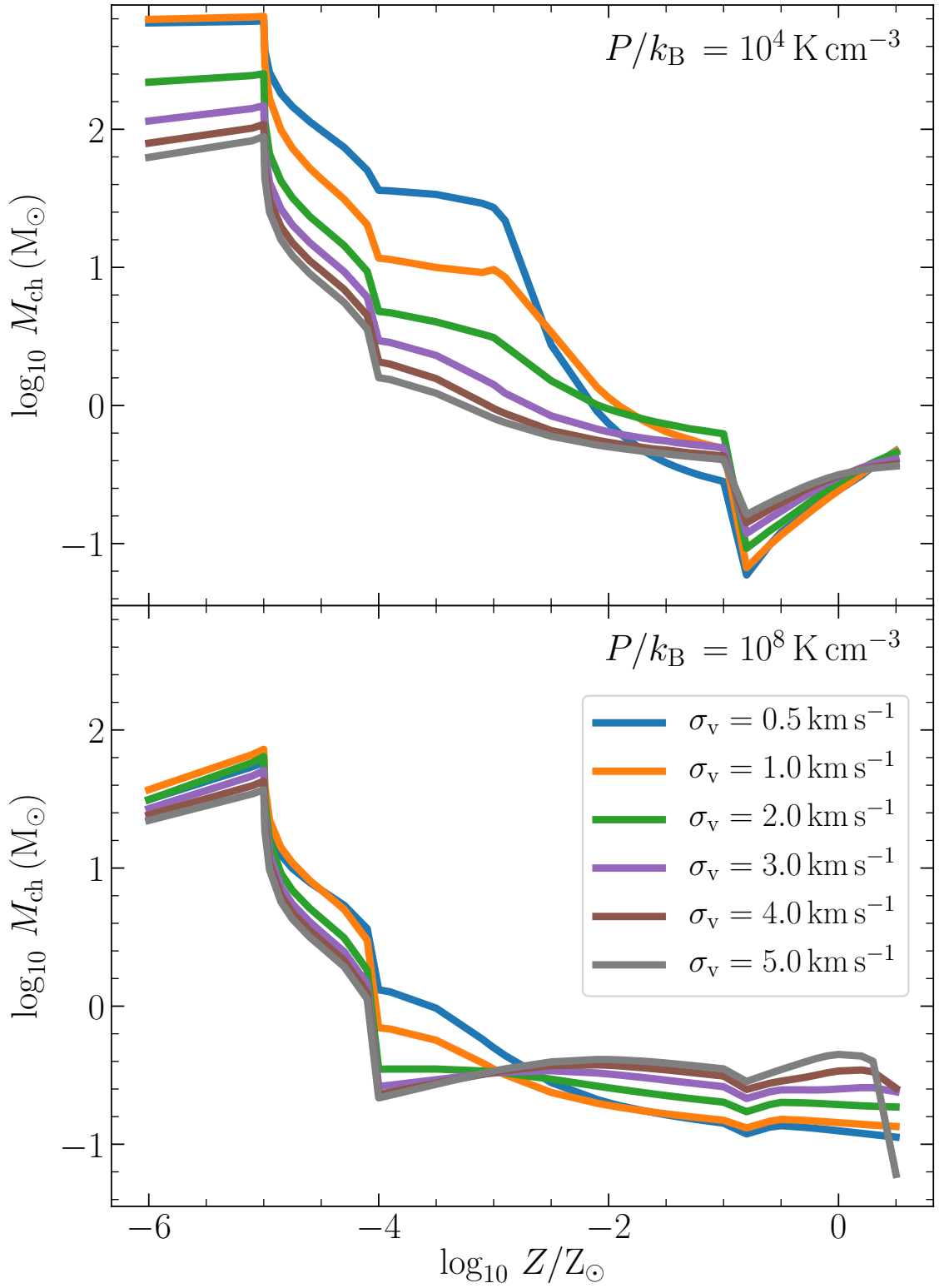
Figure 5.11: Same as Figure 5.8 but including H_2 formation heating as shown in Figure 5.10. Despite being a dominant heating process at very low metallicity, H_2 formation heating has no appreciable effect on the characteristic stellar mass.

where

$$\zeta = \zeta_{\mathrm{MW,CR}} \frac{f_{\mathrm{CR}} P}{P_{\mathrm{MW,CR}}} . \tag{5.35}$$

Here, $q_{\mathrm{CR}} = 6.5\,\mathrm{eV}$, $\zeta_{\mathrm{MW,CR}} = 3 \times 10^{-16}\,\mathrm{s}^{-1}$ is the cosmic ray primary ionisation rate per H nucleus in the Milky Way (e.g., Indriolo & McCall 2012), and the product of the two divided by μm_{H} is the cosmic ray heating rate in the Milky Way assuming that each primary ionisation yields 6.5 eV of heating. The remaining factor in equation 5.35, $f_{\mathrm{CR}} P / P_{\mathrm{MW,CR}}$, represents our assumed scaling of the cosmic ray heating rate with pressure: $P_{\mathrm{MW,CR}}/k_{\mathrm{B}} \approx 3500\,\mathrm{K\,cm}^{-3}$ is the typical cosmic ray pressure in Milky Way star-forming molecular clouds (e.g., Yusef-Zadeh et al. 2002, 2007), while f_{CR} is the ratio of cosmic ray to gas pressure in a given ISM. We compute f_{CR} from the semi-analytic models of Crocker et al. (2021, Figure 8), who express it as a function of the gas surface density Σ, which we can express in terms of the gas pressure; similar calculations are also available in Padovani et al. (2018).

We also revise our estimate of $x_{\mathrm{H\,I}}$ in the presence of cosmic rays by solving self-consistently for its equilibrium value in the H_2-dominated regime. We do so by equating the rate at which free hydrogen atoms are provided by cosmic ray ionization, $x_{\mathrm{H\,I,CR}}$, with the rate of H_2 formation on dust, $R_{\mathrm{H_2,d}}$, that we introduced in Section 5.4.1:

$$R_{\mathrm{H_2,d}} = \zeta n_{\mathrm{H}} \left(\frac{1 - x_{\mathrm{H\,I,CR}}}{2} \right) . \tag{5.36}$$

Then, we simply take $x_{\mathrm{H\,I}}$ to be the maximum of $x_{\mathrm{H\,I,CR}}$ and our fiducial estimate from equation 5.8. We adjust $x_{\mathrm{H_2}}$ consistently (equation 5.8). In practice, since $x_{\mathrm{H\,I,CR}}$ is always close to zero, our procedure amounts to changing the minimum H I fraction that prevails at high metallicity from zero to a value slightly above zero.

We show the effects of cosmic ray heating in Figure 5.12 and Figure 5.13 at the corner points of our grid; results elsewhere in the grid are qualitatively identical. We observe that heating due to cosmic rays now becomes prominent at low Z, leading to changes in the characteristic stellar mass at low Z while maintaining the qualitative trend in M_{ch} as a function of Z we know from previous sections. This is because at low Z where cosmic ray heating becomes significant, the gas temperature rises by a factor of a few, which in turn increases the mass needed to collapse (M_{BE}). The rise in the gas temperature at low P and low Z results in a jump in M_{ch} by a factor of $2 - 3$, yielding $M_{\mathrm{ch}} > 1000\,\mathrm{M_\odot}$ at $Z = 10^{-6}\,\mathrm{Z_\odot}$.

However, the above result from the model should be treated with caution. This is because we have not adjusted for the increased amount of H_2 that would form due to the increased availability of free hydrogen atoms because of cosmic ray ionization.
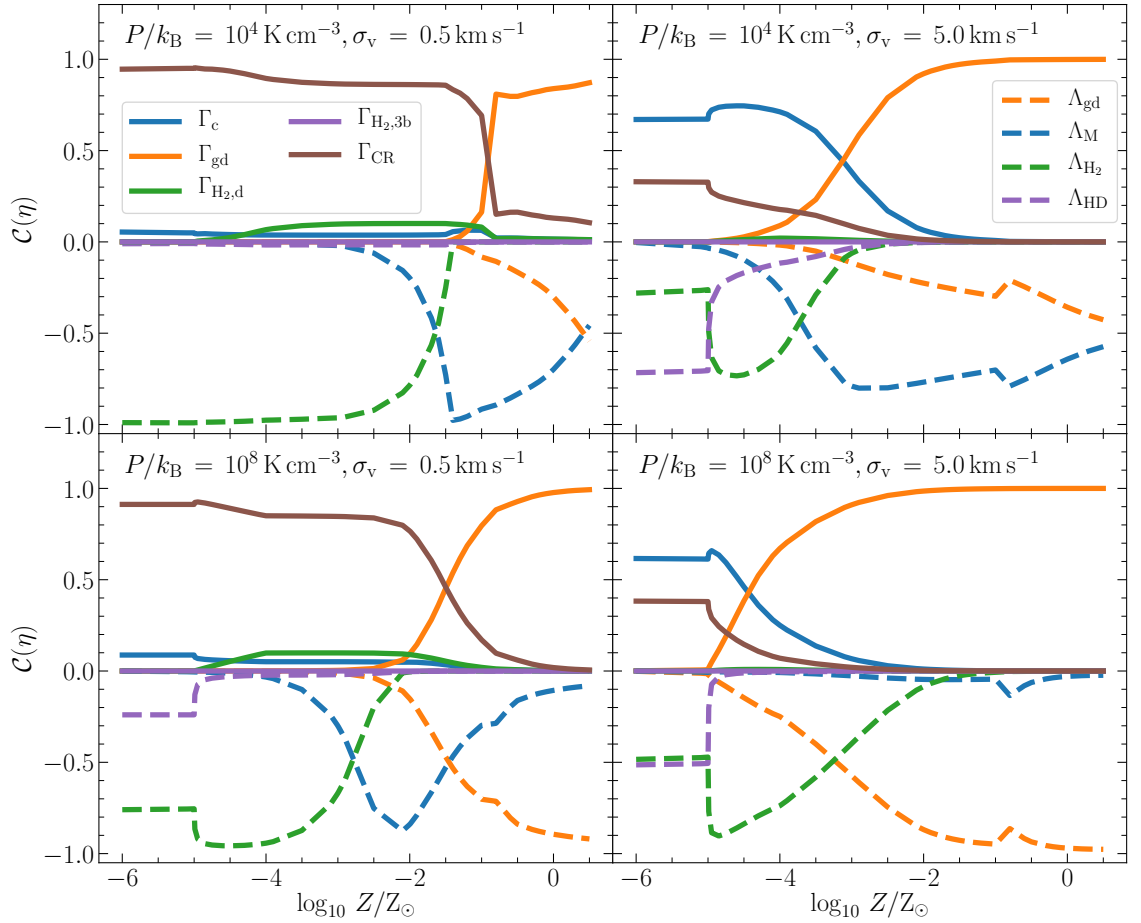
Figure 5.12: Same as Figure 5.10 but including cosmic ray heating (solid brown).

In fact, detailed modeling with time-dependent chemistry from Stacy & Bromm (2007) and Hummel et al. (2016) show that the dominant effect of cosmic rays at such low metallicities is that they indirectly provide much more gas cooling due to increased H_2 fraction, thus resulting in $10 \lesssim M_{ch}/M_\odot \ll 1000$ even when the cosmic ray strength is changed by five orders of magnitude. So, in reality, we expect cosmic ray *heating* to not play a significant role in setting the characteristic mass at very low metallicities.

While cosmic rays are of limited significance for our results at high Z, we have not accounted for the possibility that cosmic ray pressure in star-forming regions of metal-rich molecular clouds could be substantially higher than the mean pressure across the cloud due to local acceleration of cosmic rays by protostellar outflows (Padovani et al. 2016, 2020; Favre et al. 2018). Such an enhancement in cosmic ray pressure can lead to some destruction of CO molecules at high Z (Bisbas et al. 2015, 2017), at the same time leading to $T_g \gg T_d$ and hence a higher characteristic mass (because gas closer to the protostar will be hotter and thus unable to collapse; see –
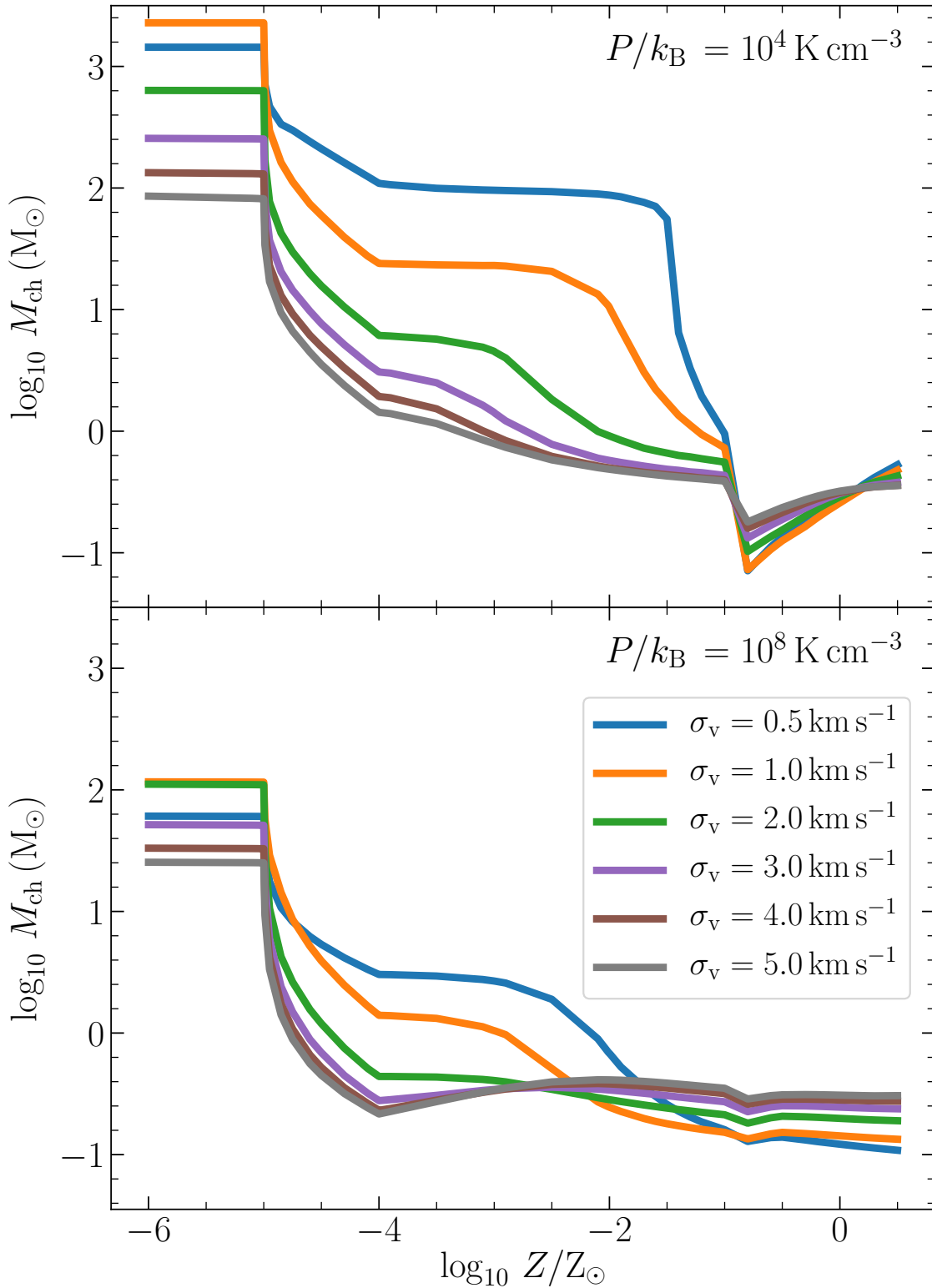
Figure 5.13: Same as Figure 5.11 but including cosmic ray heating. Cosmic rays become the dominant heating process at very low metallicity, resulting in a characteristic mass that is a factor of $2 - 3$ larger than that in the fiducial model (see, however, Section 5.4.2 where we discuss why is this not realistic).

Papadopoulos 2010; Papadopoulos et al. 2011). This effect is likely not relevant for the moment we are considering, when a protostellar core has first formed, since at this point an outflow will just have been launched, and will not yet have had time to accelerate any significant number of cosmic rays. In a clustered environment where many stars form together over time, it is possible that there could be an enhancement in cosmic rays due to acceleration by neighbouring protostars that formed earlier (e.g., Gaches & Offner 2018; Gaches et al. 2019). This will depend on the degree of clustering and the details of cosmic ray transport, and is beyond the scope of this work. Nevertheless, including cosmic rays does not change the transition metallicity at which we expect the IMF to become bottom-heavy.

5.4.3 Effects of different chemical compositions

In our fiducial model presented in Section 5.3, we adopt a plausible expression for variation of the chemical composition as a function of Z. However, the exact chemical makeup of star-forming clouds, particularly at low metallicities, is poorly known. CO has been detected from galaxies at metallicities down to ≈ 10 per cent of Solar but not lower (Rubio et al. 2015; Shi et al. 2016), so a transition from the majority of the carbon in star-forming regions being in the form of CO to C I or C II likely occurs at around this metallicity, but the lack of a reliable method of detecting "CO-dark" H_2 means that it is unclear at what metallicity a similar H I to H_2 transition occurs (e.g., Bolatto et al. 2011; Balashev et al. 2017; Jameson et al. 2018; Chevance et al. 2020).

Theoretical models predict a transition from H_2 to H I-dominated star formation at $Z \lesssim 10^{-2} Z_\odot$ (Krumholz 2012; Sternberg et al. 2021), and simulations of star formation at very low metallicities ($Z \sim 10^{-4}\,Z_\odot$) find that O I is the dominant species among all O-bearing species that make up the chemical composition at $n < 10^8\,\mathrm{cm}^{-3}$ (Chiaki et al. 2016, Figure 4). Similarly, we see from Chiaki & Yoshida (2020, Figure 8) that C I is the dominant C-bearing species at low metallicities for $n \lesssim 10^{5.5}\,\mathrm{cm}^{-3}$, and CO at high metallicities and densities. Thus, while the general results of these studies motivate the varying chemical composition we adopt for our fiducial models, they are hints only. Moreover, it is likely that, as one proceeds to lower metallicities and equilibration times become longer compared to dynamical ones, chemistry becomes increasingly non-equilibrium, such that a wide range of chemical compositions may coexist in star-forming regions of the same metallicity (Krumholz & Gnedin 2011; Krumholz 2012; Glover & Clark 2012a).

For this reason, it is important to check to what extent the major qualitative results we have obtained using our fiducial model depend on our uncertain assumptions

about chemical composition. To do so, we now fix the chemistry to one of the four main compositions we list in Section 5.2.2 for all Z, and repeat all our model calculations. We emphasise that many of these cases are not realistic – we observe that star-forming clouds are dominated by H_2 and not HI at $Z = Z_\odot$, and a CO-dominated composition at $Z \ll 10^{-2} Z_\odot$ is ruled out by observations of local metal-poor dwarf galaxies. We are intentionally exploring a range of variation much wider than plausibly exists in nature.

Figure 5.14 shows the contribution of different processes to gas thermal balance for the four different chemical compositions at fixed $P/k_B = 10^4 \, \mathrm{K\, cm^{-3}}$ and $\sigma_v = 5 \, \mathrm{km\, s^{-1}}$. We find that the qualitative behavior of the different heating and cooling processes does not vary within the chemical compositions that use atomic metal line cooling, and is similar to that of the fiducial model we use. However, using a fixed chemical composition consisting of H_2 and CO at all Z gives very different results; cooling due to CO becomes dominant at $Z < 0.1 \, Z_\odot$, and heating due to dust-gas coupling becomes dominant at all Z, driven by the much cooler gas temperature, and thus much greater dust-gas temperature difference, when CO exists at low Z. However, as noted above, a CO-dominated composition is not plausible at low metallicities.

Figure 5.15 extends this conclusion to M_{ch}; this figure is identical to the top panel of Figure 5.8, but considers fixed chemical composition. Except for the unrealistic case of CO-dominated composition at all Z, in all other cases we find the same sharp transition in M_{ch} as in our fiducial model. Thus, our results are not sensitive to the choice of the chemical composition we use.

We can understand the apparent lack of sensitivity of M_{ch} to the chemical composition as follows. At very low metallicities (primordial star formation), molecular H_2 is the dominant coolant, and the metallic composition of the gas (or dust) does not matter, thus yielding M_{ch} that is fairly constant across all the four compositions. Similarly, at very high metallicities (modern day star formation), dust takes control of the gas thermodynamics, leaving little room for metals in the gas phase to significantly impact M_{ch}. Finally, the trends in M_{ch} at intermediate metallicities $(10^{-3.5} \leq Z/Z_\odot \leq 10^{-1.5})$ for different chemical compositions are similar to that we find in the fiducial model because metal cooling dominates in both the cases.

5.4.4   Effects of a varying dust-to-metal ratio

The evolution of the dust to gas ratio δ with metallicity is observed to be linear at $Z \gtrsim 0.01 \, Z_\odot$ (Rémy-Ruyer et al. 2014; Li et al. 2019), but it is largely unknown at $Z < 0.01 \, Z_\odot$ (Galliano et al. 2018) and can even vary within the same cloud for
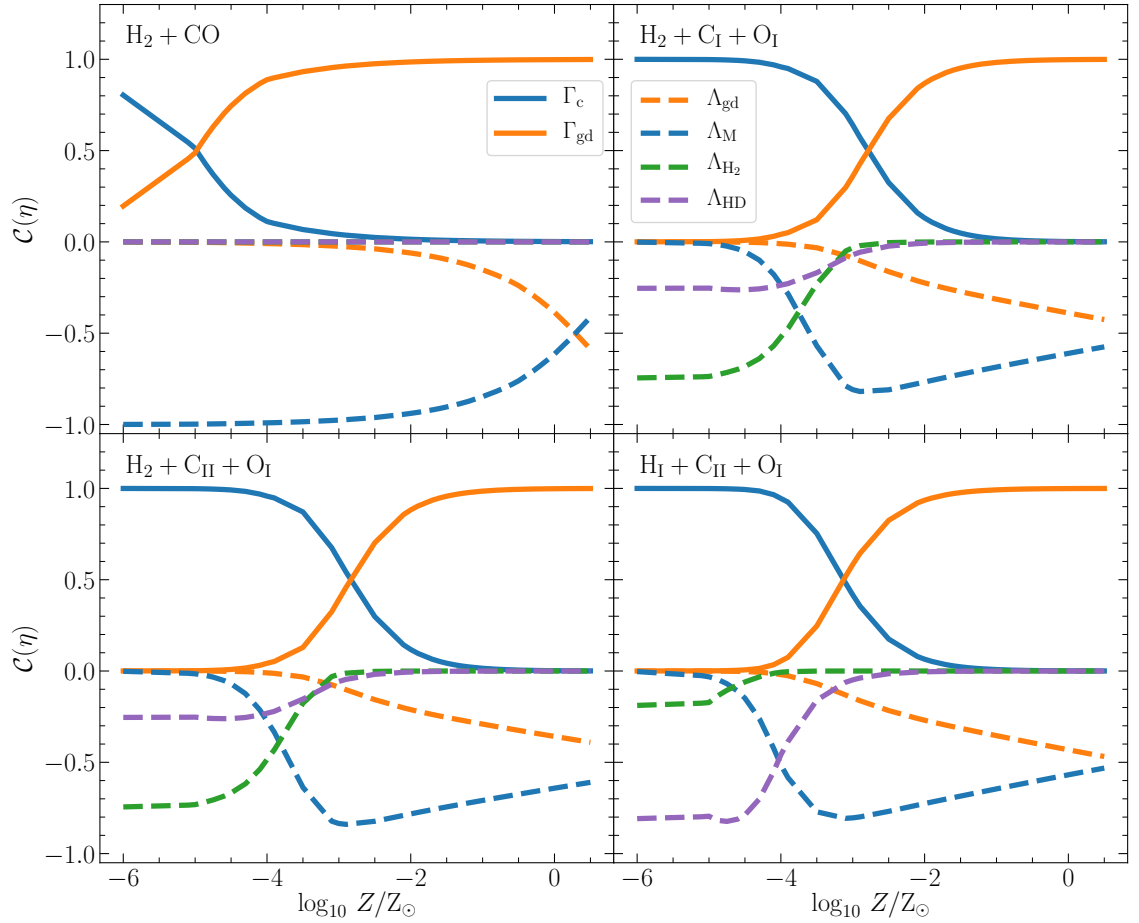
Figure 5.14: Same as Figure 5.7 but for the four different chemical compositions as noted in the panels, for a fixed $P/k_B = 10^4\,\mathrm{K\,cm^{-3}}$ and effective velocity dispersion $\sigma_v = 5\,\mathrm{km\,s^{-1}}$.

different grain sizes (Tricco et al. 2017; Bate & Lorén-Aguilar 2017). So far, we have assumed a simple linear scaling of δ with Z (see Section 5.2.2). Now, we try another scaling where we extrapolate the results of Rémy-Ruyer et al. (2014) for the variation of δ with Z down to $10^{-6}\,\mathrm{Z_\odot}$. Specifically, we set $\delta \propto Z$ for $Z \gtrsim 0.2\,\mathrm{Z_\odot}$, and $\delta \propto Z^{3.1}$ for $Z \lesssim 0.2\,\mathrm{Z_\odot}$ (Rémy-Ruyer et al. 2014, table 1), implying that δ decreases much more steeply with decreasing Z than for our fiducial scaling.

Figure 5.16 plots the gas thermal balance at the critical location that sets M_{ch} with the alternate $\delta - Z$ scaling. At low P, a comparison of Figure 5.16 with Figure 5.7 reveals that the dominance of dust and the onset of modern star formation in the case of the alternate $\delta - Z$ scaling is delayed by 0.5 dex as a function of metallicity. The effect is more dramatic at high P, and a steeper than linear decline of δ with Z causes the onset of dust-dominated modern star formation to be delayed by more than 1 dex. Nonetheless, we find from Figure 5.17 that the effects of a delay in the onset of modern star formation has no impact on the characteristic mass or
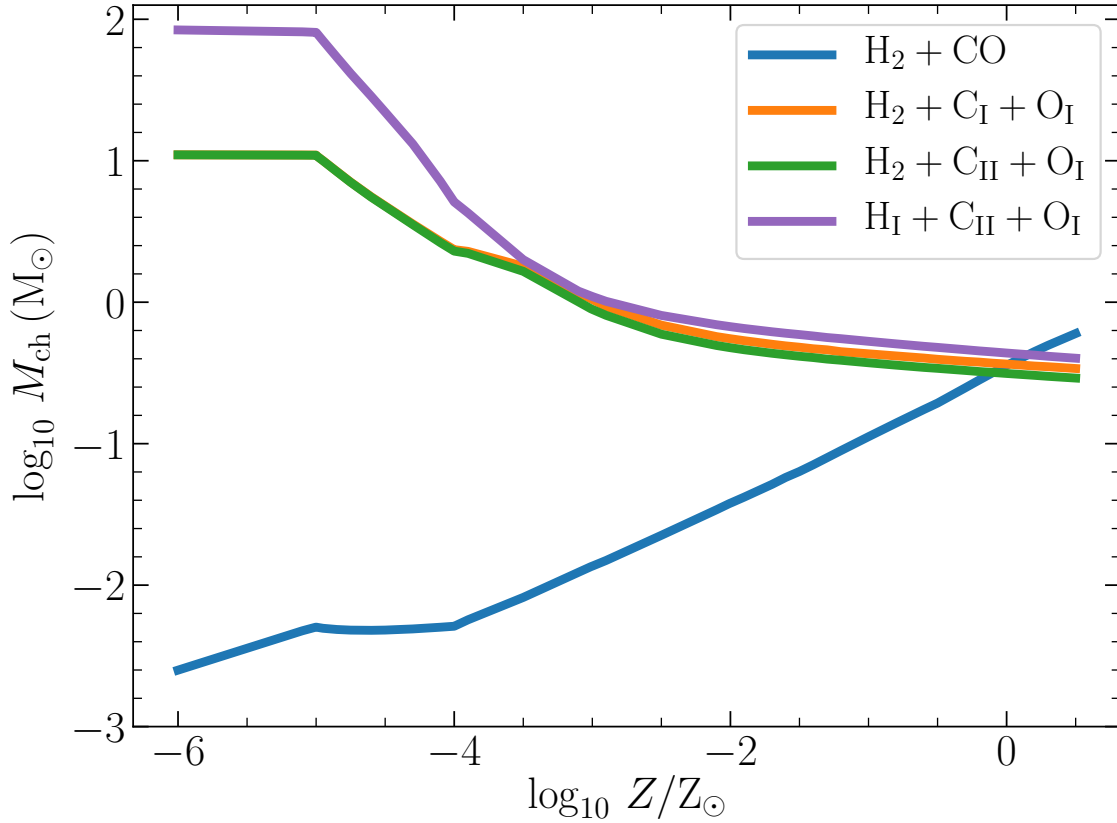
Figure 5.15: Same as the top panel of Figure 5.8 but for different chemical compositions for a fixed $P/k_B = 10^4 \, \mathrm{K\,cm^{-3}}$ and $\sigma_v = 5 \, \mathrm{km\,s^{-1}}$.

the transition from top- to bottom-heavy IMF as a function of metallicity. Given the current state of our knowledge of dust-to-metal ratio, we thus do not expect its variations to significantly impact the trends we observe in M_{ch} as a function of Z.

5.4.5   Effects of varying model parameters related to dust

Since a key driver of our work is studying the role of dust in setting M_{ch}, we now discuss how uncertainties in various model parameters related to dust can affect our results. We briefly discuss the effects of five such parameters that carry the most uncertainty – three that characterize the accretion luminosity and by extension, the underlying Chakrabarti & McKee (2005) model, and two that characterize the dust-gas energy coupling term, Ψ_{gd}. We limit this discussion to the three categories of star-forming regions we identified in Section 5.3.1 – primordial, Galactic and starburst, respectively.

1. ϵ_L – This parameter is defined in equation 5.11. If we increase its value from
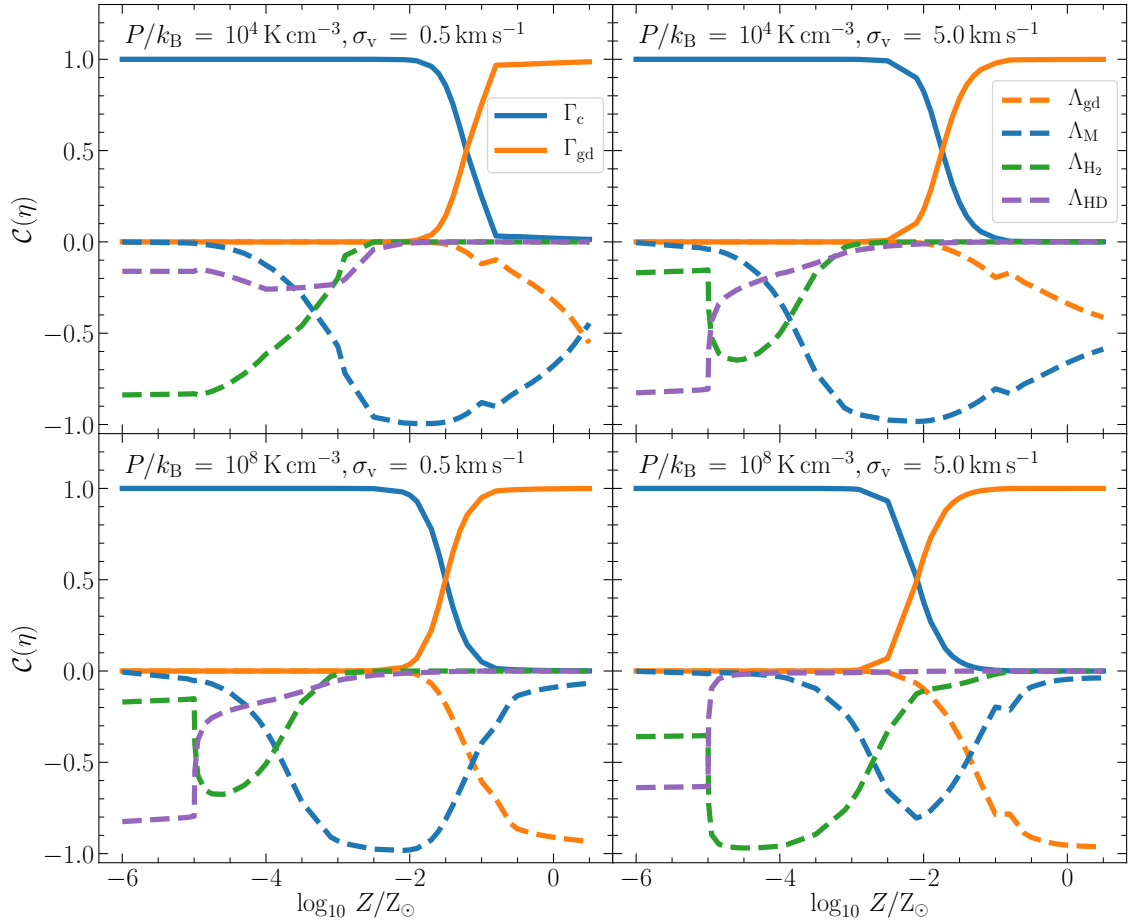
Figure 5.16: Same as Figure 5.7 but following the dust to gas ratio scaling of metallicity from Rémy-Ruyer et al. (2014). Dust dominates over a narrower range in metallicity at high P in this case as compared to the fiducial model.

0.75 to 1 (implying that accretion power does not drive any winds or outflows), we find no appreciable impact on M_{ch} in any environment. On the other hand, if we decrease it to 0.1 (implying most of the accretion power goes into winds), M_{ch} decreases by 20 and 40 per cent for the Galactic and the starburst environments, respectively, while leaving the overall trend of M_{ch} as a function of metallicity the same. The underlying physical reason that the dependence on ϵ_L is weak is that the gas temperature is relatively insensitive to the luminosity, varying between $T_d \propto L^{1/4}$ (for the limit of a completely opaque, optically thick dust atmosphere) to $T_d \propto L^{1/6}$ (for optically thin dust with Planck mean opacity that scales as $\kappa \propto T_d^2$).

2. ϵ_M – So far, we have assumed that approximately half of material infalling onto the protostar is ejected through winds. Not surprisingly, the primary effect of changing this fraction is to produce an almost proportional shift in M_{ch}, while leaving the underlying pattern of how M_{ch} varies with metallicity or and
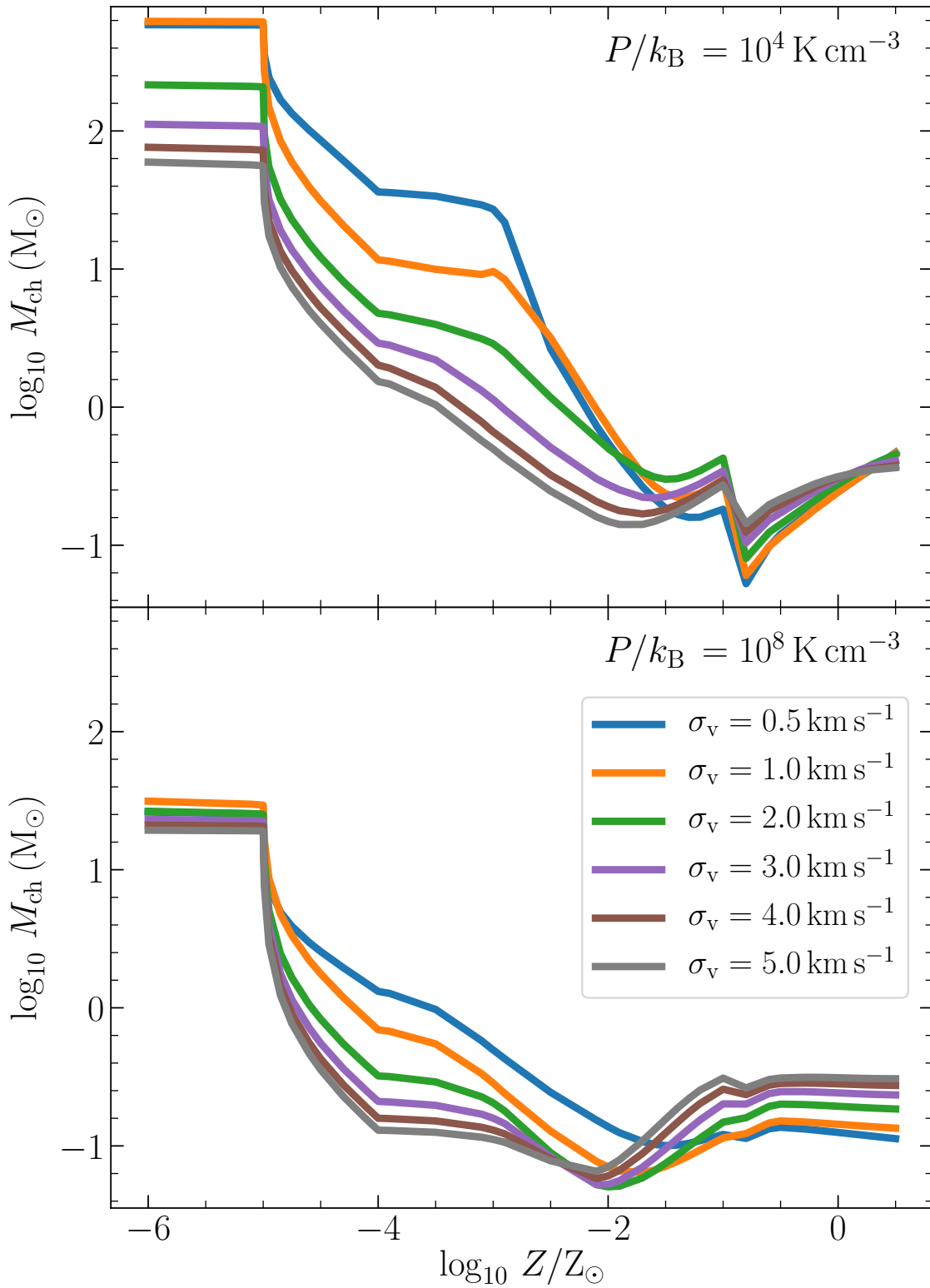
Figure 5.17: Same as Figure 5.8 but with the dust to gas ratio scaling with metallicity from Rémy-Ruyer et al. (2014). A different scaling only qualitatively impacts the characteristic stellar mass in a starburst environment.

all other parameters nearly unchanged. We note that values of ϵ_{M} outside the range $\approx 1/4 - 3/4$ are, at least in the Milky Way, ruled out by theory (Matzner & McKee 2000) and observations (Alves et al. 2007; Enoch et al. 2008), so the maximum shift in M_{ch} we expect is at the tens of percent level.

3. $\mathcal{A}$ – As we noted in Section 5.2.3, the energy yield per unit mass due to accretion is fairly constant for a wide range of protostellar masses (Krumholz 2011b). We find that variations of an order of magnitude in $\mathcal{A}$ only produce at most a 60 per cent change in M_{ch} in dust-dominated environments. Thus, we verify that uncertainties in $\mathcal{A}$ do not significantly alter our results on the evolution of M_{ch} as a function of metallicity.

4. α_{gd} – The dust-gas energy coupling goes to zero if dust-gas collisions are completely elastic such that dust does not transfer any energy to the gas during collisions. The biggest impact of completely inelastic (implying $\alpha_{\mathrm{gd}} = 1$) dust-gas collisions is in the Galactic case, where M_{ch} increases by 32 per cent. Similarly, if the collisions are nearly mostly elastic ($\alpha_{\mathrm{gd}} = 0.1$), M_{ch} decreases by 50 per cent in the Galactic case. Thus, uncertainties in α_{gd} do not significantly change our results. However, the inelasticity of the collisions is not a free parameter as it also depends on the grain size and composition (Watson & Salpeter 1972; Burke & Hollenbach 1983; D'Hendecourt et al. 1985), exploring which is beyond the scope of this work.

5. $\mathcal{S}_{\mathrm{gd}}$ – As we noted in Section 5.2.3, we have no constraints on the dust cross section per unit dust mass at low metallicities. However, this is not a problem since varying $\mathcal{S}_{\mathrm{gd}}$ by an order of magnitude only significantly impacts M_{ch} in the Galactic case, and has no significant impact at low metallicities due to the diminishing role of dust with decreasing metallicity for the assumed scalings of δ with metallicity.

5.5   Evolution of the IMF with metallicity

We next seek to put our findings here in the context of other work on the IMF as a function of metallicity, starting with observations (Section 5.5.1), then considering prior analytic work (Section 5.5.2), and finally discussing earlier simulations (Section 5.5.3). We caution that a comprehensive review of the (vast) literature on IMF variations is beyond the scope of this paper, and we refer readers to the large number of reviews that have appeared in the past decade (Bastian et al. 2010; Kroupa et al. 2013; Krumholz 2014b; Offner et al. 2014; Hopkins 2018; Lee et al. 2020). Our focus here will be specifically on variations with metallicity, and to a lesser extent,

pressure.

5.5.1   Observational evidence

Variations of the IMF have long been suspected (Kroupa 2002). Here we discuss several classes of stellar systems where previous authors have claimed IMF variation, at least potentially due to metallicity effects.

Metal-poor Milky Way stars

Based on analysis of metal-poor stars in the Milky Way halo, Suda et al. (2011, 2013) favour an IMF that transitions to bottom-heavy around [Fe/H] ~ -2 based on the abundance of carbon in carbon enhanced metal-poor stars (CEMP, Beers & Christlieb 2005); this is consistent with our finding that the era of modern day star formation begins around $Z \approx 10^{-2} \, Z_\odot$. These authors also propose an initially top-heavy Galactic IMF with a peak around $10 - 12 \, M_\odot$. Similar arguments have been made by Komiya et al. (2007) who find that the IMF of CEMP stars ([Fe/H] $\lesssim -2.5$ in their case) can be well represented by a characteristic mass $\approx 6 - 10 \, M_\odot$. Factors such as binary star formation and population synthesis also fall short at explaining the observed binary fraction of CEMP stars, requiring other phenomena such as variations in the IMF be considered (Izzard et al. 2009; Lee et al. 2014). Consistent with this analysis, and with the predictions of our model, Mattsson (2010) show that the presence of an evolving IMF that was initially top-heavy also provides good fits to the observed C/O versus O/H trends in the Galaxy (Fabbian et al. 2009).

Observations of metal-poor stars in the Milky Way also reveal an absence of carbon-normal (or CEMP-no) stars below [Fe/H] < -4 where the slope of the metallicity distribution function significantly changes (Youakim et al. 2020; Yong et al. 2021a, with the exception of the Caffau et al. 2011 star), indicating the absence of low mass stars below this metallicity that would otherwise have lived for a Hubble time (see also, Tumlinson 2006). This finding is also consistent with our finding that the transition to a bottom-heavy IMF does not occur at metallicities below $Z \approx 10^{-4} \, Z_\odot$ anywhere within the parameter space of our model. The presence of more bottom-heavy IMFs at higher metallicities that would result from a lower $M_{\rm ch}$ at high Z is also independently confirmed by observations of Wolf Rayet stars in the local Universe (Liang et al. 2021). However, we do caution that, while our models are consistent with the available evidence, the data thus far are very limited. More-over, we have predicted only the characteristic mass, not its spread. For example, simulations of both primordial (e.g., Clark et al. 2011c; Greif et al. 2011b; Sharda et al. 2020b) and modern (e.g., Bate et al. 2002; Thies et al. 2010, 2015) star for-

mation show that disc fragmentation can produce a sub-dominant population of stars with mass considerably smaller than the characteristic mass; as the example of Caffau et al. (2011)'s star shows, the detection of a single star of a particular mass and metallicity cannot be used to deduce the characteristic mass at that metallicity.

Metal-poor globular clusters and dwarf galaxies

Our model predicts that star-forming systems with $\log_{10} Z/Z_\odot \lesssim -1.5$ should have increased characteristic masses compared to more metal-rich systems – slightly higher for systems that formed at high pressure, and more substantially higher for systems that formed at low pressure. The most metal-poor globular clusters and dwarf galaxies reach this metallicity range, so in principle our model is testable by observations of such systems. However, the observational situation is highly-contested. For globular clusters De Marchi et al. (2000, 2010) find that, once one accounts for preferential evaporation of low-mass stars over ~ 10 Gyr timescales, all the globular clusters they survey are consistent with having formed with an IMF with a characteristic mass similar to that found in the Milky Way field (see also, Baumgardt 2017). By contrast, Marks et al. (2012) argue based on models for the effects of gas ejection by feedback that metal-poor clusters must have had a top-heavy IMF compared to the field. Zaritsky et al. (2014) report that characteristic masses do vary between globular clusters, but find no systematic variation with metallicity. Thus there is little consensus in the literature, and, in general, searches for IMF variation in globular clusters are challenging due to uncertainties in both the formation channels (Longmore et al. 2014; Bastian & Lardo 2018; Krumholz et al. 2019) and the dynamical evolution (Spitzer 1987; Baumgardt & Makino 2003; Leigh et al. 2012; Webb & Leigh 2015; Webb et al. 2017) of these objects. A further challenge is that the globular cluster population only reaches the edge of the ultra-low metallicity region where we expect substantial variations in $M_{\rm ch}$; in the papers discussed above, the median metallicity is close to $\log_{10} Z/Z_\odot \approx -1.5$, and clusters with $\log_{10} Z/Z_\odot < -2$ make up only ≈ 10 per cent of the sample (Zinn 1985; Harris 1996). Thus the expected signal is rather weak.

Compared to globular clusters, metal-poor dwarf galaxies suffer from fewer uncertainties about dynamical evolution, but at the price that, since they are more distant than globular clusters, observations are substantially more difficult. In the most nearby dwarfs, it is possible to measure the IMF from resolved stellar populations. Using this method, Gennaro et al. (2018) find a strong anti-correlation between the slope of the IMF and metallicity for ultra-faint Milky Way satellites, resulting in a

slightly bottom-light IMF (characteristic mass $\approx 0.5 - 0.6\,M_\odot$) at lower metallicities ($-2.5 \lesssim$ [Fe/H] $\lesssim -1.5$) for some of these galaxies as compared to the Milky Way. This would appear to be consistent with our model. However, the statistical significance of their result is marginal; if they use lognormal rather than powerlaw functional forms to fit their data, the data are consistent with having the same characteristic mass as the Milky Way at the 1σ level; more generally, El-Badry et al. (2017) show that drawing strong conclusions about the IMF in dwarf galaxies from resolved star counts is exceedingly difficult due to the limited sample sizes available. Similarly, Rossi et al. (2021) argue for a top-heavy IMF in the ultra-faint dwarf Boötes I based on simulations of its color magnitude diagram, which would be at least qualitatively consistent with our predictions (see, however, Yan et al. 2020). Nonetheless, the same caveat from El-Badry et al. (2017) likely applies.

In more distant dwarfs, only more indirect methods using unresolved stellar populations are available. Dabringhausen et al. (2009, 2010, 2012) argue for a top-heavy IMF in ultra-compact dwarf galaxies based on the large number of low mass X-ray binaries (LMXBs) found within them. However, this method does not directly probe the characteristic mass, since LMXBs come from substantially more massive stars. Moreover, analysis of a much larger sample of such galaxies has failed to confirm the existence of an LMXB excess (Pandya et al. 2016; see also, Phillipps et al. 2013 and Peacock et al. 2017). Similarly, Hoversten & Glazebrook (2008), Pflamm-Altenburg et al. (2009), Lee et al. (2009), Meurer et al. (2009), and Gunawardhana et al. (2011) all argue for IMF variation based on a variety of photometric indicators that should be sensitive to the slope of the high-mass IMF. Again, these methods do not probe the characteristic mass, and their claims are highly contested. Fumagalli et al. (2011b), Eldridge (2012), and Weisz et al. (2012) all conclude that stochastic fluctuations in IMF sampling, the star formation history, or both are sufficient to explain the observations without any need for IMF variations (however, see Weidner et al. 2013). Andrews et al. (2014) report direct measurements of the required stochastic fluctuations in low-mass clusters (though see Weidner et al. 2014 for a contrary view). In summary, we conclude that at present there is no unambiguous evidence for IMF variation in dwarf galaxies, and that, even if such evidence were found, with present methods it would provide only limited information about the characteristic mass, as opposed to the high-mass slope. JWST observations of high-redshift metal-poor dwarf satellites will help shed some light on IMF variations, if any, in these systems (Gelli et al. 2021).

Starbursts and young massive clusters

Our model predicts that starbursts and young massive clusters, which are high-pressure and often metal-rich environments, should have lower characteristic masses, and this too is a testable prediction. However, as with globulars and metal-poor dwarfs, observations of these systems are challenging. The most direct measurement is for the 30 Doradus region in the Large Magellanic Cloud, which is close enough to permit resolution of individual stars. Schneider et al. (2018) report that 30 Dor has a flatter high-mass IMF slope than is found in the Milky Way (see also, Banerjee & Kroupa 2012). While this might at first blush seem to be inconsistent with our findings, it is important to note that this study only looked at stars more massive than $15\,\mathrm{M}_\odot$ without investigating the low mass part of the IMF, and previous work on the central cluster R136 in 30 Doradus by Andersen et al. (2009) that covered stars with masses as low as $0.5\,\mathrm{M}_\odot$ did not find any IMF variations. Thus, it is quite plausible that the characteristic stellar mass in 30 Doradus is not very different from that in the Milky Way, or is even lower, even if the slope at the high mass end is flatter. Moreover, it is worth noting that, while 30 Doradus is a starburst, its metallicity is only about half of Solar, so the effects of its high pressure may be offset by its somewhat low metallicity.

All other starburst systems for which claims of IMF variation exist in the literature are more distant, and thus the evidence is more indirect. Zhang et al. (2018) and Brown & Wilson (2019) argue that the observed ratios of $^{13}\mathrm{CO}/\mathrm{C}^{18}\mathrm{O}$ in some local and high-redshift starburst galaxies provide evidence for a top-heavy IMF. Taken at face value, this again seem inconsistent with our results. However, as with 30 Dor, these observations only constrain the high mass slope of the IMF, not the characteristic mass. Moreover, Martín et al. (2019) show that isotopic ratios derived from unresolved observations may be confused by optical depth effects, leading to systematic errors.

A final caveat is that chemical evolution models that call for IMF variation implicitly assume that the ejecta of supernovae (the primary source of $^{18}\mathrm{O}$) and AGB stars (the primary source of $^{13}\mathrm{C}$) are ejected in galactic winds in the same proportion. There is no reason to believe this to be the case, and excellent reason to believe the opposite, given that models (Sharda et al. 2021d,c,e) as well as observations (Lopez et al. 2020; Cameron et al. 2021) suggest galactic winds in starbursts are preferentially enriched in supernova ejecta.

Massive early type galaxies

The centres of massive early type galaxies are very metal-rich, and, given their extremely high present-day surface densities, must have formed at very high gas pressure. There have been a number of observational results that focus on the nature of the IMF in massive early type galaxies (see the review by Smith 2020). These observations can be broadly divided into categories - one where spectroscopic measurements are taken (e.g., van Dokkum & Conroy 2010; Conroy & van Dokkum 2012; La Barbera et al. 2013; Ferreras et al. 2013, 2015; Conroy et al. 2017), and other where dynamical measurements often aided by gravitational lens modeling are used (e.g., Treu et al. 2010; Cappellari et al. 2012; McDermid et al. 2014; Smith et al. 2015; Newman et al. 2017; Oldham & Auger 2018). Some studies report a tight correlation between local metallicity and the IMF in these galaxies (Martín-Navarro et al. 2015b). While both approaches find the presence of a more bottom-heavy IMF than the Milky Way in centres of massive ellipticals (see, however, Smith et al. 2015), the systematic differences between the two methodological approaches are still not well understood (Smith 2014, 2020). Based on our results in Section 5.3.4, we expect a more bottom-heavy IMF in such an environment compared to that in the Milky Way, with a characteristic stellar mass $\lesssim 0.1\,M_\odot$ (see also, Yan et al. 2021). This result from the model seems rather robust given that the variations in M_{ch} are tiny even when we use different chemical compositions, include additional processes, or change the dust-to-metal ratio. Thus, dust-dominated star formation at high pressure that naturally leads to a more bottom-heavy stellar population is a compelling candidate to explain the observations of the centres of massive elliptical galaxies.

Recent studies have also discovered the presence of an IMF gradient in elliptical galaxies, where the central regions show a more bottom-heavy IMF than the Milky Way but the outskirts show an IMF compatible with the Milky Way (e.g., Martín-Navarro et al. 2015a; La Barbera et al. 2016; Oldham & Auger 2018; Sarzi et al. 2018; Collett et al. 2018; Parikh et al. 2018). In the context of our model, such an IMF gradient seems viable if the pressure in galaxy centres is systemically larger than that in the disc or the outskirts in elliptical galaxies (see also, Martín-Navarro et al. 2015a). Moreover, the presence of a negative metallicity gradient in early type galaxies that implies lower metallicities in the outskirts (Parikh et al. 2018) further strengthens the agreement between our model and observations. Most recently, Martín-Navarro et al. (2021) extended the spectroscopic IMF determination method to a sample of less massive quenched galaxies in the Fornax cluster. They find a strong positive correlation of metallicity with the slope of the IMF in the mass range

$0.2 - 1\,M_\odot$, indicating the presence of more high mass stars at lower metallicities, again qualitatively consistent with our model.

Cosmological observations

Claims of IMF variation based on cosmological observations represent a final observational category. Fardal et al. (2007) and Cowley et al. (2019) study the total extragalactic background radiation observed today to constrain the global star formation history. These authors also find that a universal IMF all the way to very early times is in tension with their work, and a top-heavy IMF in the past is needed to explain the observed background radiation and stellar density at the present day. In another study, Wang & Dai (2011) find that an evolving IMF that becomes increasingly top-heavy at higher redshifts (Davé 2008) can also easily reproduce the observed redshift distribution of gamma ray bursts. However, we emphasise that none of these results are unchallenged, and some are contradictory. Evidence that the IMF varies at all, let alone for the nature of that variation, remains hard to come by.

5.5.2   Comparison with theoretical models

It is also helpful to put our work in the context of previous theoretical studies, though we offer only a short summary of an extensive field; see Skillman (2008) for a review of earlier work. Some of the earliest models that studied the transition in the ISM as a function of metallicity are those of Norman & Spaans (1997) and Spaans & Norman (1997), where the authors found a phase transition occurs in the ISM between $0.03 - 0.1\,Z_\odot$. These models were however developed to study star formation in dwarf galaxies, did not include protostellar feedback, and did not explore the very metal-poor regime. Later models that followed, giving particular attention to the role of dust (Schneider et al. 2006a; Schneider & Omukai 2010), found a qualitatively similar transition in the characteristic mass (defined in these studies as the mass of a typical fragment) from highly super-solar to sub-solar as a function of metallicity (figure 5 Schneider et al. 2006a). However, the transition to a sub-solar characteristic mass occurs in these studies at very low metallicities ($Z \approx 10^{-6}\,Z_\odot$), owing to efficient dust-induced fragmentation. The difference between our results and theirs is probably due to heating of dust grains post protostar formation due to feedback.

Based on theoretical modeling of the Jeans mass in collapsing clouds including dust-gas coupling, Elmegreen et al. (2008) proposed that the reason for a universal IMF at high Z is because there is little variation in the gas temperature as a function

of metallicity for $Z \gtrsim 0.2\,Z_\odot$. This is consistent with our conclusions (see Figure 5.6), though the underlying physical picture of gas thermodynamics presented in Elmegreen et al. is quite different from ours.

Finally, number of authors have also studied how an IMF that varies in response to metallicity, pressure, star formation rate, or other large-scale galactic properties would influence a range of other galactic properties, for example present-day mass functions, photometric correlations, and rates of compact object mergers (e.g. Jeřábková et al. 2018; Guszejnov et al. 2019; Chruślińska et al. 2020). Since these authors generally seek to explore the implications of IMF variation rather than develop theoretical models for why such variation should exist, their focus is somewhat different from ours, and we will therefore not discuss these works further.

5.5.3   Comparison with simulations

Several simulations have investigated the properties of the IMF to search for variations with metallicity. These simulations can be divided in two categories – one that includes a sub-grid model for a varying IMF in cosmological simulations (e.g., Bekki 2013; Few et al. 2014; Barber et al. 2019; Gutcke & Springel 2019; Applebaum et al. 2020; Prgomet et al. 2021), and another focused on star formation where the IMF is self-consistently constructed based on fragmentation and distribution of stellar masses. We only discuss the latter approach because our work is directly comparable to those studies.

Jappsen et al. (2009) find that the change in the dominant coolant from molecular H_2 to metals at $Z \sim 10^{-3.5}\,Z_\odot$ metallicity can give rise to an apparent transition from primordial to modern day star formation based on the fragmentation characteristics (Bromm et al. 2001). While these authors did not include dust-gas coupling or protostellar feedback, they proposed that the transition in star formation is not caused by metals but by the formation of dust. Thus, our work confirms their hypothesis that it is indeed dust taking control of gas thermodynamics that sets the beginning of modern day star formation. Earlier simulations by Jappsen et al. (2005) based on idealised stiff equations of state (i.e., not directly including dust-gas coupling or protostellar feedback) found that the transition in the regime of star formation at $Z \approx 10^{-3.5}\,Z_\odot$ proposed by Bromm et al. (2001) is not real, and is simply a case of metals taking over from molecular H_2 to act as the dominant cooling agents at this metallicity. By contrast, our results suggest that the transition around $10^{-3.5}\,Z_\odot$ is indeed real. This is because the effect of metals taking over from molecular H_2 to cool the gas is directly reflected in the characteristic stellar mass, which turns out to be different for the case of metal cooling as compared to that of

molecular H_2 cooling.

Particularly noteworthy in the context of an evolving IMF are the results from numerical simulations run by Myers et al. (2011), and Chon et al. (2021). The simulation setup used by Myers et al. (2011) is similar in essence to our theoretical framework, since protostellar feedback and dust-gas coupling are the key ingredients that are common in both studies. Additionally, Myers et al. (2011) also use the Chakrabarti & McKee (2005) model to look at the evolution of the IMF as a function of metallicity. The key conclusion of Myers et al. (2011) is that varying the dust opacity by a large factor does not make any difference in fragmentation in a molecular cloud affected by protostellar radiation feedback, thus leading to a characteristic stellar mass independent of metallicity. Similar results were also obtained by Bate (2014) from their simulations of star cluster formation. However, both these works did not consider metallicities less than $0.01\,Z_\odot$, and thus they could not study the transition in star formation from primordial to modern day, nor the transition in the characteristic stellar mass as a function of metallicity that only occurs below $0.01\,Z_\odot$.

Chon et al. (2021) use hydrodynamic simulations to study the transition in the IMF as a function of Z, finding that dust already starts to control fragmentation at $Z \gtrsim 10^{-5}\,Z_\odot$ and that the IMF remains top-heavy for $Z \lesssim 10^{-2}\,Z_\odot$. They use sink particles to follow the the evolution of star clusters up to $10^{4-5}\,\mathrm{yr}$ past the onset of star formation, and include cooling due to H_2, HD, and fine structure atomic lines ($C\,\textsc{ii}$ and $O\,\textsc{i}$). However, they do not take into account the effects of protostellar feedback, which is the key ingredient in our model. While our results are broadly consistent with theirs, there are small differences. For example, we find that dust only contributes at the $\approx 10 - 30$ per cent level in setting the characteristic mass at $10^{-5} \leq Z/Z_\odot \leq 10^{-3.5}$ at all pressures, in contrast to their findings (see their figure 3). A possible explanation of this discrepancy could be that we only look at the importance of dust at the critical location where $M_{\mathrm{enc}} = M_{\mathrm{BE}}$, which occurs at relatively low n (and thus in a region of weak dust-gas coupling) in primordial-like environments, whereas they study the importance of dust at much higher densities. Another reason could be that protostellar feedback leads to much higher dust temperatures, which reduce the efficiency of dust in cooling the gas; in this context, the results of Chon et al. (2021) (as well as similar earlier results by Schneider et al. 2006a; Schneider & Omukai 2010; Dopcke et al. 2011, 2013; Nozawa et al. 2012) can be separated from ours based on the inclusion of protostellar feedback. Further progress in this area requires more simulations like those of Chon et al. (2021) where one can follow a time-dependent chemical evolution in 3D at different metallicities,

combined with protostellar feedback models such as ours to yield realistic dust temperatures, rather than ignoring feedback and treating dust solely as a coolant.

5.6   Implications for cosmic star formation history

Our result that the IMF is top-heavy in extremely-metal poor environments, and our finding of a characteristic mass set to value in the range $0.1 - 1$ $M_\odot$ in metal-rich environments, are consistent with previous work. However, the IMF for the intermediate metal-poor regime ($10^{-3.5} \lesssim Z/Z_\odot \lesssim 10^{-1.5}$) has received very limited investigation (Chiaki et al. 2018; Chon et al. 2021), despite the growing number of observed metal-poor stars with $-3.5 \lesssim$ [Fe/H] $\lesssim -1.5$ (Yong et al. 2013; Frebel & Norris 2015; Starkenburg et al. 2017; Hayes et al. 2018; Arentsen et al. 2020). Such low metallicities can exist (even if only briefly) in ISM that has been recently enriched by Population III supernovae or AGB stars (Tumlinson 2007; Nordlander et al. 2019; Ezzeddine et al. 2019; Yong et al. 2021b; Skúladóttir et al. 2021; Placco et al. 2021), or in very low mass dwarf galaxies (e.g., Leo P – McQuinn et al. 2015; J0811+4730 – Izotov et al. 2018; simulations – Emerick et al. 2018a,b). In fact, it is also proposed that a large fraction of the Universe can still exist in a metal-free regime even at redshifts as low as 5, and continue to form metal-free or extremely metal-poor stars (Muratov et al. 2013; Liu & Bromm 2020b). These results indicate the existence of an extended metal-poor phase of star formation in cosmic history.

In our models, the existence of a distinct mode of star formation at $10^{-3.5} \leq Z/Z_\odot \leq 10^{-1.5}$ is most clearly visible when we examine heating and cooling processes, which at all P and $\sigma_{\rm v}$ exhibit a metal-cooling dominated regime that separates primordial star formation from modern day star formation. However, the signal is less clear simply from examining $M_{\rm ch}$. We see from Figure 5.8 and analogous figures that the characteristic stellar mass for this regime in Z can be either sub-solar or super-solar, depending on the cloud pressure, velocity dispersion and metallicity. The exact value of $M_{\rm ch}$ in this metallicity regime depends rather sensitively on the chemical composition, as well as the effects of cosmic ray heating. As the first supernovae explode and produce copious amounts of dust within a short time ($\approx 0.1 - 10\,\mathrm{Myr}$, Sarangi et al. 2018), or binary-rich massive stellar populations and low mass AGB stars expel dust forming elements after they form, subsequent star formation can already be heavily dust-dominated (Todini & Ferrara 2001; Nozawa et al. 2003; Cherchneff & Dwek 2010; Wang et al. 2020a; Kroupa et al. 2020; Kalari et al.

2018; Gil-Pons et al. 2021; Ventura et al. 2021). Such a scenario would lead to a bottom-heavy characteristic stellar mass within a short period of time, considerably shortening the period of transitionary, metal-poor star formation.

Given these findings, we speculate that the scatter in the duration of such a transitionary star formation phase can be fairly large. In fact, the rise in metallicity in certain environments can be very sharp, thereby completely skipping the transitionary phase. Another possibility is that star formation remains fairly quiescent for a long period of time, thus delaying the onset of the modern phase. Such star formation histories (and the corresponding metallicity histories) have been retrieved through detailed SED modeling for several galaxies (Bellstedt et al. 2020; Thorne et al. 2021), although without invoking IMF variations even at very low metallicities. This implies that while we can predict when the IMF becomes bottom-heavy, we cannot place strong constraints on the time it would take for it to do so. Convolution of models like ours with studies like those of Guszejnov et al. (2017b) where the authors test different IMF models in cosmological simulations at early times will be able to quantify the scatter present in the characteristic mass at low metallicities.

5.7   Summary

In this work, we focus on understanding the evolution of the characteristic mass that sets the peak of the stellar initial mass function (IMF) as a function of metallicity. We consider collapsing dusty gas clouds that have just begun to fragment, at metallicities from $10^{-6} - 2\,Z_\odot$, and pay careful attention to how radiation feedback from the first objects to form influences subsequent fragmentation. Our work thus compliments studies that focus on fragmentation in star-forming clouds at different metallicities prior to protostar formation (e.g., Omukai et al. 2005, 2010); such an extension is necessary to correctly capture the transition to modern-day star formation, where such feedback plays a decisive role in shaping the IMF. In addition to covering a wide range in metallicity, our models also span a large range in pressure and velocity dispersion of star-forming clouds, as observed in Milky Way and dwarf galaxies (low pressure environments) to super star clusters and the centres of massive early type galaxies (high pressure environments).

We demonstrate the existence of three phases of star formation that can be separated based on the ISM metallicity: (1.) the primordial phase below $Z \lesssim 10^{-4}\,Z_\odot$ where gas cooling is dominated by molecular H_2 and HD, (2.) the transitionary phase between $10^{-4} \lesssim Z/Z_\odot \lesssim 10^{-2}$ where metal cooling dominates gas thermo-

dynamics, and (3.) the modern phase above $Z \gtrsim 10^{-2} \, Z_\odot$ where dust governs gas thermodynamics. The effects of the changes between these thermodynamic regimes is reflected in the characteristic stellar mass that sets the peak of the IMF. We find that at low pressures ($P/k_B \sim 10^4 \, \mathrm{K \, cm^{-3}}$), the characteristic stellar mass is of the order of $50 - 100 \, \mathrm{M_\odot}$ at extremely-low metallicites ($Z = 10^{-6} \, Z_\odot$), and drops down to $0.3 \, \mathrm{M_\odot}$ at $Z = Z_\odot$ (see Figure 5.8). At very high pressures ($P/k_B \sim 10^8 \, \mathrm{K \, cm^{-3}}$) and high metallicity, the characteristic stellar mass drops to $\sim 0.1 \, \mathrm{M_\odot}$ (see Figure 5.8), which is $3\times$ smaller than that we find above for a typical Milky Way molecular cloud. This provides a natural explanation for the even more bottom-heavy IMF found in early-type galaxy centres.

Our results thus suggest that the IMF became bottom-heavy around $Z \sim 10^{-2} \, Z_\odot$ in the progenitors of late type galaxies like the Milky Way, whereas it became bottom-heavy around $Z \sim 10^{-4} \, Z_\odot$ in the progenitors of massive, early type galaxies like NGC 1407. The earlier transition to a bottom-heavy IMF in early type galaxies is a result of the high-pressure ISM that existed in these galaxies. However, our models remain simplistic in the sense that they do not have the capability to predict the full distribution of the IMF. It is also possible that the trends in the characteristic mass with metallicity, velocity dispersion and pressure that we find are not noticeable in certain environments where other factors have a stronger influence on the IMF. Further advancements in our understanding of the evolution of the IMF as a function of metallicity will require chemodynamical simulations covering a wide range in metallicities coupled with models that properly account for protostellar feedback so that we can study fragmentation both pre- and post-collapse, and over metallicities ranging from the primordial to the modern.

Acknowledgements

The physics of gas phase metallicity gradients in galaxies

Context and Contribution

This chapter have been previously published as '**The physics of gas phase metallicity gradients in galaxies**', *by* **Piyush Sharda, Mark R. Krumholz, Emily Wisnioski, John C. Forbes, Christoph Federrath, and Ayan Acharyya, 2021, MNRAS, 502, 5935**. *The work is presented here exactly as in the publication. I initiated and led the idea behind this work. I have created the model described in this work. I have contributed heavily to interpretation of the results and written the majority of the paper, with inputs and suggestions from co-authors.*

Abstract

We present a new model for the evolution of gas phase metallicity gradients in galaxies from first principles. We show that metallicity gradients depend on four ratios that collectively describe the metal equilibration timescale, production, transport, consumption, and loss. Our model finds that most galaxy metallicity gradients are in equilibrium at all redshifts. When normalized by metal diffusion, metallicity gradients are governed by the competition between radial advection, metal production, and accretion of metal-poor gas from the cosmic web. The model naturally explains the varying gradients measured in local spirals, local dwarfs, and high-redshift star-forming galaxies. We use the model to study the cosmic evolution of gradients across redshift, showing that the gradient in Milky Way-like galaxies has steepened over time, in good agreement with both observations and simulations. We also predict the evolution of metallicity gradients with redshift in galaxy samples constructed using both matched stellar masses and matched abundances. Our model shows that massive galaxies transition from the advection-dominated to the accretion-dominated regime from high to low redshifts, which mirrors the transition from gravity-driven to star formation feedback-driven turbulence. Lastly, we show

that gradients in local ultraluminous infrared galaxies (major mergers) and inverted gradients seen both in the local and high-redshift galaxies may not be in equilibrium. In subsequent papers in this series, we show that the model also explains the observed relationship between galaxy mass and metallicity gradients, and between metallicity gradients and galaxy kinematics.

6.1 Introduction

Metals act as tracers of the formation and assembly history of galaxies. Tracking their evolution is crucial to understanding the various pathways a galaxy takes while it forms (Freeman & Bland-Hawthorn 2002). Metals are produced in galaxies through supernovae (Hillebrandt & Niemeyer 2000; Woosley et al. 2002), asymptotic giant branch (AGB) stars (van Winckel 2003; Herwig 2005), neutron star mergers (Thielemann et al. 2017), etc., and are consumed by low mass stars and retained in stellar remnants (Kobayashi et al. 2006; Sukhbold et al. 2016). Apart from this in-situ metal production and consumption (Pagel & Patchett 1975), metals can also be lost through outflows in the form of galactic winds (Heckman et al. 1990; Veilleux et al. 2005; Rupke 2018; Chisholm et al. 2018), or transported into the galaxy from the circumgalactic (CGM) and the intergalactic medium (IGM, Prochaska et al. 2017; Tumlinson et al. 2017), or during interactions with other galaxies, like fly-bys or mergers (e.g., Torrey et al. 2012; Grossi et al. 2020). All of these processes can be classified into four main categories: metal production (through star formation and supernovae), metal consumption (through stellar remnants and low mass stars), metal transport (through advection, diffusion, and accretion), and metal loss (galactic winds and outflows).

The distribution of metals within galaxies places important constraints on galaxy formation (Sánchez Almeida et al. 2014). One of the strongest pieces of evidence for the inside-out galaxy formation scenario is the existence of negative metallicity gradients (in the radial direction) in both the gas and stars in most galaxies. The presence of such negative radial gradients is easy to understand: in the inside-out scenario, the centre, *i.e.,* the nucleus of the galaxy forms first, and the disc subsequently forms and evolves in time. The nucleus undergoes greater astration, leading to the presence of more metals in the centre as compared to the disc, thus establishing a negative gradient. Such gradients were first observed and quantified through nebular emission lines in H II regions in the interstellar medium (ISM) by Aller (1942), Searle (1971) and Shaver et al. (1983). The decrease in metallicity is approximately exponential with galactocentric radius (Wyse & Silk 1989; Zaritsky 1992), yielding

a linear gradient in logarithmic space, with units of $\mathrm{dex\,kpc^{-1}}$. Since these early works, metallicity gradients have been measured for thousands of galaxies, both in stars and gas (see recent reviews by Kewley et al. 2019b, Maiolino & Mannucci 2019 and Sánchez 2020b). The stellar metallicity gradients are typically characterised by the abundance of iron, and are written in the form $d\log_{10}\left(\mathrm{Fe/H}\right)/dr$, whereas the gas phase metallicity gradients are characterised by the abundance of oxygen, and written as $d\log_{10}\left(\mathrm{O/H}\right)/dr$, where r is the galactocentric radius. Hereafter, we will only discuss the gas phase metallicity gradients in galaxies.

In the local Universe, samples of metallicity gradient measurements have been dramatically expanded by three major surveys: CALIFA (Calar Alto Legacy Integral Field Area, Sánchez et al. 2012), MaNGA (Mapping nearby Galaxies at Apache Point Observatory, Bundy et al. 2015), and SAMI (Sydney-AAO Multi-object Integral-field spectrograph, Bryant et al. 2015). These surveys show that local galaxies contain predominantly negative metallicity gradients, with typical values ranging between 0 and $-0.1\,\mathrm{dex\,kpc^{-1}}$. Measurements in high-$z$ ($z \lesssim 3$) galaxies are more challenging, and the samples are correspondingly smaller, but rapidly expanding (Queyrel et al. 2012; Swinbank et al. 2012; Jones et al. 2013; Stott et al. 2014; Troncoso et al. 2014; Leethochawalit et al. 2016; Wuyts et al. 2016; Förster Schreiber et al. 2018; Wang et al. 2019, 2020b; Curti et al. 2020b; Simons et al. 2020; Gillman et al. 2021).

Theoretical efforts to understand these observations are still in their infancy, with most effort thus far dedicated to understanding galaxies' global metallicities (e.g., Erb 2008; Peeples & Shankar 2011; Davé et al. 2012; Lilly et al. 2013; Dayal et al. 2013; Hunt et al. 2016; Wang & Lilly 2020; Furlanetto 2021) rather than their metallicity gradients. Early work on metallicity gradients was tuned to reproduce the present-day Milky Way metallicity gradient (e.g. Chiappini et al. 1997, 2001; Prantzos & Boissier 2000), and thus offers relatively little insight into how metallicity gradients have evolved over cosmic time and in galaxies with differing histories. More recent work has attempted to address the broader sample of galaxies, using physical models that include a range of processes: cosmological accretion, mass-loaded galactic winds, *in situ* metal production by stars, and radial gas flows (e.g., Mott et al. 2013; Jones et al. 2013; Ho et al. 2015; Carton et al. 2015; Kudritzki et al. 2015; Pezzulli & Fraternali 2016; Belfiore et al. 2019; Kang et al. 2021). However, these works generally suffer from a problem of being under-constrained: the models generally involve multiple free functions (e.g., the radial inflow velocity or mass loading factor as a function of radius and time) that are not constrained by any type of independent physical model, and fits of these free functions to the data are

often non-unique, leaving in doubt which physical processes are important in which types of galaxies.

Moreover, not all models include all possible physical processes, making them difficult to compare. For example, some of the models above assume that galactic wind metallicities are equal to ISM metallicities, contrary to observational evidence (e.g., Martin et al. 2002; Strickland & Heckman 2009a; Chisholm et al. 2018). Many models do not include metal transport processes like advection (flow of metals that are carried by a bulk flow of gas) or turbulent diffusion (metal flow that occurs due to turbulent mixing of gas with non-uniform metal concentration; e.g., de Avillez & Mac Low 2002; Greif et al. 2009; Yang & Krumholz 2012; Aumer et al. 2013; Kubryk et al. 2013; Petit et al. 2015a; Armillotta et al. 2018; Rennehan et al. 2019), despite modelling showing that these effects play an important role in setting metallicity gradients (Forbes et al. 2012).

These problems have been partly alleviated by recent radially-resolved semi-analytic models (Kauffmann et al. 2013a; Fu et al. 2013; Forbes et al. 2014a, 2019; Henriques et al. 2020; Yates et al. 2020) and cosmological simulations with enough resolution to capture disc radial structure (Pilkington et al. 2012; Gibson et al. 2013; Ma et al. 2017; Tissera et al. 2019; Hemler et al. 2021; Bellardini et al. 2021), which do at least attempt to model the dynamics of gas in galaxies self-consistently. The general result of these models (as summarised in Figure 8 of Curti et al. 2020b), is that there is only a mild evolution in metallicity gradients between $0 \leq z \leq 4$, with a slight steepening toward the present day. However, the physical origin of these results, and insights from the numerical results in general, have yet to be distilled into analytic models that we can use to understand the overall trends in the data. Thus, to this date, we lack a model that can explain the occurrence of metallicity gradients in a diverse range of galaxies from first principles. This leaves many interesting questions around gas phase metallicity gradients unanswered.

Motivated by this, we present a new theory of gas phase metallicity gradient evolution in galaxies from first principles. As with all theories of metallicity gradients, ours requires a galaxy evolution model that describes the gas in galactic discs as an input. For the purposes of developing the theory, we use the unified galactic disc model of Krumholz et al. (2018), which has been shown to reproduce a large number of observations of gas kinematics relevant to metallicity gradients, including the radial velocities of gas in local galaxies (Schmidt et al. 2016), the correlation between galaxies' gas velocity dispersions and star formation rates (SFRs; e.g., Johnson et al. 2018; Yu et al. 2019; Varidel et al. 2020), and the evolution of velocity dispersion with redshift (e.g., Übler et al. 2019). However, our metallicity model is a standalone

model into which we can incorporate any galaxy evolution model. In this paper, we present the basic formalism and results of the model, and use them to explain the evolution of metallicity gradients with redshift; in two follow-up papers we first use the model developed here to explain the dependence of metallicity gradients on galaxy mass that is observed in the local Universe (Sharda et al. 2021b), and then use the model to predict the existence of a correlation between galaxy kinematics and metallicity gradients, which we validate against observations (Sharda et al. 2021f).

We arrange the rest of the paper as follows: Section 6.2 describes the theory of metal evolution, Section 6.3 describes the equilibrium metallicity gradients generated by the theory for different types of galaxies both in the local and the high-z Universe, Section 6.4 combines the local and high-z predictions of the model to describe the cosmic evolution of metallicity gradients, and Section 6.5 discusses the limitations of the model, including special cases where the metallicity gradients may not be in equilibrium and thus the model may or may not apply. Finally, we present our conclusions in Section 6.6. For the purpose of this paper, we use $Z_\odot = 0.0134$, corresponding to $12 + \log_{10} O/H = 8.69$ (Asplund et al. 2009), Hubble time $t_{H(0)} = 13.8\,\mathrm{Gyr}$ (Planck Collaboration et al. 2018), and follow the flat ΛCDM cosmology: $\Omega_m = 0.27$, $\Omega_\Lambda = 0.73$, $h = 0.71$, and $\sigma_8 = 0.81$ (Springel & Hernquist 2003).

6.2 Evolution of metallicity

For convenience, we collect all of the symbols we define in this section in Table 6.1 and Table 6.2.

6.2.1 Evolution equations

Let us start by defining ρ_Z to be the volume density of metals at some point in space; this is related to the metallicity, Z, and gas density, ρ_g, by

$$\rho_Z = Z \rho_g. \tag{6.1}$$

The density of the metals can change due to transport – via advection with the gas or diffusion through the gas – and due to sources and sinks (e.g., production of new metals by stars or consumption during star formation). The conservation equation for metal mass is then

$$\frac{\partial \rho_Z}{\partial t} + \nabla \cdot (\mathbf{v}\rho_Z + \mathbf{j}_Z) = s_Z. \tag{6.2}$$

Table 6.1: List of fiducial parameters in the model that are common to all galaxies. All of these parameters are adopted from Table 1 in Krumholz et al. (2018), except for y and $f_{\mathrm{R,inst}}$, which we adopt from Forbes et al. (2019).

Parameter	Description	Reference equation	Fiducial value
y	Metal yield	equation 6.9	0.028
$f_{\mathrm{R,inst}}$	Fraction of metals produced that are locked in stars	equation 6.9	0.77
ϕ_y	Yield reduction factor	equation 6.13	0.1–1.0
r_0	Reference radius per kpc	equation 6.14	1
Q_{min}	Minimum Toomre Q parameter	equation 6.21	$1-2$
ϕ_Q	$1 +$ ratio of gas to stellar Toomre Q parameter	equation 6.26	2
ϵ_{ff}	Star formation efficiency per free-fall time	equation 6.30	0.015
ϕ_{mp}	Ratio of the total to turbulent pressure at the disc midplane	equation 6.30	1.4
f_{B}	Universal baryonic fraction	equation 6.33	0.17
η	Scaling factor for the rate of turbulent dissipation	equation 6.36	1.5
ϕ_{nt}	Fraction of velocity dispersion due to non-thermal motions	equation 6.36	1

Here, $\mathbf{v}$ is the gas velocity, $\mathbf{j}$ is the flux density of metals as a result of diffusion, and s_Z represents the source and sink terms. The central assumption of diffusion is that the diffusive flux is proportional to minus the gradient of the quantity being diffused (e.g., Yang & Krumholz 2012; Krumholz & Ting 2018). The slight subtlety here is that what should diffuse is not the density of metals, but the concentration of metals, *i.e.,* the flux only depends on the gradient of Z. We can therefore write down the diffusive flux as

$$\mathbf{j}_Z = -\kappa \rho_g \nabla Z \, , \tag{6.3}$$

where κ is the diffusion coefficient (with dimensions of mass/length^2). Inserting this into the continuity equation, we now have

$$\frac{\partial \rho_Z}{\partial t} + \nabla \cdot (\mathbf{v} \rho_Z - \kappa \rho_g \nabla Z) = s_Z \, . \tag{6.4}$$

We can now specialise to the case of a disc. Firstly, we assume that the disc is thin, so we can write ρ_g in terms of the surface density as $\Sigma_g = \int \rho_g dz$. We choose our coordinate system so that the disc lies in the xy plane. Integrating all quantities

Table 6.2: List of fiducial parameters that are specific to a galaxy type as listed in the last 4 columns.

Parameter	Description	Reference equation	Units	Local spiral	Local dwarf	Local ULIRG	High-z ($z = 2$)
x_{max}	Outer edge of the star-forming disc	...	r_0	15	6	3	10
v_ϕ	Rotational velocity of the galaxy	equation 6.20	$\mathrm{km\,s^{-1}}$	200	60	250	200
$f_{g,Q}$	Effective gas fraction in the disc	equation 6.21	...	0.5	0.9	1	0.7
σ_g	Gas velocity dispersion	equation 6.22	$\mathrm{km\,s^{-1}}$	10	7	60	40
β	Galaxy rotation curve index	equation 6.23	...	0	0.5	0.5	0
f_{sf}	Fraction of star-forming molecular gas	equation 6.30	...	0.5	0.2	1	1
$f_{g,P}$	Fraction of mid-plane pressure due to disc self-gravity	equation 6.30	...	0.5	0.9	1	0.7
M_{h}	Halo mass	equation 6.34	$\mathrm{M}_\odot$	10^{12}	10^{10}	10^{12}	5×10^{11}
c	Halo concentration parameter	equation 6.35	...	10	15	10	13
σ_{sf}	Gas velocity dispersion due to star formation feedback	equation 6.36	$\mathrm{km\,s^{-1}}$	7	5	9	8.5

in the z direction, the equation of mass conservation becomes

$$\frac{\partial \Sigma_Z}{\partial t} + \nabla \cdot (\mathbf{v}\Sigma_Z - \kappa\Sigma_g \nabla Z) = S_Z, \qquad (6.5)$$

where Σ_Z is the metal surface density, ∇ contains only the derivatives in the xy plane, and $S_Z = \int s_Z \, dz$. Assuming cylindrical symmetry, this reduces to,

$$\frac{\partial \Sigma_Z}{\partial t} + \frac{1}{r}\frac{\partial}{\partial r}\left(rv\Sigma_Z - r\kappa\Sigma_g \frac{\partial Z}{\partial r}\right) = S_Z, \qquad (6.6)$$

where v represents the radial component of the velocity. It is helpful to rewrite the velocity in terms of the inward mass flux across the circle at radius r, which is

$$\dot{M} = -2\pi r v \Sigma_g, \qquad (6.7)$$

where we have adopted a sign convention whereby $\dot{M} > 0$ corresponds to inward mass flow[1]. This gives

$$\frac{\partial \Sigma_Z}{\partial t} - \frac{1}{2\pi r}\frac{\partial}{\partial r}\left(\dot{M}Z\right) - \frac{1}{r}\frac{\partial}{\partial r}\left(r\kappa\Sigma_g \frac{\partial Z}{\partial r}\right) = S_Z. \qquad (6.8)$$

Similarly, since star formation is the process that is responsible for the source term, it is convenient to parameterize S_Z in terms of the star formation rate. We adopt the instantaneous recycling approximation (Tinsley 1980), whereby some fraction, $f_{\mathrm{R,inst}}$, of the mass incorporated into stars is assumed to be left in long-lived remnants (compact objects and low-mass stars), and the remainder of the mass is returned instantaneously to the ISM through Type II supernovae, enriched by newly formed metals with a yield y. Under this approximation, we have

$$S_Z = \left(y - f_{\mathrm{R,inst}}Z - \mu Z_w\right)\dot{\Sigma}_\star, \qquad (6.9)$$

where $\dot{\Sigma}_\star$ is the star formation rate surface density. The last term in equation 6.9 represents loss of metals into a galactic wind; here μ is the mass loading factor of the wind (*i.e.*, the wind mass flux is $\mu\dot{\Sigma}_\star$) and Z_w is the metallicity of the wind. Following Forbes et al. (2019, equation 41), we further parameterize the wind metallicity as

$$Z_w = Z + \xi \frac{y}{\max(\mu, 1 - f_{\mathrm{R,inst}})}, \qquad (6.10)$$

where the $1 - f_{\mathrm{R,inst}}$ limit specifies the minimum mass that can be ejected if some

---

[1]This is the opposite of the sign convention used in Forbes et al. (2012, 2014b), but consistent with the one used in Krumholz et al. (2018).

metals are ejected directly after production. The parameter ξ, which is bounded in the range $0 \leq \xi \leq 1$, specifies the fraction of metals produced that are directly ejected from the galaxy before they are mixed into the ISM. So, $\xi = 0$ corresponds to a situation when the metallicity of the wind equals the metallicity of the ISM, whereas $\xi = 1$ corresponds to the regime when all the metals produced in the galaxy get ejected in winds. Forbes et al. (2014a,b) introduced ξ to relax the assumption that metals fully mix with the ISM before winds are launched, so that $Z_w = Z$. A number of authors have shown that this assumption leads to severe difficulties in explaining observations, particularly in low-mass systems (Pilyugin 1993; Marconi et al. 1994; Mac Low & Ferrara 1999; Recchi et al. 2001, 2008; Martin et al. 2002; Robles-Valdez et al. 2017).

We can further simplify by writing down the continuity equation for the total gas surface density Σ_g, which is equation 6.8 with Z fixed to unity and $y = 0$, with an additional term for cosmic accretion,[2]

$$\frac{\partial \Sigma_g}{\partial t} - \frac{1}{2\pi r}\frac{\partial \dot{M}}{\partial r} = \dot{\Sigma}_{\rm cos} - \left(f_{\rm R,inst} + \mu\right)\dot{\Sigma}_\star , \qquad (6.11)$$

where $\dot{\Sigma}_{\rm cos}$ is the cosmic accretion rate surface density onto the disc (Oppenheimer et al. 2010; Benson 2010). If we now use this to evaluate $\partial \Sigma_Z/\partial t = \Sigma_g(\partial Z/\partial t) + Z(\partial \Sigma_g/\partial t)$ in equation 6.8, the result is

$$\Sigma_g \frac{\partial Z}{\partial t} - \frac{\dot{M}}{2\pi r}\frac{\partial Z}{\partial r} - \frac{1}{r}\frac{\partial}{\partial r}\left(r\kappa \Sigma_g \frac{\partial Z}{\partial r}\right) = \phi_y y \dot{\Sigma}_\star - Z\dot{\Sigma}_{\rm cos} , \qquad (6.12)$$

where

$$\phi_y = 1 - \frac{\mu\xi}{\max(\mu, 1 - f_{\rm R,inst})}. \qquad (6.13)$$

We refer to ϕ_y, which is bounded in the range $0 \leq \phi_y \leq 1$, as the yield reduction factor. Note that $f_{\rm R,inst}$ only appears in ϕ_y, implying that metals locked in stars are unimportant for the radial profile of metallicity as long as $\mu > 1 - f_{\rm R,inst}$.

From left to right, we can interpret the terms in equation 6.12 as follows: the first is the rate of change in the metallicity at fixed gas surface density; the second represents

---

[2]Note that equation 6.11 is identical to equation 1 of Forbes et al. (2019) except that Forbes et al. adopt instantaneous recycling only for Type II supernovae, and not for metals returned on longer timescales (e.g., Type Ia or AGB winds). While this approach is feasible in simulations and semi-analytic models, it renders analytic models of the type we present here intractable. However, this does not make a significant difference for our work because the most common gas phase metallicity tracer, O, comes almost solely from Type II supernovae. One area where our approach might cause concern is at high redshift, where the gradients are often measured through the [N II]/Hα emission line ratio, because most of the N comes from AGB stars and is released over Gyr or longer timescales (Herwig 2005).

the change due to advection of metals through the disc; the third represents the change due to diffusion of metals; finally, the terms on the right hand side are: (1.) the change in metallicity due to metal production in stars, with an effective yield $\phi_y y$ that is reduced relative to the true yield y by the factor ϕ_y, and (2.) the change in metallicity in the disc due to cosmic accretion of metal-poor gas.

The term ϕ_y represents the factor by which the effective metal yield is reduced because some fraction of metals directly escape the galaxy before they mix with the ISM. Higher values of ϕ_y imply that metals are well-mixed into the ISM, whereas lower values imply that the yield is significantly reduced by preferential ejection of unmixed metals. However, ϕ_y does not equate to the mass loading factor μ: galaxies with heavily mass-loaded winds (high μ) may still have ϕ_y close to unity if metals mix efficiently before the winds are launched; conversely, galaxies with weakly mass-loaded winds (low μ) may still have small ϕ_y if those winds preferentially carry away metals. We discuss the possible range of values for ϕ_y in more detail in Section 6.2.2 (see also, Sharda et al. 2021b).

At this point it is helpful to non-dimensionalise the system. We choose a fiducial radius r_0, which we will later take to be the inner edge of the disc where the bulge begins to dominate; for now, however, we simply take r_0 as a specified constant. We measure position in the disc with the dimensionless variable $x = r/r_0$ and time with $\tau = t\Omega_0$, where Ω_0 is the angular velocity at r_0. We further write out the profiles of gas surface density, diffusion coefficient, star formation surface density and cosmic accretion rate surface density as $\Sigma_g = \Sigma_{g0}s_g(x)$, $\kappa = \kappa_0 k(x)$, $\dot{\Sigma}_\star = \dot{\Sigma}_{\star 0}\dot{s}_\star(x)$, and $\dot{\Sigma}_{\rm cos} = \dot{\Sigma}_{\rm cos0}\dot{c}_\star(x)$ respectively. Here, the terms subscripted by 0 are the values evaluated at $r = r_0$, and $s_g(x)$, $k(x)$, $\dot{s}_\star(x)$, and $\dot{c}_\star(x)$ are dimensionless functions that are constrained to have a value of unity at $x = 1$. Note that, in principle, we could introduce a similar scaling function for $\dot{M}$; we do not do so because both observations (Schmidt et al. 2016) and theoretical models (Krumholz et al. 2018) suggest that, in steady state, $\dot{M}$ is close to constant with radius within a galactic disc. We express the metallicity as $\mathcal{Z} = Z/Z_\odot$.

Using these definitions, we can rewrite equation 6.12 as a form of the Euler-Cauchy equation (Arfken 1985; Kreyszig et al. 2011),

$$\underbrace{\mathcal{T}s_g\frac{\partial \mathcal{Z}}{\partial \tau}}_{\substack{\text{equilibrium} \\ \text{time}}} - \underbrace{\frac{\mathcal{P}}{x}\frac{\partial \mathcal{Z}}{\partial x}}_{\text{advection}} - \underbrace{\frac{1}{x}\frac{\partial}{\partial x}\left(xks_g\frac{\partial \mathcal{Z}}{\partial x}\right)}_{\text{diffusion}} = \underbrace{\mathcal{S}\dot{s}_\star}_{\substack{\text{production} \\ + \\ \text{outflows}}} - \underbrace{\mathcal{Z}\mathcal{A}\dot{c}_\star}_{\text{accretion}}. \qquad (6.14)$$

In the above equation, we have suppressed the x-dependence of s_g, k, $\dot{s}_\star$ and $\dot{c}_\star$ for

compactness, and we have defined,

$$\mathcal{T} = \frac{\Omega_0 r_0^2}{\kappa_0} \tag{6.15}$$

$$\mathcal{P} = \frac{\dot{M}}{2\pi\kappa_0\Sigma_{g0}} \tag{6.16}$$

$$\mathcal{S} = r_0^2 \frac{\dot{\Sigma}_{\star 0}}{\kappa_0\Sigma_{g0}} \left(\frac{\phi_y y}{Z_\odot}\right) \tag{6.17}$$

$$\mathcal{A} = r_0^2 \frac{\dot{\Sigma}_{\cos 0}}{\kappa_0\Sigma_{g0}}. \tag{6.18}$$

The four quantities $\mathcal{T}, \mathcal{P}, \mathcal{S}$ and $\mathcal{A}$ have straightforward physical interpretations: $\mathcal{T}$ is the ratio of the orbital and diffusion timescales, $\mathcal{P}$ is the Péclet number of the system, which describes the relative importance of advection and diffusion in fluid dynamics (e.g., Patankar 1980), $\mathcal{S}$ measures the relative importance of metal production (the numerator) and diffusion (the denominator), and $\mathcal{A}$ measures the relative importance of cosmic accretion and diffusion. $\mathcal{T}$ dictates the time it takes for a given metallicity distribution to reach equilibrium in a galaxy, whereas the other three quantities govern the type and strength of the gradients that form in equilibrium.

We will only look for the steady-state or *equilibrium* solutions to equation 6.14, so we drop the $\partial\mathcal{Z}/\partial\tau$ term. This approach is reasonable because, as we will show below, the equilibration timescale for metals is less than the Hubble time, $t_{\mathrm{H(z)}}$, for most galaxies. In our model, the time it takes for the metallicity gradient to approach an equilibrium state, t_{eqbm}, is based on the time it takes for the metal surface density to adjust to changes in metallicity triggered by each of the terms in equation 6.14,

$$\frac{1}{t_{\mathrm{eqbm}}} = \Omega_0 \frac{\left|\frac{\mathcal{P}}{x}\frac{\partial\mathcal{Z}}{\partial x}\right| + \left|\frac{1}{x}\frac{\partial}{\partial x}\left(xk s_g \frac{\partial\mathcal{Z}}{\partial x}\right)\right| + \left|\mathcal{S}\dot{s}_\star\right| + \left|\mathcal{Z}\mathcal{A}\dot{c}_\star\right|}{\mathcal{Z} s_g \mathcal{T}}. \tag{6.19}$$

If $t_{\mathrm{eqbm}} > t_{\mathrm{H(z)}}$, the metallicity gradient in the galaxy cannot attain equilibrium within a reasonable time, and the model we present below does not apply. While this is a necessary condition for metal equilibrium, it may not be sufficient. This is because if input parameters to the metallicity model (e.g., accretion rate, surface density, etc.) change on timescales much shorter than $t_{\mathrm{H(z)}}$, the equilibrium of metals will depend on that timescale. For a steady-state model like ours, it is safe to assume this is not the case, since the input galactic disc model in the next Section we use is an equilibrium model. We discuss this condition in more detail in Section 6.3 and Section 6.5.2 where we also compare t_{eqbm} with the molecular gas depletion time

that dictates the star formation timescale.

The accretion of material from the CGM can also impact metallicity in the galactic disc (Wise et al. 2012; Krumholz & Dekel 2012; Forbes et al. 2012; Taylor & Kobayashi 2015; Tumlinson et al. 2017; Schaefer et al. 2019). While this is an important consideration, in the absence of which 'closed-box' galaxy models overestimate metallicity gradients (e.g., Dalcanton 2007; Zahid et al. 2013; Kudritzki et al. 2015), it typically adds a floor metallicity at the outer edge of the galactic disc, and is of concern for simulations where the entire (star-forming as well as passive) disc up to tens of kpc is considered. CGM metallicity can also be important for long term $\left(0.1 - 1\,t_{\mathrm{H(z)}}\right)$ wind recycling (Henriques et al. 2013; Pandya et al. 2020), which we do not take into account in this model. As we show later in Section 6.2.3, we make use of this effect only as a boundary condition on the metallicity at the outer edge of the disc, and do not include it directly in the evolution equation.

This completes the basic formulation of the theory of metallicity gradients in galaxies. To further solve for the equilibrium metallicity, we now need a model of the galactic disc. We use the unified galactic disc model of Krumholz et al. (2018) for this purpose. However, we remind the reader that the metallicity evolution described by equation 6.14 can be used with other galactic disc models as well.

6.2.2   Galactic disc model

We use the unified galactic disc model of Krumholz et al. (2018) to further solve for metallicity. This model self-consistently incorporates all of the ingredients that we require as inputs: profiles of Σ_g, $\dot{M}$, κ and $\dot{\Sigma}_\star$, and the relationship between them. We refer the reader to Krumholz et al. (2018) for full details of the model, and here, we simply extract the portions that are relevant for this work.

Firstly, note that the angular velocity at r_0 is simply,

$$\Omega_0 = \frac{v_\phi}{r_0} \tag{6.20}$$

where v_ϕ is the rotational velocity of gas in the galactic disc. We can solve for the gas surface density Σ_g by requiring that the Toomre Q parameter for stars and gas is close to 1; formally, following Forbes et al. (2014a), we take $Q = Q_{\min}$, where $Q_{\min} \approx 1-2$ is the minimum Q parameter below which gravitational instability prevents discs from falling (e.g., Martin & Kennicutt 2001; Martin et al. 2002; Genzel et al. 2010; Meurer et al. 2013; Romeo & Falstad 2013; Inoue et al. 2016; Stott et al. 2016; Romeo & Mogotsi 2017). This can be re-written as (Krumholz et al. 2018,

equation 8),

$$Q_{\min} = f_{g,Q} \times Q_g \qquad (6.21)$$

where Q_g is the Toomre Q parameter for the gas alone, and $f_{g,Q}$ is the effective gas fraction in the disc (Krumholz et al. 2018, equation 9), which, based on the estimates of Σ_g (McKee et al. 2015) and gas velocity dispersion σ_g (Kalberla & Kerp 2009) is ≈ 0.5 in the Solar neighbourhood. Writing down the Toomre equation (Toomre 1964), this becomes,

$$f_{g,Q} \frac{\omega_c \sigma_g}{\pi G \Sigma_g} = Q_{\min}. \qquad (6.22)$$

Here, ω_c is the epicyclic frequency given by $\omega_c = \sqrt{2(\beta+1)}\,\Omega = \sqrt{2(\beta+1)}\,v_\phi/r$, where β is the index of the rotation curve given by $\beta = d\ln v_\phi/d\ln r$. Following Krumholz et al. (2018) and results from time-dependent numerical solutions for energy equilibrium in galactic discs (Forbes et al. 2014a), we can assume that in the steady-state, β and σ_g are independent of radius. Thus, we obtain

$$\Sigma_g = \frac{\sqrt{2(\beta+1)}\, f_{g,Q}\sigma_g v_\phi}{\pi G r Q_{\min}}. \qquad (6.23)$$

This solution provides a $1/r$ dependence for Σ_g that is somewhat at odds with observations that find an exponential dependence of Σ_g (Bigiel & Blitz 2012). However, these observations trace the entire disc (using CO as well as H I) and the Σ_g profiles show a large scatter in the inner disc, which is the focus of our work. Given these findings, we cannot conclude that a $1/r$ profile of Σ_g is unrealistic, and therefore continue to use it for our work. The quantities Σ_{g0} and $s_g(x)$ that we defined in Section 6.2.1 are thus given by

$$\Sigma_{g0} = \frac{\sqrt{2(\beta+1)}\, f_{g,Q}\sigma_g v_\phi}{\pi G r_0 Q_{\min}} \qquad (6.24)$$

$$s_g(x) = \frac{1}{x}. \qquad (6.25)$$

We can express the diffusion coefficient due to turbulent diffusion as $\kappa \approx h_g \sigma_g/3$, where h_g represents the gas scale height (Karlsson et al. 2013; Krumholz & Ting 2018) given by (Krumholz et al. 2018, equations 24 and 27),

$$h_g = \frac{\sigma_g^2}{\pi G \left(\Sigma_g + \left(\frac{\sigma_g}{\sigma_\star}\right)\Sigma_\star\right)} = \frac{\sigma_g^2}{\pi G \Sigma_g \phi_Q}, \qquad (6.26)$$

where $\Sigma_\star$ and $\sigma_\star$ is the stellar surface density and velocity dispersion, respectively,

and $\phi_Q - 1$ is the ratio of gas to stellar Toomre Q parameters. This gives

$$\kappa = \frac{\sigma_g^3}{3\pi G \Sigma_g \phi_Q} \tag{6.27}$$

Hence, the factors κ_0 and $k(x)$ that we defined in Section 6.2.1 are given by

$$\kappa_0 = \frac{Q_{\min} r_0 \sigma_g^2}{3 \phi_Q \sqrt{2(\beta+1)} f_{g,Q} v_\phi} \tag{6.28}$$

$$k(x) = x. \tag{6.29}$$

Thus, the product $\kappa_0 \Sigma_{g0} \propto \sigma_g^3 / G$ describes an effective metal flow rate in the disc due to diffusion.

To derive $\dot{\Sigma}_\star$, we can use equations 31 and 32 of Krumholz et al. (2018),

$$\dot{\Sigma}_\star = \frac{4 v_\phi f_{g,Q} \epsilon_{\rm ff} f_{\rm sf} \Sigma_g}{\pi r \sqrt{\frac{3 f_{g,P} \phi_{\rm mp}}{2(1+\beta)}}}, \tag{6.30}$$

where $\epsilon_{\rm ff}$ is the star formation efficiency per free-fall time (Krumholz & McKee 2005; Krumholz et al. 2012a; Federrath 2013b; Sharda et al. 2018, 2019b), $f_{\rm sf}$ is the fraction of gas in the cold, molecular phase that is not supported by thermal pressure, and thus forms stars (Krumholz et al. 2008, 2009b; Krumholz 2013), $f_{g,P}$ is the fraction of the mid-plane pressure due to self-gravity of the gas only, and not stars or dark matter (Krumholz et al. 2018), and $\phi_{\rm mp}$ is the ratio of the total to the turbulent pressure at the mid-plane. Following equation 6.30, we can derive $\dot{\Sigma}_{\star 0}$ and $\dot{s}_\star(x)$ as,

$$\dot{\Sigma}_{\star 0} = \frac{8(\beta+1) f_{g,Q}^2 \epsilon_{\rm ff} f_{\rm sf} \sigma_g v_\phi^2}{\pi^2 r_0^2 G Q_{\min} \sqrt{3 f_{g,P} \phi_{\rm mp}}} \tag{6.31}$$

$$\dot{s}_\star(x) = \frac{1}{x^2}. \tag{6.32}$$

Next, we consider the cosmic accretion of gas onto the disc. The functional form of $\dot{c}_\star(x)$ is not provided in the Krumholz et al. (2018) model. Within the framework of inside-out galaxy formation, $\dot{\Sigma}_{\rm cos}$ decreases with radius, as has been noted in several works (Chiappini et al. 1997, 2001; Fu et al. 2009; Courty et al. 2010; Forbes et al. 2014b; Pezzulli & Fraternali 2016; Mollá et al. 2016). In particular, we find from Colavitti et al. (2008, see their Figure 2) that $\dot{c}_\star \approx 1/x^2$ is necessary to reproduce the present day total surface mass density along the disc in the Milky Way. Additionally, a $1/x^2$ accretion profile is also identical to $\dot{s}_\star$, implying a direct correlation between star formation and accretion, as has been noticed in simulations (Davé et al. 2011).

Such a profile also means that more accretion is expected in more massive parts of the disc due to higher gravitational potential (Prantzos & Boissier 2000). Keeping these results in mind, we set $\dot{c}_\star(x) = 1/x^2$. However, we show in Appendix C.1 that changing the functional form of $\dot{c}_\star(x)$ has only modest effects on the qualitative results. Following Forbes et al. (2014a), we define

$$\dot{\Sigma}_{\cos 0} = \frac{\dot{M}_{\mathrm{h}} f_{\mathrm{B}} \epsilon_{\mathrm{in}}}{2\pi r_0^2 \int_{x_{\min}}^{x_{\max}} x \dot{c}_\star dx} \tag{6.33}$$

where $f_{\mathrm{B}} \approx 0.17$ is the universal baryonic fraction (White & Fabian 1995; Burkert et al. 2010; Planck Collaboration et al. 2016a), and ϵ_{in} is the baryonic accretion efficiency given by Forbes et al. (2014a, equation 22), which is based on cosmological simulations performed by Faucher-Giguère et al. (2011). $\dot{M}_{\mathrm{h}}$ is the dark matter accretion rate (Neistein & Dekel 2008; Bouché et al. 2010; Dekel et al. 2013) given by Krumholz et al. (2018, equation 65),

$$\dot{M}_{\mathrm{h}} \approx 39 \left(\frac{M_{\mathrm{h}}}{10^{12} \mathrm{M}_\odot} \right)^{1.1} (1+z)^{2.2} \ \mathrm{M}_\odot \, \mathrm{yr}^{-1}, \tag{6.34}$$

where the halo mass, M_{h}, can be written in terms of v_ϕ by assuming a Navarro et al. (1997) density profile for the halo as (Krumholz et al. 2018, equations 69 to 71),

$$\frac{M_{\mathrm{h}}}{10^{12} \mathrm{M}_\odot} = \left(\frac{v_\phi / \mathrm{km\,s}^{-1}}{76.17 \sqrt{\frac{c}{\ln(1+c) - c/(1+c)}}} \right)^3 (1+z)^{-3/2} \tag{6.35}$$

where c is the halo concentration parameter (Mo et al. 2010, section 7.5). It is now known that c scales inversely with halo mass (Macciò et al. 2007; Zhao et al. 2009; Dutton & Macciò 2014). For the purposes of this work, we simply adopt $c = 10$, 15 and 13 for local spirals, local dwarfs and high-z galaxies, respectively, rather than adopting more complex empirical relations (e.g., Forbes et al. 2019). Finally, note that the numerator in equation 6.33 is simply the baryonic accretion rate, $\dot{M}_{\mathrm{ext}}$.

The inflow rate required to maintain a steady state is given by the balance between radial transport, turbulent dissipation and star formation feedback (Krumholz et al. 2018, equation 49)

$$\dot{M} = \frac{4(1+\beta)\eta \phi_Q \phi_{\mathrm{nt}}^{3/2}}{(1-\beta)GQ_{\min}^2} f_{g,Q}^2 \sigma_g^3 \left(1 - \frac{\sigma_{\mathrm{sf}}}{\sigma_g} \right). \tag{6.36}$$

Here σ_{sf} is the gas velocity dispersion that can be maintained by star formation

feedback alone, η is the scaling factor for the rate of turbulent dissipation (Krumholz & Burkert 2010), and ϕ_{nt} is the fraction of gas velocity dispersion that is turbulent as opposed to thermal. While a cosmological equilibrium dictates that $\dot{M} \lesssim \dot{M}_{\mathrm{ext}}$ (and also $\dot{M}_\star \lesssim \dot{M}_{\mathrm{ext}}$, with the former being the star formation rate), it is unclear if these conditions in fact hold for observed galaxies at high redshift. We discuss this in detail in Appendix C.2, showing that these uncertainties do not affect our qualitative results on metallicity gradients.

Finally, we revisit the yield reduction factor ϕ_y that we introduced in equation 6.13. Both the mass loading factor μ and the direct metal ejection fraction ξ that are incorporated into ϕ_y are largely unknown (Creasey et al. 2013, 2015; Christensen et al. 2018). A number of authors have proposed models for μ (e.g., Creasey et al. 2013; Forbes et al. 2014b; Torrey et al. 2019; Tacchella et al. 2020), and it is believed to scale inversely with halo mass. However, there are no robust observational constraints, with current estimates ranging from 0 to 30 (Bouché et al. 2012; Newman et al. 2012; Kacprzak et al. 2014; Schroetter et al. 2015, 2019; Chisholm et al. 2017; Davies et al. 2019; Förster Schreiber et al. 2019; McQuinn et al. 2019). ξ is even less constrained by observations and theory, although observations and simulations suggest non-zero values in dwarf galaxies (e.g., Chisholm et al. 2018; Emerick et al. 2018b, 2019). For this reason we leave ϕ_y as a free parameter in the model and present solutions for metallicity evolution for a range of values. As we show in a companion paper (Sharda et al. 2021b), galaxies tend to prefer a particular value of ϕ_y based on their stellar mass, $M_\star$.

We list fiducial values of all the parameters used in the Krumholz et al. (2018) model in Table 6.1 and Table 6.2. Plugging in these parameters in equations $15-18$, we get,

$$\mathcal{T} = \frac{3\phi_Q \sqrt{2(\beta+1)} f_{g,Q}}{Q_{\min}} \left(\frac{v_\phi}{\sigma_g}\right)^2 \tag{6.37}$$

$$\mathcal{P} = \frac{6\eta \phi_Q^2 \phi_{\mathrm{nt}}^{3/2} f_{g,Q}^2}{Q_{\min}^2} \left(\frac{1+\beta}{1-\beta}\right) \left(1 - \frac{\sigma_{\mathrm{sf}}}{\sigma_g}\right) \tag{6.38}$$

$$\mathcal{S} = \frac{24\phi_Q f_{g,Q}^2 \epsilon_{\mathrm{ff}} f_{\mathrm{sf}}}{\pi Q_{\min} \sqrt{3 f_{g,P} \phi_{\mathrm{mp}}}} \left(\frac{\phi_y y}{Z_\odot}\right) (1+\beta) \left(\frac{v_\phi}{\sigma_g}\right)^2 \tag{6.39}$$

$$\mathcal{A} = \frac{3G\dot{M}_h f_{\mathrm{B}} \epsilon_{\mathrm{in}} \phi_Q}{2\sigma_g^3 \int_{x_{\min}}^{x_{\max}} x \dot{c}_\star dx} \tag{6.40}$$

where we have explicitly retained the dependence of the radial profile of cosmic accretion rate surface density in $\mathcal{A}$. Note that none of these ratios depend on r_0. Some of these parameters are dependent on other parameters: e.g., $\dot{M}_{\mathrm{h}}$ can be

expressed as a function of v_ϕ as is clear from equation 6.34 and equation 6.35.

6.2.3   Solution for the equilibrium metallicity

Now, we can combine the metallicity evolution model from Section 6.2.1 and the galactic disc model from Section 6.2.2 to obtain an analytic solution to equation 6.14 in steady-state ($\partial \mathcal{Z}/\partial \tau = 0$). The solution is

$$
\begin{aligned}
\mathcal{Z}(x) = \frac{\mathcal{S}}{\mathcal{A}} &+ c_1 x^{\frac{1}{2}\left[\sqrt{\mathcal{P}^2+4\mathcal{A}}-\mathcal{P}\right]} \\
&+ \left(\mathcal{Z}_{r_0} - \frac{\mathcal{S}}{\mathcal{A}} - c_1\right) x^{\frac{1}{2}\left[-\sqrt{\mathcal{P}^2+4\mathcal{A}}-\mathcal{P}\right]},
\end{aligned} \tag{6.41}
$$

where c_1 is a constant of integration and $\mathcal{Z}_{r_0} \equiv \mathcal{Z}(r = r_0)$. We remind the reader that $\mathcal{Z} = Z/Z_\odot$ and $x = r/r_0$ as we define in Section 6.2.1. In writing the above analytic solution, we have assumed that the metallicity at the inner edge of the disc (to which we shall hereafter refer as the central metallicity), $\mathcal{Z}_{r_0}$, is known. We show below (Section 6.3) that this approach is reasonable, because the solutions naturally tend toward a particular value of $\mathcal{Z}_{r_0}$. Thus, in practice, c_1 is the only unknown parameter in the solution. We also show later in Section 6.3 that c_1 can be expressed as a function of the metallicity gradient at r_0.

We now turn to constraining c_1. Firstly, note that $\mathcal{Z} > 0$ for all x. In practice, we ask that $\mathcal{Z} > \mathcal{Z}_{\min}$ for some fiducial $\mathcal{Z}_{\min} \approx 0.01$. For $x \gg 1$, this gives

$$
c_1 > \left(\mathcal{Z}_{\min} - \frac{\mathcal{S}}{\mathcal{A}}\right) x_{\max}^{-\frac{1}{2}\left[\sqrt{\mathcal{P}^2+4\mathcal{A}}-\mathcal{P}\right]}, \tag{6.42}
$$

where $x_{\max}$ is the outer radius of the disc at which we apply this condition[3]. Secondly, the total metal flux into the disc across the outer boundary cannot exceed that supplied by advection of gas with metallicity $\mathcal{Z}_{\mathrm{CGM}}$ into the disc, since otherwise this would imply the presence of a metal reservoir external to the disc that is supplying metals to it, which is only true in special circumstances, e.g., during or after a merger (Torrey et al. 2012; Hani et al. 2018), or due to long term wind recycling through strong galactic fountains (Grand et al. 2019). Mathematically, this condition can be written as

$$
- \underbrace{\frac{\dot{M}\mathcal{Z}}{2\pi x}}_{\text{adv. flux}} - \underbrace{\kappa\Sigma_g \frac{\partial \mathcal{Z}}{\partial x}}_{\text{diff. flux}} \geq - \underbrace{\frac{\dot{M}\mathcal{Z}_{\mathrm{CGM}}}{2\pi x}}_{\text{CGM flux}} . \tag{6.43}
$$

---

[3]The inequality is such that applying this condition at $x_{\max}$ ensures that it is also satisfied everywhere else in the disc.

For $x \gg 1$, this translates to,

$$c_1 \leq \frac{2\mathcal{P}\left(\mathcal{Z}_{\mathrm{CGM}} - \mathcal{S}/\mathcal{A}\right)}{\mathcal{P} + \sqrt{\mathcal{P}^2 + 4\mathcal{A}}} \, x_{\max}^{-\frac{1}{2}\left[\sqrt{\mathcal{P}^2 + 4\mathcal{A}} - \mathcal{P}\right]}, \tag{6.44}$$

Thus, we find that c_1 is bounded within a range dictated by the two conditions above. Given a value of c_1, we can also calculate the Σ_g-weighted and $\dot{\Sigma}_\star$-weighted mean metallicity in the model,

$$\overline{\mathcal{Z}}_{\Sigma_g} = \frac{\int_{x_{\min}}^{x_{\max}} 2\pi x \Sigma_{g0} s_g \mathcal{Z} dx}{\int_{x_{\min}}^{x_{\max}} 2\pi x \Sigma_{g0} s_g dx}, \tag{6.45}$$

$$\overline{\mathcal{Z}}_{\dot{\Sigma}_\star} = \frac{\int_{x_{\min}}^{x_{\max}} 2\pi x \dot{\Sigma}_{\star 0} \dot{s}_\star \mathcal{Z} dx}{\int_{x_{\min}}^{x_{\max}} 2\pi x \dot{\Sigma}_{\star 0} \dot{s}_\star dx}. \tag{6.46}$$

Finding $\overline{\mathcal{Z}}$ is helpful because we can use it to produce a mass-metallicity relation (MZR) that can serve as a sanity check for the model. We show in a companion paper that our model can indeed reproduce the MZR (Sharda et al. 2021b).

6.3 Equilibrium metallicity gradients

We apply our model to four different classes of galaxies: local spirals, local ultra-luminous infrared galaxies (ULIRGs), local dwarfs, and high-z galaxies. The fiducial dimensional parameters we adopt for each of these galaxy types are listed in Table 6.1 and Table 6.2. We remind the reader that the metallicity evolution model can only be applied to those galaxies where the metallicity gradient can reach equilibrium. This condition is approximately satisfied if $t_{\mathrm{eqbm}} < t_{\mathrm{H(z)}}$, where $t_{\mathrm{H(z)}}$ is the Hubble time at redshift z. We also compare t_{eqbm} with the molecular gas depletion timescale $t_{\mathrm{dep,H_2}}$, since we expect that $t_{\mathrm{dep,H_2}}$ controls the metal production timescale (hence, $\mathcal{S}$) and can potentially impact metallicity gradients. Thus, the metallicity gradients may also not be in equilibrium if $t_{\mathrm{eqbm}} \gg t_{\mathrm{dep,H_2}}$. An exception to this is for local ULIRGs, where we compare t_{eqbm} with t_{merge}, the merger timescale. This is because the dynamics of the galaxy (as dictated by its rotation curve and orbital time) are dictated by t_{merge} for local ULIRGs.

Before checking whether equilibrium is satisfied for each individual galaxy class, it is helpful to put our work in context. Considering galaxies' total metallicity (as opposed to metallicity gradient), Forbes et al. (2014b, see their Figure 15) predict that galaxies with halo masses $M_{\mathrm{h}} \geq 10^{10.5}\,\mathrm{M_\odot}$ (corresponding to $M_\star \geq 10^9\,\mathrm{M_\odot}$ – Moster et al. 2010, their Figure 4) reach equilibrium by $z \approx 2.5$. Feldmann (2015) use a linear stability analysis to show that the metal equilibration time is at most

of order the gas depletion time t_{dep}, which is small compared to $t_{\mathrm{H(z)}}$ for all massive main sequence galaxies. Similar arguments have been made by Davé et al. (2011, 2012) and Lilly et al. (2013) where the authors find that the metallicity attains equilibrium on very short timescales as compared to t_{dep}, and is thus in equilibrium both in the local and the high-z Universe. In contrast, Krumholz & Ting (2018) study metallicity fluctuations, and find that these attain equilibrium on an even shorter timescale, ~ 300 Myr. Our naive expectation is that equilibration times for metallicity gradients should be intermediate between those for total metallicity and those for local metallicity fluctuations, and thus should generally be in equilibrium. We show later in Section 6.5 that, while these expectations are in general satisfied, some galaxy classes, namely, local dwarfs with no radial inflow, local ULIRGs, and galaxies with inverted gradients, *can* be out of equilibrium. Thus, our model cannot be applied to these galaxies.

For the rest of the galaxies where the equilibrium model can be applied, we use the fiducial parameters that we list in Table 6.2, and solve the resulting differential equation to obtain $\mathcal{Z}(x)$, for different yield reduction factors. We list the resulting values of $\mathcal{T}$, $\mathcal{P}$, $\mathcal{S}$ and $\mathcal{A}$ for different galaxies in Table 6.3. To mimic the process followed in observations and simulations (e.g., Carton et al. 2018; Collacchioni et al. 2020) as well as existing models (e.g., Fu et al. 2009), we linearly fit the resulting metallicity profiles using least squares with equal weighting in logarithmic space

$$\log_{10} \mathcal{Z}\left(x\right) = \log_{10} \mathcal{Z}_{r_0} + x\nabla\left[\log_{10} \mathcal{Z}\left(x\right)\right], \tag{6.47}$$

between $x = 1$ and x_{max}, thereby excluding the innermost galactic disc where the rotation curve index is not constant, and where factors such as stellar bars can affect the central metallicity (Florido et al. 2012; Zurita et al. 2021). While it is clear from equation 6.41 that the functional form of $\mathcal{Z}$ is such that $\log_{10} \mathcal{Z}$ may not be a linear function of x in certain cases, we will continue to use the linear fit as above in order to compare with observations. We show in Appendix C.3 how the gradients change if we vary x_{min} or x_{max}. For each class of galaxy that we discuss in the subsections below, we plot a range of gradients that results from the constraints on the constant of integration c_1 (see Section 6.2.3), as well as the weighted mean metallicities, $\overline{\mathcal{Z}}_{\Sigma_g}$ and $\overline{\mathcal{Z}}_{\dot{\Sigma}_\star}$.

6.3.1   Local spirals

For local spirals, we select the outer boundary of the star-forming disc to be $15\,\mathrm{kpc}$, thus $x_{\mathrm{max}} = 15$, reminding the reader that $x = r/r_0$ where $r_0 = 1\,\mathrm{kpc}$. We first

Table 6.3: Resulting dimensionless ratios in different types of galaxies from the fiducial model based on the input parameters from Table 6.1 and Table 6.2.

Dimensionless Ratio	Description	Reference equations
$\mathcal{T}$	Ratio of orbital to diffusion timescales	equation 6
$\mathcal{P}$	Péclet number (ratio of advection and diffusion)	equation 6
$\mathcal{S}/\phi_y$	Ratio of metal production (incl. loss in outflows) and diffusion	equation 6
$\mathcal{A}$	Ratio of cosmic accretion and diffusion	equation 6
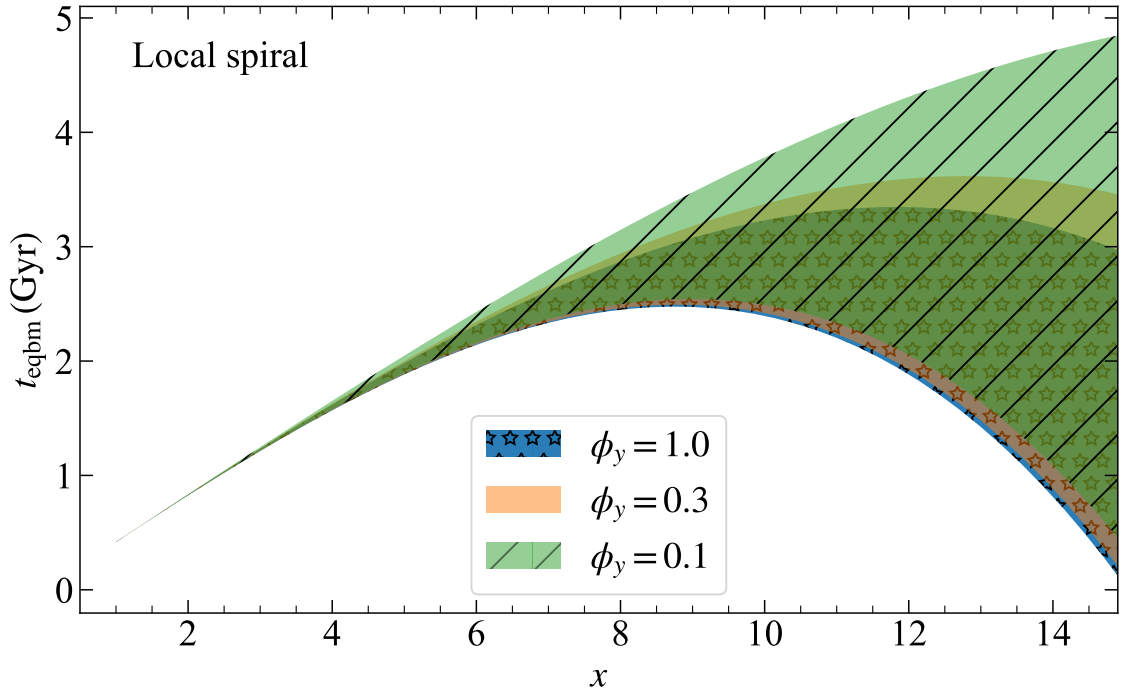
Figure 6.1: Metallicity equilibration time, t_{eqbm} plotted as a function of the dimensionless radius x for three different values of the yield reduction factor, ϕ_y, for a fiducial local spiral galaxy (see equation 6.19). Here, $x = r/r_0$, where $r_0 = 1\,\mathrm{kpc}$. The shaded bands correspond to solutions that cover all allowed values of the constant of integration c_1 in the solution to the metallicity equation (see Section 6.2.3). Since, t_{eqbm} is substantially smaller than the Hubble time $t_{\mathrm{H}(0)}$ and comparable to the molecular gas depletion time $t_{\mathrm{dep,H_2}}$, metallicity gradients in local spirals are in equilibrium.

study the metallicity equilibration time (t_{eqbm}) to see if metallicity gradients in these galaxies have attained equilibrium, so that the model can be applied to them. Figure 6.1 shows the value of t_{eqbm} we find from equation 6.19 as a function of x for local spirals for different values of the yield reduction factor, ϕ_y; the bands shown correspond to solutions covering all allowed values of the integration constant c_1. It is clear from Figure 6.1 that $t_{\mathrm{eqbm}} < t_{\mathrm{H}(0)}$ for all possible ϕ_y and c_1, so we conclude that the gradients in local spirals are in equilibrium. Additionally, $t_{\mathrm{eqbm}} \sim t_{\mathrm{dep,H_2}}$ for local spirals ($1 - 3\,\mathrm{Gyr}$, e.g., Wong & Blitz 2002; Bigiel et al. 2008; Saintonge et al. 2012; Leroy et al. 2013; Huang & Kauffmann 2014), implying that the metallicity distribution reaches equilibrium on timescales comparable to the molecular gas depletion timescale. The model also predicts that central regions of local spirals should achieve equilibrium earlier than the outskirts, however, this is somewhat sensitive to the choice of c_1 and ϕ_y as we can see from Figure 6.1 (see also, Figure 4 of Belfiore et al. 2019). Our equilibrium timescales are also consistent with our naive expectation as stated above: long compared to the timescale for local fluctuations to damp, but shorter than the time required for the total metallicity to reach equilibrium.

Figure 6.2 presents the family of radial metallicity distributions we obtain from the model for local spirals; the different lines correspond to varying choices of the outer boundary condition c_1, from the minimum to the maximum allowed. We report in the text annotations that accompany these curves the range of gas- and SFR-weighted mean metallicities $\overline{\mathcal{Z}}_{\Sigma_g}$ and $\overline{\mathcal{Z}}_{\dot{\Sigma}_\star}$, and metallicity gradients $\nabla(\log_{10} \mathcal{Z})$, spanned by the models shown. To aid in the interpretation of these results, in Figure 6.3 we also show the magnitudes of the various terms in the numerator on the right hand side of equation 6.19, which represent, respectively, the relative importance of advection, diffusion, metal production (reduced by metal ejection in outflows), and cosmological accretion in determining the metallicity gradient. We use this figure to read off which processes are dominant in different parts of the disc. While the source and the accretion terms fall off in the outermost regions due to the $1/x^2$ dependence, the advection and diffusion terms slightly increase with x, thereby resulting in a shorter metal equilibration time in the outermost regions as compared to intermediate regions, as we see in Figure 6.1. Thus, transport processes in the outer regions play an important role in establishing metal equilibrium in local spirals.

There are several noteworthy features in these plots. First, note how the solution asymptotically reaches a particular value of the central metallicity. We choose to set $\mathcal{Z}_{r_0}$ to this value, but we emphasise that the behaviour of the solution does

not depend on this choice except very close to $x = 1$: if we choose a different value of $\mathcal{Z}_{r_0}$, the solution is (by construction) forced to this value close to $x = 1$, but returns to the asymptotic limit for $x \gtrsim 1.1$. Indeed, we shall see that this is a generic feature for all of our cases: the limiting central metallicity is set by a balance between two dominant processes, and can be deduced analytically by equating the two dominant terms in equation 6.41. For the case of local spirals, the two dominant terms throughout the disc are production and accretion, as we can read off from Figure 6.3. The balance between these two processes gives

$$\mathcal{Z}_{r_0} = \frac{\mathcal{S}}{\mathcal{A}} \quad [\text{Local spirals}] . \tag{6.48}$$

This matches the conclusions of Finlator & Davé (2008) regarding the total metallicity. However, we show below in Section 6.3.2 that this conclusion holds only for local, massive galaxies, since other processes like metal transport also play a significant role in low mass galaxies as well as at high redshift. Using the above definition of $\mathcal{Z}_{r_0}$, we can now express c_1 in a more physically-meaningful way

$$c_1 = \frac{1}{\sqrt{\mathcal{P}^2 + 4\mathcal{A}}} \left. \frac{\partial \mathcal{Z}}{\partial x} \right|_{r=r_0} . \tag{6.49}$$

Thus, for local spirals, c_1 essentially describes the metallicity gradient at r_0.

Second, both the central metallicity $\mathcal{Z}_{r_0}$ and the mean metallicity $\overline{\mathcal{Z}}$ decrease with decreasing ϕ_y, as expected; we obtain mean metallicities close to Solar, as expected for massive local spirals, for ϕ_y fairly close to unity. Thus our models give reasonable total metallicities for local spirals if we assume that there is relatively little preferential ejection of metals, consistent with the results of recent simulations (Du et al. 2017; Tanner 2020; Taylor et al. 2020). Note that some semi-analytic models find a high metal ejection fraction for spirals, but self-consistently following the evolution of the CGM subsequently leads to high re-accretion of the ejected metals (Yates et al. 2020). In the language of our model, this essentially implies a high ϕ_y when averaging over the metal recycling timescale for local spirals, consistent with our expectations.

Third, and most importantly for our focus in this paper, the value of ϕ_y has little effect on the metallicity gradient, as is clear from the similar range of gradients produced by the model for different ϕ_y. Our models robustly predict a gradient $\nabla(\log_{10} \mathcal{Z}) \approx -0.07$ to 0 dex kpc^{-1}, in very good agreement with the range observed in local spirals (e.g., Zaritsky et al. 1994; Sánchez et al. 2014; Ho et al. 2015; Sánchez-Menguiano et al. 2016; Belfiore et al. 2017; Erroz-Ferrer et al. 2019;

Mingozzi et al. 2020), and within the range provided by existing simpler models of metallicity gradients (Chiappini et al. 2001; Fu et al. 2009).

Apart from the mean gradient, we can also study the detailed shape of the metal distribution with the model. For the given input parameters as in Table 6.2, the model features a nearly-flat metal distribution in the inner galaxy for all allowed values of c_1. Such flat gradients in the inner regions are commonly observed in local spirals (Moran et al. 2012; Belfiore et al. 2017; Mingozzi et al. 2020), and have been attributed to metallicity reaching saturation in these regions (Zinchenko et al. 2016; Maiolino & Mannucci 2019), although the flatness depends on the metallicity calibration used (Yates et al. 2020, Figure 4). This is also the case for our models of spirals, since the flat region corresponds to the part of the disc where the metallicity is set by the balance between metal injection and dilution by metal-poor infall (c.f. Figure 6.3). For comparison, we also show in Figure 6.2 the measured average metallicity profiles in local spirals observed in the MaNGA survey (Belfiore et al. 2017) using two different metallicity calibrations (Pettini & Pagel 2004; Maiolino et al. 2008), where we have adjusted the overall metallicity normalisation by 0.02 dex so that the model profiles overlap with the data. We see that the profiles produced by the model are in reasonable agreement with that seen in the observations (see also, Sánchez-Menguiano et al. 2018).

Several works have also noted that local spirals with higher gas fractions (at fixed mass) show steeper metallicity gradients (Carton et al. 2015; De Vis et al. 2019; Pace et al. 2020). In the language of the Krumholz et al. (2018) model, a higher gas fraction implies a higher value of $f_{g,Q}$ and $f_{g,P}$. Increasing these parameters leads to an increase in the source term $\mathcal{S}$, which gives rise to steeper metallicity gradients in the model, consistent with the above observations. Moreover, a higher gas fraction (*i.e.*, higher $f_{g,Q}$ and $f_{g,P}$) also results in a rather steep metallicity profile in the inner disc, thus giving slightly lower metallicities in the inner disc as compared to the fiducial case above, consistent with the standard picture of galaxy chemical evolution (Tinsley 1972, 1973; see also, Pace et al. 2020).

It is difficult to provide robust predictions for the metal distribution in the outer parts of the galaxy without further constraining c_1. The outer-galaxy metal distribution in the model is also sensitive to parameters like the galaxy size and the CGM metallicity. The result of these uncertainties is that depending on the choice of c_1, the model can produce both nearly-flat and quite steep metal distributions in the outer parts of the galaxy. A steep drop in the metallicity in the outer disc has been observed in several local spirals (Moran et al. 2012), but is dependent on the metallicity calibration used (Carton et al. 2015). In our models, this region corresponds to

where cosmological accretion of metal-poor gas onto the disc becomes less important than inward advection of metal-poor gas through the disc – a process whose rate we would expect to be correlated with the available mass supply in the far outer disc, as measured by H I. Note that the gradient can also flatten again in the outermost regions in the disc (Werk et al. 2011; Sánchez et al. 2014; Sánchez-Menguiano et al. 2016; Bresolin 2019); however, these regions typically have insufficient spatial resolution (Acharyya et al. 2020) as well as significant diffused ionised gas emission, both of which can cause the gradients to appear flatter than their true values (Kewley et al. 2019b, Section 6). Given the uncertainties in the model as well as observations of metallicities in the outer discs in spirals, it is not yet obvious if the metal distribution in the outer disc in the model can be validated against the available observations. Thus, we do not study these regions with our model. This analysis also shows that linear fits to the metallicity profiles is a crude approximation to the true underlying metallicity distribution in local spiral galaxies.

6.3.2 Local dwarfs

Our model can also be applied to local dwarf galaxies that can be classified as rotation-dominated, e.g., the Large Magellanic Cloud (LMC), for which $v_\phi \sim 60\,\mathrm{km\,s^{-1}}$ and $\sigma_g \sim 7\,\mathrm{km\,s^{-1}}$ (Alves & Nelson 2000). Such galaxies typically lie at the massive end of dwarfs ($M_{\star,\mathrm{LMC}} = 2 \times 10^9\,\mathrm{M_\odot}$, as reported in van der Marel 2006; Skibba et al. 2012), and possess an equilibrium gas disc to which the unified galaxy evolution model of Krumholz et al. (2018) can be applied. We set the outer disc radius to 6 kpc to find the gradient in the fiducial model, in line with the estimated gas disc size of local dwarfs ($r_{\mathrm{LMC}} \sim 4.3\,\mathrm{kpc}$, Westerlund 1990).

Figure 6.4 shows the metal equilibration time, t_{eqbm}, for local dwarfs based on the parameters we list in Table 6.1 and Table 6.2. It is clear that metallicity gradients are in equilibrium in dwarfs, since $t_{\mathrm{eqbm}} < t_{\mathrm{H}(0)}$ as in the case of local spirals (see, however, Section 6.5.2 where we show that this may not be the case under certain circumstances). Contrary to local spirals, local dwarfs show a wide range of $t_{\mathrm{dep,H_2}}$, from a few hundred Myr to several Gyr (e.g., Bolatto et al. 2011; Bothwell et al. 2014; Hunt et al. 2015; Jameson et al. 2016; Schruba et al. 2017), similar to the scatter we find in t_{eqbm} (see also, Section 6.5.2)[4].

---

[4]While it is often quoted that $t_{\mathrm{dep,H_2}}$ is smaller by a factor of $2-5$ in local dwarfs as compared to local spirals, Schruba et al. (2017) point out that this may not necessarily be true. This is because it is difficult to trace the entire molecular gas content in dwarfs, and a significant fraction of the molecular gas can be 'CO-faint' or 'CO-dark' (Bolatto et al. 2011; Jameson et al. 2018), or in quiescent molecular clouds that are not targeted in observations (Schruba et al. 2010; Kruijssen & Longmore 2014).
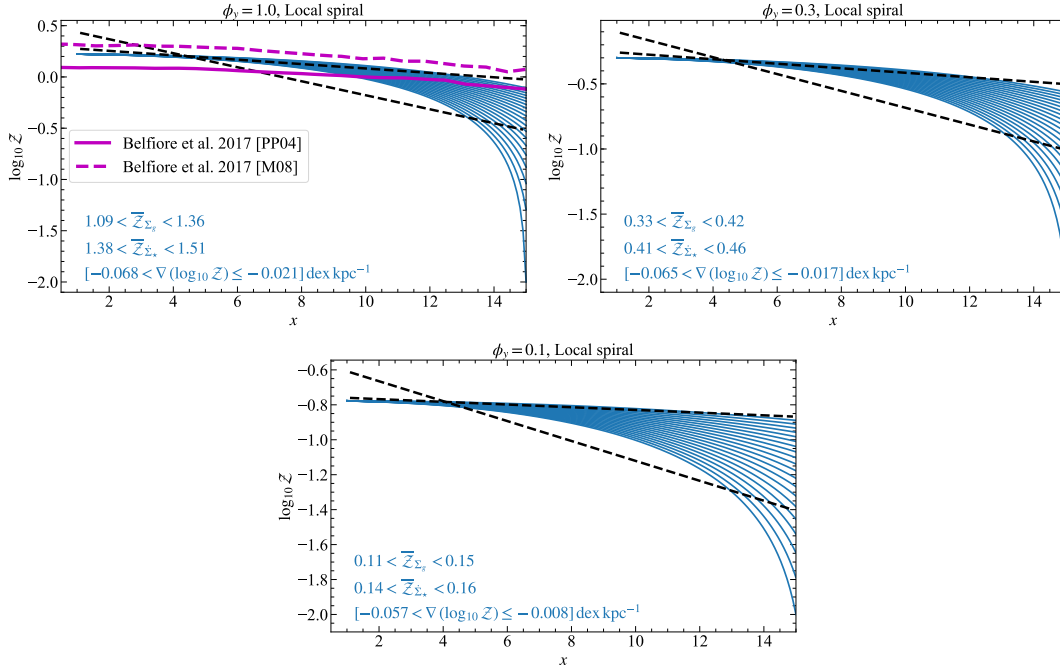
Figure 6.2: Metallicity ($\mathcal{Z} = Z/Z_\odot$; blue lines) as a function of dimensionless radius ($x = r/r_0$ with $r_0 = 1\,\mathrm{kpc}$) produced by the model for a fiducial local spiral galaxy with input parameters listed in Table 6.1 and Table 6.2, for different values of the yield reduction factor, ϕ_y. The analytic solution to the metallicity evolution equation is given by equation 6.41. The slope of the linear fit to the model gradients between $x = 1 - 15$ (black, dashed lines) gives the metallicity gradient that can be compared against simulations and observations. The blue coloured curves show the acceptable parameter space of the gradients based on the constraints on the constant of integration, c_1, using the boundary conditions criteria described in Section 6.2.3. The metallicity at the inner edge of the disc (referred to as the central metallicity in the text), $\mathcal{Z}_{r_0}$, is set by the balance between source and accretion for local spirals (see equation 6.48). $\overline{\mathcal{Z}}_{\Sigma_g}$ and $\overline{\mathcal{Z}}_{\dot{\Sigma}_\star}$ represent the range of mass-weighted and SFR-weighted mean equilibrium metallicities produced by the solution, respectively (see equation 6.46). We expect ϕ_y closer to unity for local spirals, implying that metals in these galaxies are well-mixed with the ISM before they are ejected. Finally, in the top panel we overplot the average metallicity profiles observed in local spirals in the MaNGA survey by Belfiore et al. (2017) using the PP04 (Pettini & Pagel 2004) and M08 (Maiolino et al. 2008) calibrations, adjusting the normalisation to overlap with the model profiles.
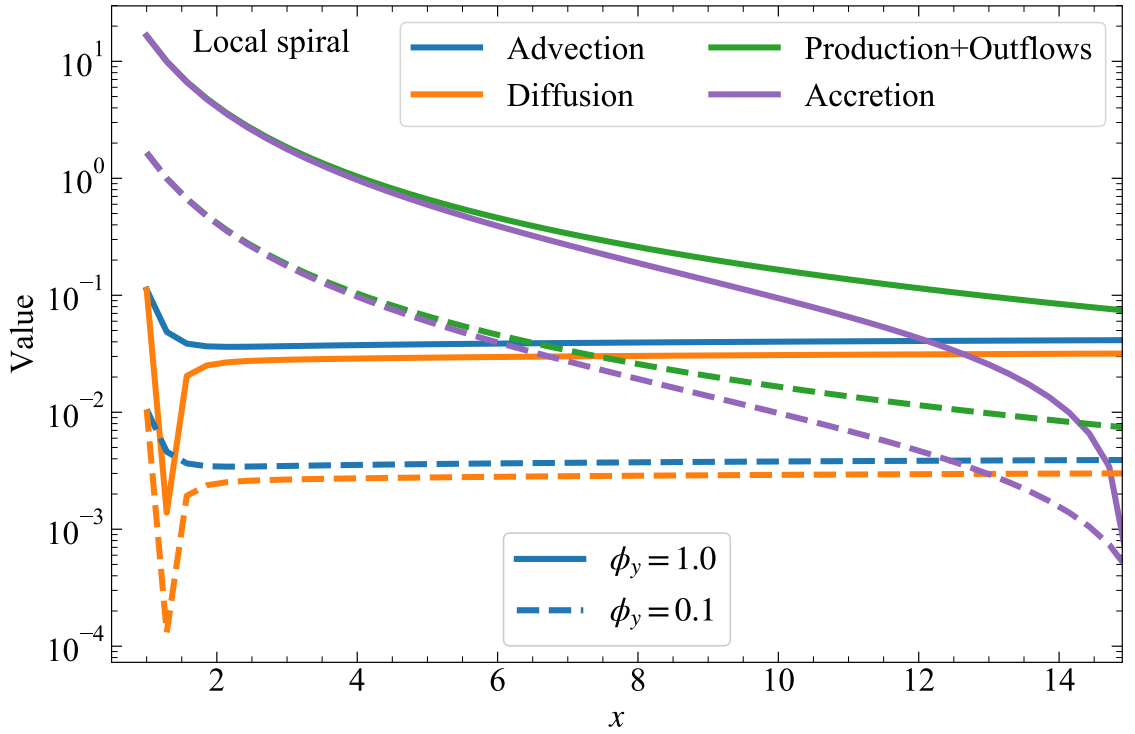
Figure 6.3: Absolute values of different terms in the numerator of equation 6.19 that collectively build the metallicity gradient in local spirals, for a fixed $\mathcal{Z}_{\text{CGM}} = 0.1$ and fixed c_1 for different yield reduction factors, ϕ_y. These terms are defined in equation 6.14. The leading terms that set the gradients in local spirals are metal production and accretion of gas onto the galaxy, whereas advection and diffusion play a subdominant role in local spirals, due to the small velocity dispersion, σ_g. Note that the sharp feature in the diffusion term near $x = 1.3$ corresponds to the location where this term passes through zero as it changes sign; the term in fact behaves smoothly everywhere, but this behaviour appears as a sharp feature when plotted on a logarithmic axis.

Having established metal equilibrium in local dwarfs, we can now study the gradients produced by the model. Figure 6.5 shows the resulting metallicity versus radius for different ϕ_y (analogous to Figure 6.2), and Figure 6.6 shows the relative importance of the various processes (analogous to Figure 6.3).

In the case of local dwarfs, we see that $\mathcal{Z}_{r_0}$ is set by the balance between advection and diffusion, giving

$$\mathcal{Z}_{r_0} = \frac{\mathcal{S}}{\mathcal{A}} + c_1 \left(1 + \frac{\sqrt{\mathcal{P}^2 + 4\mathcal{A}} - \mathcal{P}^2 - \mathcal{A}}{\sqrt{\mathcal{P}^2 + 4\mathcal{A}} + \mathcal{P}^2 + \mathcal{A}}\right) \quad [\text{Local dwarfs}] . \tag{6.50}$$

Using the above definition of $\mathcal{Z}_{r_0}$, we can express c_1 as

$$c_1 = \frac{\sqrt{\mathcal{P}^2 + 4\mathcal{A}} + \mathcal{P}^2 + \mathcal{A}}{[\mathcal{A} + (\mathcal{P} - 1)\,\mathcal{P}]\,\sqrt{\mathcal{P}^2 + 4\mathcal{A}}}\,\left.\frac{\partial \mathcal{Z}}{\partial x}\right|_{r=r_0}. \tag{6.51}$$

Central metallicities are in the range $\mathcal{Z}_{r_0} \approx 0.2 - 0.6$ depending on the choice of ϕ_y, in good agreement with that observed in local dwarfs, e.g., in the SMC and the LMC (Russell & Dopita 1992; Westerlund 1997), and M82 (Origlia et al. 2004). While $\mathcal{Z}_{r_0}$ depends only on $\mathcal{S}/\mathcal{A}$ in local spirals, it also depends on the choice of c_1 for local dwarfs, implying that it is independent of the disc properties in the former case but not in the latter.[5] Similarly, mean metallicities range from $\overline{\mathcal{Z}} \sim 0.1 - 0.5$ as ϕ_y varies from $\approx 0.1 - 1$; both observations (Martin et al. 2002; Strickland & Heckman 2009a; Chisholm et al. 2018) and numerical simulations (Emerick et al. 2018b, 2019) suggest that dwarfs suffer considerable direct metal loss, so ϕ_y considerably smaller than unity seems likely.

As opposed to spirals, our models predict that gradients are not necessarily flat in the inner regions of dwarfs, which is also consistent with observations (Belfiore et al. 2017; Mingozzi et al. 2020). The reason for this difference is due to different physical processes dominating in the two types of galaxies: accretion versus metal production in spirals, and advection versus production in dwarfs. Consequently, we predict linear gradients for local dwarfs that are steeper than the ones for local spirals at fixed ϕ_y and c_1. For the smaller values of ϕ_y expected in local dwarfs, we expect gradients in the range ~ -0.01 to $-0.15\,\mathrm{dex\,kpc^{-1}}$, implying a larger scatter in the gradients measured in local dwarfs as compared to that in local spirals, consistent with observations (Mingozzi et al. 2020, Figure 12). The metallicity profiles produced by the model for smaller values of ϕ_y are also in agreement with that observed in the MaNGA survey (Belfiore et al. 2017), as we show in Figure 6.5, where we have adjusted the overall metallicity normalization by 0.15 dex to facilitate a comparison of the data and the model profiles. Further, the larger range of gradients in low mass local galaxies as compared to massive galaxies allowed within the framework of our model is also relevant and necessary for reproducing the observed steepening of gradients with decreasing galaxy mass (Bresolin 2019, Figure 10).

Although this is not illustrated in Figure 6.5, we also find that the magnitude of the

---

[5]This dependence is also behind the sharp rise and fall near $x = 1$ seen in both the diffusion term and the metallicity profile. For the purposes of plotting, we have chosen a single value of c_1, which in turn forces all models to converge to a single $\mathcal{Z}_{r_0}$. While we could correct this by choosing different values of c_1 for different models so that they remain smooth, since the sharp feature does not affect the metallicity gradient that is our main focus in this paper, we choose for reasons of simplicity to retain the fixed c_1.
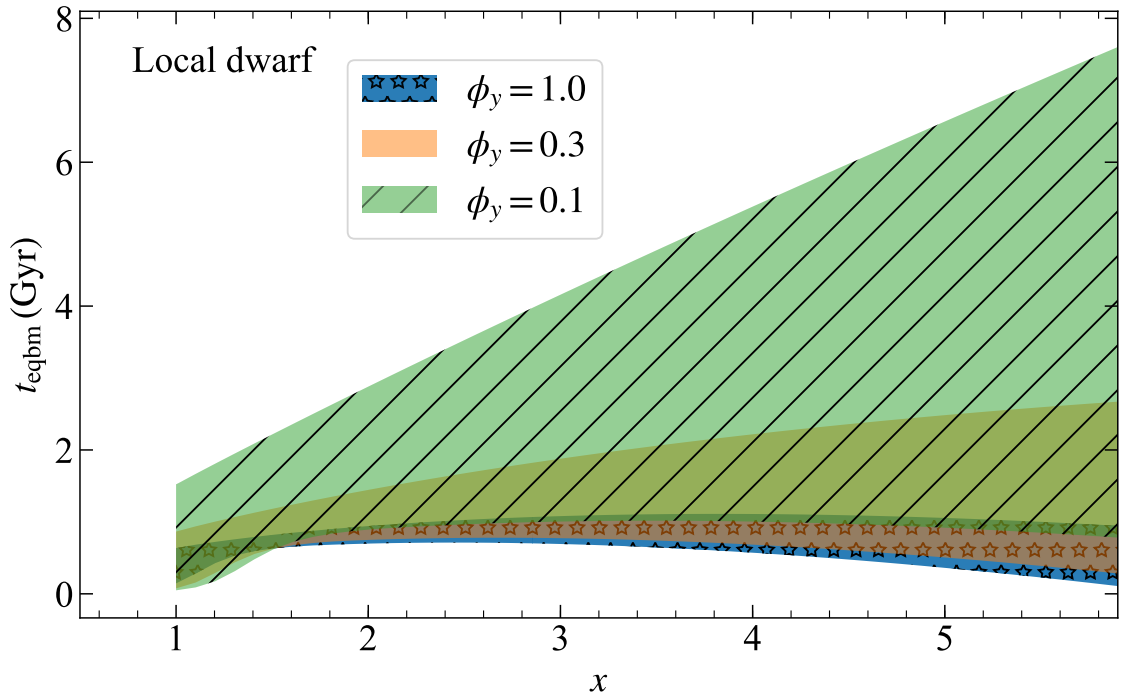
Figure 6.4: Same as Figure 6.1, but for local dwarfs. Here, $t_{\mathrm{eqbm}} < t_{\mathrm{H}(0)}$, implying that the metallicity gradients in local dwarfs are also in equilibrium, even in the case of low ϕ_y (see the text for a discussion on $t_{\mathrm{dep,H_2}}$ for local dwarfs). The corresponding metallicity gradients are plotted in Figure 6.5.

gradient is quite sensitive to both the "floor" velocity dispersion supplied by star formation, σ_{sf}, and the Toomre Q parameter, since these two jointly set the strength of advection and in this case, $\sigma_{\mathrm{sf}} \sim \sigma_g$. Thus, we expect that gradients for local dwarfs will show more scatter than those for local spirals. It is interesting to note that there is a similarly large scatter in simulations of dwarf galaxies, with some groups (e.g., Tissera et al. 2016) finding steeper gradients for dwarfs as compared to spirals whereas others (e.g. Ma et al. 2017) finding the opposite. This difference between the simulations has been attributed to the strength of feedback, which, in the language of our model, corresponds to variations in σ_{sf} and ϕ_y; thus the sensitivity of our model is at least qualitatively consistent with the strong dependence of feedback strength observed in simulations.

6.3.3   High-redshift galaxies

Massive galaxies at high-z are primarily rotation-dominated with underlying disc-like structures (Weiner et al. 2006; Förster Schreiber et al. 2009, 2018; Wisnioski et al. 2011, 2015, 2019; Wuyts et al. 2011; Di Teodoro et al. 2016; Simons et al. 2017; Übler et al. 2019). Thus, we can apply the model to these galaxies. For high-z
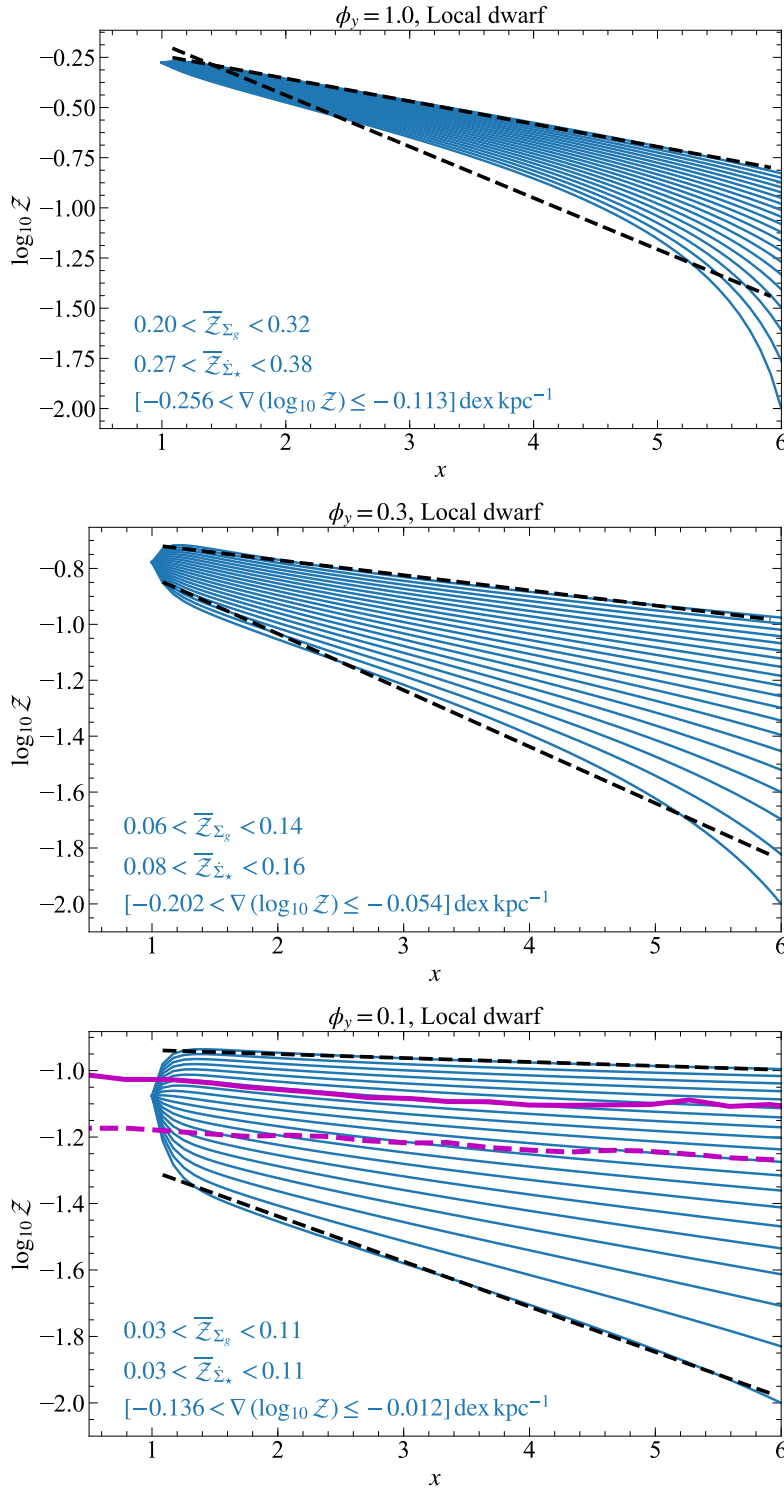
Figure 6.5: Same as Figure 6.2, but for local dwarfs. Here, $\mathcal{Z}_{r_0}$ is set by the balance between advection and diffusion, whereas metallicities in the disc are set by the balance between advection and source. The sharp rise and fall in the profile at $x = 1$ is an artefact of the choice of the constant of integration c_1 used to calculate $\mathcal{Z}_{r_0}$ (see equation 6.51). The gradients are particularly sensitive to the strength of advection for local dwarfs since turbulence due to star formation feedback is comparable to that due to gravity, $\sigma_{\rm sf} \sim \sigma_g$. When they are exactly equal, advection vanishes, and the gradients may not be in equilibrium (see Section 6.5.2). In the last panel we also plot (purple lines) the average metallicity profiles observed in local dwarfs in the MaNGA survey; see Figure 6.2.
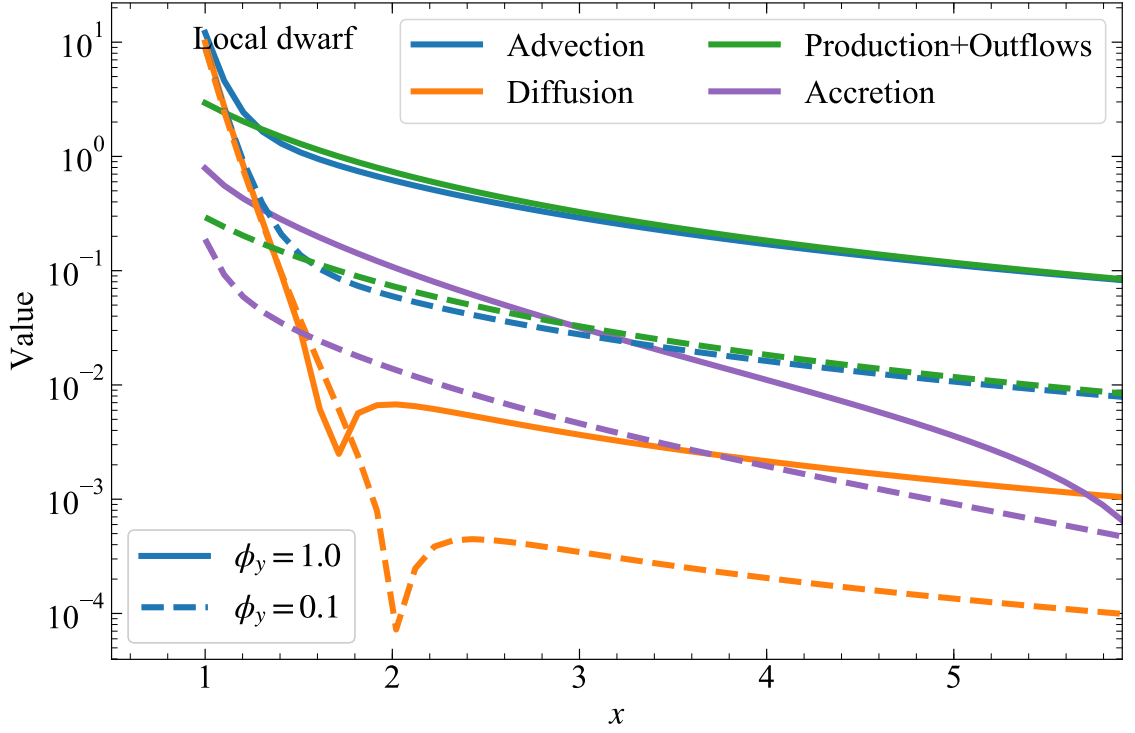
Figure 6.6: Same as Figure 6.3, but for local dwarfs. The dominant terms that set the gradients in local dwarfs are advection and diffusion (in the inner disc) and source and advection (in the outer disc).

galaxies, we set the outer disc radius to $10\,\mathrm{kpc}$ to find the gradient in the fiducial model, acknowledging that galaxies at higher redshifts are smaller than that in the local Universe (e.g., Queyrel et al. 2012; van der Wel et al. 2014). Hereafter, we work with $z = 2$ as a fiducial redshift. Figure 6.7 shows the metal equilibration time for high-z galaxies. It is clear that $t_{\mathrm{eqbm}} < t_{\mathrm{H}(z)}$, so that the equilibrium solution can be applied to these galaxies. Following Tacconi et al. (2018, 2020a), if we assume that a main sequence high-z galaxy follows $t_{\mathrm{dep,H_2}} \propto (1+z)^{-0.6}$, it implies that $t_{\mathrm{dep,H_2}} \sim 0.5 - 1.5\,\mathrm{Gyr}$ for high-z galaxies, which is comparable with t_{eqbm} as above.

Figure 6.8 shows the equilibrium metallicity distributions we obtain for a fiducial high-z galaxy with parameters listed in Table 6.1 and Table 6.2, and Figure 6.9 shows our usual diagnostic diagram comparing the importance of different processes. Examining this diagram near $x = 1$, it is clear that, as is the case for local dwarfs, the central metallicity $\mathcal{Z}_{r_0}$ is set by the balance between advection and diffusion, which gives

$$\mathcal{Z}_{r_0} = \frac{\mathcal{S}}{\mathcal{A}} + c_1 \left(1 + \frac{\sqrt{\mathcal{P}^2 + 4\mathcal{A}} - \mathcal{P}^2 - \mathcal{A}}{\sqrt{\mathcal{P}^2 + 4\mathcal{A}} + \mathcal{P}^2 + \mathcal{A}} \right) \quad [\mathrm{High} - z]\ . \qquad (6.52)$$
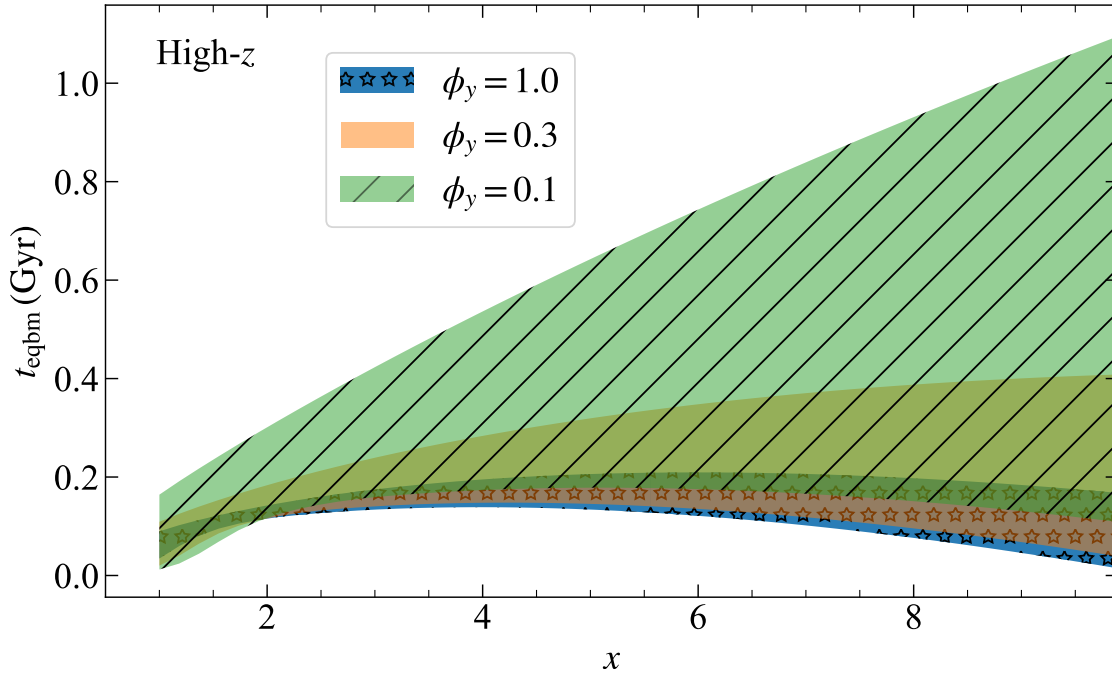
Figure 6.7: Same as Figure 6.1, but for high-z galaxies. The corresponding equilibrium metallicity gradients are plotted in Figure 6.8.

It varies between $\mathcal{Z}_{r_0} = 0.3$–0.7 depending on the value of ϕ_y, in good agreement with observed metallicities in high-z galaxies in the mass range we consider (Erb et al. 2006; Yabe et al. 2012), with c_1 same as that in equation 6.51. While the absolute metallicity depends on ϕ_y, the metallicity gradients for the most part do not – we find $\nabla(\log_{10} \mathcal{Z}) \approx -0.15$ to -0.05 dex kpc^{-1}, with order-of-magnitude variations in ϕ_y only altering these values by a few hundredths.

The gradients we find for high-z galaxies are steeper than for local spirals, and the distributions are steeper at small radii than at larger radii, the opposite of our finding for local spirals. Figure 6.9 shows why this is the case: gradients over most of the radial extent of high-z galaxies are set by the balance between source and advection, whereas accretion, which dilutes the gradients in local spirals, is sub-dominant. The fundamental reason for this change is due to the vastly higher velocity dispersions of high-z galaxies, which increase the importance of the advection term ($\mathcal{P} \propto (1 - \sigma_{\mathrm{sf}}/\sigma_g)$) while suppressing the accretion term ($\mathcal{A} \propto \sigma_g^{-3}$); this effect is partly diluted by the higher accretion rates found at high-z (equation 6.34), but the net change at high redshift is nonetheless toward a smaller role for accretion onto discs and a larger role for transport through them. We discuss this further in detail in Section 6.4.
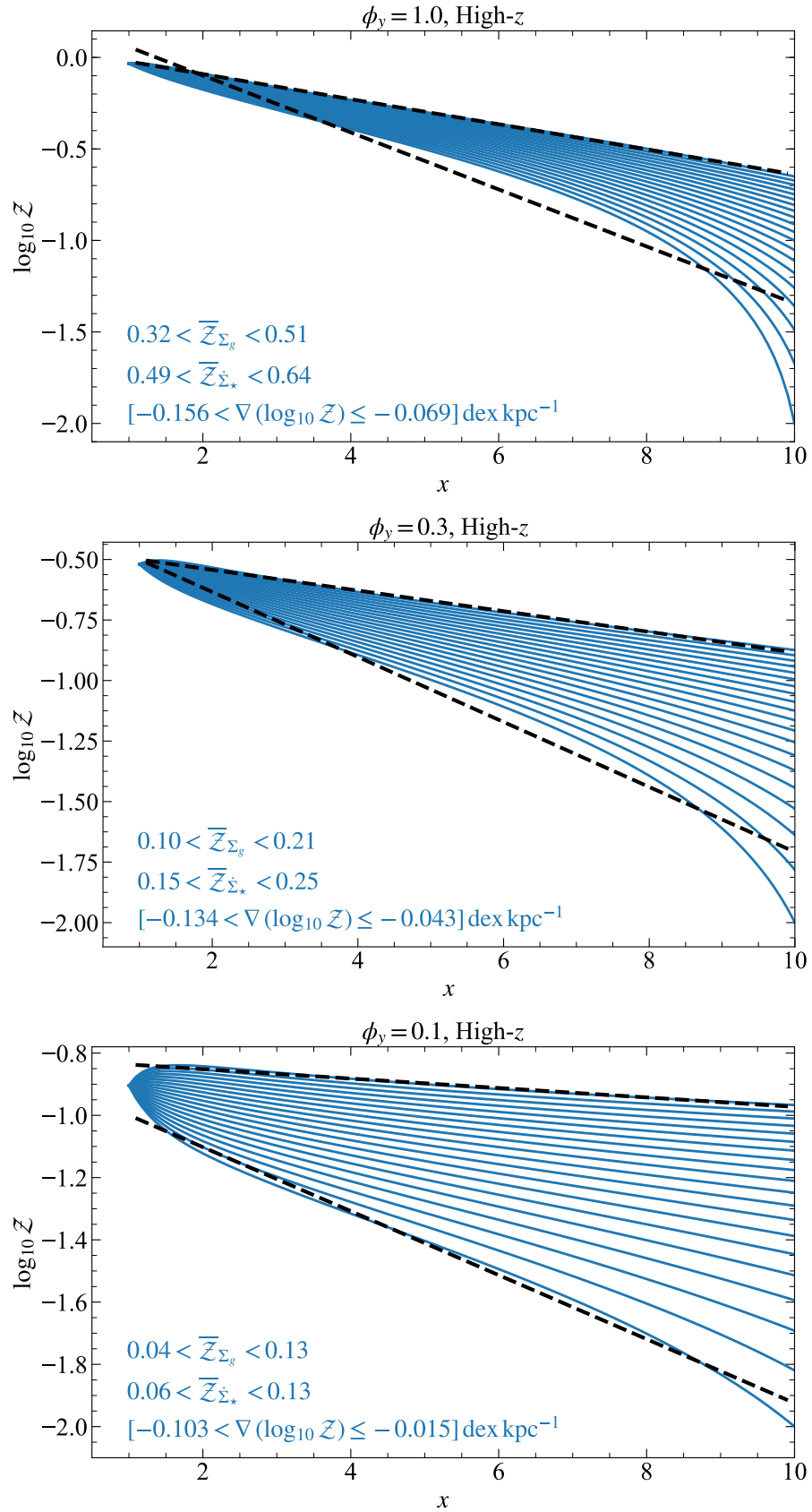
Figure 6.8: Same as Figure 6.2, but for high-z galaxies. Here, $\mathcal{Z}_{r_0}$ is set by the balance between diffusion and advection.
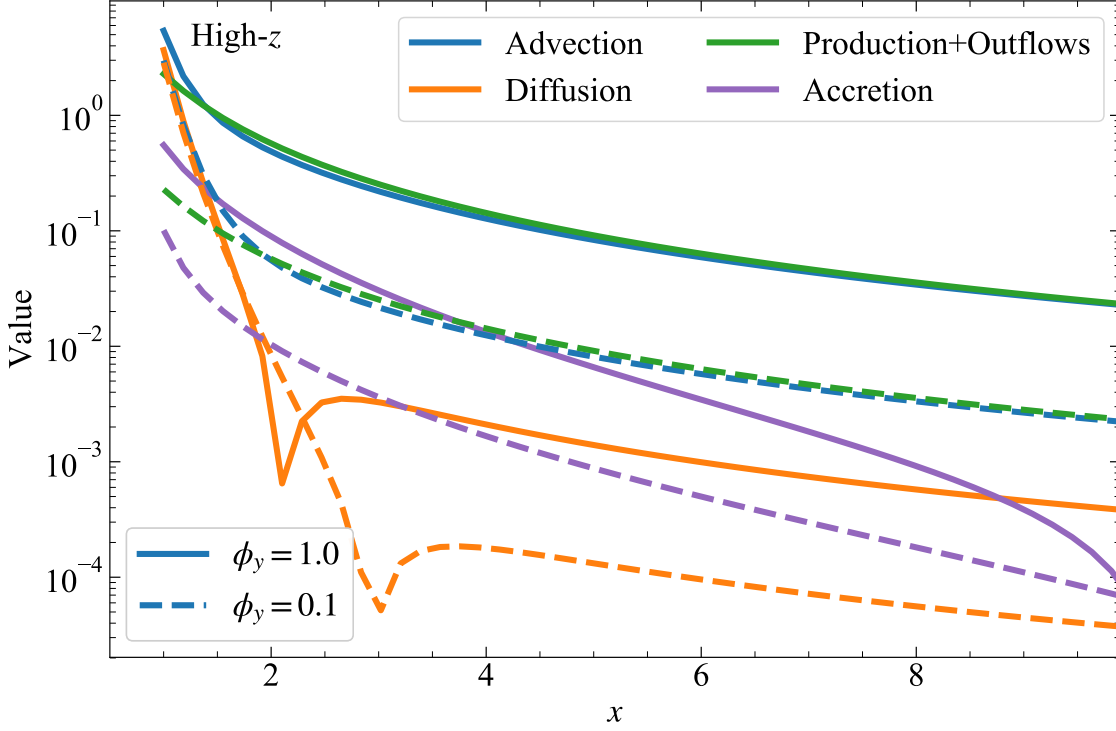
Figure 6.9: Same as Figure 6.3, but for high-z galaxies. Here, the metallicities in the disc are set by the balance between source and advection, due to efficient radial transport of the gas.

6.4   Cosmic evolution of metallicity gradients

A significant advantage of our model compared to previous analytic efforts, is that it makes meaningful predictions for how galaxy metallicity gradients have evolved across cosmic time. This is the case because we do not have the freedom to adjust parameters such as radial inflow rates and profiles of star formation rate to match any given observed galaxy. Instead, these parameters are either prescribed directly from our galaxy evolution model or depend on parameters that are directly observable (e.g., galaxy velocity dispersions). The basic inputs to our model are the halo mass M_{h} and the gas velocity dispersion σ_g as a function of z. We consider three different ways of selecting galaxies that yield different tracks of $M_h(z)$ (see below for details), while we take the evolution of $\sigma_g(z)$ from the observed correlation obtained by Wisnioski et al. (2015, see their equation 8)[6]

$$\sigma_g(z) = \frac{v_\phi(z) f_{\mathrm{gas}}(z)}{\sqrt{2\left(\beta+1\right)}}, \tag{6.53}$$

---

[6]As opposed to Wisnioski et al. (2015), we have explicitly retained the dependence of $\sigma_g(z)$ on β.

where f_{gas} is the molecular gas fraction of the galaxy (Genzel et al. 2011; Genel et al. 2012; Tacconi et al. 2013; Genzel et al. 2015; Faucher-Giguère 2018). This scaling is subject to considerable observational uncertainty, the implications of which we explore in Appendix C.2. We follow Wisnioski et al. (2015) to find f_{gas} as a function of $M_{\star}$ and z from Tacconi et al. (2013) and Whitaker et al. (2014), as it is now known that f_{gas} decreases with cosmic time and stellar mass (Leroy et al. 2008; Saintonge et al. 2011; Geach et al. 2011; Davé et al. 2012; Tacconi et al. 2013, 2018; Morokuma-Matsui & Baba 2015; Isbell et al. 2018). We note that Wisnioski et al.'s sample is limited to massive galaxies ($M_{\star} > 10^{10}\,\text{M}_{\odot}$), and there are no observations available for lower-mass galaxies. For this reason we instead follow the results of the IllustrisTNG simulations to obtain $\sigma_g(z)$ (Pillepich et al. 2019, see their Figure 12a) for stellar masses below $10^{10}\,\text{M}_{\odot}$. Finally, note that all the gradients we produce from the model in this section are in equilibrium across the redshifts we use, since $t_{\text{eqbm}} < t_{\text{H(z)}}$.

6.4.1 Trends for a Milky Way-like galaxy across redshift

We first study how the gradient in a Milky Way-like galaxy has evolved over time using our model. We only need one parameter to begin with: v_{ϕ} at $z = 0$. We set this to $220\,\text{km}\,\text{s}^{-1}$ (Bland-Hawthorn & Gerhard 2016). Then, we use equation 6.35 to calculate $M_{\text{h}}(z = 0)$ for a fixed $c = 15$. Using $M_{\text{h}}(z = 0)$ as boundary condition, we integrate equation 6.34 to find $M_{\text{h}}(z)$, keeping in mind that this equation represents an average evolution of $M_{\text{h}}(z)$ that may not necessarily apply to the Milky Way. Then, we utilize $M_{\text{h}}(z)$ to find $v_{\phi}(z)$, by changing the concentration parameter (c) as an empirical third-order polynomial fit, following Zhao et al. (2009). This ensures that as we change z, we self-consistently find M_{h} and v_{ϕ}. We adopt a simple linear variation for the outer edge of the star-forming disc, x_{max}, as a function of z such that it is 15 at $z = 0$ and 10 at $z = 2$. Similarly, we vary f_{sf} between 0.5 and 1 across redshift, keeping in mind that f_{sf} cannot be more than 1 at any redshift. For simplicity, we fix the other parameters as follows: $\beta = 0$, $f_{g,Q} = f_{g,P} = 0.5$, $\sigma_{\text{sf}} = 7\,\text{km}\,\text{s}^{-1}$, $Q_{\text{min}} = 1.5$ and $\mathcal{Z}_{\text{CGM}} = 0.1$.

We show the resulting evolution of the gradient in Figure 6.10. The model predicts a steepening of the gradient in Milky Way-like galaxies over time, with the exception of a very recent flattening, between $z \approx 0.15$ and 0. We can understand these trends in terms of the dimensionless parameters $\mathcal{S}$, $\mathcal{P}$, and $\mathcal{A}$ that describe the relative importance of *in situ* metal production, radial advection, and cosmological accretion with diffusion, respectively. The source term $\mathcal{S}$ will always make the gradients steeper because of the steep radial profile of $\dot{\Sigma}_{\star}$, and it is either $\mathcal{P}$ or $\mathcal{A}$

that balances $\mathcal{S}$ to give rise to flatter gradients. The steepest gradients at $z \approx 0.15$ correspond to when both $\mathcal{P}$ and $\mathcal{A}$ are at their weakest compared to $\mathcal{S}$. We can understand the trends on either side of this maximum in turn.

First, let us focus on the recent epoch, $z \lesssim 0.15$. During this period, cosmological accretion ($\mathcal{A}$) is more important than radial transport ($\mathcal{P}$), and accretion and metal production depend on the galaxy rotational velocity as $\mathcal{A} \propto v_\phi^{3.3}$ and $\mathcal{S} \propto v_\phi^2$, respectively. Thus, as the galaxy grows in mass, dilution by accretion gets stronger compared to metal production, leading to the recent flattening in the model. However, this can change if the metal production is underestimated, e.g., due to ignoring the contribution from long-term wind recycling (Leitner & Kravtsov 2011).

During this epoch advection is more important than accretion, $\mathcal{P} > \mathcal{A}$. The ratio of the two effects, $\mathcal{P}/\mathcal{A}$, is large at high redshift, and decreases systematically towards the present day, ultimately reaching $\mathcal{P}/\mathcal{A} \approx 1$ at $z \approx 0.15$. This transition is ultimately driven by the systematic decrease in galaxy velocity dispersions with redshift, as already discussed in the context of our high-z galaxy models (Section 6.3.3): higher velocity dispersions are strongly correlated with higher rates of radial inflow through a galaxy, so that for a Milky Way progenitor at $z \gtrsim 1$, radial inflow transports metal-poor gas into galaxy centres $\sim 10\times$ faster than cosmological accretion ($\mathcal{P}/\mathcal{A} \approx 10$) – despite the fact that the absolute accretion rate is higher at $z \gtrsim 1$ than it is today. Similarly, the ratio of radial inflow to metal production, $\mathcal{P}/\mathcal{S}$, scales with velocity dispersion as σ_g^2 (for $\sigma_g \gg \sigma_{\rm sf}$), so radial inflow also becomes more important relative to metal production as we go to higher redshift and higher velocity dispersion. This explains the flatness of gradients at high redshift[7]. This transition from radial advection being dominant to being unimportant is mirrored in the transition from gravity-driven to star formation feedback-driven turbulence from high- to low-z (Krumholz et al. 2018), as we noted earlier in Section 6.3.3.

Lastly, we find that diffusion is sub-dominant compared to both advection and accretion at all cosmological epochs, because $\mathcal{P}$ and $\mathcal{A}$ are never both less than unity at the same time. Thus, while diffusion can have some effects on the metallicity distributions, particularly towards galaxy centres (cf. Figure 6.6), as well as on metal equilibrium timescales (cf. Figure 6.1), it is generally unimportant for setting galaxy metallicity gradients.

---

[7]Note that this is a qualitatively different outcome than our comparison of local spirals and high-z galaxies in Section 6.3.1 and Section 6.3.3, where high-z galaxies were found to have steeper gradients. The difference can be understood by recalling that in Section 6.3.1 and Section 6.3.3 we were comparing galaxies with comparable rotation curve speeds v_ϕ, whereas here we are following a single growing galaxy, so v_ϕ is much smaller at high-z than at $z = 0$. This reduces $\mathcal{S}$ at high-z.

Comparison with observations

There is extensive data on the history of the Galaxy's metallicity gradient, as summarised by Mollá et al. (2019, see their Table 1), and on the history of the gradients in a number of other nearby galaxies. The general outcome of these studies is that gradients measured in H II regions (which trace the current-day metal distribution) are steeper than those measured in planetary nebulae or open clusters (which trace older populations) (Stanghellini & Haywood 2010; Stanghellini et al. 2010, 2014; Sanders et al. 2012; Stasińska et al. 2013; Magrini et al. 2016). This implies a steepening of the gradient with time in Milky Way-like galaxies, however, this should be treated with caution because measured metallicity gradients in the Galaxy are subject to large errors arising from uncertainties in estimating the ages of the planetary nebulae (Maciel et al. 2010; Cavichia et al. 2011), and due to radial migration that could result in a movement of the planetary nebulae away from their origin (Minchev et al. 2013)[8].

To allow a quantitative comparison of these observations with our model, we show measurements of the metallicity gradient for the Milky Way as a function of lookback time from Stanghellini et al. (2010) as yellow circles in Figure 6.10. The data for the Milky Way (as well as other local spirals, see Stanghellini et al. 2014) are in qualitative agreement with the predictions from our model. However, we also note that for our model to agree *quantitatively* with the measurements, we would need ϕ_y to be lower at high redshift, and increase towards unity today. Such a change in ϕ_y is plausible and is consistent with our expectation that ϕ_y should be close to unity in more massive galaxies like the present-day Milky Way, and smaller than unity in less massive galaxies with shallower potential wells, such as the Milky Way's high-z progenitors. However, the exact form of this evolution is not independently predicted by our model.

Comparison with simulations

On Figure 6.10, we also overplot results from Feedback In Realistic Environments (FIRE) simulations (Hopkins et al. 2014, 2018) of a Milky Way-like galaxy (m12i) discussed in Ma et al. (2017). This simulation finds that metallicity gradients are unstable until $z \sim 1$, after which they steepen and stabilise to an equilibrium value. This transition is primarily due to the formation of a robust galactic disc that can-

---

[8]Some earlier work reported the opposite trend, whereby the metallicity gradient in the Galaxy was initially steep and has flattened over time (Maciel et al. 2003; Mollá & Díaz 2005), while other work found little or no evolution in the gradient over time (Maciel & Costa 2013). This is a difficult measurement, and the error bars and uncertainties are large (Maciel et al. 2010; Cavichia et al. 2011; Minchev et al. 2013).

not be disrupted again due to internal or external feedback. While the quantitative trends slightly differ at some redshifts between our model and the simulation, which is not unexpected given that the exact implementation of the feedback and measurements of the gradients are different, there is a very good qualitative match. This match also implies that Milky Way-like galaxies would have had lower ϕ_y in the past as compared to the present day, as outflows were more common and stronger in the past due to higher SFR and could have ejected a larger fraction of metals not mixed with the ISM (Muratov et al. 2015; Ma et al. 2017); such a scenario has received support from recent high-resolution simulations that spatially resolve multi-phase galactic outflows, and find that the metal enrichment factor in both the cold ($< 2 \times 10^4 \, \mathrm{K}$) and hot ($> 5 \times 10^5 \, \mathrm{K}$) outflows increases with the SFR surface density (Kim et al. 2020). We can also compare our results with those of Gibson et al. (2013), where the authors study two identical simulation suites with either weak or enhanced stellar feedback, called MUGS and MaGICC, respectively (Stinson et al. 2010). The authors find that gas phase metallicity gradients are steep at high redshift in MUGS, whereas they are flat in MaGICC, clearly revealing the close correlation between feedback and metallicity gradients in galaxies. One of their simulated galaxies, MaGICC g1536, resembles the Milky Way in terms of its stellar mass, so we also compare our model results to that simulation in Figure 6.10. Again, we find qualitative similarities between the simulations and the model.

6.4.2   Trends for matched stellar mass galaxies across redshift

In this section, we study the mass-averaged trends of metallicity gradients across cosmic time. For this purpose, we use a compilation of observations of metallicity gradients in (lensed and un-lensed) galaxies spanning $0 \leq z \leq 2.5$ (Queyrel et al. 2012; Swinbank et al. 2012; Stott et al. 2014; Leethochawalit et al. 2016; Wuyts et al. 2016; Molina et al. 2017; Carton et al. 2018; Förster Schreiber et al. 2018; Wang et al. 2020b; Curti et al. 2020b), and we also include results from local surveys (Sánchez et al. 2014; Sánchez-Menguiano et al. 2016; Belfiore et al. 2017; Mingozzi et al. 2020; Acharyya et al. 2021).

Before proceeding, we warn the reader that there are many uncertainties inherent in comparing metallicity gradients across samples and across cosmic time. For example, most studies in the compiled dataset rely on strong line calibrations that use photoionisation models or electron temperature-based empirical relations to measure metallicity gradients, and the variations between different calibrations can be as high as 0.1 dex per effective half-light radius (Moustakas et al. 2010; Poetrodjojo
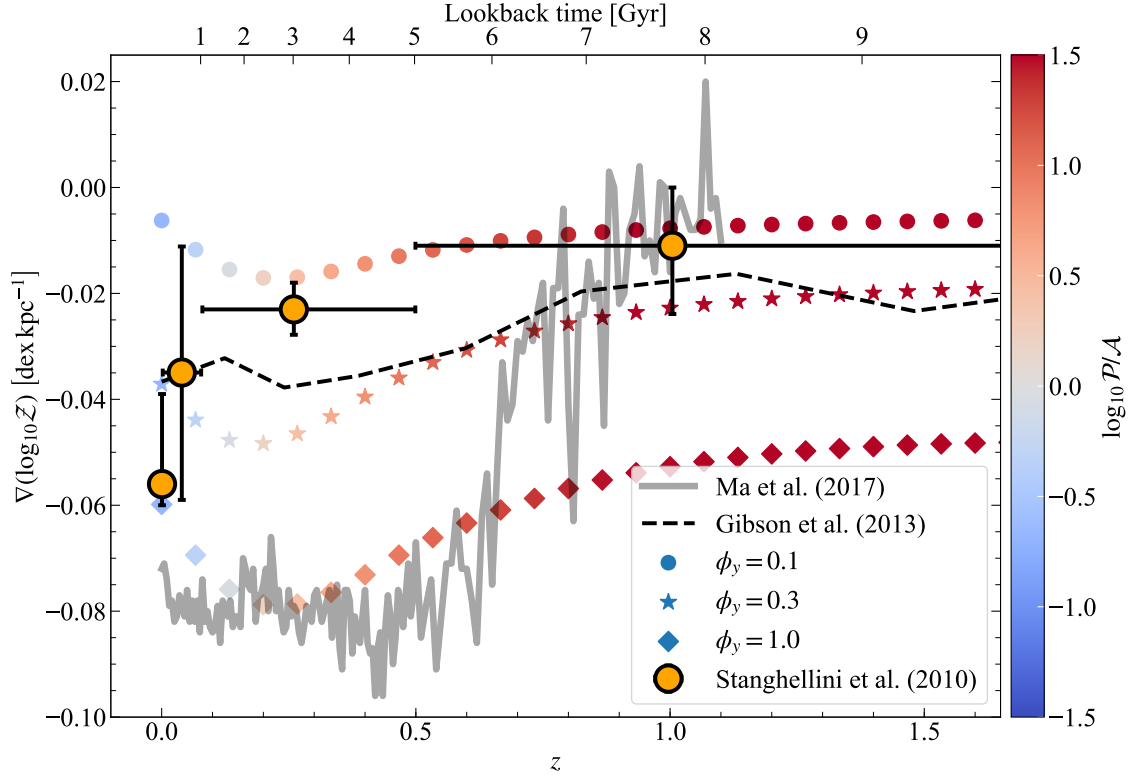
Figure 6.10: Metallicity gradient versus redshift (and lookback time) for a Milky Way-like galaxy. Different symbols show different yield reduction factors, ϕ_y, while symbol colour shows the ratio of the dimensionless numbers $\mathcal{P}/\mathcal{A}$ that describe the relative importance of radial transport and cosmological accretion, respectively. The grey curve is taken from FIRE simulations of a Milky Way-like galaxy (Ma et al. 2017) whereas the dashed, black curve is from the MaGICC g1536 simulation by Gibson et al. (2013). The orange points are from observations of H II regions, planetary nebulae and open clusters by Stanghellini & Haywood (2010), with horizontal errorbars representing the uncertainties in the ages of planetary nebulae and open clusters. The data, simulations and the model all qualitatively show that gradients in Milky Way-like galaxies have steepened over time, with the model predicting a mild flattening between $z = 0.15$ and present-day. In the model, this evolution is driven by a transition from the advection-dominated regime ($\mathcal{P}/\mathcal{A} > 1$) to the accretion-dominated regime ($\mathcal{P}/\mathcal{A} < 1$) around $z \approx 0.15$. Such a transition in metallicity gradients is mirrored in the transition in gravity-driven turbulence at high z to star formation feedback-driven turbulence at $z = 0$ (Krumholz et al. 2018).
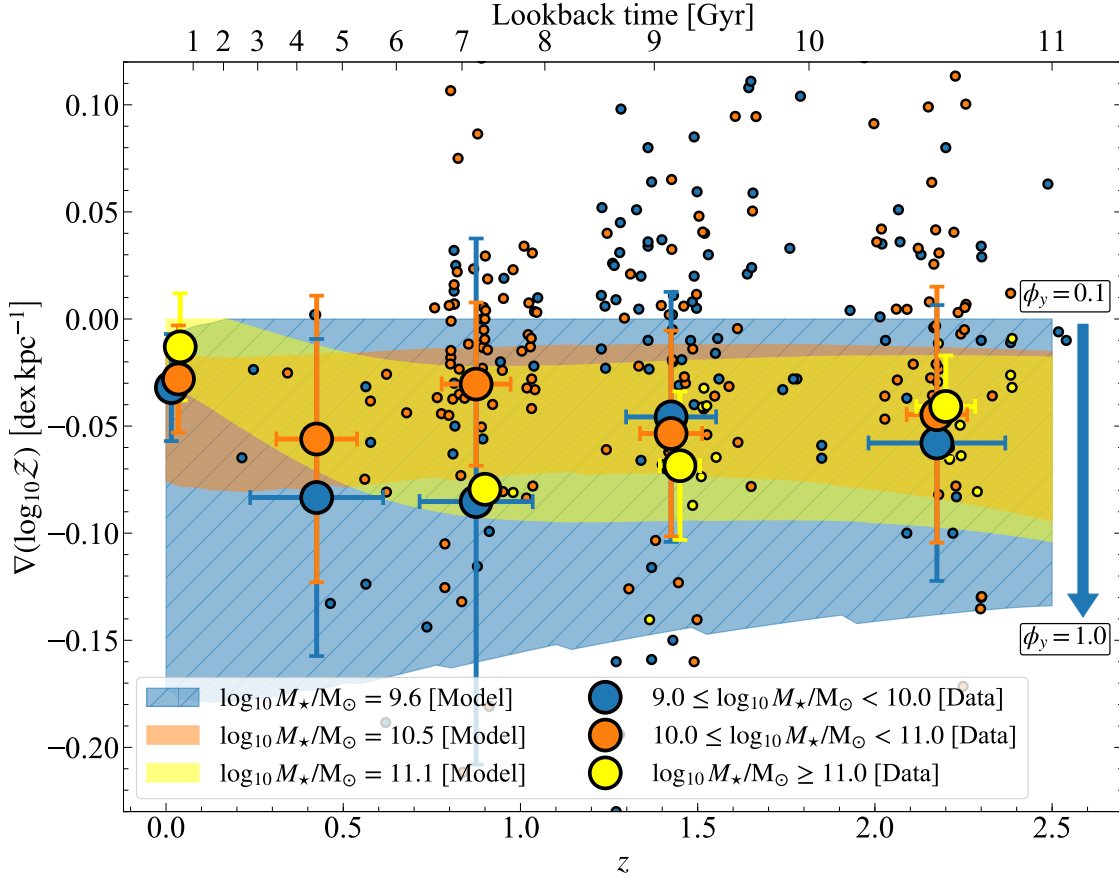
Figure 6.11: Trends in metallicity gradients as a function of redshift and lookback time. Colored markers represent individual galaxies within the three $M_\star$ bins as shown in the legend, with bigger markers representing binned averages of non-positive gradients across different redshift bins, and errorbars representing the scatter in the data within each redshift bin. The averages at $z = 0$ are taken from local surveys (Sánchez et al. 2014; Sánchez-Menguiano et al. 2016; Belfiore et al. 2017; Mingozzi et al. 2020). The high-redshift compilation data is taken from Queyrel et al. (2012); Swinbank et al. (2012); Stott et al. (2014); Leethochawalit et al. (2016); Wuyts et al. (2016); Molina et al. (2017); Carton et al. (2018); Förster Schreiber et al. (2018); Wang et al. (2020b); Curti et al. (2020b), and is inhomogeneous, with systematic issues within the different measurements (see Section 6.4.2). The colored bands represent models at three $M_\star$ values, with the spread resulting from different yield reduction factors ϕ_y, as marked by the arrow besides the shaded region. This spread in the model is largest for the low mass galaxies. While the general trend of mild evolution of gradients across redshift holds true, the models uncover the underlying variations due to galaxies transitioning from advection- to accretion-dominated regimes between $z = 2.5$ and 0, as is visible in the binned data averages. Some data points lie outside the range of the plot, and we do not include those for the purposes of studying the average trends of the data with the model.

et al. 2019, 2021c; Mingozzi et al. 2020). Further, since many high-z metallicity gradient measurements rely on nitrogen whereas low-z measurements use a larger set of (optical) emission lines, we also expect some systematic differences in these measurements with redshift (Carton et al. 2018; Kewley et al. 2019b). Using nitrogen can also lead to systematically flatter gradients due to different scalings of N/O with O/H in galaxy centres and outskirts (Schaefer et al. 2020). Lastly, it is not yet clear if strong line metallicity calibrations developed for the ISM properties of local galaxies are also applicable at high-z, where ISM electron densities, ionisation parameters, N/O ratios, or other conditions may differ from those in local galaxies (e.g., Shirazi et al. 2014; Sanders et al. 2016; Onodera et al. 2016; Kashino et al. 2017; Kaasinen et al. 2017; Kewley et al. 2019a; Davies et al. 2020). We acknowledge these biases and uncertainties in the measured sample due to different techniques and calibrations or the lack of spatial and/or spectral resolution (Yuan et al. 2013; Mast et al. 2014; Carton et al. 2017; Acharyya et al. 2020). We do not attempt to correct for these effects or homogenize the sample because our goal here is simply to get a qualitative interpretation of the data with the help of the model, and not to obtain precise measurements from these data. Future facilities like JWST and ELTs will provide more reliable metallicity measurements, thereby enabling a more robust comparison of the model with the data (Bunker et al. 2020).

We bin the data into three bins of $M_\star$: $9 \leq \log_{10} M_\star/\mathrm{M}_\odot < 10$, $10 \leq \log_{10} M_\star/\mathrm{M}_\odot < 11$ and $\log_{10} M_\star/\mathrm{M}_\odot \geq 11$. Figure 6.11 shows the individual data as well as the binned averages of non-positive gradients (represented by bigger markers) with errorbars representing the scatter in the data within different redshift bins. We only select galaxies that show non-positive gradients while estimating the average gradient in different mass bins because our model may not apply to galaxies with positive gradients, as we explore in Section 6.5.2. We bin the data in redshift such that we can avoid redshifts where there is no data due to atmospheric absorption; such a bin selection in redshift also ensures that the binned averages reflect the true underlying sample for which the averages are calculated. We have verified that our results are not sensitive to the choice of binning the data. For simplicity, we do not overplot measurements for individual galaxies at $z = 0$.

For the model, we select three representative $M_\star$ values corresponding to the mean of the three stellar mass data bins as above. Specifically, we use: $\log_{10} M_\star/\mathrm{M}_\odot = 9.6$, 10.4 and $11.1\,\mathrm{M}_\odot$ for the model. We start the calculation by selecting rotation curve speeds $v_\phi(z)$ corresponding to each of these $M_\star$ values based on the $M_\star - M_\mathrm{h}$ relation at all z (Moster et al. 2013). Given values of $M_h(z)$ and $v_\phi(z)$ corresponding to each stellar mass $M_\star$ at each redshift z, we use our model to predict the

equilibrium metallicity gradient exactly as in Section 6.4.1.

We plot the resulting range of metallicity gradients from the model points in Figure 6.11. As in other figures, the spread in the model represents different ϕ_y between 0 and 1 (note the arrow besides the shaded regions corresponding to the models). While there is a large scatter within the individual data points, the binned averages are in good agreement with the model. Note that almost one-third of the observed galaxies show inverted gradients, which may not be in metal equilibrium and thus may fall outside the domain of our model, as we explore in detail in Section 6.5.2. For the most massive galaxies, the model predicts a mild steepening of the gradients from $z = 2.5$ to 1, followed by an upturn (due to the transition from advection- to accretion-dominated regime) and flattening from $z = 1$ to 0. The available data, despite the large scatter and inhomogeneties, also seem to follow the same trend. However, the location where this upturn occurs is unknown because of the lack of data in the most massive galaxy bin around $z = 0.5$. Upcoming large surveys like MAGPI (Foster et al. 2020) that will observe massive galaxies between $z \approx 0.3 - 0.5$ will provide crucial data that can be compared against our model in the future to establish whether this upturn is indeed real.

Additionally, we can compare our results with those from the IllustrisTNG50 simulation (Hemler et al. 2021, Figure 6). While our results match theirs at low redshifts, there are certain differences at high redshifts where IlustrisTNG50 fails to reproduce the observed flattening, as already noted by the corresponding authors. We explain in a companion paper (Sharda et al. 2021f) that this difference could primarily be due to the gas velocity dispersion $\sigma_g(z)$. At high redshift, IllustrisTNG50 systematically under-predicts galaxy velocity dispersions as compared to, for example, the EAGLE simulations (Pillepich et al. 2019, Figure 12a), and the empirical relation we use from Wisnioski et al. (2015).

There is a large diversity of gradients at all redshifts (Curti et al. 2020b), particularly at low stellar mass. This observed scatter can be explained in part due to the range of ϕ_y in our model. For example, we notice from Figure 6.11 that the scatter in the model due to ϕ_y for the most massive galaxies is lower at low z than at high z. This is consistent with the trend of larger scatter in the gradients of massive galaxies at higher redshift observed in the IllutrisTNG50 simulations (Hemler et al. 2021, Figure 6). On the other hand, the scatter in the model is the largest near the upturn, where galaxies transition from advection-dominated to accretion-dominated regime. Between the three models, the scatter due to ϕ_y is the highest for the lowest $M_\star$, thus reflecting the diverse variety of gradients that can form in low-mass galaxies. This prediction of the model is consistent with observations that find strong evidence
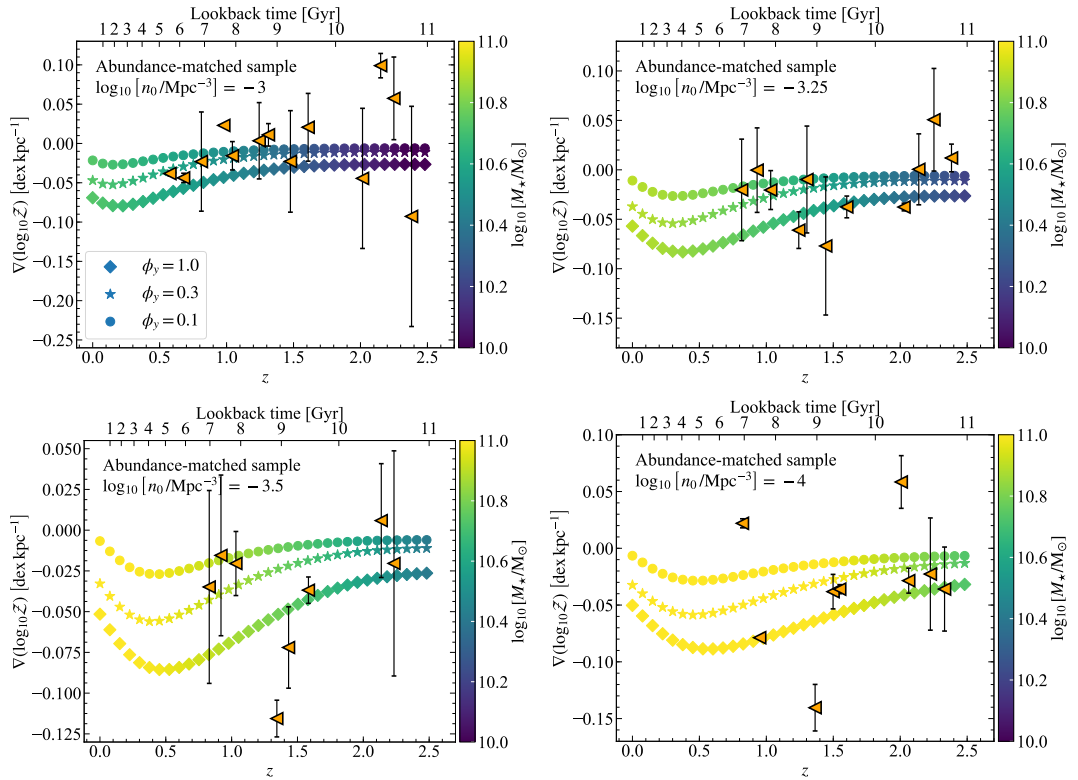
Figure 6.12: Trends in metallicity gradients as a function of z (and lookback time) for four different abundance-matched galaxy samples given a fixed comoving number density of galaxies, n_0, color-coded by $M_\star$. Abundance matching leads to the selection of more massive galaxies at lower redshifts, and can be used to collectively study gradients in local spirals and their high-z progenitors. The orange data points reflect mean gradients for a constructed abundance-matched sample from available observations, which are the same as that reported in Figure 6.11, with errorbars representing the scatter within the data. There is considerable scatter in the data, and the sample is not entirely robust given the *ex post facto* construction. Nonetheless, the model matches the observations reasonably-well.

for increased scatter in the metallicity gradients in low mass galaxies (Carton et al. 2018; Simons et al. 2020).

6.4.3   Trends for abundance-matched galaxies across redshift

Finally, we also study the evolution of metallicity gradients across an abundance-matched sample of dark matter haloes spanning a range in z[9]. Abundance-matching is based on the premise that the number density of halo progenitors should nearly remain constant across z within a comoving volume in the Universe (Mo et al.

---

[9]Abundance in the context of Section 6.4.3 refers to the abundance of galaxies in a given comoving volume in the Universe, and not the metallicity.

1996; Mo & Fukugita 1996; van Dokkum et al. 2010). It has been used to study a range of properties in local galaxies together with their high-z progenitors (e.g., Marchesini et al. 2009; Papovich et al. 2011; Trujillo-Gomez et al. 2011; Krumholz & Dekel 2012; Leja et al. 2013; Read & Erkal 2019), which is not possible with other selection criteria of galaxies (e.g., selecting galaxies with identical stellar mass, as we do in Section 6.4.2) as such galaxies evolve in time themselves (Conroy & Wechsler 2009).

Abundance matching involves assigning more massive galaxies to more massive haloes at every z; this means selecting galaxies at each z with $M_\mathrm{h}(z)$ that satisfy

$$\int_{M_\mathrm{h}(z)}^{\infty} n\left(M_\mathrm{h}, z\right) dM_\mathrm{h} = n_0 \qquad (6.54)$$

where n_0 is the target number density[10], and $n\left(M_\mathrm{h}, z\right)$ is the number of galaxies per unit mass per unit comoving cubic Mpc given by Mo & White (2002, equation 14) based on the Sheth & Tormen (1999) modification of the Press & Schechter (1974) formalism for the number density of haloes across z. Thus, using the functional form for n, we can deduce the required M_h at each z that would correspond to an abundance-matched sample for a given n_0. Following Marchesini et al. (2009) and Papovich et al. (2011), we study four sets of $\log_{10} n_0/\mathrm{Mpc}^{-3} = -3, -3.325 - 3.5$ and -4.0, respectively. For each of these n_0, we find $v_\phi(z)$ and $M_\star(z)$ using $M_\mathrm{h}(z)$ from equation 6.54, and $\sigma_g(z)$ from equation 6.53. We fix $\beta = 0$ for all galaxies since our choice of n_0 results in massive galaxies with $M_\star > 10^{10}\,\mathrm{M_\odot}$ for all $0 \leq z \leq 2.5$. For simplicity, we fix $f_{g,Q} = f_{g,P} = 0.5$ and $\sigma_\mathrm{sf} = 7\,\mathrm{km\,s^{-1}}$, the same as that for local spirals. Given that f_sf varies between 0.5 and 1 as z increases, we use a cubic interpolation to vary it between $z = 0$ and 4. We also fix $\mathcal{Z}_\mathrm{CGM} = 0.1$.

Figure 6.12 shows the cosmic evolution of gradients for an abundance-matched sample of galaxies, each panel representing a different n_0. Similar to what we have seen in prior sections, the scatter in the model is the largest at the upturn where gradients start flattening. To the best of our knowledge, there are no existing abundance-matched samples of galaxies across redshift that also contain information on metallicity gradients. However, we can construct an abundance-matched sample from the available data. We caution that constructing an abundance-matched sample from existing observations *ex post facto* is not as accurate as properly constructing the sample to start with. In the absence of the latter, we use our constructed sample to compare against the model to learn about the kinds of metallicity gradients that

---

[10]This approximation of a fixed n_0 breaks down if certain galaxies in the abundance-matched sample do not follow the stellar mass rank order, for example, due to an abrupt increment in stellar mass because of mergers, or abrupt decrement due to quenching (Leja et al. 2013).

existed in progenitors of local galaxies. For this purpose, we construct our pseudo-abundance matched sample as follows: for each target value of n_0, we first select a redshift, and use equation 6.54 to estimate the halo mass M_h corresponding to the target n_0 at that redshift. We then estimate the stellar mass of that galaxy $M_\star$ using the stellar mass-halo mass relation of Moster et al. (2013). To construct our sample set at that redshift, we then take the data collection described in Section 6.4.2 and select galaxies that have stellar masses within ± 0.05 dex of the $M_\star$ from above; this constitutes our pseudo-abundance matched sample for that redshift, from which we then measure the mean and dispersion of metallicity gradient at that redshift bin. We plot these values in Figure 6.12, along with model predictions of the metallicity gradient, which we compute from the halo mass and redshift as in previous sections. The data we obtain in this manner have considerable scatter (shown by the error-bars), but the general trends are reasonably well reproduced by the model. However, given the uncertainties in the procedure we are forced to use to construct the observed sample, it is wiser to regard the model points in Figure 6.12 as a prediction for future abundance matching measurements, rather than a rigorous comparison to existing data.

6.5   Limitations of the model

In this section, we describe the limitations of the model, first focusing on physical processes that we have excluded, and then discussing galaxies to which we cannot always apply our assumption of equilibrium.

6.5.1   Additional physics

Our model omits three possibly-important physical effects: bars, galactic fountains and long term wind recycling. With regard to the first of these, there is some evidence that gas phase metallicity gradients in the presence of bars in local spirals can be systematically shallower than those non-barred galaxies (Vila-Costas & Edmunds 1992; Zaritsky et al. 1994; Zurita et al. 2021; see, however, Sánchez-Menguiano et al. 2016, 2018). We have not included metal redistribution due to bar-driven flows, and for this reason we limit our study to gradients in the parts of a galaxy where the rotation curve slope (β) is a constant, which excludes bar-dominated regions (Bland-Hawthorn & Gerhard 2016; Martinez-Medina et al. 2020). In fact, even if we wished to include bar-driven mixing, the galaxy formation model that we use as an input in Section 6.2.2 is itself not applicable in regions where the bar dominates the dynamics of the galaxy, since it does not include the effects of bar-driven torques on gas and

SFR surface density profiles (Sun et al. 2018, 2020).

With regard to the second issue: we do not explicitly incorporate metal redistribution via galactic fountains (Bregman 1980). However, the combination of an enriched $\mathcal{Z}_{\mathrm{CGM}}$ and low ϕ_y essentially constructs a fountain process in the model that we can exploit. Semi-analytic models where the evolution of the CGM is self-consistently followed find that the CGM plays a larger role in the evolution of galaxy metallicity as it gets enriched due to outflows (Yates et al. 2020). We also note that galactic fountains, owing to their short fall-back timescale ($\sim 100-300\,\mathrm{Myr}$, Anglés-Alcázar et al. 2017) and short fall-back distance from the starting point ($\sim 1\,\mathrm{kpc}$, Spitoni et al. 2008) have been shown to play an insignificant role in the metallicity evolution of the local spiral M31 (Spitoni et al. 2013; see, however, simulations by Grand et al. 2019, where fountains are thought to transport metals to the edge of the star-forming disc). Fountains possibly have a significant effect on the far outskirts of the discs, where there are few or no local sources of metals.

There is some evidence from simulations that long term wind recycling can provide metals to the disc as it re-accretes the ejected material. These simulations also show that this recycling is independent of the halo mass (Christensen et al. 2016; Tollet et al. 2019), and can be the dominant mode of accretion of cold gas at late times. However, this recycling occurs much farther out in the disc than that we consider in our work, thus, its basic features are captured within $\mathcal{Z}_{\mathrm{CGM}}$ in the model. Additionally, while the above simulations find long term wind recycling timescale to be of the order of a Gyr, results from the EAGLE simulations find it to be comparable to $t_{\mathrm{H(z)}}$ (Mitchell et al. 2020). Thus, given these findings from simulations and the lack of direct observations, it is currently difficult to determine the importance of wind recycling for metallicity gradients.

Finally, we caution that our model is intended to apply mainly to metals whose production is dominated by type II SNe, and thus where the injection rate closely follows the star formation rate. We have not attempted to model elements produced by type Ia SNe or AGB stars. This is not a substantial problem for our intended application, however, since type II SNe do dominate production of the α elements that are most easily observable in the gas phase (Nomoto & Leung 2018). The one exception to this statement, where some caution is warranted, is nitrogen, to which AGB stars make a substantial contribution (Meynet & Maeder 2002; Herwig 2005). This matters because many of the strong-line diagnostics used at high redshift rely on the N II $\lambda6584$ line. While observers who rely on these diagnostics usually attempt to derive the O abundance by calibrating out variations in the N/O ratio (Pettini & Pagel 2004; Masters et al. 2016; Belfiore et al. 2017; Schaefer et al. 2020; see also,
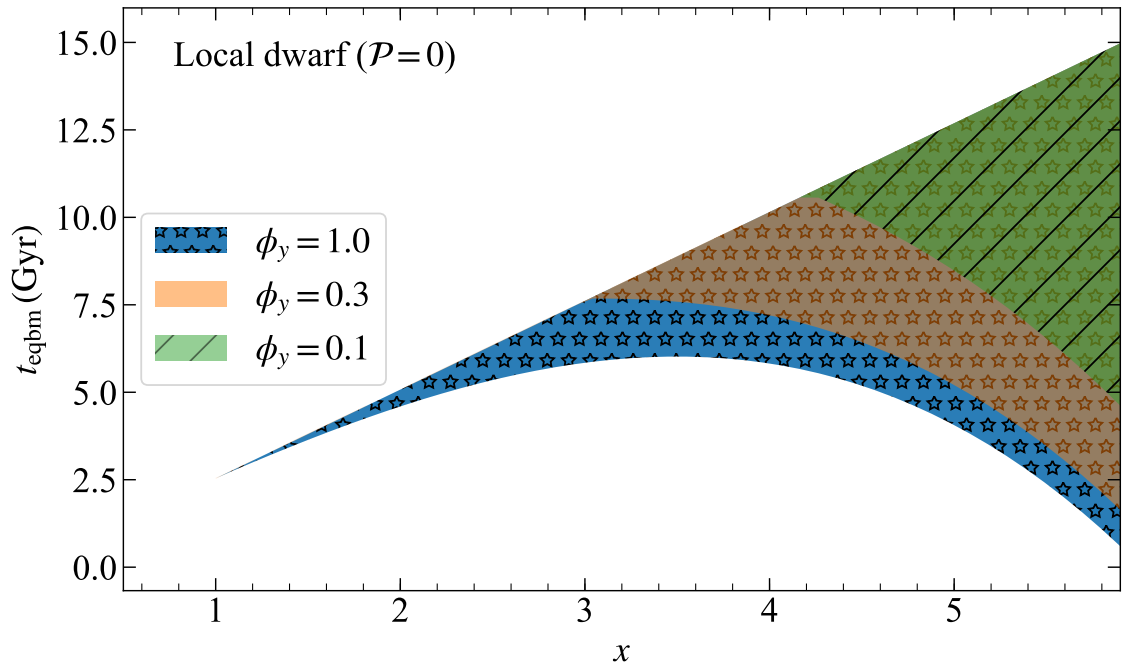
Figure 6.13: Same as Figure 6.4, but without radial inflow such that $\mathcal{P} = 0$. Here, $t_{\mathrm{eqbm}} \gtrsim t_{\mathrm{H}(0)}$, implying that the metallicity gradients in such cases in local dwarfs may or may not be in equilibrium. Thus, our equilibrium model does not necessarily apply.

Vincenzo et al. 2016), it is nevertheless the case that variations in N abundance may influence the metallicities derived at high-z, and that our model does not capture this effect.

6.5.2   Non-equilibrium metallicity gradients

There are certain classes of galaxies where we find that the metallicity distribution can be out of equilibrium, *i.e.*, $t_{\mathrm{eqbm}} \gtrsim t_{\mathrm{H}(z)}$ or $t_{\mathrm{eqbm}} \gg t_{\mathrm{dep,H_2}}$. Hence, the model cannot always be used to predict metallicity gradients in such galaxies. Nonetheless, the limitation of the equilibrium model provides interesting constraints on the evolution of such galaxies. We discuss three such cases below.

Local dwarfs without radial inflow

The balance between metal production (source) and radial transport of metals through the disc (advection, diffusion) sets the metallicity gradients in local dwarfs (cf. Section 6.3.2). It has also been suggested that turbulence in these galaxies is mainly driven by star formation feedback and not gravity (Moiseev et al. 2015; Krumholz et al. 2018), which gives rise to $\sigma_{\mathrm{sf}} \sim \sigma_g$, and the low gas velocity dispersions observed in dwarfs (Yu et al. 2019; Varidel et al. 2020). Here, we investigate
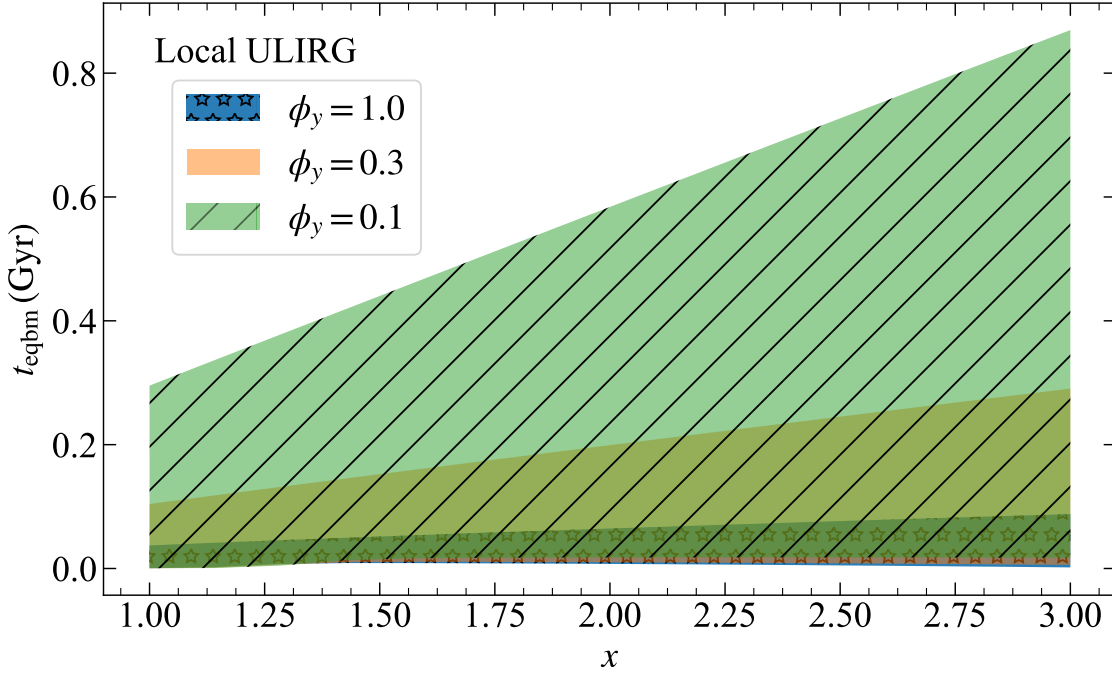
Figure 6.14: Same as Figure 6.1, but for local ultraluminous infrared galaxies (ULIRGs). Here, $t_{\mathrm{eqbm}} \sim t_{\mathrm{merge}}$, where the latter is the merger timescale of the order of $\sim\, 0.3-1\,\mathrm{Gyr}$ as seen in models (Jiang et al. 2008; Torrey et al. 2012). Thus, the metallicity gradients may not be in equilibrium throughout the merger process. In such a case, our equilibrium model for metallicity gradients cannot be applied to local ULIRGs, and the observed gradients, if any, are transient and subject to change as the merger progresses, in line with observations (Rupke et al. 2010b; Rich et al. 2012).

the case where $\sigma_{\mathrm{sf}} = \sigma_g$ such that there is no radial inflow of gas through the disc (see equation 6.36)[11].

Figure 6.13 shows the radial profile of t_{eqbm} in this case. It is clear that $t_{\mathrm{eqbm}} \gtrsim t_{\mathrm{H}(0)}$ and $t_{\mathrm{eqbm}} \gtrsim t_{\mathrm{dep,H_2}}$, especially at low ϕ_y, however, the exact values are sensitive to the choice of c_1. The reason for long metal equilibration timescales in this case is that, in the absence of advection, only diffusion and accretion are available to balance the source term. However, diffusion is weak due to the low gas dispersion ($\kappa_0 \Sigma_{g0} \propto \sigma_g^3$), and accretion is weak due to the low halo mass ($\dot{\Sigma}_{\mathrm{cos}0} \propto M_{\mathrm{h}}^{1.1}$). Thus, metallicity gradients may not attain equilibrium in the absence of radial gas inflows in local dwarfs, whereas even a small amount of advection is sufficient to restore metallicity equilibrium (cf. Figure 6.4). In the case where there is no accretion, one can expect a diverse range of metallicity gradients that are not constrained by the model. Therefore, caution must be exercised while studying metallicity gradients in such dwarfs with an equilibrium model.

---

[11]$\sigma_{\mathrm{sf}} > \sigma_g$ is not possible in equilibrium in the Krumholz et al. (2018) model.
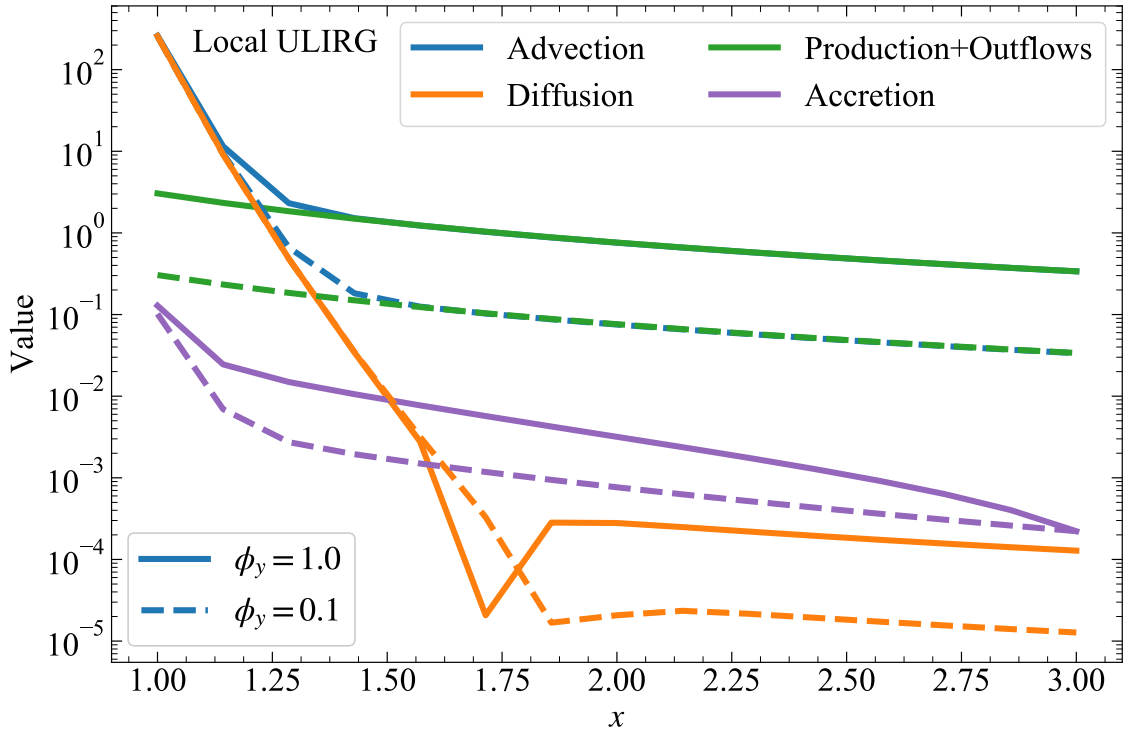
Figure 6.15: Same as Figure 6.3, but for ULIRGs, which are known to be major mergers. The non-equilibrium metallicity distribution is set by advection of gas due to tidal inflows during a merger.

At face value, this result might seem consistent with that of Forbes et al. (2014b), where the authors find that dwarf galaxies do not attain statistical equilibrium within a Hubble time (see their Figure 15; see also, Feldmann 2015; Dashyan & Dubois 2020). However, the equilibrium scenarios considered by Forbes et al. and us are not necessarily the same, and one is not a precondition of the other. Forbes et al. discuss the equilibrium for the total amount of gas or metals in a galaxy, which is a balance between inflow and outflow. The time required to reach this equilibrium is not necessarily the same as the time to equilibrate the distribution of metals *within* the galactic disc, for a given total metal content. Thus, one equilibrium time can be longer or shorter than the other.

Similarly, comparing t_{eqbm} with the metal correlation timescale for local dwarfs from Krumholz & Ting (2018), which is the time required for diffusion alone to smooth out the metallicity distribution in the azimuthal direction, reveals that azimuthal metal distribution in these galaxies reaches equilibrium substantially more quickly than the radial distribution that we study here. This is consistent with the findings of Petit et al. (2015a), who also find that metal distributions equilibrate much more quickly in the azimuthal than the radial direction.
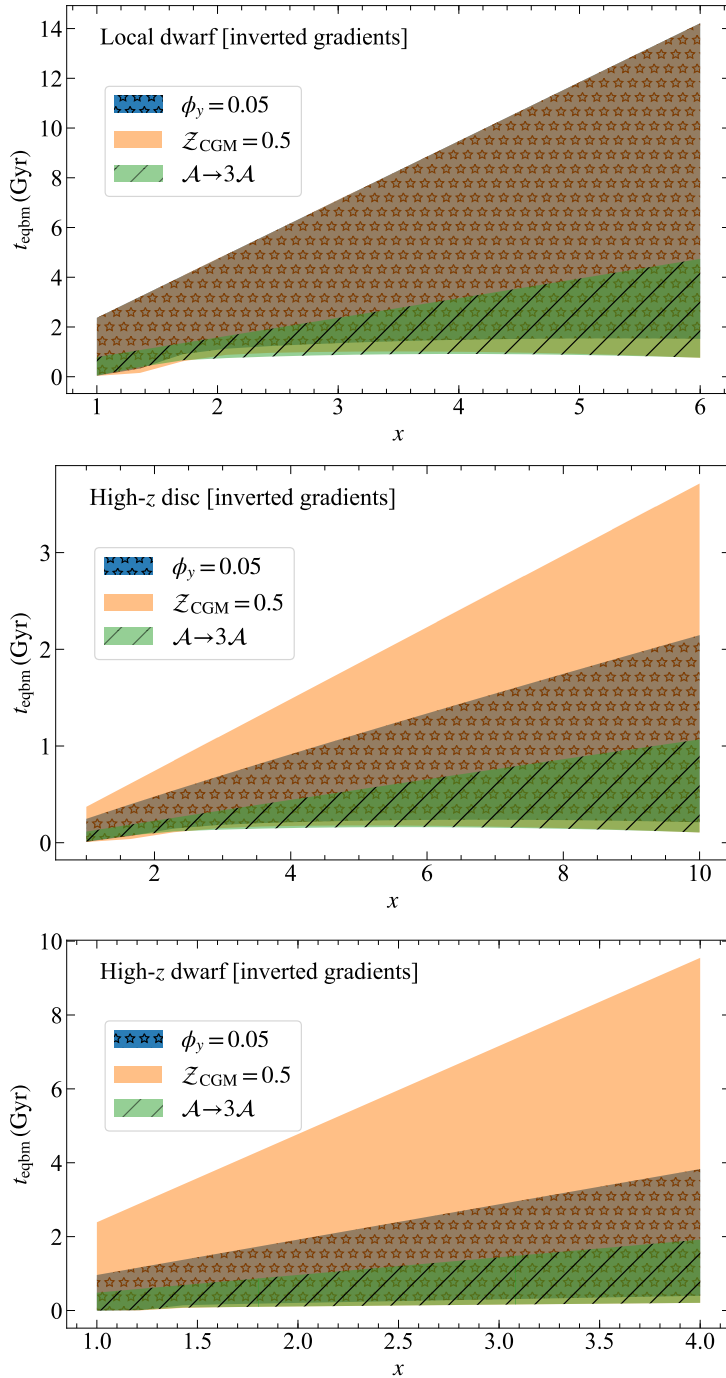
Figure 6.16: Metallicity equilibration timescale t_{eqbm} as a function of x in galaxies with inverted gradients. The first panel represents t_{eqbm} in local dwarfs. The second panel on high-z discs is identical to the class of high-z galaxies we discuss in Section 6.3.3. The third panel plots t_{eqbm} in the case of high-z dwarfs that we create by combining the fiducial parameters for local dwarfs and high-z galaxies (see Section 6.5.2 for details). The colors correspond to the different ways that can give rise to an inverted gradient in a galaxy: reduction in metal yield due to high preferential metal ejection ($\phi_y = 0.05$), enrichment of the CGM due to fountains or metal-rich flows ($\mathscr{Z}_{\mathrm{CGM}} = 0.5$), and excessive cosmic accretion ($\mathcal{A} \to 3\mathcal{A}$). The scatter in the model is due to c_1. This plot shows that inverted metallicity gradients may or may not be in equilibrium.

Local ULIRGs

Local ULIRGs are very dynamically active, and are well-known to be undergoing major mergers or have companions (Lawrence et al. 1989; Melnick & Mirabel 1990; Leech et al. 1994; Clements et al. 1996; Veilleux et al. 1999). These galaxies are often characterized by strong starburst and/or AGN-driven outflows (Veilleux et al. 1995, 2013; Soto et al. 2012; Arribas et al. 2014). They also have extremely short orbital timescales (of the order of $\sim 5\,\mathrm{Myr}$, Krumholz et al. 2018). Local ULIRGs are very compact, with discs extending out only to 2–$3\,\mathrm{kpc}$ (Downes & Solomon 1998; Rujopakarn et al. 2011). It is quite challenging to extract gas metallicities in these galaxies because the ionised gas emission lines are often dominated by shocks (Monreal-Ibero et al. 2006, 2010) and AGN activity (Ellison et al. 2013), which interfere with traditional photoionisation-based metallicity diagnostics. In addition, high levels of dust obscuration make it difficult to model the emission line spectra (García-Marín et al. 2009; Nagao et al. 2011; Piqueras López et al. 2013; Stierwalt et al. 2014). For these reasons, there are only a handful of studies that have been able to extract gas metallicities in local ULIRGs (e.g., Kewley et al. 2006a; Monreal-Ibero et al. 2007; Arribas et al. 2008; Rupke et al. 2008; Westmoquette et al. 2012; Kilerci Eser et al. 2014; Pereira-Santaella et al. 2017), and to the best our knowledge the only published studies of the metallicity gradient in ULIRGs are those of Rich et al. (2012, see their Figure 2) and Thorp et al. (2019).

The short orbital timescales of ULIRGs ensure that they return to dynamical equilibrium quickly compared to their merger timescales, which based on simulations are estimated to be $t_{\mathrm{merge}} \sim 0.3 - 1\,\mathrm{Gyr}$ (Jiang et al. 2008; Torrey et al. 2012). Thus our dynamical equilibrium model from Krumholz et al. (2018) is applicable to them. We investigate whether the metallicity distribution is also in equilibrium in Figure 6.14, which shows t_{eqbm} for local ULIRGs. It is clear that $t_{\mathrm{eqbm}} \sim t_{\mathrm{merge}}$, thus, metallicity may or may not be in equilibrium during the entire process of a merger. Our results corroborate those of Davé et al. (2012), who argue that merging galaxies should not be in equilibrium because tidal flows will fuel star formation (Barton et al. 2000; Kewley et al. 2006a; Reichard et al. 2009; Perez et al. 2011; Ellison et al. 2013; Moreno et al. 2020), making cosmic accretion irrelevant. We show this quantitatively in Figure 6.15, where advection (radial transport of gas due to tidal inflows) is the dominant term that sets the non-equilibrium metallicity distribution, and cosmic accretion is insignificant in comparison. Our results are also in line with those from simulations and observations where metallicity gradients in local ULIRGs are observed to continuously evolve and flatten as the merger progresses (Rich et al. 2012, Figure 4), implying that the metallicity distribution is not in a

steady-state. This also implies that non-equilibrium gradients in local ULIRGs are transient; assuming the galaxy settles back to being a quiescent disc after the merger, the metallicity gradient will return to the equilibrium value for a spiral galaxy on the $\sim$ few Gyr equilibrium timescale for local spirals (cf. Figure 6.1).

Given a merger rate, we can estimate the fraction of galaxies as a function of redshift that are expected to be out of metal equilibrium as $1 - e^{-\theta}$, where θ is the product of the merger rate and the metallicity equilibration timescale. Following Rodriguez-Gomez et al. (2015, Figure 9), we see that the observed average merger rate for massive galaxies ($M_\star \geq 10^{10}\,\mathrm{M_\odot}$) at $z = 0$ is less than $0.06\,\mathrm{Gyr^{-1}}$ (Lotz et al. 2011), so we expect less than 20 per cent of massive galaxies to be out of metal equilibrium at redshift zero. Similarly, based on available observational results that find a merger rate of $0.5\,\mathrm{Gyr^{-1}}$ at $z \approx 2$ (Bluck et al. 2009, 2012; Man et al. 2012), we expect less than 40 per cent of the most massive galaxies ($M_\star \geq 10^{11}\,\mathrm{M_\odot}$) to be out of metal equilibrium at redshift two. The larger fraction of galaxies that are expected to be out of metal equilibrium at high redshift could explain the inverted gradients seen in high-z observations, a topic we explore in Section 6.5.2.

Galaxies with inverted gradients

Recent observations have discovered the presence of inverted (positive) gas phase metallicity gradients in galaxies (Sánchez et al. 2014; Belfiore et al. 2017; Mingozzi et al. 2020), especially at high redshift (Cresci et al. 2010; Queyrel et al. 2012; Stott et al. 2014; Carton et al. 2018; Wang et al. 2019; Curti et al. 2020b; Wang et al. 2020b; Simons et al. 2020). Inverted gradients reflect the possibility of galaxies deviating from the classical, inside-out formation picture, at least temporarily. The three leading mechanisms that are believed to give rise to an inverted gradient are: (1.) substantial metal mass loading or merger-induced tidal flows of metal-poor gas that deprives the galaxy centre of metals, especially in dwarfs (Kereš et al. 2005; Kewley et al. 2006a; Emerick et al. 2018b, 2019; Chisholm et al. 2018; Tissera et al. 2019; see, however, Wilson et al. 2019), (2.) re-accretion of ejected metals at the outer edge of the disc from the CGM through cold, metal-rich flows or galactic fountains (Birnboim & Dekel 2003; Dekel & Birnboim 2006; Dekel et al. 2009b; Cresci et al. 2010; Crighton et al. 2013; Suresh et al. 2015), and (3.) cosmic accretion of metal-poor gas at the centre that dilutes the central metallicity (Cresci et al. 2010).

Corresponding to these three scenarios, we can produce inverted gradients in our model by coupling a moderate or high value of $\mathcal{Z}_{\mathrm{GCM}}$ (*i.e.,* addition of metal-rich gas to galaxy outskirts) with small values of ϕ_y or large values of $\mathcal{A}$ (corresponding to

depressed central metallicity due to heavy metal loss or rapid dilution by metal-poor gas, respectively). However, any inverted gradients that we get from the model are sensitive to our choice of $\mathcal{Z}_{\mathrm{CGM}}$, in the sense that we never get an inverted gradient for a sufficiently low value of $\mathcal{Z}_{\mathrm{CGM}}$. Nevertheless, regardless of the value of $\mathcal{Z}_{\mathrm{CGM}}$ that we adopt, the resulting inverted gradients may or may not be in equilibrium. We illustrate this in Figure 6.16, where we plot t_{eqbm} for local dwarfs, high-z discs (identical to high-z galaxies we discuss in Section 6.3.3), and high-z dwarfs. We introduce the latter category by combining fiducial parameters for local dwarfs and high-z galaxies from Table 6.2 in the following manner: $\beta = 0.5$, $\sigma_{\mathrm{sf}} = 7\,\mathrm{km\,s^{-1}}$, $\sigma_g = 40\,\mathrm{km\,s^{-1}}$, $v_\phi = 80\,\mathrm{km\,s^{-1}}$, $f_{g,Q} = f_{g,P} = 0.9$, $f_{\mathrm{sf}} = 0.4$, and $x_{\mathrm{max}} = 4$ at $z = 2$. The three colors in all the panels in Figure 6.16 correspond to low $\phi_y = 0.05$ (with $\mathcal{Z}_{\mathrm{CGM}} = 0.1$), high $\mathcal{Z}_{\mathrm{CGM}} = 0.5$ (with $\phi_y = 0.1$), and high accretion where we multiply our fiducial values of $\mathcal{A}$ by 3 (with $\phi_y = 0.1$, $\mathcal{Z}_{\mathrm{CGM}} = 0.1$), respectively. The shaded regions correspond to the allowed values of c_1 based on the constraints we introduced in Section 6.2.3.

We see that whether galaxies with inverted gradients are likely to be in equilibrium or not depends largely on what produces the inversion. Galaxies where the gradient inverts due to rapid accretion (high $\mathcal{A}$) have relatively short values of t_{eqbm}, and may be in equilibrium as long as the accretion lasts, while those that invert due to an influx of metal-rich gas at their outskirts (high $\mathcal{Z}_{\mathrm{GCM}}$) are almost certainly out of equilibrium; galaxies with extremely efficient metal loss (low ϕ_y) are intermediate, and may or may not be in equilibrium. Regardless of these details, the fact that many inverted gradients are not in equilibrium also hints at the possibility of them being transient (see also, Schönrich & McMillan 2017). This is because subsequent star formation in the galaxy centre (due to cold gas accretion or re-accretion of enriched gas from the CGM) will replenish the metal supply on timescales comparable to the star formation timescale, thus leading to the formation of a negative gradient again. Hence, we expect inverted gradients to be erased within a star formation timescale ($\lesssim 2\,\mathrm{Gyr}$ for massive galaxies, Leroy et al. 2008) unless they are re-established on a similar timescale. Since the processes that can cause inverted gradients (strong fountains, mergers, sudden accretion events, etc.) tend to wane with redshift, we expect that most massive galaxies will establish negative gradients by $z = 0$, though some dwarfs, which have longer equilibration (and star formation) timescales, might retain their inverted gradients to $z = 0$ or close to it.

6.6   Conclusions

In this work, we present a new theoretical model to explain the occurrence and diversity of gas phase metallicity gradients in galaxies. Starting from the conservation of metal mass, we incorporate major physical processes that can impact the distribution of metals in galaxies, namely, metal production, consumption, loss, advection, accretion and diffusion. Our first-principles based model shows that the radial metallicity gradients observed in galaxies are a natural consequence of inside-out galaxy formation. The equilibrium metallicity evolution model we present is a standalone model, but it requires inputs from a galaxy evolution model to set the galaxy properties that control metallicity. This intricate link between gas and metallicity lets us directly predict the evolution of metallicity gradients without ad hoc assumptions about galaxy properties.

The evolution of metallicities in our model depends on four dimensionless ratios: $\mathcal{T}$, $\mathcal{P}$, $\mathcal{S}$, and $\mathcal{A}$. These describe the ratio of the orbital timescale to the diffusion timescale, advection to diffusion, production (and metal ejection) to diffusion, and cosmic accretion to diffusion, respectively. Based on the input galaxy evolution model (Krumholz et al. 2018), we show how these ratios depend on various properties of the gas (cf. equation 6.37 − equation 6.40). The resulting second order differential equation of the radial distribution of metallicity has a simple analytic solution given by equation 6.41 that we use to predict a possible range of metallicity gradients as a function of galaxy properties. We use this capability to predict the metallicity gradients of local spirals, local dwarfs, and high-redshift disc galaxies, and to predict the evolution of metallicity gradients in galaxies with redshift. Below, we list our main results:

1. The time required for the metal distribution within a galaxy to reach equilibrium is smaller than the Hubble time and comparable to the molecular gas depletion time in local spirals, (most) local dwarfs, and rotation-dominated high-z galaxies. Thus, for most galaxies over most of cosmic time, the gas phase metallicity gradient is in equilibrium. Exceptions to this general trend *can* include merging galaxies, galaxies with inverted metallicity gradients, and some very low-mass local dwarf galaxies.

2. Galaxies tend to approach a particular value of central metallicity, dictated by the balance between the two dominant processes that depend on the properties of the galaxy (see below). The central metallicities we predict agree well with observations.

3. In local spirals, the two dominant processes shaping the metallicity gradient

are metal production ($\mathcal{S}$), which tries to steepen the gradient, and accretion of metal-poor gas ($\mathcal{A}$), which tries to flatten it. On the other hand, metallicity gradients in local dwarfs and high-z galaxies are set by the balance between $\mathcal{S}$ and advection of metal-poor gas from the outer to the inner parts of galaxies ($\mathcal{P}$).

4. One crucial free parameter that emerges from our model is the "yield reduction factor" ϕ_y, defined as the fraction of supernova-produced metals that mix with the ISM rather than being lost immediately in metal-enhanced galactic winds. While metallicity gradients in local spirals are not tremendously sensitive to ϕ_y, it has a significant effect on the metallicity gradients in local dwarfs and high-z galaxies. ϕ_y also impacts the absolute metallicities in all galaxies. Comparison of the model with observations reveals that massive galaxies prefer a high value of ϕ_y, whereas low-mass galaxies prefer a lower value of ϕ_y. Thus, the model predicts that low-mass galaxies undergo more preferential metal ejection, and should have more metal-enriched winds than massive galaxies. Future work should thus focus on constraining ϕ_y from observations.

As a first application of our model, we study the evolution of metallicity gradients with redshift, both within a single galaxy and over samples of galaxies at different redshifts selected to have matching stellar masses or comoving densities. Our model shows that gradients in Milky Way-like galaxies have steepened over time, in qualitative agreement with recent observations; quantitative agreement between the model and the data requires a scaling of ϕ_y such that ϕ_y was low for the Galaxy in the past as compared to today, consistent with that seen in simulations. We also predict the existence of specific signatures for the evolution of metallicity gradient with redshift as a function of stellar mass that can be tested with future surveys. We show that both the Milky Way in particular and disc galaxies in general transition from the advection-dominated ($\mathcal{P} > \mathcal{A}$) to the accretion-dominated ($\mathcal{P} < \mathcal{A}$) regime from high to low redshifts. This transition mirrors the transition from gravity-driven to star formation-driven turbulence from high to low redshifts (Krumholz et al. 2018). In companion papers, we show that this transition (along with ϕ_y) is also responsible for driving the shape of the mass-metallicity relation and the mass-metallicity gradient relation (Sharda et al. 2021b) in the local Universe, and we also apply our model to explain the relationship between metallicity gradients and gas kinematics in high redshift galaxies (Sharda et al. 2021f).

Acknowledgements

---

[12]`wolframalpha.com`
[13]`https://automeris.io/WebPlotDigitizer`

On the origin of the mass-metallicity gradient relation in the local Universe

Context and Contribution

This chapter have been previously published as **'On the origin of the mass-metallicity gradient relation in the local Universe',** *by* **Piyush Sharda, Mark R. Krumholz, Emily Wisnioski, Ayan Acharyya, John C. Forbes, and Christoph Federrath, 2021, MNRAS, 504, 53**. *The work is presented here exactly as in the publication. I initiated and led the idea behind this work. I have created the model described in this work. I have contributed heavily to interpretation of the results and written the majority of the paper, with inputs and suggestions from co-authors.*

Abstract

In addition to the well-known gas phase mass-metallicity relation (MZR), recent spatially-resolved observations have shown that local galaxies also obey a mass–metallicity gradient relation (MZGR) whereby metallicity gradients can vary systematically with galaxy mass. In this work, we use our recently-developed analytic model for metallicity distributions in galactic discs, which includes a wide range of physical processes – radial advection, metal diffusion, cosmological accretion, and metal-enriched outflows – to simultaneously analyse the MZR and MZGR. We show that the same physical principles govern the shape of both: centrally-peaked metal production favours steeper gradients, and this steepening is diluted by the addition of metal-poor gas, which is supplied by inward advection for low-mass galaxies and by cosmological accretion for massive galaxies. The MZR and the MZGR both bend at galaxy stellar mass $\sim 10^{10} - 10^{10.5} \, \mathrm{M_\odot}$, and we show that this feature corresponds to the transition of galaxies from the advection-dominated to the accretion-dominated

regime. We also find that both the MZR and MZGR strongly suggest that low-mass galaxies preferentially lose metals entrained in their galactic winds. While this metal-enrichment of the galactic outflows is crucial for reproducing both the MZR and the MZGR at the low-mass end, we show that the flattening of gradients in massive galaxies is expected regardless of the nature of their winds.

7.1   Introduction

Metals have a profound impact on galaxy formation and evolution even though their contribution to the total visible matter is less than two per cent. The symbiotic relationship between galaxies and their metal content has now been investigated in detail through numerous observations, simulations and analytic models. One of the key manifestations of this relationship is the correlation between the stellar mass of a galaxy ($M_\star$, used as a proxy for the total galaxy mass) and its global (gas phase or stellar) metallicity, Z. It is now well established that low-mass galaxies have lower Z as compared to massive galaxies. This is known as the mass metallicity relation (MZR; e.g., Kewley & Dopita 2002; Tremonti et al. 2004; Mannucci et al. 2010; Peng et al. 2015; Belfiore et al. 2017; Zahid et al. 2017; Curti et al. 2017, 2020a). The exact cause of the MZR is still debated; for example, star formation (Brooks et al. 2007), outflows (Finlator & Davé 2008; Chisholm et al. 2018), cosmic accretion or infall (Larson 1972; Davé et al. 2012), feedback (Tissera et al. 2019), and the initial mass function (IMF, Köppen et al. 2007) can all play a role in setting its shape. The shape of the MZR seen in observations has now been successfully reproduced by many simulations (e.g., Brooks et al. 2007; Davé et al. 2011, 2017; Torrey et al. 2019; Tissera et al. 2019) and theoretical models (e.g., Finlator & Davé 2008; Peeples & Shankar 2011; Lilly et al. 2013; De Lucia et al. 2020); however, the absolute normalisation of the MZR (*i.e.,* the absolute value of Z) remains uncertain due to difficulties in calibrating Z from observations (see reviews by Kewley et al. 2019b, Maiolino & Mannucci 2019 and Sánchez 2020a).

Since the pioneering works by Searle (1971), Mayor (1976) and Shaver et al. (1983), it has been known that galaxies also exhibit a gradient in the spatial distribution of metallicity, both in stars and in the gas phase, in the radial direction (e.g., Zaritsky et al. 1994; González Delgado et al. 2015; Goddard et al. 2017; Belfiore et al. 2017) as well as variations in the azimuthal direction (e.g., Luck et al. 2011; Li et al. 2013b; Ho et al. 2017, 2019; Kreckel et al. 2019). The fact that radial gradients are usually negative (*i.e.,* the centre of the galaxy is more metal-rich than the outskirts) is a key piece of evidence for the theory of inside-out galaxy formation (Mo et al. 1998;

Benson 2010; Naab & Ostriker 2017). Hereafter, we only focus on the metallicities and metallicity gradients in the ionised gas.

Thanks to the plethora of galaxies observed in the nearby Universe with large integral field spectroscopy (IFS) surveys like CALIFA (Calar Alto Legacy Integral Field Area, Sánchez et al. 2012), MaNGA (Mapping nearby Galaxies at Apache Point Observatory, Bundy et al. 2015), and SAMI (Sydney-AAO Multi-object Integral-field spectrograph, Bryant et al. 2015), we can now study the trends of metallicity gradients with different galaxy properties in a statistical sense. Like the MZR, of particular interest is the stellar mass–metallicity gradient relation (MZGR). The general consensus is that the metallicity gradient, when measured in absolute units of $\mathrm{dex\,kpc^{-1}}$, either remains independent of stellar mass up to $M_\star \sim 10^{10-10.5}\,\mathrm{M_\odot}$, then flattens toward zero gradient at higher stellar masses (Maiolino & Mannucci 2019), or shows a mild curvature around $\sim 10^{10-10.5}\,\mathrm{M_\odot}$, with flat gradients on either side (e.g., Belfiore et al. 2017). If the gradients are instead normalised by the effective radius of galaxies (r_e) and expressed in $\mathrm{dex\,}r_\mathrm{e}^{-1}$, some authors find that the MZGR is steepest around $M_\star \sim 10^{10-10.5}\,\mathrm{M_\odot}$, with flatter gradients on either side (e.g., Belfiore et al. 2017; Mingozzi et al. 2020; Poetrodjojo et al. 2021b), whereas others report a constant, characteristic $\mathrm{dex\,}r_\mathrm{e}^{-1}$ gradient for all galaxies with $M_\star > 10^{9.5}\,\mathrm{M_\odot}$ (Sánchez et al. 2012, 2014; Sánchez-Menguiano et al. 2016, 2018; Poetrodjojo et al. 2018). However, these trends in the MZGR are relatively weak as compared to the MZR, suffer observational and calibration uncertainties (Yuan et al. 2013; Acharyya et al. 2020, 2021; Poetrodjojo et al. 2021b), and to date, have received limited theoretical investigation.

The goal of this work is to provide a physical explanation for the shape of the MZGR. For this purpose, we use our recently-developed first principles model of gas phase metallicity gradients (Sharda et al. 2021b). This model is based on the equilibrium between the production, consumption, loss and transport of metals in galactic discs. It produces gas phase metallicity gradients in good agreement with a wide range of local and high-z galaxies, and shows that these gradients are in equilibrium across a diverse range of galaxy properties. We refer the reader to Sharda et al. (2021b) for a full description of the model, the gradients produced, as well as applications of the model to study the cosmic evolution of metallicity gradients and their trends with galaxy kinematics (Sharda et al. 2021f). The rest of this paper is organised as follows: Section 7.2 presents a review of the model, Section 7.3 describes the MZR produced by our model, which we use as a proof of concept to explain the MZGR in Section 7.4. Section 7.5 introduces the MZR–MZGR space in equilibrium as a new way of characterizing gas phase metallicities, and Section 7.6 summarizes our

key results. For the purpose of this paper, we use $Z_\odot = 0.0134$ for Solar metallicity, corresponding to $12 + \log_{10} O/H = 8.69$ (Asplund et al. 2009), Hubble time at $z = 0$: $t_{H(0)} = 13.8\,Gyr$ (Planck Collaboration et al. 2018), and follow the flat ΛCDM cosmology: $\Omega_m = 0.27$, $\Omega_\Lambda = 0.73$, $h = 0.71$, and $\sigma_8 = 0.81$ (Springel & Hernquist 2003).

7.2   Review of the model

In this section, we provide a brief review of the model of gas phase metallicity gradients we presented in Sharda et al. (2021b); this is intended to highlight only the results of which we will make use here, and we refer readers to the original paper for full details. In that work, we showed that the evolution of gas phase metallicity is described by the Euler-Cauchy equation

$$\underbrace{\mathcal{T}s_g\frac{\partial\mathcal{Z}}{\partial\tau}}_{\substack{\text{equilibrium}\\\text{time}}} - \underbrace{\frac{\mathcal{P}}{x}\frac{\partial\mathcal{Z}}{\partial x}}_{\text{advection}} - \underbrace{\frac{1}{x}\frac{\partial}{\partial x}\left(xks_g\frac{\partial\mathcal{Z}}{\partial x}\right)}_{\text{diffusion}} = \underbrace{\mathcal{S}\dot{s}_\star}_{\substack{\text{production}\\+\\\text{outflows}}} - \underbrace{\mathcal{Z}\mathcal{A}\dot{c}_\star}_{\text{accretion}}, \qquad (7.1)$$

where $\mathcal{Z} = Z/Z_\odot$ is the metallicity normalised to Solar, x is the radius of the disc normalised to the radius r_0 that we take to be the inner edge of the disc (i.e., $x = r/r_0$ where r is the galactocentric radius), τ is the time normalised to the orbital time at r_0, k is the normalised diffusion coefficient, and s_g, $\dot{s}_\star$, and $\dot{c}_\star$ are the normalised gas mass, star formation rate (SFR), and cosmic accretion rate per unit area of the galactic disc, respectively. From left to right, the different terms in equation 7.1 represent the equilibration time for a given metal distribution, radial advection of metals due to inflows, diffusion of metals due to concentration gradients, production of metals through star formation and loss via galactic outflows, and cosmic accretion of metal-poor gas from the circumgalactic medium (CGM), respectively. From equation 7.1, we see that $\mathcal{Z}$ is governed by four dimensionless ratios. These are $\mathcal{T}$ – the ratio of orbital to diffusion timescales, $\mathcal{P}$ – the Péclet number of the galaxy that describes the ratio of advection to diffusion (e.g., Patankar 1980; Rapp 2017), the 'source' term $\mathcal{S}$ – the ratio of metal production to diffusion, and the 'accretion' term $\mathcal{A}$ – the ratio of cosmic accretion (or infall) to diffusion.

In equilibrium, the first term goes to zero, and one can find a steady-state solution to equation 7.1 for any specified profiles of s_g, $\dot{s}_\star$, and $\dot{c}_\star$ versus radius. We set s_g and $\dot{s}_\star$ from the unified galaxy disc model of Krumholz et al. (2018), and $\dot{c}_\star$ based on cosmological simulations (e.g., Colavitti et al. 2008). For these choices, the corresponding equilibrium solution for the metallicity as a function of normalised

galactocentric radius, $\mathcal{Z}(x)$, is given by

$$\mathcal{Z}(x) = \frac{\mathcal{S}}{\mathcal{A}} + c_1 x^{\frac{1}{2}\left[\sqrt{\mathcal{P}^2 + 4\mathcal{A}} - \mathcal{P}\right]}$$
$$+ \left(\mathcal{Z}_{r_0} - \frac{\mathcal{S}}{\mathcal{A}} - c_1\right) x^{\frac{1}{2}\left[-\sqrt{\mathcal{P}^2 + 4\mathcal{A}} - \mathcal{P}\right]}, \tag{7.2}$$

where c_1 is a constant of integration that is determined by the metallicity of the CGM, $\mathcal{Z}_{\mathrm{CGM}}$, and $\mathcal{Z}_{r_0}$ is the equilibrium metallicity at r_0 that we can determine from other galaxy parameters. We can also express $\mathcal{P}$, $\mathcal{S}$ and $\mathcal{A}$ in terms of meaningful galaxy parameters using the Krumholz et al. (2018) model, which gives

$$\mathcal{T} = \frac{3\phi_Q\sqrt{2(\beta+1)}f_{g,Q}}{Q_{\mathrm{min}}}\left(\frac{v_\phi}{\sigma_g}\right)^2, \tag{7.3}$$

$$\mathcal{P} = \frac{6\eta\phi_Q^2\phi_{\mathrm{nt}}^{3/2}f_{g,Q}^2}{Q_{\mathrm{min}}^2}\left(\frac{1+\beta}{1-\beta}\right)\left(1 - \frac{\sigma_{\mathrm{sf}}}{\sigma_g}\right), \tag{7.4}$$

$$\mathcal{S} = \frac{24\phi_Q f_{g,Q}^2\epsilon_{\mathrm{ff}}f_{\mathrm{sf}}}{\pi Q_{\mathrm{min}}\sqrt{3f_{g,P}\phi_{\mathrm{mp}}}}\left(\frac{\phi_y y}{Z_\odot}\right)(1+\beta)\left(\frac{v_\phi}{\sigma_g}\right)^2, \tag{7.5}$$

$$\mathcal{A} = \frac{3G\dot{M}_h f_{\mathrm{B}}\epsilon_{\mathrm{in}}\phi_Q}{2\sigma_g^3\left[\ln x_{\mathrm{max}} - \ln x_{\mathrm{min}}\right]}. \tag{7.6}$$

Here, $\phi_Q - 1$ is the ratio of the gas to stellar Toomre Q parameters (Wang & Silk 1994; Romeo & Wiegert 2011; Romeo & Falstad 2013), β is the rotation curve index of the galaxy, $f_{g,Q}$ and $f_{g,P}$ are two slightly different measures of the effective gas fraction (Ostriker et al. 2010; Krumholz et al. 2018), Q_{min} is the Toomre Q parameter (Toomre 1964) below which discs are unstable due to gravity (e.g., Krumholz & Burkert 2010; Goldbaum et al. 2015), v_ϕ is the rotational velocity of the galaxy, σ_g is the gas velocity dispersion, η is a dimensional factor of order unity describing the rate of turbulent dissipation (Mac Low et al. 1998; Forbes et al. 2012), ϕ_{nt} is the fraction of total velocity dispersion that is in non-thermal rather than thermal motions, σ_{sf} is the maximum velocity dispersion that can be maintained by star formation feedback, ϵ_{ff} is the star formation efficiency per free-fall time (Krumholz & McKee 2005; Federrath & Klessen 2012; Padoan et al. 2012), f_{sf} is the fraction of gas that is molecular (Krumholz et al. 2009b; Krumholz 2013), ϕ_{mp} is the ratio of the total to the turbulent pressure at the mid-plane (Ostriker et al. 2010), $\dot{M}_h$ is the dark matter accretion rate onto the halo (Neistein & Dekel 2008; Bouché et al. 2010), f_{B} is the universal baryonic fraction (White & Fabian 1995; Planck Collaboration et al. 2016a), and ϵ_{in} is the baryonic accretion efficiency (Faucher-Giguère et al. 2011). We refer the readers to Sharda et al. (2021b, Tables 1 and 2) for full descriptions of

and typical values for all these parameters.

In addition to these quantities, the production term $\mathcal{S}$ depends on one additional parameter: the yield reduction factor ϕ_y, which describes the reduction in the metal yield due to preferential ejection of metals through galactic outflows. $\phi_y = 1$ corresponds to metals injected by Type II supernovae fully mixing with the interstellar medium (ISM), while $\phi_y = 0$ corresponds to all newly produced Type II supernovae metals being ejected from the galaxy immediately, without ever becoming part of the ISM.[1]

The Sharda et al. (2021b) model is distinct from earlier models for galaxy metallicity distributions in a few ways: (1.) we include all major transport processes, including advection and diffusion of metals, both of which are usually neglected, but which can become important in some regimes, as we show below; (2.) we do not make the common assumption that the wind and ISM metallicities are equal, since there is observational evidence that they are not (e.g., Martin et al. 2002; Strickland & Heckman 2009b; Chisholm et al. 2018); (3.) we derive model parameters such as the star formation rate, radial advection rate, diffusion rate, etc., from a physical model of galactic discs that is well tested against observations (Johnson et al. 2018; Yu et al. 2019; Übler et al. 2019; Varidel et al. 2020; Girard et al. 2021; Sharda et al. 2021f), rather than adopting parameterised prescriptions of unknown accuracy; (4.) our model allows us to study both global and spatially-resolved metallicity properties.

However, the model also has some important limitations that we should note. First, we derive solutions for $\mathcal{Z}(x)$ only for galaxies whose metal distributions are in equilibrium; we show in Sharda et al. (2021b) that almost all galaxies at $z = 0$ except ongoing mergers satisfy this requirement, as do the majority of galaxies out to at least $z \approx 3$. However, a major exception to this *may be* galaxies with inverted gradients; for this reason we do not study inverted gradients with this model. We also make a number of simplifying assumptions in order to obtain our analytic solutions: we assume that the rotation curve index β is a constant. We use the instantaneous recycling approximation (Tinsley 1980), which means that the model is best applied to elements that are returned to the ISM quickly via Type II supernovae, rather than over longer time scales by other nucleosynthetic sources. We assume gas accreting onto the galaxy can be described by a single, fixed metallicity, which im-

---

[1] It is important to clarify that ϕ_y is not the same as the metal outflow rate or the metal mass loading factor, since ϕ_y only describes how metals are partitioned between winds and the ISM, not the total metal mass carried by the winds. For example, a galaxy could have very low mass loading but also low ϕ_y, if the winds consisted primarily of metal-rich supernova ejecta, with very little additional ISM mass entrained.
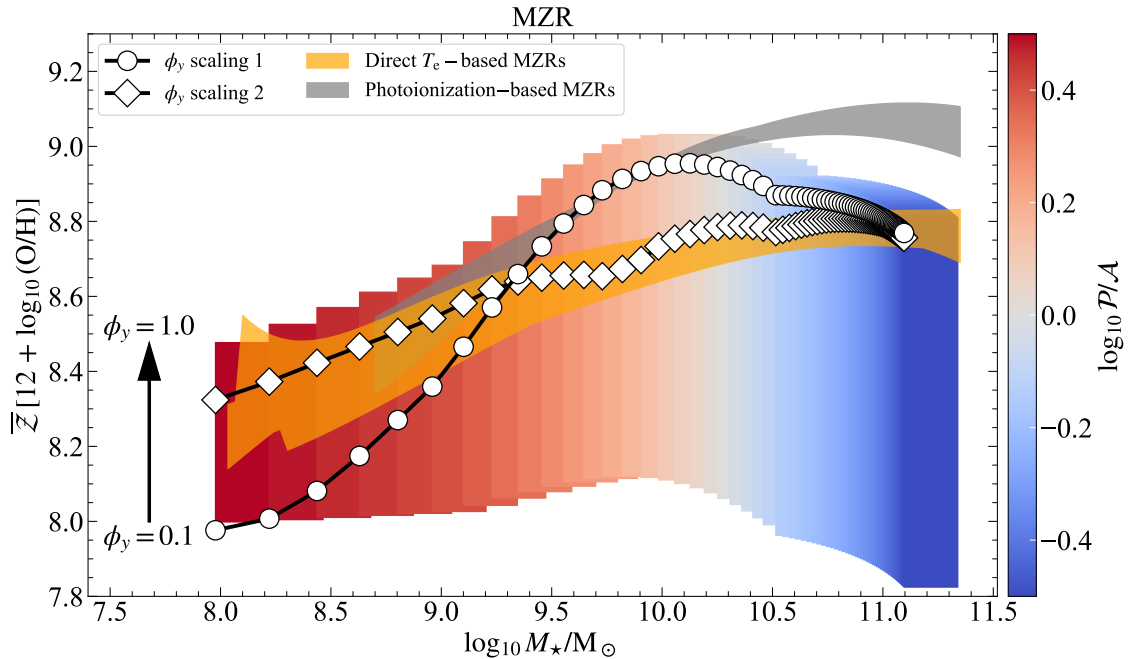
Figure 7.1: Mass–metallicity relation (MZR) in local galaxies predicted by the Sharda et al. (2021b) model, for different yield reduction factors ϕ_y, color-coded by the ratio of the Péclet number ($\mathcal{P}$) to cosmic accretion over diffusion ($\mathcal{A}$). The MZR displays a curvature around $M_\star \sim 10^{10} - 10^{10.5}\,\mathrm{M_\odot}$, corresponding to the transition from the advection-dominated ($\mathcal{P} > \mathcal{A}$) to the accretion-dominated ($\mathcal{P} < \mathcal{A}$) regime. Overlaid on the model are parameter spaces corresponding to MZRs derived from observations, using the direct T_e method (Pettini & Pagel 2004; Andrews & Martini 2013; Curti et al. 2017, 2020a), and photoionization models (Kewley & Dopita 2002; Tremonti et al. 2004; Mannucci et al. 2010), adopted from (Maiolino & Mannucci 2019, Figure 15). Finally, the white markers show model predictions using two possible empirical scalings of ϕ_y with $M_\star$. Scaling 1 is derived from observations (Chisholm et al. 2018), whereas scaling 2 is independently derived from the best match between the model MZR and the Curti et al. (2020a) MZR; details of these scalings are given in Appendix D. Our findings predict a scaling of ϕ_y with $M_\star$ where massive galaxies prefer a higher value of ϕ_y, and vice-versa. This implies that low-mass galaxies have more metal-enriched winds, consistent with observations (Chisholm et al. 2018) and simulations (Emerick et al. 2018b; Tanner 2020).

plicitly means that we neglect galactic fountains, long-term wind recycling through the CGM, and other environmental effects (e.g., the presence of satellites). Nonetheless, as we show in the next three sections that the model can successfully explain the MZR (Section 7.3), the MZGR (Section 7.4), and the relationship between the two (Section 7.5).

7.3   Mass–metallicity relation (MZR)

7.3.1   Results on the MZR from the model

Almost all the analytic models that reproduce the observed MZR do not have spatial information of the distribution of metallicities in a galaxy – these are typically developed to study global metallicities in galaxies. Although the primary focus of our work is to explain metallicity gradients by making use of the spatial information of metallicity, our model also reproduces the MZR as a proof of concept.

To produce an MZR from the model, we need an estimate of the mean metallicity in galaxies as a function of $M_\star$. For this purpose, we use the SFR-weighted mean metallicity given by Sharda et al. (2021b, equation 46)

$$\overline{\mathcal{Z}} = \frac{\int_{x_{\min}}^{x_{\max}} x \dot{s}_\star \mathcal{Z} dx}{\int_{x_{\min}}^{x_{\max}} x \dot{s}_\star dx} \, , \tag{7.7}$$

where $\dot{s}_\star(x) = 1/x^2$ is the radial distribution of star formation per unit area (Krumholz et al. 2018). We use the SFR-weighted $\overline{\mathcal{Z}}$, because it can be directly compared against available MZRs since they are inherently sensitive to the SFR as the nebular metallicities are measured in H II regions around young stars (Zahid et al. 2014). Additionally, semi-analytic models and simulations too use SFR-weighted metallicities to construct MZRs (e.g., Tissera et al. 2019; Torrey et al. 2019; Forbes et al. 2019; Yates et al. 2020).

In order to derive results in terms of $M_\star$, we treat the rotational velocity, v_ϕ, as the primary quantity that we vary. For each v_ϕ, we can estimate the corresponding halo mass $M_{\rm h}$ and halo accretion rate $\dot{M}_{\rm h}$ at $z = 0$ (Sharda et al. 2021b, equations 34–35). We convert the halo mass to $M_\star$ following the $M_{\rm h} - M_\star$ relation from Moster et al. (2013) for the local Universe. Following Sharda et al. (2021b), we keep the yield reduction factor, ϕ_y, as a free parameter and vary it between 0.1 and 1, though we note that, based on both theory and observations, ϕ_y is expected to be close to unity in massive galaxies. For all other parameters, in particular the velocity dispersion σ_g, we use the fiducial values listed in Sharda et al. (2021b, Tables 1 and 2). Specifically, we use local dwarf values for galaxies with $M_\star \leq 10^9 \, \mathrm{M}_\odot$, and local spiral values for $M_\star \geq 10^{10.5} \, \mathrm{M}_\odot$. For intermediate stellar masses, we linearly interpolate in $\log_{10} M_\star$ between these two limits for all parameters. For example, the velocity dispersions we adopt for spirals and dwarfs are $10 \, \mathrm{km \, s^{-1}}$ and $7 \, \mathrm{km \, s^{-1}}$ respectively, so we adopt $\sigma_g = (2 \log_{10} M_\star / \mathrm{M}_\odot - 11) \, \mathrm{km \, s^{-1}}$ for intermediate-mass galaxies with $10^9 \, \mathrm{M}_\odot < M_\star < 10^{10.5} \, \mathrm{M}_\odot$. We have verified that the resulting MZR and MZGR are not particularly sensitive to the choice of the $M_\star$ boundaries invoked

to classify dwarfs and spirals; we also discuss this further in Section 7.4. We set $\mathscr{Z}_{r0}$ to its equilibrium value (Sharda et al. 2021b), and set the circumgalactic medium metallicity to $\mathscr{Z}_{\mathrm{CGM}} = 0.2$ for all galaxies[2], which sets c_1. The MZR (as well as the MZGR discussed below) is insensitive to $\mathscr{Z}_{r0}$ and only weakly sensitive to $\mathscr{Z}_{\mathrm{CGM}}$ as compared to ϕ_y, so we do not vary $\mathscr{Z}_{\mathrm{GCM}}$ separately. Finally, we follow van der Wel et al. (2014) to estimate r_{e} as a function of $M_\star$, and set $x_{\min} = 0.5\,r_{\mathrm{e}}$ and $x_{\max} = 3\,r_{\mathrm{e}}$ as the range of radii x over which our model solution applies. This range of radii roughly mimics that over which metallicities are measured.

Figure 7.1 shows the resulting MZR from our model, color-coded by the ratio $\mathcal{P}/\mathcal{A}$ that describes the relative strength of advection to cosmic accretion. We remind the reader that both $\mathcal{P}$ and $\mathcal{A}$ (as well as $\mathcal{S}$) are normalised by diffusion in the model. The vertical spread in the model MZR is a result of varying ϕ_y. We also overplot the parameter space of observed MZRs from several other works based on the direct T_{e} method (Pettini & Pagel 2004; Andrews & Martini 2013; Curti et al. 2017, 2020a) and photoionization modeling (Kewley & Dopita 2002; Tremonti et al. 2004; Mannucci et al. 2010), all of which we adopt from Maiolino & Mannucci (2019, Figure 15). We see that the model is able to reproduce the MZR of the local Universe albeit with a large spread due to ϕ_y. There are several factors behind quantitative differences between the model MZR and MZRs in the literature. From the perspective of the model, these differences are attributed to the choice of the metal yield y, excluding the galaxy nucleus while finding the mean metallicities, and the absolute size of the galaxy disc. From the perspective of the MZRs we compare the model with, these differences are due to calibration and observational uncertainties, as well as limited coverage of the galaxy discs.

In order to match with the measured MZRs, the model prefers higher ϕ_y for massive galaxies and lower ϕ_y for low-mass galaxies. This implies that metals are well-mixed in the ISM in massive galaxies before they are ejected through outflows, whereas in dwarf galaxies, some fraction of metals are ejected directly before they can mix in the ISM; in other words, the best match between the model MZR and the literature MZRs predicts that dwarf galaxies have more metal-enriched winds than massive galaxies. This finding is not new and has been theorized in several works (e.g., Larson 1974; Dekel & Silk 1986; Dalcanton 2007; Finlator & Davé 2008; Lilly et al. 2013; Dayal et al. 2013; Forbes et al. 2019), simulations (Creasey et al. 2015; Ma

---

[2]This is slightly lower than the median $\mathscr{Z}_{\mathrm{CGM}} = 0.3$ found by Prochaska et al. (2017) for $z \sim 0.2$ galaxies (see also, Wotta et al. 2016, where the authors find a bimodal distribution of $\mathscr{Z}_{\mathrm{CGM}}$); however, these surveys do not cover the entire range in galaxy masses we are interested in, and we expect $\mathscr{Z}_{\mathrm{CGM}}$ to be lower in low mass galaxies. In any case, this difference does not have a significant effect on the MZGR.

et al. 2016; Christensen et al. 2018; Emerick et al. 2018b, 2019), and also has some observational evidence (Martin et al. 2002; Chisholm et al. 2018).

To further treat the question of how ϕ_y scales with $M_\star$ quantitatively, we also plot two models for this scaling. We obtain the first of these from available observations that directly constrain the ratio of wind metallicity to ISM metallicity (Chisholm et al. 2018), and the second simply by forcing the model to reproduce the observed MZR provided by Curti et al. (2020a). Appendix D describes how we obtain these scalings (and the associated uncertainties) in detail. While the shape of the first scaling is consistent with observed MZRs, the second is almost identical to the direct T_e based MZRs by construction; we include the second scaling nonetheless because there is no guarantee that the scaling we have enforced to produce the MZR will also yield the correct MZGR, a question we explore below.

Figure 7.1 shows that the MZR bends roughly where the ratio $\mathcal{P}/\mathcal{A}$ passes through unity. We can understand this behaviour as follows: the total metallicity is set by a competition between metal production (the term $\mathcal{S}$) and dilution by metal-poor gas, which can be supplied either by direct cosmological accretion onto the disc ($\mathcal{A}$) or advection of gas from the weakly-star-forming outskirts to the more rapidly-star-forming centre ($\mathcal{P}$). Each of these terms varies differently with rotation curve velocity v_ϕ, which in turn correlates with stellar mass; as shown in Sharda et al. (2021b), $\mathcal{P}$ is independent of v_ϕ,[3] while $\mathcal{S} \propto v_\phi^2$ and $\mathcal{A} \propto v_\phi^{3.3}$. In the low-mass regime, corresponding to small v_ϕ, we have $\mathcal{P} > \mathcal{A}$, implying that the metallicities are primarily set by the balance between source and advection. Since $\mathcal{P} \propto v_\phi^0$ and $\mathcal{S} \propto v_\phi^2$, as we go to smaller $M_\star$ and v_ϕ, the equilibrium metallicity drops because of lower v_ϕ and lower ϕ_y as compared to massive galaxies. On the contrary, in the high-mass regime $\mathcal{A} > \mathcal{P}$, implying that the metallicities are set by the balance between $\mathcal{A}$ and $\mathcal{S}$. Since $\mathcal{A} \propto v_\phi^{3.3}$, which is stronger than the dependence of $\mathcal{S}$ on v_ϕ, the metallicity, which is proportional to $\mathcal{S}/\mathcal{A}$, ceases to rise with $M_\star$, and instead reaches a maximum and starts to decrease. However, the decrease is rather mild, because shortly after passing the value of v_ϕ where we move into the $\mathcal{A} > \mathcal{P}$ regime, galaxies become so massive that they cease to be star-forming altogether. Thus, among star-forming galaxies, the trend of $\overline{\mathcal{Z}}$ with $M_\star$ is simply that $\overline{\mathcal{Z}}$ ceases to increase and reaches a plateau. For less massive galaxies the dominant source of metal-poor gas is advection rather than accretion. However, this only holds as long as advection is non-zero; for low mass galaxies where there is no advection (*i.e.,*

---

[3]Recall that each of these terms is expressed as the relative importance of a particular process compared to metal diffusion; thus, $\mathcal{P} \propto v_\phi^0$ does not mean that advection is equally rapid in all galaxies independent of stellar mass, just that the ratio of advection to diffusion does not explicitly depend on stellar mass.

there is no turbulence due to gravity), it falls upon cosmic accretion to balance metal production. Since cosmic accretion is much weaker in low mass galaxies, it can take a long time for this balance to approach a steady-state, which can push the gradients out of equilibrium (Sharda et al. 2021b, Section 5.1).

7.3.2 Comparison with previous work

The existence of a local gas phase MZR has been known since early analysis of data from the Sloan Digital Sky Survey (SDSS, Tremonti et al. 2004), although the absolute normalisation of the MZR remains an unsolved issue due to systematic calibration uncertainties (Kewley & Ellison 2008; Pilyugin & Grebel 2016; Brown et al. 2016; Curti et al. 2017; Barrera-Ballesteros et al. 2017; Teimoorinia et al. 2021). Despite these uncertainties, however, it is clear both that a relationship exists, and that it has a characteristic mass scale of $\sim 10^{10.5}$ M$_\odot$ at which the curvature of the relation changes (Blanc et al. 2019). Not surprisingly, there have been numerous attempts to explain these relations theoretically, and it is interesting to put our model in the context of these works. However, we caution that what follows is only a partial discussion of the (vast) literature on this topic, and refer readers to the comprehensive review by Maiolino & Mannucci (2019, Section 5.1).

The basic result from theoretical models to date is that galaxies tend to approach equilibrium between inflows, accretion, star formation and outflows, which naturally gives rise to the observed MZR (Finlator & Davé 2008; Davé et al. 2012; Lilly et al. 2013; Dayal et al. 2013; Forbes et al. 2014b). Our results are broadly consistent with this picture. However, there are some subtle differences among published models, and between existing models and ours. One important point of distinction is the extent to which outflows are metal-enriched relative to the ISM (*i.e.,* $\phi_y < 1$ in the language our model), and whether this enrichment varies as a function of galaxy mass or other properties (as is the case for our two possible scalings). As already discussed, many authors simply assume that outflows are not metal-enriched (*i.e.,* the outflow metallicity is the same as the ISM metallicity, $\phi_y = 1$ in our notation; e.g., Finlator & Davé 2008; Davé et al. 2012; Schaye et al. 2015; Hirschmann et al. 2016; Davé et al. 2017; Collacchioni et al. 2018; De Lucia et al. 2020), and produce an MZR based on this assumption. Others explicitly contemplate values of $\phi_y < 1$ (e.g., Dalcanton 2007; Spitoni et al. 2010; Peeples & Shankar 2011; Lu et al. 2015; Forbes et al. 2014b, 2019; Yates et al. 2020; Kudritzki et al. 2021). Our conclusion that reproducing the full shape of the MZR requires $\phi_y < 1$, particularly in low-mass galaxies, is consistent with the findings of the latter group of investigators. However, many of these authors do not study the relative importance of metal-

enriched outflows for dwarfs versus spirals, which we find to be important.

It is also debated whether the MZR really has a curvature at intermediate stellar masses, and if it does, whether it simply flattens out or starts to bend. While some simulations do find curvature in the MZR around $10^{10} - 10^{10.5} \, M_\odot$ (e.g., Davé et al. 2017; Torrey et al. 2019), others do not (e.g., Torrey et al. 2014; De Rossi et al. 2015; Ma et al. 2016). Our model is consistent with the former, especially if we look at the empirical scalings of ϕ_y with $M_\star$. Moreover, recent results also show that the curvature is physical and persists in the data even after observational uncertainties are accounted for (Blanc et al. 2019). However, the cause behind the curvature is not completely understood, and factors like Active Galactic Nuclei (AGN) feedback (De Rossi et al. 2017), gas recycling (Brook et al. 2014), effective gas fraction (Torrey et al. 2019), chemical saturation in the ISM of massive galaxies (Zahid et al. 2013), and a transition in galaxy regimes together with metal-enriched outflows as we show in this work can all play a role.

In addition to the models above, to which our results are directly comparable, a number of authors have studied the dependence of the MZR on factors not included in our work, like downsizing, time-dependent outflows, variations in star formation efficiencies and IMF, presence of satellites, environmental effects, etc. (e.g., Köppen et al. 2007; Cooper et al. 2008; Maiolino et al. 2008; Calura et al. 2009; Spitoni et al. 2010; Bouché et al. 2010; Hughes et al. 2013; Peng & Maiolino 2014; Genel 2016; Wu et al. 2017; Bahé et al. 2017; Lian et al. 2018a,b). However, unlike the current work, most models only study the MZR and not the MZGR, thus it is difficult to reconcile whether their conclusions hold or are self-consistent with spatially-resolved galaxy properties.

7.4 Mass-metallicity gradient relation (MZGR)

7.4.1 Results on the MZGR from the model

We use the same metallicity distributions described in Section 7.3 to compute metallicity gradients. To be consistent with the procedure most commonly used in analysing observations, we obtain the gradient by performing a linear fit to $\log_{10} \mathcal{Z}$ from $0.5 - 2.5 \, r_\mathrm{e}$ (e.g. Sánchez et al. 2012, 2014; Sánchez-Menguiano et al. 2016; Poetrodjojo et al. 2018).[4] Following the discussion on inverted gradients in Sharda

---

[4]To be consistent with observations, we only utilize metallicities till $2.5 \, r_\mathrm{e}$ to measure the gradients, as opposed to $3 \, r_\mathrm{e}$ that we use to measure $\overline{\mathcal{Z}}$.

et al. (2021b, Section 5.2.3) and the uncertainty around them being in equilibrium, we restrict the model to produce only flat or negative gradients for the purposes of studying the MZGR. Figure 7.2 shows the MZGR from our model, again color-coded by the ratio of advection to accretion ($\mathcal{P}/\mathcal{A}$). The top and the bottom panels show the metallicity gradients in $\mathrm{dex\,kpc^{-1}}$ and $\mathrm{dex\,}r_\mathrm{e}^{-1}$ units, respectively. The spread, as for the MZR, is a result of ϕ_y. The transition from the advection-dominated to the accretion-dominated regime, as in the MZR, is also visible in the MZGR. When the gradients are measured in $\mathrm{dex\,kpc^{-1}}$, this transition corresponds to the slight curvature in the MZGR that appears around $M_\star \sim 10^{10} - 10^{10.5}\,\mathrm{M_\odot}$ (top panel in Figure 7.2). When they are measured in $\mathrm{dex\,}r_\mathrm{e}^{-1}$, it corresponds to the somewhat sharper curvature around the same stellar mass (bottom panel in Figure 7.2). This finding is strong evidence for the links between the MZR and the MZGR, and also reveals that it is the same underlying physical mechanism that controls the shape of both.

While the stellar mass of the accretion-advection transition influences the location at which our model curves bend, it is not the only factor that does so. The precise location of the bend is also sensitive to parameters like $\mathcal{Z}_\mathrm{CGM}$ and ϕ_y, and both of the MZGR bend and the mass where $\mathcal{P}/\mathcal{A} = 1$ depend weakly on the limits in $M_\star$ we select for smoothly interpolating between the dwarf and spiral regimes: for example, if we lower the threshold for spirals from $10^{10.5}\,\mathrm{M_\odot}$ to $10^{10}\,\mathrm{M_\odot}$, both shift to lower stellar mass. Similarly, if we increase the threshold for dwarfs from $10^9\,\mathrm{M_\odot}$ to $10^{9.5}\,\mathrm{M_\odot}$, both shift to higher stellar mass. However, irrespective of the interpolation limits in $M_\star$, both the curvature of the MZGR and the transition from $\mathcal{P} > \mathcal{A}$ to $\mathcal{P} < \mathcal{A}$ are always present. The existence of these features is a robust prediction of the model independent of uncertain parameter choices.

The physical origin for the behaviour of the MZGR is also the same as for the MZR: gradients are at their steepest when both of the processes for smoothing them – accretion, $\mathcal{A}$, and inward advection of gas, $\mathcal{P}$, are at their weakest compared to metal production, $\mathcal{S}$. Diffusion also helps smooth gradients, but is always subdominant compared to either accretion or advection, as evidenced by the fact that we never have $\mathcal{P} < 1$ and $\mathcal{A} < 1$ simultaneously. The point where advection and accretion are weakest is roughly where galaxies are transitioning from being advection-dominated, $\mathcal{P} > \mathcal{A}$, to accretion-dominated, $\mathcal{P} < \mathcal{A}$. We emphasise that, while the exact stellar mass at which this transition occurs can be somewhat sensitive to choices of model parameters (for example, the Toomre Q of galactic discs), its existence is not; the bends in the coloured bands in Figure 7.2 that describe our model always occur irrespective of our parameter choices. Additionally, note that the minimum of the

model MZGR is not always coincident with $\mathcal{P}/\mathcal{A} = 1$; the position of the minimum is dependent on the model parameters, in particular, ϕ_y.

In Figure 7.2 we also plot MZGRs from the MaNGA (Belfiore et al. 2017), CALIFA (Sánchez et al. 2014; Sánchez-Menguiano et al. 2016) and SAMI (Poetrodjojo et al. 2018, 2021b) surveys, homogenized and corrected for spatial resolution by Acharyya et al. (2021). We adopt the $\mathrm{dex\,kpc}^{-1}$ values from Acharyya et al. (2021), and convert to $\mathrm{dex}\,r_{\mathrm{e}}^{-1}$ following the r_{e}–$M_\star$ scaling relations from van der Wel et al. (2014) to be consistent with our assumptions elsewhere[5]. We also overplot results from MaNGA based on three different metallicity calibrations by Mingozzi et al. (2020): Pettini & Pagel (2004, PP04), Maiolino et al. (2008, M08), and Blanc et al. (2015, IZI).

The first thing to notice is that the qualitative trend found in the data is in good agreement with that predicted by our model: gradients are steepest at $M_\star \sim 10^{10} - 10^{10.5}\ \mathrm{M}_\odot$, and flatten at both lower and higher masses. However, the location of the curvature in the data and the model differ by as much as $0.5 - 1\,\mathrm{dex}$ in stellar mass. This is not surprising given the uncertainties in the parameters that affect the curvature, as discussed above (e.g., interpolation limits in $M_\star$, our constant adopted value of $\mathcal{Z}_{\mathrm{CGM}}$, and the scaling of ϕ_y with $M_\star$). Moreover, it is important to recall that the data themselves are not fully secure, due to uncertainties caused by the choice of metallicity diagnostic; Poetrodjojo et al. (2021b, their Figure 11) show that the exact mass at which the MZGR bends depends on which diagnostic is used to determine the metallicity, and that these variations are reduced but still persist even after the diagnostics are homogenised. Thus, it is presently difficult to accurately determine the location of the curvature, especially given its mildness. Nonetheless, the presence of a bend seems to be robust in the data, as it is in our model.

Second, we see that similar to the MZR, this comparison of the model to the observed MZGR reveals that low-mass galaxies prefer low ϕ_y. However, the spread due to ϕ_y in the MZGR at the high-mass end is quite narrow; thus, gradients in massive galaxies are not particularly sensitive to ϕ_y, although the data suggests higher ϕ_y for the MZGR in massive galaxies (note the inverted arrows for ϕ_y on Figure 7.2 as compared to Figure 7.1). Our findings on ϕ_y being ineffective at setting gradients in massive galaxies is consistent with earlier works (e.g., Fu et al. 2013). However, our proposed explanation for the flattening of gradients in massive galaxies based on

---

[5]The qualitative trend of the MZGR remains the same for the $\mathrm{dex}\,r_{\mathrm{e}}^{-1}$ gradients reported by Acharyya et al. (2021) as compared to the ones shown in the bottom panel of Figure 7.2 using the scaling relation between r_{e}–$M_\star$, with a change in the overall normalisation of the metallicity. We have also verified that the r_{e} we find from van der Wel et al. (2014) is in very good agreement with that measured in, for example, the SAMI sample we use.
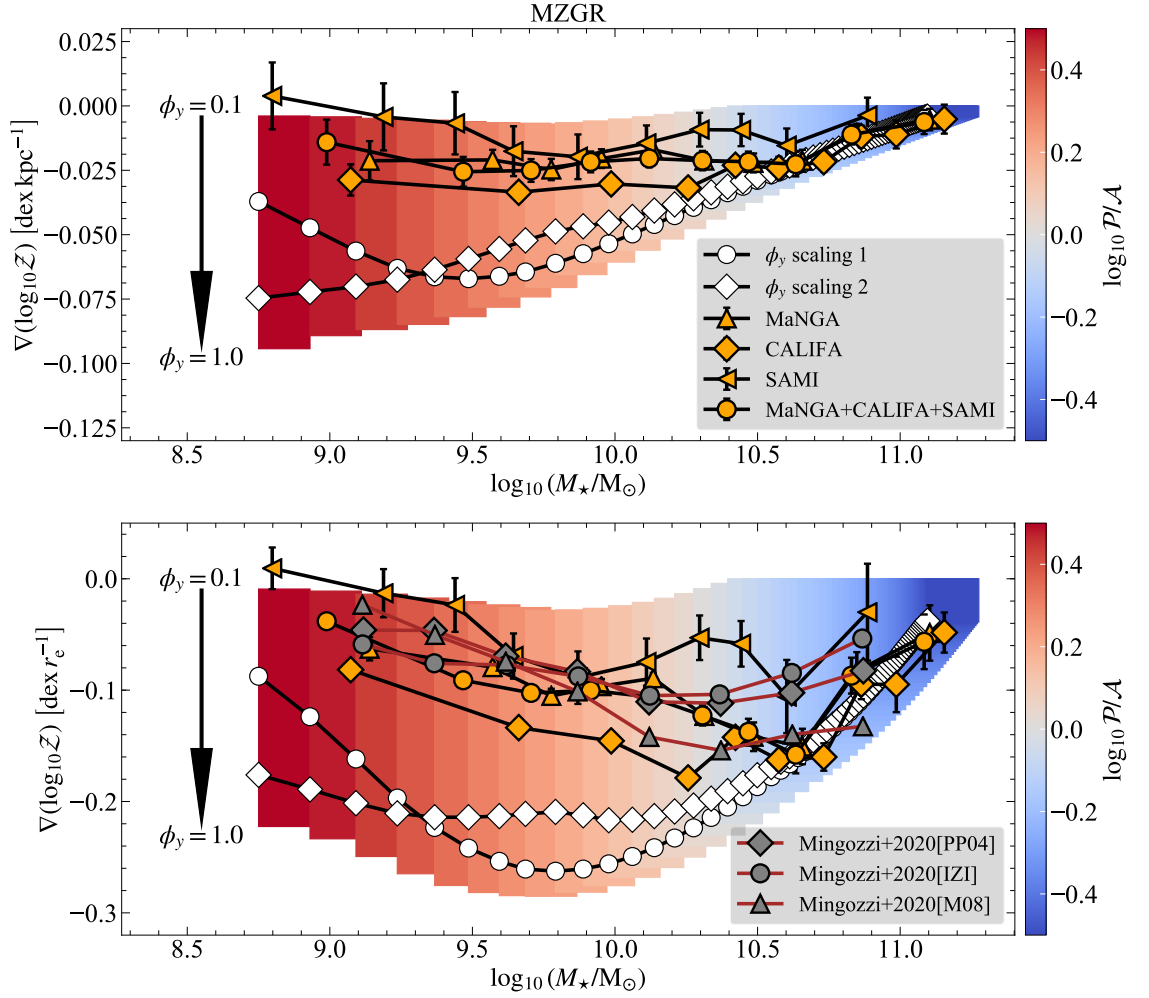
Figure 7.2: The mass–metallicity gradient relation (MZGR) for the local Universe. The coloured band shows model predictions for different yield reduction factors, ϕ_y (note the opposite direction of the arrow as compared to Figure 7.1), color-coded by the ratio of the Péclet number ($\mathcal{P}$) to cosmic accretion over diffusion ($\mathcal{A}$) in galaxies. The data to which we compare this model (orange points) are taken from a homogeneous analysis of metallicity gradients from the SAMI (Poetrodjojo et al. 2021b), MaNGA (Belfiore et al. 2017) and CALIFA (Sánchez et al. 2014) surveys, corrected for spatial resolution by Acharyya et al. (2021). To give a sense of the systematic uncertainty, grey markers denote gradients measured with different metallicity calibrations (Pettini & Pagel 2004, PP04, Maiolino et al. 2008, M08, and Blanc et al. 2015, IZI) for the MaNGA survey by Mingozzi et al. (2020). Finally, we show model predictions with two possible empirical scalings of ϕ_y with $M_\star$ (white markers); these scalings are the same as in Figure 7.1. The important conclusion from this plot is that metallicity gradients in local galaxies transition from the advection-dominated regime ($\mathcal{P} > \mathcal{A}$) to the accretion-dominated regime ($\mathcal{P} < \mathcal{A}$) as the stellar mass increases, and it is this transition that drives the shape of the MZGR. Note that the range in stellar mass covered by this figure is different than that shown in Figure 7.1, due to differences in the mass ranges covered by the available observations.

the advection-to-accretion transition differs from these studies that attributed the observed flattening to saturation of ISM metallicities (Phillipps & Edmunds 1991; Mollá et al. 2017), radially-varying star formation efficiency (Belfiore et al. 2019), or past mergers (Rupke et al. 2010a; Perez et al. 2011; Fu et al. 2013).

In Figure 7.2, we also plot model predictions using the two scalings of ϕ_y with $M_\star$ that we described in Section 7.3. These scalings are able to reproduce the high mass end of the MZGR, and yield a qualitative trend similar to that seen in the data, but quantitatively the predicted gradients from the scalings are steeper than that observed at the low mass end. In retrospect, this is not entirely unexpected given the uncertainties in the two approaches, and the fact that these scalings are sensitive to the absolute metallicity (see Appendix D). Judging from Figure 7.2, we slightly prefer scaling 2, since it is closer to the observations at intermediate stellar masses; we revisit the comparison between the two scalings in Section 7.5. Nevertheless, the fact that both the MZR and the MZGR suggest a qualitatively similar scaling between ϕ_y and $M_\star$ is an encouraging sign of consistency. However, it is difficult to derive quantitative similarities given the uncertainties in these empirical scalings.

7.4.2   Comparison with previous work

Only a handful of models exist in the literature that focus on gas phase metallicity gradients rather than global metallicities (Mott et al. 2013; Jones et al. 2013; Ho et al. 2015; Carton et al. 2015; Kudritzki et al. 2015; Pezzulli & Fraternali 2016; Schönrich & McMillan 2017; Kang et al. 2021), and even fewer that actually study the local MZGR or its equivalent (Lian et al. 2018b, 2019; Belfiore et al. 2019). Of these, the models by Lian et al. (2018b) and Belfiore et al. (2019) are closest in spirit to ours.[6] Quantitative comparison between our results and those of Lian et al. is challenging, because they do not quote measurements in dex/kpc or equivalent. Examining their plots, it seems that they also find slightly steeper gradients for intermediate mass galaxies, consistent with our findings. Similarly, Belfiore et al. find that observed gradients in local dwarfs and spirals are best reproduced by a model where the star formation timescale at each radius is proportional to the local orbital period. For massive galaxies, this scaling is quite similar to that in the Krumholz et al. (2018) galaxy model that is embedded in our metallicity model, and thus at first glance is also consistent with our findings. However, there remain substantial differences between our model and those of Lian et al. and Belfiore et al.. Neither of these studies include the effects of radial inflow or metal diffusion.

---

[6]Lian et al. (2019) focus only on low-mass satellites, so our results are not easily comparable.

Neither adopt our approach of systematically varying the highly-uncertain yield reduction factor ϕ_y: Lian et al. adopt a parameterised, time-dependent functional form that they tune in order to match stellar and gas metallicity gradient data, while Belfiore et al. assume that the ISM and outflow metallicities are equal ($\phi_y = 1$ in our terminology), contrary to our findings and inconsistent with the available observational evidence (Martin et al. 2002; Schmidt et al. 2016; Chisholm et al. 2018; Telford et al. 2019; Kreckel et al. 2020). Finally, both sets of authors explicitly fit their model parameters to the data, whereas we do not except while introducing the second scaling in ϕ_y. Thus, it is unclear to what extent the agreement between the models is simply a matter of their being enough adjustable parameters to make them behave similarly.

In addition to analytic models, semi-analytic models like L-Galaxies 2020 have also investigated the local MZGR, finding somewhat flatter gradients for massive galaxies as compared to low mass galaxies (Yates et al. 2020). The authors attribute their findings to inside-out star formation that increases the gas phase metallicity in the inner disc in massive galaxies. In the outer disc in these galaxies, Yates et al. either find metal-rich accretion from the CGM that enhances the metallicity (their 'modified' model), or metal-poor accretion that dilutes the metallicity at every radius (their 'default' model). The combined effect is to produce flatter metallicity profiles in massive galaxies in each case. They further conclude that flattening of the metallicity profiles in massive local galaxies is expected regardless of the mass-loading factors of outflows. Thus, their explanations for the trends seen in the local MZGR are consistent with the findings of our model. It is worth noting that while working with an earlier version of L-Galaxies, Fu et al. (2013) found relative metal enrichment of outflows to be more important than advection in driving gas phase metallicities. These authors also find a trend in the MZGR consistent with Yates et al. and ours.

It is also helpful to compare our results to simulations that have studied the local MZGR. For example, both Tissera et al. (2016) and Ma et al. (2017) find slightly flatter gradients for massive local galaxies in their simulations, consistent with our model and available observations. The EAGLE simulations (Schaye et al. 2015) find that metallicity gradients in their simulated galaxies are systematically shallower at $z = 0$ than those observed in the local Universe due to high star formation efficiency at all radii (Tissera et al. 2019, Figure 11). As a result, the MZGR predicted from their simulations does not show any clear trends with the stellar mass. On the other hand, the local MZGR produced by the IllustrisTNG50 simulations (Pillepich et al. 2019; Nelson et al. 2019) is in very good quantitative agreement with that produced

by our model, both in terms of the mean gradient and the scatter in gradients at a given stellar mass (Hemler et al. 2021, Figure 8). These authors suspect that gradients flatten in massive local galaxies due to AGN feedback and increasing galaxy size. While the latter of the two is consistent with the findings of Sharda et al. (2021b), the primary driver of flatter gradients in massive galaxies in our model is due to the increasing role of metallicity dilution by cosmic accretion.

7.5 The MZR–MZGR relation

In this section, we introduce a new way of looking at galaxy metallicities, by studying the MZR−MZGR correlation space. The two-fold motivation behind this is to: (1.) understand how global metallicities correlate with metallicity gradients in galaxies, because this can inform us about the correlations between global and internal dynamics of galaxies, and (2.) given that both the MZR and the MZGR require similar scaling of ϕ_y with $M_\star$ to reproduce the observations, we can study the relative importance of ϕ_y for both of these relations. An additional advantage of studying this parameter space is that it can be constructed both in observations and simulations.

In order to construct the MZR–MZGR correlation space in the model, we simply plot $\nabla(\log_{10}\mathcal{Z})$ from Figure 7.2 as a function of $\overline{\mathcal{Z}}$ from Figure 7.1. We show this in the left panel of Figure 7.3, where we color-code the model points by $M_\star$, with different curves corresponding to different ϕ_y. Note that the range in $M_\star$ is slightly different in this plot as compared to that in Figure 7.1 and Figure 7.2; thus, there are some differences visible in this plot as compared to previous figures. It is clear from this plot that ϕ_y has two distinct effects. At the high-mass end, it simply shifts the overall metallicity $-\ \overline{\mathcal{Z}} \propto \phi_y\ -$ without significantly affecting the gradient. At the low-mass end, it affects the overall metallicity, but also affects the gradient, by making it steeper for larger ϕ_y. It is also clear that the relationship between $\overline{\mathcal{Z}}$ and $\nabla(\log_{10}\mathcal{Z})$ is non-monotonic because of the same $\mathcal{P}/\mathcal{A}$ split we have seen in the MZR and the MZGR, $i.e.,$ there are two typical branches where $\overline{\mathcal{Z}}$ and $\nabla(\log_{10}\mathcal{Z})$ change monotonically with respect to one another, but the curves bend when galaxies transition from the advection-dominated to the accretion-dominated regime. Irrespective of the value of ϕ_y, this bend always occurs around $10^{10-10.5}\,\mathrm{M}_\odot$ because it is dictated by the ratio $\mathcal{P}/\mathcal{A}$ crossing unity. To demonstrate the robustness of this feature, we also overplot results for the two empirical scalings of ϕ_y with $M_\star$ that we discussed in previous sections. We see that both empirical scalings also produce a bend in the $\overline{\mathcal{Z}} - \nabla(\log_{10}\mathcal{Z})$ plane, but with rather different amounts of
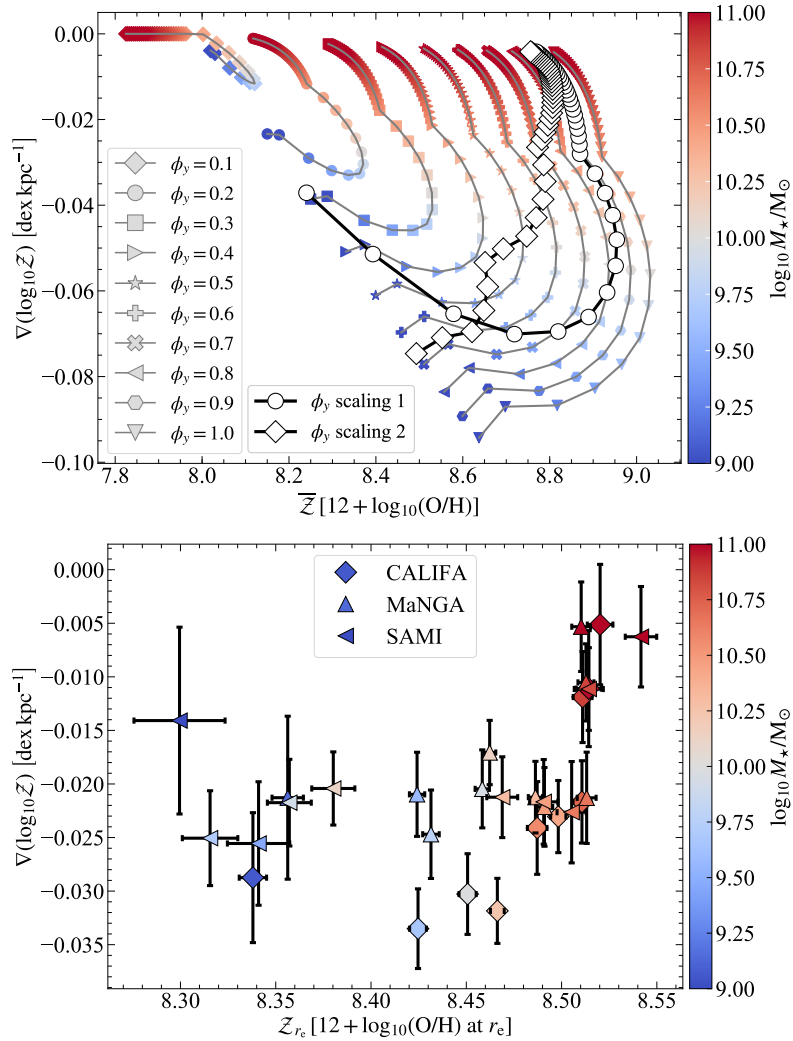
Figure 7.3: *Left panel:* MZGR–MZR space from the model for the local Universe, defined by the metallicity gradient (in $\mathrm{dex\,kpc^{-1}}$) as a function of the global (SFR-weighted) galaxy metallicity (defined as in equation 7.7). Points are color-coded by stellar mass, and different curves represent the different yield reduction factor, ϕ_y, which describes the metal-enrichment of galactic outflows. Both the MZR and the MZGR predict a scaling of ϕ_y with $M_\star$ such that low-mass galaxies prefer low ϕ_y, implying that these galaxies lose a higher proportion of the metals they produce to winds, as compared to massive galaxies. Also overlaid are the two empirical scalings of ϕ_y with $M_\star$ that are shown in Figure 7.1 and Figure 7.2. The bend seen at intermediate masses corresponds to the advection-to-accretion transition identified in Figure 7.1 and Figure 7.2. The range in $M_\star$ covered in this plot is slightly different from that in Figure 7.1 and Figure 7.2. *Right panel:* Mean metallicity gradients as a function of metallicity at the effective radius r_e in the CALIFA, MaNGA and SAMI surveys that we adopt from Acharyya et al. (2021). The observations show a similar bend compared to the predictions of the model in the MZR–MZGR space. Note, however, the differences in the axes ranges between this panel and the left panel, reflecting the difficulty of putting metallicity measurements at specific radius (r_e) and "global" metallicities on a common scale. The trends in the model as well as the data in the MZR-MZGR space remain qualitatively similar when the gradients are plotted in units of $\mathrm{dex}\,r_\mathrm{e}^{-1}$ instead of $\mathrm{dex\,kpc^{-1}}$.

curvature. Thus, a generic prediction of our model is that galaxies should lie along a bent track in $\overline{\mathcal{Z}} - \nabla(\log_{10} \mathcal{Z})$ space, with one arm closer to vertical and one closer to horizontal, but we cannot predict the exact shape of this track without a better understanding of how ϕ_y varies with $M_\star$. The trends in the model we identify in the MZR-MZGR space remain qualitatively the same when the gradients are plotted in units of $\mathrm{dex}\, r_\mathrm{e}^{-1}$, so we do not discuss them separately.

We create a parameter space similar to that above by plotting the measured metallicity gradients as a function of the measured gas phase metallicity at r_e from Acharyya et al. (2021)[7]. We show this in the right panel of Figure 7.3, color-coded with $M_\star$. The main takeaway from this figure is that the data shows a qualitatively similar bend at $M_\star \sim 10^{10.5}\,\mathrm{M}_\odot$ as the model. While this is not a one-to-one comparison between the model and the data given the former uses global metallicity whereas the latter uses metallicity at a specific location in the disc, we expect the qualitative trend (*i.e.,* the presence of the bend) to be robust given the findings in the previous sections. Similar to our observations in Section 7.4, we find that scaling 2 better reproduces the trend seen in the data. Further, like the model, the same trends in the data are also present when the gradients are plotted in units of $\mathrm{dex}\, r_\mathrm{e}^{-1}$. Thus, the model is able to identify and recover the presence of this bend in the metallicity–metallicity gradient space, and sets clear predictions for future work that will enable us to re-construct this space and facilitate a direct comparison with the model.

Hence, in addition to our findings in Section 7.3 and Section 7.4, we conclude that metal-enriched outflows play a crucial role in setting both the MZR and the MZGR for low-mass galaxies, while for high-mass galaxies, outflows play a significant role only for the MZR.

7.6   Conclusions

In this work, we present a physical explanation for the observed relation between the stellar mass and the gas phase metallicity gradient (MZGR) for galaxies in the local Universe, using the recently-developed first-principles model of gas phase metallicity gradients in galaxies given by Sharda et al. (2021b). We show that the shape of the MZGR is driven by the balance between metal advection and production for low-mass galaxies, and between cosmic accretion and metal production for

---

[7]The conversion from metallicity at r_e to mean metallicity is non-trivial and suffers considerable calibration uncertainties, both in the observations and in the model (which does not use r_e as a parameter or make an independent prediction of its location in the disc), which is why we do not attempt to create an MZR from the same observations for which we have the MZGR to directly study the MZR–MZGR space.

massive galaxies. The point where the MZGR begins to curve as the galaxy mass increases corresponds to the transition of galaxies from the advection-dominated to the accretion-dominated regime. Additionally, the best match between the model and the data naturally recovers the expected dependence of the MZGR on metal-enrichment of galactic outflows: low-mass galaxies have more metal-rich winds as compared to massive galaxies, implying that metals in low mass galaxies are not well-mixed with the ISM before ejection. This is in good agreement with observations (Martin et al. 2002; Chisholm et al. 2018) and simulations (Emerick et al. 2018b; Christensen et al. 2018; Tanner 2020).

We also present the first joint explanation for the mass-metallicity relation (MZR) and the MZGR. We find that in addition to the model successfully reproducing both the MZR and the MZGR, it has two primary commonalities: (1.) the curvature observed in both the MZR and the MZGR around a stellar mass $M_\star \approx 10^{10-10.5}\,\mathrm{M_\odot}$ have the same underlying cause, which is the shift between radial advection (in low-mass galaxies) and cosmological accretion (in more massive galaxies) as the dominant agent supplying metal-poor gas to galaxy centres, and (2.) both the MZR and the MZGR produced by the model predict that supernova-produced metals in low-mass galaxies are largely ejected before mixing with the ISM, while metals in high-mass galaxies are well-mixed with the ISM. The fact that the MZR and MZGR results are qualitatively consistent with each other is evidence for the links between global and spatially-resolved galaxy properties, though our ability to check this quantitatively is currently limited by the large uncertainties in observed metallicites.

In studying these relations, we also introduce a new way of characterizing gas phase metallicities via the MZR–MZGR correlation space. We find that the relation between the global metallicity and metallicity gradient in galaxies is non-monotonic, and bends as a result of the advection-to-accretion transition identified above. We also retrieve this bend in the available data (in metallicity gradient–metallicity at r_e space), although limitations due to the mismatch between model and data techniques prevent us from constructing the observed MZR–MZGR space exactly as we do for the model. Moreover, the MZR–MZGR space also disentangles the relative importance of metal-enriched outflows for the global metallicities and metallicity gradients: while metal-enrichment of the outflows significantly influences both the global metallicity and metallicity gradients in low-mass galaxies, in massive galaxies only the absolute metallicity is sensitive to the properties of the outflows, and gradients are flat regardless of outflow metallicity.

Acknowledgements

The role of gas kinematics in setting metallicity gradients at high redshift

Context and Contribution

This chapter have been previously published as **'The role of gas kinematics in setting metallicity gradients at high redshift'**, *by* **Piyush Sharda, Emily Wisnioski, Mark R. Krumholz, and Christoph Federrath, 2021, MNRAS, 506, 1295**. *The work is presented here exactly as in the publication. I analyzed the data, re-measured the kinematics for all galaxies and the metallicity gradients for a subset of galaxies used in this work. I have created the model described in this work. I have contributed heavily to interpretation of the results and written the majority of the paper, with inputs and suggestions from co-authors.*

Abstract

In this work, we explore the diversity of ionised gas kinematics (rotational velocity v_ϕ and velocity dispersion σ_g) and gas-phase metallicity gradients at $0.1 \leq z \leq 2.5$ using a compiled data set of 74 galaxies resolved with ground-based integral field spectroscopy. We find that galaxies with the highest and the lowest σ_g have preferentially flat metallicity gradients, whereas those with intermediate values of σ_g show a large scatter in the metallicity gradients. Additionally, steep negative gradients appear almost only in rotation-dominated galaxies ($v_\phi/\sigma_\mathrm{g} > 1$), whereas most dispersion-dominated galaxies show flat gradients. We use our recently developed analytic model of metallicity gradients to provide a physical explanation for the shape and scatter of these observed trends. In the case of high σ_g, the inward radial advection of gas dominates over metal production and causes efficient metal mixing, thus giving rise to flat gradients. For low σ_g, it is the cosmic accretion of metal-poor gas diluting the metallicity that gives rise to flat gradients. Finally, the reason for

intermediate σ_{g} showing the steepest negative gradients is that both inward radial advection and cosmic accretion are weak as compared to metal production, which leads to the creation of steeper gradients. The larger scatter at intermediate σ_{g} may be due in part to preferential ejection of metals in galactic winds, which can decrease the strength of the production term. Our analysis shows how gas kinematics play a critical role in setting metallicity gradients in high-redshift galaxies.

8.1   Introduction

Understanding the distribution of metals in galaxies is crucial to learn about galaxy formation and evolution. It is now well known that metals in both the gas and stars show a negative, radial gradient across the discs of most galaxies. Since the discovery of metallicity gradients in galactic discs (Aller 1942; Searle 1971; Shaver et al. 1983), several attempts have been made to put the measurements in context of galaxy evolution theory, as well as understand the physics driving the magnitude of the gradient by exploring trends with galaxy properties, such as mass, star formation rate (SFR), star formation efficiency, specific SFR, radial inflows, cosmic infall, etc. (see recent reviews by Maiolino & Mannucci 2019; Kewley et al. 2019b; Sánchez et al. 2021; Sánchez 2020a; Förster Schreiber & Wuyts 2020). With the advent of large resolved spectroscopic surveys using integral field unit (IFU) spectroscopy we are now able to explore the relationship between metallicity gradients and galaxy kinematics (*i.e.*, the rotational velocity v_{ϕ} and the velocity dispersion σ_{g}). There are several reasons why we would expect such a correlation to exist. For example, turbulent mixing and transport, processes whose rates are expected to scale with σ_{g}, should be important processes that influence metallicity gradients (e.g., Yang & Krumholz 2012; Forbes et al. 2014a; Petit et al. 2015b; Armillotta et al. 2018; Krumholz & Ting 2018; Kreckel et al. 2020; Li et al. 2021). Similarly, rates of cosmic infall that can dilute both the overall metallicity and its gradients should correlate strongly with halo mass, which is closely linked to v_{ϕ} (e.g., Tully & Fisher 1977; McGaugh et al. 2000; Bell & de Jong 2001; Faucher-Giguère et al. 2011). The production of metals is dictated by star formation in galaxies, and star formation feedback also impacts galaxy kinematics (e.g., Ostriker & Shetty 2011; Faucher-Giguère et al. 2013; Forbes et al. 2014a; Kim & Ostriker 2015; Goldbaum et al. 2016; Krumholz et al. 2018; Furlanetto 2021). The amount of metals lost in outflows is also expected to scale inversely with v_{ϕ} (Garnett 2002). Thus, there are several links between metallicity gradients and galaxy kinematics, and it is clear that these links likely generate a rather complex relationship between each other as well as other relevant mechanisms.

Table 8.1: Summary of the data adopted from different sources in the literature. Columns $1-3$ list the different samples, instruments used to measure emission lines and the number of galaxies N that we use from each sample, respectively. Columns $4-5$ list the range in redshift and stellar mass of the observed galaxies. Column 6 lists the spectral resolution for each instrument, and columns 7 and 8 list the PSF FWHM in arcsec and kpc, respectively. Finally, column 9 lists the references for each sample: (a.) Epinat et al. (2012), (b.) Queyrel et al. (2012), (c.) Sobral et al. (2013b), (d.) Stott et al. (2014), (e.) Swinbank et al. (2012), (f.) Carton et al. (2018), (g.) Förster Schreiber et al. (2018).

Sample	Instrument	N	z	$\log_{10} M_\star/\mathrm{M}_\odot$	R	PSF FWHM ($''$)	PSF FWHM (kpc)	Ref.
(1)	(2)	(3)	(4)	(5)	(6)	(7)	(8)	(9)
MASSIV	SINFONI	19	$0.9-1.6$	$9.4-11.0$	$2000-2640$	$0.3-1.0$	$2-7$	a, b
HiZELS	KMOS	9	≈ 0.81	$9.8-10.7$	≈ 3400	~ 0.8	~ 6	c, d
SHiZELS	SINFONI	6	$0.8-2.2$	$9.4-11.0$	≈ 4500	~ 0.1	$0.7-0.8$	e
MUSE-WIDE	MUSE	23	$0.1-0.8$	$8.3-10.6$	$1650-3800$	$0.6-0.7$	$1-5$	f
SINS/zC-SINF	SINFONI	17	$1.4-2.4$	$10.1-11.5$	$2730-5090$	$0.1-0.3$	~ 0.8	g

This connection is perhaps most readily explored at high redshift ($z \leq 2.5$), when galaxies show a more diverse range of metallicity gradients and kinematics than are found in the local Universe (Maiolino & Mannucci 2019; Förster Schreiber & Wuyts 2020; Tacconi et al. 2020b). The last decade has seen immense progress in these areas, thanks to IFU spectroscopy instruments like MUSE (Multi Unit Spectroscopic Explorer, Bacon et al. 2010), KMOS (K-band Multi Object Spectrograph, Sharples et al. 2004), SINFONI (Spectrograph for INtegral Field Observations in the Near Infrared, Eisenhauer et al. 2003; Bonnet et al. 2004), FLAMES (Fibre Large Array Multi Element Spectrograph, Pasquini et al. 2002), GMOS (Gemini Multi Object Spectrograph, Davies et al. 1997), NIFS (Gemini Near-infrared Integral Field Spectrograph, McGregor et al. 2003), and OSIRIS (OH-Suppressing InfraRed Imaging Spectrograph, Larkin et al. 2006).

Studies using these instruments have revealed that, while high-z galaxies show a diverse range of metallicity gradients, the average evolution of these gradients is rather shallow, almost non-existent (Curti et al. 2020b, Figure 8). On the other hand, there is ample evidence for redshift evolution of galaxy kinematics. In particular, σ_{g} evolves with z implying that high-z discs are thicker and more turbulent (Kassin et al. 2012; Wisnioski et al. 2015, 2019; Simons et al. 2017; Übler et al. 2019). The mass-averaged rotational velocities are also expected to evolve with time (e.g., Dutton et al. 2011; Tiley et al. 2016; Straatman et al. 2017; Übler et al. 2017; Ma et al. 2017; Glowacki et al. 2020; see, however, Tiley et al. 2019a). However, links between kinematics and metallicity gradients at high redshift have been investigated by observations only in a handful of studies (Queyrel et al. 2012; Gillman et al. 2021), most of which were limited to gravitationally-lensed samples (Yuan et al. 2011; Jones et al. 2013; Leethochawalit et al. 2016), yielding no clear connections between the two. Some simulations have also started to explore joint evolution of metallicity gradients and kinematics (Ma et al. 2017; Hemler et al. 2021), but at present theoretical work is limited to empirical examination of simulations results. No models proposed to date have quantitatively discussed the observed correlations between metallicity gradients and gas kinematics.

In a companion paper (Sharda et al. 2021b), we presented a new model for the physics of gas phase metallicity gradients from first principles. We showed that our model successfully reproduces several trends of metallicity gradients with galaxy properties, for example, the observed cosmic evolution of metallicity gradients (Sharda et al. 2021b) and the mass-metallicity gradient relation (MZGR, Sharda et al. 2021f). The goal of this paper is to apply the model to existing observations of high-redshift galaxies to investigate the relationship between metallicity gradients
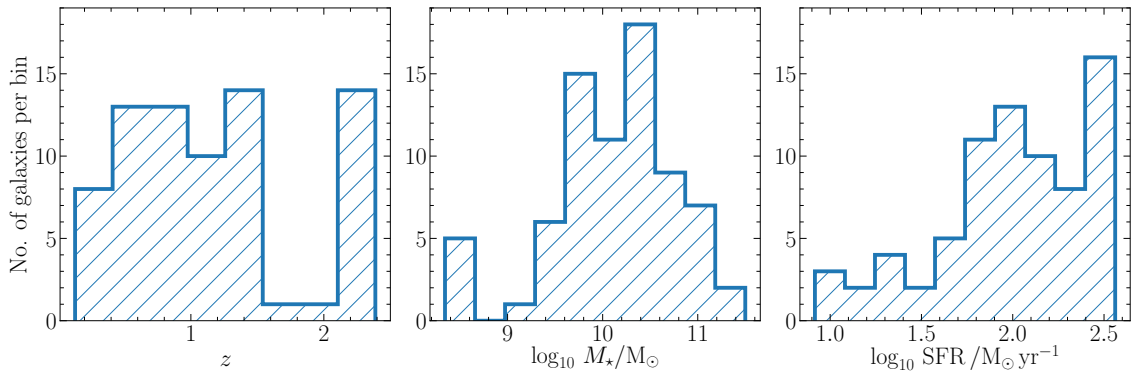
Figure 8.1: Distribution of galaxies at different redshifts (left), stellar mass (middle) and star formation rate (right) in the compiled sample used in this work.

and gas kinematics.

This paper is organized as follows: Section 8.2 describes the data on metallicity gradients and galaxy kinematics that we compile from observations, Section 8.3 presents the resulting trends we find in the data, Section 8.4 presents a discussion on the comparison of the observational data with our theoretical model, and Section 8.5 lists our conclusions. For this work, we use the ΛCDM cosmology with $H_0 = 71 \, \mathrm{km \, s^{-1} \, Mpc^{-1}}$, $\Omega_\mathrm{m} = 0.27$ and $\Omega_\Lambda = 0.73$ (Springel & Hernquist 2003). Further, we express $\mathcal{Z} = Z/\mathrm{Z_\odot}$, where $\mathrm{Z_\odot} = 0.0134$ (Asplund et al. 2009), and we use the Chabrier (2003) initial mass function (IMF).

8.2   Compiled Data and Analysis

We compile a sample of 74 non-lensed high-z ($0.1 \leq z \leq 2.5$) galaxies from the literature, studied with ground-based IFU instruments suitable for the measurement of metallicity gradients and gas kinematics. We only work with non-lensed galaxies because it is not yet clear if lens reconstructions accurately reproduce metallicity maps (Maiolino & Mannucci 2019, Section 6.7). However, we note that there is a similiar diversity of gradients from lensed galaxies (Wuyts et al. 2016; Leethochawalit et al. 2016), and including them does not change our results. We describe each of the samples we use in Section 8.2.1, and provide a summary in Table 8.1. Our database is inhomogeneous, because the sources we draw from have different sample selections, varying resolution, and use different techniques to obtain the metallicity gradients and kinematics. To alleviate some of the inhomogeneity, we reanalyse the kinematics using the same method for the full database, a process that we describe in Section 8.2.2. Additionally, where possible, we use a common metallicity diagnostic and calibration to estimate metallicity gradients. We list the database along with

the reanalysed kinematics for all 74 galaxies in Appendix E.1.

We acknowledge that there are many challenges associated with measuring metallicity gradients and kinematics in IFU observations, particularly at high-z. Metallicity measurements in H II regions rely on accurately modeling the H II-region physics, and systematic variations in the physical parameters with redshift, if any (e.g., Kewley et al. 2013a; Shirazi et al. 2014; Strom et al. 2018; Davies et al. 2020), emission line diagnostics and calibrations (e.g., Kewley & Ellison 2008; Poetrodjojo et al. 2021c), spatial and spectral resolution (e.g., Yuan et al. 2013; Mast et al. 2014), and contamination from shocks and active galactic nuclei (AGN, Kewley et al. 2013b; Newman et al. 2014). Similarly, kinematic measurements rely on model assumptions, source blending, beam smearing, and spectral resolution limits (e.g., Davies et al. 2011; Di Teodoro & Fraternali 2015; Burkert et al. 2016; Wisnioski et al. 2018). Thus, systematic errors originating from these physical and observational effects should be kept in mind in the context of our work. We note that some of the kinematic uncertainties are not captured in the quoted errors, which only account for uncertainties in the beam smearing, inclination, and instrumental resolution corrections.

8.2.1   Samples

1. *MASSIV.* We use data from the Mass Assembly Survey with SINFONI in VIMOS VLT Deep Survey (MASSIV, Contini et al. 2012) of star-forming galaxies between $1 < z < 2$. The kinematics and the metallicity gradients from this survey are described in Epinat et al. (2012) and Queyrel et al. (2012), respectively. The authors report on metallicity gradients using the [N II]/Hα ratio following the Pérez-Montero & Contini (2009) calibration. In order to be consistent with the other samples described below, we reverse the Pérez-Montero & Contini (2009) calibration to obtain the [N II]/Hα flux at different locations in the galactic disc, and use the flux to find the metallicities using the Pettini & Pagel (2004) calibration. We then use metallicities based on the Pettini & Pagel (2004) calibration to measure the metallicity gradients. We reanalyse the kinematics for this sample following the procedure described below in Section 8.2.2.

2. *HiZELS.* This sample consists of galaxies at $z \sim 0.8$ that were observed through KMOS as part of the High-z Emission Line Survey (HiZELS, Sobral et al. 2009, 2013a). The kinematics for these galaxies are reported in Sobral et al. (2013b) and the metallicity gradients in Stott et al. (2014). The metallicity gradients are measured with the [N II]/Hα ratio using the Pettini & Pagel (2004) calibration.

3. *SHiZELS.* In addition to the *HiZELS* survey above, we also use observations from the SINFONI-HiZELS survey (SHiZELS, Swinbank et al. 2012) that report on metallicity gradients and kinematics of 8 galaxies in the redshift range $0.8 - 2.2$. The gradients are measured with the [N II]/Hα ratio using the Pettini & Pagel (2004) calibration.

4. *MUSE-WIDE.* We take measurements of metallicity gradients carried out by Carton et al. (2018) for galaxies at low redshift ($0.08 < z < 0.84$) using MUSE. The authors use a forward-modeling Bayesian approach to estimate the metallicity gradients (Carton et al. 2017) from nebular emission lines (for $z \leq 0.4$, Hβ, O III, Hα, and S II, and for $z > 0.4$, O II, Hγ, Hβ, and O III). The kinematics for these galaxies are not available in the literature, so we obtain them by fitting publicly-available data (Herenz et al. 2017; Urrutia et al. 2019) using the emission line fitting code LZIFU (Ho et al. 2016). We describe this in detail in Section 8.2.2. We obtain the half-light radii for these galaxies from The Cosmic Assembly Near-infrared Deep Extragalactic Legacy Survey (CANDELS, van der Wel et al. 2012) and from 3D-HST photometry (Skelton et al. 2014).

5. *SINS/zC-SINF.* Förster Schreiber et al. (2018) report SINFONI observations of metallicity gradients and kinematics in galaxies at $z \sim 1.5 - 2.2$ from the *SINS/zC-SINF* survey, where the authors use the [N II]/Hα ratio to quantify the metallicity gradient. In order to homogenise their sample with other samples above, we use their recommended conversion factor to scale the gradients to the calibration given by Pettini & Pagel (2004). The reported kinematics for this sample are already corrected for instrumental and beam smearing effects using the approach from Burkert et al. (2016) which we utilise for the other samples in Section 8.2.2.

All the above surveys also include information on the stellar mass $M_\star$ (scaled to the Chabrier IMF where required) and the dust-corrected SFR from Hα, except for the *SINS/zC-SINF* survey. To obtain dust-corrected SFR estimates for *SINS/zC-SINF*, we use the integrated Hα fluxes reported by the authors, and scale them to find the dust-corrected Hα luminosity following Calzetti (2001), and convert it to SFR based on the Chabrier (2003) IMF following Kennicutt & Evans (2012).

Figure 8.1 shows the distributions of redshift, stellar mass and SFR of galaxies in our compiled sample from the above surveys. The distribution in redshift is quite uniform, except around $z \approx 1.7$, where there is no available data due to atmospheric absorption. This implies that the data we use are not biased towards a particular redshift. It is also clear from Figure 8.1 that the observations consist primarily of
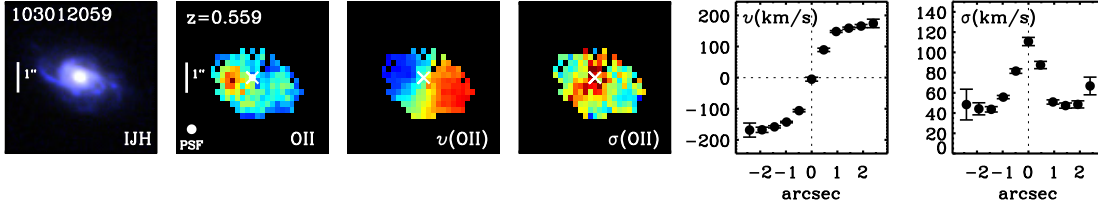
Figure 8.2: *Left to right* − observed-frame IJH color composite image from CAN-DELS HST imaging (Grogin et al. 2011; Koekemoer et al. 2011), nebular line flux with the strongest emission (O II in this case), rotational velocity v, velocity dispersion σ, as well as the 1D radial curves of v and σ derived from kinematic extractions for the galaxy G103012059 from the *MUSE-WIDE* sample.
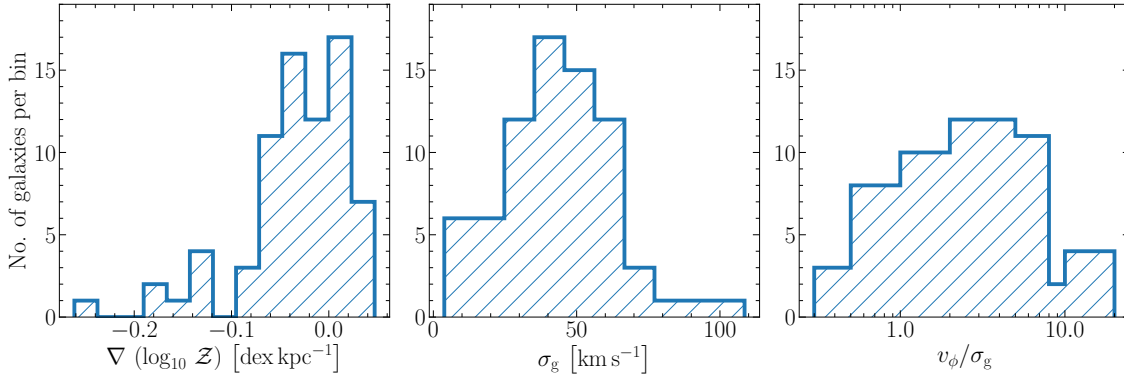
Figure 8.3: Same as Figure 8.1, but for the measured metallicity gradients (left), and reanalysed kinematics – velocity dispersion σ_{g} (middle) and the ratio of rotational velocity to velocity dispersion $v_{\phi}/\sigma_{\mathrm{g}}$ (right).

more massive ($M_{\star} > 10^{10}\,\mathrm{M}_{\odot}$) galaxies; the few low-mass galaxies ($M_{\star} \leq 10^{9.5}\,\mathrm{M}_{\odot}$) that we are able to study belong to the *MUSE-WIDE* sample. The overall sample is somewhat biased to high star formation rates: 20 per cent of the galaxies in the compiled sample have SFRs more than $3\times$ the main sequence SFR for their mass and redshift (Whitaker et al. 2012). This bias is not surprising, given that large Hα fluxes (corresponding to large SFRs) are typically necessary for spatially-resolved measurements at high redshift. However, we emphasise that the sample is not dominated by merging or interacting galaxies: based on the classifications provided by the source papers from which we draw the sample, less than 9 per cent of the galaxies are mergers or interactions. This means that our sample is not significantly affected by the flattening of gradients that typically occurs when galaxies merge (e.g., Rupke et al. 2010b; Rich et al. 2012; Torres-Flores et al. 2014; Sillero et al. 2017).

8.2.2 Kinematics

To obtain the global kinematics for each galaxy, rotational velocity v_ϕ and characteristic velocity dispersion σ_g, we use 1D velocity and dispersion curves extracted along the kinematic major axis following Wisnioski et al. (2019). Briefly, we measure the observed velocity by calculating the average of the absolute value of the minimum and maximum velocity measured along the kinematic axis and correcting for inclination. The measured velocity dispersion is calculated by taking the weighted mean of the outer data points of the 1D velocity dispersion profile. We adopt this non-parametric analysis to enable the use of galaxies with a variety of kinematic classifications. By not limiting the sample to the highest signal-to-noise disc galaxies we can investigate the metallicity gradients of galaxies with kinematic perturbations.

One dimensional kinematic extractions are directly provided for both the *HiZELS* and *SHiZELS* samples. For the *MUSE-WIDE* and *MASSIVE* samples the 1D kinematic profiles need to be measured. We use the datacubes for *MASSIV* (B. Epinat, private communication) and *MUSE-WIDE* (Herenz et al. 2017; Urrutia et al. 2019) samples to derive these. We fit the data with the emission line diagnostic package LZIFU (Ho et al. 2016). LZIFU runs spectral decomposition on IFU datacubes to produce 2D emission line and kinematic maps based on the Levenberg-Marquardt least squares method.

We first produce emission line and kinematic maps for the entire galaxy by passing the complete datacube to LZIFU. We supply an external continuum map to LZIFU that we create by finding the median flux for every spatial pixel (spaxel; e.g., *MUSE-WIDE*) or where the signal-to-noise of the continuum is negligible we simply supply a null external continuum map for the galaxies (e.g., *MASSIV*). We use the resulting flux and moment-1 maps from the fit to locate the galaxy centre and the kinematic major axis, respectively. Once the kinematic major axis and the galaxy centre are determined, we create apertures with the size of the full width at half maximum (FWHM) of the PSF across the major axis. We sum the flux in each spaxel within these apertures along the major axis. This gives a spatially-summed spectrum for every aperture, thus increasing the signal to noise ratio. We then fit the aperture spectra with LZIFU, which returns a single value of $v_\phi(r)$ and $\sigma_\mathrm{g}(r)$ for every aperture that we use to create 1D radial curves.

After we derive the global velocities and dispersions from the 1D radial curves for all galaxies in the *MASSIV*, *HiZELS*, *SHiZELS* and *MUSE-WIDE* samples, we apply inclination, instrumental resolution, and beam smearing corrections on them. To correct for inclination, we simply divide the observed velocities by $\sin(i)$, where i

is the inclination angle. We use the inclinations reported in the source papers for this purpose. Following Wisnioski et al. (2015), we add a 30 per cent uncertainty in quadrature to σ_g if it is comparable to the instrumental resolution; if σ_g is less than the instrumental resolution, we add a 60 per cent uncertainty in quadrature. To correct for beam smearing, we follow Burkert et al. (2016, Appendix A2), as done by Förster Schreiber et al. (2018, N. Förster-Schreiber, private communication). We note that this model makes the assumption that the galaxy kinematics are well described by a simple disc model. This may not apply to all galaxies in our sample, thus providing an over-correction for the beam in certain cases. The model assumes a Gaussian PSF and returns the beam-smearing correction factor based on the ratio of the stellar effective half-light radius to the beam effective half-light radius $(r_\mathrm{e}/r_\mathrm{e,b})$[1], and the ratio of the radius where the rotational velocity is calculated to the galactic effective half-light radius $(r_\mathrm{vel}/r_\mathrm{e})$. While it is straightforward to use these ratios to calculate the beam-smearing correction factor for v_ϕ, those for σ_g also depend on the mass, inclination, and redshift of the source. We incorporate a 40 per cent error in σ_g to account for uncertainties in the beam smearing correction model (Wisnioski et al. 2018, Section 3.3), however it is possible that we may overestimate or underestimate the correction factor in certain cases. We present the resulting kinematics for all galaxies in Appendix E.1, and illustrate the reanalysis procedure through a representative galaxy G103012059 (from the *MUSE-WIDE* sample) in Figure 8.2.

8.2.3   Final sample

We do not include all the galaxies that are available in the compiled surveys. We only select galaxies where the ratio of the radius at which v_ϕ is measured (r_vel) to the half-light radius, r_e, is greater than unity, as the beam-smearing correction model for v_ϕ requires $r_\mathrm{vel} > r_\mathrm{e}$. We also remove galaxies that only contain 3 or fewer resolution elements in our kinematic reanalysis, because we cannot derive a reasonable value for v_ϕ and σ_g in such cases. Further, we note that all the samples above exclude galaxies that contain contamination from active galactic nuclei (AGN), as diagnosed using the criteria described in Kewley et al. (2001, 2006b) based on the Baldwin et al. (1981, BPT) diagram. The exception to this statement is the *SINS / zC-SINF* sample, where the corresponding authors explicitly remove the contamination in gradients due to AGN for some of their galaxies. Our final sample consists of 74 galaxies with measured metallicity gradients and gas kinematics.

---

[1]The measurements of the half-light radius for the different samples are based on broadband photometry using different bands, however it has a negligible effect on the beam smearing correction factor (Nelson et al. 2016).
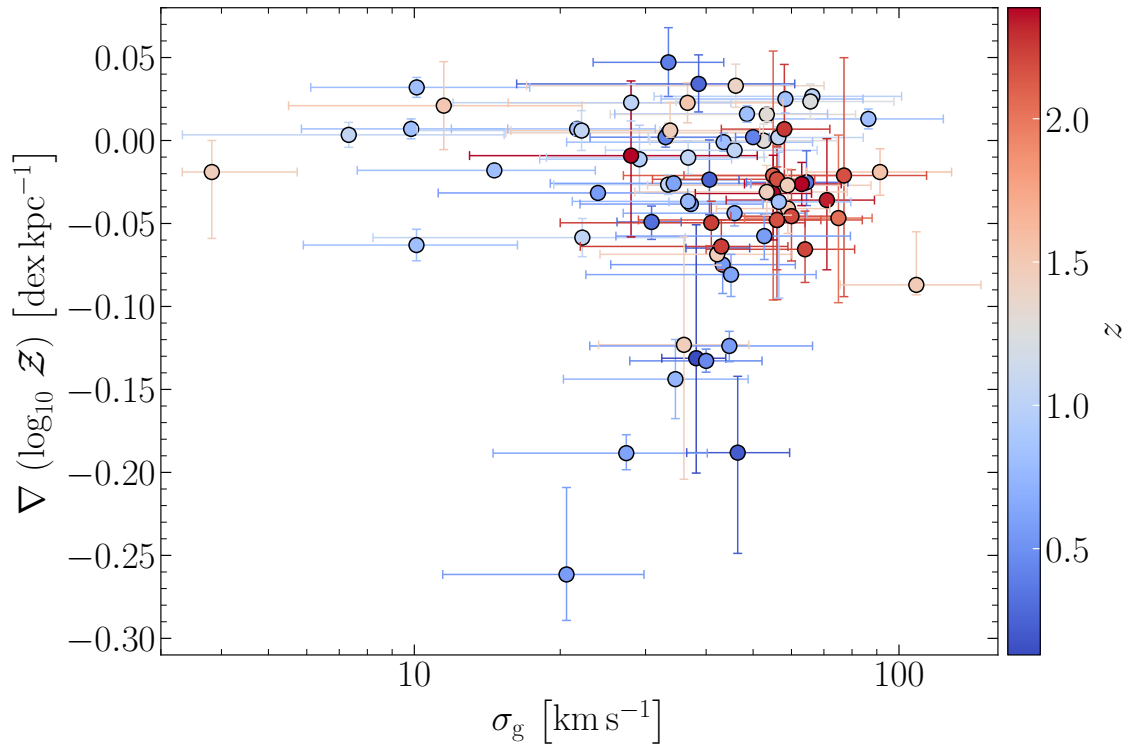
Figure 8.4: Metallicity gradients in the compiled sample of high-redshift galaxies plotted as a function of velocity dispersion σ_g, color-coded by redshift. We use the same method to derive the kinematics of all galaxies in our sample (see Section 8.2.2 for details). The quoted errorbars include uncertainties due to inclination, instrumental resolution, and beam smearing (Wisnioski et al. 2015, 2018; Burkert et al. 2016).

8.3 Results

Figure 8.3 shows the distributions of the metallicity gradients, and the resulting homogenised kinematics for all galaxies in the compiled data set. Our compilation recovers the diversity of gradients seen in the literature (by design) as well as the diversity of kinematics. This diversity is crucial for us to explore the correlations between galaxy kinematics and metallicity gradients, and is the primary driver of our work. We do not preferentially select disc galaxies however samples are likely to consist of primarily disc dominated galaxies due to the high fraction of discs at these epochs (Wisnioski et al. 2015, 2019; Stott et al. 2016; Simons et al. 2017). Another indicator of the galaxy kinematics is the ratio of the rotational velocity to the velocity dispersion, v_ϕ/σ_g (e.g., Förster Schreiber et al. 2009, 2018; Burkert et al. 2010; Kassin et al. 2014; Wisnioski et al. 2015, 2018, 2019; Jones et al. 2015; Simons et al. 2019), which is used to determine the rotational support of galaxies. We find from Figure 8.3 that while most galaxies in the sample are rotation-dominated (*i.e.*, $v_\phi/\sigma_\mathrm{g} \gtrsim 1$), around 18 per cent of the galaxies are dispersion-dominated ($v_\phi/\sigma_\mathrm{g} \lesssim$
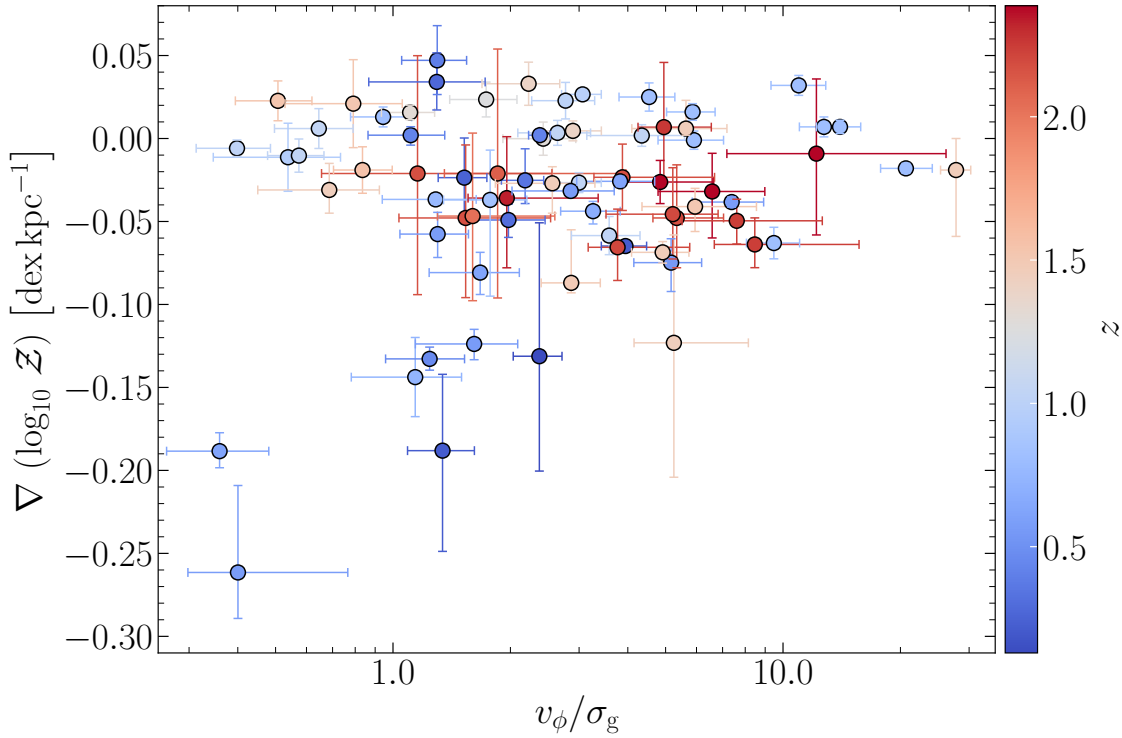
Figure 8.5: Same data as Figure 8.4, but plotted against the ratio of rotational velocity to velocity dispersion, v_ϕ/σ_g. Galaxies with $v_\phi/\sigma_g \geq 1$ are classified as rotation-dominated (and typically have a well-defined disc) whereas others are classified as dispersion-dominated (and typically have irregular structures).

1).

Figure 8.4 shows the measured metallicity gradients as a function of the reanalysed velocity dispersion σ_g, color-coded by redshift. We consider metallicity gradients as shallow or flat if the absolute strength of the gradient is less than $0.05\,\mathrm{dex\,kpc}^{-1}$. We observe that all galaxies in the sample with both high $\sigma_g (\gtrsim 60\,\mathrm{km\,s}^{-1})$ and low $\sigma_g (\lesssim 20\,\mathrm{km\,s}^{-1})$ show shallow or flat metallicity gradients, though we caution that the small velocity dispersions suffer significant uncertainties, as discussed in Section 8.2. By contrast, galaxies with intermediate σ_g $(20 - 50\,\mathrm{km\,s}^{-1})$ show both the steepest gradients $(\sim -0.25\,\mathrm{dex\,kpc}^{-1})$ and the largest scatter (~ 0.1) in gradients. We find only one galaxy with a steep gradient $(\sim -0.09\,\mathrm{dex\,kpc}^{-1})$ and high σ_g $(\sim 109\,\mathrm{km\,s}^{-1})$. Figure 8.5 shows the same data as in Figure 8.4, but as a function of v_ϕ/σ_g, thereby separating galaxies that are rotation-dominated from those that are dispersion-dominated. The main conclusion that we can draw from Figure 8.5 is that all dispersion-dominated galaxies $(v_\phi/\sigma_g \lesssim 1)$ possess shallow or flat gradients, whereas rotation-dominated galaxies $(v_\phi/\sigma_g \gtrsim 1)$ show a large scatter, and can have flat as well as steep gradients.[2] The exception to this is a

---

[2]Note, however, that this conclusion depends on the value $v_\phi/\sigma_g \sim 1$ that we choose to sepa-

couple of dispersion-dominated galaxies at $z < 1$ in the *MUSE-WIDE* sample that exhibit steep gradients. We also find from Figure 8.5 that the scatter in gradients narrows down as v_ϕ/σ_g increases. While our data compilation spans a wide redshift range, the above conclusions are not substantially different when considering just $z > 1$ versus $z < 1$. A more complete analysis exploring possible evolutionary effects requires a larger dataset.

Recent cosmological simulations like FIRE (Hopkins et al. 2014, 2018) and IllustrisTNG50 (Pillepich et al. 2018) have also explored the connection between metallicity gradients and kinematics, particularly focusing on the relation between gradients and v_ϕ/σ_g. One of the key results of both these simulations is that negative metallicity gradients only form in galaxies with $v_\phi/\sigma_\mathrm{g} > 1$ (*i.e.*, rotation-dominated systems), however, many such galaxies also show shallow gradients (Ma et al. 2017; Hemler et al. 2021). These simulations also find that dispersion-dominated galaxies always show shallow/flat gradients, consistent with mixing due to efficient feedback. However, some simulations may require more powerful radial mixing or feedback to match both kinematics and gradients (Gibson et al. 2013). We see from Figure 8.4 and Figure 8.5 that these findings are consistent with the data analysed here, with only a couple of dispersion-dominated outliers that show steep metallicity gradients.

8.4 Comparison with analytic model for metallicity gradients

In order to better understand the underlying physics that drives the diversity of metallicity gradients found in high-redshift galaxies, we compare the observations with the analytic metallicity gradient model we presented in Sharda et al. (2021b). Our model predicts the radial distribution of gas phase metallicities based on the equilibrium between production, consumption, loss and transport of metals in galaxies. It is a standalone metallicity model, but requires inputs from a galaxy evolution model to describe the properties of the gas – velocity dispersion, surface densities of gas and star formation, etc. – to solve for the metallicity. We use the galactic disc model of Krumholz et al. (2018) for this purpose, since we showed in previous works

---

rate rotation- and dispersion-dominated galaxies. If we were to use $v_\phi/\sigma_\mathrm{g} = 3$ as the break-point, for example, we would find that dispersion-dominated galaxies show a large scatter in metallicity gradients whereas rotation-dominated galaxies show shallow or flat gradients. A more precise statement, which we will see below is naturally predicted by our theoretical model, is that metallicity gradients show a very large scatter for $v_\phi/\sigma_\mathrm{g} \sim$ few, and shallow gradients on either side of this region.

that using this model allows us to successfully reproduce the observed trend of metallicity gradient with redshift (Sharda et al. 2021b), as well as the mass–metallicity and mass–metallicity gradient relations (MZR and MZGR) found in local galaxies (Sharda et al. 2021f). Note that, in what follows, we do not *fit* the model to the data while comparing the two.

8.4.1   Model description

In our model, the metallicity distribution profile in the galactic disc depends on four dimensionless ratios (equations 13, 37 – 40 in Sharda et al. 2021b),

$$\mathcal{T} \propto \left(\frac{v_\phi}{\sigma_{\rm g}}\right)^2 \text{ [metal equilibrium]}, \tag{8.1}$$

$$\mathcal{P} \propto \left(1 - \frac{\sigma_{\rm sf}}{\sigma_{\rm g}}\right) \text{ [metal advection]}, \tag{8.2}$$

$$\mathcal{S} \propto \phi_y \left(\frac{v_\phi}{\sigma_{\rm g}}\right)^2 \text{ [metal production]}, \tag{8.3}$$

$$\mathcal{A} \propto \frac{1}{\sigma_g^3} \text{ [cosmic accretion]}, \tag{8.4}$$

where we have only retained the dependencies on v_ϕ and $\sigma_{\rm g}$ for the purposes of the present study. Here, $\mathcal{T}$ is the ratio of the orbital to diffusion timescales, which describes the time it takes for a given metallicity distribution to reach equilibrium, $\mathcal{P}$ is the Péclet number of the galaxy (e.g., Patankar 1980), which describes the ratio of advection to diffusion of metals in the disc, $\mathcal{S}$ is the source term, which describes the ratio of metal production (including loss of metals in outflows) and diffusion, and $\mathcal{A}$ is the ratio of cosmic accretion (infall) to diffusion. Finally, $\sigma_{\rm sf}$ denotes the velocity dispersion that can be maintained by star formation feedback alone, with no additional energy input from transport of gas through the disc (Krumholz et al. 2018). Note that the model can only be applied in cases where the metal equilibration time (dictated by $\mathcal{T}$) is shorter than the Hubble time and shorter than or comparable to the molecular gas depletion time. If these conditions are not met, the metallicity distribution does not reach equilibrium within the galaxy. We showed in Sharda et al. (2021b, Section 5) that inverted gradients may or may not be in equilibrium, so for this work we do not apply our model to study such gradients.

The parameter ϕ_y that appears in $\mathcal{S}$ describes the reduced yield of metals in the disc due to preferential metal ejection through galactic outflows: $\phi_y = 1$ corresponds to metals being thoroughly-mixed into the interstellar medium (ISM) before ejection,

whereas $\phi_y = 0$ means that all the newly-produced metals are directly ejected before they can mix into the ISM. In line with previous works, we leave ϕ_y as a free parameter in the model. However, we showed in Sharda et al. (2021f) that our model reproduces both the local MZR and the MZGR only if ϕ_y increases with $M_\star$: low-mass galaxies prefer a lower ϕ_y, and vice-versa.

8.4.2 Model application

To produce metallicity gradients from the model, we select a value of v_ϕ and σ_g, and fix all other parameters in the model to those appropriate for high-z galaxies (Sharda et al. 2021b, Tables 1 and 2) at $z = 2$; we discuss how the results depend on the choice of redshift below. We find the spatial distribution of metallicity, $\mathcal{Z}(r)$, within $0.5 - 2.0\, r_e$ using equation 41 of Sharda et al. (2021b), which we then linearly fit in logarithmic space to obtain a metallicity gradient in dex kpc^{-1} from the model (e.g., Carton et al. 2018). We use this range in r because it is well matched to the observations ($r_{vel}/r_e \approx 2$) and the input galaxy model does not apply to the innermost regions of the galaxy.

While the choice of most of the parameters used as inputs into the metallicity model have no appreciable effect on the results, some (e.g., the Toomre Q parameter, and the circumgalactic medium metallicity $\mathcal{Z}_{CGM}$) matter at the level of tens of percent. For example, changing the Toomre Q parameter by a factor of 2 induces a 20 percent change in the metallicity gradient. The effects of changing the Toomre Q are similar to that of changing the rotation curve index β in the model, a topic we explore below in Section 8.4.2. Changing $\mathcal{Z}_{CGM}$ by ± 0.1 changes the metallicity gradient by at most ± 50 percent. This implies that increasing the CGM metallicity leads to shallower metallicity gradients. Finally, varying the redshift at which we compute the gradient by ± 1 yields changes in the gradient from ∓ 36 per cent for massive galaxies to ∓ 19 percent for low-mass galaxies. However, the overall impact of these parameters on the resulting metallicity gradients is limited compared to the dependence on ϕ_y, so in the following we focus on studying the effects of changing ϕ_y. In the main text that follows, we will continue to measure metallicity gradients in dex kpc^{-1}; we provide results on metallicity gradients measured in dex r_e^{-1}, which would potentially account for evolution in galaxy size, in Appendix E.2.

Metallicity gradient versus velocity dispersion

The left-hand panel of Figure 8.6 shows the same observational data as in Figure 8.4, now with our model as computed for a fixed $v_\phi = 105\, \text{km s}^{-1}$ (the median v_ϕ in the data). Since ϕ_y is a free parameter, we obtain a range of model predictions
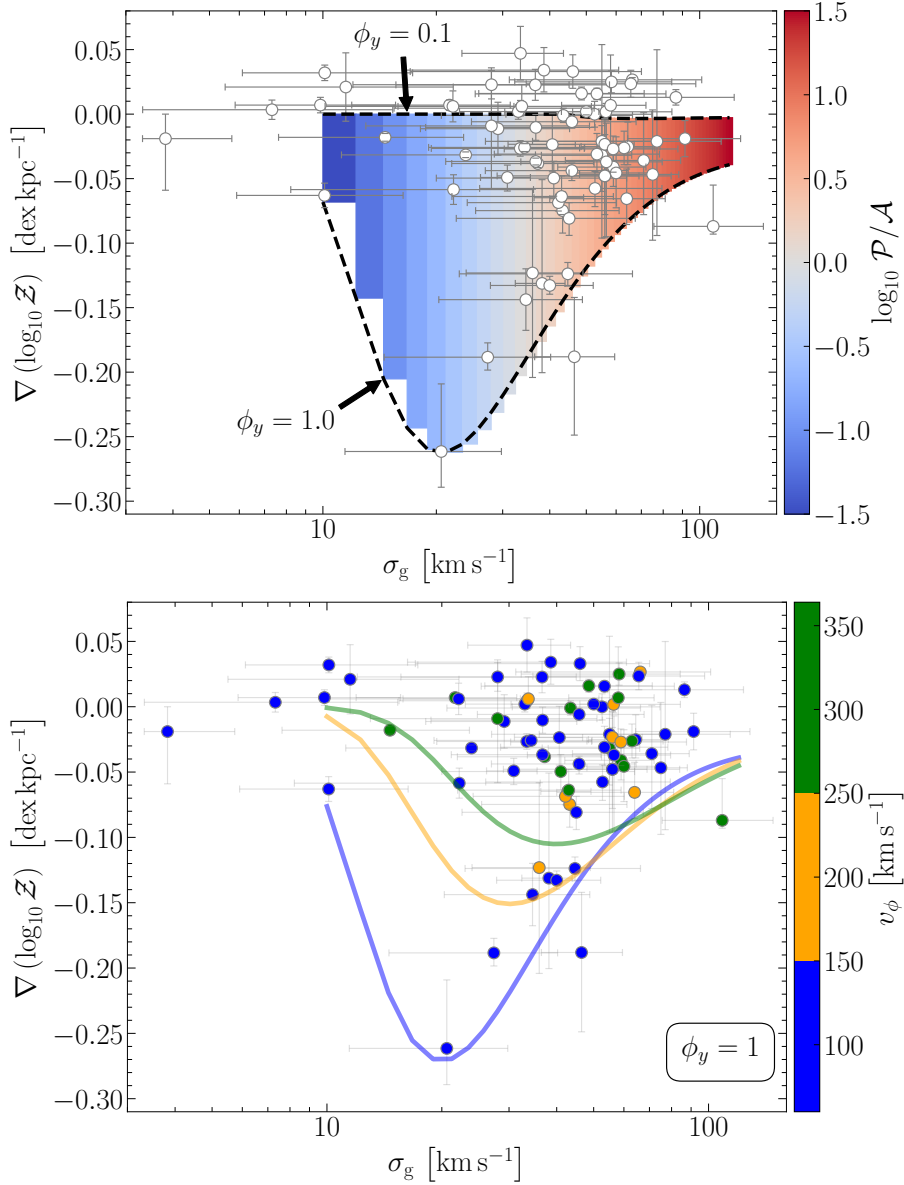
Figure 8.6: *Left panel:* Same data as Figure 8.4, but overplotted with one of the Sharda et al. (2021b) models. The model is for a high-redshift galaxy at fixed $v_\phi = 105\,\mathrm{km\,s^{-1}}$ (median v_ϕ in the data) and $z = 2$. The spread in the model (represented by the length of the colored bands) is a result of the yield reduction factor ϕ_y, which describes the preferential ejection of metals through galactic winds. Here we show models with $\phi_y = 0.1$–1, where the top and bottom dashed lines corresponds to $\phi_y = 0.1$ and 1.0, respectively. The colorbar denotes the ratio of advection of gas ($\mathcal{P}$) to cosmic accretion of metal-poor gas ($\mathcal{A}$). The steepest gradients produced by the model correspond to a transition from the accretion-dominated to the advection-dominated regime, as σ_g increases. *Right panel:* Same as the left panel, but overlaid with different models (corresponding to different v_ϕ) at $z = 2$. Only the $\phi_y = 1$ model is shown here; thus, the model curves represent the most negative gradients produced by the model for a given set of parameters. The data are also binned around the model v_ϕ as shown through the colorbar. Note that the model is not being fit to the data.
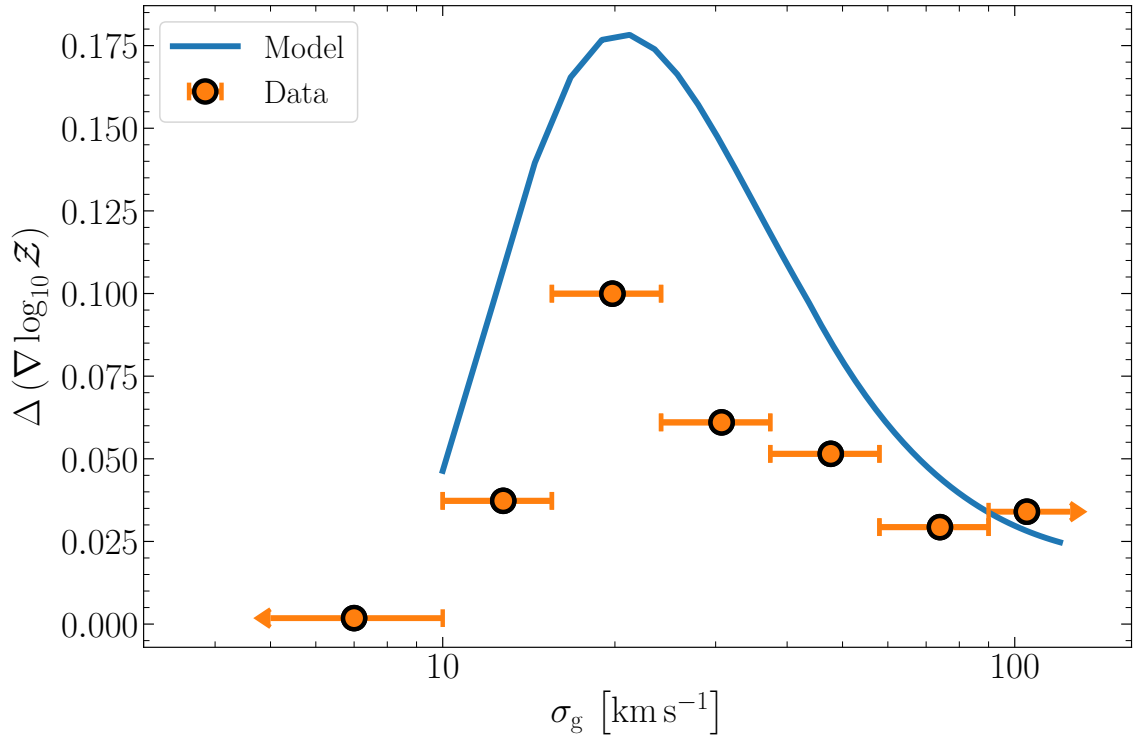
Figure 8.7: Scatter in the model metallicity gradient shown in the left panel of Figure 8.6, compared to the scatter for observed data, as a function of the gas velocity dispersion $\sigma_{\rm g}$ for a fixed rotational velocity $v_\phi = 105\,{\rm km\,s^{-1}}$ (median v_ϕ in the data). The scatter in the model is calculated as 68 per cent of the difference between the model metallicity gradients with $\phi_y = 1$ and 0.1 at every $\sigma_{\rm g}$. Errors on the scatter in the data represent the width of the bins used.

at every $\sigma_{\rm g}$; the range shown in the plot corresponds to varying ϕ_y between 0.1 and 1, as represented by the arrows on Figure 8.6. We color-code bars within this range by the ratio $\mathcal{P}/\mathcal{A}$, which describes the relative importance of advection and accretion of metal-poor gas. A key conclusion that can be drawn from this model–data comparison is that the model predicts flat metallicity gradients in galaxies with high $\sigma_{\rm g}$, irrespective of ϕ_y, in good agreement with the observational data. The model generates a uniform metallicity distribution across the disc (*i.e.,* a flat/shallow gradient) as a result of efficient radial transport of the gas. The model does not produce any steep negative ($< -0.1\,{\rm dex\,kpc^{-1}}$) metallicity gradients at high $\sigma_{\rm g}$ ($> 60\,{\rm km\,s^{-1}}$), consistent with both data and simulations.

The largest diversity in metallicity gradients in the model occurs at $\sigma_{\rm g} \approx 20 - 40\,{\rm km\,s^{-1}}$, where galaxies transition from being accretion-dominated (blue, $\mathcal{P} < \mathcal{A}$) to being advection-dominated (red, $\mathcal{P} > \mathcal{A}$). This transition in the ratio $\mathcal{P}/\mathcal{A}$ and the corresponding scatter in the steepness of the metallicity gradients are key results of the model. Moreover, the transition in $\mathcal{P}/\mathcal{A}$ from high to low values mirrors

the transition seen in σ_g from gravity-driven to star formation feedback-driven turbulence (Krumholz et al. 2018). The region around the transition is where both advection ($\mathcal{P}$) and accretion ($\mathcal{A}$) are weaker as compared to metal production ($\mathcal{S}$), resulting in steep metallicity gradients, since star formation and thus metal production are centrally peaked (Krumholz et al. 2018)[3]. The scatter near the transition arises due to the yield reduction factor ϕ_y, which can decrease the strength of $\mathcal{S}$ as compared to $\mathcal{P}$ or $\mathcal{A}$ because $\mathcal{S} \propto \phi_y$. Lastly, we note that while metal diffusion is an important process that can also flatten the gradient, it never simultaneously dominates advection and cosmic accretion, since both $\mathcal{P}$ and $\mathcal{A}$ are never less than unity at the same time.

The model is consistent with the very few data points at low σ_g, which show shallow/flat metallicity gradients. In the model, the flattening at the low-σ_g end is caused by accretion of metal-poor gas, following a $1/r^2$ profile, that dilutes the metallicity primarily in the central regions. Given the scarcity of data at low σ_g, as well as significant observational uncertainties, it is unclear whether the trend seen in the model is also present in the data. Future instruments with higher sensitivity and spectral and spatial resolution (e.g., GMTIFS, HARMONI, MAVIS, ERIS) will be able to measure low σ_g in high-redshift galaxies with higher precision (Thatte et al. 2014; Fernández-Ontiveros et al. 2017; Davies et al. 2018; Richardson et al. 2020; McDermid et al. 2020; Ellis et al. 2020), expanding the currently available sample by a considerable margin.

In the right-hand panel of Figure 8.6, we now fix $\phi_y = 1$ (implying no preferential metal ejection in winds), and look at the model differences for different values of v_ϕ. Note that v_ϕ is a proxy for stellar mass, as higher v_ϕ typically corresponds to massive galaxies in the compiled sample. The data are the same as in the left-hand panel of Figure 8.6, but now binned and color-coded by the measured v_ϕ. Thus, the model curves represent the steepest metallicity gradients that we can obtain for the given set of galaxy parameters. We emphasize that we do not fit the model to the data while plotting the model curves. It is clear that low v_ϕ (low mass) galaxies show more scatter in the model gradients as compared to high v_ϕ (massive) galaxies, consistent with observations (Carton et al. 2018; Simons et al. 2020). As v_ϕ increases, the point of inflection (or, the point of steepest gradients) shifts toward higher σ_g and toward shallower metallicity gradients. Additionally, for sufficiently high σ_g, models with different v_ϕ converge towards a lower bound for metallicity gradients, implying that

---

[3]Note that the input cosmic accretion profile in the model is also centrally peaked, similar to the SFR profile. However, as we show in (Sharda et al. 2021b, Appendix A), changing the form of the input accretion profile has only modest effects on the resulting metallicity gradients: less centrally-peaked accretion profiles give rise to slightly steeper gradients.

the flatness of metallicity gradients at high σ_g is independent of the galaxy mass (see, however, Section 8.4.2). When the data are binned in v_ϕ, they are broadly consistent with the model. Thus, the model suggests a lower limit in metallicity gradients at high velocity dispersions consistent with the compiled data.

Taken at face value, it seems from the left panel of Figure 8.6 that most galaxies in the sample favor a value of ϕ_y close to 0.1, implying a high metal enrichment in their winds. A close examination of the right panel of Figure 8.6 reveals that this is only the case for galaxies with $v_\phi < 150\,\mathrm{km\,s^{-1}}$ (*i.e.,* low-mass galaxies); galaxies with higher v_ϕ prefer both low and high values of ϕ_y. When combined with results from the local Universe showing that low-mass galaxies prefer lower ϕ_y (Sharda et al. 2021f), the finding that low-mass galaxies at high redshift also prefer lower ϕ_y is not surprising. Not only were outflows more common in the past in actively star-forming galaxies (Muratov et al. 2015), galaxies also had shallower potential wells (Moster et al. 2010) that made it easier for metals to escape via galactic winds without mixing into the ISM. This effect is more pronounced at the low-mass end, thus low-mass galaxies tend to prefer $\phi_y \sim 0.1$.

Figure 8.7 quantifies the scatter present in the model and the data as a function of σ_g. To construct a 1σ scatter in the model in the absence of *a priori* knowledge of the distribution of ϕ_y, we simply compute model gradients for $\phi_y = 1$ and 0.1 for every σ_g, and take the scatter to be 68 per cent of this range, *i.e.,* our model-predicted "scatter" is simply 68 per cent of the distance between the two black dashed lines in the left panel of Figure 8.6. To estimate the scatter in the data, we bin by σ_g such that we have one bin each for $\sigma_g < 10\,\mathrm{km\,s^{-1}}$ and $\sigma_g > 90\,\mathrm{km\,s^{-1}}$, and we divide the parameter space $10 \leq \sigma_g/\mathrm{km\,s^{-1}} \leq 90$ in five logarithmically spaced bins.

We find from Figure 8.7 that the model is able to reproduce the qualitative shape of the variation in scatter with σ_g observed in the data, but not the exact level of scatter. This is not surprising, since the true scatter expected for the model depends on the distribution of ϕ_y values in real galaxies, which is at present unknown. Future observations of galactic wind metallicity at low and high redshifts, or simulations with enough resolution to capture the hot-cold interface where mixing between SN ejecta and the ambient ISM occurs (something no current cosmological simulation possesses – Gentry et al. 2019), will enable us to constrain ϕ_y and provide a more quantitative analysis of how ϕ_y scales with galaxy mass at different redshifts.

Metallicity gradient versus rotational support

The ratio of rotation to velocity dispersion provides a quantification of the overall rotational support of a galaxy. The left-hand panel of Figure 8.8 shows the metallic-
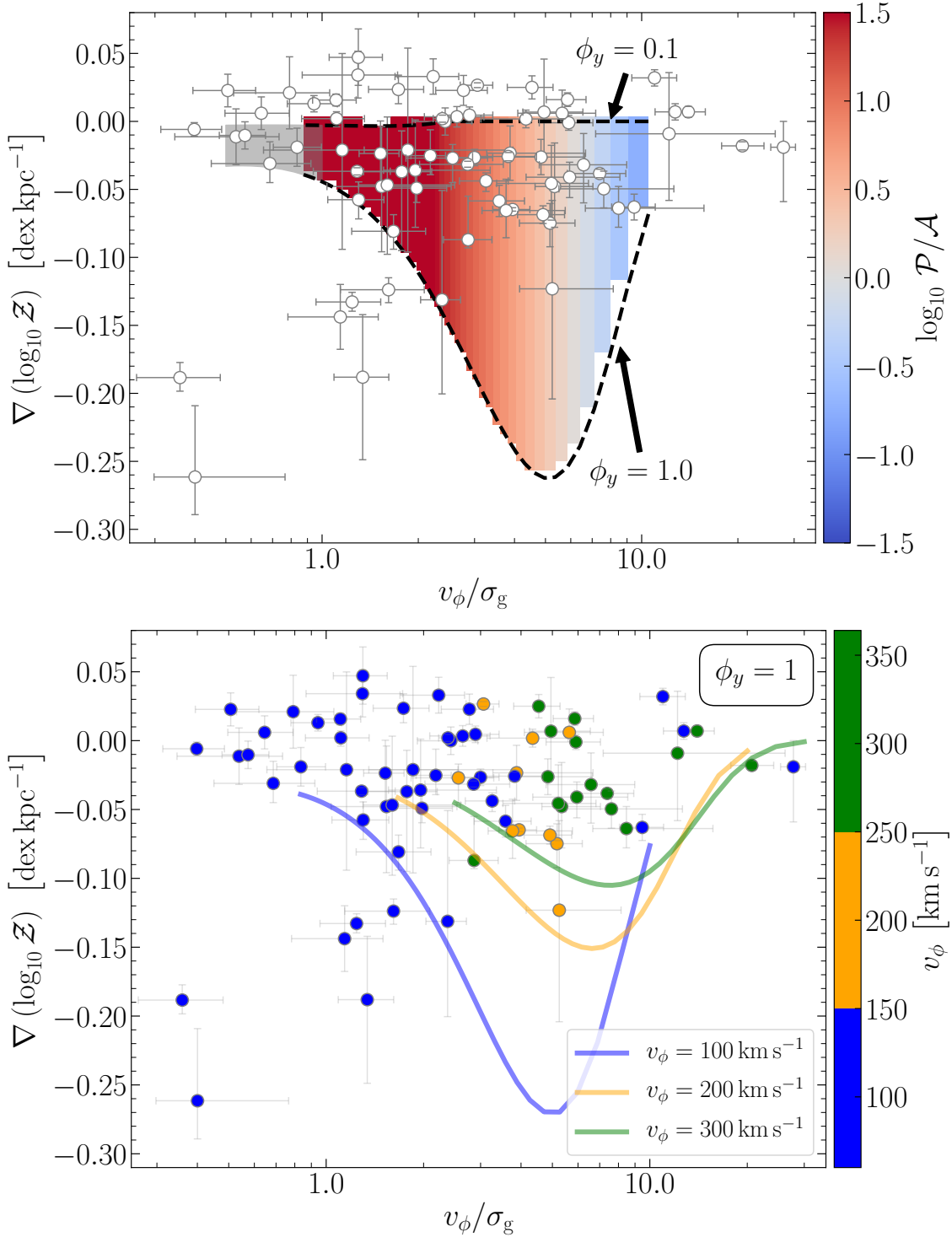
Figure 8.8: *Left panel:* Same data as in Figure 8.5, and model as in Figure 8.6 (left panel), but now plotted as a function of v_ϕ/σ_g for a fixed $v_\phi = 105\,\mathrm{km\,s^{-1}}$ (median v_ϕ in the data). The grey-shaded area corresponds to the predictions of the model for $v_\phi/\sigma_g < 1$, where the assumption of a disc-like structure likely breaks down, hence the galaxy disc model (Krumholz et al. 2018) used as an input to the metallicity model (Sharda et al. 2021b) may not be fully applicable. *Right panel:* Same as Figure 8.6 (right panel), but with metallicity gradients plotted as a function of v_ϕ/σ_g, overlaid with a set of models for different v_ϕ. The models are not fit to the data.
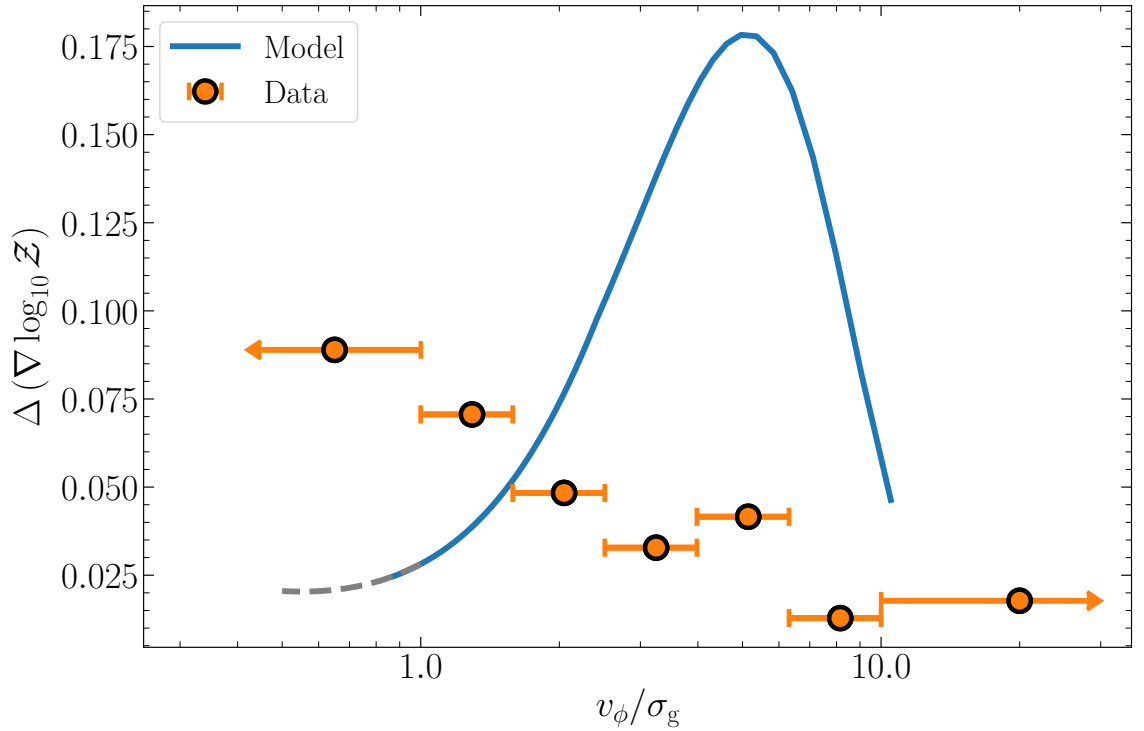
Figure 8.9: Scatter in the model metallicity gradient shown in the left panel of Figure 8.8, compared to the scatter for observed data, as a function of rotational support, $v_\phi/\sigma_{\rm g}$. The scatter in the model is calculated as 68 per cent of the difference between the model metallicity gradients with $\phi_y = 1$ and 0.1 at every $\sigma_{\rm g}$ for a fixed $v_\phi = 105\,{\rm km\,s^{-1}}$ (median v_ϕ in the data). The grey-shaded extension of the model scatter corresponds to the grey-shaded region in the left panel of Figure 8.8. Errors on the scatter in the data represent the width of the bins used.

ity gradients as a function of $v_\phi/\sigma_{\rm g}$ in the data, overplotted with the analytic model for fixed $v_\phi = 105\,{\rm km\,s^{-1}}$. The parameter space of the model denotes variations in $\mathcal{P}/\mathcal{A}$, the same as that shown in Figure 8.6. The grey-shaded region corresponds to an extrapolation of the model where it is not directly applicable because the assumption of a disc likely breaks down at $v_\phi/\sigma_{\rm g} < 1$. We first find a steepening of the gradient in the model as $v_\phi/\sigma_{\rm g}$ increases from < 1 to ~ 10, after which the gradients begin to flatten again for $v_\phi/\sigma_{\rm g} \gtrsim 10$. We can again understand this trend in terms of $\mathcal{P}/\mathcal{A}$: values of $v_\phi/\sigma_{\rm g} \gtrsim 10$ typically correspond to massive galaxies, within which strong centrally peaked accretion (large $\mathcal{A}$) flattens the gradients. Galaxies with $v_\phi/\sigma_{\rm g} \lesssim 1$ have flat gradients due to strong advection of gas through the disc (large $\mathcal{P}$) mixing and therefore homogenising the metal distribution throughout the disc. In the intermediate range of $v_\phi/\sigma_{\rm g}$, the gradients are the steepest because the production term $\mathcal{S}$ dominates over both $\mathcal{P}$ and $\mathcal{A}$.

The location of the turnover is sensitive to the value of v_ϕ, as we show in the right-hand panel of Figure 8.8. This figure is similar to the right-hand panel of Figure 8.6,

but we now show metallicity gradients as a function of $v_\phi/\sigma_{\mathrm{g}}$ for different values of v_ϕ. We see that as v_ϕ increases, the parameter space of the model shifts to flatter gradients and higher $v_\phi/\sigma_{\mathrm{g}}$. These shifts in the inflection point where galaxies transition from the advection-dominated to the accretion-dominated regime imply that massive galaxies have higher $v_\phi/\sigma_{\mathrm{g}}$ and shallower gradients as compared to low-mass galaxies.

Similar to Figure 8.6, we notice that most low-mass (low-v_ϕ) galaxies prefer a lower value of ϕ_y. The bounds provided by the model in terms of the most negative gradient it can produce (represented by $\phi_y = 1$) are consistent with the majority of the data. The four rotation-dominated ($v_\phi/\sigma_{\mathrm{g}} > 1$) outliers that we observe have v_ϕ less than $100\,\mathrm{km\,s^{-1}}$, so it is not surprising that the model does not produce a bound that is consistent with these galaxies. However, as we saw earlier in the right panel of Figure 8.6, the same outliers are within the constraints of the model when we study the trends with σ_{g}. Thus, while the agreement of the model with the lower bound in metallicity gradient as a function of σ_{g} is good, it is less so in metallicity gradient as a function of $v_\phi/\sigma_{\mathrm{g}}$. This is a shortcoming of the model, which may be a result of our fundamental approach of treating galaxies as discs breaking down as we approach $v_\phi/\sigma_{\mathrm{g}} \sim 1$, or restricting v_ϕ to a handful of values in the model.

Figure 8.9 plots the scatter in the model and the data as a function of $v_\phi/\sigma_{\mathrm{g}}$, in the same manner as that in Figure 8.7. We bin the data such that we have one bin each for $v_\phi/\sigma_{\mathrm{g}} < 1$ and $v_\phi/\sigma_{\mathrm{g}} > 10$, with five logarithmically spaced bins in between. Consistent with our findings above, we see that the model fails to reproduce the shape of the scatter as a function of rotational support. The discrepancy is largely due to restricting the model to a single value of v_ϕ whereas the data spans a wide range in v_ϕ. However, the current sample is too limited for us to bin the data in different v_ϕ bins and study the trends in the scatter by using several different values of v_ϕ in the model.

Overall, we find that the model is able to reproduce the observed non-monotonic trends (but not the scatter) between metallicity gradients and $v_\phi/\sigma_{\mathrm{g}}$, and provide a physical explanation for them. However, reproducing the full distribution of the data is beyond the scope of the model without better constraints on model parameters like ϕ_y. Additional data, particularly at high mass ($M_\star \sim 10^{10.5}\,\mathrm{M_\odot}$) and low redshift ($0 < z < 1$) would provide further constraints on the performance of the model as a function of rotational support (e.g., Foster et al. 2020).

Metallicity gradient versus rotation curve index

So far, we have only considered applications of the model that assume a flat rotation curve, $\beta = 0$, for all galaxies, where $\beta \equiv d \ln v_\phi / d \ln r$ is the index of the rotation curve. However, at high redshift when galaxies are more compact, the visible baryons are more likely to be in a baryon-dominated regime, which can give rise to non-flat rotation curves such that $\beta \neq 0$. Recent observations suggest that the inner regions of several high-z galaxies are baryon dominated (Genzel et al. 2017, 2020; Lang et al. 2017; Teklu et al. 2018; see, however, Tiley et al. 2019b), such that $\beta < 0$. Keeping these findings in mind, we now explore the effects of varying β on the metallicity gradients produced by our model.

In the context of our model, the rotation curve has several effects. First, the model is based on the premise that Toomre $Q \approx 1$, and Q depends on the epicyclic frequency and thus on β – changing β therefore changes the relationship between the gas surface density and the velocity dispersion; this manifests as a change in the source term $\mathcal{S}$, which depends on the star formation rate and thus on the gas content. Second, the rotation curve index changes the amount of energy released by inward radial flows, which alters the inflow rate required to maintain energy balance; this manifests as a change in $\mathcal{P}$.[4] From Sharda et al. (2021b, equations 38 and 39), we find that $\mathcal{P} \propto (1+\beta)/(1-\beta)$ and $\mathcal{S} \propto (1+\beta)$. Thus, $\beta < 0$ reduces both $\mathcal{S}$ and $\mathcal{P}$, weakening metal production and advection in comparison to cosmological accretion and diffusion.

Figure 8.10 shows the same model curves as in Figure 8.6, but with three different rotation curve indices, $\beta = -0.25$, 0, and 0.25. For the sake of clarity, we do not overplot the observational data in this figure. While changing β does not significantly change the range of metallicity gradients produced by the model for large v_ϕ (*i.e.,* more massive galaxies), it has some effect for galaxies with smaller v_ϕ. If $\beta < 0$, the model allows for steeper gradients (by a factor of 3) for low-mass galaxies with high $\sigma_{\rm g}$. This is because as compared to the default $\beta = 0$, the Péclet number $\mathcal{P}$ decreases by a larger factor than the source term $\mathcal{S}$ when $\beta < 0$ (Sharda et al. 2021b, equations 38 and 39). Thus, $\mathcal{S}$ dominates, giving rise to steeper gradients. On the other hand, $\mathcal{P}$ increases by a larger factor than $\mathcal{S}$ for $\beta > 0$ as compared to the default $\beta = 0$. Thus, $\mathcal{P}$ dominates, giving rise to flatter gradients. This analysis tells us that high-z galaxies with high levels of turbulence and falling rotation curves ($\beta < 0$) can still maintain a steep metallicity gradient due to the decreased strength

---

[4]Both of these effects also alter the equilibration timescale, and thus $\mathcal{T}$, but by little enough that our finding that all the galaxies under consideration are in equilibrium is unaffected. We therefore do not discuss $\mathcal{T}$ further.
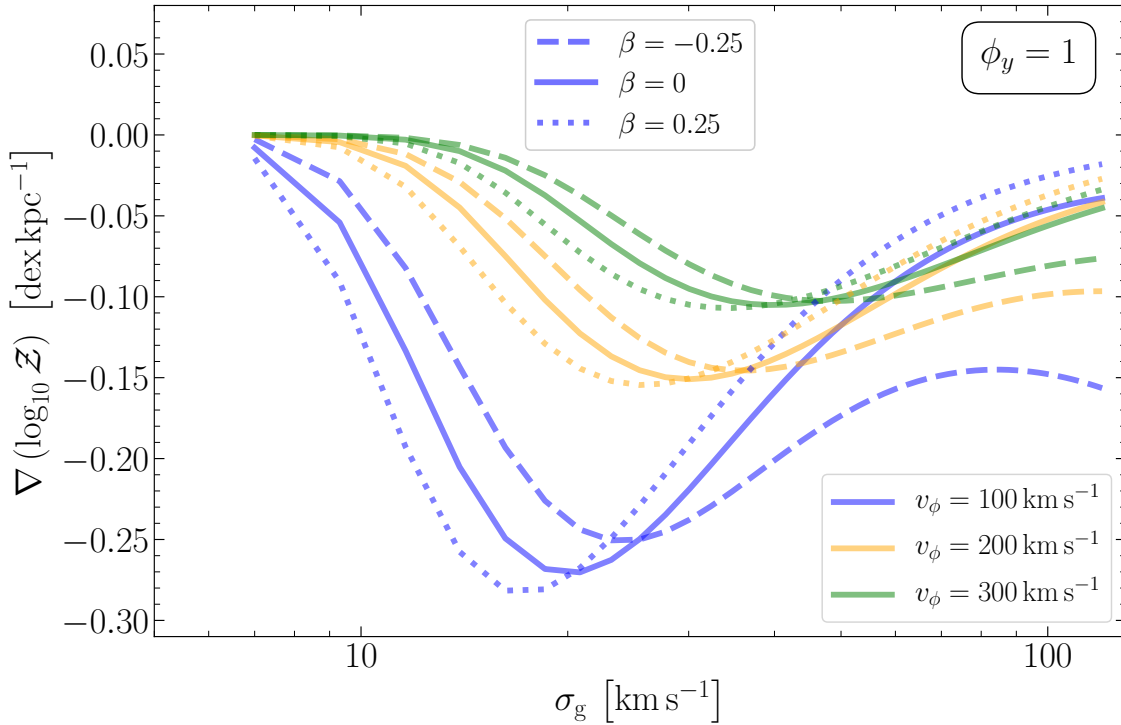
Figure 8.10: Metallicity gradients from the model for different values of v_ϕ and the rotation curve index β at fixed $z = 2$. The curves are only plotted for the highest possible yield reduction factor $\phi_y = 1$, thus providing a limit on the most negative metallicity gradient the model can produce given a set of input parameters. The main takeaway from this plot is that high-z galaxies that are very turbulent (high σ_g) but show falling rotation curves ($\beta < 0$) can still maintain a steep metallicity gradient in equilibrium.

of advection as compared to metal production.

With respect to β, a detailed comparison of the model with observational data is beyond the scope of the present study. Future observations will provide further constraints to the model parameters such as varying β and Q.

8.5   Conclusions

In this work, we explore the relationship between gas kinematics (rotational velocity v_ϕ and velocity dispersion σ_g) and gas phase metallicity gradients in star-forming galaxies at $0.1 \leq z \leq 2.5$ using a compilation of 74 galaxies across 5 ground based IFU spectroscopy samples, and our new analytic model (Sharda et al. 2021b). To partially alleviate the inhomogeneities in the compiled data that used diverse instruments and techniques, we reanalyse the kinematics for all galaxies following Förster Schreiber et al. (2018). All the samples (except for one) use the [N II]/Hα ratio and the Pettini & Pagel (2004) calibration to obtain the metallicity gradients.

We find that high-redshift galaxies that are highly turbulent ($\sigma_{\mathrm{g}} > 60\,\mathrm{km\,s^{-1}}$) show shallow or flat metallicity gradients ($> -0.05\,\mathrm{dex\,kpc^{-1}}$), whereas galaxies with intermediate levels of turbulence ($\sigma_{\mathrm{g}} \approx 20-50\,\mathrm{km\,s^{-1}}$) show comparatively the largest scatter in their measured metallicity gradients. Finally, galaxies with the lowest σ_{g} ($< 20\,\mathrm{km\,s^{-1}}$) show flat gradients, although the small number of low-σ_{g} galaxies in our sample renders this conclusion tentative. Our findings are consistent with the predictions made by simulations of galaxy formation (FIRE and IllustrisTNG50), which find that steep negative metallicity gradients only occur in galaxies that are rotation-dominated ($v_\phi/\sigma_{\mathrm{g}} > 1$), whereas all dispersion-dominated galaxies show relatively flat gradients (Ma et al. 2017; Hemler et al. 2021).

We compare the data against predictions from our recently developed model of gas phase metallicity gradients in galaxies (Sharda et al. 2021b) to provide a physical explanation for the observed trends. We find that the model is able to reproduce the observed, non-monotonic relationship between metallicity gradients and gas kinematics. Strong inward advection of gas leads to efficient metal mixing when the gas velocity dispersion is high. This mixing results in flatter gradients. However, the relationship between velocity dispersion and inward advection rate also depends on the index of the galaxy rotation curve – galaxies with falling rotation curves can maintain high velocity dispersion with relatively lower inflow rates, and thus can retain steeper metal gradients than their counterparts with flat or rising rotation curves. In contrast, the flat gradients seen with low gas velocity dispersion are due to stronger cosmic accretion of metal-poor gas which dilutes the central regions of galaxies. In these cases of high and low gas velocity dispersion, advection and accretion respectively dominate over metal production which is otherwise responsible for creating negative gradients which follow the star formation profile.

The steepest gradients as well as the largest scatter in the gradients in the model are found for intermediate velocity dispersions where both the inward advection of gas and cosmic accretion of metal-poor gas are weak compared to metal production. The scatter at intermediate velocity dispersions may arise from galaxy-to-galaxy variations in the preferential ejection of metals through galactic winds before they mix with the ISM: the most negative metallicity gradients arise in galaxies where metals mix efficiently with the ISM before ejection, while flatter gradients occur in galaxies where a substantial fraction of supernova-produced metals are ejected directly into galactic winds before mixing with the ISM. However, we note the large number of observational uncertainties which may also dominate this scatter. We also find that while metal diffusion is also an important process that contributes to flattening the metallicity gradients, it never simultaneously dominates inward

advection and cosmic accretion.

While our metallicity evolution model successfully reproduces the observed shape and scatter of the non-linear relationship between metallicity gradients and gas kinematics in high-redshift galaxies, it is in better agreement with the data in the gradient$-\sigma_{\mathrm{g}}$ space than that in the gradient$-v_{\phi}/\sigma_{\mathrm{g}}$ space. The model also cannot predict the full distribution of galaxies in either set of parameters without better constraints on the metal enrichment of outflows. The current sample only consists of 74 galaxies, and there is clearly scope for more observations of galaxies at high redshift against which we can test our inferences about the physics behind the impacts of gas kinematics on metallicity gradients.

Acknowledgements

the image-to-data tool `WebPlotDigitizer`.

Conclusions

9.1 Summary of the thesis

In this thesis, we study and explore the multi-scale structure formation in galaxies using metals as tracers. On small scales, we develop simulations and theoretical models to investigate variations in the IMF at zero and low metallicities. The IMF is fundamental to metal evolution in galaxies since it dictates the distribution of massive stars and the metal yield arising from them. On large scales, we use observations and develop theoretical models to understand the physics of metal distribution in galactic discs. By looking at the impact of metals in metal-poor ISM together with the overall distribution of metals in galaxies, this thesis is expected to equip us with some of the necessary tools and physics to understand the evolution of the first galaxies that will be observed by the ELT.

The first half of this thesis is devoted to studying the zero and low metallicity ISM, and discovering the IMF of zero and low metallicity stars. For this purpose, we use a combination of analytical models and chemo-MHD simulations. We run simulations of the formation of the first stars to investigate the impact of physical processes such as turbulence and magnetic fields on the Population III IMF. We couple the well-known MHD code FLASH to the astrochemistry package KROME, and perform a large suite of chemo-MHD simulations to overcome statistical noise. We also develop analytical models to explore thermodynamics of dusty, molecular gas at a wide range of metallicities, in order to explore variations in the peak of the IMF with ISM metallicity. The key question we attempt to answer is: when does the IMF become bottom-heavy as seen in metal-rich environments?

The key results from the first half of the thesis are:

1. Magnetic fields can grow due to dynamo amplification and provide strong support against gravity, thereby hindering fragmentation in primordial molecular clouds.

2. Magnetic fields significantly impact the IMF of the first stars, making it more

top-heavy.

3. The IMF has a strong dependence on metallicity of the ISM as different gas coolants dominate at different metallicities.

4. The characteristic mass (or the peak mass) of the IMF transitions from being top-heavy in primordial-like environments to being bottom-heavy once the metallicity exceeds $\gtrsim 1/1000\,\mathrm{Z_\odot}$.

In the second half of the thesis, we approach the role of metals from a galactic perspective, which is crucial to understanding how small-scale metal-poor environments impacted the formation of large-scale structure in the early Universe. Studying the metal distribution in galaxies at early times is necessary because it sets the scene for subsequent gas regulation, star formation, and feedback, all of which directly impact galaxy evolution. We advance existing studies by focusing on the spatially-resolved metal distribution in galaxies. Thanks to IFU spectroscopy, there has been a surge in the measurement of metallicity gradients in galaxies, but the origin of the gradient and its observed correlation with several galaxy properties remains unexplored. To address this, we develop a new first principles model of metallicity gradients in galaxies. The model parameters are tied to a galaxy evolution model, ensuring that the metals are treated self consistently with the gas in galaxies, and arbitrary tuning of model parameters is not permitted. Most importantly, unlike existing models, our model includes a treatment of metal advection and diffusion, and also allows for differential enrichment of galactic winds. The model is flexible in the sense that it can be used in conjunction with any galaxy evolution model that specifies the profiles of key galaxy properties. For the purpose of this thesis, we use the unified disc model of Krumholz et al. (2018) that has been shown to explain the trends in several galaxy properties.

The key results from the second half of the thesis are:

1. The MZGR is set by galaxies transitioning from an advection-dominated to an accretion-dominated regime as they increase in mass.

2. Simultaneously explaining the MZR and the MZGR requires that low mass galaxies preferentially loose metals in galactic winds. This implies that the metallicity of galactic winds is not always identical to the metallicity of the ISM, and preferential ejection of metals is possible.

3. The metallicity gradient of the Milky Way has evolved from being flat at early times to steep at $z = 0$.

4. Metallicity gradients have a complex dependence on gas kinematics in galaxies. Galaxies with both low and high gas velocity dispersions show flat gradients

due to efficient metal dilution and metal mixing, respectively.

This thesis thus shows how metals can be used as nature's tracers to study the multi-scale structure formation in galaxies.

9.2   Future work

There are several avenues that can be pursued to further advance our understanding of low metallicity ISM and galactic metal distributions. The early and the metal-poor Universe will be key focus areas of the next generation of astronomical facilities, and making further research in these areas worthwhile and time-critical.

9.2.1   Further   developments   in   chemo-MHD   simulations

Most zero metallicity star formation simulations have only been run for a few 1000 yr post formation of the first protostellar object. None of the current Population III star formation simulations run past the accretion phase, thus effectively hindering us from finding the 'final' distribution of stellar masses. Therefore, the mass distribution of first stars produced by these simulations cannot capture the final Population III IMF (although extrapolation to final masses using theoretical models has been attempted – Hirano et al. 2014). There are three key reasons for this: 1. as we summarize in Table 1.1, most simulations lack some or the other physical process that plays a major role in star formation and the IMF, 2. the computational expense required to run the simulations past the first collapse (due to adaptive mesh refining, etc.) can be quite high as the hydrodynamical timesteps become of the order of 1 yr, and 3. as we show in Chapter 5, overcoming the stochasticity and statistical noise in fragmentation introduced by turbulence requires running several simulations (see also, Wollenberg et al. 2020). Thus, further developments are necessary to overcome all these challenges so that we can produce the final IMF of the first stars.

The simulations we have carried out go beyond prior work by including turbulence and unordered magnetic fields. However, we do not include the effects of protostellar radiation feedback, which can be important for massive first stars (Hosokawa et al. 2011b, 2016; though, for a contrary view, see Jaura et al. 2022). Thus, including radiation feedback is the next major step in improving the existing chemo-MHD simulations. Additionally, the role of non-ideal MHD processes remains unexplored in Population III star formation. Non-ideal MHD plays a key role in influencing star formation and protostellar accretion in metal-rich star formation (Wurster &

Li 2018; Zhao et al. 2020), and can potentially play a big role in primordial star formation as well (Nakauchi et al. 2019). However, no Population III simulations to date have included non-ideal MHD; this is another frontier where further work is imperative. An attractive alternative to enable running the simulations for a longer period of time is to use GPU-based hydrodynamical codes (Schneider & Robertson 2015; Schive et al. 2018; Almgren et al. 2020; Bloch et al. 2021; Wibking & Krumholz 2022), since GPUs allow for many more zone updates per second, and provide a 10x increase in speed for the same number of CPU cores. Thus, there is a lot of scope in both numerical and astrophysical development to explore the Population III IMF.

9.2.2 Extending the simulations to low metallicity ISM

In this thesis, we have shown that there is strong evidence for IMF variations in the early, metal-poor Universe. However, we still do not know which physical and chemical processes dominate in setting its shape in metal-poor environments. A direct consequence of this is that we do not understand early metal enrichment, because the mass distribution of massive stars directly affects the integrated stellar yield of metals. A key challenge for metal-poor star formation simulations is that, at ultra-low metal abundances, all chemical processes become non-equilibrium, so it is necessary to solve the chemistry on the fly with MHD. Modelling metal-poor star formation also requires that we include a number of other physical effects – turbulence and magnetic fields (Turk et al. 2012), radiative heating of dust grains, and grain-gas coupling (Draine 2003). A large suite of such simulations is necessary to overcome stochasticity due to turbulence, and generate statistically-significant results (Sharda et al. 2020b).

Simulations of the low metallicity ISM will provide an unprecedented look at the shape and spectrum of the IMF in metal-poor environments, which will be the key to interpreting several JWST observables (see Figure 9.1). The resulting metal-poor IMF will also provide constraints on the population of gravitational wave sources in the early Universe that can be detected by the next generation of LIGO-Virgo (e.g., Deng 2021), and on ionizing sources that led to the Epoch of Reionization (Sobral et al. 2015).

Once the IMF is derived from such simulations, it will be possible to perform stochastic population synthesis of metal-poor star clusters for the first time. The resulting chemical abundances can then be compared against the measured abundances in the oldest and the most metal-poor stars (Frebel & Norris 2015). As the number of observed metal-poor stars increases thanks to LSST and SDSS V (Ivezić et al.
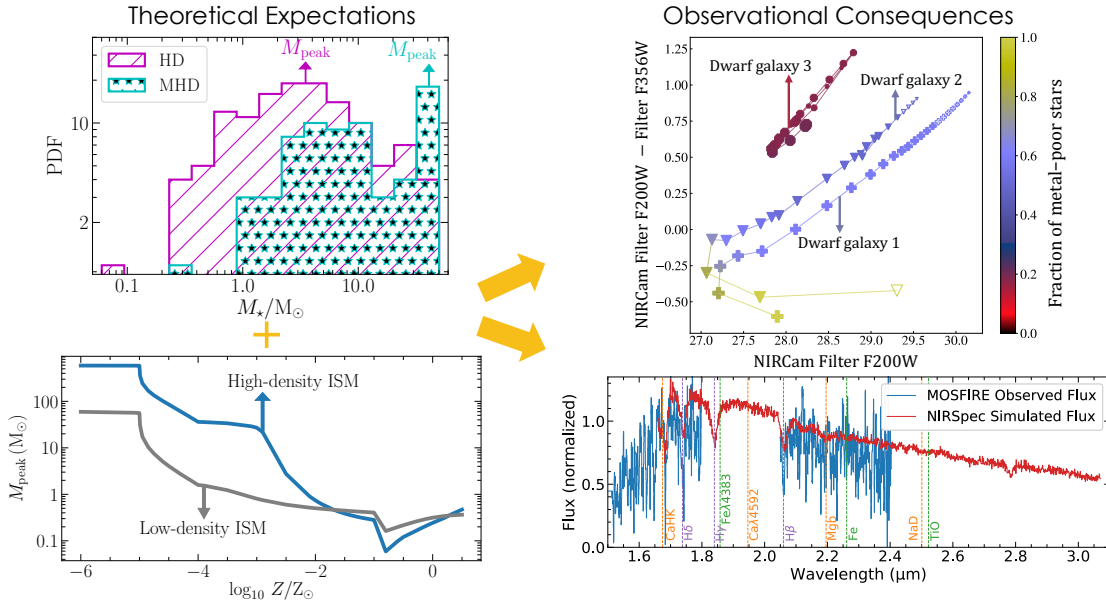
Figure 9.1: Variations in the IMF of the first stars ($Z = 0$) (top left, Sharda et al. 2020b), and in the IMF peak mass as a function of metallicity (bottom left, Sharda & Krumholz 2022). Producing the IMF at ultra-low metallicities with a corresponding metal enrichment history will be crucial to analyze JWST observables like color magnitude diagrams of the fraction of metal-poor stars in dwarf galaxies from NIRCam (top right, Gelli et al. 2021), and IMF variations at high-z measured by dynamical to stellar mass ratio using Na and Fe absorption bands from NIRSpec (bottom right, Nanayakkara et al. 2022).

2019), this will allow measurments of higher moments of chemical space (e.g., dispersion, element-element correlations) in nearby galaxies. Understanding these will require this combination of chemo-MHD simulations + stochastic population synthesis (Krumholz & Ting 2018).

9.2.3   Bridging the gap between metallicity theory and simulations

Progress in numerical techniques has led to a surge in cosmological simulations that can trace how galaxies evolve over time using metals. However, there still exist inhomegeneties and discrepancies between theoretical models such as ours with cosmological simulations, which makes it difficult to compare theory with simulations, or different theoretical models and simulations. As the amount of observational data exponentially increases thanks to large IFS surveys, there is an urgent need to homogenize the theoretical and numerical datasets to provide a consistent framework to be compared against observations (Foster et al. 2021).

One particular area where analytical, semi-analytical and numerical models need to

converge is galactic winds (and subsequently, the CGM). Using an analytic model, we have shown in this thesis that constraining the metallicity of galactic winds should be the next frontier as this is a vital but missing piece in the puzzle of galaxy evolution. However, the models do not provide any information on the nature of the winds, or where they are launched from. On the contrary, measuring differential metal enrichment of outflows is an extraordinarily difficult problem for simulations as they either do not resolve metal mixing at the interface of hot and cold ISM (e.g., Pandya et al. 2021), do not follow the evolution of the entire galaxy across cosmic time (e.g., Kim et al. 2020), or do not study both massive and dwarf galaxies (e.g., Emerick et al. 2018b). Some of these challenges can potentially be reduced by using GPU-friendly simulation codes which allow for very high resolution simulations without a significant addition in computational expense (e.g., Wibking & Krumholz 2022).

It is well known that feedback plays an important role in regulating the gas and metal budget of galaxies. However, the nature and strength of feedback significantly differs between theoretical models as well as simulations. Strong feedback results in bursty galactic discs and flat metallicity gradients, whereas weak feedback results in very steep metallicity gradients (Gibson et al. 2013; Ma et al. 2017; Hemler et al. 2021). Converging on the implementation of feedback in theory and simulations is another crucial aspect that needs to be achieved to further our understanding of evolution of metals in galaxies. This requires a better knowledge of the type of feedback processes that exist in diverse galaxies, and how they evolve over time.

9.2.4   Exploring the 2D metal distribution in galaxies

In reality, the concentration of metals not only varies in the radial direction, but also in the azimuthal direction within galactic discs. In fact, at $z > 1$, azimuthal metallicity variations possibly dominate over radial variations in galaxies (Bellardini et al. 2021, 2022) due to localised star formation and inefficient metal mixing (Dekel et al. 2009a). Reducing the dimensionality of 2D metallicity maps to 1D binned gradients also removes potentially useful data. Recent observations of local galaxies have demonstrated the power of statistical analysis of full 2D metallicity maps, finding how metal mixing correlates with physical structures like spiral arms (e.g., Kreckel et al. 2019). Such 2D statistical analyses have not been explored in distant galaxies due to the lack of sufficient resolution.

The ongoing VLT/MUSE large program MAGPI will change this situation in the near future (Foster et al. 2021). MAGPI will have more extensive galaxy coverage (by measuring metallicities out to a larger radius) at $z < 1.2$ than existing surveys,
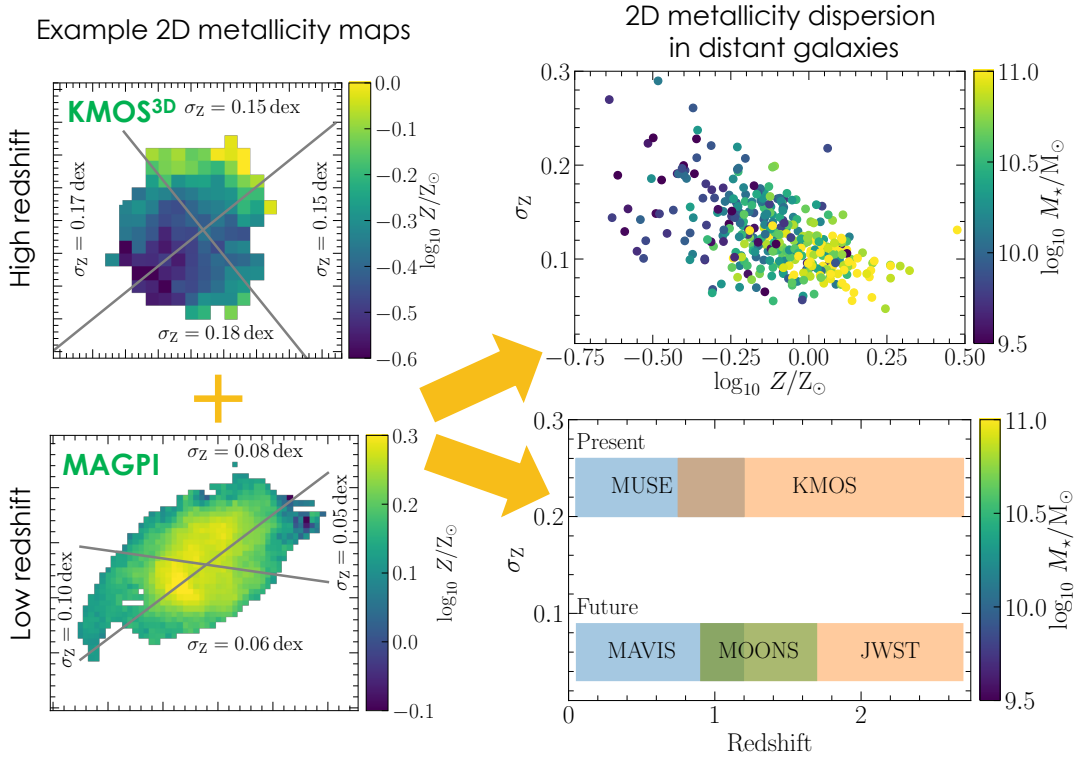
Figure 9.2: 2D metallicity variations in distant galaxies using data from the KMOS[3D] (top left, Wisnioski et al. 2019) and MAGPI surveys (bottom left, Foster et al. 2021). The metallicity maps are divided into four azimuthal segments based on the position angle (tilt) of the galaxy. σ_Z is the gradient-subtracted 2D metallicity dispersion in each segment corrected for beam smearing. Top right panel shows how σ_Z correlates with mean galaxy metallicity and galaxy mass in KMOS[3D] galaxies (Sharda et al. 2022, in prep.). A combined analysis of MAGPI and KMOS[3D] data will reveal the evolution of σ_Z across cosmic time and shed light on the internal structure of galaxies. This will set a benchmark to be tested against higher resolution data from VLT/MAVIS, VLT/MOONS, and JWST in the near future (bottom right).

and will provide 2D metallicity maps of over 1200 diverse galaxies. This will enable statistical analysis of 2D metallicity variations and exploration of possible correlations of 2D metallicity variations with galaxy properties and environment.

Additionally, archival data of several hundred galaxies is also available from the KMOS[3D] survey (Wisnioski et al. 2019). These data can be used to develop novel statistical techniques to be applied to quantify 2D metallicity variations (see Figure 9.2). Quantifying the statistics of 2D metal distributions will be integral to developing the cosmic history of 2D metallicity variations. Mapping 2D metallicity variations will in turn provide constraints on early star formation and galaxy evolution, which will set a critical benchmark to be tested against higher resolution data from VLT/MAVIS at $z < 1$, VLT/MOONS at $1 < z < 2$, and JWST at $z > 2$.

Bibliography

Abel, T., Anninos, P., Zhang, Y., & Norman, M. L. 1997, NewAs, 2, 181 (ADS entry)

Abel, T., Bryan, G. L., & Norman, M. L. 2000, ApJ, 540, 39 (ADS entry)

—. 2002, Science, 295, 93 (ADS entry)

Acharyya, A., Krumholz, M. R., Federrath, C., Kewley, L. J., Goldbaum, N. J., & Sharp, R. 2020, MNRAS, 495, 3819 (ADS entry)

Acharyya, A., Krumholz, M. R., Federrath, C., Kewley, L. J., Sànchez, F. S., & Poetrodjojo, H. 2021, MNRAS, in prep.

Adams, F. C., & Fatuzzo, M. 1996, ApJ, 464, 256 (ADS entry)

Adams, F. C., Ruden, S. P., & Shu, F. H. 1989, ApJ, 347, 959 (ADS entry)

Afflerbach, A., Churchwell, E., & Werner, M. W. 1997, ApJ, 478, 190 (ADS entry)

Aguado, D. S., Allende Prieto, C., González Hernández, J. I., & Rebolo, R. 2018, ApJ, 854, L34 (ADS entry)

Aguado, D. S., Allende Prieto, C., González Hernández, J. I., Rebolo, R., & Caffau, E. 2017, A&A, 604, A9 (ADS entry)

Ahn, K., & Shapiro, P. R. 2007, MNRAS, 375, 881 (ADS entry)

Aldrovandi, S. M. V., & Pequignot, D. 1973, A&A, 26, 33 (ADS entry)

Aller, L. H. 1942, ApJ, 95, 52 (ADS entry)

Allison, A. C., & Dalgarno, A. 1969, Atomic Data, 1, 91 (ADS entry)

Almgren, A., et al. 2020, The Journal of Open Source Software, 5, 2513 (ADS entry)

Alves, D. R., & Nelson, C. A. 2000, ApJ, 542, 789 (ADS entry)

Alves, J., Lombardi, M., & Lada, C. J. 2007, A&A, 462, L17 (ADS entry)

Amarsi, A. M., Lind, K., Asplund, M., Barklem, P. S., & Collet, R. 2016, MNRAS, 463, 1518 (ADS entry)

Ames, S. 1973, ApJ, 182, 387 (ADS entry)

Andersen, M., Zinnecker, H., Moneti, A., McCaughrean, M. J., Brandl, B., Brandner, W., Meylan, G., & Hunter, D. 2009, ApJ, 707, 1347 (ADS entry)

Andrews, B. H., & Martini, P. 2013, ApJ, 765, 140 (ADS entry)

Andrews, J. E., et al. 2014, ApJ, 793, 4 (ADS entry)

Anglés-Alcázar, D., Faucher-Giguère, C.-A., Kereš, D., Hopkins, P. F., Quataert, E., & Murray, N. 2017, MNRAS, 470, 4698 (ADS entry)

Applebaum, E., Brooks, A. M., Quinn, T. R., & Christensen, C. R. 2020, MNRAS, 492, 8 (ADS entry)

Arentsen, A., et al. 2020, MNRAS, 496, 4964 (ADS entry)

Arfken, G. 1985, Mathematical Methods for Physicists, 3rd edn. (San Diego: Academic Press, Inc.)

Armillotta, L., Krumholz, M. R., & Fujimoto, Y. 2018, MNRAS, 481, 5000 (ADS entry)

Arribas, S., Colina, L., Bellocchi, E., Maiolino, R., & Villar-Martín, M. 2014, A&A, 568, A14 (ADS entry)

Arribas, S., Colina, L., Monreal-Ibero, A., Alfonso, J., García-Marín, M., & Alonso-Herrero, A. 2008, A&A, 479, 687 (ADS entry)

Asplund, M., Grevesse, N., Sauval, A. J., & Scott, P. 2009, ARA&A, 47, 481 (ADS entry)

Astropy Collaboration et al. 2013, A&A, 558, A33 (ADS entry)

—. 2018, AJ, 156, 123 (ADS entry)

Aumer, M., White, S. D. M., Naab, T., & Scannapieco, C. 2013, MNRAS, 434, 3142 (ADS entry)

Babcock, H. W. 1961, ApJ, 133, 572 (ADS entry)

Bacon, R., et al. 2010, in Society of Photo-Optical Instrumentation Engineers (SPIE) Conference Series, Vol. 7735, Proc. SPIE, 773508 (ADS entry)

Bahé, Y. M., Schaye, J., Crain, R. A., McCarthy, I. G., Bower, R. G., Theuns, T., McGee, S. L., & Trayford, J. W. 2017, MNRAS, 464, 508 (ADS entry)

Bai, X.-N., & Stone, J. M. 2011, ApJ, 736, 144 (ADS entry)

Baierlein, R. 1978, MNRAS, 184, 843 (ADS entry)

Balashev, S. A., et al. 2017, MNRAS, 470, 2890 (ADS entry)

Baldwin, J. A., Phillips, M. M., & Terlevich, R. 1981, PASP, 93, 5 (ADS entry)

Balogh, A. 2010, Space Sci. Rev., 152, 23 (ADS entry)

Balsara, D. S., Kim, J., Mac Low, M.-M., & Mathews, G. J. 2004, ApJ, 617, 339 (ADS entry)

Banerjee, R., & Jedamzik, K. 2004, Phys. Rev. D, 70, 123003 (ADS entry)

Banerjee, R., & Pudritz, R. E. 2006, ApJ, 641, 949 (ADS entry)

Banerjee, S., & Kroupa, P. 2012, A&A, 547, A23 (ADS entry)

Barber, C., Schaye, J., & Crain, R. A. 2019, MNRAS, 482, 2515 (ADS entry)

Barinovs, Ğ., van Hemert, M. C., Krems, R., & Dalgarno, A. 2005, ApJ, 620, 537 (ADS entry)

Barrera-Ballesteros, J. K., Sánchez, S. F., Heckman, T., Blanc, G. A., & MaNGA Team. 2017, ApJ, 844, 80 (ADS entry)

Barton, E. J., Geller, M. J., & Kenyon, S. J. 2000, ApJ, 530, 660 (ADS entry)

Bastian, N., Covey, K. R., & Meyer, M. R. 2010, ARA&A, 48, 339 (ADS entry)

Bastian, N., & Lardo, C. 2018, ARA&A, 56, 83 (ADS entry)

Bastian, N., Saglia, R. P., Goudfrooij, P., Kissler-Patig, M., Maraston, C., Schweizer, F., & Zoccali, M. 2006, A&A, 448, 881 (ADS entry)

Bate, M. R. 1998, ApJ, 508, L95 (ADS entry)

—. 2005, MNRAS, 363, 363 (ADS entry)

—. 2009a, MNRAS, 392, 1363 (ADS entry)

—. 2009b, MNRAS, 392, 1363 (ADS entry)

—. 2012a, MNRAS, 419, 3115 (ADS entry)

—. 2012b, MNRAS, 419, 3115 (ADS entry)

—. 2014, MNRAS, 442, 285 (ADS entry)

—. 2019, MNRAS, 484, 2341 (ADS entry)

Bate, M. R., Bonnell, I. A., & Bromm, V. 2002, MNRAS, 332, L65 (ADS entry)

—. 2003, MNRAS, 339, 577 (ADS entry)

Bate, M. R., Bonnell, I. A., & Price, N. M. 1995, MNRAS, 277, 362 (ADS entry)

Bate, M. R., & Keto, E. R. 2015, MNRAS, 449, 2643 (ADS entry)

Bate, M. R., & Lorén-Aguilar, P. 2017, MNRAS, 465, 1089 (ADS entry)

Baumgardt, H. 2017, MNRAS, 464, 2174 (ADS entry)

Baumgardt, H., & Makino, J. 2003, MNRAS, 340, 227 (ADS entry)

Beattie, J. R., & Federrath, C. 2020, MNRAS, 492, 668 (ADS entry)

Beck, R., Brandenburg, A., Moss, D., Shukurov, A., & Sokoloff, D. 1996, ARA&A, 34, 155 (ADS entry)

Beers, T. C., & Christlieb, N. 2005, ARA&A, 43, 531 (ADS entry)

Behroozi, P. S., Wechsler, R. H., & Conroy, C. 2013, ApJ, 762, L31 (ADS entry)

Bekki, K. 2013, MNRAS, 436, 2254 (ADS entry)

Belczynski, K., Ryu, T., Perna, R., Berti, E., Tanaka, T. L., & Bulik, T. 2017, MNRAS, 471, 4702 (ADS entry)

Belfiore, F., Vincenzo, F., Maiolino, R., & Matteucci, F. 2019, MNRAS, 487, 456 (ADS entry)

Belfiore, F., et al. 2017, MNRAS, 469, 151 (ADS entry)

Bell, E. F., & de Jong, R. S. 2001, ApJ, 550, 212 (ADS entry)

Bellardini, M. A., Wetzel, A., Loebman, S. R., & Bailin, J. 2022, arXiv e-prints, arXiv:2203.03653 (ADS entry)

Bellardini, M. A., Wetzel, A., Loebman, S. R., Faucher-Giguère, C.-A., Ma, X., & Feldmann, R. 2021, MNRAS, 505, 4586 (ADS entry)

Bellstedt, S., et al. 2020, MNRAS, 498, 5581 (ADS entry)

Bendre, A. B., Subramanian, K., Elstner, D., & Gressel, O. 2020, MNRAS, 491, 3870 (ADS entry)

Benson, A. J. 2010, Phys. Rep., 495, 33 (ADS entry)

Bera, P., Shukurov, A., & Subramanian, K. 2019, Galaxies, 7, 91 (ADS entry)

Berger, M. J., & Colella, P. 1989, Journal of Computational Physics, 82, 64 (ADS entry)

Bernet, M. L., Miniati, F., Lilly, S. J., Kronberg, P. P., & Dessauges-Zavadsky, M. 2008, Nature, 454, 302 (ADS entry)

Bessell, M. S., et al. 2015, ApJ, 806, L16 (ADS entry)

Bhandare, A., Kuiper, R., Henning, T., Fendt, C., Marleau, G.-D., & Kölligan, A. 2018, A&A, 618, A95 (ADS entry)

Bhat, P., & Subramanian, K. 2014, ApJ, 791, L34 (ADS entry)

Bhat, P., Subramanian, K., & Brandenburg, A. 2016, MNRAS, 461, 240 (ADS entry)

—. 2019, arXiv e-prints, arXiv:1905.08278 (ADS entry)

Bialy, S., & Sternberg, A. 2015, MNRAS, 450, 4424 (ADS entry)

Biermann, L. 1950, Zeitschrift Naturforschung Teil A, 5, 65 (ADS entry)

Bigiel, F., & Blitz, L. 2012, ApJ, 756, 183 (ADS entry)

Bigiel, F., Leroy, A., Walter, F., Brinks, E., de Blok, W. J. G., Madore, B., & Thornley, M. D. 2008, AJ, 136, 2846 (ADS entry)

Bilitewski, T., & Schönrich, R. 2012, MNRAS, 426, 2266 (ADS entry)

Birnboim, Y., & Dekel, A. 2003, MNRAS, 345, 349 (ADS entry)

Bisbas, T. G., Papadopoulos, P. P., & Viti, S. 2015, ApJ, 803, 37 (ADS entry)

Bisbas, T. G., van Dishoeck, E. F., Papadopoulos, P. P., Szűcs, L., Bialy, S., & Zhang, Z.-Y. 2017, ApJ, 839, 90 (ADS entry)

Bitsch, B., Boley, A., & Kley, W. 2013, A&A, 550, A52 (ADS entry)

Black, D. C., & Bodenheimer, P. 1975, ApJ, 199, 619 (ADS entry)

Blackman, E. G., & Field, G. B. 2002, Phys. Rev. Lett., 89, 265007 (ADS entry)

Blanc, G. A., Kewley, L., Vogt, F. P. A., & Dopita, M. A. 2015, ApJ, 798, 99 (ADS entry)

Blanc, G. A., Lu, Y., Benson, A., Katsianis, A., & Barraza, M. 2019, ApJ, 877, 6 (ADS entry)

Bland-Hawthorn, J., & Gerhard, O. 2016, ARA&A, 54, 529 (ADS entry)

Bleuler, A., & Teyssier, R. 2014, MNRAS, 445, 4015 (ADS entry)

Bloch, H., Tremblin, P., González, M., Padioleau, T., & Audit, E. 2021, A&A, 646, A123 (ADS entry)

Bluck, A. F. L., Conselice, C. J., Bouwens, R. J., Daddi, E., Dickinson, M., Papovich, C., & Yan, H. 2009, MNRAS, 394, L51 (ADS entry)

Bluck, A. F. L., Conselice, C. J., Buitrago, F., Grützbauch, R., Hoyos, C., Mortlock, A., & Bauer, A. E. 2012, ApJ, 747, 34 (ADS entry)

Bolatto, A. D., Leroy, A. K., Rosolowsky, E., Walter, F., & Blitz, L. 2008, ApJ, 686, 948 (ADS entry)

Bolatto, A. D., et al. 2011, ApJ, 741, 12 (ADS entry)

Boley, A. C., Hartquist, T. W., Durisen, R. H., & Michael, S. 2007, ApJ, 656, L89 (ADS entry)

Bond, H. E. 1981, ApJ, 248, 606 (ADS entry)

Bonnell, I. A., & Bate, M. R. 1994, MNRAS, 269, L45 (ADS entry)

Bonnet, H., et al. 2004, in Society of Photo-Optical Instrumentation Engineers (SPIE) Conference Series, Vol. 5490, Proc. SPIE, ed. D. Bonaccini Calia, B. L. Ellerbroek, & R. Ragazzoni, 130–138 (ADS entry)

Bonnor, W. B. 1956, MNRAS, 116, 351 (ADS entry)

—. 1957, MNRAS, 117, 104 (ADS entry)

Bothwell, M. S., et al. 2014, MNRAS, 445, 2599 (ADS entry)

Bouché, N., Hohensee, W., Vargas, R., Kacprzak, G. G., Martin, C. L., Cooke, J., & Churchill, C. W. 2012, MNRAS, 426, 801 (ADS entry)

Bouché, N., et al. 2010, ApJ, 718, 1001 (ADS entry)

Bouchut, F., Klingenberg, C., & Waagan, K. 2007, Numerische Mathematik, 108, 7 (Link)

—. 2010, Numerische Mathematik, 115, 647 (Link)

Bovino, S., Grassi, T., Latif, M. A., & Schleicher, D. R. G. 2013a, MNRAS, 434, L36 (ADS entry)

Bovino, S., Schleicher, D. R. G., & Schober, J. 2013b, New Journal of Physics, 15, 013055 (ADS entry)

Brandenburg, A. 2018, Journal of Plasma Physics, 84, 735840404 (ADS entry)

Brandenburg, A., Enqvist, K., & Olesen, P. 1996, Phys. Rev. D, 54, 1291 (ADS entry)

Brandenburg, A., Kahniashvili, T., Mandal, S., Pol, A. R., Tevzadze, A. G., & Vachaspati, T. 2019, Physical Review Fluids, 4, 024608 (ADS entry)

Brandenburg, A., Nordlund, A., Stein, R. F., & Torkelsson, U. 1995, ApJ, 446, 741 (ADS entry)

Brandenburg, A., Sokoloff, D., & Subramanian, K. 2012, Space Sci. Rev., 169, 123 (ADS entry)

Brandenburg, A., & Subramanian, K. 2005, Phys. Rep., 417, 1 (ADS entry)

Bregman, J. N. 1980, ApJ, 236, 577 (ADS entry)

Bresolin, F. 2019, MNRAS, 488, 3826 (ADS entry)

Bromm, V. 2013, Reports on Progress in Physics, 76, 112901 (ADS entry)

Bromm, V., Coppi, P. S., & Larson, R. B. 2002, ApJ, 564, 23 (ADS entry)

Bromm, V., Ferrara, A., Coppi, P. S., & Larson, R. B. 2001, MNRAS, 328, 969 (ADS entry)

Bromm, V., & Larson, R. B. 2004, ARA&A, 42, 79 (ADS entry)

Bromm, V., & Loeb, A. 2003, Nature, 425, 812 (ADS entry)

Bromm, V., Yoshida, N., Hernquist, L., & McKee, C. F. 2009, Nature, 459, 49 (ADS entry)

Brook, C. B., Stinson, G., Gibson, B. K., Shen, S., Macciò, A. V., Obreja, A., Wadsley, J., & Quinn, T. 2014, MNRAS, 443, 3809 (ADS entry)

Brooks, A. M., Governato, F., Booth, C. M., Willman, B., Gardner, J. P., Wadsley, J., Stinson, G., & Quinn, T. 2007, ApJ, 655, L17 (ADS entry)

Brown, J. S., Martini, P., & Andrews, B. H. 2016, MNRAS, 458, 1529 (ADS entry)

Brown, T., & Wilson, C. D. 2019, ApJ, 879, 17 (ADS entry)

Bryant, J. J., et al. 2015, MNRAS, 447, 2857 (ADS entry)

Bundy, K., et al. 2015, ApJ, 798, 7 (ADS entry)

Bunker, A. J., NIRSPEC Instrument Science Team, & JAESs Collaboration. 2020, in Uncovering Early Galaxy Evolution in the ALMA and JWST Era, ed. E. da

Cunha, J. Hodge, J. Afonso, L. Pentericci, & D. Sobral, Vol. 352, 342–346 (ADS entry)

Burgers, J. 1948, in Advances in Applied Mechanics, Vol. 1, A Mathematical Model Illustrating the Theory of Turbulence, ed. R. V. Mises & T. V. Kármán (Elsevier), 171 – 199 (Link)

Burke, J. R., & Hollenbach, D. J. 1983, ApJ, 265, 223 (ADS entry)

Burkert, A., & Bodenheimer, P. 1993, MNRAS, 264, 798 (ADS entry)

—. 2000, ApJ, 543, 822 (ADS entry)

Burkert, A., et al. 2010, ApJ, 725, 2324 (ADS entry)

—. 2016, ApJ, 826, 214 (ADS entry)

Byler, N., Dalcanton, J. J., Conroy, C., Johnson, B. D., Levesque, E. M., & Berg, D. A. 2018, ApJ, 863, 14 (ADS entry)

Caffau, E., et al. 2011, Nature, 477, 67 (ADS entry)

Calabrò, A., et al. 2018, ApJ, 862, L22 (ADS entry)

Calura, F., Pipino, A., Chiappini, C., Matteucci, F., & Maiolino, R. 2009, A&A, 504, 373 (ADS entry)

Calzetti, D. 2001, PASP, 113, 1449 (ADS entry)

Cameron, A. J., et al. 2021, ApJ, 918, L16 (ADS entry)

Capitelli, M., Coppola, C. M., Diomede, P., & Longo, S. 2007, A&A, 470, 811 (ADS entry)

Cappellari, M., et al. 2012, Nature, 484, 485 (ADS entry)

Carilli, C. L., & Taylor, G. B. 2002, ARA&A, 40, 319 (ADS entry)

Carton, D., et al. 2015, MNRAS, 451, 210 (ADS entry)

—. 2017, MNRAS, 468, 2140 (ADS entry)

—. 2018, MNRAS, 478, 4293 (ADS entry)

Caselli, P., & Myers, P. C. 1995, ApJ, 446, 665 (ADS entry)

Casey, A. R., & Schlaufman, K. C. 2015, ApJ, 809, 110 (ADS entry)

Cassisi, S., & Castellani, V. 1993, ApJS, 88, 509 (ADS entry)

Caswell, T. A., et al. 2019, in (Zenodo) (Link)

Cattaneo, F., & Hughes, D. W. 2009, MNRAS, 395, L48 (ADS entry)

Cattaneo, F., & Tobias, S. M. 2014, ApJ, 789, 70 (ADS entry)

Cavichia, O., Costa, R. D. D., & Maciel, W. J. 2011, Rev. Mex. Astron. Astrofis., 47, 49 (ADS entry)

Cazaux, S., & Spaans, M. 2009, A&A, 496, 365 (ADS entry)

Cen, R. 1992, ApJS, 78, 341 (ADS entry)

Chabrier, G. 2003, PASP, 115, 763 (ADS entry)

Chabrier, G. 2005, in The Initial Mass Function 50 Years Later, ed. E. Corbelli, F. Palla, & H. Zinnecker, Vol. 327 (Springer), 41 (ADS entry)

Chabrier, G., Hennebelle, P., & Charlot, S. 2014, ApJ, 796, 75 (ADS entry)

Chakrabarti, S., Magnelli, B., McKee, C. F., Lutz, D., Berta, S., Popesso, P., & Pozzi, F. 2013, ApJ, 773, 113 (ADS entry)

Chakrabarti, S., & McKee, C. F. 2005, ApJ, 631, 792 (ADS entry)

—. 2008, ApJ, 683, 693 (ADS entry)

Cheera, V., & Nigam, R. 2018, Ap&SS, 363, 93 (ADS entry)

Cherchneff, I., & Dwek, E. 2010, ApJ, 713, 1 (ADS entry)

Chevance, M., et al. 2020, MNRAS, 494, 5279 (ADS entry)

Chiaki, G., Marassi, S., Nozawa, T., Yoshida, N., Schneider, R., Omukai, K., Limongi, M., & Chieffi, A. 2015, MNRAS, 446, 2659 (ADS entry)

Chiaki, G., Susa, H., & Hirano, S. 2018, MNRAS, 475, 4378 (ADS entry)

Chiaki, G., & Yoshida, N. 2020, arXiv e-prints, arXiv:2008.06107 (ADS entry)

Chiaki, G., Yoshida, N., & Hirano, S. 2016, MNRAS, 463, 2781 (ADS entry)

Chiappini, C., Matteucci, F., & Gratton, R. 1997, ApJ, 477, 765 (ADS entry)

Chiappini, C., Matteucci, F., & Romano, D. 2001, ApJ, 554, 1044 (ADS entry)

Childress, S., & Gilbert, A. D. 1995, Stretch, Twist, Fold (Springer-Verlag) (ADS entry)

Childs, H., et al. 2012, in High Performance Visualization–Enabling Extreme-Scale Scientific Insight (Taylor and Francis), 357–372

Chisholm, J., Tremonti, C., & Leitherer, C. 2018, MNRAS, 481, 1690 (ADS entry)

Chisholm, J., Tremonti, C. A., Leitherer, C., & Chen, Y. 2017, MNRAS, 469, 4831 (ADS entry)

Chon, S., & Hosokawa, T. 2019, MNRAS, 488, 2658 (ADS entry)

Chon, S., Omukai, K., & Schneider, R. 2021, MNRAS(ADS entry)

Christensen, C. R., Davé, R., Brooks, A., Quinn, T., & Shen, S. 2018, ApJ, 867, 142 (ADS entry)

Christensen, C. R., Davé, R., Governato, F., Pontzen, A., Brooks, A., Munshi, F., Quinn, T., & Wadsley, J. 2016, ApJ, 824, 57 (ADS entry)

Christensson, M., Hindmarsh, M., & Brandenburg, A. 2001, Phys. Rev. E, 64, 056405 (ADS entry)

Christlieb, N., Gustafsson, B., Korn, A. J., Barklem, P. S., Beers, T. C., Bessell, M. S., Karlsson, T., & Mizuno-Wiedner, M. 2004, ApJ, 603, 708 (ADS entry)

Chruślińska, M., Jeřábková, T., Nelemans, G., & Yan, Z. 2020, A&A, 636, A10 (ADS entry)

Ciardi, B., & Ferrara, A. 2005, Space Sci. Rev., 116, 625 (ADS entry)

Clark, P. C., Glover, S. C. O., Klessen, R. S., & Bromm, V. 2011a, ApJ, 727, 110 (ADS entry)

Clark, P. C., Glover, S. C. O., Smith, R. J., Greif, T. H., Klessen, R. S., & Bromm, V. 2011b, Science, 331, 1040 (ADS entry)

—. 2011c, Science, 331, 1040 (ADS entry)

Clarke, C. J., & Pringle, J. E. 1991, MNRAS, 249, 588 (ADS entry)

Clements, D. L., Sutherland, W. J., McMahon, R. G., & Saunders, W. 1996, MNRAS, 279, 477 (ADS entry)

Colavitti, E., Matteucci, F., & Murante, G. 2008, A&A, 483, 401 (ADS entry)

Collacchioni, F., Cora, S. A., Lagos, C. D. P., & Vega-Martínez, C. A. 2018, MNRAS, 481, 954 (ADS entry)

Collacchioni, F., Lagos, C. D. P., Mitchell, P. D., Schaye, J., Wisnioski, E., Cora, S. A., & Correa, C. A. 2020, MNRAS, 495, 2827 (ADS entry)

Collett, T. E., et al. 2018, Science, 360, 1342 (ADS entry)

Collins, D. C., Kritsuk, A. G., Padoan, P., Li, H., Xu, H., Ustyugov, S. D., & Norman, M. L. 2012, ApJ, 750, 13 (ADS entry)

Colman, T., & Teyssier, R. 2020, MNRAS, 492, 4727 (ADS entry)

Commerçon, B., Hennebelle, P., Audit, E., Chabrier, G., & Teyssier, R. 2008, A&A, 482, 371 (ADS entry)

—. 2010, A&A, 510, L3 (ADS entry)

Conroy, C., & van Dokkum, P. G. 2012, ApJ, 760, 71 (ADS entry)

Conroy, C., van Dokkum, P. G., & Villaume, A. 2017, ApJ, 837, 166 (ADS entry)

Conroy, C., & Wechsler, R. H. 2009, ApJ, 696, 620 (ADS entry)

Contini, T., et al. 2012, A&A, 539, A91 (ADS entry)

Cooke, R. J., Pettini, M., Jorgenson, R. A., Murphy, M. T., & Steidel, C. C. 2014, ApJ, 781, 31 (ADS entry)

Cooper, M. C., Tremonti, C. A., Newman, J. A., & Zabludoff, A. I. 2008, MNRAS, 390, 245 (ADS entry)

Coppola, C. M., Lodi, L., & Tennyson, J. 2011, MNRAS, 415, 487 (ADS entry)

Cornuault, N., Lehnert, M. D., Boulanger, F., & Guillard, P. 2018, A&A, 610, A75 (ADS entry)

Courty, S., Gibson, B. K., & Teyssier, R. 2010, in American Institute of Physics Conference Series, Vol. 1240, American Institute of Physics Conference Series, ed. V. P. Debattista & C. C. Popescu, 131–134 (ADS entry)

Cowley, W. I., Lacey, C. G., Baugh, C. M., Cole, S., Frenk, C. S., & Lagos, C. d. P. 2019, MNRAS, 487, 3082 (ADS entry)

Creasey, P., Theuns, T., & Bower, R. G. 2013, MNRAS, 429, 1922 (ADS entry)

—. 2015, MNRAS, 446, 2125 (ADS entry)

Creasey, P., Theuns, T., Bower, R. G., & Lacey, C. G. 2011, MNRAS, 415, 3706 (ADS entry)

Cresci, G., Mannucci, F., Maiolino, R., Marconi, A., Gnerucci, A., & Magrini, L. 2010, Nature, 467, 811 (ADS entry)

Crighton, N. H. M., Hennawi, J. F., & Prochaska, J. X. 2013, ApJ, 776, L18 (ADS entry)

Crocker, R. M., Krumholz, M. R., & Thompson, T. A. 2021, MNRAS, 502, 1312 (ADS entry)

Crutcher, R. M. 1999, ApJ, 520, 706 (ADS entry)

—. 2012, ARA&A, 50, 29 (ADS entry)

Crutcher, R. M., & Kemball, A. J. 2019, Frontiers in Astronomy and Space Sciences, 6, 66 (ADS entry)

Crutcher, R. M., Wandelt, B., Heiles, C., Falgarone, E., & Troland, T. H. 2010, ApJ, 725, 466 (ADS entry)

Cunningham, A. J., Krumholz, M. R., McKee, C. F., & Klein, R. I. 2018a, MNRAS, 476, 771 (ADS entry)

—. 2018b, MNRAS, 476, 771 (ADS entry)

Curti, M., Cresci, G., Mannucci, F., Marconi, A., Maiolino, R., & Esposito, S. 2017, MNRAS, 465, 1384 (ADS entry)

Curti, M., Mannucci, F., Cresci, G., & Maiolino, R. 2020a, MNRAS, 491, 944 (ADS entry)

Curti, M., et al. 2020b, MNRAS, 492, 821 (ADS entry)

Dabringhausen, J., Fellhauer, M., & Kroupa, P. 2010, MNRAS, 403, 1054 (ADS entry)

Dabringhausen, J., Kroupa, P., & Baumgardt, H. 2009, MNRAS, 394, 1529 (ADS entry)

Dabringhausen, J., Kroupa, P., Pflamm-Altenburg, J., & Mieske, S. 2012, ApJ, 747, 72 (ADS entry)

D'Agostino, J. J., Kewley, L. J., Groves, B. A., Medling, A., Dopita, M. A., & Thomas, A. D. 2019, MNRAS, 485, L38 (ADS entry)

Dalcanton, J. J. 2007, ApJ, 658, 941 (ADS entry)

Dalgarno, A., & Lepp, S. 1987, in IAU Symposium, Vol. 120, Astrochemistry, ed. M. S. Vardya & S. P. Tarafdar, 109–118 (ADS entry)

Dame, T. M., Hartmann, D., & Thaddeus, P. 2001, ApJ, 547, 792 (ADS entry)

Dashyan, G., & Dubois, Y. 2020, A&A, 638, A123 (ADS entry)

Davé, R. 2008, MNRAS, 385, 147 (ADS entry)

Davé, R., Anglés-Alcázar, D., Narayanan, D., Li, Q., Rafieferantsoa, M. H., & Appleby, S. 2019, MNRAS, 486, 2827 (ADS entry)

Davé, R., Finlator, K., & Oppenheimer, B. D. 2011, MNRAS, 416, 1354 (ADS entry)

—. 2012, MNRAS, 421, 98 (ADS entry)

Davé, R., Rafieferantsoa, M. H., Thompson, R. J., & Hopkins, P. F. 2017, MNRAS, 467, 115 (ADS entry)

Davies, R., et al. 2011, ApJ, 741, 69 (ADS entry)

Davies, R., et al. 2018, in Society of Photo-Optical Instrumentation Engineers (SPIE) Conference Series, Vol. 10702, Ground-based and Airborne Instrumentation for Astronomy VII, ed. C. J. Evans, L. Simard, & H. Takami, 1070209 (ADS entry)

Davies, R. L., et al. 1997, in Society of Photo-Optical Instrumentation Engineers (SPIE) Conference Series, Vol. 2871, Optical Telescopes of Today and Tomorrow, ed. A. L. Ardeberg, 1099–1106 (ADS entry)

Davies, R. L., et al. 2019, ApJ, 873, 122 (ADS entry)

—. 2020, arXiv e-prints, arXiv:2012.10445 (ADS entry)

Dayal, P., Ferrara, A., & Dunlop, J. S. 2013, MNRAS, 430, 2891 (ADS entry)

de Avillez, M. A., & Mac Low, M.-M. 2002, ApJ, 581, 1047 (ADS entry)

de Bennassuti, M., Salvadori, S., Schneider, R., Valiante, R., & Omukai, K. 2017, MNRAS, 465, 926 (ADS entry)

De Lucia, G., Xie, L., Fontanot, F., & Hirschmann, M. 2020, MNRAS, 498, 3215 (ADS entry)

De Marchi, G., Paresce, F., & Portegies Zwart, S. 2010, ApJ, 718, 105 (ADS entry)

De Marchi, G., Paresce, F., & Pulone, L. 2000, ApJ, 530, 342 (ADS entry)

De Rossi, M. E., Bower, R. G., Font, A. S., Schaye, J., & Theuns, T. 2017, MNRAS, 472, 3354 (ADS entry)

De Rossi, M. E., Theuns, T., Font, A. S., & McCarthy, I. G. 2015, MNRAS, 452, 486 (ADS entry)

De Souza, R. S., Yoshida, N., & Ioka, K. 2011, A&A, 533, A32 (ADS entry)

De Vis, P., et al. 2019, A&A, 623, A5 (ADS entry)

Dekel, A., & Birnboim, Y. 2006, MNRAS, 368, 2 (ADS entry)

Dekel, A., & Burkert, A. 2014, MNRAS, 438, 1870 (ADS entry)

Dekel, A., Sari, R., & Ceverino, D. 2009a, ApJ, 703, 785 (ADS entry)

Dekel, A., & Silk, J. 1986, ApJ, 303, 39 (ADS entry)

Dekel, A., Zolotov, A., Tweed, D., Cacciato, M., Ceverino, D., & Primack, J. R. 2013, MNRAS, 435, 999 (ADS entry)

Dekel, A., et al. 2009b, Nature, 457, 451 (ADS entry)

Deng, H. 2021, JCAP, 2021, 058 (ADS entry)

Denicoló, G., Terlevich, R., & Terlevich, E. 2002, MNRAS, 330, 69 (ADS entry)

Desch, S. J., & Mouschovias, T. C. 2001, ApJ, 550, 314 (ADS entry)

D'Hendecourt, L. B., Allamandola, L. J., & Greenberg, J. M. 1985, A&A, 152, 130 (ADS entry)

Di Teodoro, E. M., & Fraternali, F. 2015, MNRAS, 451, 3021 (ADS entry)

Di Teodoro, E. M., Fraternali, F., & Miller, S. H. 2016, A&A, 594, A77 (ADS entry)

Doi, K., & Susa, H. 2011, ApJ, 741, 93 (ADS entry)

Dolag, K., Mevius, E., & Remus, R.-S. 2017, Galaxies, 5, 35 (ADS entry)

Donnert, J., Vazza, F., Brüggen, M., & ZuHone, J. 2018, Space Sci. Rev., 214, 122 (ADS entry)

Dopcke, G., Glover, S. C. O., Clark, P. C., & Klessen, R. S. 2011, ApJ, 729, L3 (ADS entry)

—. 2013, ApJ, 766, 103 (ADS entry)

Dopita, M. A., & Evans, I. N. 1986, ApJ, 307, 431 (ADS entry)

Dopita, M. A., Kewley, L. J., Sutherland, R. S., & Nicholls, D. C. 2016, Ap&SS, 361, 61 (ADS entry)

Downes, D., & Solomon, P. M. 1998, ApJ, 507, 615 (ADS entry)

Draine, B. T. 2003, ARA&A, 41, 241 (ADS entry)

—. 2011, Physics of the Interstellar and Intergalactic Medium (Princeton University Press) (ADS entry)

Draine, B. T., Roberge, W. G., & Dalgarno, A. 1983, ApJ, 264, 485 (ADS entry)

Du, W., Wu, H., Zhu, Y., Zheng, W., & Filippenko, A. V. 2017, ApJ, 837, 152 (ADS entry)

Dubey, A., et al. 2008, in Astronomical Society of the Pacific Conference Series, Vol. 385, Numerical Modeling of Space Plasma Flows, ed. N. V. Pogorelov, E. Audit, & G. P. Zank, 145 (ADS entry)

Dubey, A., et al. 2013, in 2013 5th International Workshop on Software Engineering for Computational Science and Engineering (SE-CSE), 1–8

Duffin, D. F., & Pudritz, R. E. 2011, in IAU Symposium, Vol. 270, Computational Star Formation, ed. J. Alves, B. G. Elmegreen, J. M. Girart, & V. Trimble, 291–295 (ADS entry)

Durrer, R., & Neronov, A. 2013, A&A Rev., 21, 62 (ADS entry)

Dutton, A. A., & Macciò, A. V. 2014, MNRAS, 441, 3359 (ADS entry)

Dutton, A. A., et al. 2011, MNRAS, 410, 1660 (ADS entry)

Dyda, S., Lovelace, R. V. E., Ustyugova, G. V., Koldoba, A. V., & Wasserman, I. 2018, MNRAS, 477, 127 (ADS entry)

Ebert, R. 1955, ZAp, 37, 217 (ADS entry)

Eisenhauer, F., et al. 2003, in Society of Photo-Optical Instrumentation Engineers (SPIE) Conference Series, Vol. 4841, Proc. SPIE, ed. M. Iye & A. F. M. Moorwood, 1548–1561 (ADS entry)

El-Badry, K., Weisz, D. R., & Quataert, E. 2017, MNRAS, 468, 319 (ADS entry)

Eldridge, J. J. 2012, MNRAS, 422, 794 (ADS entry)

Ellis, S., et al. 2020, in Society of Photo-Optical Instrumentation Engineers (SPIE) Conference Series, Vol. 11447, Society of Photo-Optical Instrumentation Engineers (SPIE) Conference Series, 11447A0 (ADS entry)

Ellison, S. L., Mendel, J. T., Patton, D. R., & Scudder, J. M. 2013, MNRAS, 435, 3627 (ADS entry)

Elmegreen, B. G., Klessen, R. S., & Wilson, C. D. 2008, ApJ, 681, 365 (ADS entry)

Emerick, A., Bryan, G. L., & Mac Low, M.-M. 2018a, ApJ, 865, L22 (ADS entry)

—. 2019, MNRAS, 482, 1304 (ADS entry)

Emerick, A., Bryan, G. L., Mac Low, M.-M., Côté, B., Johnston, K. V., & O'Shea, B. W. 2018b, ApJ, 869, 94 (ADS entry)

Enoch, M. L., Evans, Neal J., I., Sargent, A. I., Glenn, J., Rosolowsky, E., & Myers, P. 2008, ApJ, 684, 1240 (ADS entry)

Epinat, B., et al. 2012, A&A, 539, A92 (ADS entry)

Epstein, R. I., Lattimer, J. M., & Schramm, D. N. 1976, Nature, 263, 198 (ADS entry)

Erb, D. K. 2008, ApJ, 674, 151 (ADS entry)

Erb, D. K., Shapley, A. E., Pettini, M., Steidel, C. C., Reddy, N. A., & Adelberger, K. L. 2006, ApJ, 644, 813 (ADS entry)

Erroz-Ferrer, S., et al. 2019, MNRAS, 484, 5009 (ADS entry)

Ezzeddine, R., et al. 2019, ApJ, 876, 97 (ADS entry)

Fabbian, D., Nissen, P. E., Asplund, M., Pettini, M., & Akerman, C. 2009, A&A, 500, 1143 (ADS entry)

Falceta-Gonçalves, D., & Kowal, G. 2015, ApJ, 808, 65 (ADS entry)

Fan, X. 2006, NewAs, 50, 665 (ADS entry)

Fardal, M. A., Katz, N., Weinberg, D. H., & Davé, R. 2007, MNRAS, 379, 985 (ADS entry)

Faucher-Giguère, C.-A. 2018, MNRAS, 473, 3717 (ADS entry)

Faucher-Giguère, C.-A., Kereš, D., & Ma, C.-P. 2011, MNRAS, 417, 2982 (ADS entry)

Faucher-Giguère, C.-A., Quataert, E., & Hopkins, P. F. 2013, MNRAS, 433, 1970 (ADS entry)

Favre, C., et al. 2018, ApJ, 859, 136 (ADS entry)

Federrath, C. 2013a, MNRAS, 436, 1245 (ADS entry)

—. 2013b, MNRAS, 436, 3167 (ADS entry)

—. 2015, MNRAS, 450, 4035 (ADS entry)

—. 2016, Journal of Plasma Physics, 82, 535820601 (ADS entry)

—. 2018, Physics Today, 71, 38 (ADS entry)

Federrath, C. 2020, in IAU Symposium, Vol. 345, IAU Symposium, ed. B. G. Elmegreen, L. V. Tóth, & M. Güdel, 43–50 (ADS entry)

Federrath, C., Banerjee, R., Clark, P. C., & Klessen, R. S. 2010a, ApJ, 713, 269 (ADS entry)

Federrath, C., Banerjee, R., Seifried, D., Clark, P. C., & Klessen, R. S. 2011a, in IAU Symposium, Vol. 270, Computational Star Formation, ed. J. Alves, B. G. Elmegreen, J. M. Girart, & V. Trimble, 425–428 (ADS entry)

Federrath, C., Chabrier, G., Schober, J., Banerjee, R., Klessen, R. S., & Schleicher, D. R. G. 2011b, Phys. Rev. Lett., 107, 114504 (ADS entry)

Federrath, C., & Klessen, R. S. 2012, ApJ, 761, 156 (ADS entry)

—. 2013, ApJ, 763, 51 (ADS entry)

Federrath, C., Krumholz, M., & Hopkins, P. F. 2017a, in Journal of Physics Conference Series, Vol. 837, Journal of Physics Conference Series, 012007 (ADS entry)

Federrath, C., Krumholz, M., & Hopkins, P. F. 2017b, in Journal of Physics Conference Series, Vol. 837, Journal of Physics Conference Series, 012007 (ADS entry)

Federrath, C., Roman-Duval, J., Klessen, R. S., Schmidt, W., & Mac Low, M. M. 2010b, A&A, 512, A81 (ADS entry)

Federrath, C., Schober, J., Bovino, S., & Schleicher, D. R. G. 2014a, ApJ, 797, L19 (ADS entry)

Federrath, C., Schrön, M., Banerjee, R., & Klessen, R. S. 2014b, ApJ, 790, 128 (ADS entry)

Federrath, C., Sur, S., Schleicher, D. R. G., Banerjee, R., & Klessen, R. S. 2011c, ApJ, 731, 62 (ADS entry)

Feldmann, R. 2015, MNRAS, 449, 3274 (ADS entry)

Feltre, A., Charlot, S., & Gutkin, J. 2016, MNRAS, 456, 3354 (ADS entry)

Fernández-Ontiveros, J. A., et al. 2017, PASA, 34, e053 (ADS entry)

Ferreras, I., La Barbera, F., de La Rosa, I. G., Vazdekis, A., de Carvalho, R. R., Falcon-Barroso, J., & Ricciardelli, E. 2013, MNRAS, 429, L15 (ADS entry)

Ferreras, I., Weidner, C., Vazdekis, A., & La Barbera, F. 2015, MNRAS, 448, L82 (ADS entry)

Few, C. G., Courty, S., Gibson, B. K., Michel-Dansac, L., & Calura, F. 2014, MNRAS, 444, 3845 (ADS entry)

Fialkov, A., Barkana, R., & Visbal, E. 2014, Nature, 506, 197 (ADS entry)

Field, G. B., & Carroll, S. M. 2000, Phys. Rev. D, 62, 103008 (ADS entry)

Fields, B. D. 2011, Annual Review of Nuclear and Particle Science, 61, 47 (ADS entry)

Finlator, K., & Davé, R. 2008, MNRAS, 385, 2181 (ADS entry)

Fisher, R. T. 2004, ApJ, 600, 769 (ADS entry)

Flock, M., Dzyurkevich, N., Klahr, H., Turner, N. J., & Henning, T. 2011, ApJ, 735, 122 (ADS entry)

Florido, E., Pérez, I., Zurita, A., & Sánchez-Blázquez, P. 2012, A&A, 543, A150 (ADS entry)

Flower, D. R., & Harris, G. J. 2007, MNRAS, 377, 705 (ADS entry)

Flower, D. R., & Pineau des Forêts, G. 2000, MNRAS, 316, 901 (ADS entry)

Fontanot, F., De Lucia, G., Xie, L., Hirschmann, M., Bruzual, G., & Charlot, S. 2018, MNRAS, 475, 2467 (ADS entry)

Forbes, J., Krumholz, M., & Burkert, A. 2012, ApJ, 754, 48 (ADS entry)

Forbes, J. C., Krumholz, M. R., Burkert, A., & Dekel, A. 2014a, MNRAS, 438, 1552 (ADS entry)

—. 2014b, MNRAS, 443, 168 (ADS entry)

Forbes, J. C., Krumholz, M. R., & Speagle, J. S. 2019, MNRAS, 487, 3581 (ADS entry)

Forgan, D., & Rice, K. 2011, MNRAS, 417, 1928 (ADS entry)

Forrey, R. C. 2013, ApJ, 773, L25 (ADS entry)

Förster Schreiber, N. M., & Wuyts, S. 2020, ARA&A, 58, 661 (ADS entry)

Förster Schreiber, N. M., et al. 2009, ApJ, 706, 1364 (ADS entry)

—. 2018, ApJS, 238, 21 (ADS entry)

—. 2019, ApJ, 875, 21 (ADS entry)

Foster, C., et al. 2020, arXiv e-prints, arXiv:2011.13567 (ADS entry)

—. 2021, PASA, 38, e031 (ADS entry)

Fragile, P. C., Anninos, P., Gustafson, K., & Murray, S. D. 2005, ApJ, 619, 327 (ADS entry)

Frank, A., et al. 2014, in Protostars and Planets VI, ed. H. Beuther, R. S. Klessen, C. P. Dullemond, & T. Henning, 451 (ADS entry)

Frebel, A., Chiti, A., Ji, A. P., Jacobson, H. R., & Placco, V. M. 2015, ApJ, 810, L27 (ADS entry)

Frebel, A., Collet, R., Eriksson, K., Christlieb, N., & Aoki, W. 2008, ApJ, 684, 588 (ADS entry)

Frebel, A., & Norris, J. E. 2015, ARA&A, 53, 631 (ADS entry)

Freeman, K., & Bland-Hawthorn, J. 2002, ARA&A, 40, 487 (ADS entry)

Fryxell, B., et al. 2000, ApJS, 131, 273 (ADS entry)

Fu, J., Hou, J. L., Yin, J., & Chang, R. X. 2009, ApJ, 696, 668 (ADS entry)

Fu, J., et al. 2013, MNRAS, 434, 1531 (ADS entry)

Fumagalli, M., da Silva, R. L., & Krumholz, M. R. 2011a, ApJ, 741, L26 (ADS entry)

—. 2011b, ApJ, 741, L26 (ADS entry)

Furlanetto, S. R. 2021, MNRAS, 500, 3394 (ADS entry)

Gabici, S., Aharonian, F. A., & Blasi, P. 2007, Ap&SS, 309, 365 (ADS entry)

Gaches, B. A. L., & Offner, S. S. R. 2018, ApJ, 861, 87 (ADS entry)

Gaches, B. A. L., Offner, S. S. R., & Bisbas, T. G. 2019, ApJ, 878, 105 (ADS entry)

Galli, D., & Palla, F. 1998, A&A, 335, 403 (ADS entry)

—. 2002, Planet. Space Sci., 50, 1197 (ADS entry)

—. 2013, ARA&A, 51, 163 (ADS entry)

Galliano, F., Galametz, M., & Jones, A. P. 2018, ARA&A, 56, 673 (ADS entry)

Gao, L., Yoshida, N., Abel, T., Frenk, C. S., Jenkins, A., & Springel, V. 2007, MNRAS, 378, 449 (ADS entry)

García-Marín, M., Colina, L., & Arribas, S. 2009, A&A, 505, 1017 (ADS entry)

Garnett, D. R. 2002, ApJ, 581, 1019 (ADS entry)

Ge, Q., & Wise, J. H. 2017, MNRAS, 472, 2773 (ADS entry)

Geach, J. E., Smail, I., Moran, S. M., MacArthur, L. A., Lagos, C. d. P., & Edge, A. C. 2011, ApJ, 730, L19 (ADS entry)

Geha, M., et al. 2013, ApJ, 771, 29 (ADS entry)

Geha, M. C. 2014, in American Astronomical Society Meeting Abstracts, Vol. 223, American Astronomical Society Meeting Abstracts #223, 314.03 (ADS entry)

Gelli, V., Salvadori, S., Ferrara, A., Pallottini, A., & Carniani, S. 2021, ApJ, 913, L25 (ADS entry)

Genel, S. 2016, ApJ, 822, 107 (ADS entry)

Genel, S., et al. 2012, ApJ, 745, 11 (ADS entry)

Gennaro, M., et al. 2018, ApJ, 855, 20 (ADS entry)

Gentry, E. S., Krumholz, M. R., Madau, P., & Lupi, A. 2019, MNRAS, 483, 3647 (ADS entry)

Genzel, R., et al. 2010, MNRAS, 407, 2091 (ADS entry)

—. 2011, ApJ, 733, 101 (ADS entry)

—. 2015, ApJ, 800, 20 (ADS entry)

—. 2017, Nature, 543, 397 (ADS entry)

—. 2020, ApJ, 902, 98 (ADS entry)

Gerola, H., & Seiden, P. E. 1978, ApJ, 223, 129 (ADS entry)

Gerrard, I. A., Federrath, C., & Kuruwita, R. 2019, MNRAS, 485, 5532 (ADS entry)

Gibson, B. K., Pilkington, K., Brook, C. B., Stinson, G. S., & Bailin, J. 2013, A&A, 554, A47 (ADS entry)

Gibson, C. H. 1996, in APS Division of Fluid Dynamics Meeting Abstracts, AD.09 (ADS entry)

Gieser, C., et al. 2021, A&A, 648, A66 (ADS entry)

Gil-Pons, P., Doherty, C. L., Gutiérrez, J., Campbell, S. W., Siess, L., & Lattanzio, J. C. 2021, A&A, 645, A10 (ADS entry)

Gillman, S., et al. 2021, MNRAS, 500, 4229 (ADS entry)

Giovannini, M. 2004, International Journal of Modern Physics D, 13, 391 (ADS entry)

Girard, M., et al. 2021, ApJ, 909, 12 (ADS entry)

Girichidis, P., Federrath, C., Banerjee, R., & Klessen, R. S. 2012, MNRAS, 420, 613 (ADS entry)

Glassgold, A. E., Galli, D., & Padovani, M. 2012, ApJ, 756, 157 (ADS entry)

Glover, S. 2005, Space Sci. Rev., 117, 445 (ADS entry)

Glover, S. C. O., & Abel, T. 2008, MNRAS, 388, 1627 (ADS entry)

Glover, S. C. O., & Clark, P. C. 2012a, MNRAS, 421, 9 (ADS entry)

Glover, S. C. O., & Clark, P. C. 2012b, MNRAS, 426, 377 (ADS entry)

—. 2016, MNRAS, 456, 3596 (ADS entry)

Glover, S. C. O., Federrath, C., Mac Low, M.-M., & Klessen, R. S. 2010, Highlights of Astronomy, 15, 405 (ADS entry)

Glover, S. C. O., & Jappsen, A.-K. 2007, ApJ, 666, 1 (ADS entry)

Glover, S. C. O., & Savin, D. W. 2009, MNRAS, 393, 911 (ADS entry)

Glowacki, M., Elson, E., & Davé, R. 2020, arXiv e-prints, arXiv:2011.08866 (ADS entry)

Goddard, D., et al. 2017, MNRAS, 466, 4731 (ADS entry)

Goldbaum, N. J., Krumholz, M. R., & Forbes, J. C. 2015, ApJ, 814, 131 (ADS entry)

—. 2016, ApJ, 827, 28 (ADS entry)

Goldsmith, P. F. 2001, ApJ, 557, 736 (ADS entry)

Gong, H., & Ostriker, E. C. 2013, ApJS, 204, 8 (ADS entry)

González Delgado, R. M., et al. 2015, A&A, 581, A103 (ADS entry)

Goodman, A. A., Benson, P. J., Fuller, G. A., & Myers, P. C. 1993, ApJ, 406, 528 (ADS entry)

Goodman, F. O. 1974, Progress In Surface Science, 5, 261 (ADS entry)

Goodman, F. O., & Wachman, H. Y. 1967, J. Chem. Phys., 46, 2376 (ADS entry)

Goodwin, S. P., Whitworth, A. P., & Ward-Thompson, D. 2004, A&A, 414, 633 (ADS entry)

Grand, R. J. J., et al. 2019, MNRAS, 490, 4786 (ADS entry)

Grassi, T., Bovino, S., Schleicher, D., & Gianturco, F. A. 2013, MNRAS, 431, 1659 (ADS entry)

Grassi, T., Bovino, S., Schleicher, D. R. G., Prieto, J., Seifried, D., Simoncini, E., & Gianturco, F. A. 2014, MNRAS, 439, 2386 (ADS entry)

Grasso, D., & Rubinstein, H. R. 2001, Phys. Rep., 348, 163 (ADS entry)

Gray, W. J., McKee, C. F., & Klein, R. I. 2018, MNRAS, 473, 2124 (ADS entry)

Greenstein, G. 1969, Nature, 223, 938 (ADS entry)

Greif, T. H. 2014, MNRAS, 444, 1566 (ADS entry)

Greif, T. H., Bromm, V., Clark, P. C., Glover, S. C. O., Smith, R. J., Klessen, R. S., Yoshida, N., & Springel, V. 2012, MNRAS, 424, 399 (ADS entry)

Greif, T. H., Glover, S. C. O., Bromm, V., & Klessen, R. S. 2009, MNRAS, 392, 1381 (ADS entry)

Greif, T. H., Johnson, J. L., Bromm, V., & Klessen, R. S. 2007, ApJ, 670, 1 (ADS entry)

Greif, T. H., Johnson, J. L., Klessen, R. S., & Bromm, V. 2008, MNRAS, 387, 1021 (ADS entry)

Greif, T. H., Springel, V., White, S. D. M., Glover, S. C. O., Clark, P. C., Smith, R. J., Klessen, R. S., & Bromm, V. 2011a, ApJ, 737, 75 (ADS entry)

—. 2011b, ApJ, 737, 75 (ADS entry)

Greif, T. H., White, S. D. M., Klessen, R. S., & Springel, V. 2011c, ApJ, 736, 147 (ADS entry)

Grete, P., Latif, M. A., Schleicher, D. R. G., & Schmidt, W. 2019, MNRAS, 487, 4525 (ADS entry)

Griffen, B. F., Dooley, G. A., Ji, A. P., O'Shea, B. W., Gómez, F. A., & Frebel, A. 2018, MNRAS, 474, 443 (ADS entry)

Grogin, N. A., et al. 2011, ApJS, 197, 35 (ADS entry)

Grossi, M., García-Benito, R., Cortesi, A., Gonçalves, D. R., Gonçalves, T. S., Lopes, P. A. A., Menéndez-Delmestre, K., & Telles, E. 2020, MNRAS, 498, 1939 (ADS entry)

Gunawardhana, M. L. P., et al. 2011, MNRAS, 415, 1647 (ADS entry)

Guszejnov, D., Hopkins, P. F., & Graus, A. S. 2019, MNRAS, 485, 4852 (ADS entry)

Guszejnov, D., Hopkins, P. F., Grudić, M. Y., Krumholz, M. R., & Federrath, C. 2018, MNRAS, 480, 182 (ADS entry)

Guszejnov, D., Hopkins, P. F., & Krumholz, M. R. 2017a, MNRAS, 468, 4093 (ADS entry)

Guszejnov, D., Hopkins, P. F., & Ma, X. 2017b, MNRAS, 472, 2107 (ADS entry)

Guszejnov, D., Krumholz, M. R., & Hopkins, P. F. 2016a, MNRAS, 458, 673 (ADS entry)

—. 2016b, MNRAS, 458, 673 (ADS entry)

Gutcke, T. A., & Springel, V. 2019, MNRAS, 482, 118 (ADS entry)

Guth, A. H. 1981, Phys. Rev. D, 23, 347 (ADS entry)

Guth, A. H., & Pi, S. Y. 1982, Phys. Rev. Lett., 49, 1110 (ADS entry)

Haemmerlé, L., Mayer, L., Klessen, R. S., Hosokawa, T., Madau, P., & Bromm, V. 2020, Space Sci. Rev., 216, 48 (ADS entry)

Hammond, A. M., Robishaw, T., & Gaensler, B. M. 2012, arXiv e-prints, arXiv:1209.1438 (ADS entry)

Han, J. L. 2017, ARA&A, 55, 111 (ADS entry)

Hani, M. H., Sparre, M., Ellison, S. L., Torrey, P., & Vogelsberger, M. 2018, MNRAS, 475, 1160 (ADS entry)

Hansen, C. J., et al. 2011, A&A, 527, A65 (ADS entry)

Harris, C. R., et al. 2020, Nature, 585, 357 (ADS entry)

Harris, W. E. 1996, AJ, 112, 1487 (ADS entry)

Harrison, E. R. 1970, MNRAS, 147, 279 (ADS entry)

Hartmann, L. 2008, Accretion Processes in Star Formation (Cambridge University Press) (ADS entry)

Hartmann, L., Calvet, N., Gullbring, E., & D'Alessio, P. 1998, ApJ, 495, 385 (ADS entry)

Hartwig, T., Clark, P. C., Glover, S. C. O., Klessen, R. S., & Sasaki, M. 2015, ApJ, 799, 114 (ADS entry)

Hartwig, T., Ishigaki, M. N., Klessen, R. S., & Yoshida, N. 2019, MNRAS, 482, 1204 (ADS entry)

Hartwig, T., et al. 2018, MNRAS, 478, 1795 (ADS entry)

Haugen, N. E., Brandenburg, A., & Dobler, W. 2004, Phys. Rev. E, 70, 016308 (ADS entry)

Hawley, J. F., Gammie, C. F., & Balbus, S. A. 1996, ApJ, 464, 690 (ADS entry)

Hayes, C. R., et al. 2018, ApJ, 852, 49 (ADS entry)

Heckman, T. M., Armus, L., & Miley, G. K. 1990, ApJS, 74, 833 (ADS entry)

Heger, A., & Woosley, S. E. 2010, ApJ, 724, 341 (ADS entry)

Hemler, Z. S., et al. 2021, MNRAS, 506, 3024 (ADS entry)

Hennebelle, P., Commerçon, B., Lee, Y.-N., & Chabrier, G. 2020a, ApJ, 904, 194 (ADS entry)

—. 2020b, ApJ, 904, 194 (ADS entry)

Hennebelle, P., & Inutsuka, S.-i. 2019, Frontiers in Astronomy and Space Sciences, 6, 5 (ADS entry)

Hennebelle, P., Lee, Y.-N., & Chabrier, G. 2019, ApJ, 883, 140 (ADS entry)

Hennebelle, P., & Teyssier, R. 2008, A&A, 477, 25 (ADS entry)

Henriques, B. M. B., White, S. D. M., Thomas, P. A., Angulo, R. E., Guo, Q., Lemson, G., & Springel, V. 2013, MNRAS, 431, 3373 (ADS entry)

Henriques, B. M. B., Yates, R. M., Fu, J., Guo, Q., Kauffmann, G., Srisawat, C., Thomas, P. A., & White, S. D. M. 2020, MNRAS, 491, 5795 (ADS entry)

Herenz, E. C., et al. 2017, A&A, 606, A12 (ADS entry)

Herwig, F. 2005, ARA&A, 43, 435 (ADS entry)

Higuchi, K., Machida, M. N., & Susa, H. 2018, MNRAS, 475, 3331 (ADS entry)

—. 2019, MNRAS, 486, 3741 (ADS entry)

Hillebrandt, W., & Niemeyer, J. C. 2000, ARA&A, 38, 191 (ADS entry)

Hindmarsh, A. C. 1980, SIGNUM Newsl., 15, 10 (Link)

Hirano, S., & Bromm, V. 2017, MNRAS, 470, 898 (ADS entry)

Hirano, S., Hosokawa, T., Yoshida, N., Omukai, K., & Yorke, H. W. 2015, MNRAS, 448, 568 (ADS entry)

Hirano, S., Hosokawa, T., Yoshida, N., Umeda, H., Omukai, K., Chiaki, G., & Yorke, H. W. 2014, ApJ, 781, 60 (ADS entry)

Hirano, S., & Yoshida, N. 2013, ApJ, 763, 52 (ADS entry)

Hirano, S., Yoshida, N., Sakurai, Y., & Fujii, M. S. 2018, ApJ, 855, 17 (ADS entry)

Hirschmann, M., De Lucia, G., & Fontanot, F. 2016, MNRAS, 461, 1760 (ADS entry)

Ho, I. T., Kudritzki, R.-P., Kewley, L. J., Zahid, H. J., Dopita, M. A., Bresolin, F., & Rupke, D. S. N. 2015, MNRAS, 448, 2030 (ADS entry)

Ho, I. T., et al. 2016, Ap&SS, 361, 280 (ADS entry)

—. 2017, ApJ, 846, 39 (ADS entry)

—. 2019, ApJ, 885, L31 (ADS entry)

Hollenbach, D., & McKee, C. F. 1979, ApJS, 41, 555 (ADS entry)

Hopkins, A. M. 2018, PASA, 35, e039 (ADS entry)

Hopkins, P. F. 2013, MNRAS, 430, 1653 (ADS entry)

Hopkins, P. F., & Christiansen, J. L. 2013, ApJ, 776, 48 (ADS entry)

Hopkins, P. F., Kereš, D., Oñorbe, J., Faucher-Giguère, C.-A., Quataert, E., Murray, N., & Bullock, J. S. 2014, MNRAS, 445, 581 (ADS entry)

Hopkins, P. F., et al. 2018, MNRAS, 480, 800 (ADS entry)

Hosking, J. G., & Whitworth, A. P. 2004, MNRAS, 347, 1001 (ADS entry)

Hosokawa, T., Hirano, S., Kuiper, R., Yorke, H. W., Omukai, K., & Yoshida, N. 2016, ApJ, 824, 119 (ADS entry)

Hosokawa, T., Offner, S. S. R., & Krumholz, M. R. 2011a, ApJ, 738, 140 (ADS entry)

Hosokawa, T., Omukai, K., Yoshida, N., & Yorke, H. W. 2011b, Science, 334, 1250 (ADS entry)

Hosokawa, T., Yoshida, N., Omukai, K., & Yorke, H. W. 2012, ApJ, 760, L37 (ADS entry)

Hoversten, E. A., & Glazebrook, K. 2008, ApJ, 675, 163 (ADS entry)

Howes, L. M., et al. 2015, Nature, 527, 484 (ADS entry)

Hoyng, P. 1988, ApJ, 332, 857 (ADS entry)

Hu, C.-Y., Sternberg, A., & van Dishoeck, E. F. 2021, arXiv e-prints, arXiv:2103.03889 (ADS entry)

Huang, M.-L., & Kauffmann, G. 2014, MNRAS, 443, 1329 (ADS entry)

Hubber, D. A., Falle, S. A. E. G., & Goodwin, S. P. 2013a, MNRAS, 432, 711 (ADS entry)

Hubber, D. A., Walch, S., & Whitworth, A. P. 2013b, MNRAS, 430, 3261 (ADS entry)

Hubber, D. A., & Whitworth, A. P. 2005, A&A, 437, 113 (ADS entry)

Hughes, T. M., Cortese, L., Boselli, A., Gavazzi, G., & Davies, J. I. 2013, A&A, 550, A115 (ADS entry)

Hummel, J. A., Stacy, A., & Bromm, V. 2016, MNRAS, 460, 2432 (ADS entry)

Hummel, J. A., Stacy, A., Jeon, M., Oliveri, A., & Bromm, V. 2015, MNRAS, 453, 4136 (ADS entry)

Hunt, L., Dayal, P., Magrini, L., & Ferrara, A. 2016, MNRAS, 463, 2020 (ADS entry)

Hunt, L. K., et al. 2015, A&A, 583, A114 (ADS entry)

Hunter, J. D. 2007, Computing in Science & Engineering, 9, 90

Hutschenreuter, S., Dorn, S., Jasche, J., Vazza, F., Paoletti, D., Lavaux, G., & Enßlin, T. A. 2018, Classical and Quantum Gravity, 35, 154001 (ADS entry)

Iapichino, L., Adamek, J., Schmidt, W., & Niemeyer, J. C. 2008, MNRAS, 388, 1079 (ADS entry)

Iapichino, L., Federrath, C., & Klessen, R. S. 2017, MNRAS, 469, 3641 (ADS entry)

Ichiki, K., Takahashi, K., Ohno, H., Hanayama, H., & Sugiyama, N. 2006, Science, 311, 827 (ADS entry)

Inayoshi, K., Kashiyama, K., Visbal, E., & Haiman, Z. 2016, MNRAS, 461, 2722 (ADS entry)

Indriolo, N., & McCall, B. J. 2012, ApJ, 745, 91 (ADS entry)

Inoue, S., Dekel, A., Mandelker, N., Ceverino, D., Bournaud, F., & Primack, J. 2016, MNRAS, 456, 2052 (ADS entry)

Isbell, J. W., Xue, R., & Fu, H. 2018, ApJ, 869, L37 (ADS entry)

Ishigaki, M. N., Tominaga, N., Kobayashi, C., & Nomoto, K. 2014, ApJ, 792, L32 (ADS entry)

—. 2018, ApJ, 857, 46 (ADS entry)

Ivezić, Ž., et al. 2019, ApJ, 873, 111 (ADS entry)

Izotov, Y. I., Thuan, T. X., Guseva, N. G., & Liss, S. E. 2018, MNRAS, 473, 1956 (ADS entry)

Izzard, R. G., Glebbeek, E., Stancliffe, R. J., & Pols, O. R. 2009, A&A, 508, 1359 (ADS entry)

Jameson, K. E., et al. 2016, ApJ, 825, 12 (ADS entry)

—. 2018, ApJ, 853, 111 (ADS entry)

Janev, R. K., Langer, W. D., & Evans, K. 1987, Elementary processes in Hydrogen-Helium plasmas - Cross sections and reaction rate coefficients (Springer) (ADS entry)

Jappsen, A.-K., Klessen, R. S., Glover, S. C. O., & Mac Low, M.-M. 2009, ApJ, 696, 1065 (ADS entry)

Jappsen, A.-K., Klessen, R. S., Larson, R. B., Li, Y., & Mac Low, M.-M. 2005, A&A, 435, 611 (ADS entry)

Jaura, O., Glover, S. C. O., Wollenberg, K. M. J., Klessen, R. S., Geen, S., & Haemmerlé, L. 2022, MNRAS(ADS entry)

Jeans, J. H. 1902, Philosophical Transactions of the Royal Society of London Series A, 199, 1 (ADS entry)

Jeřábková, T., Hasani Zonoozi, A., Kroupa, P., Beccari, G., Yan, Z., Vazdekis, A., & Zhang, Z. Y. 2018, A&A, 620, A39 (ADS entry)

Jiang, C. Y., Jing, Y. P., Faltenbacher, A., Lin, W. P., & Li, C. 2008, ApJ, 675, 1095 (ADS entry)

Joggerst, C. C., Woosley, S. E., & Heger, A. 2009, ApJ, 693, 1780 (ADS entry)

Johnson, H. L., et al. 2018, MNRAS, 474, 5076 (ADS entry)

Johnson, J. L., & Bromm, V. 2006, MNRAS, 366, 247 (ADS entry)

Jones, M. O., & Bate, M. R. 2018, MNRAS, 480, 2562 (ADS entry)

Jones, T., Ellis, R. S., Richard, J., & Jullo, E. 2013, ApJ, 765, 48 (ADS entry)

Jones, T., Sanders, R., Roberts-Borsani, G., Ellis, R. S., Laporte, N., Treu, T., & Harikane, Y. 2020, arXiv e-prints, arXiv:2006.02447 (ADS entry)

Jones, T., et al. 2015, AJ, 149, 107 (ADS entry)

Jones, T. W., Porter, D. H., Ryu, D., & Cho, J. 2011, Mem. Soc. Astron. Italiana, 82, 588 (ADS entry)

Joos, M., Hennebelle, P., Ciardi, A., & Fromang, S. 2013, A&A, 554, A17 (ADS entry)

Jørgensen, J. K., Schöier, F. L., & van Dishoeck, E. F. 2002, A&A, 389, 908 (ADS entry)

Kaasinen, M., Bian, F., Groves, B., Kewley, L. J., & Gupta, A. 2017, MNRAS, 465, 3220 (ADS entry)

Kacprzak, G. G., et al. 2014, ApJ, 792, L12 (ADS entry)

Kahniashvili, T., Brandenburg, A., & Tevzadze, A. e. G. 2016, Phys. Scr, 91, 104008 (ADS entry)

Kahniashvili, T., Maravin, Y., Lavrelashvili, G., & Kosowsky, A. 2014, Phys. Rev. D, 90, 083004 (ADS entry)

Kahniashvili, T., Maravin, Y., Natarajan, A., Battaglia, N., & Tevzadze, A. G. 2013a, ApJ, 770, 47 (ADS entry)

Kahniashvili, T., Tevzadze, A. G., Brand enburg, A., & Neronov, A. 2013b, Phys. Rev. D, 87, 083007 (ADS entry)

Kalari, V. M., Carraro, G., Evans, C. J., & Rubio, M. 2018, ApJ, 857, 132 (ADS entry)

Kalberla, P. M. W., & Kerp, J. 2009, ARA&A, 47, 27 (ADS entry)

Kang, X., Chang, R., Kudritzki, R.-P., Gong, X., & Zhang, F. 2021, arXiv e-prints, arXiv:2101.06833 (ADS entry)

Karlsson, T., Bromm, V., & Bland-Hawthorn, J. 2013, Reviews of Modern Physics, 85, 809 (ADS entry)

Kashino, D., et al. 2017, ApJ, 835, 88 (ADS entry)

Kassin, S. A., Brooks, A., Governato, F., Weiner, B. J., & Gardner, J. P. 2014, ApJ, 790, 89 (ADS entry)

Kassin, S. A., et al. 2012, ApJ, 758, 106 (ADS entry)

Kauffmann, G., Heckman, T. M., De Lucia, G., Brinchmann, J., Charlot, S., Tremonti, C., White, S. D. M., & Brinkmann, J. 2006, MNRAS, 367, 1394 (ADS entry)

Kauffmann, G., Li, C., Zhang, W., & Weinmann, S. 2013a, MNRAS, 430, 1447 (ADS entry)

Kauffmann, J., Pillai, T., & Goldsmith, P. F. 2013b, ApJ, 779, 185 (ADS entry)

Kawasaki, M., & Kusakabe, M. 2012, Phys. Rev. D, 86, 063003 (ADS entry)

Kazantsev, A. P. 1968, Soviet Journal of Experimental and Theoretical Physics, 26, 1031 (ADS entry)

Kazantsev, A. P., Ruzmaikin, A. A., & Sokolov, D. D. 1985, Zhurnal Eksperimentalnoi i Teoreticheskoi Fiziki, 88, 487 (ADS entry)

Keller, S. C., et al. 2014, Nature, 506, 463 (ADS entry)

Kennicutt, R. C., & Evans, N. J. 2012, ARA&A, 50, 531 (ADS entry)

Kereš, D., Katz, N., Weinberg, D. H., & Davé, R. 2005, MNRAS, 363, 2 (ADS entry)

Kewley, L. J., & Dopita, M. A. 2002, ApJS, 142, 35 (ADS entry)

Kewley, L. J., Dopita, M. A., Leitherer, C., Davé, R., Yuan, T., Allen, M., Groves, B., & Sutherland, R. 2013a, ApJ, 774, 100 (ADS entry)

Kewley, L. J., & Ellison, S. L. 2008, ApJ, 681, 1183 (ADS entry)

Kewley, L. J., Geller, M. J., & Barton, E. J. 2006a, AJ, 131, 2004 (ADS entry)

Kewley, L. J., Groves, B., Kauffmann, G., & Heckman, T. 2006b, MNRAS, 372, 961 (ADS entry)

Kewley, L. J., Heisler, C. A., Dopita, M. A., & Lumsden, S. 2001, ApJS, 132, 37 (ADS entry)

Kewley, L. J., Maier, C., Yabe, K., Ohta, K., Akiyama, M., Dopita, M. A., & Yuan, T. 2013b, ApJ, 774, L10 (ADS entry)

Kewley, L. J., Nicholls, D. C., Sutherland, R., Rigby, J. R., Acharya, A., Dopita, M. A., & Bayliss, M. B. 2019a, ApJ, 880, 16 (ADS entry)

Kewley, L. J., Nicholls, D. C., & Sutherland, R. S. 2019b, ARA&A, 57, 511 (ADS entry)

Kibble, T. W. B. 1980, Phys. Rep., 67, 183 (ADS entry)

Kilerci Eser, E., Goto, T., & Doi, Y. 2014, ApJ, 797, 54 (ADS entry)

Kim, C.-G., & Ostriker, E. C. 2015, ApJ, 815, 67 (ADS entry)

Kim, C.-G., et al. 2020, ApJ, 900, 61 (ADS entry)

Kim, E.-J., Olinto, A. V., & Rosner, R. 1996, ApJ, 468, 28 (ADS entry)

Kitsionas, S., et al. 2009, A&A, 508, 541 (ADS entry)

Klessen, R. 2019, Formation of the first stars, ed. M. Latif & D. Schleicher (World Scientific Publishing), 67–97 (ADS entry)

Klessen, R. S. 2018, arXiv e-prints, arXiv:1807.06248 (ADS entry)

Kobayashi, C., Umeda, H., Nomoto, K., Tominaga, N., & Ohkubo, T. 2006, ApJ, 653, 1145 (ADS entry)

Kobulnicky, H. A., & Kewley, L. J. 2004, ApJ, 617, 240 (ADS entry)

Koekemoer, A. M., et al. 2011, ApJS, 197, 36 (ADS entry)

Kolmogorov, A. N. 1941, Akademiia Nauk SSSR Doklady, 32, 16 (ADS entry)

Komiya, Y., Suda, T., Minaguchi, H., Shigeyama, T., Aoki, W., & Fujimoto, M. Y. 2007, ApJ, 658, 367 (ADS entry)

Köppen, J., Weidner, C., & Kroupa, P. 2007, MNRAS, 375, 673 (ADS entry)

Kouwenhoven, M. B. N., Goodwin, S. P., Parker, R. J., Davies, M. B., Malmberg, D., & Kroupa, P. 2010, MNRAS, 404, 1835 (ADS entry)

Kowal, G., Lazarian, A., Vishniac, E. T., & Otmianowska-Mazur, K. 2009, ApJ, 700, 63 (ADS entry)

Kratter, K. M., & Matzner, C. D. 2006, MNRAS, 373, 1563 (ADS entry)

Kraus, A. L., Ireland, M. J., Martinache, F., & Hillenbrand, L. A. 2011, ApJ, 731, 8 (ADS entry)

Krause, F., & Raedler, K. H. 1980, Mean-field magnetohydrodynamics and dynamo theory (Elsevier) (ADS entry)

Krause, F., & Roberts, P. H. 1976, Journal of Mathematical Physics, 17, 1808 (ADS entry)

Kreckel, H., Bruhns, H., Čížek, M., Glover, S. C. O., Miller, K. A., Urbain, X., & Savin, D. W. 2010, Science, 329, 69 (ADS entry)

Kreckel, K., et al. 2019, ApJ, 887, 80 (ADS entry)

—. 2020, MNRAS, 499, 193 (ADS entry)

Kreyszig, E., Kreyszig, H., & Norminton, E. J. 2011, Advanced Engineering Mathematics, tenth edn. (Hoboken, NJ, USA: Wiley)

Kritsuk, A. G., Norman, M. L., & Padoan, P. 2006, ApJ, 638, L25 (ADS entry)

Kritsuk, A. G., Norman, M. L., Padoan, P., & Wagner, R. 2007, ApJ, 665, 416 (ADS entry)

Kritsuk, A. G., Ustyugov, S. D., Norman, M. L., & Padoan, P. 2009, in Journal of Physics Conference Series, Vol. 180, Journal of Physics Conference Series, 012020 (ADS entry)

Kritsuk, A. G., et al. 2011, ApJ, 737, 13 (ADS entry)

Kronberg, P. P., Bernet, M. L., Miniati, F., Lilly, S. J., Short, M. B., & Higdon, D. M. 2008, ApJ, 676, 70 (ADS entry)

Kroupa, P. 2001, MNRAS, 322, 231 (ADS entry)

—. 2002, Science, 295, 82 (ADS entry)

Kroupa, P., Subr, L., Jeřábková, T., & Wang, L. 2020, MNRAS, 498, 5652 (ADS entry)

Kroupa, P., Weidner, C., Pflamm-Altenburg, J., Thies, I., Dabringhausen, J., Marks, M., & Maschberger, T. 2013, in Planets, Stars and Stellar Systems. Volume 5: Galactic Structure and Stellar Populations, ed. T. D. Oswalt & G. Gilmore, Vol. 5 (Springer), 115 (ADS entry)

Kruijssen, J. M. D., & Longmore, S. N. 2014, MNRAS, 439, 3239 (ADS entry)

Krumholz, M., & Burkert, A. 2010, ApJ, 724, 895 (ADS entry)

Krumholz, M. R. 2011a, ApJ, 743, 110 (ADS entry)

—. 2011b, ApJ, 743, 110 (ADS entry)

—. 2012, ApJ, 759, 9 (ADS entry)

—. 2013, MNRAS, 436, 2747 (ADS entry)

—. 2014a, MNRAS, 437, 1662 (ADS entry)

—. 2014b, Phys. Rep., 539, 49 (ADS entry)

Krumholz, M. R., Burkhart, B., Forbes, J. C., & Crocker, R. M. 2018, MNRAS, 477, 2716 (ADS entry)

Krumholz, M. R., Cunningham, A. J., Klein, R. I., & McKee, C. F. 2010, ApJ, 713, 1120 (ADS entry)

Krumholz, M. R., & Dekel, A. 2012, ApJ, 753, 16 (ADS entry)

Krumholz, M. R., Dekel, A., & McKee, C. F. 2012a, ApJ, 745, 69 (ADS entry)

Krumholz, M. R., & Federrath, C. 2019, Frontiers in Astronomy and Space Sciences, 6, 7 (ADS entry)

Krumholz, M. R., & Gnedin, N. Y. 2011, ApJ, 729, 36 (ADS entry)

Krumholz, M. R., Klein, R. I., & McKee, C. F. 2011, ApJ, 740, 74 (ADS entry)

—. 2012b, ApJ, 754, 71 (ADS entry)

—. 2012c, ApJ, 754, 71 (ADS entry)

Krumholz, M. R., Klein, R. I., McKee, C. F., Offner, S. S. R., & Cunningham, A. J. 2009a, Science, 323, 754 (ADS entry)

Krumholz, M. R., & McKee, C. F. 2005, ApJ, 630, 250 (ADS entry)

Krumholz, M. R., McKee, C. F., & Bland-Hawthorn, J. 2019, ARA&A, 57, 227 (ADS entry)

Krumholz, M. R., McKee, C. F., & Klein, R. I. 2004, ApJ, 611, 399 (ADS entry)

Krumholz, M. R., McKee, C. F., & Tumlinson, J. 2008, ApJ, 689, 865 (ADS entry)

—. 2009b, ApJ, 693, 216 (ADS entry)

Krumholz, M. R., Myers, A. T., Klein, R. I., & McKee, C. F. 2016a, MNRAS, 460, 3272 (ADS entry)

—. 2016b, MNRAS, 460, 3272 (ADS entry)

Krumholz, M. R., & Ting, Y.-S. 2018, MNRAS, 475, 2236 (ADS entry)

Kubryk, M., Prantzos, N., & Athanassoula, E. 2013, MNRAS, 436, 1479 (ADS entry)

Kudritzki, R.-P., Ho, I. T., Schruba, A., Burkert, A., Zahid, H. J., Bresolin, F., & Dima, G. I. 2015, MNRAS, 450, 342 (ADS entry)

Kudritzki, R.-P., Teklu, A. F., Schulze, F., Remus, R.-S., Dolag, K., Burkert, A., & Zahid, H. J. 2021, ApJ, 910, 87 (ADS entry)

Kulsrud, R. M. 1999, ARA&A, 37, 37 (ADS entry)

Kulsrud, R. M., & Anderson, S. W. 1992, ApJ, 396, 606 (ADS entry)

Kuruwita, R. L., & Federrath, C. 2019, MNRAS, 486, 3647 (ADS entry)

La Barbera, F., Ferreras, I., Vazdekis, A., de la Rosa, I. G., de Carvalho, R. R., Trevisan, M., Falcón-Barroso, J., & Ricciardelli, E. 2013, MNRAS, 433, 3017 (ADS entry)

La Barbera, F., Vazdekis, A., Ferreras, I., Pasquali, A., Cappellari, M., Martín-Navarro, I., Schönebeck, F., & Falcón-Barroso, J. 2016, MNRAS, 457, 1468 (ADS entry)

Lang, P., et al. 2017, ApJ, 840, 92 (ADS entry)

Langer, W. D. 2009, in Astronomical Society of the Pacific Conference Series, Vol. 417, Submillimeter Astrophysics and Technology: a Symposium Honoring Thomas G. Phillips, ed. D. C. Lis, J. E. Vaillancourt, P. F. Goldsmith, T. A. Bell, N. Z. Scoville, & J. Zmuidzinas, 71 (ADS entry)

Larkin, J., et al. 2006, in Society of Photo-Optical Instrumentation Engineers (SPIE) Conference Series, Vol. 6269, Proc. SPIE, 62691A (ADS entry)

Larson, R. B. 1969, MNRAS, 145, 271 (ADS entry)

—. 1972, Nature Physical Science, 236, 7 (ADS entry)

—. 1974, MNRAS, 169, 229 (ADS entry)

Latif, M. A., & Schleicher, D. R. G. 2015, MNRAS, 449, 77 (ADS entry)

—. 2016a, A&A, 585, A151 (ADS entry)

—. 2016b, A&A, 585, A151 (ADS entry)

Latif, M. A., Schleicher, D. R. G., & Schmidt, W. 2014, MNRAS, 440, 1551 (ADS entry)

Latif, M. A., Schleicher, D. R. G., Schmidt, W., & Niemeyer, J. 2013a, ApJ, 772, L3 (ADS entry)

—. 2013b, MNRAS, 432, 668 (ADS entry)

Launay, J. M., & Roueff, E. 1977, A&A, 56, 289 (ADS entry)

Law, D. R., et al. 2016, AJ, 152, 83 (ADS entry)

Lawrence, A., Rowan-Robinson, M., Leech, K., Jones, D. H. P., & Wall, J. V. 1989, MNRAS, 240, 329 (ADS entry)

Lee, J. C., et al. 2009, ApJ, 706, 599 (ADS entry)

Lee, J.-E., Lee, S., Dunham, M. M., Tatematsu, K., Choi, M., Bergin, E. A., & Evans, N. J. 2017, Nature Astronomy, 1, 0172 (ADS entry)

Lee, Y.-N., & Hennebelle, P. 2018, A&A, 611, A89 (ADS entry)

—. 2019, A&A, 622, A125 (ADS entry)

Lee, Y.-N., Offner, S. S. R., Hennebelle, P., André, P., Zinnecker, H., Ballesteros-Paredes, J., Inutsuka, S.-i., & Kruijssen, J. M. D. 2020, Space Sci. Rev., 216, 70 (ADS entry)

Lee, Y. S., Suda, T., Beers, T. C., & Stancliffe, R. J. 2014, ApJ, 788, 131 (ADS entry)

Leech, K. J., Rowan-Robinson, M., Lawrence, A., & Hughes, J. D. 1994, MNRAS, 267, 253 (ADS entry)

Leethochawalit, N., Jones, T. A., Ellis, R. S., Stark, D. P., Richard, J., Zitrin, A., & Auger, M. 2016, ApJ, 820, 84 (ADS entry)

Leigh, N., Umbreit, S., Sills, A., Knigge, C., de Marchi, G., Glebbeek, E., & Sarajedini, A. 2012, MNRAS, 422, 1592 (ADS entry)

Leitner, S. N., & Kravtsov, A. V. 2011, ApJ, 734, 48 (ADS entry)

Leja, J., Speagle, J. S., Johnson, B. D., Conroy, C., van Dokkum, P., & Franx, M. 2020, ApJ, 893, 111 (ADS entry)

Leja, J., van Dokkum, P., & Franx, M. 2013, ApJ, 766, 33 (ADS entry)

Leja, J., et al. 2019, ApJ, 877, 140 (ADS entry)

Lemaster, M. N., & Stone, J. M. 2009, ApJ, 691, 1092 (ADS entry)

Lepp, S., & Shull, J. M. 1984, ApJ, 280, 465 (ADS entry)

Lepp, S., Stancil, P. C., & Dalgarno, A. 2002, Journal of Physics B: Atomic, Molecular and Optical Physics, 35, R57 (Link)

Leroy, A. K., Walter, F., Brinks, E., Bigiel, F., de Blok, W. J. G., Madore, B., & Thornley, M. D. 2008, AJ, 136, 2782 (ADS entry)

Leroy, A. K., et al. 2013, AJ, 146, 19 (ADS entry)

Lesaffre, P., & Balbus, S. A. 2007, MNRAS, 381, 319 (ADS entry)

Lewis, B. T., & Bate, M. R. 2018, MNRAS, 477, 4241 (ADS entry)

Li, P. S., Norman, M. L., Mac Low, M.-M., & Heitsch, F. 2004, ApJ, 605, 800 (ADS entry)

Li, Q., Narayanan, D., & Davé, R. 2019, MNRAS, 490, 1425 (ADS entry)

Li, S., Frank, A., & Blackman, E. G. 2013a, ApJ, 774, 133 (ADS entry)

Li, Y., Bresolin, F., & Kennicutt, Robert C., J. 2013b, ApJ, 766, 17 (ADS entry)

Li, Z., Krumholz, M. R., Wisnioski, E., Mendel, J. T., Kewley, L. J., Sánchez, S. F., & Galbany, L. 2021, MNRAS, 504, 5496 (ADS entry)

Li, Z. Y., Banerjee, R., Pudritz, R. E., Jørgensen, J. K., Shang, H., Krasnopolsky, R., & Maury, A. 2014, in Protostars and Planets VI, ed. H. Beuther, R. S. Klessen, C. P. Dullemond, & T. Henning, 173 (ADS entry)

Li, Z.-Y., Krasnopolsky, R., & Shang, H. 2013c, ApJ, 774, 82 (ADS entry)

Lian, J., Thomas, D., Li, C., Zheng, Z., Maraston, C., Bizyaev, D., Lane, R. R., & Yan, R. 2019, MNRAS, 489, 1436 (ADS entry)

Lian, J., Thomas, D., Maraston, C., Goddard, D., Comparat, J., Gonzalez-Perez, V., & Ventura, P. 2018a, MNRAS, 474, 1143 (ADS entry)

Lian, J., et al. 2018b, MNRAS, 476, 3883 (ADS entry)

Liang, F.-H., Li, C., Li, N., Zhou, S., Yan, R., Mo, H., & Zhang, W. 2021, arXiv e-prints, arXiv:2101.03217 (ADS entry)

Liao, W.-T., Turk, M., & Schive, H.-Y. 2019, arXiv e-prints, arXiv:1911.07898 (ADS entry)

Lilly, S. J., Carollo, C. M., Pipino, A., Renzini, A., & Peng, Y. 2013, ApJ, 772, 119 (ADS entry)

Lipovka, A., Núñez-López, R., & Avila-Reese, V. 2005, MNRAS, 361, 850 (ADS entry)

Lique, F., Kłos, J., Alexander, M. H., Le Picard, S. D., & Dagdigian, P. J. 2018, MNRAS, 474, 2313 (ADS entry)

Lique, F., Werfelli, G., Halvick, P., Stoecklin, T., Faure, A., Wiesenfeld, L., & Dagdigian, P. J. 2013, J. Chem. Phys., 138, 204314 (ADS entry)

Liu, B., & Bromm, V. 2018, MNRAS, 476, 1826 (ADS entry)

—. 2020a, MNRAS, 495, 2475 (ADS entry)

—. 2020b, MNRAS, 497, 2839 (ADS entry)

Liu, B., Meynet, G., & Bromm, V. 2021, MNRAS, 501, 643 (ADS entry)

Longmore, S. N., et al. 2014, in Protostars and Planets VI, ed. H. Beuther, R. S. Klessen, C. P. Dullemond, & T. Henning, 291 (ADS entry)

Lopez, L. A., Mathur, S., Nguyen, D. D., Thompson, T. A., & Olivier, G. M. 2020, ApJ, 904, 152 (ADS entry)

López-Barquero, V., Farber, R., Xu, S., Desiati, P., & Lazarian, A. 2016, ApJ, 830, 19 (ADS entry)

Lotz, J. M., Jonsson, P., Cox, T. J., Croton, D., Primack, J. R., Somerville, R. S., & Stewart, K. 2011, ApJ, 742, 103 (ADS entry)

Low, C., & Lynden-Bell, D. 1976, MNRAS, 176, 367 (ADS entry)

Lu, Y., Blanc, G. A., & Benson, A. 2015, ApJ, 808, 129 (ADS entry)

Luck, R. E., Andrievsky, S. M., Kovtyukh, V. V., Gieren, W., & Graczyk, D. 2011, AJ, 142, 51 (ADS entry)

Ma, X., Hopkins, P. F., Faucher-Giguère, C.-A., Zolman, N., Muratov, A. L., Kereš, D., & Quataert, E. 2016, MNRAS, 456, 2140 (ADS entry)

Ma, X., Hopkins, P. F., Feldmann, R., Torrey, P., Faucher-Giguère, C.-A., & Kereš, D. 2017, MNRAS, 466, 4780 (ADS entry)

Mac Low, M.-M., & Ferrara, A. 1999, ApJ, 513, 142 (ADS entry)

Mac Low, M.-M., Klessen, R. S., Burkert, A., & Smith, M. D. 1998, Phys. Rev. Lett., 80, 2754 (ADS entry)

Macciò, A. V., Dutton, A. A., van den Bosch, F. C., Moore, B., Potter, D., & Stadel, J. 2007, MNRAS, 378, 55 (ADS entry)

Machida, M. N., & Doi, K. 2013, MNRAS, 435, 3283 (ADS entry)

Machida, M. N., Matsumoto, T., Hanawa, T., & Tomisaka, K. 2005, MNRAS, 362, 382 (ADS entry)

Machida, M. N., Matsumoto, T., & Inutsuka, S.-i. 2008a, ApJ, 685, 690 (ADS entry)

Machida, M. N., & Nakamura, T. 2015, MNRAS, 448, 1405 (ADS entry)

Machida, M. N., Omukai, K., Matsumoto, T., & Inutsuka, S.-i. 2006, ApJ, 647, L1 (ADS entry)

—. 2008b, ApJ, 677, 813 (ADS entry)

Machida, M. N., Omukai, K., Matsumoto, T., & Inutsuka, S.-I. 2009, MNRAS, 399, 1255 (ADS entry)

Maciel, W. J., & Costa, R. D. D. 2013, Rev. Mex. Astron. Astrofis., 49, 333 (ADS entry)

Maciel, W. J., Costa, R. D. D., & Idiart, T. E. P. 2010, A&A, 512, A19 (ADS entry)

Maciel, W. J., Costa, R. D. D., & Uchida, M. M. M. 2003, A&A, 397, 667 (ADS entry)

Madden, S. C., et al. 2020, A&A, 643, A141 (ADS entry)

Magg, M., et al. 2020, MNRAS, 498, 3703 (ADS entry)

Magrini, L., Coccato, L., Stanghellini, L., Casasola, V., & Galli, D. 2016, A&A, 588, A91 (ADS entry)

Maio, U., Khochfar, S., Johnson, J. L., & Ciardi, B. 2011a, MNRAS, 414, 1145 (ADS entry)

Maio, U., Koopmans, L. V. E., & Ciardi, B. 2011b, MNRAS, 412, L40 (ADS entry)

Maiolino, R., & Mannucci, F. 2019, A&A Rev., 27, 3 (ADS entry)

Maiolino, R., et al. 2008, A&A, 488, 463 (ADS entry)

Maki, H., & Susa, H. 2004, ApJ, 609, 467 (ADS entry)

—. 2007, PASJ, 59, 787 (ADS entry)

Malapaka, S. K., & Müller, W.-C. 2013, ApJ, 778, 21 (ADS entry)

Man, A. W. S., Toft, S., Zirm, A. W., Wuyts, S., & van der Wel, A. 2012, ApJ, 744, 85 (ADS entry)

Mannucci, F., Cresci, G., Maiolino, R., Marconi, A., & Gnerucci, A. 2010, MNRAS, 408, 2115 (ADS entry)

Marchand, P., Tomida, K., Tanaka, K. E. I., Commerçon, B., & Chabrier, G. 2020, ApJ, 900, 180 (ADS entry)

Marchesini, D., van Dokkum, P. G., Förster Schreiber, N. M., Franx, M., Labbé, I., & Wuyts, S. 2009, ApJ, 701, 1765 (ADS entry)

Marconi, G., Matteucci, F., & Tosi, M. 1994, MNRAS, 270, 35 (ADS entry)

Marks, M., Kroupa, P., Dabringhausen, J., & Pawlowski, M. S. 2012, MNRAS, 422, 2246 (ADS entry)

Martell, S. L., et al. 2017, MNRAS, 465, 3203 (ADS entry)

Martin, C. L., & Kennicutt, Robert C., J. 2001, ApJ, 555, 301 (ADS entry)

Martin, C. L., Kobulnicky, H. A., & Heckman, T. M. 2002, ApJ, 574, 663 (ADS entry)

Martín, S., Muller, S., Henkel, C., Meier, D. S., Aladro, R., Sakamoto, K., & van der Werf, P. P. 2019, A&A, 624, A125 (ADS entry)

Martín-Navarro, I., La Barbera, F., Vazdekis, A., Falcón-Barroso, J., & Ferreras, I. 2015a, MNRAS, 447, 1033 (ADS entry)

Martín-Navarro, I., et al. 2015b, ApJ, 806, L31 (ADS entry)

—. 2021, arXiv e-prints, arXiv:2107.14243 (ADS entry)

Martinez-Medina, L. A., Pichardo, B., & Peimbert, A. 2020, MNRAS, 496, 1845 (ADS entry)

Masson, J., Chabrier, G., Hennebelle, P., Vaytet, N., & Commerçon, B. 2016, A&A, 587, A32 (ADS entry)

Mast, D., et al. 2014, A&A, 561, A129 (ADS entry)

Masters, D., Faisst, A., & Capak, P. 2016, ApJ, 828, 18 (ADS entry)

Masunaga, H., & Inutsuka, S.-i. 2000, ApJ, 531, 350 (ADS entry)

Masunaga, H., Miyama, S. M., & Inutsuka, S.-i. 1998, ApJ, 495, 346 (ADS entry)

Matese, J. J., & O'Connell, R. F. 1970, ApJ, 160, 451 (ADS entry)

Mathew, S. S., & Federrath, C. 2020a, MNRAS, 496, 5201 (ADS entry)

—. 2020b, MNRAS, 496, 5201 (ADS entry)

—. 2021, MNRAS(ADS entry)

Matthews, M. J., Petitpas, G., & Aceves, S. M. 2011, Applied Physics Letters, 99, 081906 (Link)

Mattsson, L. 2010, A&A, 515, A68 (ADS entry)

Matzner, C. D., & McKee, C. F. 2000, ApJ, 545, 364 (ADS entry)

Mayor, M. 1976, A&A, 48, 301 (ADS entry)

Mayor, M., & Vigroux, L. 1981, A&A, 98, 1 (ADS entry)

McDermid, R. M., et al. 2014, ApJ, 792, L37 (ADS entry)

—. 2020, arXiv e-prints, arXiv:2009.09242 (ADS entry)

McDowell, J. C. 1986, MNRAS, 223, 763 (ADS entry)

McGaugh, S. S., Schombert, J. M., Bothun, G. D., & de Blok, W. J. G. 2000, ApJ, 533, L99 (ADS entry)

McGregor, P. J., et al. 2003, in Society of Photo-Optical Instrumentation Engineers (SPIE) Conference Series, Vol. 4841, Instrument Design and Performance for Optical/Infrared Ground-based Telescopes, ed. M. Iye & A. F. M. Moorwood, 1581–1591 (ADS entry)

McKee, C. F., & Krumholz, M. R. 2010, ApJ, 709, 308 (ADS entry)

McKee, C. F., & Ostriker, E. C. 2007, ARA&A, 45, 565 (ADS entry)

McKee, C. F., Parravano, A., & Hollenbach, D. J. 2015, ApJ, 814, 13 (ADS entry)

McKee, C. F., Stacy, A., & Li, P. S. 2020, MNRAS, 496, 5528 (ADS entry)

McKee, C. F., & Tan, J. C. 2003, ApJ, 585, 850 (ADS entry)

—. 2008, ApJ, 681, 771 (ADS entry)

McQuinn, K. B. W., van Zee, L., & Skillman, E. D. 2019, ApJ, 886, 74 (ADS entry)

McQuinn, K. B. W., et al. 2015, ApJ, 812, 158 (ADS entry)

Meece, G. R., Smith, B. D., & O'Shea, B. W. 2014, ApJ, 783, 75 (ADS entry)

Meiksin, A., & Whalen, D. J. 2013, MNRAS, 430, 2854 (ADS entry)

Melnick, J., & Mirabel, I. F. 1990, A&A, 231, L19 (ADS entry)

Meneguzzi, M., Frisch, U., & Pouquet, A. 1981, Phys. Rev. Lett., 47, 1060 (ADS entry)

Meru, F., & Bate, M. R. 2011, MNRAS, 411, L1 (ADS entry)

Meurer, G. R., Zheng, Z., & de Blok, W. J. G. 2013, MNRAS, 429, 2537 (ADS entry)

Meurer, G. R., et al. 2009, ApJ, 695, 765 (ADS entry)

Meynet, G., & Maeder, A. 2002, A&A, 381, L25 (ADS entry)

Mielke, S. L., Peterson, K. A., Schwenke, D. W., Garrett, B. C., Truhlar, D. G.,
    Michael, J. V., Su, M.-C., & Sutherland, J. W. 2003, Phys. Rev. Lett., 91, 063201
    (ADS entry)

Minchev, I., Chiappini, C., & Martig, M. 2013, A&A, 558, A9 (ADS entry)

Mingozzi, M., et al. 2020, A&A, 636, A42 (ADS entry)

Mitchell, G. F., & Deveau, T. J. 1983, ApJ, 266, 646 (ADS entry)

Mitchell, P. D., Schaye, J., & Bower, R. G. 2020, MNRAS, 497, 4495 (ADS entry)

Miville-Deschênes, M.-A., Murray, N., & Lee, E. J. 2017, ApJ, 834, 57 (ADS entry)

Mo, H., van den Bosch, F. C., & White, S. 2010, Galaxy Formation and Evolution
    (Cambridge University Press) (ADS entry)

Mo, H. J., & Fukugita, M. 1996, ApJ, 467, L9 (ADS entry)

Mo, H. J., Jing, Y. P., & White, S. D. M. 1996, MNRAS, 282, 1096 (ADS entry)

Mo, H. J., Mao, S., & White, S. D. M. 1998, MNRAS, 295, 319 (ADS entry)

Mo, H. J., & White, S. D. M. 2002, MNRAS, 336, 112 (ADS entry)

Mocz, P., Burkhart, B., Hernquist, L., McKee, C. F., & Springel, V. 2017, ApJ, 838,
    40 (ADS entry)

Moffatt. 1978, Magnetic Field Generation in Electrically Conducting Fluids, Cam-
    bridge Monographs on Mechanics (Cambridge University Press) (Link)

Moiseev, A. V., Tikhonov, A. V., & Klypin, A. 2015, MNRAS, 449, 3568 (ADS en-
    try)

Molina, F. Z., Glover, S. C. O., Federrath, C., & Klessen, R. S. 2012, MNRAS, 423,
    2680 (ADS entry)

Molina, J., Ibar, E., Swinbank, A. M., Sobral, D., Best, P. N., Smail, I., Escala, A.,
    & Cirasuolo, M. 2017, MNRAS, 466, 892 (ADS entry)

Mollá, M., & Díaz, A. I. 2005, MNRAS, 358, 521 (ADS entry)

Mollá, M., Díaz, Á. I., Ascasibar, Y., & Gibson, B. K. 2017, MNRAS, 468, 305 (ADS entry)

Mollá, M., Díaz, Á. I., Cavichia, O., Gibson, B. K., Maciel, W. J., Costa, R. D. D., Ascasibar, Y., & Few, C. G. 2019, MNRAS, 482, 3071 (ADS entry)

Mollá, M., Díaz, Á. I., Gibson, B. K., Cavichia, O., & López-Sánchez, Á.-R. 2016, MNRAS, 462, 1329 (ADS entry)

Monreal-Ibero, A., Arribas, S., & Colina, L. 2006, ApJ, 637, 138 (ADS entry)

Monreal-Ibero, A., Arribas, S., Colina, L., Rodríguez-Zaurín, J., Alonso-Herrero, A., & García-Marín, M. 2010, A&A, 517, A28 (ADS entry)

Monreal-Ibero, A., Colina, L., Arribas, S., & García-Marín, M. 2007, A&A, 472, 421 (ADS entry)

Moran, S. M., et al. 2012, ApJ, 745, 66 (ADS entry)

Moreno, J., et al. 2020, MNRAS, tmp (ADS entry)

Morokuma-Matsui, K., & Baba, J. 2015, MNRAS, 454, 3792 (ADS entry)

Mosquera Cuesta, H. J., & Lambiase, G. 2009, Phys. Rev. D, 80, 023013 (ADS entry)

Moster, B. P., Naab, T., & White, S. D. M. 2013, MNRAS, 428, 3121 (ADS entry)

Moster, B. P., Somerville, R. S., Maulbetsch, C., van den Bosch, F. C., Macciò, A. V., Naab, T., & Oser, L. 2010, ApJ, 710, 903 (ADS entry)

Mott, A., Spitoni, E., & Matteucci, F. 2013, MNRAS, 435, 2918 (ADS entry)

Moustakas, J., Kennicutt, Robert C., J., Tremonti, C. A., Dale, D. A., Smith, J.-D. T., & Calzetti, D. 2010, ApJS, 190, 233 (ADS entry)

Mowla, L., van der Wel, A., van Dokkum, P., & Miller, T. B. 2019, ApJ, 872, L13 (ADS entry)

Mueller, K. E., Shirley, Y. L., Evans, Neal J., I., & Jacobson, H. R. 2002, ApJS, 143, 469 (ADS entry)

Muratov, A. L., Gnedin, O. Y., Gnedin, N. Y., & Zemp, M. 2013, ApJ, 773, 19 (ADS entry)

Muratov, A. L., Kereš, D., Faucher-Giguère, C.-A., Hopkins, P. F., Quataert, E., & Murray, N. 2015, MNRAS, 454, 2691 (ADS entry)

Myers, A. T., Klein, R. I., Krumholz, M. R., & McKee, C. F. 2014a, MNRAS, 439, 3420 (ADS entry)

—. 2014b, MNRAS, 439, 3420 (ADS entry)

Myers, A. T., Krumholz, M. R., Klein, R. I., & McKee, C. F. 2011, ApJ, 735, 49 (ADS entry)

Myers, A. T., McKee, C. F., Cunningham, A. J., Klein, R. I., & Krumholz, M. R. 2013, ApJ, 766, 97 (ADS entry)

Naab, T., & Ostriker, J. P. 2017, ARA&A, 55, 59 (ADS entry)

Nagakura, T., & Omukai, K. 2005, MNRAS, 364, 1378 (ADS entry)

Nagao, T., Maiolino, R., Marconi, A., & Matsuhara, H. 2011, A&A, 526, A149 (ADS entry)

Nakamura, F., & Umemura, M. 2002, ApJ, 569, 549 (ADS entry)

Nakauchi, D., Omukai, K., & Susa, H. 2019, MNRAS, 488, 1846 (ADS entry)

Nanayakkara, T., Esdaile, J., Glazebrook, K., Espejo Salcedo, J. M., Durre, M., & Jacobs, C. 2022, PASA, 39, e002 (ADS entry)

Navarro, J. F., Frenk, C. S., & White, S. D. M. 1997, ApJ, 490, 493 (ADS entry)

Neistein, E., & Dekel, A. 2008, MNRAS, 383, 615 (ADS entry)

Nelson, D., et al. 2019, MNRAS, 490, 3234 (ADS entry)

Nelson, E. J., et al. 2016, ApJ, 828, 27 (ADS entry)

Newman, A. B., Smith, R. J., Conroy, C., Villaume, A., & van Dokkum, P. 2017, ApJ, 845, 157 (ADS entry)

Newman, S. F., et al. 2012, ApJ, 761, 43 (ADS entry)

—. 2014, ApJ, 781, 21 (ADS entry)

Ng, Y., & Vachaspati, T. 2010, Phys. Rev. D, 82, 023008 (ADS entry)

Nolan, C. A., Salmeron, R., Federrath, C., Bicknell, G. V., & Sutherland, R. S. 2017, MNRAS, 471, 1488 (ADS entry)

Nomoto, K., Kobayashi, C., & Tominaga, N. 2013, ARA&A, 51, 457 (ADS entry)

Nomoto, K., & Leung, S.-C. 2018, Space Sci. Rev., 214, 67 (ADS entry)

Nordlander, T., Amarsi, A. M., Lind, K., Asplund, M., Barklem, P. S., Casey, A. R., Collet, R., & Leenaarts, J. 2017, A&A, 597, A6 (ADS entry)

Nordlander, T., et al. 2019, MNRAS, 488, L109 (ADS entry)

Norman, C. A., & Spaans, M. 1997, ApJ, 480, 145 (ADS entry)

Nozawa, T., Kozasa, T., & Nomoto, K. 2012, ApJ, 756, L35 (ADS entry)

Nozawa, T., Kozasa, T., Umeda, H., Maeda, K., & Nomoto, K. 2003, ApJ, 598, 785 (ADS entry)

Oesch, P. A., et al. 2016, ApJ, 819, 129 (ADS entry)

Oey, M. S., & Shields, J. C. 2000, ApJ, 539, 687 (ADS entry)

Offner, S. S. R., Clark, P. C., Hennebelle, P., Bastian, N., Bate, M. R., Hopkins, P. F., Moraux, E., & Whitworth, A. P. 2014, in Protostars and Planets VI, ed. H. Beuther, R. S. Klessen, C. P. Dullemond, & T. Henning, 53 (ADS entry)

Offner, S. S. R., Klein, R. I., McKee, C. F., & Krumholz, M. R. 2009a, ApJ, 703, 131 (ADS entry)

Offner, S. S. R., Klein, R. I., McKee, C. F., & Krumholz, M. R. 2009b, ApJ, 703, 131 (ADS entry)

Offner, S. S. R., Kratter, K. M., Matzner, C. D., Krumholz, M. R., & Klein, R. I. 2010, ApJ, 725, 1485 (ADS entry)

Ogle, P., Boulanger, F., Guillard, P., Evans, D. A., Antonucci, R., Appleton, P. N., Nesvadba, N., & Leipski, C. 2010, ApJ, 724, 1193 (ADS entry)

Oldham, L., & Auger, M. 2018, MNRAS, 474, 4169 (ADS entry)

Oliphant, T. E. 2006, A guide to NumPy, Vol. 1 (Trelgol Publishing USA)

O'Meara, J. M., Tytler, D., Kirkman, D., Suzuki, N., Prochaska, J. X., Lubin, D., & Wolfe, A. M. 2001, ApJ, 552, 718 (ADS entry)

Omukai, K. 2000, ApJ, 534, 809 (ADS entry)

—. 2001, ApJ, 546, 635 (ADS entry)

Omukai, K., Hosokawa, T., & Yoshida, N. 2010, ApJ, 722, 1793 (ADS entry)

Omukai, K., & Nishi, R. 1998, ApJ, 508, 141 (ADS entry)

Omukai, K., Schneider, R., & Haiman, Z. 2008, ApJ, 686, 801 (ADS entry)

Omukai, K., Tsuribe, T., Schneider, R., & Ferrara, A. 2005, ApJ, 626, 627 (ADS entry)

Onodera, M., et al. 2016, ApJ, 822, 42 (ADS entry)

Oppenheimer, B. D., Davé, R., Kereš, D., Fardal, M., Katz, N., Kollmeier, J. A., & Weinberg, D. H. 2010, MNRAS, 406, 2325 (ADS entry)

Origlia, L., Ranalli, P., Comastri, A., & Maiolino, R. 2004, ApJ, 606, 862 (ADS entry)

O'Shea, B. W., Nagamine, K., Springel, V., Hernquist, L., & Norman, M. L. 2005, ApJS, 160, 1 (ADS entry)

O'Shea, B. W., & Norman, M. L. 2007, ApJ, 654, 66 (ADS entry)

Ossenkopf, V., & Henning, T. 1994, A&A, 291, 943 (ADS entry)

Ostriker, E. C., McKee, C. F., & Leroy, A. K. 2010, ApJ, 721, 975 (ADS entry)

Ostriker, E. C., & Shetty, R. 2011, ApJ, 731, 41 (ADS entry)

Pace, Z. J., Tremonti, C., Schaefer, A. L., Stark, D. V., Witherspoon, C. A., Masters, K. L., Drory, N., & Zhang, K. 2020, arXiv e-prints, arXiv:2012.12887 (ADS entry)

Padoan, P., Haugbølle, T., & Nordlund, Å. 2012, ApJ, 759, L27 (ADS entry)

Padoan, P., & Nordlund, Å. 2011, ApJ, 730, 40 (ADS entry)

Padoan, P., Nordlund, A., & Jones, B. J. T. 1997, MNRAS, 288, 145 (ADS entry)

Padovani, M., Ivlev, A. V., Galli, D., & Caselli, P. 2018, A&A, 614, A111 (ADS entry)

Padovani, M., Marcowith, A., Hennebelle, P., & Ferrière, K. 2016, A&A, 590, A8 (ADS entry)

Padovani, M., et al. 2020, Space Sci. Rev., 216, 29 (ADS entry)

Pagel, B. E. J., Edmunds, M. G., Blackwell, D. E., Chun, M. S., & Smith, G. 1979, MNRAS, 189, 95 (ADS entry)

Pagel, B. E. J., & Patchett, B. E. 1975, MNRAS, 172, 13 (ADS entry)

Pandya, V., Mulchaey, J., & Greene, J. E. 2016, ApJ, 819, 162 (ADS entry)

Pandya, V., et al. 2020, ApJ, 905, 4 (ADS entry)

—. 2021, MNRAS, 508, 2979 (ADS entry)

Pantaleone, S., Enrique-Romero, J., Ceccarelli, C., Ferrero, S., Balucani, N., Rimola, A., & Ugliengo, P. 2021, ApJ, 917, 49 (ADS entry)

Papadopoulos, P. P. 2010, ApJ, 720, 226 (ADS entry)

Papadopoulos, P. P., Thi, W.-F., Miniati, F., & Viti, S. 2011, MNRAS, 414, 1705 (ADS entry)

Papovich, C., Finkelstein, S. L., Ferguson, H. C., Lotz, J. M., & Giavalisco, M. 2011, MNRAS, 412, 1123 (ADS entry)

Pariev, V. I., & Colgate, S. A. 2007, ApJ, 658, 114 (ADS entry)

Pariev, V. I., Colgate, S. A., & Finn, J. M. 2007, ApJ, 658, 129 (ADS entry)

Parikh, T., et al. 2018, MNRAS, 477, 3954 (ADS entry)

Pasquini, L., et al. 2002, The Messenger, 110, 1 (ADS entry)

Patankar, S. V. 1980, Numerical heat transfer and fluid flow, Series on Computational Methods in Mechanics and Thermal Science (Hemisphere Publishing Corporation (CRC Press, Taylor & Francis Group)) (Link)

Peacock, M. B., et al. 2017, ApJ, 841, 28 (ADS entry)

Peebles, P. J. E. 1968, ApJ, 153, 1 (ADS entry)

Peeples, M. S., & Shankar, F. 2011, MNRAS, 417, 2962 (ADS entry)

Peng, Y., Maiolino, R., & Cochrane, R. 2015, Nature, 521, 192 (ADS entry)

Peng, Y.-j., & Maiolino, R. 2014, MNRAS, 438, 262 (ADS entry)

Pereira-Santaella, M., Rigopoulou, D., Farrah, D., Lebouteiller, V., & Li, J. 2017, MNRAS, 470, 1218 (ADS entry)

Pérez, F., & Granger, B. E. 2007, Computing in Science and Engineering, 9, 21 (Link)

Perez, J., Michel-Dansac, L., & Tissera, P. B. 2011, MNRAS, 417, 580 (ADS entry)

Pérez-Montero, E., & Amorín, R. 2017, MNRAS, 467, 1287 (ADS entry)

Pérez-Montero, E., & Contini, T. 2009, MNRAS, 398, 949 (ADS entry)

Peters, T., Klessen, R. S., Mac Low, M.-M., & Banerjee, R. 2010, ApJ, 725, 134 (ADS entry)

Petit, A. C., Krumholz, M. R., Goldbaum, N. J., & Forbes, J. C. 2015a, MNRAS, 449, 2588 (ADS entry)

—. 2015b, MNRAS, 449, 2588 (ADS entry)

Pettini, M., & Pagel, B. E. J. 2004, MNRAS, 348, L59 (ADS entry)

Pezzulli, G., & Fraternali, F. 2016, MNRAS, 455, 2308 (ADS entry)

Pflamm-Altenburg, J., Weidner, C., & Kroupa, P. 2009, MNRAS, 395, 394 (ADS entry)

Phillipps, S., & Edmunds, M. G. 1991, MNRAS, 251, 84 (ADS entry)

Phillipps, S., Young, A. J., Drinkwater, M. J., Gregg, M. D., & Karick, A. 2013, MNRAS, 433, 1444 (ADS entry)

Pilkington, K., et al. 2012, A&A, 540, A56 (ADS entry)

Pillai, T., Kauffmann, J., Wyrowski, F., Hatchell, J., Gibb, A. G., & Thompson, M. A. 2011, A&A, 530, A118 (ADS entry)

Pillepich, A., et al. 2018, MNRAS, 473, 4077 (ADS entry)

—. 2019, MNRAS, 490, 3196 (ADS entry)

Pilyugin, L. S. 1993, A&A, 277, 42 (ADS entry)

Pilyugin, L. S., & Grebel, E. K. 2016, MNRAS, 457, 3678 (ADS entry)

Pineda, J. L., et al. 2017, ApJ, 839, 107 (ADS entry)

Piqueras López, J., Colina, L., Arribas, S., & Alonso-Herrero, A. 2013, A&A, 553, A85 (ADS entry)

Pirogov, L. E. 2009, Astronomy Reports, 53, 1127 (ADS entry)

Placco, V. M., et al. 2016, ApJ, 833, 21 (ADS entry)

—. 2021, ApJ, 912, L32 (ADS entry)

Planck Collaboration et al. 2016a, A&A, 594, A13 (ADS entry)

—. 2016b, A&A, 594, A19 (ADS entry)

—. 2018, arXiv e-prints, arXiv:1807.06209 (ADS entry)

Plewa, T. 2001, in IAU Symposium, Vol. 200, The Formation of Binary Stars, ed. H. Zinnecker & R. Mathieu, 563 (ADS entry)

Poetrodjojo, H., D'Agostino, J. J., Groves, B., Kewley, L., Ho, I. T., Rich, J., Madore, B. F., & Seibert, M. 2019, MNRAS, 487, 79 (ADS entry)

Poetrodjojo, H., et al. 2018, MNRAS, 479, 5235 (ADS entry)

—. 2021a, MNRAS, 502, 3357 (ADS entry)

—. 2021b, MNRAS, 502, 3357 (ADS entry)

—. 2021c, MNRAS, 502, 3357 (ADS entry)

Pollack, J. B., Hollenbach, D., Beckwith, S., Simonelli, D. P., Roush, T., & Fong, W. 1994, ApJ, 421, 615 (ADS entry)

Prantzos, N., & Boissier, S. 2000, MNRAS, 313, 338 (ADS entry)

Press, W. H., & Schechter, P. 1974, ApJ, 187, 425 (ADS entry)

Prgomet, M., Rey, M. P., Andersson, E. P., Segovia Otero, A., Agertz, O., Renaud, F., Pontzen, A., & Read, J. I. 2021, arXiv e-prints, arXiv:2107.00663 (ADS entry)

Price, D. J., & Bate, M. R. 2007, MNRAS, 377, 77 (ADS entry)

—. 2009, MNRAS, 398, 33 (ADS entry)

Prieto, J., Jimenez, R., & Martí, J. 2012, MNRAS, 419, 3092 (ADS entry)

Prochaska, J. X., et al. 2017, ApJ, 837, 169 (ADS entry)

Pudritz, R. E. 1981a, MNRAS, 195, 897 (ADS entry)

—. 1981b, MNRAS, 195, 881 (ADS entry)

Pudritz, R. E., & Norman, C. A. 1986, ApJ, 301, 571 (ADS entry)

Queyrel, J., et al. 2012, A&A, 539, A93 (ADS entry)

Radhakrishnan, K., & Hindmarsh, A. C. 1993, US Dept of Energy OSTI Technical Report

Raedler, K. H. 1986, in ESA Special Publication, Vol. 251, Plasma Astrophysics, ed. T. D. Guyenne & L. M. Zeleny, 569 (ADS entry)

Rapp, B. 2017, Microfluidics: Modeling, Mechanics and Mathematics (Elsevier)

Read, J. I., & Erkal, D. 2019, MNRAS, 487, 5799 (ADS entry)

Recchi, S., Matteucci, F., & D'Ercole, A. 2001, MNRAS, 322, 800 (ADS entry)

Recchi, S., Spitoni, E., Matteucci, F., & Lanfranchi, G. A. 2008, A&A, 489, 555 (ADS entry)

Rees, M. J. 1976, MNRAS, 176, 483 (ADS entry)

Regan, J. A., & Downes, T. P. 2018, MNRAS, 475, 4636 (ADS entry)

Reichard, T. A., Heckman, T. M., Rudnick, G., Brinchmann, J., Kauffmann, G., & Wild, V. 2009, ApJ, 691, 1005 (ADS entry)

Rémy-Ruyer, A., et al. 2014, A&A, 563, A31 (ADS entry)

Rennehan, D., Babul, A., Hopkins, P. F., Davé, R., & Moa, B. 2019, MNRAS, 483, 3810 (ADS entry)

Riaz, R., Bovino, S., Vanaverbeke, S., & Schleicher, D. R. G. 2018, MNRAS, 479, 667 (ADS entry)

Rich, J. A., Torrey, P., Kewley, L. J., Dopita, M. A., & Rupke, D. S. N. 2012, ApJ, 753, 5 (ADS entry)

Richardson, M. L. A., Routledge, L., Thatte, N., Tecza, M., Houghton, R. C. W., Pereira-Santaella, M., & Rigopoulou, D. 2020, MNRAS, 498, 1891 (ADS entry)

Rincon, F. 2019, Journal of Plasma Physics, 85, 205850401 (ADS entry)

Ripamonti, E., & Abel, T. 2004, MNRAS, 348, 1019 (ADS entry)

Robles-Valdez, F., Rodríguez-González, A., Hernández-Martínez, L., & Esquivel, A. 2017, ApJ, 835, 136 (ADS entry)

Rocha, M., Peter, A. H. G., Bullock, J. S., Kaplinghat, M., Garrison-Kimmel, S., Oñorbe, J., & Moustakas, L. A. 2013, MNRAS, 430, 81 (ADS entry)

Rodríguez-Fernández, N. J., Martín-Pintado, J., de Vicente, P., Fuente, A., Hüttemeister, S., Wilson, T. L., & Kunze, D. 2000, A&A, 356, 695 (ADS entry)

Rodriguez-Gomez, V., et al. 2015, MNRAS, 449, 49 (ADS entry)

Rogachevskii, I., & Kleeorin, N. 2003, Phys. Rev. E, 68, 036301 (ADS entry)

—. 2004, Phys. Rev. E, 70, 046310 (ADS entry)

Rogachevskii, I., Kleeorin, N., & Brandenburg, A. 2018, Journal of Plasma Physics, 84, 735840502 (ADS entry)

Romeo, A. B., & Falstad, N. 2013, MNRAS, 433, 1389 (ADS entry)

Romeo, A. B., & Mogotsi, K. M. 2017, MNRAS, 469, 286 (ADS entry)

Romeo, A. B., & Wiegert, J. 2011, MNRAS, 416, 1191 (ADS entry)

Rosen, A. L., & Krumholz, M. R. 2020, AJ, 160, 78 (ADS entry)

Rosen, A. L., Krumholz, M. R., McKee, C. F., & Klein, R. I. 2016, MNRAS, 463, 2553 (ADS entry)

Rossi, M., Salvadori, S., & Skúladóttir, Á. 2021, MNRAS, 503, 6026 (ADS entry)

Rubio, M., Elmegreen, B. G., Hunter, D. A., Brinks, E., Cortés, J. R., & Cigan, P. 2015, Nature, 525, 218 (ADS entry)

Ruediger, G., Elstner, D., & Stepinski, T. F. 1995, A&A, 298, 934 (ADS entry)

Rujopakarn, W., Rieke, G. H., Eisenstein, D. J., & Juneau, S. 2011, ApJ, 726, 93 (ADS entry)

Rupke, D. 2018, Galaxies, 6, 138 (ADS entry)

Rupke, D. S. N., Kewley, L. J., & Barnes, J. E. 2010a, ApJ, 710, L156 (ADS entry)

Rupke, D. S. N., Kewley, L. J., & Chien, L. H. 2010b, ApJ, 723, 1255 (ADS entry)

Rupke, D. S. N., Veilleux, S., & Baker, A. J. 2008, ApJ, 674, 172 (ADS entry)

Russell, S. C., & Dopita, M. A. 1992, ApJ, 384, 508 (ADS entry)

Ruzmaikin, A., Sokolov, D., & Shukurov, A. 1988a, Nature, 336, 341 (ADS entry)

Ruzmaikin, A. A., Sokolov, D. D., & Shukurov, A. M. 1988b, Magnetic Fields of Galaxies, Vol. 133 (Springer) (ADS entry)

Ryu, D., Schleicher, D. R. G., Treumann, R. A., Tsagas, C. G., & Widrow, L. M. 2012, Space Sci. Rev., 166, 1 (ADS entry)

Saga, S., Tashiro, H., & Yokoyama, S. 2018, Phys. Rev. D, 98, 083518 (ADS entry)

Saigo, K., Matsumoto, T., & Umemura, M. 2004, ApJ, 615, L65 (ADS entry)

Saintonge, A., et al. 2011, MNRAS, 415, 32 (ADS entry)

—. 2012, ApJ, 758, 73 (ADS entry)

Sakuma, M., & Susa, H. 2009, ApJ, 698, 155 (ADS entry)

Salpeter, E. E. 1955, ApJ, 121, 161 (ADS entry)

Sánchez, S. F. 2020a, ARA&A, 58, 99 (ADS entry)

—. 2020b, ARA&A, 58, 99 (ADS entry)

Sánchez, S. F., Walcher, C. J., Lopez-Cobá, C., Barrera-Ballesteros, J. K., Mejía-Narváez, A., Espinosa-Ponce, C., & Camps-Fariña, A. 2021, Rev. Mex. Astron. Astrofis., 57, 3 (ADS entry)

Sánchez, S. F., et al. 2012, A&A, 538, A8 (ADS entry)

—. 2014, A&A, 563, A49 (ADS entry)

Sánchez Almeida, J., Elmegreen, B. G., Muñoz-Tuñón, C., & Elmegreen, D. M. 2014, A&A Rev., 22, 71 (ADS entry)

Sánchez-Menguiano, L., et al. 2016, A&A, 587, A70 (ADS entry)

—. 2018, A&A, 609, A119 (ADS entry)

Sanders, N. E., Caldwell, N., McDowell, J., & Harding, P. 2012, ApJ, 758, 133 (ADS entry)

Sanders, R. L., et al. 2016, ApJ, 816, 23 (ADS entry)

—. 2021, ApJ, 914, 19 (ADS entry)

Santos-Lima, R., de Gouveia Dal Pino, E. M., & Lazarian, A. 2012, ApJ, 747, 21 (ADS entry)

Sarangi, A., Matsuura, M., & Micelotta, E. R. 2018, Space Sci. Rev., 214, 63 (ADS entry)

Sarzi, M., Spiniello, C., La Barbera, F., Krajnović, D., & van den Bosch, R. 2018, MNRAS, 478, 4084 (ADS entry)

Saslaw, W. C., & Zipoy, D. 1967, Nature, 216, 976 (ADS entry)

Savin, D. W., Krstić, P. S., Haiman, Z., & Stancil, P. C. 2004, ApJ, 606, L167 (ADS entry)

Schaefer, A. L., Tremonti, C., Belfiore, F., Pace, Z., Bershady, M. A., Andrews, B. H., & Drory, N. 2020, ApJ, 890, L3 (ADS entry)

Schaefer, A. L., et al. 2019, ApJ, 884, 156 (ADS entry)

Schauer, A. T. P., Whalen, D. J., Glover, S. C. O., & Klessen, R. S. 2015, MNRAS, 454, 2441 (ADS entry)

Schauer, A. T. P., et al. 2017, MNRAS, 467, 2288 (ADS entry)

Schaye, J., et al. 2015, MNRAS, 446, 521 (ADS entry)

Schekochihin, A. A., Cowley, S. C., Hammett, G. W., Maron, J. L., & McWilliams, J. C. 2002, New Journal of Physics, 4, 84 (ADS entry)

Schekochihin, A. A., Cowley, S. C., Taylor, S. F., Maron, J. L., & McWilliams, J. C. 2004, ApJ, 612, 276 (ADS entry)

Schive, H.-Y., ZuHone, J. A., Goldbaum, N. J., Turk, M. J., Gaspari, M., & Cheng, C.-Y. 2018, MNRAS, 481, 4815 (ADS entry)

Schleicher, D. R. G., Banerjee, R., Sur, S., Arshakian, T. G., Klessen, R. S., Beck, R., & Spaans, M. 2010, A&A, 522, A115 (ADS entry)

Schleicher, D. R. G., Galli, D., Glover, S. C. O., Banerjee, R., Palla, F., Schneider, R., & Klessen, R. S. 2009, ApJ, 703, 1096 (ADS entry)

Schmidt, T. M., Bigiel, F., Klessen, R. S., & de Blok, W. J. G. 2016, MNRAS, 457, 2642 (ADS entry)

Schmidt, W., Federrath, C., Hupp, M., Kern, S., & Niemeyer, J. C. 2009, A&A, 494, 127 (ADS entry)

Schneider, E. E., & Robertson, B. E. 2015, ApJS, 217, 24 (ADS entry)

Schneider, F. R. N., et al. 2018, Science, 359, 69 (ADS entry)

Schneider, N., et al. 2015, A&A, 578, A29 (ADS entry)

Schneider, R., Ferrara, A., Salvaterra, R., Omukai, K., & Bromm, V. 2003, Nature, 422, 869 (ADS entry)

Schneider, R., Hunt, L., & Valiante, R. 2016, MNRAS, 457, 1842 (ADS entry)

Schneider, R., & Omukai, K. 2010, MNRAS, 402, 429 (ADS entry)

Schneider, R., Omukai, K., Bianchi, S., & Valiante, R. 2012, MNRAS, 419, 1566 (ADS entry)

Schneider, R., Omukai, K., Inoue, A. K., & Ferrara, A. 2006a, MNRAS, 369, 1437 (ADS entry)

Schneider, R., Salvaterra, R., Ferrara, A., & Ciardi, B. 2006b, MNRAS, 369, 825 (ADS entry)

Schober, J., Schleicher, D., Federrath, C., Glover, S., Klessen, R. S., & Banerjee, R. 2012a, ApJ, 754, 99 (ADS entry)

Schober, J., Schleicher, D., Federrath, C., Klessen, R., & Banerjee, R. 2012b, Phys. Rev. E, 85, 026303 (ADS entry)

Schober, J., Schleicher, D. R. G., Federrath, C., Bovino, S., & Klessen, R. S. 2015, Phys. Rev. E, 92, 023010 (ADS entry)

Schöier, F. L., van der Tak, F. F. S., van Dishoeck, E. F., & Black, J. H. 2005, A&A, 432, 369 (ADS entry)

Schönrich, R., & McMillan, P. J. 2017, MNRAS, 467, 1154 (ADS entry)

Schrinner, M., Rädler, K.-H., Schmitt, D., Rheinhardt, M., & Christensen, U. R. 2007, Geophysical and Astrophysical Fluid Dynamics, 101, 81 (ADS entry)

Schroder, K., Staemmler, V., Smith, M. D., Flower, D. R., & Jaquet, R. 1991, Journal of Physics B Atomic Molecular Physics, 24, 2487 (ADS entry)

Schroetter, I., Bouché, N., Péroux, C., Murphy, M. T., Contini, T., & Finley, H. 2015, ApJ, 804, 83 (ADS entry)

Schroetter, I., et al. 2019, MNRAS, 490, 4368 (ADS entry)

Schruba, A., Leroy, A. K., Walter, F., Sand strom, K., & Rosolowsky, E. 2010, ApJ, 722, 1699 (ADS entry)

Schruba, A., et al. 2017, ApJ, 835, 278 (ADS entry)

Scoville, N., et al. 2017, ApJ, 837, 150 (ADS entry)

Searle, L. 1971, ApJ, 168, 327 (ADS entry)

Seiden, P. E., Schulman, L. S., & Gerola, H. 1979, ApJ, 232, 702 (ADS entry)

Seifried, D., Banerjee, R., Klessen, R. S., Duffin, D., & Pudritz, R. E. 2011, MNRAS, 417, 1054 (ADS entry)

Seifried, D., Banerjee, R., Pudritz, R. E., & Klessen, R. S. 2013, MNRAS, 432, 3320 (ADS entry)

Semenov, D., Henning, T., Helling, C., Ilgner, M., & Sedlmayr, E. 2003, A&A, 410, 611 (ADS entry)

Sharda, P., Federrath, C., da Cunha, E., Swinbank, A. M., & Dye, S. 2018, MNRAS, 477, 4380 (ADS entry)

Sharda, P., Federrath, C., & Krumholz, M. R. 2020a, MNRAS, 497, 336 (ADS entry)

—. 2020b, MNRAS, 497, 336 (ADS entry)

Sharda, P., Federrath, C., Krumholz, M. R., & Schleicher, D. R. G. 2021a, MNRAS, 503, 2014 (ADS entry)

Sharda, P., & Krumholz, M. R. 2022, MNRAS, 509, 1959 (ADS entry)

Sharda, P., Krumholz, M. R., & Federrath, C. 2019a, MNRAS, 490, 513 (ADS entry)

Sharda, P., Krumholz, M. R., Wisnioski, E., Acharyya, A., Federrath, C., & Forbes, J. C. 2021b, MNRAS, 504, 53 (ADS entry)

—. 2021c, MNRAS, 504, 53 (ADS entry)

Sharda, P., Krumholz, M. R., Wisnioski, E., Forbes, J. C., Federrath, C., & Acharyya, A. 2021d, MNRAS, 502, 5935 (ADS entry)

Sharda, P., Wisnioski, E., Krumholz, M. R., & Federrath, C. 2021e, MNRAS, 506, 1295 (ADS entry)

—. 2021f, MNRAS, 506, 1295 (ADS entry)

Sharda, P., et al. 2019b, MNRAS, 487, 4305 (ADS entry)

Sharples, R. M., et al. 2004, in Society of Photo-Optical Instrumentation Engineers (SPIE) Conference Series, Vol. 5492, Proc. SPIE, ed. A. F. M. Moorwood & M. Iye, 1179–1186 (ADS entry)

Shaver, P. A., McGee, R. X., Newton, L. M., Danks, A. C., & Pottasch, S. R. 1983, MNRAS, 204, 53 (ADS entry)

Sheth, R. K., & Tormen, G. 1999, MNRAS, 308, 119 (ADS entry)

Shi, Y., Wang, J., Zhang, Z.-Y., Gao, Y., Hao, C.-N., Xia, X.-Y., & Gu, Q. 2016, Nature Communications, 7, 13789 (ADS entry)

Shima, K., & Hosokawa, T. 2021, arXiv e-prints, arXiv:2102.06312 (ADS entry)

Shirazi, M., Brinchmann, J., & Rahmati, A. 2014, ApJ, 787, 120 (ADS entry)

Shu, F. H., Adams, F. C., & Lizano, S. 1987, ARA&A, 25, 23 (ADS entry)

Shu, F. H., Li, Z.-Y., & Allen, A. 2004, ApJ, 601, 930 (ADS entry)

Sigl, G., Olinto, A. V., & Jedamzik, K. 1997, Phys. Rev. D, 55, 4582 (ADS entry)

Silk, J. 1983, MNRAS, 205, 705 (ADS entry)

Sillero, E., Tissera, P. B., Lambas, D. G., & Michel-Dansac, L. 2017, MNRAS, 472, 4404 (ADS entry)

Silverman, J. D., et al. 2008, ApJ, 679, 118 (ADS entry)

Simons, R. C., et al. 2017, ApJ, 843, 46 (ADS entry)

—. 2019, ApJ, 874, 59 (ADS entry)

—. 2020, arXiv e-prints, arXiv:2011.03553 (ADS entry)

Singh, N. K., Rogachevskii, I., & Brandenburg, A. 2017, ApJ, 850, L8 (ADS entry)

Skelton, R. E., et al. 2014, ApJS, 214, 24 (ADS entry)

Skibba, R. A., et al. 2012, ApJ, 761, 42 (ADS entry)

Skillman, E. D. 2008, in Low-Metallicity Star Formation: From the First Stars to
    Dwarf Galaxies, ed. L. K. Hunt, S. C. Madden, & R. Schneider, Vol. 255 (IAU),
    285–296 (ADS entry)

Skúladóttir, Á., et al. 2021, ApJ, 915, L30 (ADS entry)

Smith, R. J. 2014, MNRAS, 443, L69 (ADS entry)

—. 2020, ARA&A, 58, 577 (ADS entry)

Smith, R. J., Hosokawa, T., Omukai, K., Glover, S. C. O., & Klessen, R. S. 2012,
    MNRAS, 424, 457 (ADS entry)

Smith, R. J., Lucey, J. R., & Conroy, C. 2015, MNRAS, 449, 3441 (ADS entry)

Snaith, O. N., Park, C., Kim, J., & Rosdahl, J. 2018, MNRAS, 477, 983 (ADS entry)

Sobral, D., Matthee, J., Darvish, B., Schaerer, D., Mobasher, B., Röttgering,
    H. J. A., Santos, S., & Hemmati, S. 2015, ApJ, 808, 139 (ADS entry)

Sobral, D., Smail, I., Best, P. N., Geach, J. E., Matsuda, Y., Stott, J. P., Cirasuolo,
    M., & Kurk, J. 2013a, MNRAS, 428, 1128 (ADS entry)

Sobral, D., et al. 2009, MNRAS, 398, 75 (ADS entry)

—. 2013b, ApJ, 779, 139 (ADS entry)

Soto, K. T., Martin, C. L., Prescott, M. K. M., & Armus, L. 2012, ApJ, 757, 86
    (ADS entry)

Spaans, M., & Norman, C. A. 1997, ApJ, 483, 87 (ADS entry)

Spitoni, E., Calura, F., Matteucci, F., & Recchi, S. 2010, A&A, 514, A73 (ADS en-
    try)

Spitoni, E., Matteucci, F., & Marcon-Uchida, M. M. 2013, A&A, 551, A123 (ADS en-
    try)

Spitoni, E., Recchi, S., & Matteucci, F. 2008, A&A, 484, 743 (ADS entry)

Spitzer, L. 1987, Dynamical evolution of globular clusters (Princeton University Press) (ADS entry)

Springel, V. 2005, MNRAS, 364, 1105 (ADS entry)

Springel, V., & Hernquist, L. 2003, MNRAS, 339, 289 (ADS entry)

Stacy, A., & Bromm, V. 2007, MNRAS, 382, 229 (ADS entry)

—. 2013, MNRAS, 433, 1094 (ADS entry)

—. 2014, ApJ, 785, 73 (ADS entry)

Stacy, A., Bromm, V., & Lee, A. T. 2016, MNRAS, 462, 1307 (ADS entry)

Stacy, A., Bromm, V., & Loeb, A. 2011, MNRAS, 413, 543 (ADS entry)

Stacy, A., Greif, T. H., & Bromm, V. 2010, MNRAS, 403, 45 (ADS entry)

—. 2012, MNRAS, 422, 290 (ADS entry)

Stacy, A., Pawlik, A. H., Bromm, V., & Loeb, A. 2014, MNRAS, 441, 822 (ADS entry)

Staemmler, V., & Flower, D. R. 1991, Journal of Physics B Atomic Molecular Physics, 24, 2343 (ADS entry)

Stahler, S. W., Palla, F., & Salpeter, E. E. 1986, ApJ, 308, 697 (ADS entry)

Stahler, S. W., Shu, F. H., & Taam, R. E. 1980, ApJ, 241, 637 (ADS entry)

Stancil, P. C., Lepp, S., & Dalgarno, A. 1998, ApJ, 509, 1 (ADS entry)

Stanghellini, L., & Haywood, M. 2010, ApJ, 714, 1096 (ADS entry)

Stanghellini, L., Magrini, L., Casasola, V., & Villaver, E. 2014, A&A, 567, A88 (ADS entry)

Stanghellini, L., Magrini, L., Villaver, E., & Galli, D. 2010, A&A, 521, A3 (ADS entry)

Starkenburg, E., et al. 2017, MNRAS, 471, 2587 (ADS entry)

—. 2018, MNRAS, 481, 3838 (ADS entry)

Stasińska, G., Peña, M., Bresolin, F., & Tsamis, Y. G. 2013, A&A, 552, A12 (ADS entry)

Steenbeck, M., Krause, F., & Rädler, K. H. 1966, Zeitschrift Naturforschung Teil A, 21, 369 (ADS entry)

Steigman, G. 2007, Annual Review of Nuclear and Particle Science, 57, 463 (ADS entry)

Stenrup, M., Larson, Å., & Elander, N. 2009, arXiv e-prints (ADS entry)

Stepinski, T. F., & Levy, E. H. 1990, ApJ, 362, 318 (ADS entry)

Sternberg, A., Gurman, A., & Bialy, S. 2021, arXiv e-prints, arXiv:2105.01681 (ADS entry)

Sternberg, A., Le Petit, F., Roueff, E., & Le Bourlot, J. 2014, ApJ, 790, 10 (ADS entry)

Sternberg, A., & Neufeld, D. A. 1999, ApJ, 516, 371 (ADS entry)

Stevenson, D. J. 2003, Earth and Planetary Science Letters, 208, 1 (ADS entry)

Stierwalt, S., et al. 2014, ApJ, 790, 124 (ADS entry)

Stinson, G. S., Bailin, J., Couchman, H., Wadsley, J., Shen, S., Nickerson, S., Brook, C., & Quinn, T. 2010, MNRAS, 408, 812 (ADS entry)

Stone, J. M., Hawley, J. F., Gammie, C. F., & Balbus, S. A. 1996, ApJ, 463, 656 (ADS entry)

Stott, J. P., et al. 2014, MNRAS, 443, 2695 (ADS entry)

—. 2016, MNRAS, 457, 1888 (ADS entry)

Straatman, C. M. S., et al. 2017, ApJ, 839, 57 (ADS entry)

Strickland, D. K., & Heckman, T. M. 2009a, ApJ, 697, 2030 (ADS entry)

—. 2009b, ApJ, 697, 2030 (ADS entry)

Strom, A. L., Steidel, C. C., Rudie, G. C., Trainor, R. F., & Pettini, M. 2018, ApJ, 868, 117 (ADS entry)

Subramanian, K. 1999, Phys. Rev. Lett., 83, 2957 (ADS entry)

—. 2016, Reports on Progress in Physics, 79, 076901 (ADS entry)

Suda, T., Yamada, S., Katsuta, Y., Komiya, Y., Ishizuka, C., Aoki, W., & Fujimoto, M. Y. 2011, MNRAS, 412, 843 (ADS entry)

Suda, T., et al. 2013, MNRAS, 432, L46 (ADS entry)

Sugimura, K., Matsumoto, T., Hosokawa, T., Hirano, S., & Omukai, K. 2020, ApJ, 892, L14 (ADS entry)

Sukhbold, T., Ertl, T., Woosley, S. E., Brown, J. M., & Janka, H. T. 2016, ApJ, 821, 38 (ADS entry)

Sun, J., et al. 2018, ApJ, 860, 172 (ADS entry)

—. 2020, ApJ, 901, L8 (ADS entry)

Sur, S., Brandenburg, A., & Subramanian, K. 2008, MNRAS, 385, L15 (ADS entry)

Sur, S., Federrath, C., Schleicher, D. R. G., Banerjee, R., & Klessen, R. S. 2012, MNRAS, 423, 3148 (ADS entry)

Sur, S., Pan, L., & Scannapieco, E. 2014, ApJ, 784, 94 (ADS entry)

Sur, S., Schleicher, D. R. G., Banerjee, R., Federrath, C., & Klessen, R. S. 2010, ApJ, 721, L134 (ADS entry)

Suresh, J., Bird, S., Vogelsberger, M., Genel, S., Torrey, P., Sijacki, D., Springel, V., & Hernquist, L. 2015, MNRAS, 448, 895 (ADS entry)

Susa, H. 2013, ApJ, 773, 185 (ADS entry)

—. 2019, ApJ, 877, 99 (ADS entry)

Susa, H., Doi, K., & Omukai, K. 2015, ApJ, 801, 13 (ADS entry)

Susa, H., Hasegawa, K., & Tominaga, N. 2014, ApJ, 792, 32 (ADS entry)

Swinbank, A. M., Sobral, D., Smail, I., Geach, J. E., Best, P. N., McCarthy, I. G., Crain, R. A., & Theuns, T. 2012, MNRAS, 426, 935 (ADS entry)

Tacchella, S., Forbes, J. C., & Caplar, N. 2020, MNRAS, 497, 698 (ADS entry)

Tacconi, L. J., Genzel, R., & Sternberg, A. 2020a, arXiv e-prints, arXiv:2003.06245 (ADS entry)

—. 2020b, ARA&A, 58, 157 (ADS entry)

Tacconi, L. J., et al. 2013, ApJ, 768, 74 (ADS entry)

—. 2018, ApJ, 853, 179 (ADS entry)

Tan, J. C., Beltrán, M. T., Caselli, P., Fontani, F., Fuente, A., Krumholz, M. R., McKee, C. F., & Stolte, A. 2014, Protostars and Planets VI, 149 (ADS entry)

Tan, J. C., & Blackman, E. G. 2004, ApJ, 603, 401 (ADS entry)

Tanaka, K. E. I., Tan, J. C., & Zhang, Y. 2017, ApJ, 835, 32 (ADS entry)

Tanaka, T., & Haiman, Z. 2009, ApJ, 696, 1798 (ADS entry)

Tanner, R. 2020, ApJ, 899, 108 (ADS entry)

Tashiro, H., & Sugiyama, N. 2006, MNRAS, 372, 1060 (ADS entry)

Taylor, P., & Kobayashi, C. 2015, MNRAS, 448, 1835 (ADS entry)

Taylor, P., Kobayashi, C., & Kewley, L. J. 2020, MNRAS, 496, 4433 (ADS entry)

Teimoorinia, H., Jalilkhany, M., Scudder, J. M., Jensen, J., & Ellison, S. L. 2021, MNRAS, 503, 1082 (ADS entry)

Teklu, A. F., Remus, R.-S., Dolag, K., Arth, A., Burkert, A., Obreja, A., & Schulze, F. 2018, ApJ, 854, L28 (ADS entry)

Telford, O. G., Werk, J. K., Dalcanton, J. J., & Williams, B. F. 2019, ApJ, 877, 120 (ADS entry)

Thatte, N. A., et al. 2014, in Society of Photo-Optical Instrumentation Engineers (SPIE) Conference Series, Vol. 9147, Ground-based and Airborne Instrumentation for Astronomy V, ed. S. K. Ramsay, I. S. McLean, & H. Takami, 914725 (ADS entry)

Thielemann, F. K., Eichler, M., Panov, I. V., & Wehmeyer, B. 2017, Annual Review of Nuclear and Particle Science, 67, 253 (ADS entry)

Thies, I., Kroupa, P., Goodwin, S. P., Stamatellos, D., & Whitworth, A. P. 2010, ApJ, 717, 577 (ADS entry)

Thies, I., Pflamm-Altenburg, J., Kroupa, P., & Marks, M. 2015, ApJ, 800, 72 (ADS entry)

Thomas, L. B. 1967, in Rarefied Gas Dynamics, Volume 1, Vol. 1, 155 (ADS entry)

Thorne, J. E., et al. 2021, MNRAS, 505, 540 (ADS entry)

Thorp, M. D., Ellison, S. L., Simard, L., Sánchez, S. F., & Antonio, B. 2019, MNRAS, 482, L55 (ADS entry)

Tiley, A. L., et al. 2016, MNRAS, 460, 103 (ADS entry)

—. 2019a, MNRAS, 482, 2166 (ADS entry)

—. 2019b, MNRAS, 485, 934 (ADS entry)

Tinsley, B. M. 1972, A&A, 20, 383 (ADS entry)

—. 1973, ApJ, 186, 35 (ADS entry)

—. 1980, Fund. Cosmic Phys., 5, 287 (ADS entry)

Tissera, P. B., Pedrosa, S. E., Sillero, E., & Vilchez, J. M. 2016, MNRAS, 456, 2982 (ADS entry)

Tissera, P. B., Rosas-Guevara, Y., Bower, R. G., Crain, R. A., del P Lagos, C., Schaller, M., Schaye, J., & Theuns, T. 2019, MNRAS, 482, 2208 (ADS entry)

Tobias, S. M., & Cattaneo, F. 2013, Nature, 497, 463 (ADS entry)

Tobin, J. J., et al. 2016, ApJ, 818, 73 (ADS entry)

Todini, P., & Ferrara, A. 2001, MNRAS, 325, 726 (ADS entry)

Tokovinin, A., & Moe, M. 2020, MNRAS, 491, 5158 (ADS entry)

Tollet, É., Cattaneo, A., Macciò, A. V., Dutton, A. A., & Kang, X. 2019, MNRAS, 485, 2511 (ADS entry)

Tomida, K., Okuzumi, S., & Machida, M. N. 2015, ApJ, 801, 117 (ADS entry)

Tomida, K., Tomisaka, K., Matsumoto, T., Hori, Y., Okuzumi, S., Machida, M. N., & Saigo, K. 2013, ApJ, 763, 6 (ADS entry)

Toomre, A. 1964, ApJ, 139, 1217 (ADS entry)

Torres-Flores, S., Scarano, S., Mendes de Oliveira, C., de Mello, D. F., Amram, P., & Plana, H. 2014, MNRAS, 438, 1894 (ADS entry)

Torrey, P., Cox, T. J., Kewley, L., & Hernquist, L. 2012, ApJ, 746, 108 (ADS entry)

Torrey, P., Vogelsberger, M., Genel, S., Sijacki, D., Springel, V., & Hernquist, L. 2014, MNRAS, 438, 1985 (ADS entry)

Torrey, P., et al. 2019, MNRAS, 484, 5587 (ADS entry)

Tremonti, C. A., et al. 2004, ApJ, 613, 898 (ADS entry)

Treu, T., Auger, M. W., Koopmans, L. V. E., Gavazzi, R., Marshall, P. J., & Bolton, A. S. 2010, ApJ, 709, 1195 (ADS entry)

Tricco, T. S., Price, D. J., & Laibe, G. 2017, MNRAS, 471, L52 (ADS entry)

Troncoso, P., et al. 2014, A&A, 563, A58 (ADS entry)

Truelove, J. K., Klein, R. I., McKee, C. F., Holliman, II, J. H., Howell, L. H., & Greenough, J. A. 1997, ApJ, 489, L179 (ADS entry)

Trujillo-Gomez, S., Klypin, A., Primack, J., & Romanowsky, A. J. 2011, ApJ, 742, 16 (ADS entry)

Tseliakhovich, D., & Hirata, C. 2010, Phys. Rev. D, 82, 083520 (ADS entry)

Tsukamoto, Y., Iwasaki, K., Okuzumi, S., Machida, M. N., & Inutsuka, S. 2015a, ApJ, 810, L26 (ADS entry)

—. 2015b, MNRAS, 452, 278 (ADS entry)

Tsukamoto, Y., Okuzumi, S., Iwasaki, K., Machida, M. N., & Inutsuka, S.-i. 2017, PASJ, 69, 95 (ADS entry)

Tully, R. B., & Fisher, J. R. 1977, A&A, 500, 105 (ADS entry)

Tumlinson, J. 2006, ApJ, 641, 1 (ADS entry)

—. 2007, ApJ, 665, 1361 (ADS entry)

Tumlinson, J., Peeples, M. S., & Werk, J. K. 2017, ARA&A, 55, 389 (ADS entry)

Tumlinson, J., Venkatesan, A., & Shull, J. M. 2004, ApJ, 612, 602 (ADS entry)

Turk, M. J., Abel, T., & O'Shea, B. 2009, Science, 325, 601 (ADS entry)

Turk, M. J., Oishi, J. S., Abel, T., & Bryan, G. L. 2012, ApJ, 745, 154 (ADS entry)

Turk, M. J., Smith, B. D., Oishi, J. S., Skory, S., Skillman, S. W., Abel, T., & Norman, M. L. 2011, ApJS, 192, 9 (ADS entry)

Turner, J. L., Beck, S. C., & Ho, P. T. P. 2000, ApJ, 532, L109 (ADS entry)

Turner, M. S., & Widrow, L. M. 1988, Phys. Rev. D, 37, 2743 (ADS entry)

Tytler, D., Fan, X.-M., & Burles, S. 1996, Nature, 381, 207 (ADS entry)

Übler, H., et al. 2017, ApJ, 842, 121 (ADS entry)

—. 2019, ApJ, 880, 48 (ADS entry)

Urban, A., Martel, H., & Evans, Neal J., I. 2010, ApJ, 710, 1343 (ADS entry)

Urrutia, T., et al. 2019, A&A, 624, A141 (ADS entry)

Vachaspati, T. 1991, Physics Letters B, 265, 258 (ADS entry)

Vale Asari, N., Couto, G. S., Cid Fernandes, R., Stasińska, G., de Amorim, A. L., Ruschel-Dutra, D., Werle, A., & Florido, T. Z. 2019, MNRAS, 489, 4721 (ADS entry)

Van Borm, C., Bovino, S., Latif, M. A., Schleicher, D. R. G., Spaans, M., & Grassi, T. 2014, A&A, 572, A22 (ADS entry)

van der Marel, R. P. 2006, in The Local Group as an Astrophysical Laboratory, ed. M. Livio & T. M. Brown, Vol. 17 (Cambridge University Press), 47–71 (ADS entry)

van der Tak, F. F. S., Lique, F., Faure, A., Black, J. H., & van Dishoeck, E. F. 2020, Atoms, 8, 15 (ADS entry)

van der Tak, F. F. S., van Dishoeck, E. F., Evans, Neal J., I., & Blake, G. A. 2000, ApJ, 537, 283 (ADS entry)

van der Wel, A., et al. 2012, ApJS, 203, 24 (ADS entry)

—. 2014, ApJ, 788, 28 (ADS entry)

van Dokkum, P. G., & Conroy, C. 2010, Nature, 468, 940 (ADS entry)

van Dokkum, P. G., et al. 2008, ApJ, 677, L5 (ADS entry)

—. 2010, ApJ, 709, 1018 (ADS entry)

Van Rossum, G., & Drake, F. L. 2009, Python 3 Reference Manual (Scotts Valley, CA: CreateSpace)

van Winckel, H. 2003, ARA&A, 41, 391 (ADS entry)

Varidel, M. R., et al. 2020, MNRAS, 495, 2265 (ADS entry)

Vaytet, N., Commerçon, B., Masson, J., González, M., & Chabrier, G. 2018, A&A, 615, A5 (ADS entry)

Vaytet, N., Tomida, K., & Chabrier, G. 2014, A&A, 563, A85 (ADS entry)

Vazza, F., Brüggen, M., Gheller, C., & Wang, P. 2014, MNRAS, 445, 3706 (ADS entry)

Vazza, F., Brunetti, G., Kritsuk, A., Wagner, R., Gheller, C., & Norman, M. 2009, A&A, 504, 33 (ADS entry)

Veilleux, S., Cecil, G., & Bland-Hawthorn, J. 2005, ARA&A, 43, 769 (ADS entry)

Veilleux, S., Kim, D. C., & Sanders, D. B. 1999, ApJ, 522, 113 (ADS entry)

Veilleux, S., Kim, D. C., Sanders, D. B., Mazzarella, J. M., & Soifer, B. T. 1995, ApJS, 98, 171 (ADS entry)

Veilleux, S., et al. 2013, ApJ, 776, 27 (ADS entry)

Ventura, P., et al. 2021, arXiv e-prints, arXiv:2108.04471 (ADS entry)

Verner, D. A., & Ferland, G. J. 1996, ApJS, 103, 467 (ADS entry)

Vila-Costas, M. B., & Edmunds, M. G. 1992, MNRAS, 259, 121 (ADS entry)

Vilchez, J. M., & Esteban, C. 1996, MNRAS, 280, 720 (ADS entry)

Vincenzo, F., Belfiore, F., Maiolino, R., Matteucci, F., & Ventura, P. 2016, MNRAS, 458, 3466 (ADS entry)

Virtanen, P., et al. 2020a, Nature Methods (ADS entry)

—. 2020b, Nature Methods, 17, 261 (ADS entry)

Vishniac, E. T., & Brandenburg, A. 1997, ApJ, 475, 263 (ADS entry)

Viviani, M., Käpylä, M. J., Warnecke, J., Käpylä, P. J., & Rheinhardt, M. 2019, ApJ, 886, 21 (ADS entry)

Vogelsberger, M., Genel, S., Sijacki, D., Torrey, P., Springel, V., & Hernquist, L. 2013, MNRAS, 436, 3031 (ADS entry)

Vogelsberger, M., et al. 2014, MNRAS, 444, 1518 (ADS entry)

Waagan, K. 2009, Journal of Computational Physics, 228, 8609 (ADS entry)

Waagan, K., Federrath, C., & Klingenberg, C. 2011, Journal of Computational Physics, 230, 3331 (ADS entry)

Wagstaff, J. M., Banerjee, R., Schleicher, D., & Sigl, G. 2014, Phys. Rev. D, 89, 103001 (ADS entry)

Wang, B., & Silk, J. 1994, ApJ, 427, 759 (ADS entry)

Wang, E., & Lilly, S. J. 2020, arXiv e-prints, arXiv:2009.01935 (ADS entry)

Wang, F. Y., & Dai, Z. G. 2011, ApJ, 727, L34 (ADS entry)

Wang, L., Kroupa, P., Takahashi, K., & Jeřábková, T. 2020a, MNRAS, 491, 440 (ADS entry)

Wang, P., Li, Z.-Y., Abel, T., & Nakamura, F. 2010, ApJ, 709, 27 (ADS entry)

Wang, X., et al. 2019, ApJ, 882, 94 (ADS entry)

—. 2020b, ApJ, 900, 183 (ADS entry)

Warnecke, J., Rheinhardt, M., Tuomisto, S., Käpylä, P. J., Käpylä, M. J., & Brandenburg, A. 2018, A&A, 609, A51 (ADS entry)

Watson, W. D., & Salpeter, E. E. 1972, ApJ, 174, 321 (ADS entry)

Webb, J. J., & Leigh, N. W. C. 2015, MNRAS, 453, 3278 (ADS entry)

Webb, J. J., Vesperini, E., Dalessandro, E., Beccari, G., Ferraro, F. R., & Lanzoni, B. 2017, MNRAS, 471, 3845 (ADS entry)

Weidner, C., Kroupa, P., & Maschberger, T. 2009, MNRAS, 393, 663 (ADS entry)

Weidner, C., Kroupa, P., & Pflamm-Altenburg, J. 2013, MNRAS, 434, 84 (ADS entry)

—. 2014, MNRAS, 441, 3348 (ADS entry)

Weiner, B. J., et al. 2006, ApJ, 653, 1027 (ADS entry)

Weingartner, J. C., & Draine, B. T. 2001, ApJ, 548, 296 (ADS entry)

Weisz, D. R., et al. 2012, ApJ, 744, 44 (ADS entry)

Welsh, L., Cooke, R., & Fumagalli, M. 2021, MNRAS, 500, 5214 (ADS entry)

Werk, J. K., Putman, M. E., Meurer, G. R., & Santiago-Figueroa, N. 2011, ApJ, 735, 71 (ADS entry)

Westerlund, B. E. 1990, A&A Rev., 2, 29 (ADS entry)

—. 1997, The Magellanic Clouds (Cambridge University Press) (ADS entry)

Westmoquette, M. S., Clements, D. L., Bendo, G. J., & Khan, S. A. 2012, MNRAS, 424, 416 (ADS entry)

Whitaker, K. E., van Dokkum, P. G., Brammer, G., & Franx, M. 2012, ApJ, 754, L29 (ADS entry)

Whitaker, K. E., et al. 2014, ApJ, 795, 104 (ADS entry)

White, D. A., & Fabian, A. C. 1995, MNRAS, 273, 72 (ADS entry)

Wibking, B. D., & Krumholz, M. R. 2022, MNRAS(ADS entry)

Widrow, L. M. 2002, Reviews of Modern Physics, 74, 775 (ADS entry)

Widrow, L. M., Ryu, D., Schleicher, D. R. G., Subramanian, K., Tsagas, C. G., & Treumann, R. A. 2012, Space Sci. Rev., 166, 37 (ADS entry)

Wiesenfeld, L., & Goldsmith, P. F. 2014, ApJ, 780, 183 (ADS entry)

Wilson, T. J., et al. 2019, ApJ, 874, 18 (ADS entry)

Wilson, W. E., et al. 2011, MNRAS, 416, 832 (ADS entry)

Wise, J. H., & Abel, T. 2007, ApJ, 665, 899 (ADS entry)

Wise, J. H., Turk, M. J., & Abel, T. 2008, ApJ, 682, 745 (ADS entry)

Wise, J. H., Turk, M. J., Norman, M. L., & Abel, T. 2012, ApJ, 745, 50 (ADS entry)

Wisnioski, E., et al. 2011, MNRAS, 417, 2601 (ADS entry)

—. 2015, ApJ, 799, 209 (ADS entry)

—. 2018, ApJ, 855, 97 (ADS entry)

—. 2019, ApJ, 886, 124 (ADS entry)

Wollenberg, K. M. J., Glover, S. C. O., Clark, P. C., & Klessen, R. S. 2020, MNRAS, 494, 1871 (ADS entry)

Wong, T., & Blitz, L. 2002, ApJ, 569, 157 (ADS entry)

Woosley, S. E., Heger, A., & Weaver, T. A. 2002, Reviews of Modern Physics, 74, 1015 (ADS entry)

Wotta, C. B., Lehner, N., Howk, J. C., O'Meara, J. M., & Prochaska, J. X. 2016, ApJ, 831, 95 (ADS entry)

Wright, E. L. 2006, PASP, 118, 1711 (ADS entry)

Wu, P.-F., Zahid, H. J., Hwang, H. S., & Geller, M. J. 2017, MNRAS, 468, 1881 (ADS entry)

Wu, Y., Wei, Y., Zhao, M., Shi, Y., Yu, W., Qin, S., & Huang, M. 2004, A&A, 426, 503 (ADS entry)

Wünsch, R., Walch, S., Dinnbier, F., & Whitworth, A. 2018, MNRAS, 475, 3393 (ADS entry)

Wurster, J. 2021, MNRAS, 501, 5873 (ADS entry)

Wurster, J., & Bate, M. R. 2019, MNRAS, 486, 2587 (ADS entry)

Wurster, J., Bate, M. R., & Price, D. J. 2018, MNRAS, 475, 1859 (ADS entry)

—. 2019, MNRAS, 489, 1719 (ADS entry)

Wurster, J., & Lewis, B. T. 2020, MNRAS, 495, 3795 (ADS entry)

Wurster, J., & Li, Z.-Y. 2018, Frontiers in Astronomy and Space Sciences, 5, 39 (ADS entry)

Wurster, J., Price, D. J., & Bate, M. R. 2017, MNRAS, 466, 1788 (ADS entry)

Wuyts, E., et al. 2016, ApJ, 827, 74 (ADS entry)

Wuyts, S., et al. 2011, ApJ, 742, 96 (ADS entry)

Wyse, R. F. G., & Silk, J. 1989, ApJ, 339, 700 (ADS entry)

Xu, H., O'Shea, B. W., Collins, D. C., Norman, M. L., Li, H., & Li, S. 2008, ApJ, 688, L57 (ADS entry)

Xu, H., Wise, J. H., Norman, M. L., Ahn, K., & O'Shea, B. W. 2016, ApJ, 833, 84 (ADS entry)

Xu, S., & Lazarian, A. 2016, ApJ, 833, 215 (ADS entry)

—. 2020, ApJ, 899, 115 (ADS entry)

Xu, W., & Kunz, M. W. 2021, MNRAS(ADS entry)

Yabe, K., et al. 2012, PASJ, 64, 60 (ADS entry)

Yan, Z., Jerabkova, T., & Kroupa, P. 2021, arXiv e-prints, arXiv:2107.03388 (ADS entry)

Yan, Z., Jeřábková, T., & Kroupa, P. 2020, A&A, 637, A68 (ADS entry)

Yang, C.-C., & Krumholz, M. 2012, ApJ, 758, 48 (ADS entry)

Yates, R. M., Henriques, B. M. B., Fu, J., Kauffmann, G., Thomas, P. A., Guo, Q., White, S. D. M., & Schady, P. 2020, arXiv e-prints, arXiv:2011.04670 (ADS entry)

Yong, D., et al. 2013, ApJ, 762, 26 (ADS entry)

—. 2021a, MNRAS, 507, 4102 (ADS entry)

—. 2021b, Nature, 595, 223 (ADS entry)

Yoshida, N., Oh, S. P., Kitayama, T., & Hernquist, L. 2007, ApJ, 663, 687 (ADS entry)

Yoshida, N., Omukai, K., Hernquist, L., & Abel, T. 2006, ApJ, 652, 6 (ADS entry)

Youakim, K., et al. 2020, MNRAS, 492, 4986 (ADS entry)

Young, M. D., & Clarke, C. J. 2016, MNRAS, 455, 1438 (ADS entry)

Yu, X., et al. 2019, MNRAS, 486, 4463 (ADS entry)

Yuan, T. T., Kewley, L. J., & Rich, J. 2013, ApJ, 767, 106 (ADS entry)

Yuan, T. T., Kewley, L. J., Swinbank, A. M., Richard, J., & Livermore, R. C. 2011, ApJ, 732, L14 (ADS entry)

Yusef-Zadeh, F., Law, C., & Wardle, M. 2002, ApJ, 568, L121 (ADS entry)

Yusef-Zadeh, F., Wardle, M., & Roy, S. 2007, ApJ, 665, L123 (ADS entry)

Zahid, H. J., Dima, G. I., Kudritzki, R.-P., Kewley, L. J., Geller, M. J., Hwang, H. S., Silverman, J. D., & Kashino, D. 2014, ApJ, 791, 130 (ADS entry)

Zahid, H. J., Geller, M. J., Kewley, L. J., Hwang, H. S., Fabricant, D. G., & Kurtz, M. J. 2013, ApJ, 771, L19 (ADS entry)

Zahid, H. J., Kudritzki, R.-P., Conroy, C., Andrews, B., & Ho, I. T. 2017, ApJ, 847, 18 (ADS entry)

Zaritsky, D. 1992, ApJ, 390, L73 (ADS entry)

Zaritsky, D., Colucci, J. E., Pessev, P. M., Bernstein, R. A., & Chandar, R. 2014, ApJ, 796, 71 (ADS entry)

Zaritsky, D., Kennicutt, Robert C., J., & Huchra, J. P. 1994, ApJ, 420, 87 (ADS entry)

Zhang, K., et al. 2017, MNRAS, 466, 3217 (ADS entry)

Zhang, Z.-Y., Romano, D., Ivison, R. J., Papadopoulos, P. P., & Matteucci, F. 2018, Nature, 558, 260 (ADS entry)

Zhao, B., Caselli, P., Li, Z.-Y., Krasnopolsky, R., Shang, H., & Nakamura, F. 2016, MNRAS, 460, 2050 (ADS entry)

Zhao, B., et al. 2020, Space Sci. Rev., 216, 43 (ADS entry)

Zhao, D. H., Jing, Y. P., Mo, H. J., & Börner, G. 2009, ApJ, 707, 354 (ADS entry)

Zinchenko, I. A., Pilyugin, L. S., Grebel, E. K., Sánchez, S. F., & Vílchez, J. M. 2016, MNRAS, 462, 2715 (ADS entry)

Zinn, R. 1985, ApJ, 293, 424 (ADS entry)

Zovaro, H. R. M. 2020, PhD thesis, Australian National University, Australia (ADS entry)

Zubko, V., Dwek, E., & Arendt, R. G. 2004, ApJS, 152, 211 (ADS entry)

Zurita, A., Florido, E., Bresolin, F., Pérez, I., & Pérez-Montero, E. 2021, MNRAS, 500, 2380 (ADS entry)

Zweibel, E. G. 2006, Astronomische Nachrichten, 327, 505 (ADS entry)

Convergence study of Population III star formation simulations

It is well known that hydrodynamic simulations of star and galaxy formation can be highly sensitive to the resolution or level of refinement that can be achieved (Commerçon et al. 2008; Meru & Bate 2011; Snaith et al. 2018). In the case of primordial star formation, the Jeans scale (and the fragmentation scale) depends on the resolution and thus plays a key role in setting the mass distribution of sink particles (Glover 2005; Stacy et al. 2010). Hence, it is necessary to check if the fragmentation we observe in our simulations is scale-dependent. For this purpose, we repeat three runs with variable γ_{H_2} (to which we refer in this appendix as runs A, B and C) from our total sample of 40 at four different resolutions with 12, 13, 14 and 15 levels of refinement, respectively (see Section 2.3.1 for a description of the levels of refinement). We select these three runs to represent cases of low, medium, and high fragmentation, respectively, at the resolution used in the main text (14 levels). To check for convergence, we compare the state of the runs at SFE = 3.5%, rather than 5% as in the main text. This is a pragmatic choice driven by the high computational cost of attempting to reach SFE = 5% at the highest resolution. Table A.1 shows the number of sinks formed, which remains unchanged between resolutions 14 and 15 for all the three runs, suggesting that our results are converged. We find further evidence of convergence at resolution 14 by plotting the CDF of the mass of sink particles accumulated from the three runs at every resolution, as we show in Figure A.1. In fact, the mean sink particle mass also remains the same at resolutions 14 and 15 in all the three runs. While the fragmentation pattern is not identical as we increase the resolution, we do not expect that it should be, since the flows are ultimately chaotic. These differences, however, do not appear to affect the first order characteristics of primordial cloud collapse that we study in this work.

Table A.1: Summary of outcomes for three sets of variable γ_{H_2} runs (A, B, C) carried out at multiple resolutions (12, 13, 14 and 15) with different random turbulent fields. $N_{\rm sink}$ denotes the number of sink particles at SFE = 3.5% and dx is the unit cell length at the highest level of refinement corresponding to the resolution used.

Property	Resolution	dx	Run A	Run B	Run C
	12	30 au	2	4	2
	13	15 au	2	6	5
$N_{\rm sink}$	14	7.6 au	3	6	13
	15	3.8 au	3	6	13
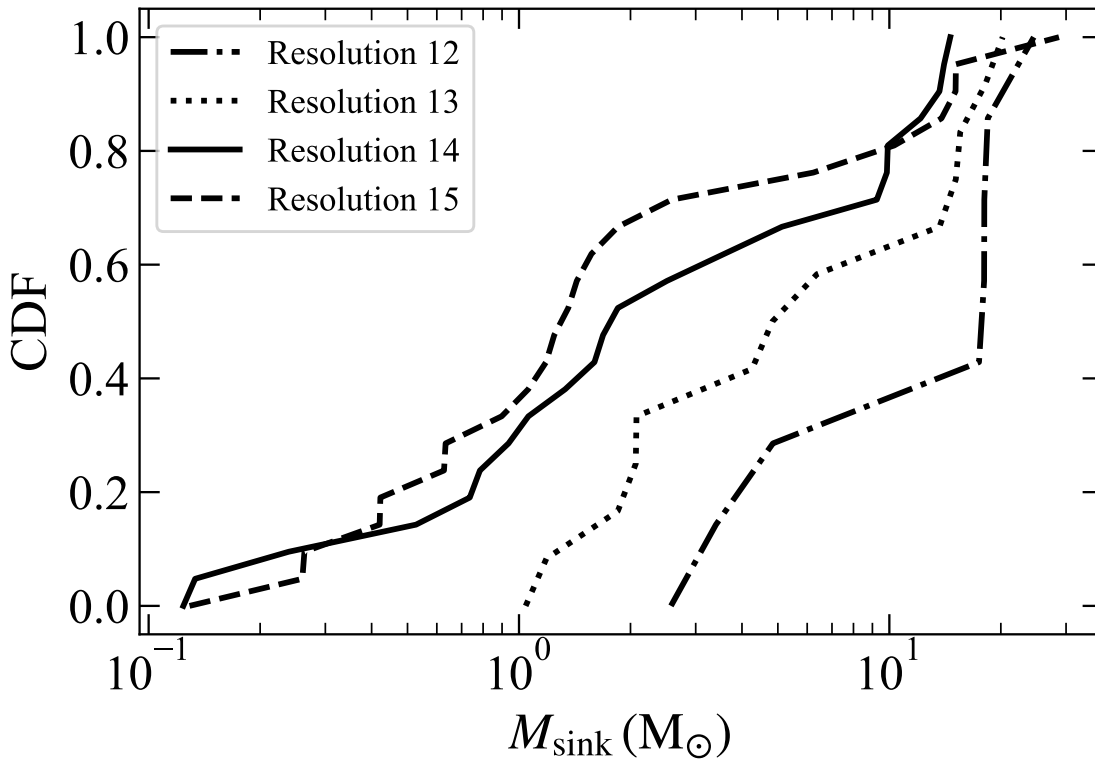
Figure A.1: CDF of the sink particle mass accumulated over the three runs (A, B, C; see Table A.1) at every resolution.

Effects of Jeans resolution on cooling in Population III star formation simulations

The morphological evolution of the weak field runs changes significantly when we use 64 cells per Jeans length instead of 32. As discussed in Section 4.3.1, in the higher resolution case the simulation develops a near-spherical bubble of gas at temperatures of $\approx 3000 - 6000$ K that expands over time; Turk et al. (2012) noticed a similar phenomenon in their highest-resolution simulations. To determine whether this bubble is associated with the presence of a magnetic field, we repeat the run shown in Figure 4.1 with identical gas initial conditions, but with no magnetic field, at resolutions of 32 (J32) and 64 (J64) cells per Jeans length. Figure B.1 shows the density-weighted temperature projections for the J32 and J64 runs. Given that we observe the same phenomenon as in the magnetic field runs, i.e., a hot bubble appears in J64 but not in J32, we conclude that the presence of the bubble is not solely due to magnetic fields.

Instead, we find that the key distinction between runs where we do and do not form bubbles is how well we resolve the temperature jump across the accretion shocks where matter falls onto the disc. To illustrate this point, we focus on a particular location inside the bubble, which we refer to as p_1 hereafter, at a radial distance of $r_1 = 400$ au from the star, located in the plane of the disc, as indicated by the '+' in Figure B.1. Figure B.2 shows profiles of ρ, T, P, v_r and c_s along a radial ray passing through this point, at two times: just before and just after the bubble reaches p_1. We refer to the profile measured immediately before the bubble reaches our sample point as the "Pre-Shock" profile (blue in Figure B.2), and the one immediately after as the "Post-Shock" profile (orange in Figure B.2).

Table B.1 lists the properties of the gas at p_1 at times corresponding to the pre-shock and post-shock snapshots shown in Figure B.2. The ratios of densities, tempera-
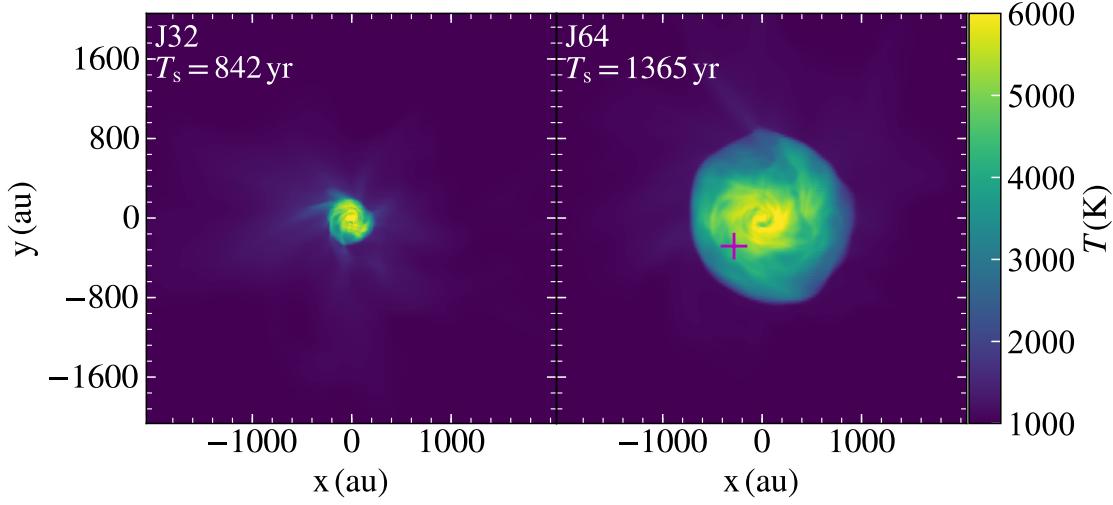
Figure B.1: Density-weighted projections of temperature for the J32 and J64 runs at the end of the simulation, when the SFE has reached 5 percent. The '+' marker denotes the sample point p_1 where we calculate the cooling length as the shock front travels through it earlier in the simulation.

Table B.1: Pre-shock properties at point p_1 as obtained from Figure B.2 in the J64 run. The quantity x_q is the mass fraction of species q.

Property	Pre-Shock	Post-Shock
$n\,(\mathrm{cm}^{-3})$	2.6×10^9	6.2×10^9
$T\,(\mathrm{K})$	1350	3110
x_{H}	0.76	0.76
$x_{\mathrm{H_2}}$	2.9×10^{-3}	1.2×10^{-3}
x_{D}	4.6×10^{-5}	4.6×10^{-5}
x_{HD}	4.0×10^{-7}	1.5×10^{-7}
$x_{\mathrm{H+}}$	1×10^{-8}	4×10^{-8}
$x_{\mathrm{D+}}$	4×10^{-11}	7×10^{-11}
$\Gamma_{\mathrm{rad}}\,(\mathrm{erg/cm^3/s})$	4.8×10^{-14}	8.9×10^{-17}
$\Gamma_{\mathrm{chem}}\,(\mathrm{erg/cm^3/s})$	NA	4.3×10^{-15}
$E_{\mathrm{T}}\,(\mathrm{erg/cm^3})$	7.3×10^{-4}	3.8×10^{-3}
$t_{\mathrm{cool}}\,(\mathrm{yr})$	477	27428
$t_{\mathrm{diss\,H_2}}\,(\mathrm{yr})$	∞	55

tures, and pressures in the pre- and post-shock conditions are as expected from the Rankine-Hugoniot jump conditions for non-radiative shocks.

Using the post-shock values, we can calculate the total volumetric cooling rate via radiation, Γ_{rad}, and via chemical reactions, Γ_{chem} (important at high temperature, where endothermic dissociation of H_2 is a significant coolant) from KROME. The time it will take for the gas to cool, t_{cool}, depends on the cooling rate and the thermal
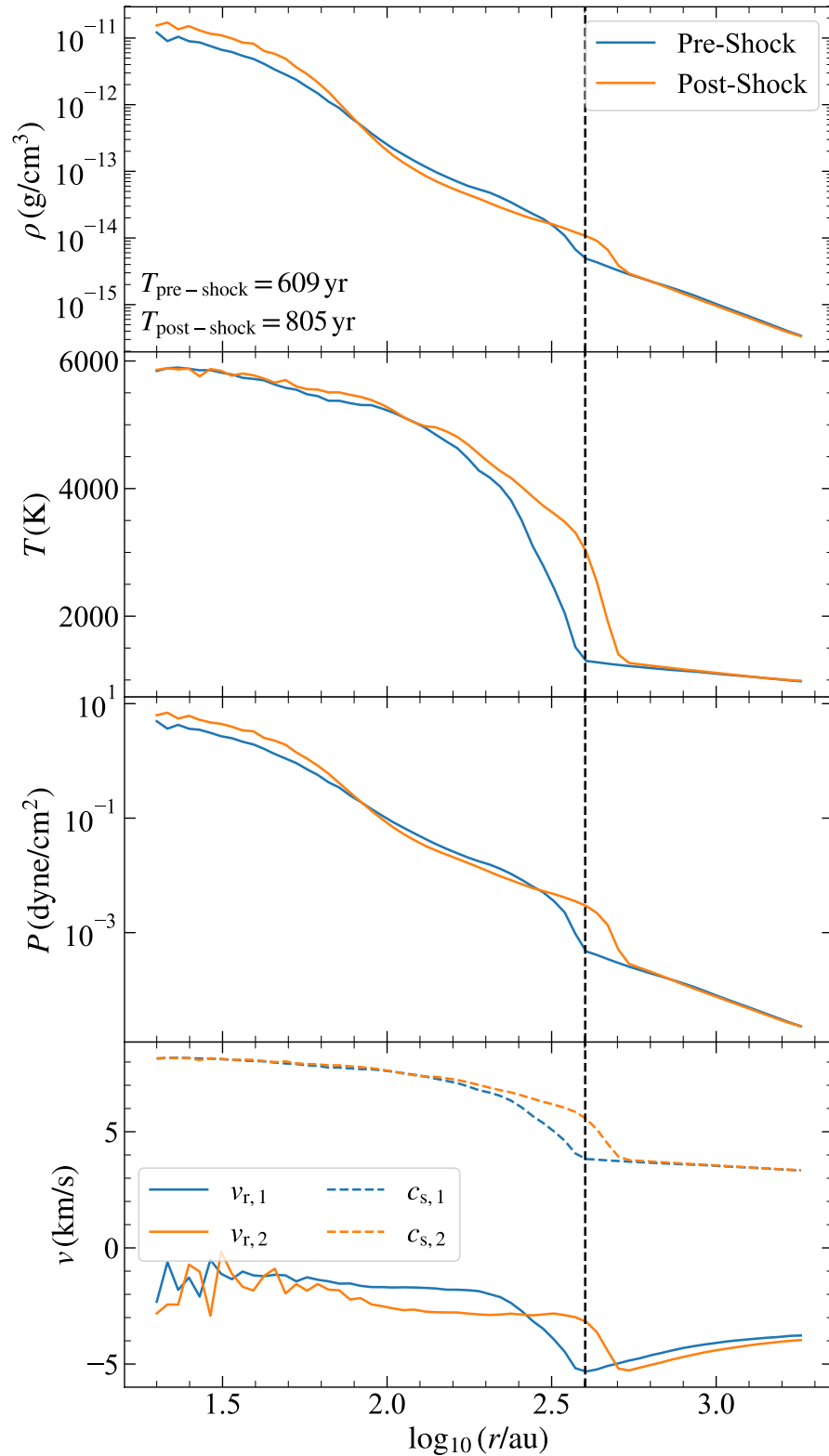
Figure B.2: Profiles of density, temperature, pressure and radial velocity along a radial ray passing through our sample point p_1 (Figure B.1) at two times, just before (labelled "Pre-Shock") and just after (labelled "Post-Shock") the edge of the hot bubble reaches p_1, at a distance $r_1 = 400\,\mathrm{au}$ from the central star (indicated by the dashed vertical line). The time it takes for the gas to traverse the width of the shock is 204 yr.
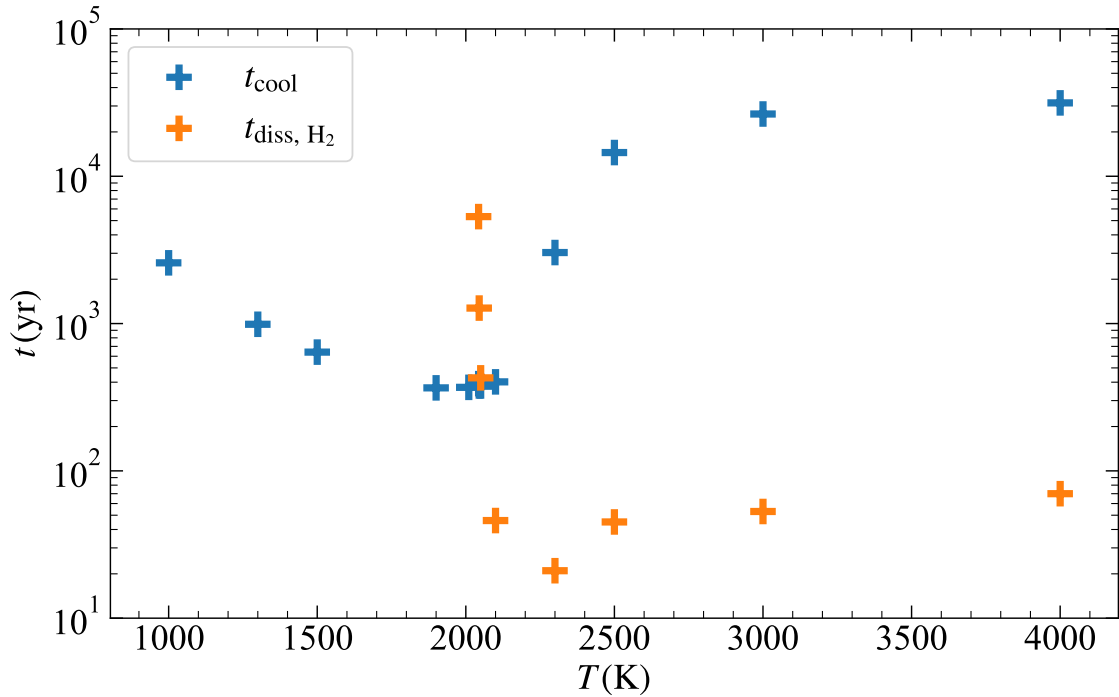
Figure B.3: The cooling and H_2 dissociation timescales as a function of temperature, for the fixed post-shock chemical composition and density as listed in Table B.1. At lower temperatures, $t_{\mathrm{diss\,H_2}}$ is infinity since there is no net dissociation of H_2. At higher temperatures, the molecular gas dissociates faster than it can cool.

energy per unit volume, E_{T},

$$t_{\mathrm{cool}} = \frac{E_{\mathrm{T}}}{\Gamma_{\mathrm{rad}} + \Gamma_{\mathrm{chem}}} \,, \qquad (\mathrm{B.1})$$

where $E_{\mathrm{T}} = (3/2)n k_{\mathrm{B}} T$, and k_{B} is the Boltzmann constant[1]. Similarly, the time it takes for H_2 to dissociate can be given by,

$$t_{\mathrm{diss,\,H_2}} = \frac{x_{\mathrm{H_2}}}{-\dot{x}_{\mathrm{H_2}}} \,, \qquad (\mathrm{B.2})$$

where $x_{\mathrm{H_2}}$ is the H_2 mass fraction, and $\dot{x}_{\mathrm{H_2}}$ is the rate of change in the H_2 mass fraction; by convention, if $\dot{x}_{\mathrm{H_2}} \geq 0$, we take $t_{\mathrm{diss,\,H_2}} = \infty$. We see that the pre-shock conditions are characterised by rapid cooling ($t_{\mathrm{cool}} \sim 500$ yr) and no dissociation, while the post-shock conditions are characterised by much slower cooling ($t_{\mathrm{cool}} \sim 27,000$ yr) and rapid dissociation ($t_{\mathrm{diss\,H_2}} \sim 50$ yr). The reason for the much longer cooling time is the fact that, at the ≈ 3000 K temperature found in the post-shock region, most collisions between H_2 molecules and H atoms lead to collisional

---

[1]Note that the factor of 3/2 implicitly assumes the gas is monoatomic, and thus ignores the effect of H_2 on the adiabatic index; given the very small H_2 fraction ($\sim 10^{-3}$) in the pre-shock gas, this approximation is reasonable.

dissociation rather than to excitation followed by radiative de-excitation.

In order to understand why resolution matters, it is helpful to consider how the cooling and dissociation times depend on temperature. Figure B.3 shows these quantities as a function of temperature for the post-shock chemical composition and density. The key feature to notice is that the thermal and chemical regime changes sharply at ≈ 2000 K. Now, consider how material on the low-temperature side of this jump evolves as it encounters a shock. In the limit of infinite resolution, the shock has a width of the order of the particle mean free path. Given $n \sim 10^9\,\mathrm{cm}^{-3}$ and a typical cross-section for neutral species $\sim 10^{-16}\,\mathrm{cm}^2$, the shock width is $\sim 10^7\,\mathrm{cm}$. The time to traverse this distance at $\sim 1\,\mathrm{km\,s^{-1}}$ is $\sim 100\,\mathrm{s}$, which is tiny as compared to any radiative or chemical timescale. Thus, if this gas crosses a strong shock, its temperature increases by the usual factor $(\gamma + 1)/(\gamma - 1)$, without time for any radiative cooling to occur. If the gas is initially at $1300\,\mathrm{K}$, as is the case for our pre-shock sample point, this causes it to jump from the left to the right side of the $2000\,\mathrm{K}$ discontinuity in Figure B.3. At that point, H_2 dissociates faster than the gas is able to cool, and we get into the high-temperature, slow-cooling regime that characterises our post-shock region. Thus, the gas never cools.

Now, consider the case where the shock is broadened to a size $\sim 4\Delta x$, a typical shock width imposed by artificial viscosity (e.g., Creasey et al. 2011; Hubber et al. 2013a). If the resolution inside the region is $23\,\mathrm{au}$, as is the case in the J32 run, then the time required to traverse the shock region is greatly increased to $\sim 92\,\mathrm{au}/1\,(\mathrm{km\,s^{-1}}) = 436\,\mathrm{yr}$. Interestingly, this is comparable to the pre-shock cooling time. The net effect is that the gas cools at the same time it is traversing the broadened shock, and thus never crosses over to the right side in Figure B.3. It remains cool and with a significant fraction of H_2, exactly as we observe in the J32 run. On the other hand, if we double the Jeans resolution, then the time to traverse the shock is halved, and we are in the regime where the hydrodynamic time to cross the shock is smaller than the cooling time. Thus the temperature goes up, and we get to the right side of the jump at $2000\,\mathrm{K}$ in Figure B.3, where $t_{\mathrm{diss\,H_2}} \ll t_{\mathrm{cool}}$. Once in this regime, the gas does not have enough time to cool before it dissociates, leading to the formation of a hot, H_2-poor bubble as we observe in the J64 run. This discussion also explains why a magnetic field, though not critical to the phenomenon we have identified, can nonetheless influence it: magnetic pressure helps mediate the shock (e.g., Fragile et al. 2005; Li et al. 2013a), and thus changes the rate at which gas heats or cools as it passes the shock front.

Thus, while our motivation to use a higher Jeans resolution was to better resolve the action of the small-scale dynamo, this result, along with earlier findings of Turk

et al. (2012), implies that a higher Jeans resolution is also critical for capturing the thermal and chemical changes that occurs across shocks.

Uncertainties in the metallicity gradient model

C.1 Functional form of cosmic accretion rate surface density

Here, we describe how the solutions change if we pick a different functional form for the radial profile of cosmological accretion, $\dot{c}_\star(x)$. Note that we must numerically solve for these functional forms, because analytic solutions either do not exist or are so complex in functional form that a numerical integration is preferable. Specifically, we experiment with $\dot{c}_\star(x) = 1/x$ and $\dot{c}_\star(x) = 1$.

Figure C.1, Figure C.2, and Figure C.3 show metallicity profiles with different $\dot{c}_\star(x)$ for local spirals, local dwarfs, and high-z galaxies with $\phi_y = 1$, respectively; we use $\phi_y = 1$ because this maximises the dependence on $\dot{c}_\star(x)$ – smaller ϕ_y values suppress variations. Note that the dimensionless parameters $\mathcal{P}$ and $\mathcal{S}$ are identical to that used in the Section 6.3 for the corresponding galaxies, but that $\mathcal{A}$ differs due to its dependence on $\dot{c}_\star$ (equation 6.40). We see that changing the profile of $\dot{c}_\star(x)$ has no noticeable effect for local dwarfs or high$-z$ galaxies. This is because cosmic accretion is not a dominant term in the metallicity model for these galaxies, and the metallicities are instead mainly set by source, advection and diffusion.

The profile of $\dot{c}_\star(x)$ does matter for local spirals; as $\dot{c}_\star(x)$ flattens, metallicities in the inner regions of the disc reach higher values whereas the outer regions of the disc become more metal poor, thus leading to somewhat steeper gradients. For the most extreme case of constant $\dot{c}_\star(x)$, gradients are ≈ -0.05 dex kpc^{-1} steeper than our fiducial model. Thus, if the cosmic accretion profiles in local spirals are flatter than that we use in the main text, we expect slightly steeper gradients from the metallicity model, which is largely due to the SFR that we input from the galaxy evolution model. This is because under the input galaxy evolution model of
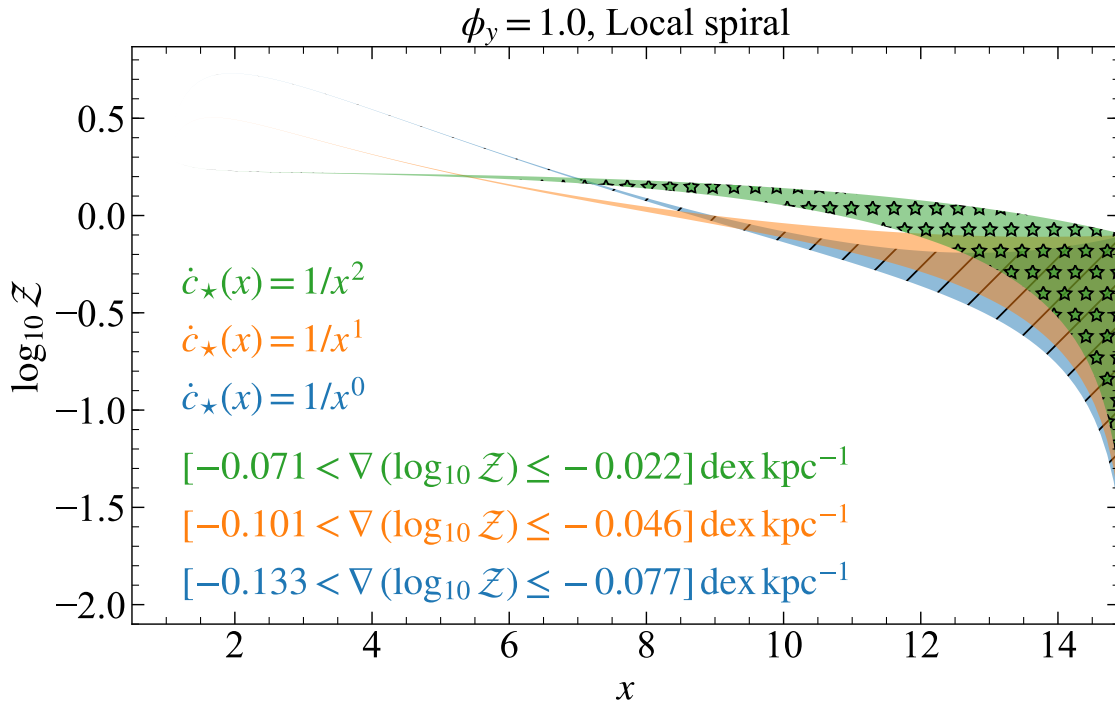
Figure C.1: Same as Figure 6.2 but with different functional forms for cosmic accretion, namely, $\dot{c}_\star = 1/x^2$ (the one we use in the main text), $1/x$ and 1, respectively. Flatter cosmic accretion profiles make the gradients steeper (within a factor of 2).

Krumholz et al. (2018) where the SFR varies as $1/x^2$, flatter accretion profiles will dilute the metallicity in the metal-deficient outer regions by the same amount as that in the metal-rich inner regions, thus giving a larger difference between metallicities in the inner and outer regions in the disc.

C.2   Uncertainties in cosmological evolution of accretion and velocity dispersion

Our predictions of metallicity gradient evolution depend on a scaling of σ_g with z derived from high-z galaxy observations (Wisnioski et al. 2015), and a scaling of $\dot{M}_h$ with z derived from cosmological simulations (Neistein & Dekel 2008; Faucher-Giguère et al. 2011). Since these two methods of deriving the scaling are very different, it is important to comment on any possible discrepancies between the two, and if they affect our results. Indeed, there is what appears at first glance to be an inconsistency: as we noted in Section 6.2.2, cosmological equilibrium demands that the inflow rate $\dot{M}$ through the disc (and, the star formation rate $\dot{M}_\star$) be similar to or less than the accretion rate onto the galaxy $\dot{M}_{\rm ext}$, in order to conserve the total mass. In terms of our model, the above condition translates into $\mathcal{P}/\mathcal{A} \lesssim \ln x_{\rm max}$
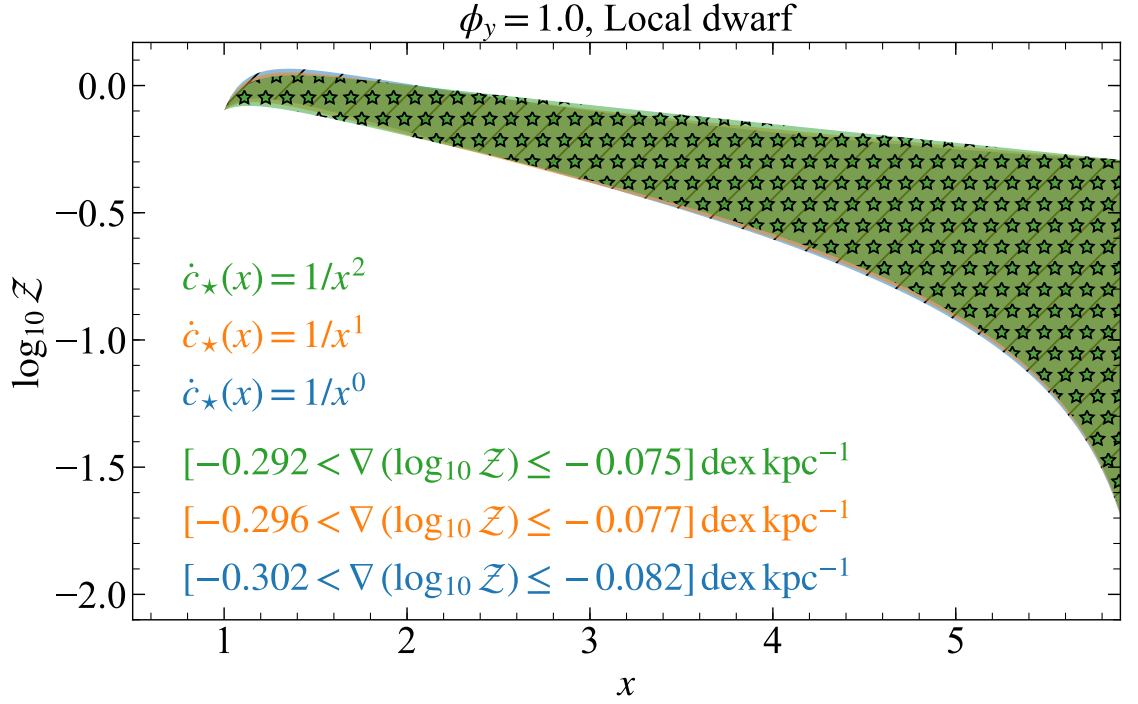
Figure C.2: Same as Figure C.1 but for local dwarfs. Changing the functional form of $\dot{c}_\star(x)$ has no impact on the metallicity distributions in local dwarfs.
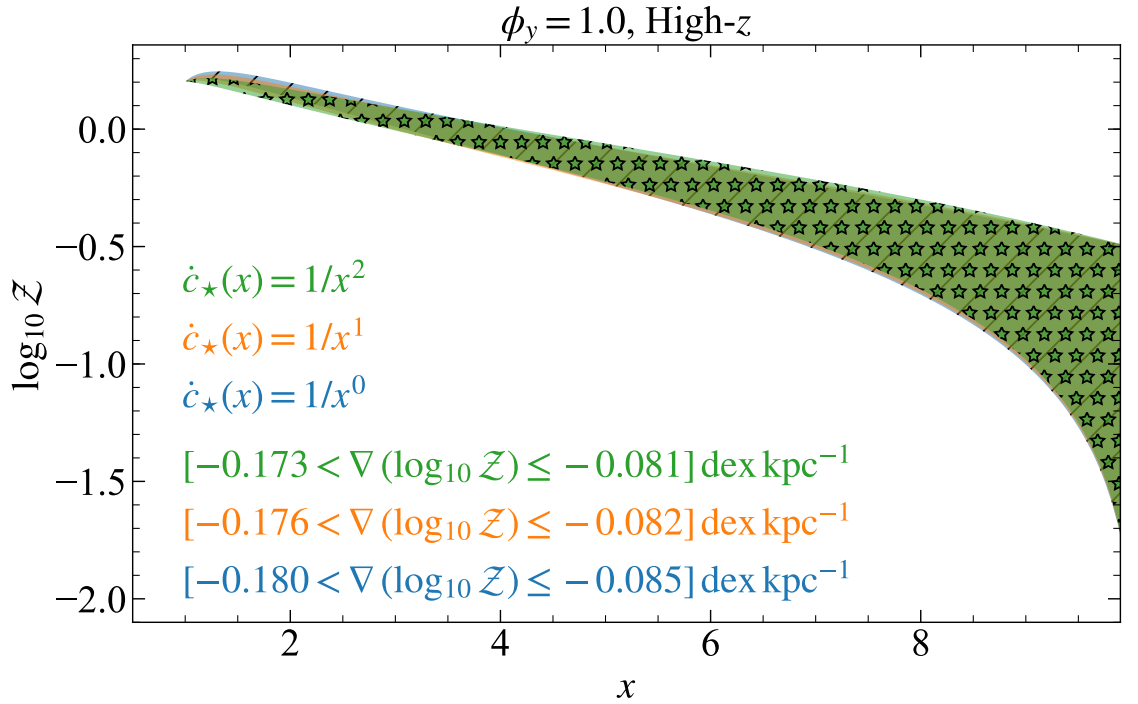
Figure C.3: Same as Figure C.1 but for high-z galaxies. Similar to local dwarfs, changing the functional form of $\dot{c}_\star(x)$ has no impact on the metallicity distributions in high-z galaxies.

for $\dot{c}_\star = 1/x^2$. However, in many cases, our adopted scalings of σ_g and $\dot{M}_h$ with z give considerably larger values of $\mathcal{P}/\mathcal{A}$ at high-z. This discrepancy is simply a manifestation of the known problem that galaxies at $z \sim 2$ have star formation rates $\dot{M}_\star > \dot{M}_{\text{ext}}$ (Erb 2008; Behroozi et al. 2013; Scoville et al. 2017); high-z galaxies obey the same observed scaling between star formation rate and velocity dispersion as local galaxies (Krumholz et al. 2018; Varidel et al. 2020), and since the inflow rate is directly set by σ_g, $\dot{M}_* > \dot{M}_{\text{ext}}$ directly implies $\dot{M} > \dot{M}_{\text{ext}}$.

The discrepancy between star formation rates (and velocity dispersions) and expected cosmological accretion rates has several possible explanations, but from the standpoint of our model for metallicity gradients, we can divide these into two main categories. One is that galaxies near the epoch of peak star formation do in fact form stars and move mass inward faster than their mean cosmological accretion rates, either because mass that was ejected at an earlier epoch falls back onto the galactic outskirts (e.g., Christensen et al. 2016; Tollet et al. 2019), or because of large angular momentum mismatch between the infalling material and the disc that triggers a sufficiently large radial inflow (Mayor & Vigroux 1981; Bilitewski & Schönrich 2012; Pezzulli & Fraternali 2016), or because galaxies accumulate large gas reservoirs at $z \gtrsim 2$, which then flow into the star-forming portion of the disc due to compaction events (Dekel et al. 2009a; Dekel & Burkert 2014), interactions (Rupke et al. 2010a) or mergers (Hani et al. 2018) at $z \sim 2$. In these cases, the model we present is sufficient and we do not need to make any changes, since in such cases galaxies can maintain a large $\mathcal{P}/\mathcal{A}$ for a considerable time.

The other possibility is that the $\dot{M}_\star$ measured at high-z are overestimated (e.g., Leja et al. 2019, 2020), thus altering the $\sigma_g - \dot{M}_*$ relationship; this is functionally equivalent to overestimating σ_g at fixed $\dot{M}_\star$. Such an overestimate in high-redshift galaxies could plausibly be due to beam smearing, inclination uncertainty, and similar resolution-dependent (and thus redshift-dependent) factors (Davies et al. 2011; Di Teodoro & Fraternali 2015). This would have a significant impact on $\mathcal{P}/\mathcal{A}$ because $\mathcal{P}/\mathcal{A} \propto \sigma_g^3$. To study the effects this can have on our results, we reproduce the expected cosmic evolution of metallicity gradient for the Milky Way in the model (cf. Figure 6.10), but using σ_g obtained from equation 6.53 reduced by a factor of $(1 + z)$, in line with the redshift scaling of the limits of spectral resolution of different instruments (McDermid et al. 2020, Figure 2.3). Figure C.4 presents the resulting metallicity gradients from the model, where the maximum $\log \mathcal{P}/\mathcal{A}$ is only 0.6. The qualitative shape of the model changes slightly for $z > 0.5$. However, ϕ_y remains the primary factor that drives the model gradients closer to the observed gradients across cosmic time. The main difference from our fiducial model is that
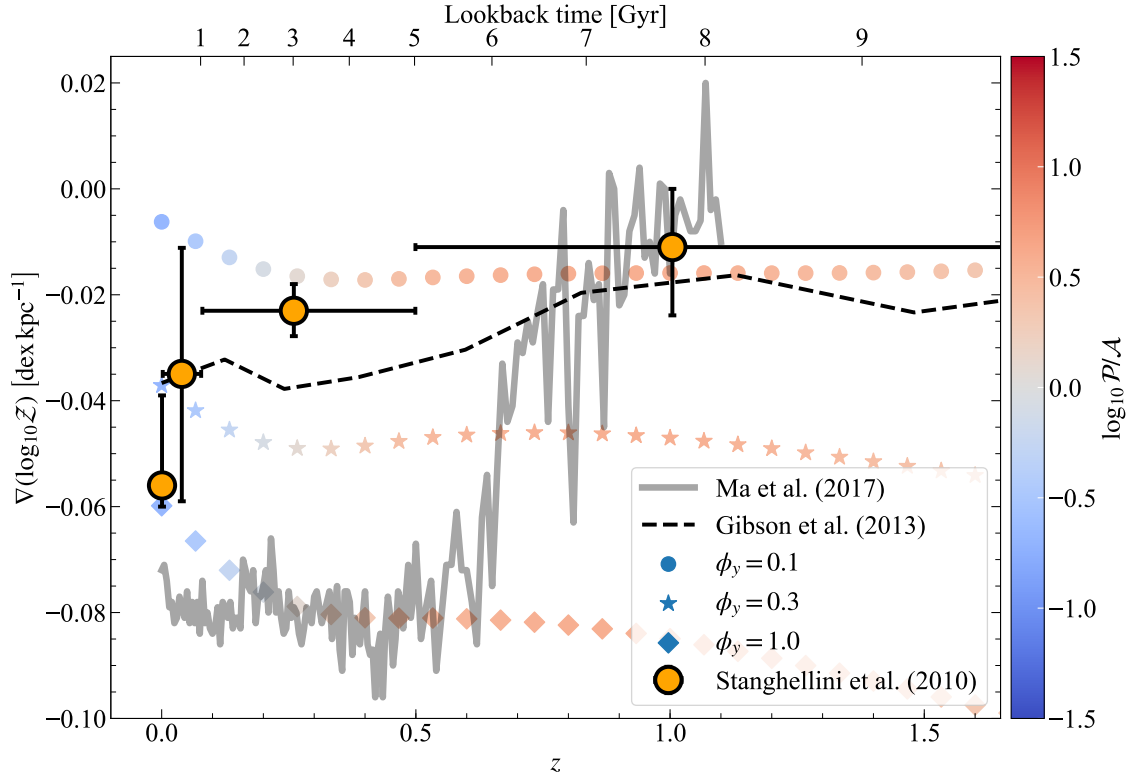
Figure C.4: Same as Figure 6.10, but with $\sigma_g(z)$ reduced by a factor of $1 + z$ as compared to equation 6.53 (see Appendix C.2 for a discussion).

steep gradients become possible at high-z if ϕ_y is close to unity, because a smaller $\mathcal{P}/\mathcal{A}$ implies weaker homogenisation of the ISM by inward advection of metal-poor gas.

C.3 Dependence on the location of disc edges

In the main text, we non-dimensionalize the solution in terms of x, where $x = r/r_0$ and we adopt a fiducial value of $r_0 = 1\,\mathrm{kpc}$, finding solutions for x in the range $(x_{\min}, x_{\max})$, with $x_{\min} = 1$ and $x_{\max}$ chosen based on observations of the sizes of the star-forming region for different galaxies. To explore the sensitivity of our results to the choice of our range in x, we show in Figure C.5 how the equilibrium gradients change in local spirals if we increase $x_{\max}$ from the fiducial 15 used in the main text to 20, noting that the qualitative trends remain the same across all types of galaxies. Increasing $x_{\max}$ leads to higher metallicities at each location in the disc, with slightly higher mean metallicities and shallower metallicity gradients. This is because increasing $x_{\max}$ decreases $\mathcal{A}$ since it means that there is a larger disc for the same total cosmic accretion rate (see equation 6.34 and equation 6.40). Thus, the ratio $\mathcal{S}/\mathcal{A}$ that appears in $\mathcal{Z}$ (see equation 6.41) increases, giving higher $\mathcal{Z}(x)$.
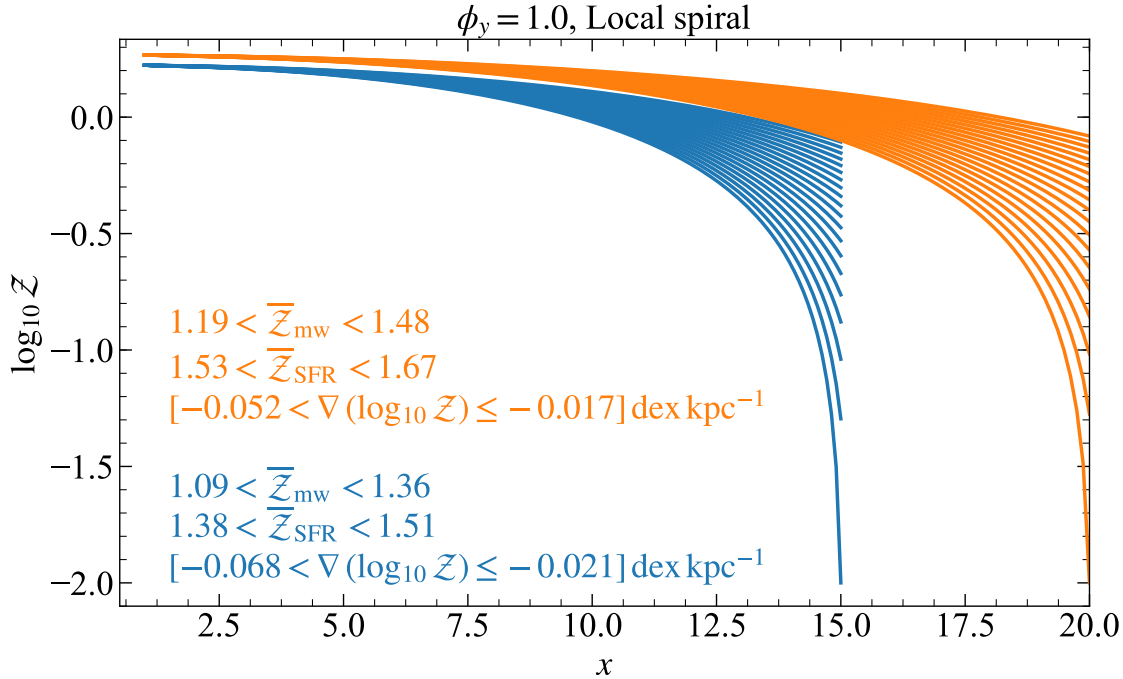
Figure C.5: Metallicity gradients as shown in the main text in Section 6.3, but with an alternate value of the edge of the star-forming disc, x_{max}. The profile of the distribution is preserved in each case, with slight variations in the absolute metallicities and metallicity gradients, with diminishing differences for decreasing ϕ_y. Larger galaxies (in each galaxy class) show higher mean metallicity and flatter gradients.

Further, this increment in $\mathcal{S}/\mathcal{A}$ is reduced if $\phi_y < 1$ because $\mathcal{S} \propto \phi_y$. Thus, for lower ϕ_y, changing x_{max} does not lead to any appreciable change in $\mathcal{Z}(x)$. Similarly, if we shift the inner edge of the galactic disc (where the rotation curve flattens out) by decreasing it to $x_{min} = 0.5$ (or increasing it to 2), the solution allows for slightly higher (lower) mean metallicities, and steeper (shallower) gradients.

Thus, this analysis implies that in galaxies where the transition from the star-forming disc to the bulge occurs at smaller galactic radius, the galaxy could potentially build slightly steeper metallicity gradients. Conversely, in galaxies where the star-forming disc is larger, we expect slightly shallower metallicity gradients. However, these variations remain insignificant compared to the scatter introduced due to other parameters, particularly ϕ_y. Thus we do not regard variations in x_{min} or x_{max} as a substantial uncertainty in the model.

Scaling of the yield reduction factor with stellar mass

Comparing our analytic model with observations of the MZR and the MZGR discussed in the main text suggests a scaling of the yield reduction factor ϕ_y with stellar mass $M_\star$. In this appendix, we explore ways to directly retrieve this scaling using two different methods. The two scalings introduced below capture the qualitative essence of how ϕ_y should scale with $M_\star$, albeit with significant uncertainties.

1. *Scaling 1:* We make use of the observations reported in Chisholm et al. (2018) to derive a scaling of ϕ_y with $M_\star$. The authors report on the ratio of the wind to the ISM metallicity, $\mathcal{Z}_w/\mathcal{Z}$, as well as the metal mass loading factor for galaxies of different masses. We perform a linear fit to their data to obtain $\mathcal{Z}_w/\mathcal{Z}$ as a function of $M_\star$. To find how the metal mass loading factor varies as a function of $M_\star$, we use the scaling provided by Denicoló et al. (2002) which provides the best fit to the data. Then, we use $\mathcal{Z}_w/\mathcal{Z}$ and the metal mass loading factor to find the mass loading factor μ as a function of $M_\star$. Using $\mathcal{Z}_w/\mathcal{Z}$ and μ, it is straightforward to compute ϕ_y (Sharda et al. 2021b, equations 10 and 13)

$$\phi_y = 1 - \mu \mathcal{Z} \frac{\mathrm{Z}_\odot}{y} \left(\frac{\mathcal{Z}_w}{\mathcal{Z}} - 1 \right) , \tag{D.1}$$

where y is the yield of metals from core collapse supernovae. Before we proceed further, it is important to point out the caveats of this approach. Firstly, Chisholm et al. only observed 7 galaxies across a wide range of $M_\star$ ($\sim 10^7 - 10^{11}\,\mathrm{M}_\odot$), so the coverage in stellar mass is very sparse. Secondly, the ISM metallicities for the galaxies used in Chisholm et al. are non-homogeneous; for example, some are stellar metallicities and some are gas metallicities. Thirdly, some galaxies in this dataset are undergoing mergers, and show diluted metallicities as compared to isolated galaxies of the same
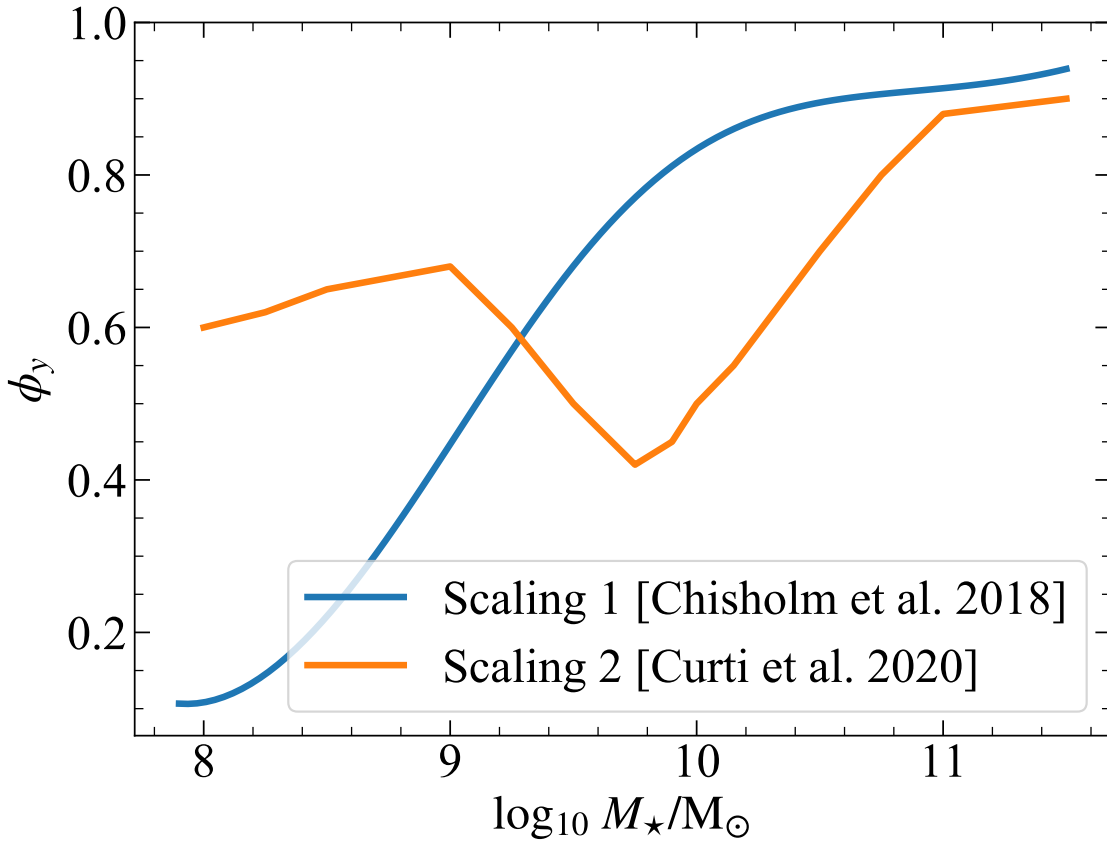
Figure D.1: Scalings of the yield reduction factor ϕ_y with $M_\star$, obtained using the two approaches described in Appendix D. Scaling 1 is from observations (Chisholm et al. 2018) whereas scaling 2 is from the best match between the model MZR and the Curti et al. (2020a) MZR.

mass. Keeping these caveats in mind, and noting that ϕ_y is sensitive to the absolute value of $\mathcal{Z}$ as we see from equation D.1, we simply increase the ISM metallicities quoted in Chisholm et al. by 0.3 dex, which has the effect of bringing them into closer alignment with the observed MZR; without this increment, the least and the most massive galaxies in the sample ($M_\star \approx 10^7$ and $10^{10.7} \, \mathrm{M}_\odot$, respectively) would have a metallicity $\mathcal{Z} = 0.03$ and 0.5, respectively, placing them well below the observed MZR. We do not re-scale the ratio $\mathcal{Z}_w/\mathcal{Z}$ because it is not sensitive to the absolute value of $\mathcal{Z}$. With this adjustment, we show the resulting scaling of ϕ_y with $M_\star$ in Figure D.1. This is our first model scaling.

2. *Scaling 2:* In this approach, we simply find the best match between the model MZRs and the Curti et al. (2020a) MZR by eye, where we take the latter to be the representative MZR in the local Universe. We note that there is no particular reason to prefer the latter MZR over other available MZRs, especially given the uncertainties in the absolute normalisation of metallicities.

However, for the sake of developing a scaling of ϕ_y with $M_\star$ from this approach, we will continue with this MZR. We plot the resulting scaling in Figure D.1. Interestingly, while the general trend of ϕ_y increasing with $M_\star$ still holds, we find an inflection at intermediate masses where ϕ_y is the lowest. However, we do not place great weight on this finding, given the large uncertainties in both the choice of MZR and its absolute value. From the standpoint of our model predictions, the main difference between this scaling and our first scaling is that this scaling gives a shallower trend in ϕ_y with $M_\star$, such that ϕ_y reaches a minimum value of only ≈ 0.5 even for very low-mass galaxies.

Database of high-redshift galaxies

E.1 Compiled data with reanalysed kinematics

Table E.1: Compiled database of metallicity gradients and reanalysed kinematics utilized in this work. Columns $1-9$ list the parent sample, galaxy ID, redshift, stellar mass, star formation rate, half-light radius (in arcsec), metallicity gradient, rotational velocity, and velocity dispersion, respectively. See Section 8.2 and Table 8.1 for the list of references for each sample.

Sample	Galaxy ID	z	$\log_{10} \frac{M_\star}{M_\odot}$	$\log_{10} \frac{\text{SFR}}{M_\odot \, \text{yr}^{-1}}$	$r_\text{e}\,('')$	$\frac{\nabla(\log_{10}\mathcal{Z})}{\text{dex}\,\text{kpc}^{-1}}$	$v_\phi/\text{km}\,\text{s}^{-1}$	$\sigma_\text{g}/\text{km}\,\text{s}^{-1}$
(1)	(2)	(3)	(4)	(5)	(6)	(7)	(8)	(9)
MASSIV	20106882	1.40	9.73	1.58	0.42	$0.033^{+0.013}_{-0.013}$	103^{+13}_{-13}	46^{+24}_{-29}
MASSIV	20116027	1.53	9.83	1.63	0.50	$0.023^{+0.012}_{-0.012}$	19^{+5}_{-5}	37^{+21}_{-21}
MASSIV	20147106	1.52	9.84	1.96	0.14	$0.021^{+0.027}_{-0.027}$	9^{+6}_{-6}	12^{+11}_{-6}
MASSIV	20214655	1.04	9.76	1.71	0.18	$0.003^{+0.008}_{-0.008}$	19^{+8}_{-8}	7^{+8}_{-4}
MASSIV	20386743	1.05	9.62	1.60	0.33	$0.006^{+0.012}_{-0.012}$	14^{+6}_{-6}	22^{+10}_{-12}
MASSIV	20461235	1.03	10.10	0.98	0.49	$-0.059^{+0.012}_{-0.012}$	80^{+17}_{-17}	22^{+14}_{-14}
MASSIV	140083410	0.94	9.81	1.57	0.24	$-0.011^{+0.021}_{-0.021}$	16^{+11}_{-11}	29^{+16}_{-11}
MASSIV	140217425	0.98	10.58	2.30	1.12	$0.027^{+0.002}_{-0.002}$	203^{+23}_{-23}	66^{+35}_{-35}
MASSIV	140545062	1.04	10.34	1.36	0.36	$-0.027^{+0.006}_{-0.006}$	100^{+23}_{-23}	33^{+16}_{-14}
MASSIV	220014252	1.31	10.52	2.30	0.40	$0.016^{+0.004}_{-0.004}$	59^{+14}_{-14}	53^{+28}_{-28}
MASSIV	220015726	1.29	10.51	2.03	0.33	$0.000^{+0.010}_{-0.010}$	128^{+48}_{-48}	53^{+22}_{-22}
MASSIV	220376206	1.24	10.41	2.40	0.63	$0.024^{+0.011}_{-0.011}$	114^{+14}_{-14}	66^{+32}_{-31}
MASSIV	220397579	1.04	9.97	2.16	0.37	$-0.010^{+0.010}_{-0.010}$	21^{+5}_{-5}	37^{+16}_{-18}
MASSIV	220544103	1.40	10.45	2.07	0.67	$0.005^{+0.006}_{-0.006}$	97^{+28}_{-28}	33^{+19}_{-18}
MASSIV	220544394	1.01	10.08	1.70	0.42	$0.023^{+0.011}_{-0.011}$	78^{+19}_{-19}	28^{+17}_{-16}
MASSIV	220576226	1.02	10.05	1.82	0.27	$-0.006^{+0.005}_{-0.005}$	18^{+6}_{-6}	46^{+22}_{-21}
MASSIV	220578040	1.05	10.46	1.32	0.47	$0.002^{+0.007}_{-0.007}$	245^{+103}_{-103}	56^{+28}_{-26}
MASSIV	220584167	1.47	10.95	2.31	0.85	$-0.069^{+0.007}_{-0.007}$	207^{+42}_{-42}	42^{+18}_{-18}

MASSIV	910193711	1.56	9.73	2.30	0.27	$-0.019^{+0.014}_{-0.014}$	76^{+16}_{-16}	91^{+37}_{-27}
HiZELS	CFHT-NBJ-1709	0.81	10.70	0.93	0.27	$0.007^{+0.006}_{-0.006}$	125^{+33}_{-33}	10^{+6}_{-4}
HiZELS	CFHT-NBJ-1739	0.80	10.60	1.06	0.79	$-0.001^{+0.006}_{-0.006}$	257^{+51}_{-51}	43^{+23}_{-23}
HiZELS	CFHT-NBJ-1740	0.81	10.40	0.95	0.65	$0.016^{+0.005}_{-0.005}$	285^{+60}_{-60}	49^{+23}_{-23}
HiZELS	CFHT-NBJ-1745	0.82	9.80	0.75	0.54	$0.025^{+0.009}_{-0.009}$	264^{+47}_{-48}	58^{+26}_{-26}
HiZELS	CFHT-NBJ-1759	0.80	10.30	1.11	0.54	$-0.018^{+0.003}_{-0.003}$	302^{+44}_{-44}	15^{+9}_{-7}
HiZELS	CFHT-NBJ-1774	0.81	9.80	0.62	0.50	$0.013^{+0.006}_{-0.006}$	82^{+24}_{-24}	86^{+37}_{-32}
HiZELS	CFHT-NBJ-1787	0.81	10.60	1.08	0.85	$0.007^{+0.004}_{-0.004}$	303^{+27}_{-27}	22^{+10}_{-10}
HiZELS	CFHT-NBJ-1790	0.81	9.90	0.67	0.22	$0.032^{+0.006}_{-0.006}$	111^{+31}_{-31}	10^{+7}_{-4}
HiZELS	CFHT-NBJ-1795	0.81	9.80	0.81	0.39	$-0.063^{+0.010}_{-0.010}$	96^{+26}_{-26}	10^{+6}_{-4}
SHiZELS	HiZELS1	0.84	10.03	0.30	0.23	$-0.037^{+0.030}_{-0.058}$	100^{+26}_{-26}	57^{+23}_{-23}
SHiZELS	HiZELS7	1.46	9.81	0.90	0.43	$-0.019^{+0.019}_{-0.040}$	106^{+18}_{-18}	4^{+2}_{-1}
SHiZELS	HiZELS8	1.46	10.32	0.85	0.36	$0.006^{+0.017}_{-0.004}$	190^{+26}_{-26}	34^{+18}_{-18}
SHiZELS	HiZELS9	1.46	10.08	0.78	0.48	$-0.027^{+0.010}_{-0.018}$	151^{+46}_{-46}	59^{+29}_{-29}
SHiZELS	HiZELS10	1.45	9.42	1.00	0.27	$-0.031^{+0.016}_{-0.014}$	37^{+19}_{-19}	53^{+25}_{-25}
SHiZELS	HiZELS11	1.49	11.01	0.90	0.15	$-0.087^{+0.032}_{-0.006}$	311^{+42}_{-42}	109^{+39}_{-33}
MUSE-WIDE	G103012059	0.56	10.25	1.37	0.72	$-0.075^{+0.014}_{-0.017}$	223^{+40}_{-40}	43^{+18}_{-18}
MUSE-WIDE	G118011046	0.58	10.54	1.28	1.36	$-0.038^{+0.003}_{-0.003}$	275^{+29}_{-29}	37^{+15}_{-15}
MUSE-WIDE	G105002016	0.34	10.31	0.25	0.45	$-0.025^{+0.019}_{-0.014}$	141^{+11}_{-11}	64^{+14}_{-16}
MUSE-WIDE	G122003050	0.21	9.97	0.02	1.44	$-0.065^{+0.001}_{-0.001}$	169^{+37}_{-37}	43^{+6}_{-6}
MUSE-WIDE	G102021103	0.25	9.22	-0.68	0.78	$-0.024^{+0.024}_{-0.021}$	62^{+15}_{-15}	41^{+6}_{-6}
MUSE-WIDE	G105012048	0.68	10.39	1.07	0.92	$-0.044^{+0.006}_{-0.008}$	149^{+27}_{-27}	46^{+19}_{-19}
MUSE-WIDE	G104005033	0.40	8.64	-0.72	0.90	$0.047^{+0.021}_{-0.021}$	43^{+10}_{-10}	33^{+10}_{-10}
MUSE-WIDE	G107029135	0.74	9.75	0.84	0.50	$-0.144^{+0.024}_{-0.024}$	39^{+22}_{-22}	35^{+14}_{-14}

MUSE-WIDE	G101001006	0.31	8.64	-0.65	0.64	$-0.049^{+0.010}_{-0.011}$	61^{+28}_{-28}	31^{+5}_{-5}
MUSE-WIDE	G114007070	0.13	8.66	-1.50	1.46	$-0.131^{+0.080}_{-0.069}$	91^{+22}_{-22}	38^{+6}_{-6}
MUSE-WIDE	G108016127	0.21	8.50	-1.05	0.62	$-0.188^{+0.046}_{-0.061}$	62^{+19}_{-19}	46^{+13}_{-10}
MUSE-WIDE	HDFS3	0.56	9.75	1.39	1.34	$-0.032^{+0.002}_{-0.002}$	68^{+17}_{-17}	24^{+13}_{-13}
MUSE-WIDE	HDFS6	0.42	9.40	-0.02	0.60	$0.002^{+0.005}_{-0.006}$	37^{+12}_{-12}	33^{+10}_{-10}
MUSE-WIDE	HDFS7	0.46	9.49	0.19	0.73	$-0.133^{+0.007}_{-0.007}$	50^{+17}_{-17}	40^{+12}_{-12}
MUSE-WIDE	HDFS8	0.58	10.00	1.12	0.30	$-0.058^{+0.013}_{-0.014}$	69^{+21}_{-21}	53^{+27}_{-27}
MUSE-WIDE	HDFS9	0.56	9.49	0.96	0.42	$-0.124^{+0.009}_{-0.010}$	72^{+33}_{-33}	45^{+22}_{-22}
MUSE-WIDE	HDFS11	0.58	9.31	0.52	0.17	$-0.262^{+0.052}_{-0.028}$	8^{+15}_{-4}	21^{+9}_{-9}
MUSE-WIDE	UDF1	0.62	10.60	1.19	1.34	$-0.026^{+0.003}_{-0.003}$	131^{+13}_{-13}	34^{+15}_{-15}
MUSE-WIDE	UDF2	0.42	9.89	-0.07	0.58	$0.002^{+0.003}_{-0.003}$	119^{+12}_{-12}	50^{+4}_{-4}
MUSE-WIDE	UDF3	0.62	10.13	0.82	0.86	$-0.081^{+0.012}_{-0.013}$	75^{+25}_{-25}	45^{+22}_{-22}
MUSE-WIDE	UDF4	0.77	10.06	1.26	0.98	$-0.037^{+0.003}_{-0.003}$	47^{+19}_{-19}	37^{+16}_{-16}
MUSE-WIDE	UDF7	0.62	9.39	0.70	0.68	$-0.188^{+0.011}_{-0.010}$	10^{+5}_{-3}	27^{+13}_{-13}
MUSE-WIDE	UDF10	0.28	8.34	-0.81	0.64	$0.034^{+0.018}_{-0.017}$	50^{+16}_{-16}	39^{+22}_{-22}
SINS / zC-SINF	Q2343-BX389	2.17	10.61	1.76	0.74	$-0.048^{+0.032}_{-0.030}$	299^{+40}_{-21}	56^{+13}_{-15}
SINS / zC-SINF	Q2346-BX482	2.26	10.26	1.53	0.72	$0.007^{+0.039}_{-0.034}$	287^{+63}_{-30}	58^{+14}_{-15}
SINS / zC-SINF	Q2343-BX513	2.11	10.43	1.23	0.31	$-0.021^{+0.075}_{-0.075}$	102^{+64}_{-26}	55^{+24}_{-28}
SINS / zC-SINF	Q1623-BX599	2.33	10.75	1.73	0.29	$-0.036^{+0.037}_{-0.042}$	139^{+62}_{-36}	71^{+18}_{-27}
SINS / zC-SINF	Q2343-BX610	2.21	11.00	1.56	0.53	$-0.066^{+0.023}_{-0.020}$	241^{+62}_{-38}	64^{+17}_{-24}
SINS / zC-SINF	Deep3a-15504	2.38	11.04	1.73	0.72	$-0.026^{+0.013}_{-0.013}$	305^{+138}_{-80}	63^{+13}_{-15}
SINS / zC-SINF	Deep3a-6004	2.39	11.50	1.92	0.61	$-0.032^{+0.023}_{-0.028}$	362^{+109}_{-126}	55^{+11}_{-17}
SINS / zC-SINF	Deep3a-6397	1.51	11.08	1.63	0.69	$-0.041^{+0.011}_{-0.015}$	351^{+138}_{-107}	59^{+13}_{-17}
SINS / zC-SINF	ZC400528	2.39	11.04	1.69	0.29	$-0.009^{+0.045}_{-0.049}$	341^{+184}_{-89}	28^{+23}_{-15}

SINS / zC-SINF	ZC400569N	2.24	11.11	1.59	0.85	$-0.064^{+0.016}_{-0.014}$	364^{+138}_{-64}	43^{+16}_{-21}
SINS / zC-SINF	ZC400569	2.24	11.21	1.63	0.88	$-0.050^{+0.013}_{-0.014}$	312^{+19}_{-13}	41^{+23}_{-21}
SINS / zC-SINF	ZC403741	1.45	10.65	1.33	0.26	$-0.123^{+0.065}_{-0.081}$	189^{+73}_{-36}	36^{+13}_{-12}
SINS / zC-SINF	ZC406690	2.20	10.62	1.80	0.83	$-0.046^{+0.028}_{-0.027}$	313^{+88}_{-107}	60^{+16}_{-15}
SINS / zC-SINF	ZC407302	2.18	10.39	1.78	0.43	$-0.023^{+0.020}_{-0.020}$	217^{+71}_{-40}	56^{+11}_{-25}
SINS / zC-SINF	ZC407376S	2.17	10.14	1.51	0.19	$-0.021^{+0.071}_{-0.073}$	89^{+65}_{-45}	77^{+37}_{-41}
SINS / zC-SINF	ZC407376	2.17	10.40	1.65	0.65	$-0.048^{+0.044}_{-0.048}$	86^{+24}_{-20}	56^{+28}_{-27}
SINS / zC-SINF	ZC412369	2.03	10.34	1.62	0.36	$-0.047^{+0.050}_{-0.051}$	120^{+40}_{-27}	75^{+13}_{-27}

E.2   Effects of galaxy size

Galaxies evolve significantly in size in the range of redshifts we cover in this work (e.g., Mowla et al. 2019). Thus, size evolution could potentially explain some of the trends observed in the data that we compile. A common approach to take the galaxy size into account is to express the metallicity gradient as a value normalised to the effective half-light radius, *i.e.,* in units of $\mathrm{dex}\,\mathrm{r}_\mathrm{e}^{-1}$ (e.g., Belfiore et al. 2017), rather than an absolute gradient measured in $\mathrm{dex}\,\mathrm{kpc}^{-1}$. In this appendix, we study how our results change if we examine normalised rather than absolute gradients. For this purpose, we use the half-light radii reported by the source works we use to compile the observed data (see Table E.1). The model sits in the natural space of kpc as guided by the input self-similar galaxy evolution model (Krumholz et al. 2018), and does not provide an independent estimate of r_e as a function of galaxy mass. Thus we simply use the mean of the observed half-light radii for galaxies falling in each v_ϕ bin (see Figure 8.4) to obtain the model metallicity gradients in units of $\mathrm{dex}\,\mathrm{r}_\mathrm{e}^{-1}$. We caution that this approach limits our ability to make a fair comparison of the model with the data on metallicity gradients normalised by galaxy size, since we are using the measured effective radii directly in the comparison, rather than predicting them self-consistently.

Figure E.1 shows the same data and model as in the right panels of Figure 8.6 and Figure 8.8, but with the metallicity gradients expressed in the units of $\mathrm{dex}\,\mathrm{r}_\mathrm{e}^{-1}$. As expected based on the results in the main text, we find that the results do not significantly change even when the galaxy size is taken into account while studying the trends between metallicity gradients and gas kinematics.
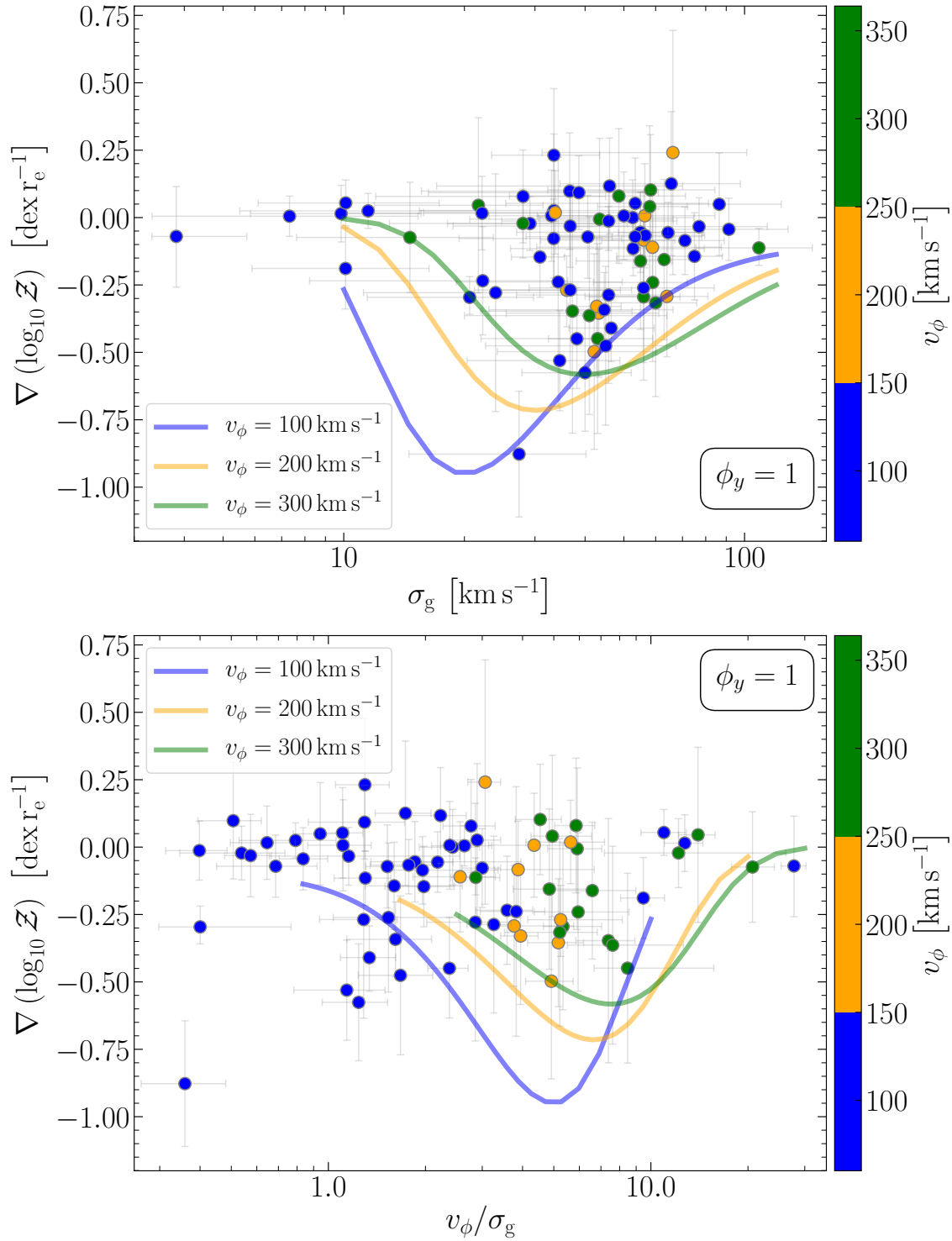
Figure E.1: *Left panel:* Same as the right panel of Figure 8.6, but now the metallicity gradients are normalized to the galaxy size and expressed in $\mathrm{dex\,r_e^{-1}}$. *Right panel:* Same as the right panel of Figure 8.8, but with metallicity gradients expressed in $\mathrm{dex\,r_e^{-1}}$.